Proceedings of the Second Eurasian Conference

NUCLEAR SCIENCE AND ITS APPLICATION

16-19 September 2002
Almaty, Republic of Kazakhstan

PRESENTATIONS

Volume I

"Nuclear energy: present status and perspectives; nuclear non-proliferation"

"Basic problems of nuclear physics"

Almaty - 2003

II Eurasian Conference on

NUCLEAR SCIENCE AND ITS APPLICATION

September 16-19, 2002, Almaty, Republic of Kazakhstan, *PRESENTATION,* Vol.I: "Nuclear energy: present status and perspectives; nuclear non-proliferation", "Basic problems of nuclear physics". - Almaty, Institute of Nuclear Physics NNC RK, 2003, – 526p.

ISBN 9965-9214-5-8

ISBN 9965-9214-5-8
© Institute of Nuclear Physics NNC RK, 2003

INTERNATIONAL ADVISORY BOARD

Chairman: V.S. Shkolnik (Kazakhstan)

K. Burns (IAEA)
M. Betti (European Commission)
E. Birol (Turkey)
M.E. Dzhakishev (Kazakhstan)
N.N. Gerasimenko (Russia)
W. Greiner (Germany)
K.A. Gridnev (Russia)
S.S. Hecker (USA)
E.M. Ibragimova (Uzbekistan)
R.I. Ilkaev (Russia)
B.I. Imanakunov (Kyrgyzstan)
Yu.A. Izrael (Russia)
V.G. Kadyshevskii (Russia)
I.B. Khaybullin (Russia)
A.A. Kist (Uzbekistan)
F.F. Komarov (Byelorussia)
M. Kroening (ISTC)
Sh. Kubono (Japan)
M.A. Kurbanov (Azerbaijan)
J.D.B. Lambert (USA)
R.S. Madatov (Azerbaijan)
I.I. Mustafaev (Azerbaijan)
A.D. Nikulin (Russia)
T.O. Orozobakov (Kyrgyzstan)
A. Özmen (Turkey)
R.J. Peterson (USA)
A.D. Pogrebnjak (Ukraine)
W. Potter (USA)
C. Rolfs (Germany)
U.S Salikhbaev (Uzbekistan)
K.M. Salikhov (Russia)
Zh.S. Takibaev (Kazakhstan)
H. Yavuz (Turkey)
T.M. Zhantikin (Kazakhstan)

ORGANIZATIONAL COMMITTEE

Chairman: Sh.T. Tukhvatulin (Kazakhstan)

V.M. Alekhina (Kyrgyzstan)
P. Arikan (Turkey)
F. Aykol (Turkey)
R.M. Bayazitov (Russia)
G. Buyan (Turkey)
S. Can (Turkey)
N. Cetinkaya (Turkey)
K.M. Donbaev (Kazakhstan)
A.D. Duysebaev (Kazakhstan)
V. Dzhazairov-Kakhramanov (Kazakhstan)
R.M. Fardarli (Azerbaijan)
A.M. Gasanov (Azerbaijan)
M.B. Halitligil (Turkey)
T.S. Koroleva (Kyrgyzstan)
T.A. Kozhamkulov (Kazakhstan)
T.A. Kuketaev (Kazakhstan)
V.I. Kukulin (Russia)
Sh.M. Makhkamov (Uzbekistan)
S. Mamatibraimov (Kyrgyzstan)
B.N. Mukashev (Kazakhstan)
T.M. Muminov (Uzbekistan)
K. Olimov (Uzbekistan)
O.S. Pivovarov (Kazakhstan)
V.S. Rusakov (Russia)
V.R. Rustamov (Azerbaijan)
B.A. Suleymanov (Azerbaijan)
A. Tanrikut (Turkey)
I.L. Tazhibayeva (Kazakhstan)
A.Zh. Tuleyushev (Kazakhstan)
Yu.S. Vasil'ev (Kazakhstan)
Zh.R. Zhotabaev (Kazakhstan)
R. Yarmukhamedov (Uzbekistan)
T.N. Kvochkina– Secretary (Kazakhstan)

COORDINATORS FROM THE COUNTRIES-ORGANIZERS

A.A. Garibov - Azerbaijan
K.K. Kadyrzhanov - Kazakhstan
I.A. Vasilev - Kyrgyzstan
N. Birsen - Turkey
B.S. Yuldashev - Uzbekistan

COUNTRIES CO-ORGANIZERS OF THE CONFERENCE

Azerbaijan, Kazakhstan, Kyrgyzstan, Turkey, Uzbekistan

CONFERENCE ORGANIZERS

Ministry of Energy and Mineral Resources
of the Republic of Kazakhstan (RK)

Atomic Energy Committee RK

National Nuclear Center RK

Institute of Nuclear Physics NNC RK

Nuclear Society RK

Engineering Academy RK

The Organizers would like to express their gratitude to the following organizations for their sponsorship and financial supports, through which this Conference was made possible:

Turkish Atomic Energy Authority (TAEK)

International Science and Technology Center (ISTC)

Islamic Development Bank (IDB)

NATO

Dear Colleagues!

On behalf of the Ministry of Energy and Mineral Resources of the Republic of Kazakhstan, International Advisory Board and the Organizational Committee I would like to welcome you at the Second Eurasia Conference "Nuclear Science and its Applications". The first conference was organized by the Turkish Atomic Energy Committee in cooperation with Azerbaijan, Kazakhstan, Kyrgyz Republic and Uzbekistan and took place in Izmir, Turkey.

The present Conference will cover a wide range of topics that are of great importance for the developing countries in Eurasia. The problems to be considered include present state and prospective of the nuclear power industry development, fundamental issues of nuclear physics and radiation solid state physics, regional problems of nuclear non-proliferation. Considerable attention at the Conference will be paid to the problems of radiation ecology and application of nuclear technologies in economy, medicine and agriculture.

I hope that with your help the Conference that hosted today the distinguished scientists and many leading specialists from 15 countries will be successful scientific forum stimulating further international cooperation and contacts, will give rise to more detailed and thorough investigations in the key fields of contemporary basic and applied nuclear physics, will help to expand its geography.

Let me express my best wishes to the participants of the Conference in their fruitful work, interesting scientific discussions and pleasant impressions on places of interest and cultural events in Almaty and vicinity.

Minister of Energy and Mineral
Resources RK V.S. Shkolnik

PREFACE

The Second Eurasian Conference on *Nuclear Science and its Application* was held from 16th to 19th September 2002 at Almaty, Republic of Kazakhstan (RK).

The Conference was organized by Ministry of Energy and Mineral Resources RK, Atomic Energy Committee RK, National Nuclear Center RK, Institute of Nuclear Physics NNC RK with joint efforts of Turkish Atomic Energy Authority, Academy of Science of Azerbaijan, National Academy of Science of Kyrgyzstan and Uzbekistan Academy of Science.

The scientific programme of the Conference was arranged in following areas:

- Nuclear energy: present status and perspectives
- Basic problems of nuclear physics
- Radiation solid - state physics
- Application of nuclear technologies in industry, medicine and agriculture
- Regional problems of nuclear non-proliferation.

Within framework of the Conference was held Advanced Research Workshop "*Environmental Protection Against Radioactive Pollution*"

These Proceedings is a collection of the invited talks at the plenary sessions, oral contributions given by the speakers at the parallel sessions and poster presentations.

During the meeting, the participants presented new interesting results and discussed widely future plans about exciting new prospects.

Around 270 scientists and experts from 16 countries took part in the Conference.

We would like to thank all participants for their attendance and contributions to the Conference. We are very grateful to all members of the International Advisory Board and Organizing Committee for their efforts to make this Conference successful.

Coordinators of the Conference

A.A.Garibov (Azerbaijan), K.K. Kadyrzhanov (Kazakhstan)
I.A. Vasilev (Kyrgyzstan), N. Birsen (Turkey), B.S. Yuldashev (Uzbekistan)

CONTENTS

Nuclear energy: present status and perspectives
Regional problems of nuclear non-proliferation

SAFETY REGULATION INFRASTRUCTURE OF PEACEFUL USE OF ATOMIC ENERGY IN THE REPUBLIC OF KAZAKHSTAN 11
Kim A., Yeligbayeva G., Zhantikin T.

THE DUTIES, THE RESPONSIBILITIES AND THE JURISDICTIONS OF TURKISH ATOMIC ENERGY AUTHORITY (TAEK) AND THE NEW PROJECTS THAT TAEK IS PRESENTLY INVOLVED 18
Öner Önder

INTERNATIONAL PROJECT ON INNOVATIVE NUCLEAR REACTORS AND FUEL CYCLE 28
Cherepnin Yu.S., Bezzubtsev V.S., Gabaraev B.A.

A SIMPLE APPROACH FOR PRE-LOCA ANALYSIS OF MTR TYPE RESEARCH REACTORS 33
Yılmazer A., Yavuz H.

ACTIVITIES ON METU –TWO PHASE FLOW TEST FACILITY 41
Yesın A.O.

AUTOMATED HYDROGEN AND İTS İSOTOPES MEASURİNG SYSTEM AT IVG.1M REACTOR 49
Chikhray Y., Shestakov V., Kulsartov T., Kenzhin E.

DETERMINISTIC AND PROBABILISTIC ANALYSIS OF PWR PRESSURE VESSEL INTEGRITY FOR DIFFERENT TRANSIENT CONDITIONS 59
Oya Özdere Gülol, Üner Çolak

DOSE ASSESSMENT AROUND YENIKOY COAL-FIRED POWER PLANT DUE TO MEASURED GROSS ALPHA RADIOACTIVITY LEVELS IN FLYING ASH OF THE PLANT 71
Tayfun Büke

ENVIRONMENTAL IMPACT OF NUCLEAR INDUSTRY AND POWER GENERATION IN THE RUSSIAN FEDERATION: ASSESSMENT OF CONTRIBUTION TO GENERAL ECOLOGICAL DAMAGE 78
Vetrov V. A.

EVALUATION OF CORE HEATUP IN CASE OF TOTAL LOSS OF POOL WATER OF TRIGA REACTORS 85
Tayfun Büke, Hasbi Yavuz

EXPERIMENTAL STUDY OF HEAT TRANSFER IN A THIN VERTICAL RECTANGULAR CHANNEL 91
Arikan İbrahim, Baykal Adnan, Adalioğlu Ulvi, Yavuz Hasbi

HEU-LEU MIXED CORE ANALYSIS FOR TR-2 97
Turgut Mehmet Hulusi

PUBLIC AWARENESS ON NUCLEAR ENERGY 105
Aykol Fethiye, Özkan Reşat, Atila Berrak, Hangül Gökhan, Aksu Levent M.

Basic problems of nuclear physics

CHARGED-PARTICLE TRANSFER REACTIONS AND NUCLEAR ASTROPHYSICS PROBLEM 111
Artemov S.V, Yarmukhamedov R., Yuldashev B.S. Burtebaev N., Duysebaev A.D., Kadyrzhanov K.K.

THRESHOLDS, CLUSTERS and ASTROPHYSICS 128
Peterson R..J.

A RESEARCH OF THE TWO-AVALANCHE EVENTS BY A METHOD OF AN IONIZATION CALORIMETER AND X-RAY FILMS AT THE ENERGIES $E>10^{13}$ EV. 135
Sadykov T. Kh.

A NOVEL APPROACH FOR THE COUPLING POTENTIAL IN COUPLED-CHANNELS FORMALISM 139
Boztosun I., Burtebayev N., Dzhazairov-Kakhramanov V.

ABOUT INVESTIGATION OF NUCLEAR REACTIONS WITH ION BEAMS CHANNELING AND COLLIDING INSIDE CRYSTAL 145
Takibayev N. Zh.

ABOUT LIMIT MASSES OF ELEMENTARY PARTICLES 151
Ibadova Umida and Safarova Zamira

ABOUT TOTAL KINETIC ENERGY DISTRIBUTION BETWEEN FRAGMENTS OF BINARY FISSION 159
Khugaev A.V., Koblik Yu.N., Pikul V.P., Ioannou P.,Dimovasili E.

ALPHA-PARTICLE STATES AND α-CONDENSATE IN NUCLEAR MATTER 163
Gnilozub I.A., Kurgalin S.D and Tchuvil'sky Yu.M

ANGULAR DEPENDENCE OF A TWO-PROTONS CORRELATION FUNCTION IN p+A AND d+A INTERACTIONS AT 3 AGeV 169
Afanasiev S.V., Anisimov Yu.S., Bondarev V.K., Driablov D.K., Isupov A.Yu., Ivanov V.I., Litvinenko A.G., Malakhov A.I., Migulina I.I., Penev V.N., Starikov A.Yu., Titov O.A.

DEFINITION OF THE MASS OF BOUND STATE 176
Dineykhan M., Baizhanova Zh., Jahanshir A., Sakhyev S.K.

DETERMINATION OF DYNAMICAL QUADRUPOLE DEFORMATION OF NUCLEI AT NUCLEAR CAPTURES OF HEAVY IONS 181
Khugaev A.V., Koblik Yu.N., Pikul V.P. Jovliev U., Nasirov A.K., Muminov A.I., Pavly K.V., Poliak Yu.V., Vdovkin P.O.

DIAGRAM METHODS IN NUCLEAR REACTION THEORY 190
Blokhintsev L.D.

DISPLAYING OF FORMATION OF ATOMIC CLUSTERS IN RADIOACTIVE LUTETIUM OXIDE FILMS 196
Kartashov V.M., Troitskaya A.G.

EFFECT OF PHOTON INTERACTION DEPTH IN THE DETERMINATION OF ABSOLUTE EFFICIENCY OF HPGe DETECTOR FOR LIQUID VOLUME SOUCE 202
Demirel H., Yücel H., Çetiner M.A. , Çetiner B., Yurtseven İ., Demircioğlu B., Karadeniz. H and Özmen A.

ELASTIC AND INELASTIC DIFFRACTION INTERACTIONS OF NUCLEONS AND LIGHT NUCLEI AT INTERMEDIATE AND HIGH ENERGIES 216
(Review of the theoretical results and experimental data)
Ismatov Ye.I., Kuterbekov K.A., Djuraev Sh.Kh., Esanniyazov Sh.F., Strigina S.B., Fazylov M.I.

ELASTIC NUCLEUS-NUCLEUS INTERACTION WITHIN THE DIFFRACTION THEORY OF MULTIPLE SCATTERING 235
Yuldashev B.S., Ismatov Ye.I., Kuterbekov K.A., Fazylova Z.F., Fazylov M.I.

ELASTIC SCATTERING OF PROTONS ON ^{8}Li NUCLEUS IN INVERSE KINEMATICS 244
Zhusupov M.A., Ibraeva E.T., Imambekov O., Sanfirova A.B.

ENERGY DEPENDENCE OF MACROSCOPIC AND SEMI-MICROSCOPIC POTENTIAL PARAMETERS FOR ALPHA-PARTICLES IN THE RANGE OF ENERGIES 20 - 80 MeV 250
Kuterbekov K.A., Zholdybayev T.K., Sadykov B.M., Mukhambetzhan A. Penionzhkevich Yu.E., Kukhtina I.N.

FROM STORAGE ION TRAP TO EFFECTIVE ACCUMULATOR-COLLAIDER OF ACCELERATED FUSIONING HYDROGEN NUCLEI 266
Tarantin N.I.

HIGH-EFFECTIVE POSITION-TIME SPECTROMETER IN ACTUAL MEASUREMENTS OF LOW INTENSITY REGIONS OF ELECTRON SPECTRA 267
Babenkov M.I., Zhdanov V.S.

HYDROGEN PLASMA ION SOURCE WITH SEPARATION OF IONS IN BEAM BY MASS COMPOSITION 273
Nazarenko L.M., Yakushev E.M., Stakhov O.V., Mit' A.G., Elengeev A.K., Alkozhaev N.

HYPOTHESIS OF FUNDAMENTAL MASS AND CONCRETE EXPERIMENTAL CONSEQUENCES AT ULTRAHIGH ENERGIES 277
Ibadov R.M.

INFLUENCE OF HIGHER ORDER ABERRATIONS ON THE RESOLUTION ABILITY OF MIRROR OBJECTIVE FREE FROM THE THIRD ORDER SPHERICAL ABERRATION 288
Bimurzaev S.B., Serikbaeva G.S. and Yakushev E.M.

INVESTIGATION of SPACE – TIME-OF-FLIGHT FOCUSING PROPERTIES of TWO –DIMENSIONAL ELECTRONIC MIRRORS with CURVILINEAR AXIAL TRAJECTORY 295
Bimurzaev S.B., Iskakova Z.D. andSarsenbaeva N.S.

INVESTIGATION OF PARTICLE CORRELATIONS BY THE METHOD OF DEFINITION OF RAPIDITY INTERVALS DENSITY IN INELASTIC COLLISIONS OF NUCLEI 305
Boos E.G., Izbasarov M., Zastrozhnova N.N.

MASS DEPENDENCE OF MACROSCOPIC AND SEMI-MICROSCOPIC POTENTIAL PARAMETERS FOR ALPHA-PARTICLES IN THE RANGE OF ENERGIES 20 - 80 MeV 309
Kuterbekov K.A., Zholdybayev T.K., Sadykov B.M., Mukhambetzhan A., Penionzhkevich Yu.E., Kukhtina I.N.

MASS SPECTROMETER WITH TWO ION SOURCES 326
Glickman L.G., Mit' A.G.

MAXIMAL HEAT LOADING OF THE ELECTROSTATIC DEFLECTOR'S SEPTUM AT THE CYCLOTRON 329
A. Arzumanov, A. Borissenko

MEASUREMENT OF ABSOLUTE GAMMA RAY EMISSION PROBABILITY OF 1001 keV FROM THE DECAY OF ^{234m}Pa 335
Çetiner B., Karadeniz H., Yücel H., Özgür İ., Çetiner M.A., Özmen A.

MEASUREMENT OF MASS DISTRIBUTIONS OF FISSION FRAGMENTS ^{235}U INDUCED BY THERMAL NEUTRONS IN ASYMMETRIC AREA 342
Jovliev U., Koblik Yu.N., Khugaev A.V., Muminov A.I., Nasirov A.K., Pavliy K.V., Pikul V.P., Polyak Yu.V.

MEASUREMENT OF THERMAL NEUTRON CROSS SECTION AND RESONANCE INTEGRAL FOR ^{139}La(n,γ)^{140}La REACTION BY ACTIVATION METHOD USING CADMIUM RATIOS 347
Yücel H., Karadağ M., Çetiner M.A., Tan M. and Özmen, A.

MEASUREMENT OF TIME STRUCTURE AND THE INTERNAL BEAM INTENSITY AT THE CYCLOTRON 362
Arzumanov A.,. Gorkovets M, Koptev V.

MEASUREMENTS OF GROUND, FIRST EXCITED-STATE ENERGY AND WIDTH OF ^{5}He VIA d-^{7}Li REACTION 367
Baykal Adnan, Tarcan Gökçe, Reyhancan Iskender Atilla and Erduran M. Nizamettin

MULTIPLE PRODUCTION OF PARTICLES IN ANTIPROTON - PROTON ANNIHILATION AT MOMENTUM 22.4 GeV/c 373
Boos E.G., Temiraliev T., Pokrovsky N.S., Samoilov V.V.

NEW DATA ON THE ANOMALOUSLY DELAYED PARTICLES IN CORE REGION OF THE ABOVE-THE-KNEE EXTENSIVE AIR SHOWERS 378
Antonova V.P., Chubenko A.P., Baigubekov A.S., Kryukov S.V., Kupchishin A.I., Oskomov V.V., Sadykov T.Ch., Shepetov A.L., Vildanova L.I., Zastrozhnova N.N.

ON THE PROPERTIES AND APPLICATIONS OF RELATIVISTIC DUFFIN-KEMMER-PETIAU EQUATION 385
Boztosun I. and Taskin F., Burtebayev N.

ON THE STRUCTURE OF THE HAMILTONIAN OF QCD STRING 401
Dineykhan M., Ashimov D.S., Jahanshir A., Sakhyev S.K.

PREDICTION OF CATASTROFE THEORY FOR HEAVY IONS COLLISION AT HIGH ENERGIES 410
Kuchin I.A.

PRODUCTION OF Pd-103 RADIONUCLIDE AT THE CYCLOTRON 417
Arzumanov A., Berger V., Gorodiskaya N., Knyazev A., Popov Yu.

PROMPT GAMMA-RAY NEUTRON ACTIVATION ANALYSIS (PGNAA) SYSTEM BY USING A 740 GBq ^{241}Am-Be NEUTRON SOURCE 422
Çetiner M.A., Yücel H., Demirbaş A., Demirel H., Bozkurt A., Turhan Ş. and Özmen A.

RADIAL AND LATITUDINAL GRADIENTS OF GALACTIC PROTONS 432
Kazkenov Ye.K., Aitmuhambetov A.A., Ashirov R.R.

RADIATION ASPECTS ON THE EARTH'S SURFACE DURING SOLAR FLARES 438
Mansurov K.Zh., Aitmuhambetov A.A.

REACTIONS OF MASSIVE NUCLEI FOR HEAVY AND SUPERHEAVY ELEMENTS 444
Fazio G., Giardina G., Lamberto A., Muminov A.I., Nasirov A.K., Yakhshiev U.T., Palamara R., Ruggeri R.

REGENERATION OF ENRICHED ^{98}Mo FROM WASTE ^{99m}Tc GENERATORS 455
Khujaev S., Mirzaeva N.A., Ashrapov U.T., Nushtaeva L.B., Berdieva M.

SEARCH OF CORRELATION BETWEEN A FLOW LOW ENERGY OF SPACE PARTICLES AND PERTURBATION IN TERRESTRIAL CRUST. 459
Babaev M.K., Baigubecov A.S., Martyanov I.S., Sadykov T.Kh., Zastrozhnova N.N.

SEARCH OF THE RESONANCE E_{55}^{+++} IN ANTIPROTON-PROTON INTERACTIONS AT THE MOMENTUM 22.4 GeV/c 463
Temiraliev T.

STATUS OF CYCLOTRON BASED RADIOISOTOPES PRODUCTION IN ALMATY 467
Arzumanov A., Berdinova N., Borisenko A., Chumikov G., Gorodisskaya N., Knyazev A., Koptev V., Popov Yu., Sychikov G., Zhetltov D.

STUDY OF FINAL STATE RESONANCE IN PHOTODESINTEGRATION REACTIONS 474
Takibayev N.Zh., Lennik S.G., Livetsova A.S.

THE QUARK BAG FORMFACTOR IN THE MODEL OF INDEPENDENT PARTICLES 481
Rasulov E.A.

THE H_N METHOD FOR SOLVING LINEAR TRANSPORT EQUATION: THEORY AND APPLICATIONS 487
Tezcan C., Kaşkaş A. and Güleçyüz M. Ç.

THE SIMPLE METHOD FOR ADAPT TIME SAMPLING OF THE ANALOG SIGNAL 496
Babaev M.K., Baigubecov A.S., Kalinin Yu.G., Martyanov I.S., Sadykov T.Kh., Zastrozhnova N.N.

THE STATIONARY GENERATOR OF THE TECHNETIUM - 99M 499
Ashrapov U.T., Khujaev S.

THE VIBRATIONAL STATES IN THE SKYRME MODEL 504
Abdulvagabova S.K.

UPGRADE OF THE GIBS SPECTROMETER AT THE NUCLOTRON ACCELERATOR FOR INVESTIGATION OF CHARGE EXCHANGE REACTIONS 510
Aksinenko V.D., Kondratiev V.P., Krasnov L.V., Lukstins J., Matyushin V.T., Nurgozhin N.N., Richvitsky V.S., Saitov I.S., Tyatyushkina O.Yu.

AUTHOR INDEX 516

Nuclear energy: present status and perspectives

Regional problems of nuclear non-proliferation

SAFETY REGULATION INFRASTRUCTURE OF PEACEFUL USE OF ATOMIC ENERGY IN THE REPUBLIC OF KAZAKHSTAN

A. Kim, G. Yeligbayeva, T. Zhantikin

Atomic Energy Committee of the Republic of Kazakhstan
Almaty, Kazakhstan

1. Introduction

The Republic of Kazakhstan one of the new independent countries of the former Soviet Union is located immediately to the south of Russian Federation and west of China. It encompasses over 2.7 million sq. km of land area and has a population of over 14 million. Before disintegration of the Soviet Union, Kazakhstan had no own legislative base in the field of atomic energy use and had no state bodies, called to execute the control at observance of security measures by atomic energy use. Since 1991, after getting of the sovereignty, Kazakhstan started developing of its own legislative and regulative system in this area. In accordance with the Decrees of President appropriate structures in Kazakhstan were created. They are: Atomic Energy Agency, as a main Supervising governmental body, National Nuclear Centre combining all nuclear related scientific institutes, and National Corporation of Atomic Energy and Industry Enterprises KATEP. On 14 February 1994 Kazakhstan joined the International Atomic Energy Agency.

The general purpose of activity in the field of atomic energy use in Kazakhstan is safely and effective ensuring safety of the present and future generations and environment protection from radioactive contamination both by normal and extraordinary situation and maintenance of nuclear weapon non-proliferation regime.

According to those tasks the Republic of Kazakhstan needs the effective system for the assurance and guarantees for protection of population and environment against the possible negative influence of atomic energy usage and system for the control of radioactive materials.

2. Factors, affecting on nuclear and radiation safety in Kazakhstan

The situation in the field of nuclear and radiation on a territory of the Republic of Kazakhstan is formed currently by the following main factors.

- *Activity of the enterprises of uranium mining and milling industry, including geological exploration of uranium*

As is known, the Kazakhstan takes one of the first places in the world on quantity of prospected uranium stocks (about 50 % of uranium stocks of former USSR). A long time (more than 40 years) development more than 20 deposits was

conducted. The enterprises of this industry branch are located practically on all territory of Kazakhstan. Ulba metallurgical plant in the East of the country produces nuclear fuel for NPP. At realization prospecting, and processing processes on uranium mining and milling enterprises were made radioactive waste, total weight which is about 220 million tones with activity 250 thousand Ci more.

- *Power and research reactors*

In Kazakhstan there are 5 nuclear installations, including one nuclear power plant BN-350 in Aktau-city, and four research nuclear reactors of the National Nuclear Centre. One of them is located in Almaty, and three of them are located in Kurchatov-city (on the territory of the former Semipalatinsk Test Site).

Potential radiation danger of nuclear installation exists directly only during their technological activity, in duration 30-40 years, i.e. less vital term of one human generation. After closing of nuclear reactors the direct danger disappears, but there is the special danger of a fulfilled nuclear fuel and a radioactive waste, formed for a time of operation of object.

At the present time NNP BN-350 reactor is shut down. The decommissioning procedure of this reactor has started pursuant to the Governmental Decree of 22 April 1999.

All research reactors operated currently.

- *Nuclear explosions*

As a result of conduction of nuclear explosions (about 500 atmospheric and underground explosions for military and peaceful purposes) on Semipalatinsk Test Site and other sites were formed the waste of low activity on a surface and average activity in cavities of explosions as a kind of melt mountain mass.

The volumes of the waste are evaluated as 12.3 million tonnes with activity of surface contamination of 11.6 thousand Ci and underground contamination 12.87 million Ci.

- *Activity of the enterprises of mining and milling of commercial minerals containing radioactive elements*

Number of Kazakhstan deposits of polimetalls, phosphors rare earth contains uranium, which at a production of ores is extracted together with main ores and, as a rule, is not divided and can be accumulated in concentrates, and more often leaves in tailing. On some coal deposits top of a part coal are also accompanied uranium. This coal will not be realised as a fuel, and is subject to radioactive waste management. During the study of the territory with oil deposits were find the areas with soil and industry equipment contamined by natural radionuclides Ra-226 and Th-232. Radioactive waste of this group makes 1.57 million tonnes with total activity of 520 Ci.

- *Use of radioisotopes in medicine, industry and scientific research*

In Kazakhstan in many branches of medicine, industry and scientific research use a kind of radiation sources. Every year about 100 thousand of sources with total activity up to 25,000 Ci are using. Annually 10 thousand of sources more set out for storage. The radionucleads types of sources are from H-3 to Am-241.

The solution of problems of nuclear and radiation safety of the population and waste safety is possible only at availability of the necessary legislative base and with system of the state regulation of radiation safety.

3. Legislative base

Before disintegration of the Soviet Union the documents, regulating safety of activity in given area in Kazakhstan, were the Norms of Radiation Safety NRB 76 / 87, Basic Sanitary Rules OSP- 72/ 87 and various departmental documents. State Committee on Safely Atomic Energy Use Supervision of USSR (Gosatomnadzor) executed the control in this field.

After getting of the sovereignty in 1991 to the Republic of Kazakhstan were begun and carried out till the present time work on the creation of legislative base in the field of atomic energy use and radioactive waste management based on main principles of International Basic Safety Standards. Thus experience in the field of the nuclear right of a number of advanced countries, such as Germany, Finland Russia, Ukraine was used.

At the present time in Kazakhstan there is the following legislation base in this field:

In 1997, April 14 the Law on Atomic Energy Use was adopted. The Act defines nuclear energy concepts, sets out a structure for the peaceful use of nuclear energy, the protection of public health and environment, the non-proliferation of nuclear weapons and nuclear and radiation safety. It authorizes the Government to designate those State Bodies, which regulate nuclear and radiation safety and the licensing of various types of nuclear activity. That is the basic Law in the nuclear legislation of the country.

In 1998, April 23 the second Law of the nuclear legislation of Kazakhstan was adopted. It is Law on Radiation Safety of Population. This Law aims to protect the population from adverse effects of lionizing radiation. It deals with the right of individuals in the context of such safety, the duties of users of lionizing radiation sources and the responsibilities of State bodies.

Others Laws of the Republic of Kazakhstan in this field are:

- on Sanitary-epidemiological Happiness of the Population;
- on Protection of the Environment;
- on Bowels and Bowels Use;
- on Licensing;

- on Social Protection of Citizens, affected by the nuclear tests at Semipalatinsk Test Site;

Others legislative acts in this field are
- The Decrees of the President, Decrees of Parliament and Government;
- Decrees about bodies of state management, regulation and inspections;
- System of the rules and norms of nuclear and radiation safety;
- System of state standards and rules;
- System of the documentation of ministerial regulation;

In addition 100 regulation documents more, including acts of Soviet Union and developed in Kazakhstan, as well as Norms of Radiation Safety NRB-99, developed and accepted in Russian Federation in 1999 used now, and Regulation for the Safe Transport of Radioactive Materials, which was elaborated on the base of IAEA Transport Regulation, 1996 Edition No. TS-R-1, and adopted in 1 March 1999.

Republic of Kazakhstan have signed and joined such international treaties and conventions as Treaty on the Non-Proliferation of Nuclear Weapons, Convention on Nuclear Safety, Joint Convention on the Safety of Spent Fuel Management and on the Safety of Radioactive Waste Management. Thus, Republic of Kazakhstan took obligation to execute the International requirements of safe atomic energy use.

4. System of state nuclear and radiation safety regulation

President, Parliament and Government of Kazakhstan, realizing the high national responsibility in discharging the functions took a decision to create a system of State radiation safety regulation.

Various State bodies are responsible for the following functions.

In accordance with the nuclear legislation of the country Atomic Energy Agency (since 1999 Atomic Energy Committee (KAEC)) is defined as Central regulatory body in the field of supervision for nuclear and radiation safety.

According to the provision on KAEC adopted by Governmental Decree of 23 September 2000 No.1442, it is responsible for:

- Realization of State Policy in the field of safely atomic energy use.
- State control of nuclear, radioactive and special non-nuclear materials, dual-use goods. Providing Regime of Non Proliferation Nuclear Weapons, nuclear and radiation Safety during the using of atomic energy.
- Export and import control of nuclear materials, technologies, equipment, special non-nuclear materials, dual-use goods and equipment, radioactive sources and isotope goods.
- Preparation of Annual reports connected with safety status of entities using atomic energy.

- Development of acts, regulations, standards, rules in the field of atomic energy use.
- Licensing all types of activities in the field of atomic energy use.
- Consideration and concordance of papers bottomed safety of nuclear installation during the all stages their life cycle.
- State account and control of nuclear materials and supervision for providing of physical protection during their storage, transport and use.
- Providing and Coordination of co-operation of Kazakhstan Institutions with IAEA and other International organizations in the field of atomic energy use.
- Emergency preparedness.
- Coordination and organization of research and scientific activity in the country and participation in the international co-operation in the field of atomic energy use.
- Preparation of proposals for upgrading and improvement of legislation of the Republic of Kazakhstan in the field of atomic energy use.
- Other functions.

The Ministry on Health of the Republic of Kazakhstan with its sanitary-epidemiology stations provides medical services necessary for the protection of the public and employees at risk. It is responsible in context of its competence for regulating and inspecting the manufacture, use, storage, transport of nuclear materials and radioactive sources. It also carries out the account all radioactive sources and gives the sanction to work with sources, renders the medical help to personal, which works with nuclear materials.

The Ministry of Environmental Protection is responsible for protection of the environment against radioactive contamination. It co-ordinates the work on study of a radiation situation in Kazakhstan and executes the State ecological examination of the projects.

Others Ministries and Departments of the Republic of Kazakhstan with their responsibility are.

Ministry of Energy and Mineral Resources is responsible for the co-ordination of all scientific activity in the field of atomic energy use. It also organizes the verification of the scientific soundness of technical projects.

The Ministry of Internal Affairs verifies the fire safety and physical protection standards of all facilities which use atomic energy or in which radioactive waste is managed.

The Agency on Emergency Situations is responsible for monitoring compliance with measures on the prevention of emergency situations and sets out measures to protect the public against radiation exposure in the event of such situation. The Department of Safety of Industry and Mines, within this Agency, is responsible for the regulating of industrial equipment.

All those State Bodies are the first level of the system of regulation.

The various national institutions carrying out the direct radiation control and measurements form the second level.

The institutes of the National Nuclear Centre of the Republic of Kazakhstan (Ministry of Energy and Mineral Resources) are controlling the radiation situation at the all territories of nuclear test sites and carried out the measurements of concentrations of radionuclides in soil and water here.

State enterprise "Hydromet" with its network (Ministry Environmental Protection) carried out control of global fall of the radioactive substances at the territory of the country.

Joint Stock Company "Volkovgeology" (Kazatomprom, Ministry of Energy and Mineral Resources) executes the radiation monitoring at the objects of uranium mining and milling.

The control of external irradiation dose and levels of radionuclides in soil, water, food and other products is also carried out by laboratories under the Ministry of Agriculture and different scientific laboratories and various research institutes of appropriate profile.

5. The system of nuclear material control in Kazakhstan

In 1993 Kazakhstan joined the Nuclear Weapon Non-Proliferation Treaty as a non-weapon state, in connection with which in 1994 a Safeguard Agreement was singed with IAEA. This Agreement was enforced in 1995 by Degree of the President f the republic. The state System for Accountancy of Nuclear Materials was developed: The accounting system includes the database operation for nuclear material of each key measurement points, the reporting to government body, annual checks of operability of the system by physical inventory. All the works on organization and account of nuclear materials are carried out within the frameworks of regulatory requirements developed by supervising body. Currently, all facilities are safeguarded under IAEA safeguarding standards, through IAEA inspections. Annually, IAEA verifies all nuclear materials at all Kazakhstan nuclear facilities. Now additional Protocol to this Agreement is being prepared for signature.

System for nuclear export and import control of the Republic meets recommendations of International organizations. The government reporting system discloses the existence of all nuclear material and its transfer intended for interaction through the export control system and the nuclear control accounting system. Principles of the System are defined in the Nuclear Export Control Law, and the mechanisms for implementation of the control are established din the set of the Governmental Decrees. The standard operating procedure is the primary means for regulating exports and determines the mechanism for the realization of export control policy. The nuclear materials export and import is conducted on the basis of license issued by special state body, and in case of transit via Kazakhstan – by

governmental permission. Recent decision of the Nuclear Suppliers Group to accept application of Kazakhstan to loin this group can be considered as an indication of correspondence of the state export control system to international standards.

A work is going on upgrading of a system for combating of illicit trafficking of nuclear and radioactive materials.

6. Conclusion

At the present time in Kazakhstan:

In the field of nuclear legislation the Laws on the Atomic Energy Use and on Radiation Safety of Population are elaborated with using of international experience in this area and adopted by Parliament of the Republic of Kazakhstan. National Regulation for the Safe Transport of Radioactive Materials was elaborated on the base of IAEA Transport Regulation, 1996 Edition No. TS-R-1, and adopted in 1999. The Law on Export Control established norms for state control of goods.

In the nuclear material control Kazakhstan has established a system for nuclear material accountancy and control. This system will strengthen state control of nuclear materials providing more effective work for safeguards and security of the materials in peaceful use of atomic energy in the country.

The State system, which includes the number of Ministries, Agencies and Committees of Kazakhstan, for the supervision and regulation in the field of nuclear and radiation safety, for safeguards and security of the materials was created. Atomic Energy Committee controlled all types of nuclear activity by means of licensing and inspection and inspections.

THE DUTIES, THE RESPONSIBILITIES AND THE JURISDICTIONS OF TURKISH ATOMIC ENERGY AUTHORITY (TAEK) AND THE NEW PROJECTS THAT TAEK IS PRESENTLY INVOLVED

ÖNER Önder

Turkish Atomic Energy Authority, Ankara, Turkey

Abstract

The TAEK, reporting to the Prime Minister, has the duty to determine the national policy and the related plans and programs for the peaceful use of nuclear energy for the benefit of Turkey. The TAEK consist of a President, three Vice Presidents, an Atomic Energy Commission, an Advisory Council, Specialized Departments and Divisions and Research and Training Centers.

At present TAEK is dealing with the following new projects:

1. The seismic safety and upgrading of TR-1 and TR-2 research reactors in the Cekmece Nuclear Research and Training Center in Istanbul.
2. The construction of a 500 kev linear electron accelerator in Saraykoy, Ankara.
3. The construction of a 30 Mev proton and 15 Mev deuteron accelerator (cyclotron type) in Saraykoy, Ankara.

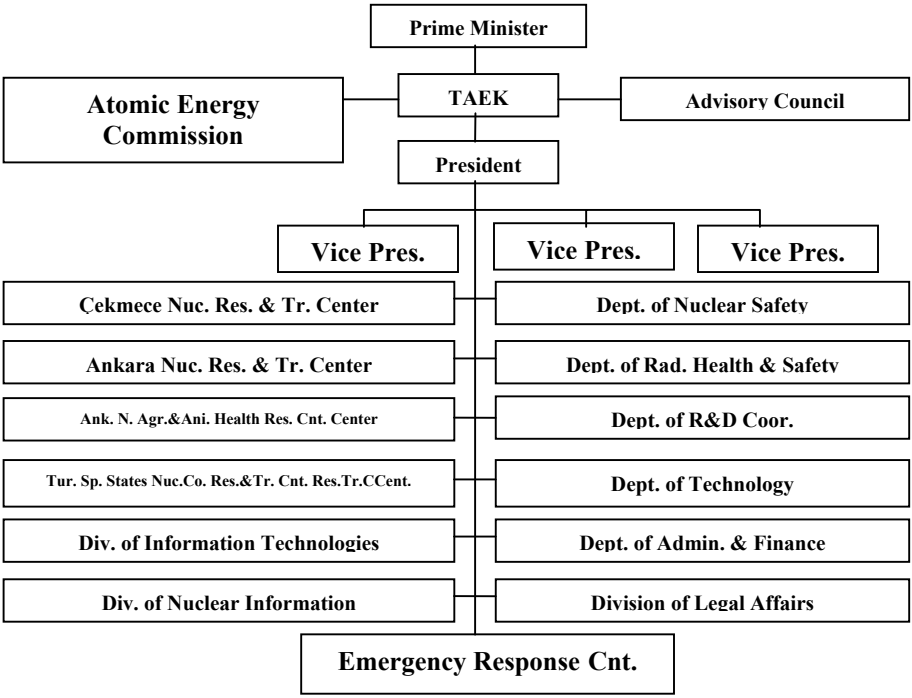
1. Historical Information about TAEK

Following the first Geneva conference in 1955 for expanding peaceful uses of nuclear energy, Turkey was one of the first countries to commence activities in the nuclear field. Turkish Atomic Energy Authority (TAEK) was established in 1956. Turkey was one of the founding member of the International Atomic Energy Agency (IAEA) when it is established in 1957. Turkey has signed the non-proliferation treaty and the comprehensive nuclear test ban treaty.

2. The Duties, the Responsibilities and the Jurisdictions of TAEK

- Act as a nuclear regulatory body,
- Carry out research and development in nuclear field,
- Support, promote and coordinate all nuclear activities in Turkey,
- Develop and implement regulations for physical protection, safeguards and illicit trafficking of nuclear materials,
- Establish cooperation with other countries and international organizations.

3. The General Administrative Structure of TAEK



3.1. The President's Office

President of TAEK: The President of TAEK assigned by and reported to the Prime Minister of Turkey. His assignment has to be approved by the President of Turkey. The President of TAEK ensures that the duties given to the TAEK by the Atomic Energy Authority Act are carried out within the principles and programs determined by the Atomic Energy Commission (AEC). The President represents and governs the TAEK and is his executive officer and the chairman of the AEC.
Vice Presidents of TAEK: There are three Vice Presidents assigned by the Prime Minister and approved by the President of Turkey. Their duties are to assist the president in his work. The Vice Presidents are the member of AEC.

3.2. Atomic Energy Commission

Structure: Chaired by the President of TAEK, consist of three Vice Presidents, one member each from Ministries of National Defense, Foreign Affairs, Energy and Natural Resources, and four faculty member active in education and research in the nuclear field. The members other than President and Vice Presidents of TAEK are assigned by the Prime Minister for four years term.

Duties:

- Determines the working principles and programs of TAEK,
- Prepares the draft acts and statutes related to the nuclear field,
- Follows and evaluates the work of TAEK,
- Prepares and submits the budget of TAEK to Prime Minister for approval.

3.3. Advisory Council

Structure: The Advisory Council consist of the faculty members teaching in the nuclear field, and the experts from other related institutions and organizations. The council members are appointed by the Prime Minister among the individuals proposed by the AEC. Local and foreign experts may be invited to the Council meetings for consultation.

Duties: The Advisory Council investigates the topics specified by the AEC and submit his conclusions and recommendations to the Chairman of the Commission.

3.4. Research Centers

3.4.1. Cekmece Nuclear Research and Training Center (CNAEM):

CNAEM was found in 1961 on the Coast of Kucukcekmece Lake near City of Istanbul and covers an area of 3200 acres. CNAEM mainly involved in various aspects of nuclear research, development and applications as well as the training activities. The first Turkish nuclear reactor TR-1 (1MW) was built at CNAEM in 1961. Later in 1981, due to the increasing demand in research and radioisotope production 5 MW TR-2 nuclear reactor was built.

These reactors were used for research and training and for the production of radioisotopes for medicine, agriculture and industry and for neutron activation analyses.

3.4.2. Ankara Nuclear Research and Training Center (ANAEM):

ANAEM was found in the Campus of University of Ankara in 1961. The main activities of this center are to carry out research in basic and applied fields using nuclear techniques and provide training in nuclear field. A linear electron accelerator and a proton and deuteron cyclotron will soon be built for this center for research, training and radioisotope production.

3.4.3. Ankara Nuclear Agriculture and Animal Health Research Center (ANTHAM):

Lalahan Animal Health Nuclear Research Institute was found in Ankara in 1981. This Institute was combined with the Agriculture Research Section of ANAEM to establish ANTHAM at Saraykoy near City of Ankara in 1999. The main activities of this Center is to carry out research in the field of agriculture, animal science, food preservation and sterilization using nuclear techniques and train the researchers working in other relevant institutes in Turkey.

3.4.4. Turkish Speaking States Nuclear Cooperation, Research and Training Center (TUDNAEM):

TAEK has started cooperating with nuclear institutes in Turkish Speaking Countries and signed protocols for cooperation in peaceful uses of nuclear energy in the late 1990's. As a result of this, a new Research and Training Center was found at TAEK Headquarters in Ankara for organizing the nuclear cooperation among Turkish Speaking Countries in 1999.

3.5. Departments

3.5.1. Nuclear Safety Department (NGD):

- Licensing and inspection of nuclear installations and other nuclear fuel cycle facilities,
- Provide measures for environmental safety of nuclear installations and other nuclear fuel cycle facilities,
- Provide measures for physical protection, safeguards and illicit trafficking of nuclear material,
- Provide measures for disposing of radioactive waste and spent fuel coming from nuclear installations and other nuclear fuel cycle facilities.

3.5.2. Radiological Health And Safety Department (RGD):

- Licensing and inspection of persons or organizations keeping, using, importing, exporting, transporting, storing and trading radioactive materials and radiation producing devices,
- Enforce insurance obligation for permitting above activities,
- Provide measures for disposing of radioactive waste coming from the use of radioactive material and radiation producing devices.

3.5.3. Research, Development & Coordination Department (AGK):

- In nuclear field, conduct or assist conducting training courses within the country and support students and TAEK personnel for training abroad,
- Distribute grants obtained from domestic or foreign sources for all kinds of studies in the nuclear field,
- International and public relations and translations.

3.5.4. Technology Department (TD):

- Investigate R&D on nuclear fuel, raw nuclear material and nuclear reactor systems not intended for power production,
- Perform duties related to quality assurance, economic analyses and industrial relations in the nuclear field.

3.5.5. Department of Administrative and Financial Affairs (IMID):

Perform the services related to personnel, general services, archives, construction, supply, budget, and accounting.

3.6. Divisions

3.6.1. Division of Information Technologies (BET)

Carries out and coordinates the following,

- Infrastructure development,
- System analysis and software development,
- e-Turkey integration,
- Internal and external WEB sites development

3.6.2. Division of Nuclear Information (NE)

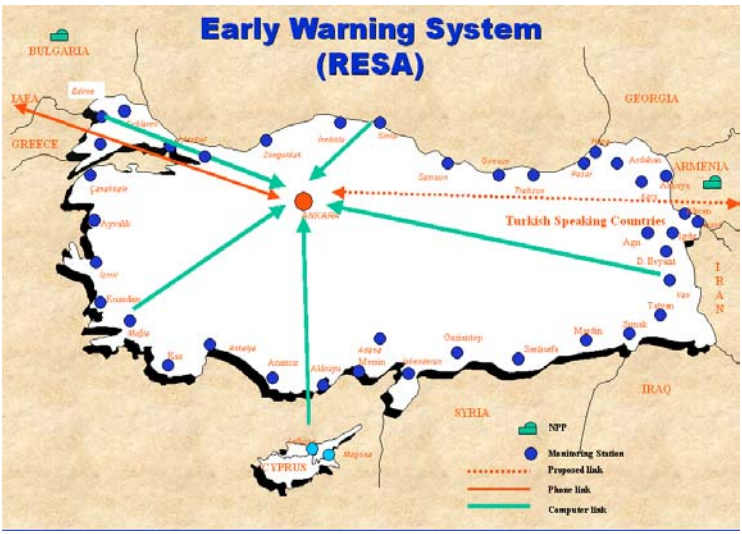
Provides nuclear data and publication to researchers through the INIS system of International Atomic Energy Agency.

3.6.3. Legal Affairs (HM)

- Deals with the ordinary legal problems of TAEK,
- Deals with the Nuclear Law related problems of TAEK,
- Deals with nuclear agreements and treaties.

3.7. Emergency Response Center

Turkey is initiated his own Environmental Radiation Monitoring System for early warning of nuclear emergencies (RESA). Over 60 radiation-monitoring stations have been installed at various locations through out Turkey and Cyprus. The monitoring locations have been selected by taking into account topographic and climatic characteristic of the region as well as the distance and locations of nuclear power plants in neighboring countries. The Emergency Response Center is located in TAEK headquarters in Ankara and has the computer links to monitoring stations and phone link to IAEA as shown in the following map.



4. New Projects

4.1. TR-1 and TR-2 Nuclear Research Reactors and their Seismic Safety Assessment and Upgrading

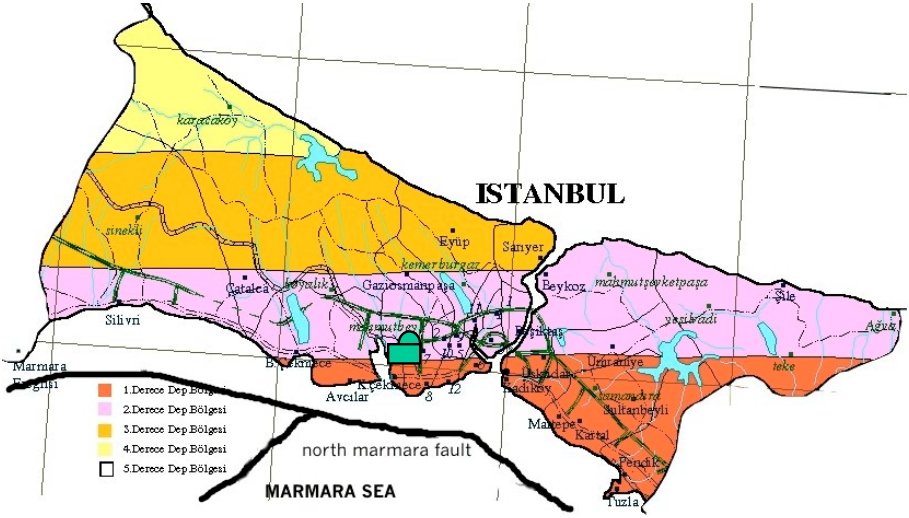
TR-1 Research Reactor: TR-1 is an open pool type of reactor with a nominal power of 1 MW. It was design and erected by American Machine and Foundry Company of USA between 1959 and 1961 in CNAEM in the Coast of Kucukcekmece Lake, 20 miles west of Istanbul City. The TR-1 reached its first criticality in January 1962. The reactor fuel is 93 % enriched uranium and it is light water moderated, cooled and reflected. The reactor is equipped with 6 radial beam tubes, one through tube and a thermal column. The TR-1 is located in the smaller part of the pool. It was used for radioisotope production, neutron beam experiments, in-core irradiation for neutron activation analysis and training. It was shut down in 1977 due to the installation of TR-2 reactor components.

TR-2 Research Reactor: During early 1970's, a power increase in TR-1 reactor was considered but later decided to build 5 MW TR-2 reactor in the larger part of the TR-1 pool. The TR-2 reactor is also open pool type with MTR fuel elements of 93 % and 19.9 % enriched uranium, reflected by beryllium blocks and moderated and cooled by light water. It was designed in 1974 jointly by engineers from CNAEM and from the Centre d'Etudes Nucléaries de Grenoble, France. The Belgonuclearie from Belgium was the main contractor for the supply of equipment and installation of reactor components. During the installation of TR-2, the pool is lined with a 3 mm stainless steel sheet for water tightness and building construction modified to maintain a certain level of air tightness. The TR-2 reactor reached its first criticality in December 1981. It is used for radioisotope production (mainly Tc-99 and Ir-192), in-core irradiation for neutron activation analysis and training. The TR-2 is shut down in 1995 for an extended period for the seismic evaluation and the necessary upgrading of TR-1 and TR-2 reactors' building and components.

The Assessment of the Seismic Safety: TR-1 and TR-2 reactors' common building was built between 1959 and 1961. At that time, a site-specific design bases earthquake was not considered in the design of the building. A devastating earthquake (magnitude of 7.4) occurred in Turkey at Eastern Marmara Sea on August 17, 1999. A few buildings were collapsed in Avcılar a district of City of Istanbul, where about 5 km away from TR-1 & TR-2 research reactors. The seismic instruments at the reactor-building basement and at the ground floor of another building at CNAEM site were recorded the peak acceleration values during this earthquake. They were 0.12 g and 0.18 g respectively. An inspection of the reactor building by experts after the earthquake showed that there was no damage on the reactor building, systems and components.

Considering the occurrence of a Review Level Earthquake (RLE) of similar magnitude as the one mentioned above in the north Marmara Sea fault line, where

is about 20 km south of the reactor site, a maximum ground level acceleration at the TR-1 & TR-2 reactors' building was calculated as 0.4g. Following is the earthquake-zoning map for Istanbul Province, also showing the north Marmara Sea fault line. The location of Reactors shown as green domed building.



Using this 0.4 g value, a finite element structural model of the reactor building was developed and a dynamic soil-structure interaction analysis was performed. The generic time histories, obtained from Turkish Seismic Design Response Spectra, were used to check the seismic capacity of the structure. The soil degradation that occurs during an earthquake was also considered in the analysis. A static analysis of a fixed–base model of the reactor building was also performed. The seismic safety of TR-1 and TR-2 reactors' building was evaluated using the results of both analyses.

Upgrading: The critical structural elements checked in the building against earthquake loads were reinforced concrete shear walls surrounding the building at the basement, the reinforced concrete frames in the superstructure and the infill brick walls,

The safe shutdown equipments and components and their anchorages or attachments are also analyzed under the effect of the RLE,

As a result of these analyses, an extensive upgrading on civil structures found necessary,

The upgrading needs for the equipment and components will be minimal,

The design work for upgrading of the civil structures and upgrading work for the equipment and components will soon be started.

4.2. The Construction of 500 kev and 20 mA Linear Electron Accelerator

The Accelerator: A 500 kev DC power linear electron accelerator has been purchased from Vivirad company in France through a grand obtained from an IAEA's technical cooperation program. We are waiting the design specification of the building, which will house the accelerator from Vivirad Company. As soon as the specification received, the building will be design and constructed in Saraykoy near city of Ankara. Following the completion of the building construction, the Company will install the accelerator.

Specifications:

- Maximum beam energy is 500 kev and changeable between 300-500kev.
- Maximum beam current is 20 mA and changeable between 1-20 mA.
- Maximum electron dose rate is 10^6 Gy/sec,
- Scans the electrons in a 61 cm path.

Proposed Use of the Accelerator:

- The electron radiation treatment of films and plastics produce cross-linking and polymerization in these organic materials, resulting improvement in their physical properties. For example, the molecular weight of bulk polymers can be tailored by depolymerization with electron beam,
- The treatment of coatings and adhesives on woods, metals and polymers with electron beam eliminates the need for chemical catalysts or solvent and therefore eliminates the pollution and occupational safety problems associated with corrosive or toxic agents. In addition, it also eliminate the need of heat treatment to save energy,
- The radiation treatment of rubber increases its strength,
- When an energetic electron beam pass through the water it produces very active chemical agents called free radicals. Then, these free radicals decompose the toxic organic compounds in wastewater and contaminated surface and groundwater to disinfect them,
- The free radicals are also produced from water vapor in flue gases coming out from coal and oil fired power plants when the effluent exposed by an electron beam. These free radicals, converted the SO_x and NO_x pollutants into sulfuric and nitric acid respectively. At this phase, if we inject ammonia to the effluent, these acids are neutralized by ammonia to form ammonium salts. These salts are solid materials and can easily be removed from the effluent. They can be used as fertilizer,
- The electron radiation treatment of surgical tool from top and bottom can sterilize the tools killing the bacteria, virus and other germs.

4.3. The Construction of a 30 Mev Proton & 15 Mev Deuteron Cyclotron

The Cyclotron: A bidding was called in July this year for the manufacturing, installation and testing of a cyclotron to accelerate protons to 30 Mev and deuterons to 15 Mev. The tender will include the construction of the buildings, which will house the cyclotron and its associated laboratories, and the supply of the laboratory equipments. It is expected that the civil construction will start next summer. The manufacturing, installation and testing of systems and components including civil construction will last 30 months.

The Proposed Use: The cyclotron will be used for the production of I-123, In-111, Ga-67, Tl-201, F-18, Rb-81 and Pd-103 radioisotopes. From these radioisotopes radio-pharmaceuticals will be produced in hot laboratories for medical applications. The cyclotron will also be used for the training and the scientific research.

Specifications:

- The cyclotron will be capable of accelerating both protons and deuterons,
- The beam energy will be variable and the maximum for protons will be 30 Mev and for deuterons 15 Mev,
- The total beam current for the protons will be 350 μA and deuterons 30μA,
- There will be two main beam port, each with switching magnet,
- Two beam line from each port will be obtained, having a total of four beam line,
- Three beam line will be used for radioisotopes production and one for training and research,
- There will be two hot laboratories for the production of radio-pharmaceuticals from Tl-201, In-111, Pd-103, Ga-67 and F-18,
- There will be two separate hot laboratories for the production of radio-pharmaceuticals from I-123 and Rb-81,
- There will be other labs for quality control and other activities.

References

1. Altınyollar, A. ,et al., Re-assessment of the seismic safety of TR-2 research reactor and dose calculations.60

INTERNATIONAL PROJECT ON INNOVATIVE NUCLEAR REACTORS AND FUEL CYCLE

Cherepnin Yu.S., Bezzubtsev V.S., Gabaraev B.A.

RDIPE named after N.A. Dollezhal, Ministry for Atomic Energy, Russia

Positive changes are taking place recently in the world nuclear power. In some leading countries electric power generation by NPP has grown, the rates of construction and completion of new power units are intensifying. Great efforts are made to improve safety of operating NPP, to use nuclear fuel efficiently, to solve the problems of spent fuel and radioactive waste. Meanwhile, there is a burst of activity in developing new reactor technologies to overcome the drawbacks of traditional nuclear power, i.e. insufficient safety, spent fuel and waste management problems, potential proliferation risks and low economic competitiveness compared to fossil fuel energy sources.

Enhancement of international cooperation in nuclear power should be mentioned among the most important events in this respect. Here, the following are noteworthy: International project implemented by three Agencies OECD\IEA, OECD\NEA, IAEA for comparative evaluation of new projects in nuclear power, development of Generation IV reactors undertaken by the USA in collaboration with some Western countries and, finally, the Initiative by the President of Russia V.V. Putin on combining efforts of interested Member States under the aegis of IAEA in considering the issues of energy supply of mankind sustainable development, including radical problem solving in nuclear weapons nonproliferation and environmental recovery of the Earth.

The 44-th session of IAEA General Conference in September, 2000, supported the Initiative by the RF President and appealed to all the Member States concerned to combine their efforts under the aegis of IAEA in the INPRO (International Project on Innovative Nuclear Reactors and Fuel Cycles) for considering and choosing the most acceptable nuclear technologies of the 21st century, making allowance for shortages of today's nuclear power.

The objectives of INPRO are as follows:

– to help to ensure that nuclear energy is available to contribute in fulfilling, in a sustainable manner, energy needs in the 21st century;

– to bring together all interested Member States, both technology holders and technology users, to consider jointly the international and national actions required to achieve desired innovations in nuclear

reactors and fuel cycles that use sound and economically competitive technology, and are based – to the extent possible – on systems with inherent safety features and minimize the risk of proliferation and the impact on the environment;

– to create a process that involves all relevant stake holders that will have an impact on, draw from, and complement both the activities of existing institutions and ongoing initiatives at national and international levels.

The necessary Organizational Structures have been set up at IAEA for implementation of the INPRO: Steering Committee comprising as officials from Member States of the Project; International Co-ordinating Group of Experts (ICG); Technical Expert Groups comprising experts from Member States.

Technical and administrative support of the Project is rendered by IAEA Secretariat directly. All the Project activities were subdivided into two Phases.

Phase I – elaboration of user requirements and selection of criteria for the comparison of different nuclear technologies. The work is carried out along the five subject groups:

- Resources, Demand, Economics;
- Safety;
- Spent Fuel and Waste;
- Resistance to Nuclear weapons Proliferation;
- Environment.

Let us point out the most essential current requirements to future nuclear technologies in line with each of the subject categories suggested.

Analysis of energy development scenarios in the next 100 years, of nuclear power role and place made in the project framework, suggests that nuclear power in the course of this century will remain the factor of secondary importance, while its share in the world energy mix may vary within 5-20%, depending on development scenario and region. Resumption of nuclear power development on the basis of open uranium fuel cycle will lead to full exhaustion of relatively cheap uranium raw materials resources by the end of the century. There is a need to

develop new fuel technologies on the basis of nuclear fuel conversion to overcome the shortage of resources.

Under today's conditions more enhanced requirements will be made to new projects in reference to Safety. The main requirement is a guarantee of health protection of the population residing near a nuclear power unit in case of occurrence of any accidents. Accidents at NPP resulting in radioactive material releases hazardous for life, shall be prevented largely by inherent safety means in the nuclear technologies used.

New nuclear technologies must produce as minimal as practicable amount of Radioactive Waste, providing for burning up and transmutation of actinides and long-lived fission products. It is advisable to envisage extraction of Sr and Cs from irradiated fuel along with some other fission products for their possible utilization as heat and radiation sources, as well as of J, Tc and, possibly other long-lived nuclides for their subsequent transmutation. Technology of innovative fuel regeneration shall assure RW decontamination from actinides, J, Tc, Sr, Cs to the extent that, after RW supervised cooling down in interim storages, will permit bringing RW long-term toxicity in the points of its final disposal to the level equivalent to radiotoxicity of uranium recovered from the bowels of the earth along with its radioactive decay products.

Today hazard of Nuclear Proliferation has become one of the main challenges. Accordingly, the relevant requirement to innovative nuclear power necessitates closing of nuclear weapons proliferation channels relating to nuclear power by gradual phasing out from nuclear power of technologies and processes aimed at uranium enrichment and plutonium extraction (and then ^{233}U, as well) from equilibrium composition fuel circulating in closed fuel cycle, and by assuring high radioactivity of fuel as a means of technological protection, which impedes its unauthorized use, first of all for its direct use in nuclear weapons.

Requirements for the Environment shall embrace all stages of nuclear activities from ore mining to waste disposal. Methods of uranium mining, permitting co-extraction of its long-lived decay products (^{230}Th, ^{226}Ra, ^{231}Pa), shall be developed for initial source materials recovery, if they promote easy remediation of the mining area. Operation of NPP and external fuel cycle processes shall not give rise to upsetting the composition, structure, functional arrangement of NPP natural environment (the state of ecosystems in the vicinity of NPP site). Normal operation of NPP shall provide radiation and toxic safety of ecosystems in the NPP location; radiation and toxic effects on all groups of residents in the region, which are not in excess of sanitary standards; the absence of intolerable response of the ground and water ecosystems of the region, impairing sanitary and hygienic living standards of population residing near NPP; the absence of chemical contamination of natural environment, which may give rise to contamination of atmospheric air, water and foodstuffs intolerable for people.

Formulation of requirements and criteria for assessing nuclear technologies is just a portion of the INPRO Phase I. The issue of elaborating a methodology for nuclear power innovative projects evaluations is no less important, which is the final aspect to be addressed at the Phase I. Comparative evaluation of technologies should be made relying on definite enough and clear rules. The methodology shall incorporate a variety of criteria on diverse approaches, therefore, a multi-criterion approach should be employed. The method of selecting shall also make allowance for national features regarding specific indices relating to the economics, safety, nuclear weapons non-proliferation, waste management and social sphere.

After completion of the INPRO Phase I, bearing in mind the recommendations made by the Steering Committee, the Phase II will be started by agreement with the countries involved in the Project.

At the Phase II the available innovative nuclear technologies will be subjected to project screening to reveal the ones, which can potentially be chosen for implementation by the Member States involved in the new International Project. At that Phase the Member States concerned will be able to assess the potentialities and drawbacks of diverse technologies of innovative reactors and fuel cycles to define the most promising technologies using the methodologies and criteria elaborated at the Phase I of the Project.

Actual activities in the INPRO began in January, 2001. The Member States involved in the Project appointed their representatives to the Steering Committee and several meetings of the Committee were carried out. International group of experts staffed by representatives of 13 countries of Europe, Asia and America was formed and started its work in Vienna in May, 2001.

By now the International group of experts in IAEA has already drawn up a draft of report on formulating basic user requirements and criteria for nuclear power innovative projects evaluation along all the subject group considered. Currently, the period of the report agreement by the Member States is underway. International conference in Vienna “Innovative Technologies for Nuclear Fuel Cycles and Nuclear Power”, scheduled for June, 2003, will be a culmination of the INPRO Phase I. Major results of the INPRO Phase I implementation will be presented in detail, the available nuclear technologies and technologies under development will be discussed.

In Russia particular significance is attached to the INPRO, hence, the relevant organizational structures for its actual support were set up in January, 2001 and a plan of measures was developed. In the middle of 2001 a special Decree by the RF Government was issued naming leading executors of the INPRO in Russia in the Minatom of the RF and RRC “Kurchatov Institute”. Specific lists of measures pertinent to participation and the tasks set for Russian institutions within the INPRO were formulated in the relevant orders by Minatom of the RF.

A Board of Directors of Russian research institutions headed by academician E.P. Velikhov, was set up for scientific and methodological support of

the INPRO activities. Heads of Russian research organizations attracted for the project activities became members of the Board. The main objectives of the Board of Directors are: making of recommendations on Russia position towards all aspects of the INPRO; consideration and review of research and technical results of the INPRO phases; scientific and methodological support of the INPRO; information-analytic and propagandistic support of the INPRO.

In subsequent phases of the INPRO Russia will present its innovative developments in reactor technologies. Currently they are: GT-MGR (module high-temperature gas reactor); BN-800 (fast neutron reactor with sodium coolant); BREST – fast neutron reactor with inherent safety. The BREST concept is considered to be the most revolutionary one. NPP with fast neutron reactors and on-site fuel cycle is among its distinctive features. Plutonium nitrides and non-enriched uranium will be used as nuclear fuel at the NPP mentioned. Lead at a temperature of 420°C - 540°C will serve as coolant. Self-provision with fuel after the initial loading, using on-site fuel cycle with simultaneous reprocessing of radioactive waste, is a unique feature of the NPP. The BREST technology meets largely the nuclear power user requirements which have been formulated in the INPRO, and even now, at the stage of design the pilot-demonstration facility, it arouses interest of specialists and potential users.

A SIMPLE APPROACH FOR PRE-LOCA ANALYSIS OF MTR TYPE RESEARCH REACTORS

[1]Yılmazer A., [2]Yavuz H.

[1]Turkish Atomic Energy Authority, Ankara,
[2]Istanbul Technical University, Nuclear Energy Institute, Turkey

Abstract

In this study, it is intended to analyze early phases of a protected loss of coolant accident (LOCA) for TR-2 Research Reactor at Istanbul, and to show the applicability of the presented model to the other similar types of research reactors. The transient situation since the time when coolant is beginning to be lost throughout one or more of the main coolant pipes which were supposed to be broken guillotine-like to the time when the core is totally uncovered is investigated.

The modeling of the problem was separated into two phases; in the first phase when the water level of the pool is being decreased in a pre-estimated time-dependent way calculated by using Modified Bernoulli Equation, the conservation equations are solved by a usual implicit finite difference algorithm. The later phase, when water level reaches to the top level of fuel plates and begins to decrease until the bottom of the core, needs some modifications to the approach used for the first phase. Because, the coolant channels among fuel plates are filled with air when the level goes below, and the fuel plates are being cooled by air above the water level. This complexity is resolved using a moving boundary approach in the numerical solution. A Lagrange type interpolation approximation for the derivatives along with interface conditions in the neighborhood of the air-water interface was imported to the numerical algorithm. The analysis is performed for a nominal channel.

1. Introduction

As a result of the work carried out worldwide aiming at the conversion of research reactors from HEU to LEU, remarkable effort has been spent on re-evaluation of the safety of the current research reactors. Most of the reports concerning safety assessments were published by IAEA in a special edition of 5 volumes [1]. An important part of safety assessment of research reactors is the safety calculations requiring the simulation of events belonging to the two wide categories of accidents; reactivity insertion accidents and loss of flow accidents.

It has been customary to consider two transient cases in the analysis of reactivity accidents; protected transients in which the reactor was not shut down by the scram signal and unprotected or self-limited transients in which the reactor was shut down by the scram signal. Unprotected reactivity transients have been matter of interest in the past [2] and recently [3,4] since they are determinant of the reactivity insertion limits for clad melting temperature. However, simulation of unprotected loss of flow transients for pool type research reactors is a rather new research interest [5,6].

The most important accident among the inventory of research reactors is the loss of coolant accident (LOCA). The former studies on LOCA were direct accident experiments during the years when first research reactors had been built. Spert experiments are of these kind of studies [7]. In 1980s, within the framework of IAEA supported reduced enrichment project for test and research reactors, a computer code (3D-AIRLOCA) was developed for MTR type reactors' LOCA analysis [8]. As another IAEA supported research project, 3D-AIRLOCA was adapted to THEAP-I computer code in Democritus Nuclear Research Centre, which could only be used in LOCA analysis of MTR type research reactors [9]. THEAP-I code was used for Turkish TR-2 Reactor and given results in conformity with the experiments [10].

Most of the work concerning LOCA of research reactors in the literature has been done for the latest phase of the accident where the core was totally uncovered and being cooled by natural circulation of air. Whereas, partial LOCA analysis could be especially important for high flux and power MTR type reactors when reactor core is partially covered with water [11]. There is a gap in the literature for the analysis of the phase until the core is totally uncovered. For our purpose, Turkish TR-2 Reactor is taken as an illustrative case. It is our aim to investigate the transient situation since the time when coolant is beginning to be lost throughout one or more of the main coolant pipes to the time when the core is totally uncovered.

2. Modeling

2.1. Loss of pool water

TR-2 Reactor is a 5 MW MTR type research reactor which is inside a partitioned pool along with dismantled TR-1 Reactor. Two primary cooling pipes of the reactors and one common diffuser pipe back to reactor pool penetrate pool wall. One or more of these three pipes is supposed to be broken guillotine-like at the outside of the pool wall (as a result of expected earthquake in Istanbul or a terrorist bombing, etc.). For the pipe under consideration, Extended Bernoulli Equation could be written throughout the streamline, which is from pool surface to the point where the pipe is broken outside the pool as

$$\int_1^4 \frac{\partial v}{\partial t} ds + \frac{P_4}{\rho_4} + \frac{v_4^2}{2} + g z_4 = \frac{P_1}{\rho_1} + \frac{v_1^2}{2} + g z_1 - \Delta P_t \tag{1}$$

where subscripts 1 and 4 denote respectively pool surface and break point, t is time, v is coolant velocity, P is pressure, ρ is density, g is gravity acceleration, z is altitude from pool base. The last term on the right hand side of the above equation is the total pressure drop along the streamline consisting of core pressure drop and pipe pressure drop

$$\Delta P_t = \Delta P_c + \Delta P_b \tag{2}$$

where each value is determined experimentally as a function of flow-rate [12]. Noticing

$P_4 = P_1 = P_{atm}$, $\rho_1 \cong \rho_4, v_1 \cong 0$ (reactor pool surface velocity is too low),

$g(z_1 - z_4) = h$

first term of the left hand side of equation (1) could be arranged as

$$\int_1^4 \frac{\partial v}{\partial t} ds = \int_1^2 \frac{\partial v}{\partial t} ds + \int_2^3 \frac{\partial v}{\partial t} ds + \int_3^4 \frac{\partial v}{\partial t} ds \cong \int_2^3 \frac{\partial v}{\partial t} ds + \int_3^4 \frac{\partial v}{\partial t} ds = L_c \frac{dv_c}{dt} + L \frac{dv_4}{dt} \tag{3}$$

where subscripts 2 and 3 denote respectively core inlet , core outlet, L_c is the height of the core, v_c is the mean water velocity in the core, L is the total length of the broken pipe, v_4 is the mean water velocity in the pipe. Inserting (3) into (1) we get

$$L_c \frac{dv_c}{dt} + L \frac{dv_4}{dt} + \frac{v_4^2}{2} = gh - \Delta P_t \tag{4}$$

Continuity of mass could be written as the equality of the flowrates along the core and the pipe as following

$$v_c A_c = v_4 A_4 \Rightarrow v_c = \frac{v_4 A_4}{A_c} \tag{5}$$

where A_c is the total flow area of the core and A_4 is the pipe cross sectional area.

Equation (4) could be arranged for v_4 using (5)

$$\left(L_c \cdot \frac{A_4}{A_c} + L\right) \frac{dv_4}{dt} + \frac{v_4^2}{2} = gh - \Delta P_t \tag{6}$$

In order to calculate mean water velocity in the core (v_c) and height of water level(h), non-linear equation(6) was solved together with equations (2) and (5) using below discretization in time

$$(L_c.\frac{A_4}{A_c}+L)\frac{v_4(t+\Delta t)-v(t)}{\Delta t}+\frac{v_4^2(t)}{2}=g.h(t)-\Delta P(t) \qquad (7)$$

with the initial condition *h(0)=initial level of the pool* and using an iterative method. As an example of results of the above calculations, change of the pool level and the mean water velocity in the core with time are given in Figure 1 and Figure 2 respectively.

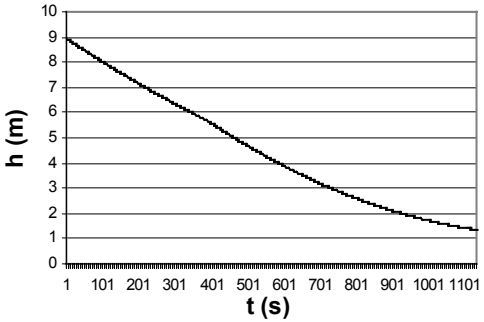


Figure 1. Variation of pool level with time for the case of break of the difussor pipe

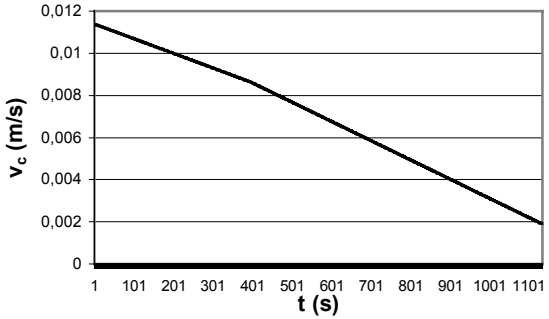


Figure 2. Variation of mean core water velocity with time for the case of break of the difussor pipe

2.2. Thermal-Hydraulics Model of Coolant Channels

Consider a typical pool-type research reactor with MTR-type fuel elements of rectangular geometry, cooled and moderated with light water. A one-dimensional core is considered, consisting of a coolant channel of width l_w and a fuel plate of width l_p. Incompressible slug flow of velocity v is assumed to take place on the plate surface through a heat transfer coefficient h.

The equations for local coolant temperatures T_b and fuel surface temperature T_w [13] are

$$q''(z,t) = \rho_p l_p C_p \frac{\partial T_w}{\partial t} + 2h(T_w(z,t) - T_b(z,t)) \qquad (8)$$

$$2h(T_w(z,t) - T_b(z,t)) = \rho \frac{W}{W'} l_w C_w \frac{\partial T_b}{\partial t} + \rho v \frac{W}{W'} l_w C_w \frac{\partial T_b}{\partial z} \qquad (9)$$

Where t is time, z is axial coordinate, $q''(z,t)$ is the local heat flux, ρ is density, c is specific heat, and the subscripts b and f denote respectively the coolant and the fuel.

2.3. Numerical Solution

Steady state calculations are performed for the above equations by taking time-derivative terms as zero and using a standard finite difference scheme. For this purpose, axial coolant channel is divided into 60 meshes.

First Phase

Postulated accident begins with the reactor's shut down by scram signal when one or more pipes are broken guillotine-like. In the first phase of the accident when the pool level is being decreased in a pre-estimated time-dependent way as calculated before, equations a usual implicit finite difference algorithm solves (8) and (9).

Second Phase

In the later phase, when water level reaches to the top level of fuel plates and begins to decrease until the bottom of the core, the coolant channels among fuel plates are filled with air and the fuel plates are being cooled by air above the water level (Figure 3). This complexity is resolved using a moving boundary approach in the numerical solution. A Lagrange type interpolation approximation for the derivatives along with interface conditions in the neighborhood of the air-water interface was imported to the numerical algorithm.

Using Lagrange Interpolation Formula, we get the spatial derivatives for airside ($z < s(t)$) at time $j\Delta t$

$$\frac{\partial T_a}{\partial z} = \frac{1}{\Delta z}\left(-\frac{p}{p+1}T_{i-1,j} - \frac{1-p}{p}T_{i,j} + \frac{1}{p(p+1)}T_B\right), \quad z = i\Delta z \tag{10}$$

$$\frac{\partial T_a}{\partial z} = \frac{1}{\Delta z}\left(\frac{p}{p+1}T_{i-1,j} - \frac{p+1}{p}T_{i,j} + \frac{(2p+1)}{p(p+1)}T_B\right), \quad z = s(t) \tag{11}$$

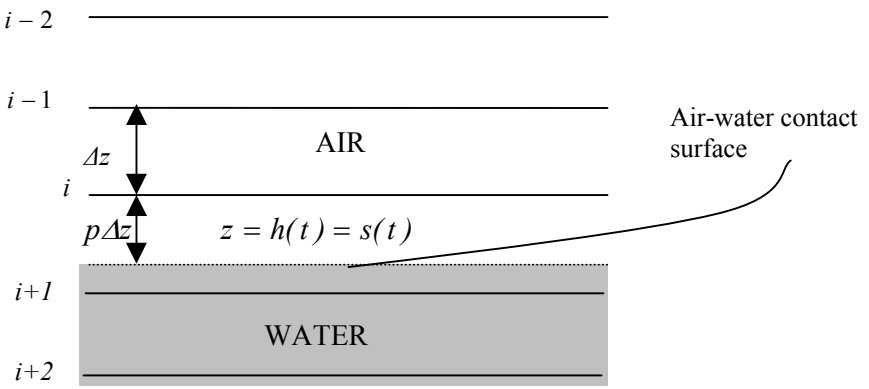


Figure 3. Discretization when water level falls between meshes *i* and *i+1*

Similarly for the water side $z > s(t)$

$$\frac{\partial T_b}{\partial z} = \frac{1}{\Delta z}\left(\frac{p}{p-1}T_{i+1,j} + \frac{1-p}{2-p}T_{i+2,j} - \frac{1}{(1-p)(2-p)}T_B\right), \quad z = (i+1)\Delta z \tag{12}$$

$$\frac{\partial T_b}{\partial z} = \frac{1}{\Delta z}\left(\frac{2p-3}{(1-p)(2-p)}T_B + \frac{2-p}{1-p}T_{i+1,j} - \frac{(1-p)}{(2-p)}T_{i+2,j}\right), \quad z = s(t) \tag{13}$$

For the meshes, which are not in the neighborhood of the interface a usual implicit finite difference scheme is used.

3. Results and conclusion

As an illustrative case of the results, the diffuser pipe is assumed broken guillotine-like at the exit of the pool wall. Calculation is based on taking initial pool water temperature and ambient air temperature as 35 ^{o}C and 30 ^{o}C respectively. Temperature distributions of coolant water and fuel surface temperature when the pool level is just on the top of the core which is the latest state of first phase are given in Figure 4. Figure 5 shows the temperature distributions of air and fuel surface as the latest state of the phase 2 when the water level is just below the core.

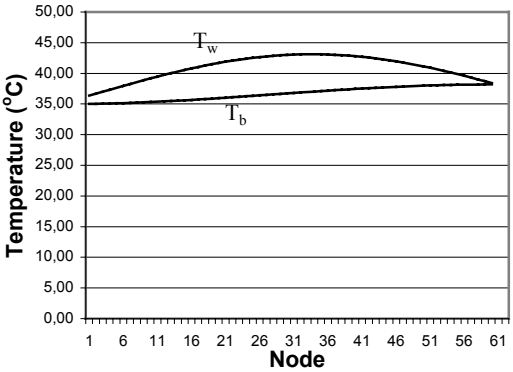


Figure 4. Temperature distributions of coolant water and the fuel surface when the pool level is just on the top the core

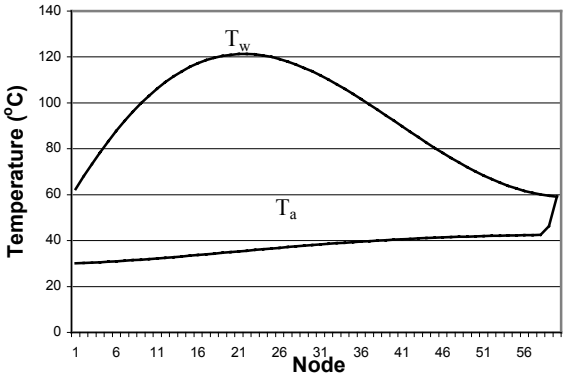


Figure 5. Temperature distributions of air and fuel surface when the water level is just below the core.

It could be observed from the Figures that a considerable increase in the fuel temperature as coolant water is replaced with the air when pool level falls. The considered model lets someone start with obtained data as an initial condition to analyze further stages of LOCA when the core is totally uncovered and the residual heat is removed via natural circulation of air.

Comparison of the predicted temperatures with experimental results is desired to evaluate the applicability of the model for analyzing the early phase of LOCA for MTR type research reactors.

References

1. IAEA, 1992. Research reactor core conversion guidebook, IAEA, Report IAEA-TECDOC-643.
2. Woodruff, W.L., 1984. A kinetics and thermal-hydraulics capability for the analysis of research reactors, Nuclear Technology 64, 196-206.
3. Mirza, A.M., Khanam, S., Mirza, N. M., 1998, Simulation of reactivity transients in current MTRs, Annals of Nuclear Energy 25, 1465-1484.
4. Nasir, R., Mirza, N. M., S. M., 1999. Sensitivity of reactivity insertion limits with respect to safety parameters in a typical MTR, Annals of Nuclear Energy 26, 1517-1535.
5. Housiadas, C., 2000, Simulation of loss-of-flow transients in research reactors, Annals of Nuclear Energy 27, 1683-1693.
6. Housiadas, C., 2002, Lumped parameters analysis of coupled kinetics and thermal-hydraulics for small reactors, Annals of Nuclear Energy 29, 1315-1325.
7. US Atomic Energy Commission, “National Reactor Testing Station”, 1962-1964, IDO-Reports of petroleum company.
8. Cheung, Y. K., Glower, J.P., 1982.,3D-AIRLOCA Loca Analysis Code for Research and Test Reactors, Transactions of American Nuclear Society 41, 655.
9. Bartzis, J.G., 1989, THEAP-I Micro-Computer Version, Democritus Nuclear Research Center.
10. Sevdik, B., Yavuz, H., 1998, Experimental measurement for plate temperatures of MTR fuel elements cooled in stagnant air and comparison with computed results, Kerntechnik 63, 267-272.
11. IAEA, 1980, Research Reactor Core Conversion From Highly Enriched Uranium to the use of Low Enriched Uranium Fuels Guidebook, International Atomic Energy Agency, Report IAEA-TECDOC-233.
12. ÇNAEM, 1997, Safety Analysis Report of TR-2, Çekmece Nuclear Research and Training Centre, Istanbul (In Turkish).
13. Klein, J., Mishima, K., TRANSV2: A Thermal Hydraulics Code for Research Reactors.

ACTIVITIES ON METU –TWO PHASE FLOW TEST FACILITY

Yesın A.O.

Ankara, Turkey

1. Introduction

A Joint Research Project Agreement was made between Atomic Energy of Canada Limited (AECL), Turkish Atomic Energy Authority (TAEK) and Middle East Technical University (METU). The objectives of this Joint Research Project are: to investigate the two-phase behavior of a scaled CANDU-6 Inlet Header under natural circulation conditions in order to provide experimental data to improve the understanding of Header behavior and to reduce the uncertainties associated with existing Header models used in the CATHENA system thermalhydraulic code; to construct an experimental two-phase flow test facility in the Mechanical Engineering Department of METU for supporting graduate level research activities in the Department ; and to increase the experience and knowledge of TAEK's staff on nuclear safety by direct involvement in safety related research activities.

In some postulated loss of coolant accidents in CANDU-6 reactor, two-phase (water-steam) conditions can appear in the cooling circuit and the ability of the coolant to remove heat from the fuel channel is influenced by how the Inlet Header distributes water and steam to the Feeders. Understanding of the Header's behavior is very important due to complexity of the phase distribution in this type of geometry. Void fraction and mass flow rate in the Feeders are two crucial parameters for determination of flow distribution. In addition unwanted flow oscillations and reversal may occur within the Feeders and their affects should be observed closely.

2. Description of the Test Facility

To investigate the Inlet Header behavior qualitatively and quantitatively Two-Phase Flow Test Facility (TPFTF) was constructed in the Mechanical Engineering Department of METU. The Test Facility is composed of a transparent and scaled CANDU-6 Inlet Header and 5 Feeders. Each Feeder is connected to the lower half of the Header. A globe valve is placed in each Feeder to obtain the required flow rate in the Feeders and to simulate the flow resistance. The other components of the Test Facility are: 100 lt water-storage tank, water-circulating pump of maximum 2 kg/s flow rate, air compressor of 10 bars maximum pressure, three air storage tanks, an air-water mixer. Water and air mixture is analogous to the postulated water and steam mixture in the CANDU Heat Transport System. The

Header and the Feeders are made of transparent PVC and acrylic (Figure 1). Distilled water is used in a closed circulation loop to prevent accumulation of lime within the component. The instant water and air flow rates are measured by a turbine flow meter and by an orificemeter, respectively. The volumetric flow rate values in air and water supply lines are used in arranging different void fractions at the Header inlet.

Two-phase (air-water) mixture fills the Header before entering the Feeders. The Header has a cylindrical shape with a diameter of 194 mm and length of 1200 mm. The Feeders are connected to the Header via flanges at different angles . Three of the Feeders have inlet diameters of 34.5 mm and two of them have 25.4 mm. There are 1 ¼" and 1" globe valves on larger and smaller Feeders, respectively, to adjust the fluid flow rate. In each Feeder, there is an impedance probe to measure the average void fraction within the Feeder.

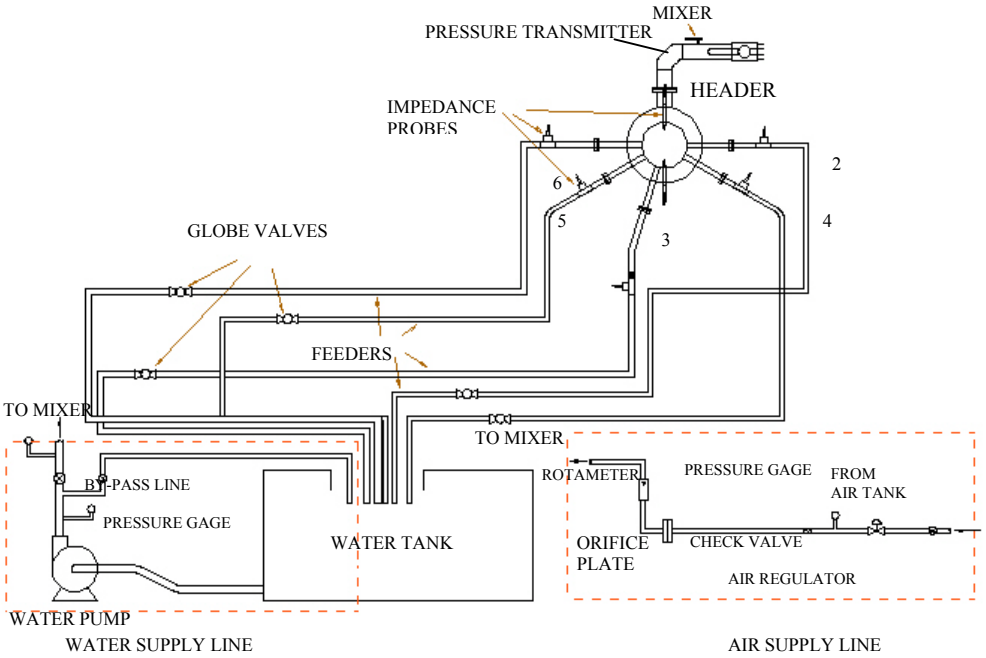


Fig.1 Side View of the Test Facility

The pressure difference between the upstream and downstream of the globe valves is measured by differential pressure transmitters to estimate the flow rate of the

water-air mixture. Pressure drop at different void fractions and at different valve openings are recorded and utilized in the quantification of the two-phase flow.
The outputs of all impedance probes, differential pressure transmitters, turbine flowmeter, air orificemeter and pressure transducers are converted to Volt signals and are supplied to the Data Acquisition System.

3. Two-phase Flow Rate Measurements

The mass flow rate measurements in the Feeders are performed with a differential pressure producer, namely a globe valve. The globe valves mounted on the TPFTF are manually operated, plug-type valve with T-pattern body. The fluid flow has to make some turns through the valve which causes a pressure drop. The pressure loss of two-phase flow in the globe valve is measured with a Differential Pressure Transmitter (DP transmitter) in the 0-100 psi (0 - 6.89 bars) range. This value is then related to valve opening and void fraction and is correlated to estimate the mass flow rate of two-phase flow in each Feeder. The required straight length of pipe is allowed at the upstream and downstream of the globe valve to provide a fully developed flow in the measuring section.

The results of the Two-phase flow rate measurements in a Feeder of 34.5 mm. inner diameter by using a 1 ¼ ” globe valve will be briefly presented [1] :

5 different void fractions (0%, 10%, 20%, 30%, 40%) and 7 different valve openings (10%, 17%, 23%, 36%, 49%, 62%, 100%) were studied. Due to three order of magnitude difference between densities of air and water, mass flow rate of water can be treated as the two-phase mass flow rate.

The calibration of the globe valve was accomplished by simultaneously recording the output signals of the DP transmitter and collecting the water passing through the valve. The collected water was weighed by an electronic balance with an accuracy of $\pm$ 20 g. The milliAmper output signals were converted to Volt signals of 1 V – 5V corresponding to minimum and maximum values before entering the data acquisition card.

4. The Effect of Valve Opening on Pressure Drop across The Globe Valve

The effect of valve opening was investigated by fixing the void fraction and changing the valve opening. As an example, in Figure 2 the relationship between the water flow rate and the pressure drop for 40 % void fraction is shown. It is seen that for a given mass flow rate, pressure drop increases as the valve opening decreases [1].

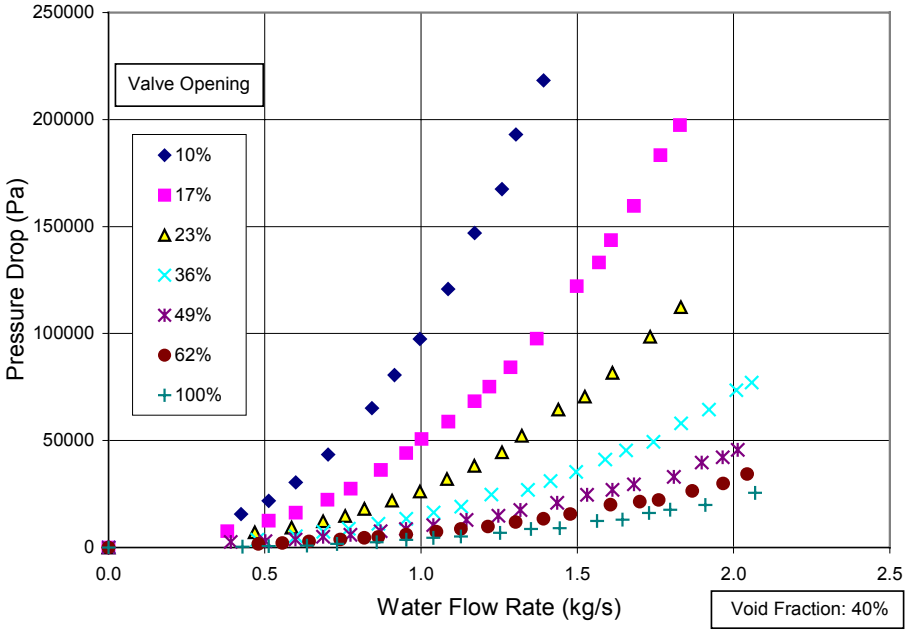


Fig. 2 The Effect of Valve Opening on Pressure Drop (Void Fraction: 40%)

5. The Effect of Void Fraction on Pressure Drop across The Globe Valve

Effect of void fraction was investigated by fixing the valve opening and changing the void fraction. As an example, in Figure 3 the relationship between the water flow rate and the pressure drop for 10 % valve openings is shown. It is seen that for a given mass flow rate, pressure drop increases as the void fraction increases[1].

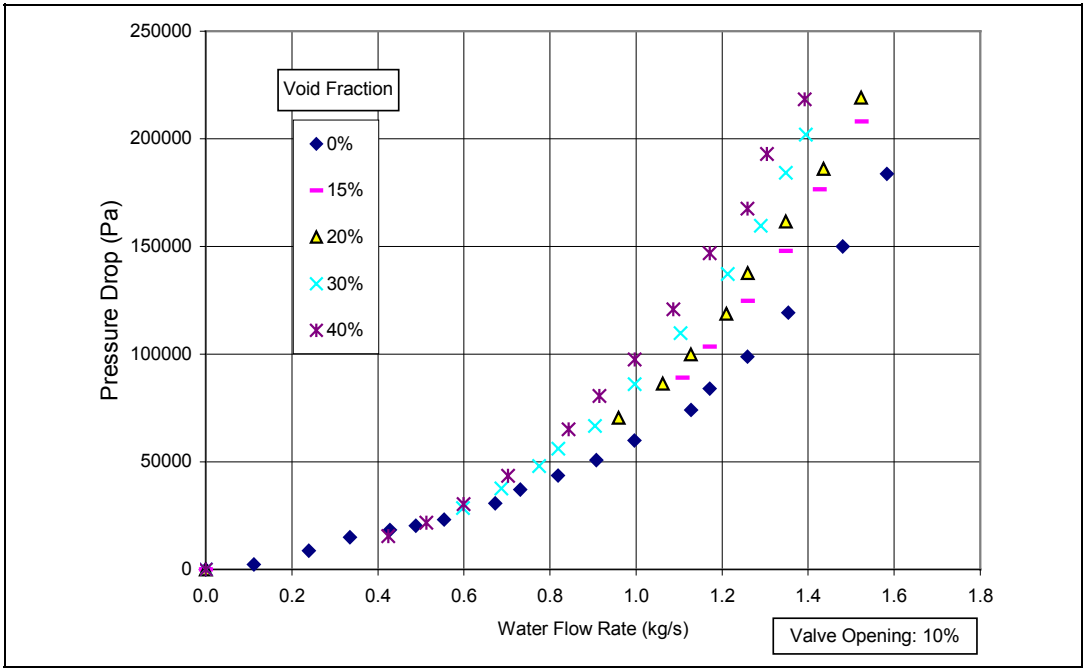


Fig. 3. The Effect of Void Fraction on Pressure Drop (Valve Opening: 10%)

6. Correlation of Two-phase Mass Flow Rate

Two-phase mass flow rate can be correlated in terms of three parameters: pressure drop across the globe valve ΔP, void fraction α and valve opening percentage N.

To correlate the results and to find an association between independent and dependent variables, Sigmaplot2001 software is utilized which can perform a multivariable nonlinear regression. The most suitable formulation is found by a trial and error procedure. Using this approach, two-phase mass flow rate can be correlated as follows:

$$\dot{m}_{tp} = \frac{0.0176 * \Delta P^{0.5059} - 1.136 * 10^{-5} * \Delta P - 0.0058}{5.0835 * (0.9477)^{N} + (1.0058)^{\alpha} + 0.0337} \qquad (1)$$

Equation 1 estimates mass flow rate in kg/s. The unit of pressure drop is Pascal. Void fraction and valve openings are defined as percentages, but they have to be entered into the equation by multiplying with 100. For example; if the void fraction or valve opening is 0.1 (i.e. 10 %), then it has to be entered as 10 into Equation 1.

The range of applicability of this correlation is: Pressure drop across the globe valve 0 -220 000 Pa, void fraction 0 – 40 %, valve opening 10 –100 % [1].

For Equation 1, the coefficient of determination (R^2) value is 0.982 which shows that the fit has a good agreement with the experimental data. Uncertainty analysis for this correlation indicates that ± 9% relative uncertainty occurs in the predictions of Equation 1.

7. Void Fraction Measurement by Impedance Probe Technique

The electrical impedance of a flowing fluid consists of resistive and capacitive components. Void fraction measurement in gas- liquid flow by impedance probe technique is based on the significant difference in the electrical properties between two phases such as resistance and capacitance. The excitation is assured by an AC voltage source to eliminate the polarisation effect and electrochemical attack. The excitation frequency which determines the resistive and capacitive characteristics of a measured impedance. When the excitation frequency is low enough especially under 1 MHz depending on the probe geometry, the impedance of the probe is resistive. Increasing the excitation frequency greater than 1MHz results in decreasing the value of resistance term and approaching the value of capacitive term to the resistive term depending on the probe's geometry. The existing probes on the TPFTF are of short single-ended configuration. Short single-ended probes are intended to be used for applications where it is necessary to make a real time measurement distinction between water and air. The probe consists of a stainless steel rod sheated by a Rulon insulator. Rulon material has a low friction coefficient and it is capable of performing under severe temperature (-240 to +278.8 ^{o}C) conditions. It has a high chemical resistance, low moisture absorption and a dielectric constant of about 2.5. The probe is inserted through the pipe wall by means of a Conax fitting. Wire leads are attached to the protruding end of the rod and to the fitting. These leads are connected to the measuring circuit. Probe configuration on the Feeders is shown in Figure 4. Probe tip is inserted inside the probe body with the distance of the half of the diameter. The impedance probes were placed at each Feeder at different inclination due to the position of the Feeder.

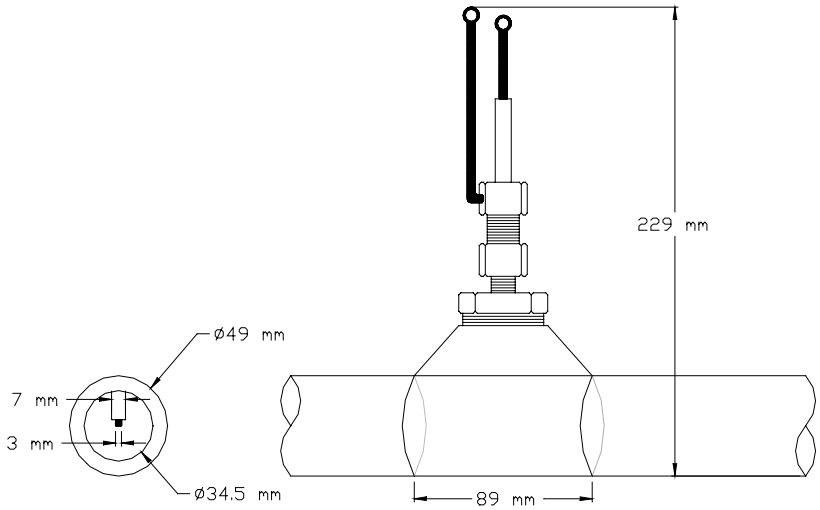


Fig. 4. Schematic view of impedance probe on the Feeders

8. Calibration of the Impedence Probe

Two-phase fluid temperature is found to have a strong effect on the measured impedance which causes a considerable shift in probe voltage output in all water medium. To eliminate the voltage shift due to the changes in fluid temperature, a non-dimensional probe output voltage may be defined in terms of the probe voltage outputs in all water (V_{OW}) and in all air(V_{OA}) media measured at the beginning of each experimental run [2].

$$\overline{V} = \frac{V_m - V_{OW}}{V_{OA} - V_{OW}} \qquad (2)$$

where V_m is the average of 300 instantaneous voltage outputs measured in 30 seconds. This sampling frequency is selected to obtain more reliable average values and to minimize the effect of two-phase flow regime.

During calibration process of an impedance probe the excitation frequency is selected as 500 Hz to minimize the water temperature effect on probe impedence. Calibration tests covered a range of water volume flow rate of 0 to 0.00183 m^3/s, air volume flow rate of 0 to 0.00185 m^3/s, water temperature of 21.2 to 25.6 ^oC, air temperature of 21.5 to 26 ^oC.

A curve fit is applied to the data relating the void fraction and non-dimensional probe voltage output. Calibration data and curve fit of a sample probe is shown in Figure 5 [2].

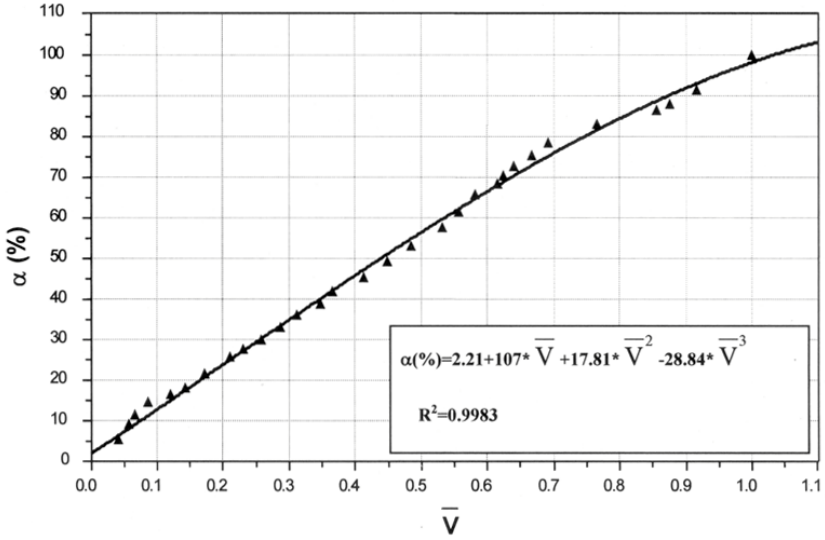


Fig.5. Calibration data and curve fit of a sample probe.

9. Acknowledgements

Mr.Mustafa Barış Kaya and Mr.Tufan Hosanoglu worked as researchers in the Joint Research Project and carried out the investigations related to the flow rate measurement and void fraction measurement in the TPFTF, respectively. Middle East Technical University, Turkish Atomic Energy Authority and Atomic Energy of Canada Limited are acknowledged for their generous sponsorship.

References

1. Mustafa Baris Kaya, "Flow Rate Measurements in A Two-Phase Flow System", M.S. Thesis, Mechanical Eng.Dept., Middle East Technical University, Ankara, September 2001.
2. Tufan Hosanoglu, "Void Fraction Measurement in A Two-Phase Flow System With Impedance Probe Technique", M.S. Thesis, Mechanical Eng.Dept., Middle East Technical University, Ankara, January 2002.

AUTOMATED HYDROGEN AND ITS ISOTOPES MEASURING SYSTEM AT IVG.1M REACTOR

Chikhray Y., Shestakov V., Kulsartov T.[1)], Kenzhin E.[2)]

[1)] SRIETP KazNU, Almaty, Kazakhstan
[2)]IAE NNC, Kurchatov, Kazakhstan

1. Abstract

For radiation studies of prospective materials for fusion application it is almost absolutely necessary to monitor hydrogen and its isotopes (deuterium and especially tritium) as well as theirs combinations (HD, D_2H, and so on) during irradiation experiment. As far as fusion reactions are based on tritium as fuel, insomuch it is important to monitor tritium behavior in examined materials. For example it is very crucial to know neutron irradiation performance of tritium breeding materials which are going to be used in fusion reactor blanket (such as lithium-containing ceramics and eutectics, beryllium, beryllides and so on).

Presented here hydrogen monitoring system is dedicated for real-time registration of hydrogen (and its isotopes) concentration changes within two volumes of experimental device during irradiative material testing experiment at IVG1M reactor of Kazakhstan National Nuclear Center.

2. System description: history of upgrades

Initially the hydrogen/tritium monitoring system at IVG1M reactor was designed for experimental studies of irradiation stimulated hydrogen permeation (diffusion) through some tested structural steels and alloys and was based on omegatron-type mass-analyzer IPDO-1 (Omegatron-type Indicator of Partial pressures).

At it is well known, omegatron mass-analyzer is of radio-frequency type. For omegatron it means that sweep parameter, which allows production of wide mass-spectrum, is its operating frequency. With our constant magnet IPDO-1 is capable to register masses from hydrogen to lower hydro carbonates with operating frequency range from 2.5 MHz downto 50 kHz. Initially such a system had provided only analogous registration of one gas (continuously) or up to 3-4 gases measurements (with manual set-up of respective omegatron operating frequencies).

Due to consideration of measurement accuracy and according to geometry of experiment the omegatron probe with electrometer for mass-spectrum signal amplification should be located as close as possible to attached experimental volume that is under irradiation and which gaseous content is under monitoring. At IVG1M reactor that minimal distance is about 3 meters with use of flexible metal-reinforced vacuum hose. Omegatron and electrometer are located at reactor upper

cover plate (premise 200), nearby the experimental channel where experimental device with tested material is installed (see Figure 1). At the same time the distance between omegatron and measurement control room (premise 203), where the source of omegatron operating frequency, voltmeter (or ADC) and computer are located, is much longer (about 30 meters)

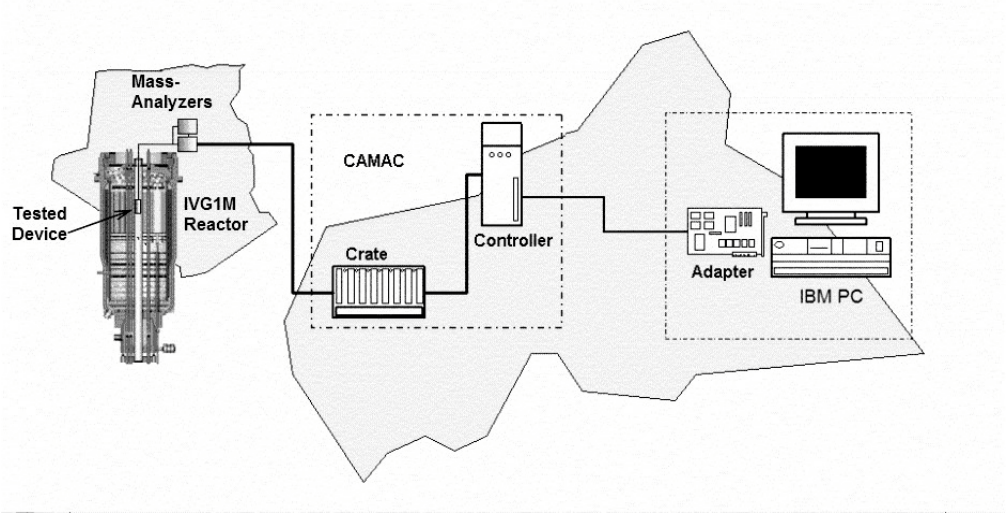


Figure 1. Outline of hydrogen monitoring system at IVG1M reactor

Historically the first upgrade of legacy measuring system had consisted in replacing of original source of IPDO-1 spectrometer's operating frequency (LC-oscillator mechanically controlled with variable capacity C) with digitally controlled frequency synthesizer with the same frequency range. As it is known, PLL-synthesizer (Phase Locked Loop) could provide quantized values of frequency with its excellent stability within very wide range while its quantum (step) is sufficiently small. We designed such a synthesizer in CAMAC standard (Computer Application for Measurements And Control) with purpose to provide fast and reliable 16-bit control over omegatron operating frequency. To digitize analogue signal from omegatron probe electrometer a 20-bit delta-sigma CAMAC Analog-to-Digital Converter (ADC) was used. Then a standard IBM PC was used to communicate with those two CAMAC-modules located in CAMAC crate through PC adapter – CAMAC crate-controller link. At last that hardware was supplemented with appropriate software so allowing registration of wide mass-spectrum of gases in studied volume and time log of any number of pre-selected masses as well (hydrogen/deuterium/tritium, for example). In that way the first variant of automated hydrogen monitoring system was created (refer to simplified outline at Figure 1). Figure 2 presents the example of mass-spectrum registered with that system during technological pup-out of experimental device installed in

experimental channel while content of hydro-carbonate and water is being controlled.

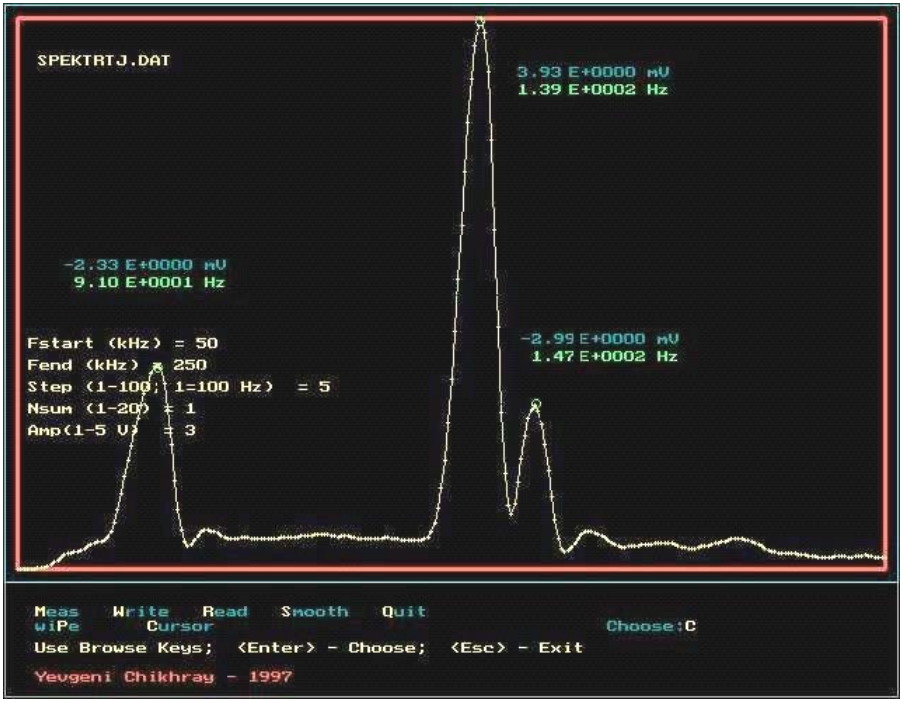


Figure 2. An example of omegatron mass-spectrum from studied chamber in reactor channel registered during technological annealing (frequency window from 50 to 250 kHz). Residual peaks of hydrocarbon and water triplet (bigger one) are present

Further modernization of monitoring system was directed on extension of its measurement capabilities with addition of second mass-analyzer. This upgrade was motivated by necessity to control chemical composition of atmosphere in two operational volumes of experimental installation (in inlet and outlet sides, for example) during the same irradiation experiment. Such a capability is especially important for comparative experiments with two materials and for experiments on evaluation of diffusion parameters (with method of hydrogen permeation, for example). Therefore the second mass-analyzer MX6407-P (for light masses only) was introduced to installation.

MX6407-P is another type of radio-frequency spectrometer. The main difference of this kind of mass-spectrometers from omegatron-type one is that its sweep parameter is deflection voltage while operating frequency remains stable.

Beside that this variant of mass-analyzer has some specifics because it was designed for operating in descent module of space vehicle to Venus for relatively short life-time. Due to that restriction and to limitation on weigh and size it was supplied only with very simple means to provide it operability. It was a very all-sufficient system that starts continuous scanning of mass-spectrum spectrum of light masses (2-6) after it's turned on without any possibility to control it or even to stop it. Therefore some modifications were needed to provide computer control over this spectrometer. Our analysis of its electronics had showed that easiest way to provide its controllability was to replace its original blocking-oscillator of deflection voltage with digitally controlled source.

Figure 3 shows principal scheme of such high-voltage DAC (digital-to-analog converter) which provides negative voltage for ion beam deflection within 30-300V range with 0.3V step and excellent stability. In contrast to omegatron spectrometer, where high stability of operating frequency was provided with frequency synthesizer, the stability of original MX6407-P source of operating frequency still remains insufficient. So we cannot be sure about the position of peaks in its mass-spectrum versus deflection voltage and therefore the simplest solution is to register full spectrum of light masses at each measurement point and to seek peaks later (if it drifts). Figure 4 shows exemplary 3D-view of time evolution of MX6407-P spectrum from Lithium-Led eutectics under neutron irradiation. There are three peaks (masses) from left to the right: hydrogen H_2, HT, and tritium T_2. Time axis is "directed" from front to background.

Finally additional CAMAC modules were introduced to electronic equipment: one for digital control of this high-voltage DAC and second (relay multiplexer) for switching outputs of both mass-analyzers to one ADC input. Also the software for such control and measurement was revised and updated respectively. That is the current state of hydrogen-tritium monitoring system at IVG1M reactor now. Its main technical parameters are given below.

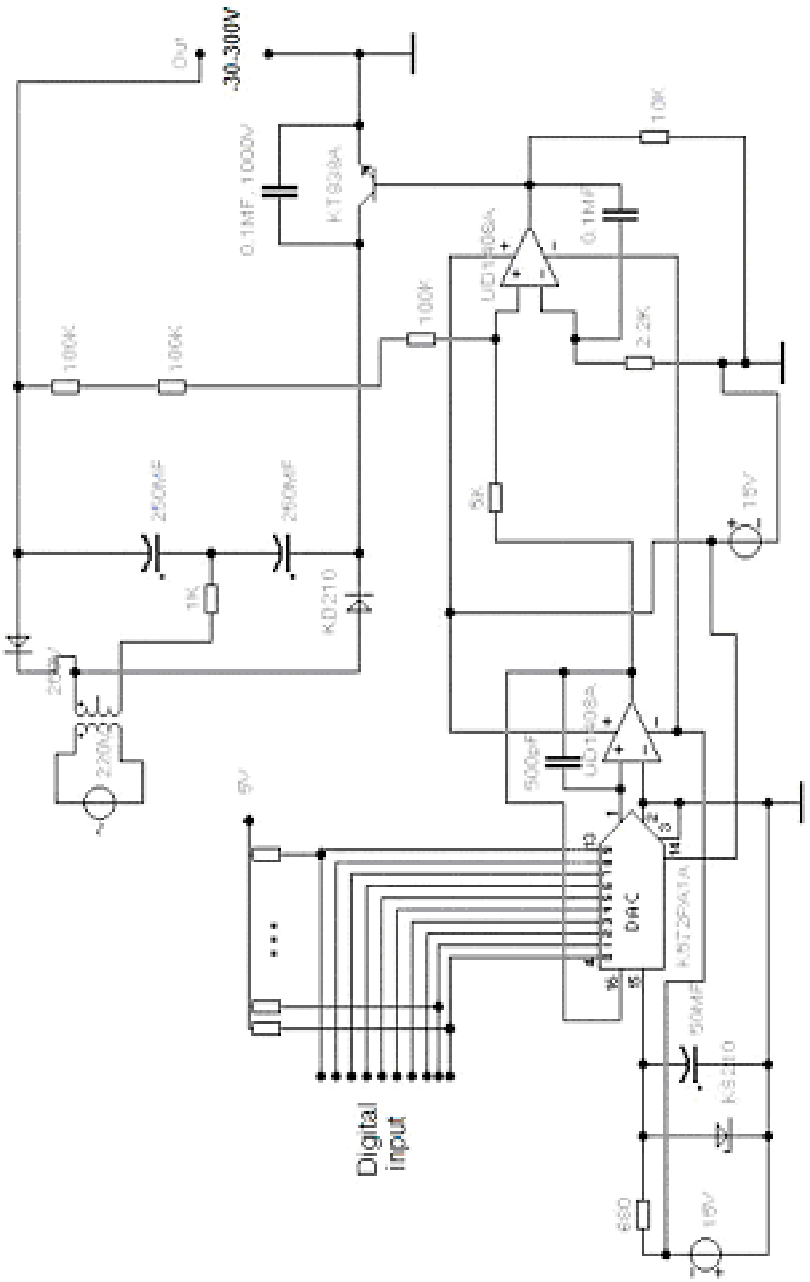


Figure 3. High-voltage DAC for MX6407-P mass-analyzer.

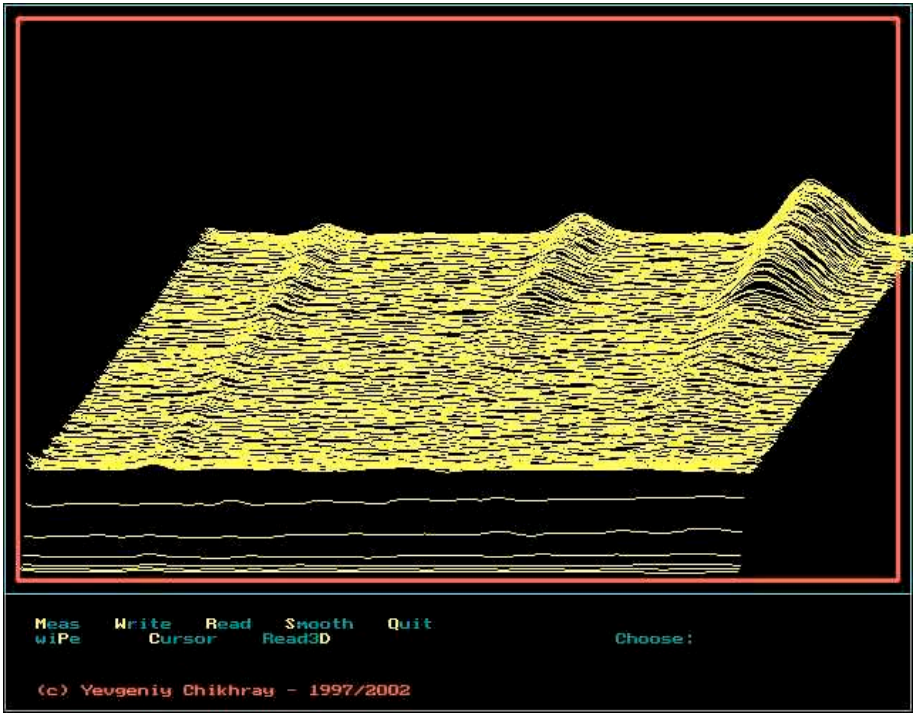


Figure 4. An exemplary 3D-view of time evolution of MX6407-P spectrum from Lithium-Led eutectics under neutron irradiation (penetration through MANET steel). Increase of peaks is caused by increase of neutron flux.

3. System Content and Parameters

System consists of:

- Radio-frequency probe of omegatron mass-spectrometer (IPDO-1);
- Electrometric amplifier of omegatron probe signal;
- CAMAC PLL-synthesizer of omegatron operating frequency;
- Radio-frequency mass-spectrometer MX6407-P;
- CAMAC High-voltage scanning DAC for MX6407-P;
- CAMAC controller (crate-controller);
- CAMAC double delta-sigma ADC 701A (20-bit effective resolution);
- CAMAC Relay multiplexer
- Adapter card (ISA interface) for data link between IBM PC and crate-controller;
- IBM PC

System provides data acquisition and processing during four-hour reactor power session with following technical characteristics:

- Number of measuring channels: 2 (one-channel operation is possible)
- Mass number ranges:
  - 2-60 (for omegatron)
  - 2-6 (for MX6407-P)
- Maximal relative sensitivity to hydrogen:
  - 1 %vol (for MX6407-P)
  - 2%vol (for omegatron)
- Maximal pressure of studied medium: 0.001 Pa
- Minimal registered partial pressure of hydrogen 10^{-8} Pa
- Omegatron frequency sweep range: 30- 2300 kHz, step 100 Hz
- MX6407 sweep voltage: 30-300 V, step 0.2V
- Input signals: analogous, 10^{-5}-10.0V voltage
- Channel sampling frequency: up to 0,1 Hz

Post-measurement processing of raw data includes:

- Archive file loading (with possibility of data superposition for comparison);
- Detail graphical analysis of data (possibility to retrieve information of each measured point exactly from the spectrum image);
- Filtering of measured data arrays (digital non-shifting filtering) with Save and Print functions;
- Function of graphical "Print Screen".

4. System Operation

General view of mass-analyzers at reactor cover and system control desk is presented on Figure 5. Huge vacuum system that is important part of entire experimental installation as well as cable path for operating frequency and analogous signals from/to CAMAC-modules and other communications are not shown and described here. Temperature over experimental device and pressure within experimental channel are controlled with regular reactor means independently.

System allows conducting of automated simultaneous real-time sampling and registration of chemical composition of gases in operational volumes of two chambers of experimental installation (in inlet and outlet sides, for example). Automated measurement system provides possibility to measure under irradiation wide (full) mass-spectrum over all possible masses of omegatron mass-analyzer or to carry-out partial scan in specified window of masses (see Figure 2).



Mass-analyzers at reactor top cover (premise 200)



Measurement control workstation (premise 203)

Figure 5. Automated Hydrogen/Tritium measurement system at IVG1M reactor

Such a regime is usually used before reactor's full power mode or even at some certain moments of experiment with purpose to check vacuum condition over studied material. Usually (in most cases) the experiment consist in simultaneous measurement of up to four masses concentration changes in one chamber (with omegatron) and registration of spectrum of light masses (2-6) in second chamber (with MX6407). Under such mode computer switches ADC input to omegatron output, sets operating frequency of synthesizer according to needed mass and after certain time delay samples the output signal from mass-analyzer. And so on until all needed masses would be measured. After that multiplexer switches ADC input to second output (of MX6407) and high-voltage DAC starts its scan (see Figure 4). Real system time of each measurement point and both type of measured data (set of values from omegatron and 250-point array from MX6407) are stored in one file, which could be processed later (see figure 6,7).

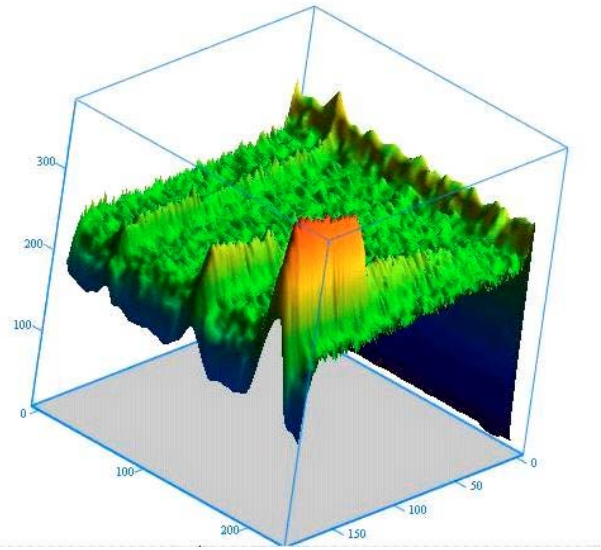


Figure 6. Three-dimensional view of experimental (registered with MX6407-P) unfiltered data array processed with MathCAD. Data file is the same as on Fig. 4.

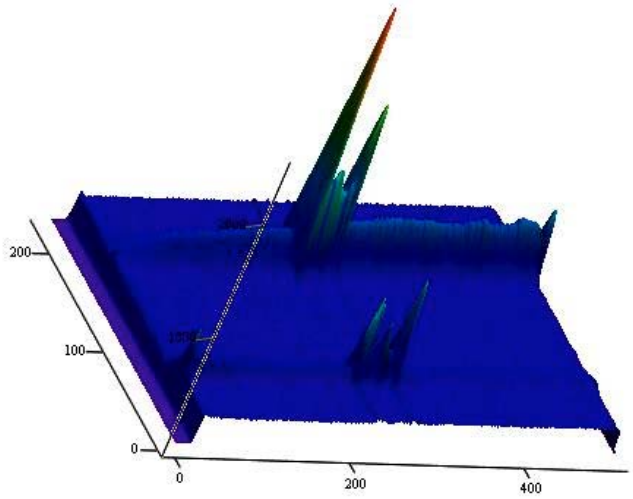


Figure 7. An exemplary 3D-view of time evolution of MX6407-P spectrum from Lithium-Led eutectics under neutron irradiation (penetration through F82H steel).

Also system software could operate in data analysis mode, providing digital filtering and graphical analysis of data when measurements are finished. Choices of measurement type, data presentation, experiment duration, sampling rate and recording are provided by graphical user interface based on IBM PC graphical terminal. Software is functioning in MS-DOS or Windows operational systems environment.

5. Conclusion

Automated hydrogen (and its isotopes) measuring system is established at IVG1M reactor of Kazakhstan National Nuclear Center. Described automated system is used for investigation of hydrogen/tritium behavior in perspective materials within the frame of international program of ITER-DEMO Thermonuclear Reactor.

DETERMINISTIC AND PROBABILISTIC ANALYSIS OF PWR PRESSURE VESSEL INTEGRITY FOR DIFFERENT TRANSIENT CONDITIONS

Oya Özdere Gülol[a], *Üner Çolak*[b]

[a] Turkish Atomic Energy Authority, Nuclear Safty Department, Ankara,
[b] Hacettepe University, Department of Nuclear Engineering, Beytepe, Ankara, Turkey.

Abstract

In this study, nuclear reactor pressure vessel analysis is performed via deterministic and probabilistic methods for six different transient conditions which may cause pressurized thermal shock. A classical four loop PWR with SA533B type ferritic steel pressure vessel is analyzed. Deterministic analysis is performed for obtaining change in material properties and mechanical state of vessel against temperature and pressure changes. In probabilistic analysis, failure probabilities for vessel beltline region welds are calculated. VISA II computer code is employed for both deterministic and probabilistic analysis.

1. Introduction

Pressure vessel is the most critical component of a nuclear reactor since it contains core, its internals and control mechanisms at high temperature and pressure. Neutron fluence, high pressure, temperature, and stresses arising from these loads are important points concerned in pressure vessel integrity analysis. It is of special importance for pressurized water reactors since they operate at higher pressures and neutron fluxes when compared to boiling water reactors [1,2]. Pressure vessel contains the primary side of the coolant loop. It prevents the release of radioactive substances to environment.

Reactor vessels are designed and manufactured according to strict regulations including the safety margins. The reactor vessel steels are chosen among steels of high fracture toughness, high yield strength and low radiation embrittlement. Therefore, change in material properties must be taken into account in design of vessel.

Since there is no actual failure of pressure vessels, there is no real data for pressure vessel failure, therefore, the probabilistic methods play an important role in analysis as well as deterministic approaches.

There are two types of events which endanger the integrity of pressure vessel; overcooling transients and cold repressurization. Cold repressurization

occurs when system pressure is increased significantly at startup. Overcooling transients happen by the injection of cold emergency core cooling system due to break or leak at the primary system. In this study, six overcooling transients are analyzed. These events are; large main steam line break (LMSLB), small main steam line break (SMSLB), loss of heat sink (LOHS), small break LOCA (SBLOCA), large break LOCA of 50 cm^2 (LBLOCA50) and large break LOCA of 200 cm^2 (LBLOCA200) break. Vessel Integrity Simulation Analysis (VISA II) code is employed deterministic and probabilistic calculations.

2. Description of Vessels and Transients

2.1. Reactor Pressure Vessel and Materials

A classical four loop PWR is subjected to our study. Reactor pressure vessel characteristics are presented in Table 1.

Overall hight	13 660 mm
Inside diameter	4394 mm
Wall thickness opposite core	215 mm
Dry weight of pressure vessel	434 800 kg
Normal operating pressure	15.98 MPa
Design pressure	17.13 MPa
Normal operation coolant inlet temperature	288 °C
Normal operation coolant outlet temperature	327 °C

Table 1. Characteristic of PWR reactor pressure vessel

Reactor pressure vessel steels are chosen among high fracture toughness materials. Two common ferritic steels employed in light water reactor vessels are SA508 and SA533B. In this study, SA533B type steel, which is commonly used in newer vessels is employed. The copper, nickel and phosphorus constitutients of SA533B and its weld material are presented in Table 2.

Constitutient (w/o)	*base*	*weld*
Cu	0.14	0.055
Ni	0.58	0.97
P	0.013	0.022

Table 2. Constitutient of PWR base and weld steel

Weld material is important in pressure vessel failure analysis since pressure vessel welds are the most susceptible parts which may lead to vessel rupture. SA508 type vessel steel is composed of circumferentially oriented welds while SA533B type is composed of three circumferential and six axially oriented welds.

Copper, nickel, and phosphorus are the most important elements in pressure vessel steel analysis. Since copper precipitation under irradiation is the most well known embrittlement mechanism, it is of prime importance in fracture toughness and nil ductility temperature prediction. Nickel was added to improve the hardenability of ferritic steels. Moreover, phosphorus content is important in most cases and phosphorus embrittlement mechanism must be analyzed and understood in detail.

2.2. Neutron Fluence

Fast neutron fluence used in the analysis includes neutrons with energies greater than 1 MeV. Neutron fluence in pressurized water reactor is in the $1\text{-}10\times 10^{19}$ neutrons / cm^2 range. In this study, the neutron fluence at inner vessel wall is chosen to be an average value of 4×10^{19} neutrons / cm^2.

Fluence distribution in the vessel wall is modelled by the relation;

$$\phi = \phi_O \times \exp(-0.0945\ x)$$

where x is the depth in centimeters from the inner vessel surface.

2.3 Description of Transients

Small main steam line break transient is characterized by a break of 3.2 cm^2. All component operations and operator actions were assumed to be taken properly to deal with the accident after cold emergency cooling water was injected. Because of the isolation of auxiliary feedwater, the cooling rate becomes lower, and eventually the temperature starts to increase gradually. Large main steam line break transient is similar to small main steam line break at event sequence. The size of the break is 33.6 cm^2. both of the transients occur at full power. Both transients last at the end of 8000 seconds.

Loss of heat sink at full power is characterized as the simultaneous loss main feedwater and auxiliary feedwater. Because of cold emergency cooling water injection, coolant temperature decreased rapidly, but pressure decreased simultaneously by opening the pressurizer relief valve. Transient takes 5500 seconds.

In small break LOCA, the transient happens at full power and transent time is 8000 seconds. The temperature starts to decrease with cold emergency cooling water injection. System pressure decreases rapidly because the coolant

flow rate through the break was greater than the charging and emergency cooling water flow rate.

Large break LOCA occurs in the hot leg of primary coolant loop when the reactor is at full power. The size of the break is 50 cm^2. Temperature starts to decrease with cold emergency core cooling water injection. Accumulator tank is employed since pressure decreases to 1 MPa. No significant increase in pressure or temperature is observed since the break is greater than the charging. Transient lasts at the end of 5000 seconds.

In large break LOCA, the size of the break is 200 cm^2. Since discharge rate of coolant is higher, system introduces a sharper decrease in pressure and temperature. Total transient time is 3000 seconds.

Figures 1 and 2 present temperature and pressure histories for main steam line break transients. Figure 3 and 4 presents temperature and pressure histories for loss of heat sink transient. Figure 5 and 6 represents temperature and pressure history of large break LOCA of 50 cm^2 transient. Figure 7 and 8 represents temperature and pressure history of large break LOCA of 200 cm^2 transient.

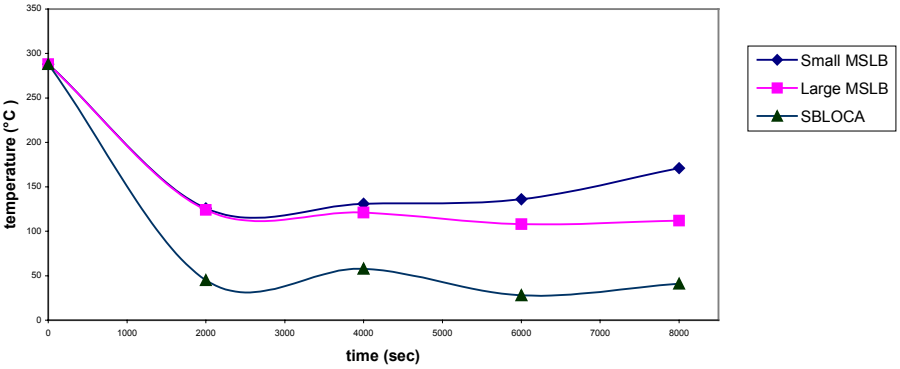


Figure 1 Temperature Histories for Main Steam Line Break and Small Break LOCA Transients

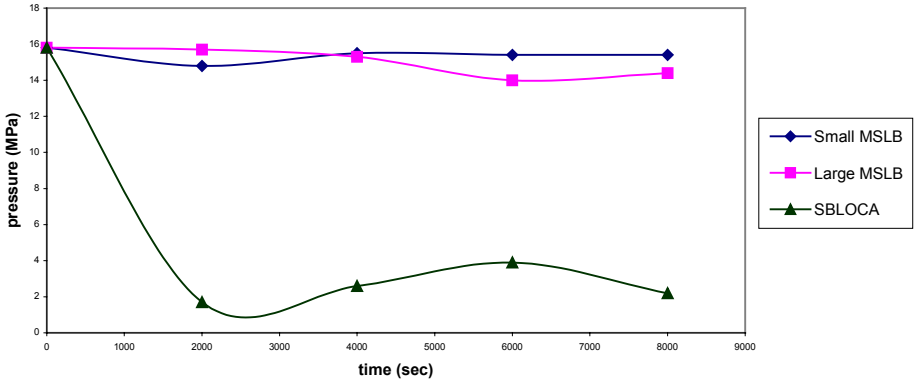


Figure 2 Pressure Histories for Main Steam Line Break Transients

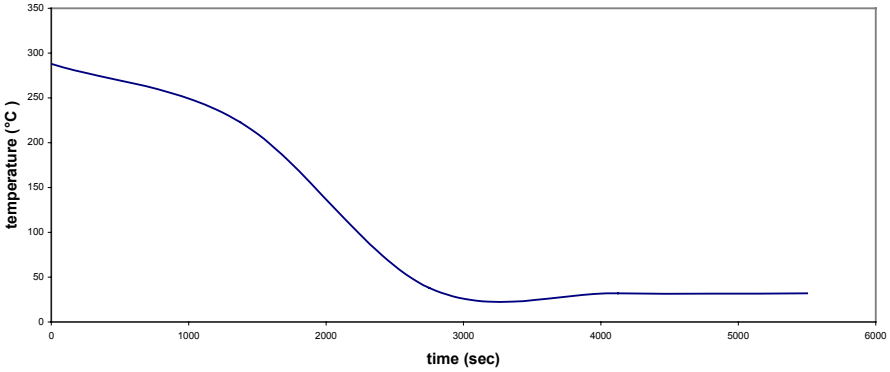


Figure 3 Temperature History for Loss of Heat Sink Transient

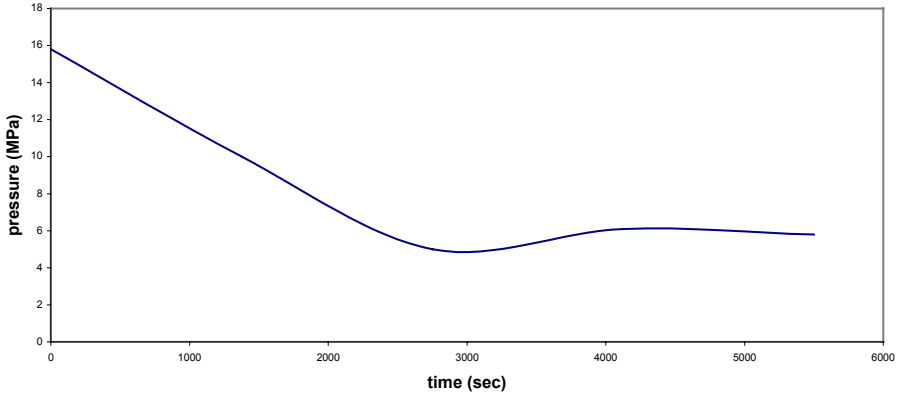


Figure 4 Pressure History for Loss of Heat Sink Transient

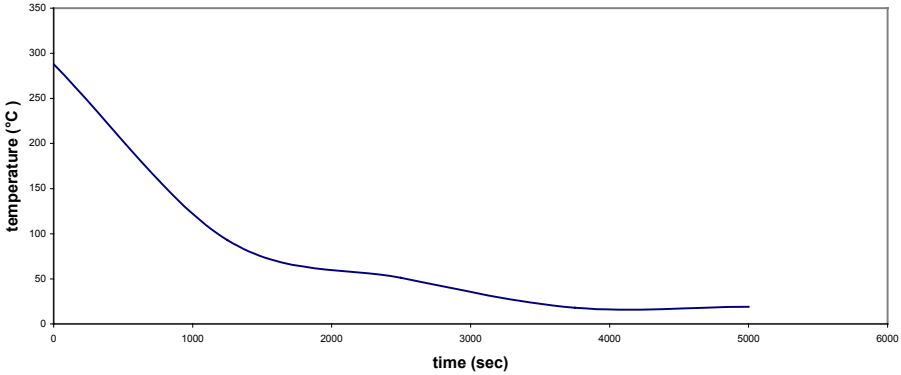


Figure 5 Temperature History for Large Break LOCA Transient (50 cm^2)

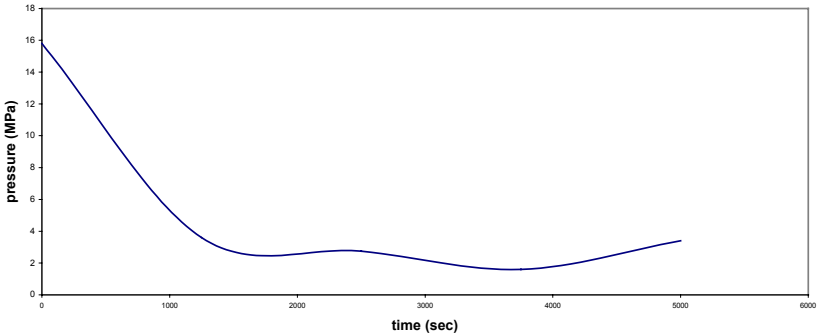


Figure 6 Pressure History for Large Break LOCA (50 cm^2)

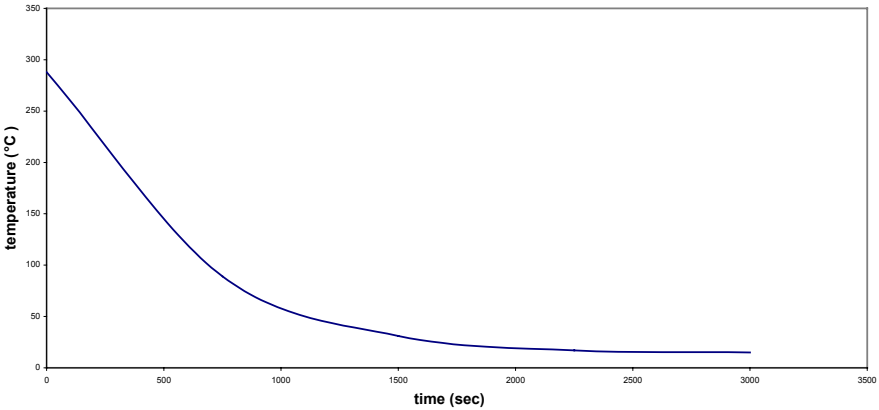


Figure 7 Temperature History for Large Break LOCA Transient (200 cm^2)

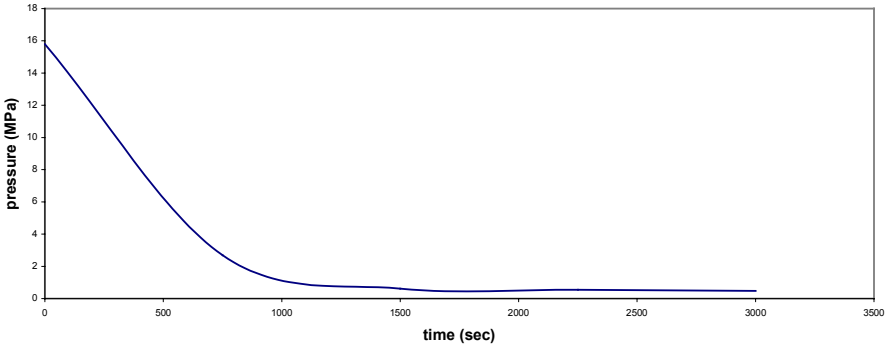


Figure 8 Pressure History for Large Break LOCA Transient (200 cm^2)

3. Analysis

Pressure vessel integrity analysis is composed of deterministic and probabilistic parts.

3.1 Deterministic Analysis

Deterministic analysis is composed of heat transfer analysis and stress analysis. The term 'fracture mechanics analysis' includes stress and heat transfer analyses as well as the calculation of crack tip stress intensity factors.

VISA II code calculates crack tip stress intensity factors and the corresponding values of crack tip temperatures, initiation, and arrest toughness values for various crack depths. Stainless steel vessel clad is taken into consideration in calculations. Deterministic analysis provides an input to probabilistic analysis.

In fracture mechanical analysis, linear elastic material behavior is assumed. Linear elastic fracture mechanics (LEFM) is the base approach for calculations. The fracture toughness values are calculated based on copper and nickel content, neutron fluence, and initial value of nil ductility temperature, RT_{NDTO}. The radiation induced shift in RT_{NDT} is calculated employing the USNRC Regulatory Guide 1.99 Revision 2.

In transient analysis, the temperature difference between the inner and outer walls is calculated. During an overcooling transient, the stainless steel cladding at vessel inner wall tends to increase the thermal stresses since thermal expansion coefficient of clad metal is higher than thermal expansion coefficient of

vessel base metal. Also thermal conductivity of cladding is lower than that for base metal which intensifies the temperature difference between vessel inner and outer surfaces. Table 3 and Table 4 represent the temperature differences between inner and outer walls at different times of the transient.

As can be seen from Tables 3 and 4, the temperature difference between inner and outer walls reaches the maximum value at the first half of the transient. The vessel wall faces the maximum difference of 176 °C among the other transients. This means that the temperature stress on vessel wall is maximum for loss of heat sink transient. Temperature gradients tend to decrease after the first half of the transient after the ECCS is activated.

Another point to be observed s the positive gradient of fracture toughness due to rapid cooling of the vessel wall. The stress intensity factors for longitudinally and axially oriented flaws are also modelled in this study. Especially longitudinally oriented flaws are of prime concern for pressure vessel analysis since they have a greater contribution to vessel failure.

time	ΔT (°X)	time	ΔT (°X)	time	ΔT (°X)
0.1 T_{SMSLB}	83	0.1 T_{LMSLB}	83	0.1 T_{SBLOCA}	130
0.2 T_{SMSLB}	104	0.2 T_{LMSLB}	105	0.2 T_{SBLOCA}	158
0.3 T_{SMSLB}	88	0.3 T_{LMSLB}	90	0.3 T_{SBLOCA}	127
0.4 T_{SMSLB}	60	0.4 T_{LMSLB}	65	0.4 T_{SBLOCA}	84
0.5 T_{SMSLB}	37	0.5 T_{LMSLB}	43	0.5 T_{SBLOCA}	52
0.6 T_{SMSLB}	21	0.6 T_{LMSLB}	30	0.6 T_{SBLOCA}	38

Table 3. Temperature Difference Between Inner and Outer Vessel Walls for Main Steam Line Break and Small Break LOCA Transients

time	ΔT (°X)	time	ΔT (°X)	time	ΔT (°X)
0.1 T_{LOHS}	-24	0.1 $T_{LBLOCA50}$	91	0.1 $T_{LBLOCA200}$	83
0.2 T_{LOHS}	21	0.2 $T_{LBLOCA50}$	137	0.2 $T_{LBLOCA200}$	142
0.3 T_{LOHS}	92	0.3 $T_{LBLOCA50}$	145	0.3 $T_{LBLOCA200}$	172
0.4 T_{LOHS}	150	0.4 $T_{LBLOCA50}$	134	0.4 $T_{LBLOCA200}$	180
0.5 T_{LOHS}	176	0.5 $T_{LBLOCA50}$	119	0.5 $T_{LBLOCA200}$	163
0.6 T_{LOHS}	165	0.6 $T_{LBLOCA50}$	57	0.6 $T_{LBLOCA200}$	148

Table 4. Temperature Difference Between Inner and Outer Vessel Walls for Large Break LOCA and Loss of Heat Sink Transients

3.2 Probabilistic Analysis

The probabilistic analysis employs Monte Carlo techniques to assess the probability of vessel failure. Generally, Monte Carlo methods are used to determine the probability distribution of a function of random variables. This is accomplished by making a large number of evaluations using different sets of sampled values of the random variables. The sample values are obtained by generating random variables.

For each iteration, the simulated values of initial nil ductility temperature, fluence at the inner vessel wall, flaw size, flaw location, copper content and nickel content are selected from their respective distributions. The simulation of the flaw location includes determination of 1) specific weld, of the many welds in vessel, in which flaw is located, and 2) location of the flaw within the vessel wall thickness. With these results fixed for one iteration, the code steps through the time history of transient. For each time step, the applied stress intensity factor at the crack tip is taken from the stored values from the deterministic portion of the code. The fluence at the crack tip is calculated and the sampled value of fluence at the inner vessel wall of the RPV. The value of the shift in nil ductility temperature is calculated using the sampled copper and nickel values and the attenuated neutron fluence. The value of the shift is added to the sampled initial nil ductility temperature to obtain the adjusted RT_{NDT}. The value of fracture toughness, K_{IC}, is sampled and compared to the applied stress intensity factor at this point. Crack growth initiates if K_{IC} is less than the applied stress intensity factor. I f crack initiation does not occur, the simulation moves to the next time step. If initiation occurs, the crack is extended 0.25 inch and the crack arrest toughness, K_{Ia} is simulated. The mean value of K_{Ia} is calculated using the values of RT_{NDT}, fluence and temperature at the crack tip. If crack arrest occurs, the simulation moves to the next time step; if not, the crack is extended another 0.25 inch and a new value of K_{Ia} is simulated. This process continues until either the vessel fails or transient is completed. Table 5 shows the results of probabilistic analysis.

Transient	P_i	P_f	P_O
SMSLB	1×10^{-4}	1×10^{-4}	1×10^{-8}
LMSLB	1×10^{-4}	1×10^{-4}	1×10^{-8}
LOHS	9.7×10^{-1}	2×10^{-2}	1.9×10^{-3}
SBLOCA	1.8×10^{-1}	4.7×10^{-2}	8.4×10^{-3}
LBLOCA50	5.9×10^{-1}	1.4×10^{-1}	8.2×10^{-2}
LBLOCA200	9×10^{-1}	1.2×10^{-1}	1×10^{-2}

Table 5. Results of Probabilistic Analysis

P_i represents the probability of initiation of a flaw in vessel beltline region weld material where P_f represents the probability of failure of that flaw. The overeall probability, P_O is the failure probability of a vessel weld due to a flaw initiated, which is the product of Pi and P_f. Another point to be considered is that circumferentially and axially oriented flaws on circumerentially and axially oriented welds are modelled in analysis. But the flaws which lead to failure are axially oriented on axial welds of pressure vessel beltline region. Large break LOCA of 50 cm^2 pipe break is the most critical of the transients analyzed for pressure vessel integrity. Large break LOCA of 200 cm^2 and small break LOCA comes after the transient. Since the discharge rate of coolant and addition of cold water from emergency core cooling system is high especially for LOCA transients, the result is not surprising.

Another screening criterion applied in pressure vessel integrity analysis is the shift in nil ductility temperature due to transient. Large Break LOCA of 50 cm^2 causes the highest shift in pressure vessel with 84°C. The shift nil ductility temperature values for four transients are similar. Table 6 presents the shift in nil ductility temperatures for transients analyzed.

Transient	ΔRT_{NDT} (°C)
SMSLB	51
LMSLB	75
LOHS	83
SBLOCA	68
LBLOCA50	84
LBLOCA200	82

Table 6. Shift in Nil Ductility Temperatures due to Transients Analyzed

4. Conclusions

In this study, pressure vessel integrity analysis is carried for a Westinghouse design PWR. The most limiting conditions for pressure vessel are resulted from overcooling of vessel and overpressurization. Six overcooling transients are analyzed in this study, these are; small main steam line break, large main steam line break, loss of heat sink, small break loca, large break loca of 50 cm^2 and large break loca of 200 cm^2 pipe break.

The most susceptible part of pressure vessel against failure is the beltline region where the core is located. In a SA533B forged steel pressure vessel, there exists circumferential and axial welds on the beltline region. The study analyzed the cracks located longitudinally and axially on those welds. The results showed

that crack initiation and failure only occurred on axially oriented welds and the cracks were longitudinally oriented.

Pressure vessel integrity analysis is performed by the calculation of shift in nil ductility temperature, the stress distribution on vessel wall, and the probability of initiation of a crack located on vessel beltline region welds to predict the probability of vessel failure. USNRC Reegulatory Guide 1.99 Revision 2 is employed in predicting the shift in RT_{NDT}. The vessel faces the highest shift of 84°C in large break loca transient of 50 cm^2 pipe break. According to the current US regulatory practice, 10 CFR 50.61 Regulatory Guide 1.154, the screening criteria for shift in nil ductility temperature is 149°C for circumferential welds and 132°C for plates and forgins. These temperatures for the pressure vessel analyzed in this study remains below the specified limits in all transient cases.

References

1. International Comparative Assessment Study of Pressurized Thermal Shock in Reactor Pressure Vessels, NUREG/CR-6651, ORNL/TM – 1999/231, 1999.
2. N.K. Mukhopadhyay, T.V. Pavan Kumar, J.Chattopadhyay, B.K. Dutta, H.S. Kushwoha, V.V. Raj, International Journal of Pressure Vessel and Piping, 75 (1999), 1055.
3. O.Ozdere, Deterministic and Probabilistic Analysis Under Pressurized Thermal Shock, Hacettepe University, Master of Science Thesis, 2000.
4. U.Colak, O.Ozdere, Journal of Nuclear Materials, 297 (2001), 271.
5. A. Simonen, K.I. Johnson, A.M. Liebetrau, D.W. Engel, E.P. Simonen, VISA II A Computer Code for Predicting the Probability of Reactor Pressure Vessel Failure, NUREG/CR-4486 PNL-5775, 1986.

DOSE ASSESSMENT AROUND YENIKOY COAL-FIRED POWER PLANT DUE TO MEASURED GROSS ALPHA RADIOACTIVITY LEVELS IN FLYING ASH OF THE PLANT

Tayfun Büke

Muğla University, Faculty of Science and Letters, Physics Department, Muğla-Turkey

Abstract
The gross alpha radioactivity levels in ash wasted from Yeniköy coal-fired power plant have been measured. And then radiation dose calculations have been carried out by the code CAP88-PC around the plant environment by using the maximum measured gross alpha activity in the flying ash samples as a radioactive source. 16 wind sectors and 20 mesh distances are used around the facility in the calculation. The results obtained from the calculations are under the dose limits of International Commission of Radiation Protection and it does not any risk for public health around the plant environment.

1. Introduction

YPP (Yeniköy Power Plant) is located in Muğla province to produce electricity since some important part of lignite reserve of Turkey is in this region and it has a power of 2x210 MW.
Lignite in Muğla province contains some uranium as all lignite does. Lignite in uranium passes to ash with a higher concentration during the firing process in furnace chamber at 1000 ^{o}C. While well-burned ash goes to the plant chimney, the others are not burned perfectly which are called slag ashen drops the furnace chamber floor. The radioactive in flying ash is released to the atmosphere, depending on the efficiency of the plant's chimney emission control equipment [1]. The major potential pathway which might result in increased radiation doses to people are inhalation of flying ash, ingestion of food grown in contaminated soil or direct radiation exposure from the increased deposited radioactivity when flying ash are released from the plant chimney [2].
In this study, the gross alpha radioactivity levels in ash wasted from the plant have been measured. And then radiation dose calculations have been carried out by the code CAP88-PC [3] around the plant environment by using the measured gross alpha activity in the flying ash as a radioactive source. The meteorological data obtained for Yeniköy from Turkish State Meteorological Service [4] are processed to find wind frequencies for 16 directions. The population distribution around the plant is obtained from Turkish State Institute of Statistics [5] according to the last census.

2. Experimental procedures

Approximately 3 kg of each type of ash was taken in the plastic bags from YPP in 3 different time. 100 g from each type of the ash sample in the plastic bags was transferred into the beakers. The ash samples in the beakers were dried, homogenized, and sieved. Four sediments were prepared by the procedure given in Reference (6) from each sample in the same way.

The gross alpha radiation counting were measured by Ludlum Model 43-10 alpha sample counter [7]. And the gross alpha counts in ash sample [A_α : Bq/kg] can be calculated by [6,8]:

$$A_\alpha = \frac{G - B}{60 * T * E * Q} \tag{1}$$

Where G is the gross sample counts; B is the background counts; T is the counting time (min.); E is the alpha efficiency at sample density thickness (cpm/dpm); Q is the sample weight (kg) and 60 is the conversion factor from dpm to Bq.

The alpha efficiency [E : cpm/dpm]; at sample density thickness [x: mg/cm^2] is obtained for absorption data generated experimentally as follows:

$$E = \frac{0.39 + 1.762x}{1 + 6.397x + 1.439x^2} \quad , \quad x \le 8.5 \ mg/cm^2 \tag{2}$$

The maximum deviation is 3.36 % between the experimental values and the results obtained from Eq.(2). This fitted equation is used in Eq (1). Statistical error in all measurements

[σ : Bq/kg] are calculated from the equation which is given as [6]:

$$\sigma = \frac{\pm 1.96 * \sqrt{G + B}}{60 * T * E * Q} \tag{3}$$

The gross alpha radioactivity levels in ash wasted from YPP have been calculated by using Eqs. (1) to (3). Calculated results are given in Table 1.

Table-1. The gross alpha activities in ash samples

Sample No.	Sampling date	Sample type	Gross alpha activity (Bq/kg)
1	08.06.2000	Flying ash	538 ± 95
2	08.06.2000	Slag ashen	362 ± 53
3	21.06.2000	Flying ash	542 ± 85
4	21.06.2000	Slag ashen	368 ± 54
5	29.06.2000	Flying ash	525 ± 78
6	29.06.2000	Slag ashen	351 ± 55

Due to low level of radioactivity of samples, the measuring time was 18000 s. All the results given in Table 1 are average of the four calculations to get the good statistics.

3. Radiation hazard calculations

Radiation dose calculations have been carried out by the code CAP88-PC around the plant environment by using the maximum measured gross alpha activity in the flying ash samples as a radioactive source. The CAP88-PC (Clean Air Act Assessment Package) is a set of computer programs, databases and associated utility programs for estimation of dose and risk from radioisotope emissions to air on a personal computer.

It uses a modified Gaussian plume equation to estimate the average dispersion of radioisotopes released from up to six emitting sources for a circular grid of distances and directions for a radius of up to 80 kilometers around the facility. Plume rise can be calculated assuming either a momentum or buoyant-driven plume. The plume centerline remains at effective stack height unless gravitational settling of particulates produces a downward tilt, or until meteorological conditions change.

Annual nuclide release rate for gross alpha activity [Q: Bq/y] is calculated from the relation given by:

$$Q = \dot{m} A_{\alpha} L \tag{4}$$

Where $\dot{m}$ is the ash emission rate from the plant chimney (kg/y) [9], A_{α} is the measured maximum gross alpha activity in flying ash (Bq/kg) and L is the plant loading factor.

The presence and behavior of radioisotopes in ash wasted from the plant have been studied by using the gamma isotopic analysis method [10]. Ash samples contain approximately 90% ^{238}U and 10% ^{232}Th in total according to the results obtained from the gamma isotopic analysis method. Therefore, it is assumed that the nuclide inventories contain same percentage isotopes in nuclide release rate and it is also assumed that only alpha radioactive isotopes considered in both of complex chains.

Plume rise is calculated by using the momentum plume model since ash emission velocity at the chimney exit is known. An average lid for the assessment area is provided as part of the input data.

The agricultural data like beef cattle density, milk cattle density and land fraction cultivated for vegetable crop and others input to the code for Yeniköy to the dispersion data to estimate uptake of emitted radioisotopes into the food chain.

The meteorological data obtained from Turkish State Meteorological Service for Yeniköy region is processed to find out the stability array file for 16 directions.

The stability array file consists of 4 different wind frequencies, one for each of the

16 wind directions and 6 Pasquill stability category. 16 records are entered for each Pasquill stability category and wind frequencies.
The program uses a population file for dose calculations. The population file contains the location description, latitude, and longitude of the facility, the number of distances and population for each distance according to 16 wind directions in counterclockwise order starting with North and 20 distances are used for each wind directions. The distances are edge points of each sector and are entered in the population file in kilometers.
The Population distribution file is prepared around the plant for 20 distances of each wind direction and this file is used in dose calculation. Input parameters used in radiation dose calculations are given in Table 2 [4,5,9,11].

Table-2. Input parameters used in the calculation

Explanation	Values
Grid distances, (m)	1500, 3950, 6400, 8850, 11300, 13750, 16200, 18650, 21100, 23550, 26000, 28450, 30900, 33350, 35800, 38250, 40700, 43150, 45600, 48000.
Annual precipitation in Yeniköy, (m/y)	0.49
Annual ambient temperature in Yeniköy, (^{o}C)	19
Height of lid, (m)	400
Chimney height, (m)	200
Chimney inner diameter at the exit, (m)	6
Ash emission velocity at the chimney exit, (m/s)	2.5
Ash emission rate from the chimney, (kg/y)	9.47×10^{5}
Plant loading factor	75%
Maximum measured gross alpha activity in flying ash, (Bq/kg)	542
Annual nuclide release rate, (Bq/y)	5.18×10^{8}
Radioisotope list in the escaping ash	^{238}U and ^{232}Th complex chains
Meat ingestion per person, (kg/y)	22.9
Leafy vegetable ingestion per person, (kg/y)	117
Produce ingestion, (kg/y)	118
Milk ingestion per person, (L/y)	6

4. Conclusions

Measured total gross alpha radioactivity levels in ash samples of the plant are given in Table 1. It is seen that the radioactivity levels in flying ash are slightly greater than the slag ashen for all ash samples. This is an expected result, because of the slag ashen is not fired as well as flying ash.

Calculated effective dose equivalent rate values including all radioisotopes and pathways effect around the plant environment by CAP88-PC code are given in Table 3. It is seen that the maximum effective dose equivalent rate is **0.54 μSv/y**. This value is recommended by the International Commission of Radiation Protection and it do not any risk for public health around the plant environment.
In this study, the effective dose equivalent rate values obtained around the facility by CAP88-PC code are depend on the measured gross alpha activities in a known time period. It is necessary and important to make radioactivity measurements in the ash samples of YPP periodically to check the radioactivity levels in ash samples for radiological dose assessment, since YPP works and burned lignite continuously. If there is an increase radioactivity levels of the ash samples which means that lignite with high concentrations is burned. In this case, authorized persons have to take require precaution to protect public from the radiation hazards.

*Table-3. Effective dose equivalent rate (**in μSv/y**) around YPP environment*

Distance (km)	**N**	**NNW**	**NW**	**WNW**	**W**	**WSW**	**SW**	**SSW**
1.50	0.0000	0.0000	0.0000	0.0330	0.0000	0.0000	0.0000	0.0000
3.95	0.0000	0.0620	0.0190	0.0000	0.0000	0.0000	0.0000	0.0000
6.40	0.0000	0.0540	0.0170	0.0000	0.0780	0.0000	0.1200	0.0000
8.85	0.0000	0.0000	0.0000	0.0000	0.0760	0.1500	0.0000	0.0000
11.30	0.0000	0.0000	0.0160	0.0250	0.0670	0.1300	0.0000	0.0000
13.75	0.0900	0.0420	0.0140	0.0220	0.0580	0.1100	0.0000	0.1000
16.20	0.0790	0.0370	0.0130	0.0200	0.0000	0.0980	0.0000	0.0910
18.65	0.0000	0.0330	0.0120	0.0180	0.0000	0.0000	0.0000	0.0800
21.10	0.0620	0.0000	0.0110	0.0000	0.0400	0.0000	0.0000	0.0000
23.55	0.0550	0.0270	0.0100	0.0150	0.0000	0.0000	0.0000	0.0000
26.00	0.0500	0.0240	0.0000	0.0000	0.0330	0.0000	0.0000	0.0000
28.45	0.0450	0.0220	0.0094	0.0130	0.0000	0.0000	0.0000	0.0000
30.90	0.0000	0.0210	0.0089	0.0000	0.0000	0.0000	0.0000	0.0000
33.35	0.0000	0.0190	0.0086	0.0000	0.0000	0.0000	0.0000	0.0000
35.80	0.0000	0.0180	0.0082	0.0000	0.0000	0.0000	0.0000	0.0000
38.25	0.0000	0.0180	0.0083	0.0000	0.0000	0.0000	0.0000	0.0000
40.70	0.0000	0.0170	0.0080	0.0000	0.0000	0.0000	0.0000	0.0000
43.15	0.0000	0.0160	0.0078	0.0000	0.0000	0.0000	0.0000	0.0000
45.60	0.0000	0.0000	0.0000	0.0000	0.0000	0.0000	0.0000	0.0000
48.00	0.0000	0.0000	0.0074	0.0000	0.0000	0.0000	0.0000	0.0000

Table-3. Continues

Distance (km)	S	SSE	SE	ESE	E	ENE	NE	NNE
1.50	**0.5400**	0.0000	0.0000	0.0000	0.0450	0.0000	0.0000	0.0000
3.95	0.0000	0.0000	0.0000	0.0000	0.0000	0.0000	0.0000	0.0000
6.40	0.0000	0.1600	0.0000	0.0000	0.0000	0.0000	0.0750	0.0000
8.85	0.0000	0.0000	0.0680	0.0000	0.0000	0.0000	0.0000	0.0610
11.30	0.3500	0.1400	0.0000	0.0000	0.0000	0.0000	0.0610	0.0000
13.75	0.0000	0.1200	0.0000	0.0000	0.0000	0.0000	0.0000	0.0482
16.20	0.2600	0.1100	0.0490	0.0000	0.0000	0.0000	0.0000	0.0000
18.65	0.0000	0.0940	0.0000	0.0000	0.0000	0.0000	0.0000	0.0380
21.10	0.0000	0.0000	0.0390	0.0000	0.0000	0.0000	0.0000	0.0000
23.55	0.0000	0.0000	0.0000	0.0000	0.0000	0.0000	0.0000	0.0310
26.00	0.0000	0.0000	0.0000	0.0000	0.0000	0.0000	0.0000	0.0000
28.45	0.0000	0.0000	0.0000	0.0000	0.0000	0.0000	0.0000	0.0000
30.90	0.0000	0.0000	0.0000	0.0000	0.0000	0.0000	0.0000	0.0000
33.35	0.0000	0.0000	0.0000	0.0000	0.0000	0.0000	0.0000	0.0000
35.80	0.0000	0.0000	0.0000	0.0000	0.0000	0.0000	0.0000	0.0000
38.25	0.0000	0.0000	0.0000	0.0000	0.0000	0.0000	0.0000	0.0000
40.70	0.0000	0.0000	0.0000	0.0000	0.0000	0.0000	0.0000	0.0000
43.15	0.0000	0.0000	0.0000	0.0000	0.0000	0.0000	0.0000	0.0000
45.60	0.0000	0.0000	0.0000	0.0000	0.0000	0.0000	0.0000	0.0000
48.00	0.0000	0.0000	0.0000	0.0000	0.0000	0.0000	0.0000	0.0000

References

1. *Kınacı, S. R.:* Energy and radioactive environment, Proceedings of National Fifth Energy Conference, Ankara, Turkey, (1990), p.213.
2. *Eral, M.:* Determination of uranium in ash-wasted from a thermal power plant and effect of them on the environment, Proceedings of Environment-87 Symposium, Izmir, Turkey, (1987), p.E-1.
3. *Parks, B.; Chaki, S. P. E.:* CAP88-PC Version 2.0 Updated User's Guide, EPA 402-R-00-004, 2000.
4. Annual Meteorological Conditions in Yeniköy, Turkish State Meteorological Service, Ankara, Turkey, 2000.
5. Population by District, Sub-district and Villages for Muğla, Republic of Turkey Prime Ministry State Institute Statistics, Ankara, Turkey, 1997, p.8.
6. Gross Alpha and Beta for Various Matrices, Laboratory Procedures Manual, Part B, Revision No:12, ORISE/ESSAP, 2001, p.3.

7. Instruction Manual for Ludlum Model 43-10 Alpha Sample Counter, Ludlum Measurements, Inc., Texas, USA, 1992, p.1.
8. *Scarpitta, C. S.:* Preparation and Validation of Gross Alpha/Beta Samples Used in EML's Quantity Assessment Program, EML-592, New York, USA, 1997, p.25.
9. *Selçuk, N.; Atımtay, A.; Uslu, O.; Cirik, Ş.; Vurdu, H.; Tuncel, G.; Kaya, Z.; Evirgen, M.; Yurteri, C.:* Scientific Committee Report for Kemerköy Thermal Power Plant, Ankara, Turkey, 1995, p.9.
10. *Akyüz, T.; Varinlioğlu, A.; Köse, A.; Derman, D.:* Gamma isotopic analysis in flying ash samples collected from several thermal power plants, Proceedings of VII. National Nuclear Sciences and Technology Conference, Istanbul Technical University, Institute for Nuclear Energy, Istanbul, Turkey, (1996), p.239.
11. Technical Report for Yeniköy Power Plant, Yeniköy Power Plant Administration Office, Muğla, Turkey, 1998.

ENVIRONMENTAL IMPACT OF NUCLEAR INDUSTRY AND POWER GENERATION IN THE RUSSIAN FEDERATION: ASSESSMENT OF CONTRIBUTION TO GENERAL ECOLOGICAL DAMAGE

V.A. Vetrov

Institute of Global Climate and Ecology, Moscow, Russia

1. Introduction

The objective of the study was to assess a relative impact of nuclear industry and power generation on natural resources (consumption and detriment) and environmental pollution in the Russian Federation. Both kinds of impact – consumption or detriment of resources and contamination – were considered as general ecological damage. The general aim was to provide rationale for the sound strategy and priorities in addressing protective measures for resources and the environment at the national and regional governance levels. ***Industry in total, atomic and fossil-fuel power production, motor transport, housing and communal services*** were taken into consideration as principal sectors of the economy, causing detriment of resources and contamination of the environment.

Estimates were derived from data found in reviews published by federal environmental protection authorities [1-12]. The impact of major sectors of economy on the environment and natural resources was estimated through analyzing chemical and radioactive releases, as well as air, water, land and forest contamination levels in those economic regions and provinces where major nuclear plants were located. Pollutant maximum permissible concentrations (MPC) for natural environment media (ambient air, natural water, soil) as adopted in the RF were used as evaluation criteria. A relative pollution index taking into account the gross product value in the given sector of economy was proposed for the purposes of economic assessment of ecological damage.

2. Consumption of natural resources

2.1. Fresh water.

Table 1 presents the basic data on surface and ground water resources and major consumption items. One can see, that in 1998-2000 atomic industry demand shared less 10% of fresh water consumption by the industry. The far less impact of atomic industry was revealed in contaminated waste water discharges into fresh surface waters – about 1.4% of annual total industry waste water effluents, but 30% of the volume discharged from all electric power plants.

Table 1. The basic data on water resources consumption in 1998-2000.

Item	*Resource/ consumption,* km^3/a	*Relative*
Surface water resource (SWR) (annual river flux from the territory of the RF)	4310	
Predicted ground water resource (GWR) *incl.* ready for use	317 19.8	
Total consumption from all sources in 1998 (TC) *Incl. fresh water*: from surface sources from underground sources for industry needs	 87.4 70.4 11.6 39.1	 1.6% of SWR 60% of GWR 45% of TC
Consumption of fresh water by atomic industry	3.8	4.4% of TC

In general, there have been no problems for Russian economy in water supply needs so far except the problem of uncontaminated fresh water supply for special industrial technologies.

2.2. Land resources.

Some major items of available land use in the RF in 1998-2000 are presented in Table 2.

Table 2. Major items of available land use in 1998-2000.

Item	*Area, ha*	*Relative*
Total available land (TAL)	$1710 \cdot 10^6$	
Industry and infrastructure lands (IIL) Annual variations of counted lands	$18 \cdot 10^6$ $\sim 0{,}5 \cdot 10^6$	11% of TAL 3% of IIL
Land used by atomic industry enterprises	$<0{,}2 \cdot 10^6$	~1% of IIL

Average specific (relative to produced energy unit) value of land area occupied by atomic enterprises is about 4 times less, than for coal energy production and 2.5 less than for gas energy production plants. In general, atomic industry has pretty modest land use indexes relative to other industrial sectors of economy.

2.3. Biological resources – wood.

Wood is one of the most important kind of biological resources used for industrial purposes. Table 3 shows the situation in wood resources of the RF in 1998-2000, that can be assessed as quite satisfactory, at least in quantitative sense.

In particular, atomic industry is not mentioned in the list of major wood consumers.

Table 3. Major items of wood consumption in 1998-2000.

Item	*Value*	*Relative*
Total available standing wood stock (AWS)	$81{,}9 \cdot 10^9$ m^3	
Annual stock increase (ASI)	$0{,}87 \cdot 10^9$ m^3/a	~1% of AWS
Permitted stock cutting (PSC)	$0{,}51 \cdot 10^9$ m^3/a	65% of ASI
Real cutting	$0{,}11 \cdot 10^9$ m^3 /a	13% of AWS 22% of PSC

2.4. Fuel: fossil and uranium.

As the population of the RF is about 2% of the world population Russia has 7 -15 % oil, 35-38 % gas, 36 % coal of established world resources [12]. Values of average consumption security (ratio "consumption / current production") for established principal mineral fuel resources is presented at Table 4.

Table 4. Consumption security of established resources [12].

Fuel	*Consumption security (years)*
Oil	50
Natural gas	80
Coal	>600
Uranium: atomic industry as a whole (energy production + export)	50-60
Uranium: atomic energy production (status quo)	200
Uranium: atomic industry with respect to development rate and increased established stock	100-150

A brief analysis shows, that oil and gas sharing less 25% of total fossil fuel stock effect more than 80% of energy production. At the same time uranium together with coal, covering about 76% of total fuel stock (36% +40%) give only 13% of energy production. These estimations should be reckoned as dramatic lack of fuel balance. Therefore, energy production in Russia is getting more and more dependent on one fuel source – natural gas. Decreasing gas consumption must be set off by more intensive development of atomic and coal energy production.

3. Contamination of the environment

3.1. Atmospheric pollution

About 50% of the RF population live under permanent toxic impact of chemical atmospheric pollution, more than 20 millions live in towns where annual average concentrations exceed 10 MPC's. High contamination levels in urban environment result from ***dust and soot, SO_2, NO_x, CO, CO_2, CS_2, HF, NH_3, Cl, formaldehydes, benz(a)pyrene, methilmercaptan*** and other chemicals. Emissions of industrial gases and particulate remain the major sources of dangerous chemical air pollution in each province concerned. Sectors of economy mostly contributing to air pollution are ***automobile transport, fossil-fuel power generation, chemistry, oil refinery, pulp and paper, metallurgy, mining, machine-building, municipal waste treatment and heat production***.

Industrial emissions of phytotoxic and green-house gases (GHG) have become a prior threat of disturbing the chemical of the atmosphere and consequently global radiation balance. Data in Table 5 demonstrate comparison of specific (per energy unit, kW·h) GHG emissions (mass C equivalent, g) for different energy production modes.

Table 5. Specific emissions of green-house gases by different sectors of energy production.

Sector: source of energy	*Specific emission, $gC_{eq}/kW{\cdot}h$*
Organic fuel (wood, lignine)	260-370
Coal	260-360
Oil	220-250
Natural gas	120-190
Hydroenergetics	6-70
Atomic energy	3-6

Index **φ,** as specific polluted air volume ("ecological price") was calculated for each of the main sectors of economy, responsible for mostly urban atmospheric pollution, with respect to annual:production (Rb/a) in a sector **"i"**:

$$\varphi_i = P_i / (MPC)\cdot M_i \quad [m^3/Rb]$$

where P_i is the total annual emission, g/a; **MPC** – as above, g/m^3; M_i is the monetary value of annual production of i-sector, Rb/a. Values of φ_i were calculated for selected sectors taking into account emissions of dust, SO_2, CO, NO_x, Pb, radioactive matter (Table 6). Results of this simple monitory analysis evidently show, that mostly "dirty" sectors of economy would be fossil-fuel power generation and motor (automobile) transport. "Ecological price" of atomic energy

looks quite negligible - more than five orders of magnitude less than the price of fossil-fuel combustion. According to reported data atomic power and industry plants make no adverse effect on the ambient air quality in impact areas.

Table 6. Specific (per Rb production) volumes of air polluted by major sources of emissions.

Sector of economy	Industry, total	Motor vehicles	HOUSING/ Communal	Fossil-fuel power generation	Nuclear industry, total	Nuclear power generation
φ_i, m^3/Rb	25 200	12 400	2 100	98 300	16 000	0.6

3.2.Contamination of natural waters.

Water quality in most natural fresh water bodies fails to meet the standards, more than 50% of volume of fresh water resources are classified as different degrees of "dirty". The most widespread pollutants are represented by ***oil products, phenols, organic matter, metals, nitrogen compounds***, etc. Major sources of water pollution are: ***industrial wastewater, agriculture, communal effluents, wash-off from polluted watershed***.

Of the vast amount of surface freshwater resources in Russia, it is only in the Techa River (the Mayak Combined Works impact zone, Urals, Ob river basin) that the technogenous ^{90}Sr concentrations are close to or exceed its MPC for drinking water.

3.3. Contamination and degradation of land (soil).

Table 7 presents data that can be used for general assessment of land status in the RF.

Table 7. Characteristics of land status in the RF in 1998-2000.

Area of economy use lands	*Status*
>50% of the land area in 51 members of the RF - about 4 millions km^2 total	*rank: "Environment crisis"*
48% of the RF territory, 40 members of the RF	*Priority problem: land contamination*
25% of the territory of the RF, 22 members of the RF	*Priority problem: land man-caused degradation*
Abandoned land as result of radioactive contamination: 4-5 thousand km^3 (0,1% of area, ranked as "environment crises")	*Good fertility*

As it can be concluded from the data in Table 7 and from a comprehensive review of the situation at regions no atomic enterprise or a site is mentioned in the list of economy enterprises, responsible for contamination and degradation of land. Most of the latter ones belong to ***mining, fossil fuel energy production, housing-communal services (HCS), agriculture*** and other sectors of economy. Therefore, major factors causing soil degradation and agricultural land losses (hundreds of thousand km^2) comprise industrial pollution, bad cultivation and technogenous disturbance. The lands abandoned due to radioactive contamination (3-4 thousand km^2) cannot be ranked as "environmental crisis" areas, since they have not lost their natural fertility.

3.4. Losses and contamination of forests.

Table 8 presents forest areas lost in1998 caused by major harmful effects.

Table 8. Annual losses of forest stands in the RF in 1998.

Cause of loss		*Area, km^2/a*
	Total	2790
Ecological causes:	total	93
Incl.: Pests		*31*
Wild animals		*11*
Forest diseases		*51*
Man-made causes:	total	87
Incl.: Industry pollution		*1*
Natural disasters		153
Fires		2459

The total area of forests lost in the RF as a result of radioactive contamination throughout the nuclear history (mainly, Kyshtym and Chernobyl areas) is approximately 20 km^2, that is four times less than forest area, damaged by cumulative man-made factors during just 1998 (Table 8).

4. Conclusion

Simple comparative consideration and analysis shows, that atomic industry as a whole and leading nuclear enterprises in particular are out of the list of major sources of hazardous detriments of natural resources, pollution and damage of the environment both in the country and in the provinces of their location.

References (all in Russian):

1. Governmental Report "About the Status of the Environment in the Russian Federation in 1999" – Goscomecologia, Moscow, 2000, , 579 pp.
2. Governmental Report "About the Status of the Environment in the Russian Federation in 1998" – Goscomecologia, Moscow, 1999, 573 pp.
3. Governmental Report "About the Status of the Environment in the Russian Federation in 1994" – Goscomecologia, Moscow, 1995, 339 pp.
4. Review of the Environmental Contamination in the Russian Federation in 1999. – Federal Service of the Russia on Hydrometeorology and Monitoring of the Environment. Moscow, 2000.
5. Review of the Environmental Contamination in the Russian Federation in 1998. – Federal Service of the Russia on Hydrometeorology and Monitoring of the Environment. Moscow,1999.
6. Annual Review of Surface Water Quality in the Russian Federation in 1998 – Gidrometeoizdat, Sankt-Petersburg, 1999.
7. Radiation Status of the Russia and Neighboring States Territories in 1998 – Annual reveiw. Ed. by K.P.Makhonko - Gidrometeoizdat, Sankt-Petersburg, 2000, 255 pp.
8. Radiation Status of the Russia and Neighboring States Territories in 1996 – Annual reveiw. Ed. by K.P.Makhonko - Gidrometeoizdat, Sankt-Petersburg, 2000, 165 pp.
9. Radiation Status of Russia and Neighboring States Territories in 1995 – Annual reveiw. Ed. by K.P.Makhonko - Gidrometeoizdat, Sankt-Petersburg, 1996, 308 pp.
10. The State Water Cadaster. Official Edition.-Moscow, 1995.
11. Industry in Russia. Off. Ed. – Goscomstat Rossii. Moscow, 1998.
12. Basic Concepts of Energetic Strategy of Russia for the period till 2020. – Mintopenergo of the RF, Moscow, 1999.

EVALUATION OF CORE HEATUP IN CASE OF TOTAL LOSS OF POOL WATER OF TRIGA REACTORS

Tayfun Büke[1] *and Hasbi Yavuz*[2]

[1] Muğla University, Faculty of Science and Letters, Physics Department, Muğla-Turkey
[2] Istanbul Technical University, Institute for Nuclear Energy, Maslak-Istanbul-Turkey

Abstract
An analytical study has been undertaken of the transient thermal behavior of ITU TRIGA Mark-II Reactor following a highly improbable total loss of pool water.
A computer model has been developed to predict transient temperatures of the uncovered core cooled by natural convection of air in the core coolant channel. The fuel element decay power versus time, starting from the moment of the coolant loss is used in the calculations.
Results obtained from the calculation shows that the maximum fuel temperature will never be exceeded under any conditions of coolant loss according to maximum operating power density.

1. Introduction

The reactor core is surrounded by water, which acts as moderator, reflector, coolant and biological shield in an open pool research reactor. An accident that could lead to water loss in the pool, and consequently, to direct exposure of the fuel elements in the reactor core to the air, will be followed by substantial fuel element temperature increases due to fuel element residual decay heat. It is essential to demonstrate, that such a temperature increase does not lead to excessive core melting and significant radioactive material release into the reactor building and consequently to the environment in the case of total loss of the tank water under accident conditions [1].
Several studies have been developed to predict transient temperatures of the uncovered core, cooled by natural air convection [2-6].
In this study, lumped-parameter model is used to evaluate fuel element temperature, which respect to time for ITU TRIGA Mark-II reactor fuel elements following total loss of pool water. The fuel element decay power versus time, starting from the moment of the coolant loss is used for the calculations. The calculated results shows that the maximum temperature will never be exceeded under any conditions of total coolant loss according to maximum operating power density.

2. Mathematical model

According to the lumped parameter model, the heat balance expression for fuel element can be written as [7]:

$$\rho_f c_f V_f \frac{dT_f}{dt} = P(t) - \mu(T_f - T_\infty) \tag{1}$$

Where T_f are average fuel element temperature and the remaining notations are given in Table-1.

The following assumptions are made in the calculations: Reactor was operated for an infinite time at maximum power until the moment of coolant loss, coolant loss is total and instantaneous, the only heat removing mechanism is air free convection and air temperature and convective heat transfer coefficient are assumed constant in the coolant channel. The calculations are restricted to an equivalent simple unit cell consisting of zirconium rod, fuel meat, cladding and coolant.

Thermal resistance coefficient (μ) is obtained by solving the steady-state, one dimensional heat conduction equation in the fuel element for cylindrical geometry as follows:

$$\mu = \frac{\pi H_f}{\frac{1}{4k_f} - \frac{r_f^2 + r_z^2}{8k_f(r_f^2 - r_z^2)} - \frac{r_z^4}{2k_f(r_f^2 - r_z^2)^2}\ln\frac{r_z}{r_f} + \frac{1}{2k_c}\ln\frac{r_c}{r_f} + \frac{1}{2r_c h_m}} \tag{2}$$

$P(t)$ is the decay heat in Eq.(1). Consistent with most of the Safety Analysis report of the TRIGA type reactors, one assumes that the reactor has been operating at its nominal power for an extended period of time so that the heat produced immediately after shut down is given by [6]:

$$P(t) = P_O\left(0.023178e^{-0.078t} + 0.05625t^{-0.2}\right) \tag{3}$$

After substituting Eq.(3) into the Eq.(1) one can get linear differential equation of the form:

$$\frac{dT_f}{dt} + AT_f = +Be^{-0.078t} + Ct^{-0.2} + D \tag{4}$$

Where the coefficients *A, B, C, D* are constants given as follows

$$A = \frac{\mu}{\rho_f c_f V_f}\ ,\ B = \frac{P_o 0.023178}{\rho_f c_f V_f}\ ,\ C = \frac{P_o 0.05625}{\rho_f c_f V_f}\ ,\ D = \frac{\mu T_\infty}{\rho_f c_f V_f} \tag{5}$$

Differential equation given in Eq.(4) with the initial condition $T_f(t=0)=T_{fo}$ is solved analytically after $Ct^{-0.2}$ term expanded to Taylor series expansion. The solution of Eq.(4) is:

$$T_f(t)=\frac{D}{A}+Se^{-At}+\frac{B}{(A-0.078)}e^{-0.078t}+Ce^{-At}\sum_{n=0}^{\infty}\frac{A^n t^{(n+0.8)}}{n!(n+0.8)} \tag{6}$$

Where;

$$S=T_{fo}-\frac{B}{(A-0.078)}-\frac{D}{A} \tag{7}$$

In this study, a computer program in Fortran-77 language is written to solve $T_f(t)$ in Eq. (6) for different fuel element power levels and convective heat transfer coefficients. Input parameters for the ITU TRIGA Mark-II reactor are used in the computer program given in Table 1 [8]. One should note that since the model represents only one fuel element, the highest power element was represented. The initial power of this element was calculated by the code TRIGLAV [9].

Table 1. Physical parameters used in the calculations

Explanation	Symbol	Value
Fuel element density	ρ_f	6.10 (g/cm^3)
Specific heat of fuel element	c_f	0.479 (J/g. ^{o}C)
Volume of fuel element	V_f	405.10 (cm^3)
Thermal conductivity of fuel meat	k_f	0.1758 (W/cm. ^{o}C)
Thermal conductivity of clad	k_c	0.1665 (W/cm. ^{o}C)
Radius of zirconium	r_z	0.3175 (cm)
Radius of fuel meat	r_f	1.8161 (cm)
Radius of fuel element	r_c	1.8669 (cm)
Fuel length	H_f	38.100 (cm)
Convective heat transfer coefficient	h_m	5.05 (W/m^2 ^{o}C)
Initial fuel element temperature	T_{fo}	35 (^{o}C)
Air temperature in the coolant channel	T_∞	25 (^{o}C)
Power of the fuel element	P_o	5686 (W)

3. Results and conclusions

In this study, an analytical study has been proposed to calculate average fuel temperature of the ITU TRIGA Mark-II reactor fuel elements following total loss of water for different power levels of the fuel element and different convective heat transfer coefficients. Results of calculations are shown in Fig. (1) to (3).

The sensitivity studies conducted show that different correlation or initial temperatures will lead to different values of peak temperature, but some general conclusions can be drawn:

The maximum temperature to which the fuel can increase is **900 ^{o}C** without substantial yielding of the clad or subsequent release of fission products [8]. This temperature will never be exceeded under any conditions of coolant loss if the maximum fuel element power is less than **20 kW.**

For fuel element power **5.686 kW;** which is the maximum power of the fuel element in the ITU TRIGA Mark-II reactor core. The maximum fuel temperature reaches to approximately **600 ^{o}C at 10800 s**. when the heat transfer coefficient of the air is taken as **0.0505 W/m^2.^{o}C**.

The fuel temperature rise to a maximum value of approximately **275 ^{O}C** for the maximum element power of **6 kW** if the coolant is lost immediately after reactor shutdown according to the safety report of the ITU TRIGA Mark-II reactor. This temperature is calculated **258 ^{o}C** in this study.

The deviation according to the safety report result comes from the mathematical models and heat transfer coefficients are used in the calculations.

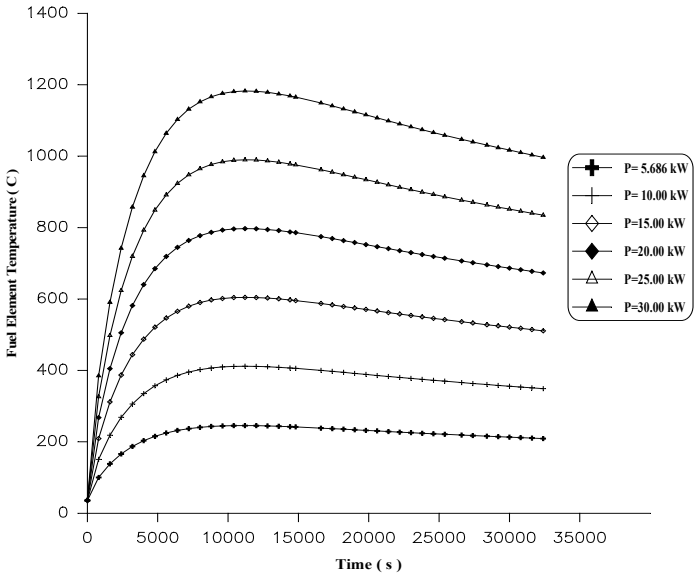


Fig. 1. Fuel element temperatures versus time for different power levels (h=5.05 W/m^2. ^{0}C)

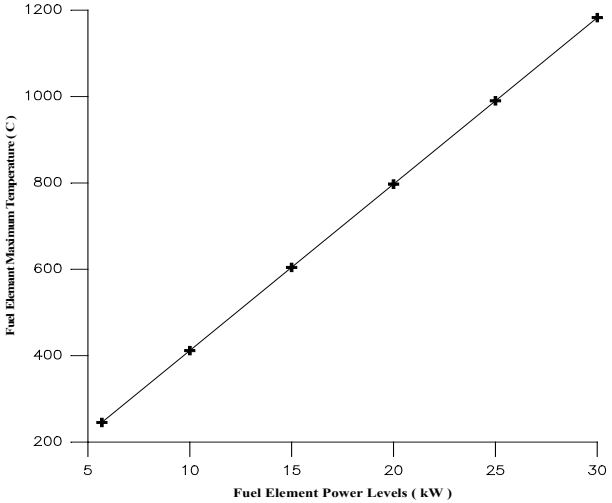


Fig. 2. Fuel element maximum temperatures versus different power levels ($h=5.05$ $W/m^2.\ ^0C$)

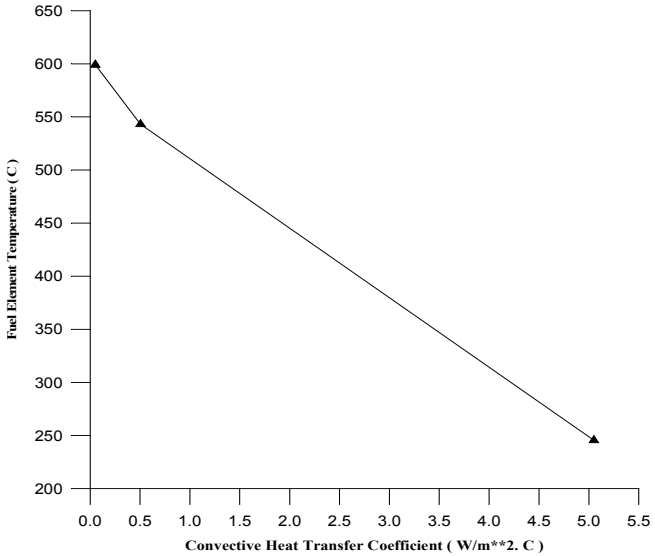


Fig. 3. Fuel element temperatures versus different convective heat transfer coefficients (P=5.686 kW, t=10800 s.)

References

1. *Rogers, J. T.; Veeder, J.; Lamari, M.:* Transient Thermal Behavior of an SES-10 Reactor Following a Loss of Pool Water Accident. International Conference on Nuclear Simulations, Canadian Nuclear Society, Montreal, June 2-4, 1993
2. *Skreba, S.; Sprünken, H.; Unger, H.:* Investigation of the transition from forced to natural convection in the research reactor Munich II Nuclear Engineering and Design, 215 (2002) 15-25
3. *Xinian, Z.; Weijun, G.; Bing, H.; Shifei, S.:* Transient Analysis of the Passive Residual Heat Removal System. Nuclear Engineering and Design, 206 (2001) 105-111
4. *Hazi, G.; Mayer, G.; Farkas, I.; Makovi, P.; El-Kafas, A.A.:* Simulation of a Small Loss of Accident by Using RETINE V1.0D Code. Annals of Nuclear Energy, 28 (2001) 1583-1594
5. *Sevdik, B.; Yavuz, H.*: Experimental Measurements for Plate Temperatures of MTR Fuel Elements Cooled in Stagnant Air and Comparison with Computed Results. Kerntechnik 63 (1998) 5-6
6. *Atieri, S.; Lana, F.; Pedroni, P.:* Maximum Temperature After Loss of Coolant and Pulse Operation at the TRIGA LENA Plant: New Evaluation for Licensing Purpose. Ninth European TRIGA Users Conference, Casaccia, Italy, October 7-9, 1986
7. *Housiadas, C.:* Lumped Parameters Analysis of Coupled Kinetics and Thermal-Hydraulics for Small Reactors, Annals of Nuclear Energy 29 (2002) 1315-1325
8. Safety Analysis Report for the ITU TRIGA Mark-II Reactor August 1978
9. *Persic, A.; Ravnik, M.; Slavic, S.; Zagar, T:,* TRIGLAV- A Program Package for Research Reactor Calculations. J. Stefan Institute Report, IJS-DP-7862, Ljubljana, 1998

EXPERIMENTAL STUDY OF HEAT TRANSFER IN A THIN VERTICAL RECTANGULAR CHANNEL

Arikan İbrahim, Baykal Adnan, Adalioğlu Ulvi
[1]Yavuz Hasbi

Cekmece Nuclear Research and Training Center, Istanbul – Turkey
Istanbul Technical University, Institute of Energy, Maslak, Istanbul – Turkey

Abstract

Free convection cooling processes are often used in nuclear technology as well as in the vertical channel type structures of some systems, in electronic circuit board cooling and many other fields. TR-2 Reactor at Cekmece Nuclear Research and Training Centre (CNRTC) is a pool type research reactor with plate type fuel elements. The narrow vertical cooling channels of this reactor have a width of 2.1 mm. In case of an accident or a loss of cooling event, the heat in these channels are transfered by natural convection. An experimental setup was constructed to simulate the TR-2 cooling channels. Dummy fuel plates were heated by a DC source and temperature measurements were taken by copper-constantan thermocouples situated at different points. Cooling fluid is air. For several different powers and channel gaps the temperatures had been measured. The average Nu and Ra numbers were calculated for the channel and compared with the numerical results.

1. Introduction

The cooling of vertical plates in which energy is generated has become considerably important in recent years. The cooling of printed circuit boards of electronic devices by natural convection can be given as an example.

In nuclear reactor accident conditions, the cooling has been carried out by natural convection after the failure of the cooling systems. In plate type fueled, pool type reactors (MTR) cooling occurs in parallel narrow vertical channels in the direction from top to bottom. In case of a pump failure the cooling is supplied by natural convection from bottom to top.

A lot of theoretical and experimental studies were done for laminar flow with different fluids in narrow vertical channels (**1-6**). TR-2 is a 5 MW, plate type fueled, pool type research reactor. This reactor has 23 plane fuel plates per element which has 22 cooling channels between these plates and 2 cooling channels at the outer sides. Channels are narrow, vertical and rectangular having dimensions of 61 cm x 0.21 cm x 6.54 cm (**7**). A feedback dynamic analysis model was developed

for the safety analysis report of TR-2 Reactor. According to this model, reactor shuts down after pump failure and during the first 250 sec. no boiling occurs (**8**). It is also experimentally shown that, when the cooling channels of the used fuel elements are open to air, they can be cooled by natural convection (**9**).

In this study, an experimental setup was constructed to simulate the TR-2 cooling channels. The cooling fluid is air. At several powers and channel gaps the temperatures had been measured at different points. The average Nu and Ra numbers were calculated for the channels. These values were compared with the numerical results.

2. Experimental Set-up

In order to simulate the cooling channels of TR-2 an experimental setup was made for studying the cooling by air (**Fig.-1**). The geometry is shown in **Fig.-2**. The plates have a height of L, and spacing of b. Each fuel plate consists of two aluminum plates, heating resistances between these plates which also have two electrical isolation plates at the inner surface. Aluminum plates have 1 mm. thickness and same dimensions of the real plates. A mica plate, surrounded by resistance wire with identical intervals provides a homogen heating source. It was tried to make the heating source of the plates identical with each other. The sensitivity reduced up to 0.01 ohm between two resistance wires. Power was supplied by a 0-200 V, 0-7.5 A DC source. Channel width between plates was provided by sticks with different thicknesses. Seven thermocouples were used to measure the surface temperatures along the channel. The channel inlet, outlet temperatures and ambient temperature were measured by using other thermocouples. The temperature of the isolated outer faces of the two plates were also measured with thermocouples situated outside of each plate. On outer side of the plates there are 5 cm. wool-stone for thermal isolation. The thermocouples were sticked on the plate surfaces with a resin which is durable up to 120^{o}C. In the construction of the thermocouples copper and constantant wires (diameter 0.2 mm) were welded in electrical arc in vacuum. The voltage was read on each thermocouple with a single precise multimeter (1 μV sensitivity) and a scanner with 32 channels.

Channel gap values (2.1, 4, 6 and 8 mm) and the power given to the plates (2-20 W) are the input variables in the experiment. For a given channel gap and power, the temperatures at the inside of the plate surfaces, at the channel inlet and outlet, at the outside of the isolation material and ambient temperatures were measured.

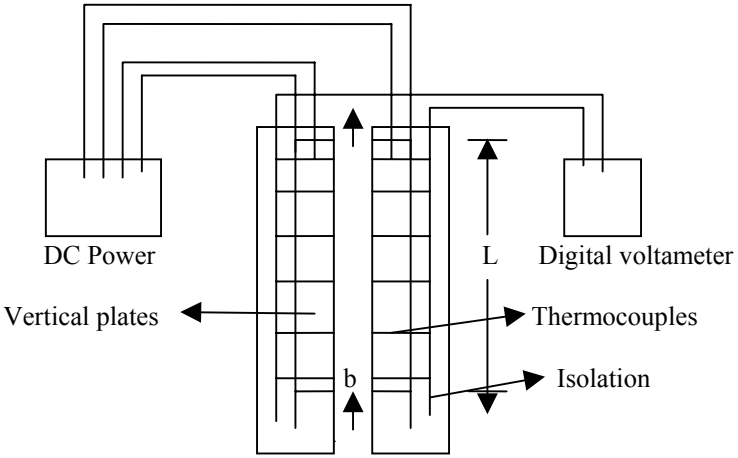


Figure - 1: Experimental apparatus

3. Experimental Data Analysis

A vertical rectangular channel with a height of L and a channel gap of b is heated through the walls, the fluid inside the channel starts to rise due to the decrease of the fluid density (**Fig.- 2**).

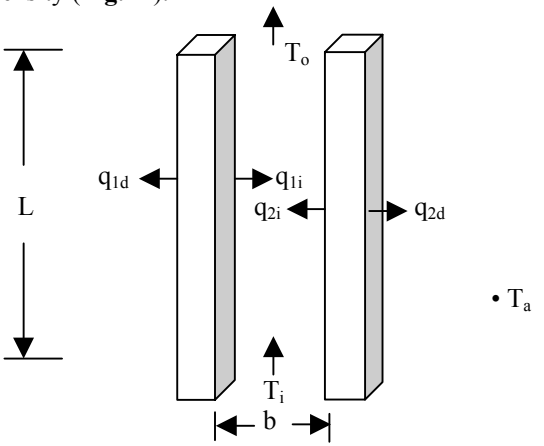


Figure - 2: Geometry of the vertical parallel plates and related parameters

In the analysis, the plate temperatures are the arithmetic means of the temperatures measured on the plates. The temperature of the fluid T_c is calculated as

$$T_c = \frac{T_i + T_o}{2},$$

where T_i and T_o is the fluid temperatures measured at the inlet and outlet of the channel.

The net heat given to the channel is taken as the heat produced at the plates minus the heat loss from outside of the plates.

Nusselt number, Nu, is calculated using net heat flux, q, mean temperature of the walls, T_w, temperature of fluid, T_c, channel gap, b, and the thermal conductivity of the fluid, k, as

Rayleigh number, Ra, is also calculated for each case.

$$Nu = \frac{qb}{k\left(T_w - T_c\right)},$$

where: g : Constant of gravitational acceleration,

β : Fluid thermal expansion coefficient,

$$Ra = \frac{g\beta q b^5}{L\nu\alpha k},$$

L : Plate height,

ν : Fluid kinematic viscosity,

α : Fluid thermal diffusivity,

The Nu and Ra numbers has been found by changing the plate power and channel width are shown in Table-1.

Table – 1: Experimental parameters

Power (w)	b= 2.1 mm		b= 4 mm		b= 6 mm		b= 8 mm	
	Ra	Nu	Ra	Nu	Ra	Nu	Ra	Nu
2	0.01088	0.3155	0.3262	0.5614	2.4708	0.8462	10.6290	1.11
4	0.01876	0.2930	0.7835	0.5763	4.3184	0.8979	18.5630	1.201
5	0.02187	0.2728	1.1340	0.5707	6.1054	0.9067	25.9450	1.233
7	0.03806	0.3557	1.5445	0.5918	8.7941	0.9156	40.0560	1.361
10	0.05099	0.3399	1.8972	0.5970	11.756	0.9382	53.5190	1.446
15	0.06229	0.2944	2.1620	0.5866	17.887	1.0363	79.8790	1.517
18	0.08798	0.3890	2.9845	0.6243	24.271	1.1399	94.9700	1.60
20	0.08583	0.3520					95.8330	1.615

The variation of Nusselt versus Rayleigh is given **Fig.-3**.

By using the least squares techniques for the values in **Fig.-3**

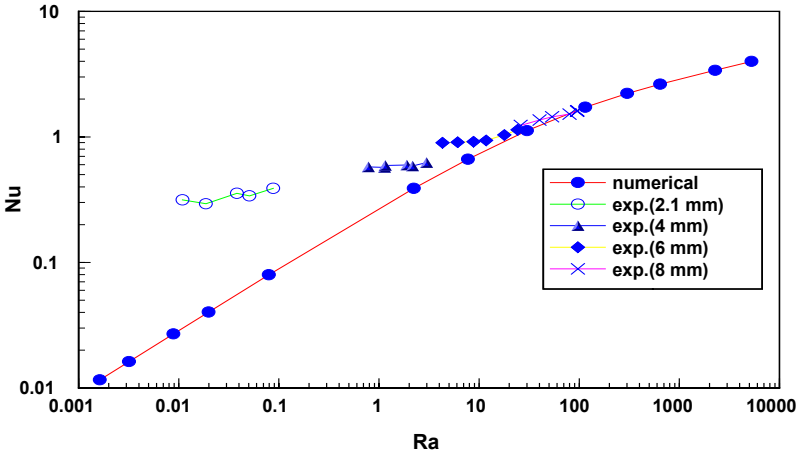


Figure – 3: Nusselt number as a function of Reyleigh number

$$Nu = A(Ra)^{B}\left(\frac{b}{L}\right)^{C}$$

equation can be found.

Here; A = 8.966
B = 0.1061
C = 0.5228
and R-square value is

$$R^2 = 0.8815$$

Simplified forms of Navier-Stokes equations for free convection cooling and incompressible flows were solved. Flow and temperature distributions inside the channel and some integral parameters, such as Nu number, were obtained (**10**). The results of this theory and the experimental study were compared. Numerical Nu and Ra is shown in **fig.- 3**.

4. Results

When the fluid is air and as the gap increased the experimental values approach to the theoretical values.

When the gap of the channel is narrow the Navier – Stokes equation can not be applicable since side layers interact each other and numerical solution results are different than the experimental values.

References

1. J. R. Bodoia, J. F. Osterle, " The Developent of Free Convection between Heated Vertical Plates", Jour. of Heat Transfer, 40-44, Feb. 1962.
2. W. Aung, L. S. Fletcher, V. Sernas, "Developing Laminar Free Convection Between Vertical Flat Plates with Asymmetric Heating", Int. Jour. Heat Mass Tranfer, Vol 15, 2293-2308, 1972.
3. A. M. Dalbert, F. Penot, J. L. Peube, "Convection Naturelle Laminaire dans un Canal Vertical Chauffe a Flux Constant", Int. Jour. Heat Mass Transfer, Vol. 24, No. 9, 1463-1473, 1981.
4. R.A. Wirtz, R. J. Stutzman, "Experiments on Free Convection between Vertical Plates with Symetric Heating", Jour. Heat Transfer, Vol. 104, 501-507, Aug. 1982.
5. T. Usui, M. Kaminaga, Y. Sudo, "Combined Fored and Free Convective Heat Transfer Characteristics in a Narrow Vertical Rectangular Channel with 2.5 mm in Gap Heated form Both Sides", Jour. Nucl. Scien. Tech., 26(6), 580-590, June 1989.
6. K. Kato, T. Takarada, H. Miyazaki, H. Sato, N. Nakagawa, "Heat in a Channel between Vertical Electronic Circuit Boards Cooed by Naturel Air Convection", Jour. Chem. Engin. Japan, Vol. 24, No. 5, 568-574, 1991.
7. D. Öner et al., TR-2 Safety Analysis Report, 1981 (Turkish).
8. H. İ. Arıkan, U. Adalıoğlu, "The New Version of TR-2 Transient Analaysis Code of AIREK-MOD and It's Application", CNAEM, TR 27, 1985 (Turkish).
9. B. Sevdik, "The Loss of Coolant Accident for The MTR Type Research Reactors", I.T.U., P.H.D.Thesis, 1994 (Turkish).
10. U. Adalıoğlu, H. İ. Arıkan, A. Baykal, H. Yavuz, "Flow and Cooling in Narrow Vertical Rectangular Channels", CNAEM, TR 333, 1997 (Turkish).

HEU-LEU MIXED CORE ANALYSIS FOR TR-2

TURGUT Mehmet Hulusi

TAEK, Çekmece Nuclear Research and Training Center, İstanbul-TURKEY

Abstract

Core conversion calculations have been carried out for different core loadings of the TR-2 reactor in order to find out the optimum design for the radioisotope production. Using HEU and LEU fuel elements in the mixed core also introduced additional peaking problems to be eliminated. Five group structure is used for the burnup dependent cross-section libraries that are generated by EPRI-CELL code. 2D diffusion-depletion code GEREBUS is used for the reactivity and burnup calculations.

New graphite and Be reflectors have been added to the periphery of the core to enhance the reactivity and the discharge burnup levels. Two water boxes have been placed inside the reactor core in order to increase the radioisotope production. The activity levels of the irradiation samples, core excess reactivities, power peaking factors, and the anti-reactivities of the control blades have been calculated for various loadings. After the optimization studies, it is found that these modifications have yielded higher production rates and a uniform distribution in the activity levels of the irradiation samples.

One irradiation and two standard LEU fuel elements have already been loaded to the TR-2 core without any operational or safety related problems. The agreement between the calculations and the experiments are quite good for the operated 13 cycles.

1. Introduction

TR-2 is a plate type research reactor with an operational power of 5 MW. The initial fuel has 93 % enrichment. Core conversion calculations have been carried out at ANL-USA [1, 2]. The initial core has been modified several times according to the irradiational and operational needs [3, 4, 5, 6].

The insertion of the first LEU elements inside the core was made at the 13^{th} cycle. Two fresh standart LEU elements were placed on the opposite sides at the periphery of the core. One fresh irradiatinal LEU element was also introduced on the other side at the periphery. This mixed core has been operated for 371.9 MWD's without any operational and safety related problems.

Most of the HEU fuels have already been burned above 40 %. The aim is to increase the discharge burnup of the available HEU fuels as much as possible before the shippent to USA. So, further combinations of the mixed HEU-LEU loading were planned according to the operational needs. Many different core

loadings have been tested for this purpose. The ones that have higher radioisotope production yields have been chosen for detailed studies.

2. Cross sectıon lıbrarıes and codes

Few group (5, and 10) burnup dependent cross-sections for HEU and LEU fuels were generated for different core regions using EPRI-CELL code [7]. The RABANL integral transport option of MC^2-2 code [8] was used to accurately account for the resonance self-shielding of U-238. Transport corrected effective cross-sections were used for the control rod regions [9].

Two and 3-dimensional diffusion and burnup calculations were carried out by DIF3D [10], REBUS-3 [11] and GEREBUS codes [12]. Control rods CR-1 and CR-2 were assumed to be partially inserted in the burnup calculations during each cycle in order to reflect the criticality adjustments made throughout the operations. Five group libraries were used in most of the calculations. Ten group structure was only used for the calculation of safety parameters.

3. Optımızatıon calculatıons

Optimization calculations have been carried out for the maximization of the radioisotope production, after the tracing calculations up to the 13^{th} cycle. All the available 12 Be elements and some additional graphite reflectors were used around the core in order to enhance the neutron fluxes in the reactor core and the discharge burnup levels of the fuel elements. Some of the water boxes which are at the periphery were moved inside the core in order to increase the radioisotope production. MoO_3 is irradiated in order to obtain Tc-99m isotope. TeO_2 is irradiated for the production of I-131 isotope.

Many core designs have been tested in order to find an optimum loading. The proposals of the reactor operation group were also calculated. The excess reactivities and related cycle lengths, control rod anti-reactivities, the values and positions of the power peaking factors (PPF's), and Mo-99 activities were calculated for every loading. The optimum positions found for the Tc-99m isotope turned out to be again the most suitable places for the I-131 production.

4. Comparison of the results with experiments

After long discussions, most of the cases were eliminated and the experiments were made for the chosen two core loadings which are given in Figure-1 (C13K and C13AD). The Mo activities at the water boxes and irradiation elements are also included in the figure. The calculated and measured excess reactivities and the control rod worths are given in Table-1. The absolute and relative thermal flux distribution are given in Figure-2. The thermal flux profiles along the axis passed over the water boxes are given for the two cases in Figure-3. Large increase in the fluxes can be observed for the case C13K which contains 2 water boxes inside the reactor core. Relative Mo activities given in Table-2 also

reflects this increase (% 66-130). As can be seen from these two tables and from Figure-2, the agreement between the calculations and the experiments are quite satisfactory. The deviations mainly come from the impossibility to reflect the control rod movements in the calculations.

5. Short discussion on the different core lodings

There are several possibilities for the TR-2 core loading and the optimum is based on the utilization of the reactor. Some of them may be eliminated due to lower activities or higher peaking values. For the moment C13K seems to be satisfactory for todays irradiational needs. C13HB is also a possibility for the increased demads due large number of irradiation positions. C13F3 is another possibility for higher activities. Decision will be made according to that days conditions.

6. Final remarks

Results of these mixed core and optimization calculations can be summarized as follows :

- The agreement between calculations and the experiments seems to be reasonable.
- There are many loading possibilities for the TR-2, and the decision can be made according to irradiational needs or other utilization factors.
- Radioisotope production can be maximized by new loading patterns. Especially insertion of water boxes inside the reactor will increase the yields up to % 66-130. This is also verified by the experiments.
- Optimization studies have yielded higher production rates and in addition a uniform distribution in the activity levels of the irradiation samples.
- Replacing Be and graphite reflectors around the core will also inrease the production rates and the discharge burnup levels.
- The discharge burnup levels of the HEU elements can further be increased only by the mixed core loading.
- The PPF's become more important in mixed core analysis. Loading patterns should be adjusted for each step for the minimization of the peaks untill the full conversion to LEU equilibrium core.
- No operational or safety related problems were observed during the initial phase of the mixed core during 371.9 MWD's of operation.

Table-1: Calculated and measured reactivities for the 2 core loadings

	C13K		**C13AD**	
	Calculations	Measurements	Calculations	Measurements
Core excess reactivity [pcm]	**3744**	**3720**	**6868**	**6867**
SR-1 worth [pcm]	5822	4503	6219	4511
SR-2 worth [pcm]	5755	5231	5936	4294
CR-1 worth [pcm]	5847	3991	6051	4402
CR-2 worth [pcm]	5748	4146	5734	4394

Table-2: Relative Mo activities for the 2 core loadings

Calculation name		% increase			
C13K	**C13AD**	Calculations	Average	Measurements	Average
WB45 /	WB25	66.0	68.2	68.2	66.1
WB65 /	WB85	70.5		64.0	
WB45 /	WB23	125.1	130.2	-	-
WB65 /	WB83	135.3		-	
IE55 /	IE55	15.7	12.0	-8.0	3.4
IE57 /	IE57	8.3		14.8	

^{22}W	^{32}WB	^{42}Be	^{52}Be	^{62}Be	^{72}DIF	^{82}W
^{23}C	^{33}Be*	^{43}S115	^{53}S113	^{63}S106	^{73}Be*	^{83}C
^{24}C	^{34}S116	--- C011 ---	^{54}S104	--- C013 ---	^{74}S118	^{84}C
^{25}Be	^{35}LS01	^{45}WB **16470**$^{+}$	I002 0 0 **15094**	^{65}WB **16420**	^{75}LS02	^{85}Be
^{26}C	^{36}S105	--- C018 ---	^{56}S103	--- C014 ---	^{76}S117	^{86}C
^{27}C	^{37}Be*	^{47}S11 2	L101 0 0 **8120**	^{67}S11 0	^{77}Be*	^{87}C
^{28}W	^{38}C	^{48}Be	^{58}Be	^{68}Be	^{78}C	^{88}W

C13K

^{22}W	^{32}C	^{42}Be	^{52}Be	^{62}Be	^{72}DIF	^{82}W
^{23}WB **7316**	^{33}Be*	^{43}S110	^{53}S112	^{63}S115	^{73}Be*	^{83}WB **6979**
^{24}Be	^{34}S116	--- C013 ---	^{54}S101	--- C017 ---	^{74}S118	^{84}Be
^{25}WB **9921**	^{35}S117	^{45}S114	I001 0 0 **13051**	^{65}S111	^{75}S105	^{85}WB **9628**
^{26}C	^{36}LS01	--- C012 ---	^{56}S108	--- C015 ---	^{76}LS02	^{86}C
^{27}C	^{37}Be*	^{47}S10 6	L101 0 0 **7501**	^{67}S10 4	^{77}Be*	^{87}C
^{28}W	^{38}C	^{48}Be	^{58}Be	^{68}Be	^{78}C	^{88}W

C13AD

^{28}W	^{27}C	^{26}WB **7630**	^{25}WB **9222**	^{24}Be	^{23}C	^{22}W
^{38}C	^{37}Be*	^{36}S105	^{35}LS01	^{34}S116	^{33}Be*	^{32}WB
^{48}Be	^{47}S112	--- C018 ---	^{45}S103	--- C011 ---	^{43}S115	^{42}Be
^{58}Be	LI01 0 0 **7701**	^{56}S109	I002 0 0 **12502**	^{54}S104	^{53}S113	^{52}Be
^{68}Be	^{67}S110	--- C014 ---	^{65}S102	--- C013 ---	^{63}S106	^{62}Be
^{78}C	^{77}Be*	^{76}S117	^{75}LS02	^{74}S118	^{73}Be*	^{72}DIF
^{88}W	^{87}C	^{86}WB **7570**	^{85}WB **9168**	^{84}Be	^{83}C	^{82}W

C13AB

^{28}W	^{27}C	^{26}C	^{25}Be	^{24}C	^{23}C	^{22}W
^{38}C	^{37}Be*	^{36}S105	^{35}LS01	^{34}S116	^{33}Be*	^{32}WB
^{48}Be	^{47}S112	--- C018 ---	^{45}S103	--- C011 ---	^{43}S115	^{42}Be
^{58}Be	LI01 0 0 **8875**	^{56}S109	I002 0 0 **13085**	^{54}S104	^{53}WB **14169**	^{52}Be
^{68}Be	^{67}S110	--- C014 ---	^{65}S102	--- C013 ---	^{63}S106	^{62}Be
^{78}C	^{77}Be*	^{76}S117	^{75}LS02	^{74}S118	^{73}Be*	^{72}DIF
^{88}C	^{87}C	^{86}C	^{85}Be	^{84}C	^{83}C	^{82}C

C13BB

^{28}C	^{27}C	^{26}Be	^{25}Be	^{24}Be	^{23}C	^{22}C
^{38}C	^{37}LS01	^{36}S106	^{35}WB **14057**	^{34}S112	^{33}S105	^{32}WB
^{48}Be	^{47}S115	--- C018 ---	^{45}S102	--- C011 ---	^{43}S110	^{42}Be
^{58}Be	WB **12233**	^{56}S109	I002 0 0 **12257**	^{54}S111	^{53}WB **14991**	^{52}Be
^{68}Be	^{67}S116	--- C014 ---	^{65}S103	--- C013 ---	^{63}S113	^{62}Be
^{78}C	^{77}LS02	^{76}S118	^{75}WB **14136**	^{74}S104	^{73}S117	^{72}DIF
^{88}C	^{87}C	^{86}Be	^{85}Be	^{84}Be	^{83}C	^{82}C

C13HB

^{28}C	^{27}C	^{26}Be	^{25}Be	^{24}Be	^{23}C	^{22}C
^{38}C	^{37}S106	^{36}S105	^{35}LS01	^{34}S116	^{33}S110	^{32}WB
^{48}Be	^{47}S113	--- C018 ---	^{45}WB **15756**	--- C011 ---	^{43}S102	^{42}Be
^{58}Be	S111	^{56}S107	WB **18279**	^{54}S114	^{53}S109	^{52}Be
^{68}Be	^{67}S104	--- C014 ---	^{65}WB **15755**	--- C013 ---	^{63}S103	^{62}Be
^{78}C	^{77}S115	^{76}S117	^{75}LS02	^{74}S118	^{73}S112	^{72}DIF
^{88}C	^{87}C	^{86}Be	^{85}Be	^{84}Be	^{83}C	^{82}C

C13F3

$^{+}$) :	Mo activity	W:	Pool Water	S115:	HEU Standart fuel element No.115
C:	Graphite block	WB:	Water Box	LS01:	LEU Standart fuel element No.011
Be:	Be block	DIF:	Dry Irradiation Facility	I002:	HEU Irradiation fuel element No.002
Be*:	Be block with hole	C011:	HEU Control fuel element No.011	LI01:	LEU Irradiation fuel element No.001

Figure-1: TR-2 core loadings and calculated Mo activities

33 Be*	4.708 **727** 642	4.756 **734** 665	4.635 **715** 607	73 Be*
3.922 **605** 603	5.119 **790** -	5.256 **811** 707	5.066 **782** -	3.880 **599** 481
3.048 **470** 408	WB	6.479 **1000** 1000	WB	3.035 **468** 327
2.851 **440** 475	3.475 **536** -	4.027 **621** 617	3.329 **514** -	2.861 **442** 355
37 Be*	3.358 **518** 560	3.106 **479** 611	3.326 **513** 433	77 Be*

C13K

33 Be*	5.022 **880** 612	5.080 **890** 646	4.986 **873** 611	73 Be*
4.370 **765** 511	4.933 **864** -	5.710 **1000** 752	5.685 **996** -	4.305 **754** 489
3.358 **588** 451	4.512 **790** 639	5.576 **977** 1000	4.455 **780** 533	3.227 **565** 402
2.228 **390** 258	2.775 **486** -	3.725 **652** 494	2.846 **498** -	2.172 **380** 212
37 Be*	2.772 **485** 424	2.736 **479** 535	2.792 **489** 375	77 Be*

C13AD

4.708 → Thermal flux/10^{13} (Calculation)
727 → Relative thermal flux (Calculation)
642 → Relative thermal flux (Experimental)

Figure-2: Absolute and relative thermal flux distributions for the 2 core loadings

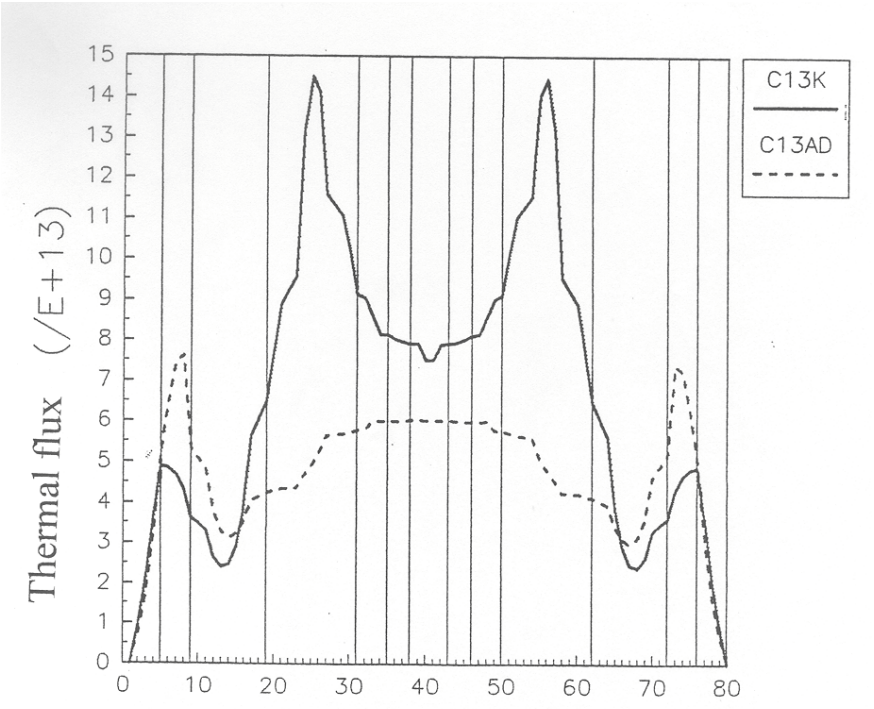


Figure-3 : Thermal flux profiles for the 2 core loadings

References

1. T. Aldemir, M.H. Turgut, M.M. Bretscher, J.L. Snelgrove, «A Feasibility Study Con-cerning the Conversion of the TR-2 Reactor from Using Highly Enriched Uranium to Light Enriched Uranium», ÇNAEM-R-217 (1982)
2. M.H. Turgut, T. Türker, «Core Conversion Calculations for the TR-2 Reactor; Part A : Neutronics Calculations», ÇNAEM-AR-308 (Feb., 1993)
3. M.H. Turgut, «Neutronic Calculations of the TR-2 Reactor Present Core», ÇNAEM Technical Report No : 30 (Sept., 1986)
4. M.H. Turgut, «Density Search Calculations for the Siliside Fuels», ÇNAEM Technical Report No : 37 (Dec., 1986)
5. M.H. Turgut, «Optimization of the Usage of the Remaining HEU Fuel», ÇNAEM Tech-nical Report No : 42 (Sept., 1987)
6. M.H. Turgut, G. Üstün, «Calibration Calculations for the TR-2 Reactor», ÇNAEM-AR-245 (Apr., 1988)

7. [B.A. Zolotar, et.al.,«EPRI-CELL Code Description», Advanced Recycle Methodology Program System Documentation, Part II, Chapter 5, Electric Power Research Institute (Sept., 1977)
8. H. Henryson III, B.J. Toppel, and C.G. Stenberg, «MC^2-2 : A Code to Calculate Fast Neutron Spectra and Multigroup Cross-Sections», Argonne National Laboratory Report, ANL-8144 (June, 1976)
9. M.M. Bretscher, «Blackness Coefficients, Effective Diffusion Parameters, and Control Rod Worths for Thermal Reactors», Argonne National Laboratory Report, ANL/RERTR /TM-5 (Sept., 1984)
10. K.L. Derstine, «DIF3D: A Code to Solve One-, Two-, and Three-Dimensional Finite-Difference Diffusion Theory Problems», Argonne National Laboratory Report, ANL-82-64 (Apr., 1984)
11. [B.J. Toppel, «A Users Guide for the REBUS-3 Fuel Cycle Analysis Capability», Ar-gonne National Laboratory Report, ANL-83-2 (March ,1983)
12. M. Console, A. Daneri and E. Salina, «EREBUS: A Multigroup Diffusion Program in two Dimension», FN-E-88 (FIAT, 1967) (GEREBUS is GKSS version of EREBUS code)

PUBLIC AWARENESS ON NUCLEAR ENERGY

Aykol Fethiye, Özkan Reşat, Atila Berrak, Hangül Gökhan,
[1]Aksu Levent M.

Turkish Atomic Energy Authority, Ankara, Turkey
[1]Gazi University, Ankara, Turkey

The Globalization process resulted from the rapid scientific, technological, economical and political developments made the sustainability a very important issue. One of the important problems created by the globalization process is the energy problem. Energy is a must for all the countries of the world and nuclear energy is an integral part of it. Nuclear energy is a sophisticated and proven technology in the production of electricity. There are 438 nuclear power plants in 32 different countries producing 18'% of the total electricity demand of the World. However in spite of putting its hallmark to the twentieth century as the "atom era" it still creates grave public reaction in many countries in the world.
One of the most important problems of the nuclear industry is the preparation, application and sustaining the necessary programs for the public acceptance of nuclear energy. The nuclear programs faced grave reaction from the start. This was partly due to the tragic memoirs of the atomic bombs dropped on Hiroshima and Nagasaki and partly due to the sensationalism of the mass media. Chernobyl accident, one of the biggest global tragedies coupled with those, caused the problem to be much more aggravated. TMI accident was a very big set back for the use of nuclear energy. However the Chernobyl, which was to take place seven years latter absolutely, destroyed the public trust that had taken so long to re-establish after TMI. The accident took place in complete accordance with the disaster scenarios of the anti nuclear lobby with a loss of human life. Most people thought that it was the end of the nuclear programs. However the situation did not turned out as they expected. Some Western countries used it as an opportunity to inform the public in a much effective manner. For instance in countries like England this opportunity was taken to enlighten the public about the nuclear related issues. They include such information to their educational curricula. They strictly emphasized that such an accident was not possible in Western reactors.

The situation in Turkey.
The concerns and the fears of the public against the nuclear related issues mainly stem from the fear of nuclear power plants and associated accidents. Before going into this I would like to brief you on the general attitude of the Turkish media.
The way that the Turkish media deal with the nuclear related issues is unique. The anti nuclear lobby became particularly effective after the Chernobyl accident and

they started an anti nuclear campaign with the claims that the Turkish people were forced to drink radioactive tea after the Chernobyl accident. Unfortunately this campaign found certain support among the technocrats as well. The opinions of the other countries became balanced within a few years. However the news published in one of the major newspapers of Turkey in 1992 took the Chernobyl accident at the top of the agenda. We call this second Chernobyl incident. This caused many of the impartial people in the country to take a negative stance against the nuclear energy.

The anti-nuclear lobby waged a very effective campaign against the construction of a nuclear power plant in Akkuyu region. The supporters of anti nuclear chorus went to that region in the protest organized at the anniversary of the atom bomb dropped on Hiroshima. They never mentioned the fact that Japan, who had the bitterest experience with the nuclear power, had 52 nuclear power plants on its soil. Nevertheless the lobby was successful and the Turkish government had to postpone the Akkuyu project. However the government stated that the postponement was due to economic concerns.

The anti nuclear opinions are generally centered on the view that Turkey has other means of energy and she doesn't need nuclear energy at the moment. The effect of the Chernobyl is exaggerated beyond any proportion. They also claim that many countries are giving up nuclear energy as an option for the energy demand. The danger of the nuclear waste, the destruction of nature and the earthquake susceptibility of Akkuyu region are continuously emphasized in a very distorted manner.

The Turkish press is open to influence and close to censure since it acts upon the general principle of "free news, secret source and free comment ". The way of conveying news mostly contains personal comments. For instance as we witnessed during the Chernobyl accident a news concerning the radiation in tea is generally published with an article telling the adverse effects of radiation together with a picture of a baby born with a handicapped body.

Major part of the Turkish press adapts sensational newsman ship and draws its strategies accordingly. This is the natural consequence of the race to get the biggest portion from the advertisement cake. Therefore they prefer the sensational approach to the news rather than the approach of truth. This choice becomes highly apparent in nuclear related issues. An article concerning the nuclear energy is generally published with a picture of an environmental disaster or a nuclear accident. The problem of nuclear waste, Chernobyl accident, its victims and its environmental impact and nuclear weapons are some of their most popular material.

The comments are generally made by the writers of paper. The pressmen are mainly affected by three factors, namely the source of the news, the educational level of the pressman and his/her mission or worldview.

The source of the news is important because if it is an environmental organization the way of presenting news is based upon the most tragic developments possible. If the source is economically oriented then the economic dimensions of the event become apparent. If it is a scientific source then the presentation is multi sided containing the environmental advantages and disadvantages, its impact upon the human health, loss and profit balance.

The education of the newsman is of great importance. Although nuclear energy is a highly technical subject most of the reporters working in the media are social subject oriented. They either can't get grasp on the subject and report the news accordingly or misunderstand the point and the resulting news becomes inadequate and dismays the public.

The mission of the writer is also important. A writer who undertakes a green or environmental protection mission, feels obliged to display an anti nuclear approach no matter how much his or her logic drives him or her to investigate the event.

The attitude of the government also determines the approach of the media. If the government is pro-nuclear and the supporters display pro-nuclear and the opposition, which generally constitute the majority, display anti-nuclear approach.

The media, which considers itself as the supervisor on behalf of the public, takes the events in very critical manner. The dose of this criticism increases in a sensitive issue such as nuclear energy and the news are presented in the eyes of the environmental organizations.

However we have to accept one very important fact. The world had a very unfortunate Chernobyl accident and Turkey was affected from it in a very bad way. The reason why media adapts such a sentimental and opposing manner towards nuclear related issues mainly stems from it.

As we summarized the attitude of the Turkish press, we can now dwell upon what and why they are against or for the nuclear energy as a whole. The main criticisms and the fears against the nuclear energy, which are centered around the nuclear power plants, are as follows:

- High installation, maintenance and dismantling costs,
- Risk of accident,
- Waste management,
- The economic crisis prevailing in Turkey at present,
- The high-energy production cost,
- The prolonged period of construction of a nuclear plant,
- The concept of the "technology left by the whole world " since Germany and Sweden decided to leave the nuclear energy in their energy production policies,
- Adverse impact on environment and human health,
- The risk of earthquake,
- Having a NPP does not mean having nuclear technology,
- The risk of developing atomic weapons,

- There are other less harmful ways in producing energy,
- The transport of nuclear waste through Turkish straights (which is highly popular nowadays).

The opinions in favor of the nuclear power are:

- It is clear and safe,
- It is the only viable alternative for the anticipated energy gap of the country in future.

The opinions expressed in the media reveal that the people are not fully cognizant of the other uses of nuclear energy and nuclear technology such as in medicine and agriculture.

I would like to show you some of the news appeared in the Turkish media as a striking example of the biased views and the views in supports of the nuclear power



NO TO NPPs. TAKE GOKOVA AS AN EXAMPLE

Note: Gokova is a thermal power plant . This card was distributed to almost all sections of the society . This is an striking example of the gross distortion of the facts which the anti nuclear looby used in its propaganda

All these show the importance of starting necessary studies to inform the public on nuclear related issues. However there are certain difficulties as regards to it. The main problems are the following:

1. To inform the public about the high level and sophisticated technology involved with the nuclear applications is extremely difficult.
2. The budgets of the related authorities to cope with such a gigantic task is highly inadequate.
3. There are certain bureaucratic barriers against the people involved.

The experience gained from other countries showed us that the price to be paid for not dealing against this sort of anti propaganda on time is very high. Therefore timely intervention against the anti nuclear chorus is one of the key factors to succeed against them.
One of the most important activities of TAEK relating to the human performance is public information, which is the major obstacle against the future of the nuclear energy. The main activities of TAEK related to public information are as follows:

- Various publications (booklets, brochures and periodicals),
- A White paper and a related CD distributed to the wide section of the society ranging from the local authorities to high ranking officials,
- School and group visits,
- TV programs,
- Meetings, congress, conferences and seminars. The recent seminars given by the

IAEA and TAEK experts to the parliamentarians and two major universities of the country were highly successful. Most of the parliamentarians who were not able to attend this seminar asked for the related documents from TAEK. There are also demands from the various universities and local governors of the country for the organization of the similar seminars in their cities.
There was a preliminary survey concerned, with the nuclear energy and technology, on university students and university personnel. We are planning to extend this survey in scope and apply it to the policymaking bodies, governmental and non-governmental organizations, military and civil personnel, secondary education institutes in other words almost all sections of the society. Turkish Statistical Institute promised that they would help us in the evaluation of the resulting data.
The writings and articles published in Turkish press regarding to nuclear related issues are carefully collected by the Department of Research, Development and Coordination on daily basis. The articles, which require a response from TAEK, are immediately answered. We are also following the TV programs made on the same subjects (and attending them when necessary) asking the records of the programs from the related channels.
The points, which are to be taken into account when dealing with the public as regards to nuclear issues, are the following:

- Be friendly and talk friendly,
- Don’t forget the target needs to be informed,
- Don’t describe but explain using healthy discussions,
- Don’t simplify but clarify,
- Don’t try to use the statistics but tell the truth,
- Don’t use confusing numbers but give examples,

- Don't hesitate, be stable,
- Don't use details and decide on a central message.

Although Turkish Atomic Energy Authority (TAEK) has carried out similar studies for a long time, there was a TAEK and IAEA initiated TC project entitled "Public Awareness on the Nuclear Field" in order to carry out these activities in a much more coordinated manner. There are many ways to wage an effective campaign against the anti nuclear fringes. One of the most effective ways is establishing an exhibition center on nuclear related issues. This will enable us to show the facilities and related problems in a visualized manner. The biggest goal of this project is establishing an exhibition center, which would extremely useful to cope with the anti nuclear propaganda disseminated by various quarters. As it is known that the people believe what they see, more than what they hear.

The activities planned within the scope of the project on Public awareness in nuclear field are as follows:

- To carry out continuous public education programs,
- To include the nuclear related issues in school curricula,
- To prepare excursion tours to Çekmece Nuclear Research and Training Center to show people our nuclear research reactor and other facilities,
- To emphasize the advantage of the nuclear technology comparing it with other means of obtaining energy,
- To establish close ties with the parliamentarians and other decision making bodies,
- To form good relations with media and give them first hand unbiased facts,
- To publish necessary documents appealing to the all sections of the society,
- To use all forms of communication to convey our message such as making films distributing CDs and using Internet,
- To prepare an extensive survey form to be distributed to parliamentarians, the local authorities, high schools, NGOs, civil and military personnel,
- To establish an exhibition center open to the public.

Some of the studies have been started and will continue in the future.
Thank you very much for your attention.

References

1. Nuclear Energy and Information "Informing Parliamentarians on Nuclear Energy" Seminar, Prague, Czech Republic, 28-30 November 1994.
2. B.Gül Göktepe, The investigation of the Behavior of Mass Media against the NPPs (Personal communications).

Basic problems of nuclear physics

CHARGED-PARTICLE TRANSFER REACTIONS AND NUCLEAR ASTROPHYSICS PROBLEM

[1]*Artemov S.V,* [1]*Yarmukhamedov R.,* [1]*Yuldashev B.S.*
[2]*Burtebaev N.,* [2]*Duysebaev A.D.,* [2]*Kadyrzhanov K.K.*

[1]Institute of Nuclear Physics, Tashkent, Uzbekistan
[2]Institute of Nuclear Physics NNC PK, Almty, Kazakhstan

1. Introduction

A reliable estimation of rates of different nuclear astrophysical processes responsible for the light elements abundance (for example, $^{6,7}Li$, *Be*, *B, C, N,* O etc.) is one of the most actual problems of the modern nuclear astrophysics [1]. In this turn, solution of this problem is impossible without obtaining the very-low energy cross sections or equivalently its the astrophysical S –factors for such reactions as $^{2,3}H(\alpha,\gamma)^{6,7}Li$, $^{3}He(\alpha,\gamma)^{7}Be$, $^{7}Be(p,\ \gamma)^{8}B$, $^{12,13}C(p,\ \gamma)^{13,14}N$, $^{12}C(\alpha,\gamma)^{16}O^{*}$ etc. For example, the cross sections for the $^{2,3}H(\alpha,\gamma)^{6,7}Li$ and $^{7}Be(p,\ \gamma)^{8}B$ reactions at solar energies *(~20 keV)* play a crucial role for determination of the $^{6,7}Li$ and ^{8}B creations in the Big-Bang nucleosynthesis and in the solar neutrinos, respectively[2-6].

The impressive improvements in our understanding of these processes have been made in the past decades [1-8]. For example, it is now revealed that electron neutrinos ($\nu_e^{'}s$) obtained from the $^{7}Be(p,\ \gamma)^{8}B$ reaction in the Sun oscillate into $\nu_\mu^{'}s$ and/or $\nu_\tau^{'}s$ [8]. However, some uncertainties connected with both the extrapolation of measured cross sections to rather low energies region and the theoretical predictions for them still exist and they may considerably influence upon the predictions of the solar model [1]. Note that the theoretical predictions are the consistently 3 and 1.7 times higher than the measured neutrino fluxes observed in the Homestake and GALLEX experiments, respectively.

One of possible solutions of this problem is based on the idea about the fact that due to strong Coulomb repulsion of colliding particles and rather low value of the binding energy of the captured particles (proton or α -particle) at stellar energies the direct capture reaction of astrophysical interest proceeds through the tail of the overlap integral, that in this tail region is completely determined by the Coulomb interaction, the binding energy and the respective asymptotic normalization coefficient (ANC) (or equivalently its the nuclear vertex constant (NVC)) [9]. The $^{2,3}H(\alpha,\gamma)^{6,7}Li$, $^{7}Be(p,\ \gamma)^{8}B$ and $^{12}C(p,\ \gamma)^{13}N$ reactions are typical examples for such direct capture reactions. From here it follows that astrophysical S –factors for such direct processes can be correctly determined through indirect measurements of ANC's(or NVC's) for the virtual decays $^{6}Li\rightarrow \alpha+ d$, $^{7}Li\rightarrow \alpha+ t$,

$^{8}B \rightarrow p + {}^{7}Be$ and $^{13}N \rightarrow p + {}^{12}C$ that may be obtained from peripheral proton and α-particle transfer reactions [10-12]. A use of these ANC' (or NVC's) and others as an input parameter for the direct amplitudes of different capture reactions has now been done in works [13-20].

In this review work we will summarize results of the low-energy cross sections (or astrophysical *S*- factors) for the $^{2,3}H(\alpha,\gamma)^{6,7}Li$, $^{7}Be(p,\gamma)^{8}B$ and $^{12}C(p,\gamma)^{13}N$ reactions obtained within ANC approach as well as note areas where additional experimental and theoretical works are called for. At first below we briefly describe the theoretical approach that has usually been used to extract the ANC's.

2. Three-body model and DWBA

Here we present the three-body model of consideration of the peripheral charged particle transfer reaction

$$\alpha + (\beta\gamma) \rightarrow (\alpha\gamma) + \beta, \qquad (1)$$

where γ is a transferred particle. Our consideration is based on the assumptions that (i) near the main peak in the angular distribution of the reaction (1) a dominant contribution gives part of the common amplitude of the reaction (1) having the nearest to the physical region ($-1 \le z \le 1$) singularity at $z \rightarrow \zeta$, where $z = -\mathbf{k_i}\,\mathbf{k_f}/k_i\,k_f = \cos\theta$, ($\mathbf{k_i}$ and $\mathbf{k_f}$ is the momentum of particle $\alpha(\beta)$ in c.m.s. of the reaction (1) and θ is the scattering angle in the c.m.s.) and ζ is the nearest singularity generated by the pole diagram (Fig.1*a*) describing transfer mechanism of the particle γ, (ii) rescattering effects in the initial and final states of the reaction (1) must be taken into account within the optical model and, at last, (iii) all possible subsequent Coulomb rescattering in the intermediate state, which are described by diagrams Fig.1*b,c* and etc, can be taken into account within the dispersion theory of the direct transfer reaction.

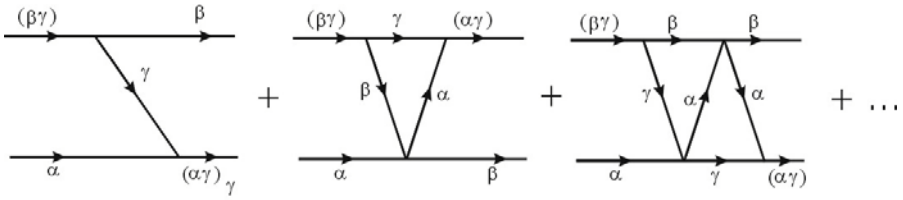


Fig.1. Diagrams describing transfer of the particle γ and taking into account all possible subsequent Coulomb rescattering of the particles α, $\beta$and γ in the intermediate state.

As it is shown in works [22,23], within the framework of the three-body Faddeev's formalism the leading singular at $z \rightarrow \zeta$term of the reaction (1) amplitude in the momentum representation is given as

$$M^{TBDWPA} = M^{DWBA} + \Delta M\,, \tag{2}$$

$$M^{DWBA} = \left\langle \Psi^{(-)}_{\mathbf{k_f}} I_{\alpha\gamma} \left| V^N_\alpha + \Delta V^C_\beta \right| I_{\beta\gamma}\, \Psi^{(+)}_{\mathbf{k_i}} \right\rangle, \tag{3}$$

$$\Delta M = \left\langle \Psi^{(-)}_{\mathbf{k_f}} I_{\alpha\gamma} \left| \Delta V^C_\beta G_C \Delta V^C_\alpha \right| I_{\beta\gamma}\, \Psi^{(+)}_{\mathbf{k}_i} \right\rangle, \tag{4}$$

where $I_{\alpha\gamma}$ ($I_{\beta\gamma}$) is the overlap integral in the momentum representation for the wave functions of the bound state ($\alpha\gamma$) (($\beta\gamma$)) in the (α+γ)-((β+γ)-) configuration depending on the relative momentum $\mathbf{q}_{\alpha\gamma}$($\mathbf{q}_{\beta\gamma}$) of the center of mass of nuclei α and γ (β and γ), $\Psi^{(+)}_{\mathbf{k_i}}(\Psi^{(+)}_{\mathbf{k_f}})$ is the distorted waves in the initial (final) state of the reaction (1) in the momentum representation, $V^N_\beta(V^N_\alpha)$ is the nuclear potential between particles of the pair ($\alpha\gamma$) (($\beta\gamma$)), $\Delta V^C_\beta = V^C_\beta + V^C_\gamma - V^C_f, \Delta V^C_\alpha = V^C_\alpha + V^C_\gamma - V^C_i$, V^C_β, V^C_γ and V^C_α are the Coulomb potential between particles of the pairs ($\alpha\gamma$), ($\alpha\beta$) and ($\beta\gamma$) respectively, $V^C_i(V^C_f)$ is an optical Coulomb potential in the initial (final) state of the reaction (1) and G_C is the three-particle (α, β and γ) Green's function. In the expression (2)-(4) the amplitude M^{DWBA} is so-called the "post"-form of the DWBA amplitude, which is the sum of zeroth and first terms of the expansion of a transition operator in M^{TBDWPA} in a series in ΔV^C_β. The amplitude ΔM involves high-orders (the second and more) of the terms of such an expansion in $\Delta V^C_{\alpha,\beta}$.

2.1. Modified "post"-form of DWBA

We briefly consider a use of the DWBA for extracting ANC from an analysis of the peripheral transfer reaction (1). Usually the radial overlap integral $I_{\sigma\delta;l_{\sigma\delta}j_{\sigma\delta}}(r_{\sigma\delta})$ (σ and δ =α and γ or β and γ) is replaced by model wave function of the bound state (σδ) as

$$I_{\sigma\delta;l_{\sigma\delta}j_{\sigma\delta}}(r_{\sigma\delta}) = S^{1/2}_{\sigma\delta;l_{\sigma\delta}j_{\sigma\delta}} \varphi_{n_{\sigma\delta}l_{\sigma\delta}j_{\sigma\delta}}(r_{\sigma\delta}.)\,, \tag{5}$$

where $\varphi_{n_{\sigma\delta}l_{\sigma\delta}j_{\sigma\delta}}(r_{\sigma\delta})$ is solution normalized to unity of the one-particle radial Schrdinger equation with the Woods-Saxon potential, $l_{\sigma\delta}(j_{\sigma\delta})$ is the orbital angular (total) momentum of the particles σ and δ in the bound state (σδ), $S_{\sigma\delta;l_{\sigma\delta}j_{\sigma\delta}}$ is the spectroscopic factor for the bound state (σδ) in the (σ+δ)-configuration with quantum numbers $l_{\sigma\delta}$ and $j_{\sigma\delta}$. Note that the ANC $C_{\beta\gamma;l_{\beta\gamma}j_{\beta\gamma}}$ determines the

normalization of the tail of the radial overlap integral $I_{\beta\gamma;l_{\beta\gamma}j_{\beta\gamma}}(r_{\beta\gamma})$ at $r_{\beta\gamma} > R_N$ by relation

$$I_{\beta\gamma;l_{\beta\gamma}j_{\beta\gamma}}(r_{\beta\gamma}) \approx C_{\beta\gamma;l_{\beta\gamma}j_{\beta\gamma}} \frac{W_{-\eta_{\beta\gamma};l_{\beta\gamma}+1/2}(2\kappa_{\beta\gamma}r_{\beta\gamma})}{r_{\beta\gamma}}, \qquad (6)$$

where R_N is the nuclear interaction radius between particles β and γ, $W_{-\eta_\beta;l_{\beta\gamma}j_{\beta\gamma}}(2\kappa_{\beta\gamma}r_{\beta\gamma})$ is the Whittaker function, which describes also the asymptotic behavior of the bound state wave function $\varphi_{n_{\beta\gamma}l_{\beta\gamma}j_{\beta\gamma}}(r_{\beta\gamma})$, $\kappa_{\beta\gamma} = \sqrt{2\mu_{\beta\gamma}\varepsilon_{\beta\gamma}}$., $\varepsilon_{\beta\gamma}$ is the binding energy of the bound state *(βγ)* in the *(β+γ)*-channel, $\mu_{\beta\gamma}$ is the reduced mass of particles β and γ, $\eta_{\beta\gamma}$ is the Coulomb parameter for the bound state *(βγ)* .The ANC $C_{\beta\gamma;l_{\beta\gamma}j_{\beta\gamma}}$ is related to the NVC $G_{\beta\gamma;l_{\beta\gamma}j_{\beta\gamma}}$ for the virtual decay *(βγ)→β+γ* by [9]

$$G_{\beta\gamma;l_{\beta\gamma}j_{\beta\gamma}} = -i^{\eta_{\beta\gamma}+l_{\beta\gamma}} \frac{\sqrt{\pi}}{\mu_{\beta\gamma}} C_{\beta\gamma;l_{\beta\gamma}j_{\beta\gamma}}, \qquad (7)$$

where the antisymmetrization factor due to identical nucleons absorbed in the ANC.

The differential cross section in the "post"-form of the DWBA is parameterised in terms of the product of the $S_{\beta\gamma;l_{\beta\gamma}j_{\beta\gamma}}$ and $S_{\alpha\gamma;l_{\alpha\gamma}j_{\alpha\gamma}}$ and can be written as [23]

$$\frac{d\sigma^{DWBA}}{d\Omega} = \sum_{j_{\alpha\gamma}\ j_{\beta\gamma}} C^2_{\beta\gamma;l_{\beta\gamma}\ j_{\beta\gamma}} C^2_{\alpha\gamma;l_{\alpha\gamma}\ j_{\alpha\gamma}} R^{DWBA}_{l_{\beta\gamma}\ j_{\beta\gamma}\ l_{\alpha\gamma}\ j_{\alpha\gamma}}, \qquad (8)$$

$$R^{DWBA}_{l_{\beta\gamma}j_{\beta\gamma}l_{\alpha\gamma}j_{\alpha\gamma}} = \frac{\sigma^{DWBA}_{l_{\beta\gamma}j_{\beta\gamma}l_{\alpha\gamma}j_{\alpha\gamma}}}{b^2_{\beta\gamma;l_{\beta\gamma}j\beta\gamma}b^2_{\alpha\gamma;l_{\alpha\gamma}j_{\alpha\gamma}}}, \qquad (9)$$

where $\sigma^{DWBA}_{l_{\beta\gamma}j_{\beta\gamma}l_{\alpha\gamma}j_{\alpha\gamma}}$ is the reduced DWBA cross section [24] and it is assumed that only one value of $l_{\beta\gamma}$ and $l_{\alpha\gamma}$ are contribute. It should be stressed that the expression (8) and (9) take into account the fact that the ANC $C_{\beta\gamma;l_{\beta\gamma}j_{\beta\gamma}}$ and the single-particle ANC, $b_{\beta\gamma;l_{\beta\gamma}j_{\beta\gamma}}$, for the model wave function $\varphi_{n_{\beta\gamma}l_{\beta\gamma}j_{\beta\gamma}}(r_{\beta\gamma})$ coincide [23], i.e.,

$$S_{\beta\gamma;l_{\beta\gamma}j_{\beta\gamma}}\, b^2_{\beta\gamma;l_{\beta\gamma}j_{\beta\gamma}} = C^2_{\beta\gamma;l_{\beta\gamma}j_{\beta\gamma}} \ . \qquad (10)$$

Note that for peripheral transfer reactions only $r_{\beta\gamma} > r^0_{\beta\gamma}$ and $r_{\alpha\gamma} > r^0_{\alpha\gamma}$ give a contribution to the DWBA radial integrals [25,26], where $r^0_{\sigma\delta}$ is the nuclear interaction radius between σand δ particles in the bound state (σδ). From here it follows that the $\sigma^{DWBA}_{l_{\beta\gamma}j_{\beta\gamma}l_{\alpha\gamma}j_{\alpha\gamma}}$ is not practically sensitive to the variation of the cut off radius at $r_{cut} < r^0_{\beta\gamma}$ and $r_{cut} < r^0_{\alpha\gamma}$ in the initial and final states, respectively. In this case entering in the expression for $\sigma^{DWBA}_{l_{\beta\gamma}j_{\beta\gamma}l_{\alpha\gamma}j_{\alpha\gamma}}$ the bound state wave functions $\varphi_{n_{\beta\gamma}l_{\beta\gamma}j_{\beta\gamma}}(r_{\beta\gamma})$ and $\varphi_{\alpha\gamma;l_{\alpha\gamma}j_{\alpha\gamma}}(r_{\alpha\gamma})$ can be approximated by its asymptotic forms. Therefore, in the expression (6) in the stripping peak the dependence on parameters (the radius r_o and the diffuseness *a*) of the Woods-Saxon potential, which is usually used for a calculation of the bound sate wave functions $\varphi_{n_{\sigma\delta}l_{\sigma\delta}j_{\sigma\delta}}(r_{\sigma\delta})$ (σδ= βγ and αγ), enters through the product of the single-particle ANC's, $b_{\beta\gamma;l_{\beta\gamma}j_{\beta\gamma}}\ b_{\alpha\gamma;l_{\alpha\gamma}j_{\alpha\gamma}}$. Then the function $R^{DWBA}_{l_{\beta\gamma}j_{\beta\gamma}l_{\alpha\gamma}j_{\alpha\gamma}}$ must be nearly independent on $b_{\beta\gamma;l_{\beta\gamma}j_{\beta\gamma}}$ and $b_{\alpha\gamma;l_{\alpha\gamma}j_{\alpha\gamma}}$ for the peripheral transfer reactions [25,26].

2.2. Three-body Coulomb effects: The generalized method of distorted waves pole approximation

In this subsection we briefly present the theoretical scheme of generalization of "post'-form of the DWBA, given by the expression (8) and (9), taking into account three-particle (α, β and γ) Coulomb dynamic transfer mechanism for the peripheral transfer reaction (1). In works [21,22] within the framework of the dispersion theory for the Sub-barrier direct nuclear reaction of charged- particle transfer the three-body distorted wave pole approximation (TBDWPA) has been proposed and explicit form of the peripheral partial amplitudes M^{TBDWPA}_l at $l >> 1$ of the exact amplitude M^{TBDWPA} and its leading singular at $z \to \zeta$ term have been derived. It was shown that the explicit forms for the partial amplitudes of the exact amplitude M^{TBDWPA}, M^{TBDWPA}_l, at $l >> 1$ and the peripheral partial amplitudes of the DWBA amplitude M^{DWBA}, M^{DWBA}_l, at $l >> 1$have identical dependence on the orbital angular momentum *l*, but the absolute values of these partial amplitudes are different. At $l >> 1$for their ratio, which is

denoted by R_γ, the explicit expression has been derived as $R_\gamma = \frac{M_l^{TBDWPA}}{M_l^{DWBA}}, l >> 1.$

The fact that the main contribution to the amplitude of the peripheral transfer reaction (1) comes from peripheral partial-waves amplitudes M_l^{TBDWPA} for $l >> 1$, the inclusion of the term ΔM, taking into account all possible subsequent Coulomb rescatterings between the α, βandγ particles in the transfer mechanism, to the amplitude M^{DWBA} can be done by mean of multiplying the DWBA amplitude, M^{DWBA}, near z→ζ by $R_\gamma$also [22]

$$M^{TBDWPA}(\mathrm{k_i}, \mathbf{k_f}) \approx R_\gamma M^{DWBA}(\mathbf{k_i}, \mathbf{k_f}), \qquad z \to \zeta. \tag{12}$$

Then the differential cross section near the main peak for the peripheral reaction (1) with taking into account the three-particle Coulomb dynamic transfer mechanism can be rewritten as

$$\frac{d\sigma^{TBDWPA}}{d\Omega} = \left| R_\gamma \right|^2 \frac{d\sigma^{DWBA}}{d\Omega}, \tag{13}$$

where the factor $|R_\gamma|^2$ takes into account the influence of high-orders of the terms over $\Delta V^C_{\alpha,\beta}$ containing in the expression (2) on the amplitude of the "post"-form of DWBA. The explicit form of the factor $|R_\gamma|^2$ can be found in [22]. As it is seen from the relation (13) the value of the factor $|R_\gamma|^2$allows us to estimate scale of an influence of the term ΔMon the extracted values of ANC's obtained within the DWBA approach.

3. Peripheral proton and α-particle transfer reaction and the $^{208}Pb(^6Li, \alpha d)^{208}Pb$ Coulomb break up for the $^{2,3}H(\alpha,\gamma)^{6,7}Li$, $^7Be(p,\gamma)^8B$and $^{12}C(p,\gamma)^{13}N$ reactions

It is well known that in the standard solar models the solar neutrino fluxes are determined through the very low- energy cross section $\sigma(E)$ or respective its the astrophysical *S*- factor *S(E)* [6]. Note that the cross section $\sigma(E)$ is related to the astrophysical *S*- factor *S(E)* as

$$\sigma(E) = e^{-2\pi\eta} S(E)/E, \tag{14}$$

where η is the Summerfield parameter for colliding particles.

The cross section $\sigma(E)$ for the direct radiative capture reaction A(a,γ)B has the form as

$$\sigma(E) = N\left|\left\langle I_{Aa}(\mathbf{r}_{Aa})\middle|O(\mathbf{r}_{Aa})\middle|\Psi_{\mathbf{k}}^{(+)}(\mathbf{r}_{Aa})\right\rangle\right|^2 , \qquad (15)$$

where N is kinematic factor, $O(\mathbf{r}_{Aa})$ is the electromagnetic transition operator, $\Psi_{\mathbf{k}}^{(+)}$ is the scattering wave function in the colliding particles A and a and $k = \sqrt{2\mu_{Aa}E}$. If the dominant contribution to the radial amplitude of the direct capture A(a,γ)B reaction comes from the region of $r_{Aa} > r_{Aa}^0$, entering in (15) the radial overlap integral $I_{Aa;l_{Aa}j_{Aa}}(r_{Aa})$ can be replaced by its asymptotic expression (6). In this case the ANC $C_{Aa;l_{Aa}j_{Aa}}$ for the virtual decay B$\rightarrow$ A+a is just found from the peripheral transfer reactions.

As it was mentioned above the $^{2,3}H(\alpha,\gamma)^{6,7}Li$ reactions are one of source of the $^{6,7}Li$ formation in the early Universe [2-5].A direct measurement of the cross section σ *(E)* the $d(\alpha,\gamma)^6Li$ reaction has been done down up to energies E ~ *0.7 MeV*[4], and the indirect measured data in the energy region of $100 \le E \le 600$ *keV* have uncertainties more than 30 % [7,27] . A reliable estimation of ^8B high-energy neutrinos flux from the Sun produced via the $^7Be(p,\gamma)^8B$ reaction is an unsolved problem of the solar neutrino problem so far. So knowledge of the astrophysical *S*-factor *S(E)* , $S_{17}(0)$, plays a important role in solution of this problem within existing solar models [6]. Besides, the $^{12}C(p,\gamma)^{13}N$reaction is the first one in the CNO-cycle and it plays an important role at nuclear energy generation in massive stars [28-30] and as a source of low energy solar neutrinos in the GALLEX experiment [1,31].

In the last years considerable experimental and theoretical progress have been made for determining astrophysical S- factors ,S_{24}(E), S_{34}(E),S_{17}(E)and$S_{1\ 12}$(E), for the d(α,γ)^{6}Li, t(α,γ)^{7}Li ^{7}Be(p,γ)^{8}B and ^{12}C(p,γ)^{13}N reactions, respectively, at stellar energies (E ~ 25 keV). A use of the peripheral character of the direct capture amplitude of these reactions is one of such approach. Therefore, according to EQS.(14) and (15), the overall normalization of the direct astrophysical S-factors for each from the d(α,γ)^{6}Li,t(α,γ)^{7}Li , ^{7}Be(p,γ)^{8}B and ^{12}C(p, γ)^{13}N reactions may be determined by the ANC's (or NVC's) for the virtual decays6Li$\rightarrow$ α+ d, 7Li$\rightarrow$ α+ t, ^{8}B$\rightarrow$ p+ ^{7}Be and ^{13}N$\rightarrow$ p+ ^{12}C. These ANC's have been found from an analysis of the differential cross sections of the d(^{6}Li,d)^{6}Li, d(^{7}Li,t)^{6}Li and ^{208}Pb(^{6}Li,αd) ^{208}Pb Coulomb break up processes[21,7] as well as of the peripheral proton transfer ^{14}N(^{13}C, ^{14}N)^{13}C [32],^{14}N (^{7}Be,^{8}B) ^{13}C [17] and ^{12,13}C(^{3}He,d)^{13,14}N [11,33,34] reactions. Below we present the results of an analysis of these processes to obtain the indirect measured ANC's for the virtual decays ^{6}Li$\rightarrow$ α+ d, ^{7}Li$\rightarrow$ α+ t, ^{8}B$\rightarrow$ p+^{7}Be and ^{13}N$\rightarrow$ p+^{12}C and to use them for determining the astrophysical S- factors S_{24}(E), S_{34}(E), S_{17}(E) and $S_{1\ 12}$(E), at stellar energies.

3.1. $D(^6Li,d)^6Li$, $D(^7Li,t)^6Li$and $^{208}Pb(^6Li, \alpha d)\ ^{208}Pb$ Coulomb break up processes for the $^{2,3}H(\alpha,\gamma)^{6,7}Li$reactions

As it was mentioned above a direct measurement of the astrophysical S-factor, S_{24}exp (E), for the d(α,γ)^{6}Li reaction covers the energy region of E ≥ 700 keV[4]. The indirect measured data for S_{24}exp (E) in the energy region of 100 ≤ E ≤ 600 keV were obtained in [27] from an analysis of the ^{208}Pb(^{6}Li,αd)^{208}Pb Coulomb break up taking into account only the E2- contribution, while a E1-contribution is noticeable for extracting reliable data for S_{24}exp (E) at astrophysical low energies [35,7] .

In work [7]the new data for $S_{24}^{exp}(E)$ in the energy region of $130 \le E \le 250$ *keV* have been obtained by using the information about the NVC for the virtual decay $^6Li \to \alpha + d$ gotten within framework of the three-body method of an analysis of the same Coulomb break up taking into account the E1- and E2- contributions, including their interference by correct way. The obtained data have uncertainties not less 30 % and that are displayed in Figs.2 and 3.

From Fig.2 it is seen that the obtained in [7] results for the NVC for the virtual decay $^6Li \to \alpha + d$ are in a good agreement with the independent estimations for NVC $G^2_{\alpha d:01}=0.41\pm0.06$ *fm* obtained in [21] from an analysis of the peripheral $d(^6Li,d)^6Li$ reaction with correct taking into account the three-particle (α-d-d) Coulomb dynamic transfer mechanism (Fig.4*a*) and $G^2_{\alpha d:01}=0.42\pm0.02$ *fm* obtained in [37] from an analysis of the α-d – scattering.

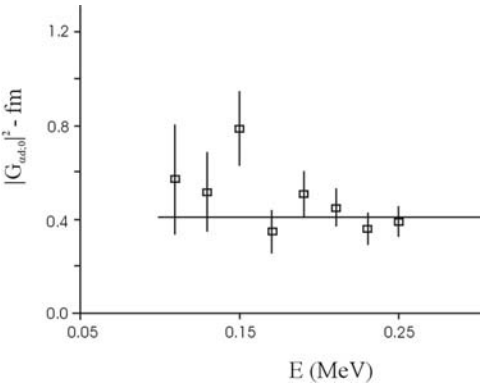


Fig.2. The value $\left|G_{\alpha d;01}\right|^2$ for the virtual decays $^6Li \to \alpha + d$. The square points (solid line) are the results from work [7] ([20] and [37]).

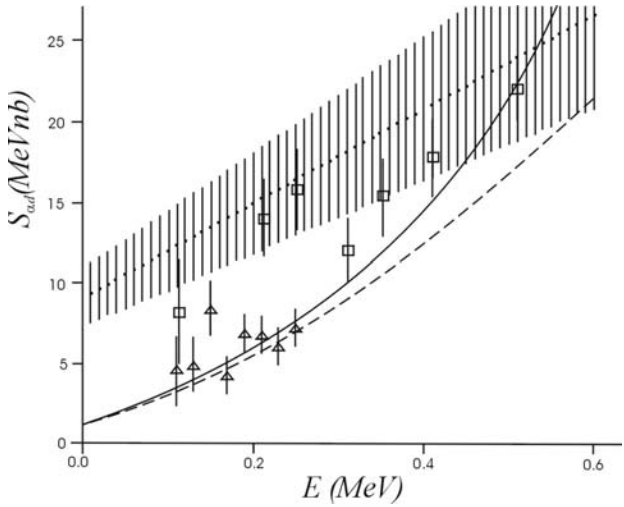


Fig. 3. The astrophysical S- factor for the $d(\alpha,\gamma)^6Li$ reaction. The triangle (square) are the results from [7]([27]). The solid (dashed) line are the results of calculation from [13,14]([13]) for the E1- and E2- multipoles taking Coulomb-nuclear (Coulomb) α-d scattering. The dashed band is the results of the interpolation formula $S_{\alpha d}(E)=(9.1\pm1.8+(29.2\pm6.6)E)MeVnb$ [27].

From Fig.3 it is seen that for $S_{24}^{exp}(E)$ (triangle points) significant energy dependence occurs in the contrast to the data (square points) of a paper [27] obtained with taking into account only the E2-contribution. From Fig.3 it is also seen that a good agreement between the $S_{24}^{exp}(E)$ data obtained in [7] and the theoretical predictions (solid line) obtained by authors of works [13,14] occurs. Note that in works [12,13] the information about the NVC for the virtual decay $^6Li \rightarrow \alpha + d$ from works [21,37] has been used. It should be stressed that the data $S_{24}^{exp}(E)$ obtained in [7] confirms the conclusion of a paper [4] that the production rate of ^6Li via the $d(\alpha,\gamma)^6Li$ reaction in Big-Bang nucleosynthesis is sufficiently small. However a presence of rather more uncertainties for the $S_{24}^{exp}(E)$ requires carrying out news direct measurement of the cross sections of the $d(\alpha,\gamma)^6Li$ reaction at energies E less than 600 keV in order to do a final conclusion.

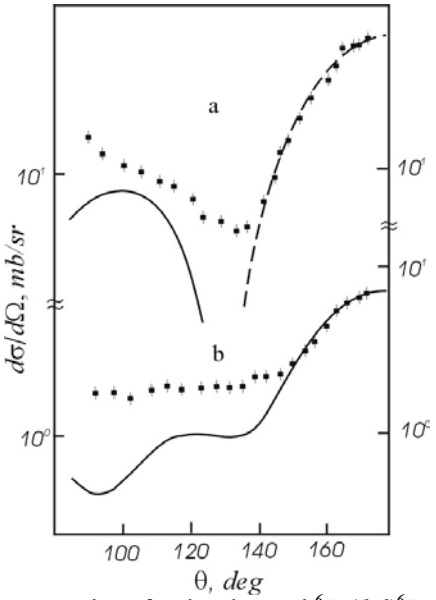


Fig. 4. The differential cross sections for the changed $^6Li(d,d)^6Li$ scattering *(a)* and $^7Li\ (d,t)^6Li$ reaction *(b)* at E_d= 12 MeV. The curves are the results of the DWBA-calculation from [21].

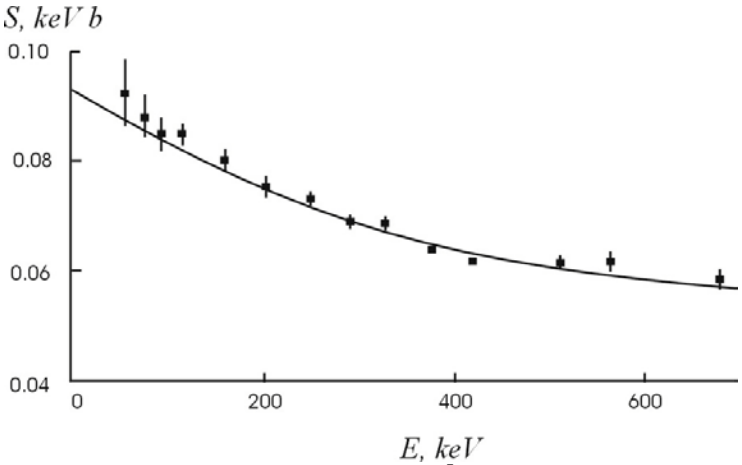


Fig. 5. The astrophysical S- factor for the $t(\alpha,\gamma)^7Li$ reaction [39]. The curve is the result of calculation from work [15]

In Figs. 4*b* and 5 the results of an analysis of the peripheral $d(^7Li,t)^6Li$ reaction performed in [21] with correct taking into account the three-particle (α-d-t) Coulomb dynamic transfer mechanism and of the experimental astrophysical S-factor, $S_{34}^{exp}(E)$, for the $t(\alpha,\gamma)^7Li$ reaction [39] performed in [15] are shown, respectively. The NVC- value for the virtual decay $^7Li \rightarrow \alpha + t$ $G^2_{\alpha t:1\ 3/2}=0.46$ *fm* obtained in [21] is a good agreement with a value of $G^2_{\alpha t:1\ 3/2}=0.49$ *fm* [15]. The result for $S_{34}(0)$ is $S_{34}(0)= 0.093$ *keVb* [15], which agrees well with the result of $S_{34}(0)\approx 0.1$ *keVb* [40,41].

3.2. $^{13}C(^3He,d)^{14}N$, $^{14}N(^{13}C,\ ^{14}N)^{13}C$ and $^{14}N\ (^7Be,^8B)\ ^{13}C$ reactions for $^7Be(p,\gamma)^8B$

The differential cross section (DCS) for the $^{13}C(^3He,d)^{14}N$ reaction have been measured in a ^3He beam with energies *34* and *42 MeV* from the 150-cm cyclotrons of the Institute of Nuclear Physics (Tashkent, Uzbekistan) and of the Institute of Nuclear Physics of the National Nuclear Center of Kazakhstan (Almaty) [33]. The experimental DCS's for this reaction populating the ground state of ^{14}N and its the DWBA predictions are shown in Fig.6.

The normalization factor between the experimental and the DWBA calculated DCS determine the ANC (or NVC) for the virtual decay $^{14}N \rightarrow p + ^{13}C$ with dominating $l_{p^{13}C}=1$ and $j_{p^{13}C}=1/2$, since the ANC for the virtual decay $^3He \rightarrow d+p$ is known [25,42]. The obtained results are presented in Table 1.

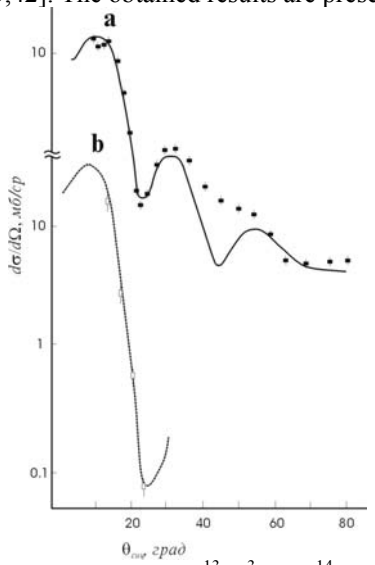


Fig. 6. The differential cross section of the $^{13}C(^3He,d)^{14}N$ reaction at E_{3He} =34 MeV (*a)* and E_{3He} = 42 MeV (*b*) populating the ground state of ^{14}N and their comparison with DWBA (solid line)from work[33].

The measured in works [32,17] angular distributions for the peripheral proton transfer $^{14}N(^{13}C, ^{14}N)^{13}C$ and $^{14}N (^{7}Be,^{8}B) ^{13}C$ reactions populating the ground state of ^{13}C and their comparison with DWBA are shown in Figs.7 and 8. The obtained values of ANC's for the virtual decays $^{14}N \rightarrow p+ ^{13}C$ and $^{8}B \rightarrow p+ ^{7}Be$ are presented in Table 1. Besides, we also estimate an influence of the three-body Coulomb effects, which are describe by the factor $|\ R_p\ |^2$, on the extracted within DWBA values of ANC's. They are also given in Table 1. As it is seen from Table 1 the three-body Coulomb effects contribute noticeably on the absolute value of DCS in the stripping peak of the $^{14}N(^{13}C, ^{14}N)^{13}C$ and $^{14}N (^{7}Be,^{8}B) ^{13}C$ reactions. Therefore, an influence of these effects cannot be neglected , as it has been done in works [17,32,33].

Table 1. The factor $|\mathbf{R_\gamma}|^2$, the adopted NVC's ($\mathbf{G^2\alpha\gamma;}l_{\alpha\gamma}\, j_{\alpha\gamma}$) and ANC's ($\mathbf{C^2\alpha\gamma;}l_{\alpha\gamma}\, j_{\alpha\gamma}$) for the virtual decay $\mathbf{(\alpha\gamma)\rightarrow\alpha+\gamma.}$

Reaction $\alpha+(\beta\gamma)\rightarrow\beta+(\alpha\gamma)$	$\mathbf{E_{lab}}$ (MeV)	Virtual decay	$\lvert R_\gamma\rvert^2$	$G^2\alpha\gamma;l_{\alpha\gamma}\, j_{\alpha\gamma}$(fm)		$C^2\alpha\gamma;l_{\alpha\gamma}\, j_{\alpha\gamma}$(fm^{-1})	
				DWBA	*TBDWBA*	DWBA	TBDWBA
$d+^{6}Li\rightarrow d+^{6}Li$	12 [21]	$^{6}Li\rightarrow\alpha+d$	0.954	0.42 ± 0.06	0.46 ± 0.06	5.39 ± 0.77	5.26 ± 0.77
$d+^{7}Li\rightarrow t+^{6}Li$	12 [21]	$^{7}Li\rightarrow\alpha+t$	0.703	0.64	0.45	13.6	9.55
$^{12}C+^{3}He\rightarrow d+^{13}N$	34; 42 [11,34]	$^{13}N\rightarrow p+^{12}C$	0.983	0.37	0.36	2.34	2.34
$^{13}C+^{3}He\rightarrow d+^{14}N$	34 [33]	$^{14}N\rightarrow p+^{13}C$	1.020	3.20	3.14	19.9	19.5
$^{13}C+^{14}N\rightarrow ^{13}C+^{14}N$	162.0 [32]	$^{14}N\rightarrow p+^{13}C$	0.799	2.99	3.34	18.6	20.8
$^{7}Be+^{14}N\rightarrow ^{13}C+^{8}B$	85.0 [17]	$^{8}B\rightarrow p+^{7}Be$	0.470	0.0671 ± 0.0078	0.128	0.371 ± 0.043	0.706

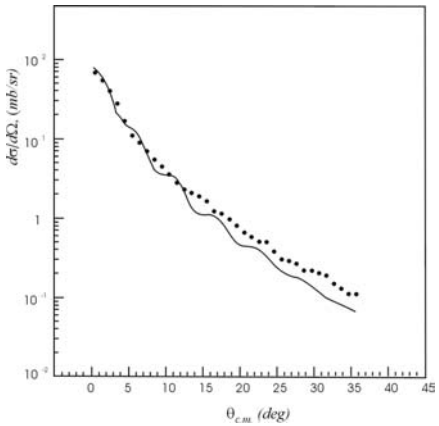


Fig. 7. The differential cross section of the ^{14}N(^{13}C, ^{14}N)^{13}C reactionpopulating the ground state of ^{13}C and their comparison with DWBA (solid line) from work [32].

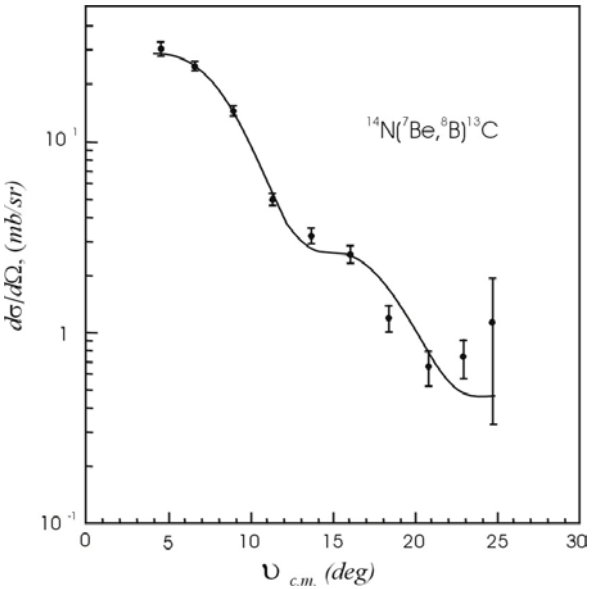


Fig. 8. The differential cross section of the ^{14}N (^{7}Be, ^{8}B) ^{13}C reactions populating the ground state of ^{13}C reaction populating the ground state of ^{13}C and their comparison with DWBA (solid line) from work [17].

In work [17] the extracted ANC for the virtual decay $^8B \rightarrow p + {}^7Be$ has been used to determine the $^7Be(p, \gamma)^8B$ capture rate. It is $S_{17}(0) = 17.3 \pm 1.8$ *eVb*, which is in agreement with early recommended value 19^{+4}_{-2} *eVb* [1] and is noticeable less than the recent recommended in work [43] value of $S_{17}(0) = 22.3 \pm 0.7(exp) \pm 0.5(theor)$ *eVb*.

A use of ANC for the virtual decay $^8B \rightarrow p + {}^7Be$ obtained by us taking into account an influence of the factor $|R_p|^2$ on the DWBA calculations leads to $S_{17}(0) = 31.6 \pm 3.6$ *eVb*, which is also noticeably more than the recommended in work [43] value of $S_{17}(0)$. One of the possible reason of the observed discrepancy between results of work [43] and of $S_{17}(0) = 31.6 \pm 3.6$ *ebb* can be apparently connected with unacceptable accuracy of TBDWPA for using the $^{14}N\,(^7Be, ^8B)\,^{13}C$ reaction since this reaction is near so-called to the«dramatic» case [22] because of a value of $\eta_{p^{13}C} + \eta_{p^{7}Be}$ is near to a natural number (= 1.929).

3.3. $^{12}C(^3He, d)^{13}N$reaction and $^{12}C(p, \gamma)^{13}N$capture

The $^{12}C(^3He,d)^{13}N$reaction at energies of ^3Hebeam *34* and *42 MeV* has been studied in the 150-cm cyclotrons of the Institute of Nuclear Physics (Tashkent, Uzbekistan) and the Institute of Nuclear Physics of the National Nuclear Center of Kazakhstan (Almaty)as well as on the 120-cm cyclotron of the Institute of Nuclear Research of Moscow State University (Russia) [33]. The measured differential cross sections of this reaction populating the ground state of ^{13}N and their comparison both DWBA are shown in Fig.9. The extracted values of ANC for the virtual decay $^{13}N \rightarrow p + {}^{12}C$ both from DWBA – analysis [33] and with taking into account the three-body Coulomb effects [11,34] are also presented in Table 1. It is seen that an influence of the three-body Coulomb effects on the calculated cross sections in the stripping peak is about 2 %.

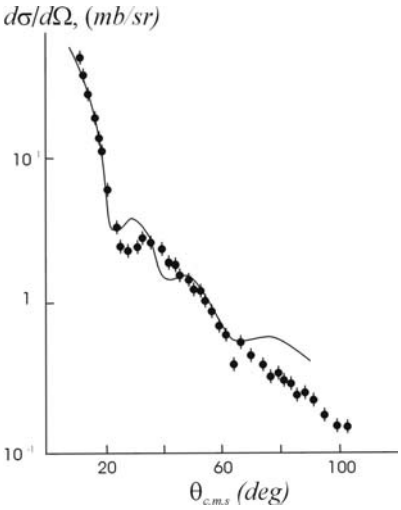


Fig. 9. The differential cross section of the $^{12}C(^{3}He,d)^{13}N$ reaction at E_{3He} =34 MeV populating the ground state of ^{13}N [33] and their comparison with DWBA (solid line) from work[11].

The extracted ANC for calculating the astrophysical *S*- factor of the $^{12}C(p, \gamma)^{13}N$ reaction at stellar energies has been used [20]. The recommended value of $S_{1\,12}(0) = 1.54 \pm 0.08$ *keVb* . The determined $S_{1\,12}(E)$ have been also used for a calculation of the $^{12}C(p, \gamma)^{13}N$ reaction rates as a function of stellar temperature $T_9(10^{-3} \leq T_9 \leq 10)$. A noticeable difference (up to 15%) occurs between the results of [20] and the early recommended that of given in [44] within stellar temperature, including solar temperature.

4. Conclusion

In this review work the ANC approach of a calculation of the astrophysical *S*- factors for the $^{2,3}H(\alpha,\gamma)^{6,7}Li$, $^{7}Be(p, \gamma)^{8}B$ and $^{12}C(p, \gamma)^{13}N$ reactions at stellar energies is considered. It is demonstrated that the ANC approach, that takes into account the information about the ANC-values previously obtained from an analysis of peripheral proton and α-particle transfer reactions as a input parameter in the direct capture amplitude, can be used as independent method of determining the direct capture cross sections (or the astrophysical S- factors) at solar energies *(~20 keV)* for which measurements of capture cross sections are practically

impossible directly due to them extremely smallest. It is shown that a reliability of the ANC approach depends on the applicability of the traditional "post"- or "prior"- form DWBA to obtain the ANC-value, and the DWBA approach should be modified by correct taking into account of the three-particle Coulomb dynamic transfer mechanism to get required in the ANC approach information about ANC's with highest precision as possible.

From this point of view it is felt that there is also a necessity in the future improvement of DWBA formalism within the framework of the subsequent three-body distorted wave method in which the three-particle Coulomb effects must be correctly taken into account by means of inclusion in the full transition operator all high –orders of the terms over $\Delta V^{C}_{\alpha,\beta}$.

At last, it is of great interest to carry out a similar study for the other peripheral one-particle transfer reactions and respective them radiative capture reactions. For this aim joint use of the existing facilities of accelerators of the Institute of Nuclear Physics (Tashkent, Uzbekistan) and of the Institute of Nuclear Physics of the National Nuclear Center of Kazakhstan (Almaty) would be highly encouraged.

One of authors (R.Y.) thanks the Abdus Salam ICTP for the hospitality in Trieste during July 2002, where the work has been completed.

References

1. E. G. Adelberger et al. Rev.Mod.Phys. 70(1998)1265.
2. D.N.Schramn , R.V.Wagoner. Ann.Rev.Nucl.Sci.27(1977)37.
3. R.V.Wagoner. Astrophys.J.Suppl.Ser.18(1969)247.
4. R.G.H.Robertson et al. Phys.Rev.Lett.47(1981)1867.
5. K.M.Nollett, M.Lemoine, D.N.Scharmm. Phys.Rev.C56(1997)1144.
6. J.N.Bahcall. Neutrino Astrophysics. Cambridge University Press.1989.
7. S.B.Igamov , R.Yarmukhamedov. Nucl.Phys.A673(2000)509.
8. Q.R.Ahmad et al. Phys.Rev.Lett.87(2001)071301.
9. L.D.Blokhintsev, I.Borbely, E.I.Dolinskii. Sov.J.Part.Nucl.8(1977)485.
10. H.M.Xu et al. . Phys.Rev.Lett.739(1994)2027.

11. R.Yarmukhamedov. Phys.Atomic Nucl.60(1997)1126.
12. A.M.Mukhamedzhanov et al. Phys.Rev.C56(1997)1302.
13. S.B.Igamov , R.Yarmukhamedov. Phys.Atomic Nucl.58(1995)1317.
14. A.M.Mukhamedzhanov et al. Phys.Rev.C52(1995)3483.
15. S.B.Igamov, T.Tursunmuratov, R.Yarmukhamedov. Phys.Atomic Nucl.60(1997)1126.
16. A.Azhari et al. Phys.Rev.Lett.82(1999)3960.
17. A.Azhari et al. . Phys.Rev.C60(1999)055803.
18. A.Sattarov et al. Phys.Rev.C60(1999)035801.
19. C.R.Brune et al. Phys.Rev.Lett.83(1999)4025.
20. S.B.Igamov, T.Tursunmuratov, R.Yarmukhamedov. Proc. the 3th Inter.Conf.Nucl.and Radiative Phys. 4-7 June 2001,Almaty,Kazakhstan,Par.2,p.**
21. G.V.Avakov et al. Sov.J.Nucl.Phys.43(1986)524.
22. Sh.S.Kajumov, A.M.Mukhamedzhanov, R.Yarmukhamedov, I.Borbely.Z.Phys.A336(1990)297.
23. A.Goncharov et al. Sov.J.Nucl.Phys.35(1982)383.
24. R.M.Devries. Phys.Rev.C8(1973)951.
25. I.R.Gulamov, A.M.Mukhamedzhanov, G.K.Nie. Phys.Atomic Nucl.58(1995)1689.
26. A.M.Mukhamedzhanov et al. Phys.Rev.C56(1997)1302.
27. J.Kiener et al. Phys.Rev.C44(1991)2195.
28. E.M.Burbidge et al. Rev.Mod.Phys. 29(1957)54.
29. C.A.Barns. Adv.Nucl.Phys. 41(1971)133.
30. C.Rolfs , W.S.Rodney. Cauldrous in the Cosmos (University of Chicago, Chicago,1988).
31. T.A.Kirsten. . Rev.Mod.Phys.71(1999)1213.
32. L.Trache et al. . Phys.Rev.C58(1998)2715.
33. S.V. Artemov et al. Phys.Atomic Nucl.59(1996)454.
34. S.V. Artemov et al.Izv.RAN.Seriya Fiz.66(2002)55.
35. N.A.Burkova et al.Phys.Lett.B248(1990)15.
36. M.G.Bingham et al. Nucl.Phys.A173(1971)265.
37. L.D.Blokhintsev et al. Phys.Rev.C48(1993)2390.
38. M.G.Bingham et al. Nucl.Phys.A175(1971)374.
39. C.R.Brune, R.W.kavanagh, C.Rolfs.Phys.Rev.C50(1994)2205.
40. K.Langanke. Nucl.Phys.A457(1986)351.
41. P.Mohr et al.Phys.Rev.C48(1993)1420
42. L.D.Blokhintsev, S. Rasulev, R.Yarmukhamedov. Sov. J. Nucl. Phys. 44(1986)758.
43. A.R.Junghans et al.Phys.Rev.Lett.88(2002)041101.
44. C.Angulo et al.Nucl.Phys.A656(1999)3.

THRESHOLDS, CLUSTERS and ASTROPHYSICS

Peterson R. J.

Boulder, CO, USA

For further nucleosynthesis to continue, very simple nuclear systems must combine so as to jump the gaps of unbound nuclei at A=5 and A=8. Multinucleon processes are thus required. Since these components are usually very rare in the sites of nucleosynthesis, these reactions need help from resonances to succeed. The most famous case is the triple-alpha mechanism, first proceeding through an S-wave resonance at ^{8}Be, unbound by only 92 keV, and then through the 0^{+}; 0 state of ^{12}C for a net resonance energy of 379 keV. Is this conjunction of nuclear states of exactly appropriate quantum numbers and a set of binding energies due to some fundamental principle, or is this just a doubly-fortunate coincidence?

This paper examines other cases in light nuclei where a nuclear state of just the right energy, quantum numbers and structure is found where needed to enhance multinucleon reactions.

One clue was a strong state in ^{10}Be strongly populated in 3-nucleon transfer reactions on ^{7}Li.[l] We repeated this measurement with higher resolution for the ^{7}Li(α,p)^{10}Be reaction, to determine that the state at 17.79 MeV has a spin of 2^{-}, suited to S-wave capture of ^{3}H onto ^{7}Li [2], matching the strong resonance in direct ^{3}H capture. [3] We thus note that this reaction provides another way for nucleosynthesis to proceed across the A=5 and 8 gaps, and that the direct transfer reaction can be used in place of difficult direct capture studies. Nucleon transfer is also a direct means to examine subthreshold resonant states.

Another example is the ^{7}Li(^{3}He,p)^{9}Be reaction, recently studied at very low energies. [4] The resonance seen at higher energies in this ^{3}He study should be seen in the direct ^{7}Li(α,n)^{10}B reaction, by analogy to the case for the ^{3}H resonance and the (α,p) direct reaction, but a search of the literature (via www-nds.iaea.or.at, click in NSR) found no relevant study.

The new astrophysical S-factor for ^{7}Li(^{3}He,p)^{9}Be permits us to compare this one reaction to cross the A=8 gap to the triple-alpha process. The triple-alpha process requires common nuclei, but with a reaction rate proportional to the cube of the alpha density. The ^{3}He + ^{7}Li reaction uses much rarer nuclei, but has a lower Coulomb barrier and has a rate proportional only to the square of the density. Figure 1 shows the ratio of these two reaction rates, scaled from a previous calculation by the new S-factor. We take N(^{3}He) = 10^{-4} N(α) and N(^{7}Li)=10^{-9} N(α), at two N(α) values.

Extreme differences are too readily found for thesse calculations, but there is clearly a range of temperatures and densities where the two rates are not hugely

different. We are encouraged to seek other multinucleon reactions that could prove to be important pathways to nucleosynthesis.

Striking sharp peaks at high excitations were found in $^{12,13}C(\alpha,p)^{15,16}N$ reactions.[5] Usually such narrow peaks would indicate high spins, with little astrophysical significance. Here, however, the states were shown to be due to three nucleon transfer to the s-d shell, where the difference in structure from the states to be formed by neutron decay might be expected to create longer lifetimes. These $(sd)^3$ states are known to occur in cluster calculations in light nuclei. [6] Incidentally, these cluster calculations also indicate clearly the three-alpha structure of the ^{12}C 0^+ state at 7.6 MeV, as required for the triple-alpha process. [7]

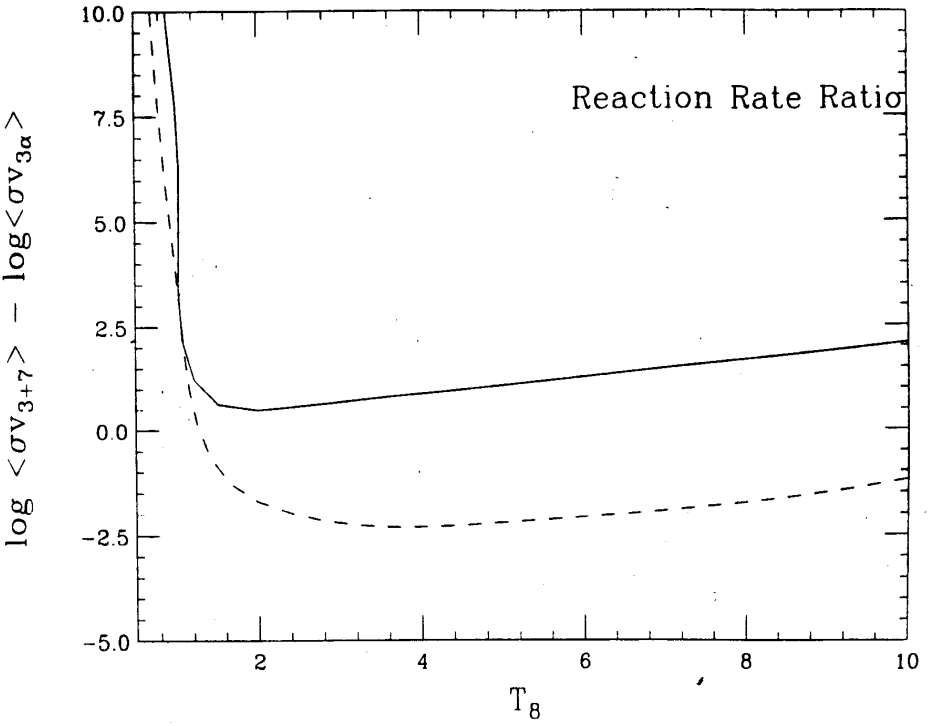


Fig. 1 The computed ratio of thermonuclear reaction rates for two means to jump the A=8 gap is shown for alpha particle densities of 10^{22} (solid) and 10^{26} (dashed) cm^{-3}, using a new measurement of the astrophysical S-factor for the $^7Li(^3He,p)^9$ reaction.[4] The denominator of the ratio is the rate for the triple-alpha drocess.

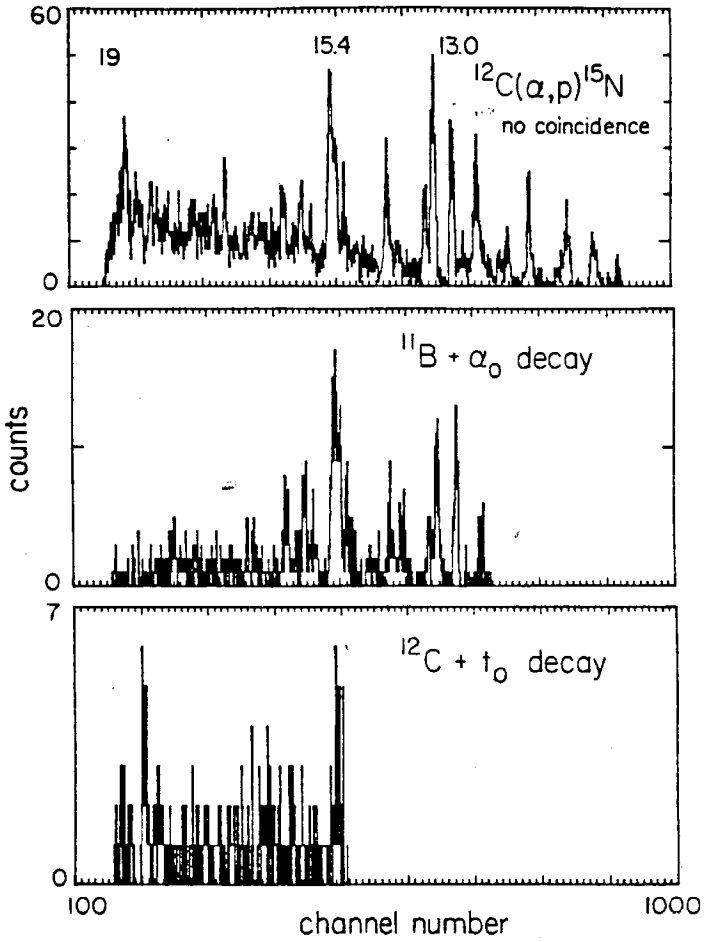


Fig.2 Singles and coincident spectra for the $^{12}C(\alpha,p)^{15}N$ reaction are shown. [8]

We examined the particle decay of these sharp states from the $^{12,13}C(\alpha,p)^{15,16}N$ reactions using Si detector telescope systems. [8] Figure 2 shows the ^{15}N spectra without coincidence and with coincidences for alpha decay to the ground state of ^{11}B and the triton decav to the ground state of ^{12}C. Other spectra without coincidences obtained better energy resolution for the protons using tighter kinematics, and showed the 15.4 MeV state to have a width of no more than 40 keV. The 15.3 MeV state is the sharp stretched $13/2^+$ configuration for $(d5/2)^3$, and has a a high centrifugal barrier to prevent its particle decay.

Note that the states strongly populated by the direct reaction also have strong decays to the alpha channel and to the triton channel. We see the same structures by the direct transfer, a hypothetical alpha capture on ^{11}B and hypothetical triton capture on ^{12}C. The triton transition is found for a state within 0.6 MeV of the ^{12}C + ^{3}H threshold.

Figure 3 shows the corresponding singles spectrum for ^{13}C(α,p)^{16}N. The total energy of the sharp peak at 11.75 MeV lines up with the 15.3 and 15.4 MeV sharp peaks in ^{15}N, presumably because of a simple coupling system. [5] The coincidence spectrum however showed no events for alpha or triton decay of these states in ^{16}N, which we understand as due to the very high neutron penetrabilities for this very neutron-rich system, going faster than the charged particle decays.

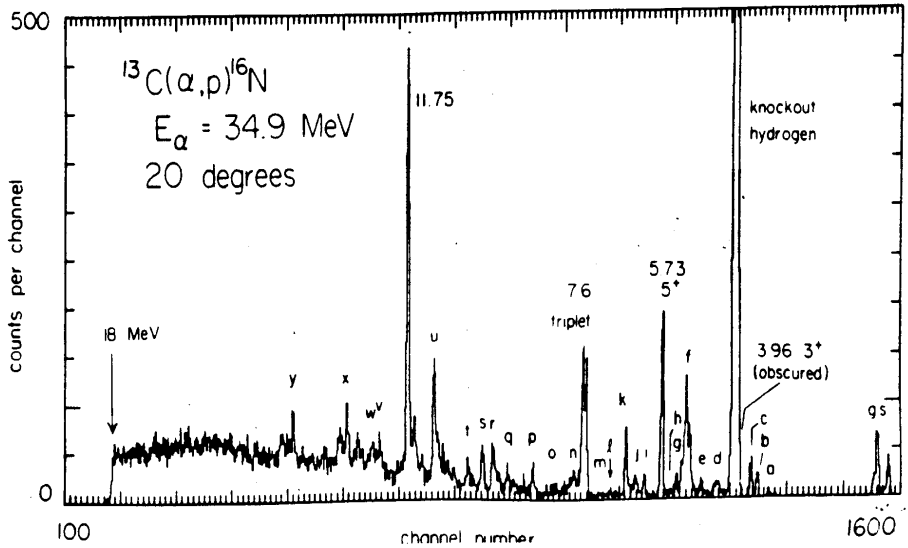


Fig. 3. A singles spectrum for the ^{13}C(α,p)^{16}N reaction also shows sharp states at high excitations, but no alpha or triton decays are seen from these. [8]

These are only examples of some applications of multinucleon transfer reactions for spectroscopic studies perhaps relevant to nucleosynthesis. In these, and other cases, the relevant states are found at just the relevant energies. This makes one suspect that there is a fundamental energy, symmetry and statistical explanation for this phenomenon.

A very different example with the same result of specific states being found at just the binding energy of their constituents is found in pion inelastic scattering on

light nuclei. The states in this case are high-spin stretched states, of little relevance to astrophysics.

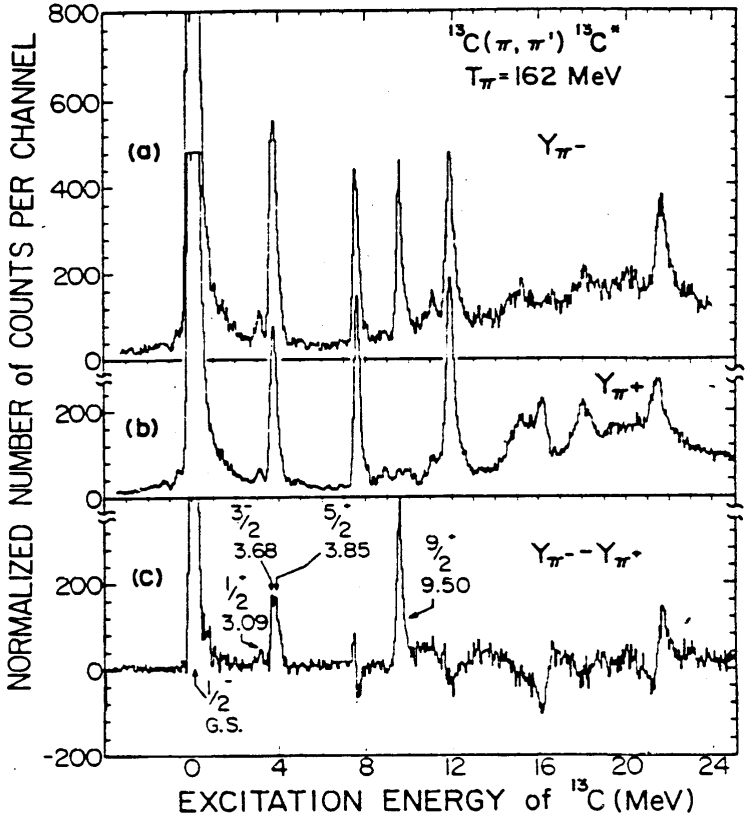


Fig. 4. Pion inelastic spectra for both charge states, and their difference, are shown. [9] Note the neutron-like positive asymmetries for certain states.

At the beam energy of about 180 MeV these pion reactions follow the isospin coupling rules of the 3-3 or delta resonance, with neutrons and π^- interacting 9 times more strongly than neutrons and π^+, and conversely. We can do experiments to form an isospin interferometer, using the pion asymmetry

$$A_\pi = \frac{d\sigma_- - d\sigma_+}{d\sigma_- + d\sigma_+}$$

Figure 4 shows π^+, π^- and difference spectra for ^{13}C [9]. The states of high asymmetry are noted in this and other cases to lie very near relevant single particle threshold. The 9.50 MeV $9/2^+$ state of ^{13}C is only 100 keV from a combination of a $d_{5/2}$ particle state in ^{13}C and the ^{12}C first 2^+ state. A compilation is found in [10], but more cases have since been discovered in nuclei from A=7 to A=17. The observed asymmetries are plotted in Fig. 5, as the energy difference between the nuclear state and the relevant separation energies. There is somewhat of a correlation, with greater asymmetries (stronger single-neutron or single-proton) responses the nearer the state is to the appropriate threshold.

For two very different kinds of nuclear reaction, direct cluster transfer reactions and resonant energy pion scattering, we note a correlation in many cases of the observed structure or partitions in the spectra to occur to states lying very near the separation energies making up those very partitions. These effects do come from some specific calculations, for instance the Resonating Group Method in [7], but there is also likely to be a more universal and fundamental reason. Discovery of such a principle would have particular value to nuclear astrophysical processes, where cluster transfers are increasingly known to be important.

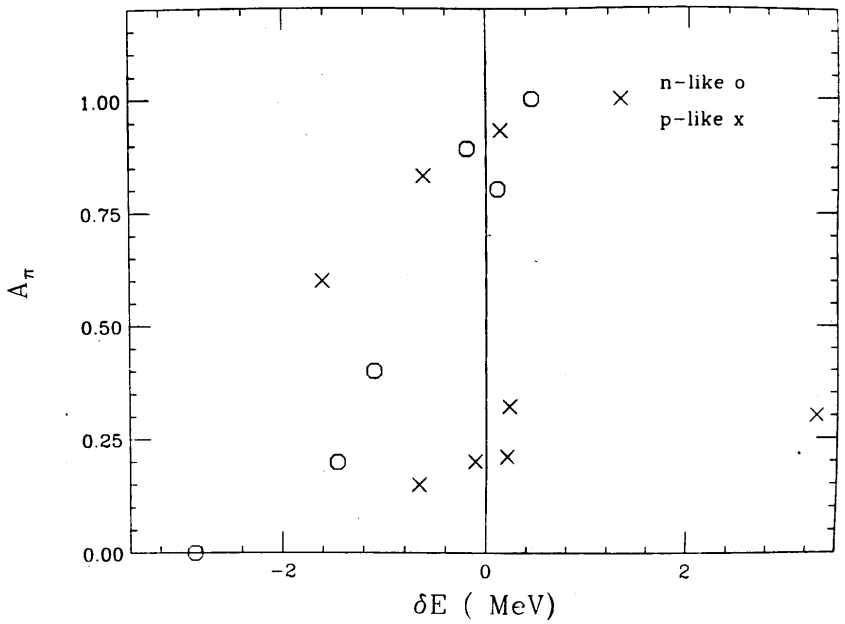


Fig. 5 Measured pion asymmetries for a number of transitions in light nuclei are plotted as a function of the difference of their excitation energies from the appropriate single-particle separation energies. Circles show positive asymmetries, or neutron-like transitions, and crosses show positive or proton-like asymmetries.

Acknowledgements. This work was supported by the US Department of Energy and the University of Colorado.

References

1. N. T. Burtebaev et al., Izv. Akad. Nauk SSR 39, 2160 (1975)
2. S. Hamada et al., Phys. Rev. C49, 3192 (1994)
3. D.R. Brune et al., Phys. Rev. C43, 875 (1991)
4. J. Yan et al., Phys. Rev C 65, 048801
5. J. J. Hamill, R. J. Peterson and M. Yasue, Nucl. Phys. A408, 21 (1983)
6. H. Furutani et al., Prog. Theo. Phys. 68, 193 (1980)
7. Y. Suzuki and M. Takahashi, Phys. Rev. C65, 064318 ((2002)
8. J. J. Hamill, PhD thesis, University of Colorado (1982) unpublished
9. S. J. Seestrom et al., Phys. Rev. Lett. 22, 1447 (1981) but check
10. R. J. Peterson, Physica Scripta T5, (1982)

A RESEARCH OF THE TWO-AVALANCHE EVENTS BY A METHOD OF AN IONIZATION CALORIMETER AND X-RAY FILMS AT THE ENERGIES E>10^{13} EV

T. Kh. Sadykov

Institute of Physics and Technology, MES RK, Almaty, Kazakhstan

Abstract

In the paper the analysis of two-jet events registered in an ionization calorimeter and roentgen-emulsion chamber (REC) is given. Is showed that for avalanches generated in the target, the quantity of a cross impulse considerably increases. The share of such events makes ~ 0,05 % from a total number of events, select according to the criteria of events.

In a paper of the Japanese-Brazilian collaboration [1], published in 1979, informed recording binocular events registered in X-rays emulsion chamber (X-REC), exposed at the altitude of 5200 m above see level. It is necessary to mark, that in 1977 we have reported [2] about registration of similar class of events, which one we have termed - as two-jet events. We carried on further investigation of two-jet events using of the information from an ionization calorimeter in combination to X-REC.

The experimental data were obtained on installation by the area 9 m^2. She consist of an ionization calorimeter by width of 980 g/cm^2, which one consists of six rows of ionization chambers. X-REC placed on a calorimeter and completely covered its area. The photolayers of X-REC, containing two PT-6 X-ray films and P-2T nucleus - emulsion, were under 1,2,3 and 4 cm of lead. At the altitude 6 and 11 meters above X-REC were installed two targets by width 22 g/cm^2 and area 60 m^2. The geometrical factor of installation was peer 13 str/m^2 [3]. The summary exposure of a handled experimental material made 17,2 m^2 year.

On a calorimeter the events caused by interactions, both single hadrons, and multiple hadrons were analyzed. Thus it was required, that the trunks of avalanches should do not intercross lateral faces of a calorimeter. In case of group slope of hadrons the spatial-disjointed avalanches were taken, i.e. the events, for which energy and trajectory each nuclear electromagnetic cascade (NEC) it is possible to find. Energy NEC was determined with precision 25 %. The coordinates of a shower were determined with precision 10 -15 cm.

X-REC in basic were intended for measuring energy of g-quanta and definition of their spatial performances. The relative accuracy of measuring of energies of g-quanta is peer 20-30 %. The threshold made 100 % of recording, particular on a differential energy spectra, for a nuclear emulsion 0.5 TeV, for a X-

ray film - 1,5 TeV. At integrating g-quanta in the set the measure (test) were applied: on a zenith angle $\pm 3^0$, on azimuth $\pm 20^0$. Gamma-quanta energy was determined with precision 20 %. The coordinates of gamma-quanta on a X-ray film were erected with precision 100 microns.

The bond between electronic - nuclear avalanches in a calorimeter and electron-photon cascades in X-REC was erected by comparison spatial and energy parameters of the studying events: in coordinates X and Y in a plane X-REC, azimuth and zenith angles, aggregate energy of g-quanta in X-REC and energy electron-photon cascade in an ionization calorimeter. For each event it was required, that the probability of chance comparison should be $< 5\ 10^{-2}$ [4].

In the table 1 the items of information on an overall performance of installation are presented. It is necessary to mark, that the avalanches transiting through lateral faces of a calorimeter and also multi-trunk events, in which one the direction and energy of avalanches was not possible to select did not account. In total of such cases was typed about 25 %.

Table 1. Results of comparison of events registered in an ionization calorimeter and X-REC

N, X-REC	Time-work IK,hour	An overall performance IK	Number of events with N (E > 1,5 TeV)
12	4416	0,74	400
13	4000	0,66	427
14	4235	0.81	518
15	3915	0,75	212
Total	16567		1557

On each event on X-REC it was necessary several avalanches in a calorimeter. We applied rather strong measure (tests) of takeoff, as a result of which ~85 % of events on X-REC managed to be connected with avalanches in a calorimeter. The remaining not compared events on X-REC (~15 %) have arisen because of an odds in the performances superior requirement of comparison.

Thus, practically events retrieved in X-REC, with avalanches registered in an ionization calorimeter uniquely were identified.

In a fig. 1 the integrated energy distribution of events registered in an ionization calorimeter (light mugs -1) is given. A spectrum of disjointed two-avalanche-type parallel events (dark mugs -2) here is submitted (shown). These spectrums are featured by an exponential function $N(>E_0) \sim (E_0)^{-a}$ with exponents $a_1 = 1{,}60 \pm 0{,}02$ for all events and $a_2 = 1{,}5 \pm 0{,}3$ for two-avalanche-type parallel events. The delta circuits - 4 show a spectrum of nonparallel two-avalanche-type events, which one enter geometrically concurrent, and also not traversed avalanches. Such events it is revealed 320. By an exponential function they are not

featured. Probably, it is possible to explain them simultaneous (4mcs) by slope of independent avalanches on a calorimeter, and also availability of interactions with a major cross impulse is low-level above a calorimeter. The daggers submit - 3(shown) a spectrum of two-avalanche-type parallel events in a calorimeter.

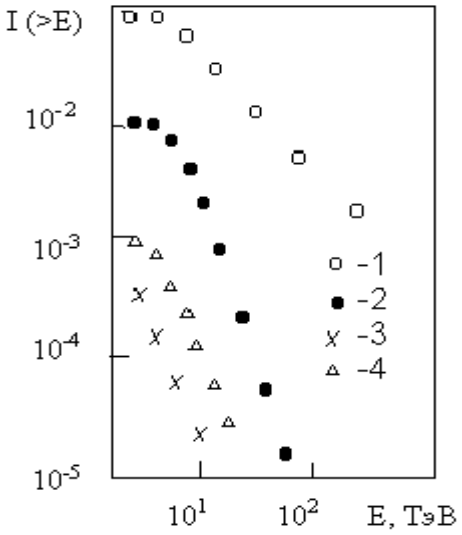


Fig. 1. Explanation in the text

For examination of a put problem on an ionization calorimeter the two-avalanche-type events selected. From them those were considered only, the trajectory which one converged in the target to one point. The performances of such events are submitted (shown) in the table 2.

Table 2. The performances of the compared showers, the trajectory which one was intercrossed in the target

№ event	№ of a shower	E_0, TeV	E_1, TeV	L, cm	H, m	$P_\perp$, ГэВ/cm^2
1	1 2	14,2 1,8	0,5 0,7	140	6.10	1587
2	1 2	3,6 2,6	1,2 0,8	133	6.21	1033
3	1 2	19,2 5,6	2,7 2,4	649	11.37	424

In the table 2 E_0 - energy of a shower particular on an ionization calorimeter, E_1 - energy of gamma-quantum particular on a nuclear emulsion, L - distance between gamma-quantum, H - medial distance from the target up to X-REC.

If to interpret formation of two-jet events as effect (result) of decay of an intermediate system [2], from a kinematics relation it is possible to spot mass of this hypothetical system:

$$M_0 = R \sqrt{E_1 E_2} / Hc^2$$

here R- distance between avalanches; $E_{1,2}$ - energy of each jet; H- height of their generation. In the table 2 the values $P_\perp$ for each event are given. In the given operation M_0~9 GeV/c^2; it is necessary to note, that in this case there is a speech about complete mass, instead of about allocated in a neutral builder, as it is usually made [2]. The business that availability of the information from an ionization calorimeter allows to determine the size E_0 without engaging the prior guesses about value K_γ - shares of energy transferred (handed) in gamma-quantum.

Was earlier shown that the combined effect of sampling on ΣE_γ and steeply dipping energy distribution gives in uprating quantity Kγ [3]. The experimental value Kγ=0,36, instead of 0,2, which one is given in operation [2]. If to accept this value Kγ and to use for definition of mass geminiona in [2], is gained M_0=13 ГeV/c^2, that with allowance for of methodical and experimental errors is compounded with our effect.

For 12510 h of operation of an ionization calorimeter with $E_0 \geq 1{,}0$ TeV 5780 events were registered. Among them 300 two-jet nonparallel avalanches selected. After careful measuring three compared showers were detected the trajectories which one geometrically were intercrossed in the target.

Thus, the showers with anomalously major cross impulses (~1000 GeV/c^2) are watched. The amount makes them ~0,05 % from a total number of the registered avalanches with $E_0 \geq 1.0$ TeV.

Reference

1. Bellandi J., Cardoso I.L. et al. Baryon pair production with large decay g-vaive. 6-th ICRC. Kyoto, Japan, 1979, v.7, p. 350-357.
2. Takibaev G.S., Sadykov T.Kh. Pair formation pion of clusters in the field of energies 25 TeV. Izv. AN Kaz. SSR. 1977, № 4, p. 15-19.
3. Alibekov M.I., Amanov K.A. et al. Quantums of high energies in a composition of nuclear avalanches at a level of mountains. Multiple formation of hadrons. Alma-Ata, 1983, p. 208-231.
4. Babaev M.K., Eremenko Yu. A. About events with large transfers momentum registered. 15-th ICRC. Munchen, 1977, V.7, p. 178-183.

A NOVEL APPROACH FOR THE COUPLING POTENTIAL IN COUPLED-CHANNELS FORMALISM

[1]I. Boztosun, [2]N. Burtebayev, [2]V. Dzhazairov-Kakhramanov

[1]Department of Physics, Erciyes University, 38039 Kayseri-Turkey
[2]Institute of Nuclear Physics, Almaty, Republic of Kazakhstan

Abstract

A number of serious problems have continued to plague the study of the $^{16}O+^{28}Si$, $^{12}C+^{24}Mg$ and $^{12}C+^{12}C$ systems for the last 40 years. The explanation of anomalous large angle scattering data; the reproduction of the oscillatory structure near the Coulomb barrier; the out-of-phase problem between theoretical predictions and experimental data; the consistent description of angular distributions together with resonance and excitation functions data are just some of these problems. These are long standing problems that have persisted over the years and do represent a challenge calling for a consistent framework to resolve these difficulties within a unified approach. Traditional frameworks have failed to describe these phenomena within a single model and have so far only offered different approaches where these difficulties are investigated separately from one another. The present work offers a plausible framework where all these difficulties are answered. Not only it improves the simultaneous fits to the data of these diverse observables, achieving this within a unified approach for a number of nuclear systems over wide energy ranges, but it departs for its coupling potential from the standard formulation. This new feature could provide new insight in the dynamics of these reactions. It also leads to new predictions especially concerning resonance phenomena in these systems which could form the basis for some new experimental investigation.

Introduction

The elastic and inelastic scattering of light heavy-ions have stimulated a great deal of interest over the last 40 years. There has been extensive experimental effort to measure the elastic and inelastic scattering data as well as their 90^0 and 180^0 excitation functions. A large body of experimental data for these systems is available (see [1,2,3] and references therein). Although most of the theoretical models proposed so far provide reasonably good fits, no unique model has been proposed that explains consistently the elastic and inelastic scattering data over a wide energy range without applying any *ad hoc* approaches. Consequently, the following problems continue to exist for light heavy-ion reactions: (1) explanation of anomalous large angle scattering data, 'ALAS'; (2) reproduction of the oscillatory structure near the Coulomb barrier; (3) the lack of the correct oscillatory structure between theoretical predictions and experimental data; (4) simultaneous fits of the individual angular distributions, resonances and excitation functions (for

the $^{12}C+^{12}C$ system in particular); (5) the magnitude of the mutual-2^+ excited state data in the $^{12}C+^{12}C$ system is unaccounted for; (6) the deformation parameters (β values): previous calculations require β values that are at variance with the empirical values and are physically unjustifiable.
Therefore, in this paper, we are concerned with the measured experimental data for $^{12}C+^{12}C$, $^{16}O+^{28}Si$ and $^{12}C+^{24}Mg$ in an attempt to find a global model, which simultaneously fits the elastic and inelastic scattering data for the ground and excited states in a consistent way over a wide energy range.

The Standard Coupled-Channels (CC) Model

Although three different reactions are analyzed, we are only going to show some of the results for the $^{12}C+^{12}C$ reaction. The details of the models and a complete set of the results for all the reactions will be published in [4,5,6,7]. We describe the interaction between ^{16}O and ^{28}Si nuclei with a deformed optical potential. The real potential has the square of a Woods-Saxon (WS) shape *i.e.*

$$V_N(r) = -V_0 / (1+\exp(r-R)/a)^2$$

with V_0=706.5 MeV, $R=r_0(A_p^{1/3}+A_t^{1/3})$ with r_0=0.749 fm and a=1.4 fm. The parameters of the real potential were fixed as a function of energy and were not changed in the present calculations. The Coulomb potential with radius 5.56 fm was also added.
The imaginary part of the potential was as the sum of a WS volume and surface potentials *i.e.*

$$W(r)=-W_V\, f(r,R_V,a_V)+4W_S a_S\, df(r,R_S,a_S)/dr$$

$f(r,R,a) = 1/(1+\exp((r-R)/a))$ with W_V=59.9 MeV, a_V=0.127 fm and W_S=25.0 MeV, a_S=0.257 fm. These parameters were also fixed in the calculations and only their radii increased linearly with energy according to the following formulae.

$$R_V = 0.06084E_{CM}-0.442 \quad \text{and} \quad R_S = 0.2406E_{CM}-2.191$$

Since the target nucleus ^{28}Si is strongly deformed, it is essential to treat its collective excitation explicitly in the framework of the CC formalism. It is assumed that the target nucleus has a static quadrupole deformation, and that its rotation is described in the framework of the collective model. It is therefore taken into account by deforming the real optical potential in the following way

$$R(\theta,\varphi)= r_0A_t^{1/3}[1+\beta_2Y_{20}(\theta,\varphi)]$$

where β_2=-0.64 is the deformation parameter of the target nucleus, ^{28}Si. In the present calculations, the first two excited states of the target nucleus ^{28}Si: 2^+ (1.78

MeV) and 4^+ (4.62 MeV) were included and the 0^+-2^+-4^+ coupling scheme was employed. The reorientation effects for 2^+ and 4^+ excited states were also included. The calculations were performed with a modified version of the code CHUCK [8]. Using the standard coupled-channels theory, we found, as other authors had found, that it was impossible to describe consistently the elastic and inelastic scattering of this and other reactions we considered.

New Coupling Potential

The limitations of the standard coupled-channels theory in the analyses of these reactions compelled us to look for another solution. Therefore, a second-derivative coupling potential, as shown in figure 1, has been used in the place of the usual first-derivative coupling potential.

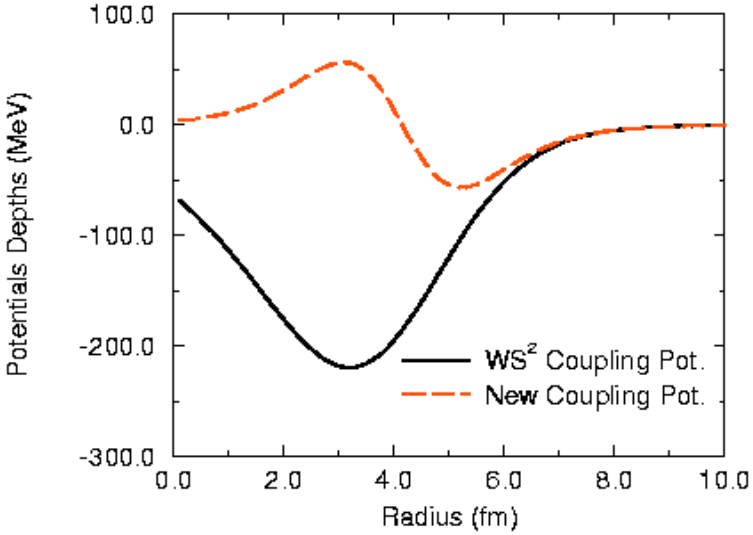


Figure 1: For $^{16}O+^{28}Si$, the comparison of the *standard coupling potential* which is the first derivative of the central potential and our *new coupling potential*, parameterized as the 2nd derivative of WS shape and has V=155.0 MeV, R=4.16 fm and a=0.81 fm.

The interpretation of this new coupling potential will be given in the forthcoming paper [4]. Here we employed the same method with small changes in the potential parameters. The empirical deformation parameter (β_2) is used in these calculations.

Results

$$^{16}O+^{28}Si$$

The first system we consider is ^{16}O + ^{28}Si, which shows anomalous large angle scattering (ALAS). In the present work, we consider an extensive *simultaneous* investigation of the elastic and the inelastic scattering of this system at numerous energies from E_{Lab}=29.0 MeV to 142.5 MeV over the whole angular range up to 180^0. In this energy range, the excitation functions for the ground and 2^+ states are also analyzed [5,6,7]. Excellent agreement with the data was obtained.

$$^{12}C+^{24}Mg$$

The second example we have considered is ^{12}C+^{24}Mg. Fifteen complete angular distributions of the elastic scattering of ^{12}C+^{24}Mg system were measured at energies around the Coulomb barrier and were published recently [2]. We have studied these fifteen complete elastic scattering angular distributions. Excellent agreement with the experimental data was obtained by using this new coupling potential.

$$^{12}C+^{12}C$$

The final system we have considered is that of ^{12}C+^{12}C, which has been studied extensively over the last 40 years. There has been so far no model, which fits consistently the elastic, inelastic scattering data and mutual excited state data as well as the resonances and excitation functions. Another problem is the predicted magnitude of the excited state cross-sections, in particular for the mutual-2^+ channel. The conventional coupled-channels model underestimates its magnitude by a factor of at least two and often much more [10,11,12]. We have also observed this in our conventional coupled-channels calculations as shown in figure 2 with dashed lines. There are also resonances observed at low energies, which have never been fitted by a potential, which also fits either the angular distributions or the excitation functions.

Using our new coupling potential, we have been able to fit the energy average of all the available ground, single-2^+, mutual-2^+ and the backgrounds in the integrated cross-sections of Cormier [9] as well as the main gross features of the 90^0 excitation function [3] simultaneously.

In sum, while these three systems show quite different properties and problems, a unique solution has come from a new coupling potential. The approach outlined here is universal and applicable to all the systems. Studies using this new coupling potential may lead to new insights into the formalism and a new interpretation of these systems.

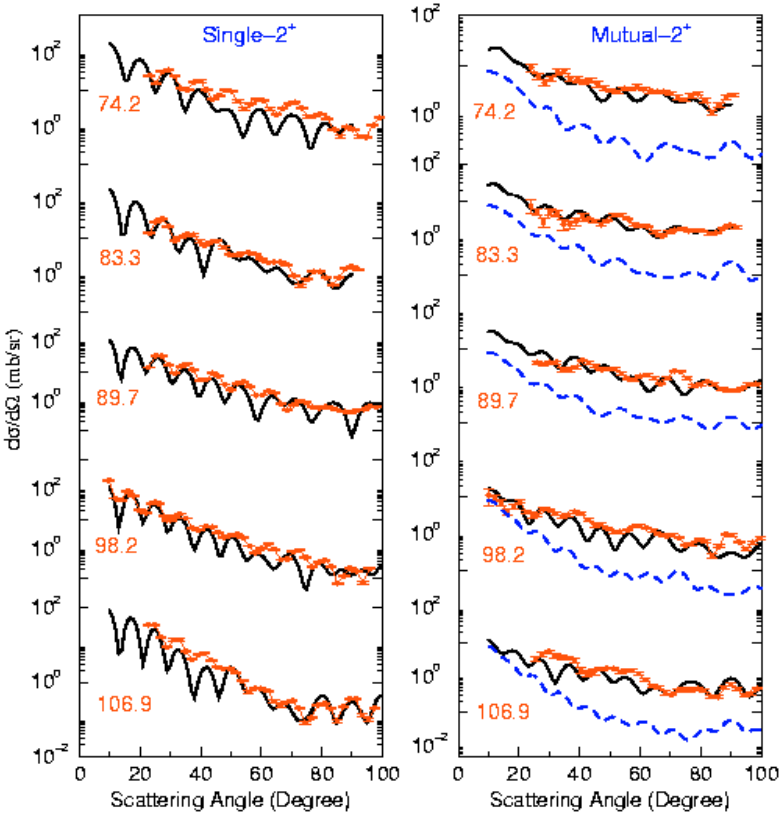


Figure 2: The $^{12}C+^{12}C$ system: The results of the single and mutual-2^+ states. The solid lines are the results of the *new coupling potential*, while the dashed lines are the results of *standard coupled-channels* model, shown only for the mutual case.

Acknowledgments

Special thanks to B. Buck, A. Merchant, Y. Nedjadi, B. Fulton, G. R. Satchler, D. Brink and N. A. Odman for valuable discussions and providing some data. I. Boztosun also would like to thank the Turkish Council of Higher Education (YÖK), Oxford and Erciyes Universities, Turkey, for their financial support.

Reference

1. P. Braun-Munzinger and J. Barrette, Phys. Reports **87** (1982) 209.
2. W. Sciani *et al*, Nucl. Phys. **A620** (1997) 91.
3. R. G. Stokstad *et al*, Phys. Rev. **C20** (1979) 655.
4. I. Boztosun and W.D.M. Rae, Phys. Rev C **63** 054607.
   I. Boztosun and W.D.M. Rae, Phys. Rev. C **64** 054607 (2001)
   I. Boztosun and W.D.M. Rae, Phys. Rev. C **65** 024603 (2002)
   I. Boztosun, Phys. Rev. C **66** 024610 (2002).
5. I. Boztosun and W.D.M. Rae, Proceedings of the 7th International Conference on Clustering Aspects of Nuclear Structure and Dynamics, Edited by M. Korolija, Z. Basrak and R. Caplar, World-Scientific-2000 (143).
6. I. Boztosun and W.D.M. Rae, Physics Letter **518B** 229.
7. I. Boztosun, Physics of Atomic Nuclei (Yadernaya Fizika) **65**, No 4, 607 (2002).
8. P. D. Kunz, CHUCK, An optical model search code, unpublished.
9. T. M. Cormier *et al*, Phys. Rev. Lett. **40** (1978) 924.
10. R. Wolf *et al*, Z. Phys. **A305** (1982) 179.
11. Y. Sakuragi *et al*, Proceedings of the 7th International Conference on Clustering Aspects of Nuclear Structure and Dynamics, Edited by M. Korolija, Z. Basrak and R. Caplar, World-Scientific-2000 (138).
12. P. E. Fry, DPhil Thesis, University of Oxford (1997), unpublished.

ABOUT INVESTIGATION OF NUCLEAR REACTIONS WITH ION BEAMS CHANNELING AND COLLIDING INSIDE CRYSTAL

Takibayev N. Zh.

Almaty, Kazakhstan

The problem of energy generation with using of nuclear fusion has been already developed near 50 years and by different ways [1-11]. All of these ways are very interesting for physics but do not give success yet for utilization. May be in ten years or a little more the big projects like "Tokomak" will come to the acting reactor but new idea or methods can leads to useful results too.

It is offered to develop a new direction of investigations on a joint of disciplines: nuclear physics and crystal physics. Another words, we'll try to stimulate the fusion reactions by placing in crystal body the crossing accelerated beams of particles and keeping conditions for channeling of these beams in crystal.

The nuclear interactions of light ions channeled inside crystal can be considered. The technique of crossing particle beams is developed quite well, especially, for the high-energy range. The phenomenon of fast-ion channeling in crystals is well known, being thoroughly studied [12,13]. It is of interest that to combine these phenomena, i.e., to consider the crossing channeled beams of light nuclei inside a crystal.

Let's consider the colliding beams of the accelerated particles (beams of light nuclei) in hollow. It is clear the probability of collisions between particles of beams is close to zero, that is a consequence of low density of particles in the beams. The simple magnification of density conducts to effect "spreading" in every beam and technically is not justified, at least, in region of not high energies. Other situation can arise, if the beams collide inside a crystal, when each of beams will be in a mode of a channeling in ranked medium (i.e. inside and along the crystal planes or axes). We suppose that the energy of the accelerated particles of beams can be not high, but sufficient for a channeling, i.e. nearly Mev or a little more.

It is known that under certain conditions and properties of a crystal (energies and incidence angles of particles on a surface of a crystal etc.) there is an effect of a channeling of particles deep into of crystal along its axes or planes. It is important, that the losses of energy of particles in this case become considerably smaller. It means that investigation of properties of the crystal and its radiation becomes possible as well as the effects of the ordered structure medium impact on the excitation or resonance processes in compound systems [14-16].

The entering macro-beam breaks up to set of mini-beams going along the next planes of a crystal (a plane channeling) or axes of a crystal (an axial

channeling). Approximately, the plane channeling can be described as a motion of a charged particle between two charged planes. The phenomenon partly reminds effect of glissade of a full speed body along a demarcation surface of two mediums.

Beam of particles channeled in crystal

The essential fact is the process of formation of a channeling beam and its effective squeezing by planes of a crystal. The focusing of a beam is caused by effective interplanar potential repelling particles of a beam from planes deep into in interplanar space.

Density of particles in a channeling beam - ρ(x), differs from density initial one. Distance between knots of a lattice is accepted for 1, density of entering beams is considered as homogeneous: $\rho_0 = 1$ (Fig.1).

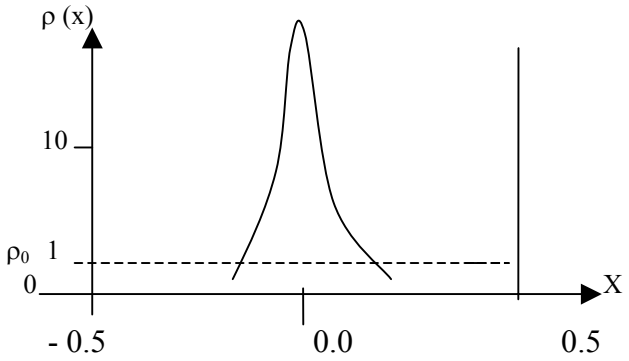


Fig. 1

In a crystal distance between planes of a lattice d ~ 10^{-8} cm. Picking a crystal and optimum requirements for a channeling of particles it is possible to achieve pinch of density of a beam in central field on two and more orders. Thereof the field of a preferred channeling, where 90 % of particles of a beam focused, will have the reference sizes with a diameter $D_c \sim 10^{-10} \div 10^{-11}$ cm.

More composite experiment guesses, that the channeling beams of particles can be guided towards each other. Then their trajectories will be intercrossed many times on the channeling path inside a crystal (see Fig.2).

It will be already equivalent to a situation, when a diameter of a tube, in which particle fly towards each other, exceeds only on the order or two the effective size R_{eff} of colliding particles $R_{eff} \sim 10^{-12} \div 10^{-13}$ cm. Experimental data and the theoretical calculations for beams of protons of energy about 1 Mev give value for the channeling length: $\chi \sim 10^{-3}$ cm.

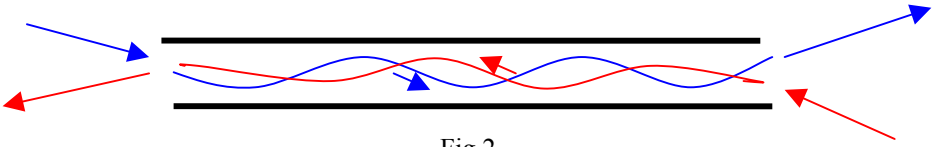


Fig.2.

In some of cases the phenomenon of hyper-channeling is happened for particles, which takes place in the most favorable kinematics requirements. Length of hyper-channeling can be $\chi_H \sim 100\ \chi$ or more. The number of particles getting in a mode of hyper-channeling reaches quantity 20-30 % from number all of channeling particles.

It is possible to tell, that the efficiency of interaction of colliding particles in a mode of hyper-channeling becomes greater on two order and more. In recalculation on one colliding particle, it gives $R_{eff} \sim 10^{-11}$ cm and more, i.e. $R_{eff} \approx D_c$. Thus, the effective size of interaction area of particles on colliding beams, channeled in a crystal, can appear equal to the size of the field of a channeling.

On the other hand, kinetic energy in system of two crossing channeling particles will be enough to run through Coulomb barrier $E_{kin} > Z_A Z_B e^2 / R_{AB}$, where $R_{AB} \approx 10^{-13}$ cm. In this case the probability of nuclear fusion reaction will become sufficient to investigate the phenomenon and may be to obtain nuclear fusion products or generate energy.

However, it demands high density of particles on colliding beams. Moreover, a high density of beams, i.e. high concentration of energy incoming inside of a crystal, can destroy crystalline medium.

While the estimates can be given the following. It is known that at pumping up of energy more than 10^{+15} W/cm^2 leads to the destruction of a crystal. Such energy corresponds to densities of colliding beams about 2 Mev in section of 10^{-16} cm^2. In this case, for example, the beams of accelerated protons with energy 1 Mev, the each colliding particle will meet the partner on a path of a channeling, even once.

The required currents in beams of particles from the accelerator can be achieved already now. The problem, however, consists in questions of a focusing and microfocusing of colliding beams. It is necessary for magnification of density of beams impinging on a surface of a crystal, on 5 and more orders, in comparison with density of beams gained from the accelerator.

The solution of a question of sync and spatial orientation of beams colliding in a crystalline foil (in a working band) also is required.

It is important to estimate that occurs faster: process of a channeling in crystal or process of destruction of a crystal. The destruction of a crystal may also be the result of nuclear reaction occurred in a crystal. In this case the system for

keeping up of the process can become an effective expedient of a drain of surplus energy from a working band. The different engineering solutions here are possible.

Fusion reactions between particles channeling in crystal

The development of the investigations includes a substantiation of an opportunity of controllable nuclear fusion processes, based on nuclear reactions realized inside a crystal. Such reactions are supposed to be explored on colliding channeling beams of light nuclei in crystal. The energies of nuclei are guessed not so high (about several Mev).

The medium of ordered structure (crystal) and the beam of accelerated light ions are proposed to be used for stimulation of the fusion reactions as well as for investigation of the effects of energy generation. For instance,

$$d + t \rightarrow n + {}^4He + 17.6 \text{ MeV or } d + {}^3He \rightarrow p + {}^4He + 18.3 \text{ MeV}$$

with using beams of d-particles and ${}^3H$ or ${}^3He$ ones.

A series of experiments can be bound to study of efficiency of these reactions in a crystal. The processes of nuclear fusion on channeling beams of light ions inside a crystal can be implemented in different variants. But all of them should use to some extent focalizing properties of ranked structure (crystal).

More composite variant guess to use of the phenomenon of resonant "swelling" of a nucleus participating in reaction up to is abnormal of the major sizes. Thus cross section of the nuclear reaction sharply grows.

The idea consists in excitation of particles of one of beams before their collisions. The resonant excited state should have the major abnormal effective size (as small bound system). As resonant particles the nuclei can be chosen which have small resonant neutron excitations.

Reactions of excitation of ions having abnormally large, efficient radii are of special interest. Opportunity for generation of particle beams in anomalous states is urgent and attractive too.

Settling excited states can be carried out by exterior action, for example, laser irradiation. It is possible to view excited nuclei channeling in a crystal as a potential radiant of neutrons, for example, resonant states of heavy nuclei (^{106}Cd, ^{150}Sm, etc.).

If the colliding beams of particles will consist of nuclei of ^{3}He, the reaction

$$^3\text{He} + \text{n} \rightarrow {}^4\text{He} + 20.5 \text{ Mev}$$

is possible with high probability. And the nuclear fusion becomes effective. Really, the efficiency will be obliged is abnormal to the major size excited (or resonant) states of a nucleus A*, for which $R_{eff} \sim 10^{-10}$ cm and more.

Other variant of study of nuclear reactions inside a crystal is bound to formation of nuclei - targets in volume of a crystal. In this case there are the direct beam and target nuclei, preliminary implanted in a crystal to a fixed depth.

For example, in case of implantation of atoms ^{6}Li in a crystal and then channeling of a beam of deuterons the pure reaction is possible:

$$d + {}^6Li \rightarrow \alpha + \alpha + 22.4 \text{ Mev},$$

i.e. reaction without harmful radioactive by-products on an output.

The formation of crystals is possible also, in which knots the nuclei - targets (light ions) are located. Search of temperature modes, when the phenomenon of a channeling still takes place, and the thermal oscillations conduct to magnification of probability of collisions of these light ions with channeling particles, can also be an object of examinations.

At examinations of channeling beams in crystals the investigation can go about study as interactions of the accelerated particles with nuclei of the crystal, and interactions between introduced (colliding or implanted) particles.

The cases are interested, when the ranked structure of a crystal will influence the characteristics of the processes. Such influence will be especial considerable for resonant transitions, which effective size is comparable with the size of a channeling area.

Summary

The essence of examinations of a direction can consist in the following:

- Study of influence of ranked structure (medium) on the characteristic of nuclear reactions;
- Definition of an opportunity and efficiency of fusion reactions;
- Search of a resonance excitation of channeling particles (nuclei) and crystal.

The main practical research problem can become a scientific substantiation of operation possibility in principle the engine installations of a new type based on nuclear fusion reactions of channeling particles in a crystal.

The physics of channeling beams of particles having composite interior structure, processes of their excitation, nuclear reactions inside a crystal represents a new perspective scientific direction of investigations.

It concerns the research of properties, both crystal, and channeling particles in crystal (stimulated transitions, decays and radiation).

All investigations as a whole are unwrapped in a new scientific direction, which is possible to term " Nuclear reactions in crystals ".

References

1. Hawryluk R.J., et al. "Fusion plasma experiments on TFTR: A 20 year retrospective". Phys. Plasm., 1998, V 5, p. 1577-1589.
2. Cheng E.T., Peng Y. K., et al "Study of spherical tokamak based volumetric neutron source". Fusion Engineering and Design, 1998, V 38, p. 219-255.
3. Annual report of Naka Fusion Research Establishment from April 1, 1998 to March 31, 1999. JAERI - Rev. 1999, N 99-022, i - xvi, p. 1 - 118.
4. JAERI Developed new technique for continuous operation of JT - 60. Atoms Jap., 2000, V 44, p. 16.
5. Selemir V.D., Karelin V.I. et al Trudy uchenukh yadernykh tcentrov Rossii, 1998, Vol. 6, p. 160 - 170.
6. US - Japan Workshop on Laser Fusion. Execut. Newslett./ Fusion Power Assoc., 1998, V 20, N 5, 3.
7. Dittrich T.R., Haan S.W., et al "Reduced scale national ignition facility capsule design". Phys. Plasm., 1998, V 5, 3708-3713.
8. Gernshtein S.S., Petrov Yu.V., Ponomapev L.I. Uspekhi Fizicheskikh nauk, 1990, v. 160, p. 158.
9. Karnakov B.M. Soros obraz. J., 1999, N 12, p. 62-67.
10. Dimov G.I. Fizika plazmy, 1997, Vol. 23, p. 883 - 908.
11. Lavrent'ev O.O. Ukr. Fiz. J. 1998, Vol. 43, p. 1100 - 1111.
12. Kumakhov M.A. "Izluchenie kanallirovannykh chastits v kristallakh", Moscow, Energoatomizdat, 1986.
13. Kashlev Yu.A., Sadykov N.M. Teoreticheskaya i matematicheskaya fizika, Vol. 116, p, 1998 .
14. Merkur'ev S.P., Faddeev L.D. "Kvantovaya teoriya rasseianiya dlya sistem neskol'kikh chastits", Moscow, Nauka, 1985 .
15. Takibayev N., Pen'kov F. Yadernaya Fizika, Vol. 57, p. 1300 - 1308, 1994.
16. Takibayev N. Reports of National Academy of Sciences Republic of Kazakhstan, 2000, Vol 5, p. 34.

ABOUT LIMIT MASSES OF ELEMENTARY PARTICLES

IBADOVA Umida and SAFAROVA Zamira

Department of Theoretical Physics and Computer Sciences, Samarkand State University, Samarkand, 703004, Uzbekistan

Abstract

The simple examples of spontaneous breaking of various symmetries for the scalar theory with fundamental mass have been considered. Higgs' generalizations on "fundamental mass" that was introduced into the theory on a basis of the five-dimensional de Sitter space. The connection among "fundamental mass", "Planck's mass" and "maximons" has been found. Consequently, the relationship among G- gravitational constant and other universal parameters can be established.

1. Introduction

The concept of mass having its root from deep antiquity (including Galileo's Pisans experiment, theoretical research of the connection of a mass with the Einstein's energy etc.) still remains fundamental. Every theoretical and experimental research in classical physics and quantum physics associated with mass is a step to the discernment of Nature. Besides mass, the other fundamental constants such as Plank's constant and the speed of light also play the most important role in the modern theories. The first one is related to quantum mechanics and the second one is related to the theory of relativity.

Nowadays the properties and interactions of elementary particles can be described more or less adequately in terms of local fields that are affiliated with the lowest representations of corresponding compact groups of symmetry. It is known that mass of any body is composed of masses of its comprising elementary particles. The mass of elementary particles is the Kasimir's operator of the noncompact Paunkare group, and those representations of the given group, that are being used in Quantum Field Theory (QFT), and it can take any values in the interval of $0 \le m < \infty$. Two particles, today referred to as elementary particles, can have masses distinct one from another by many orders. For example, the vectorial bosons with the mass of ~$10^{15} GeV$ take place in GUT modules, whereas the mass of an electron is only ~0,5 10^{-3} GeV. Formally, the standard QFT remains logical in a case when the mass of particles can be compared with the mass of automobiles. The modern QFT does not forbid such a physically meaningless extrapolation. Perhaps, it is a principal defect of the theory? In 1965 Markov put forward a hypothesis [1], according to which the spectrum of masses of elementary particles must jump into discontinuity on the "Plank's mass" $m < m_{Plank} = \sqrt{\hbar c / G}$, well-known universal constants $\hbar$, c and G-

gravitational constant take place in this expression. Markov named particles of a limiting mass as "maximums". In works V.G.Kadyshevsky and his students [2,3] in the quantum theory of a field on a strict mathematical basis the parameter " fundamental mass " which alongside with parameters of the standard quantum theory to play an essential role in physics at high energy is entered.

In the given work, we have strived for the connection of the universal constants (h, c, G), "Plank's mass", "maximon" and "fundamental mass" on a basis of the spontaneous breaking of symmetry.

2. On Quantum Field Theory with a new parameter fundamental mass

Here we will cite briefly the major ideas of quantum field theory (QFT), in which the four-dimensional momentum space is a constant curvature space with a large radius M.

The construction of the sequential Quantum Field Theory (QFT) with a new, universal scale in the superhigh energy region- Fundamental Mass M emanates to V.G. Kadyshevsky's work [2] and his students [3].

The parameter M is called fundamental mass and its inverse $l = \hbar / M \cdot c$ fundamental length. The fundamental mass fixes a new universal scale of theory in the high-energy region. The standard QFT is recovered in the "flat limit" $M \to \infty$. Recall that fundamental mass M is a new hypothetical parameter of mass dimension, which should be as universal as $\hbar$, c or Newtonian gravitational constant G and serve as characteristic scale in the region of high energies.

A key role in the approach developed belongs to the five-dimensional configuration representation. Being four-dimensional in its essence the theory admits a specific local Lagrangian formulation in which the dependence of fields on auxiliary fifth coordinate is local too. Internal symmetries in this formalism generate gauge transformations localized in the same five-dimensional configuration space. The de Sitter space has a constant curvature. Depending on its sign there are two possibilities

$$p_0^2 - p_1^2 - p_2^2 - p_5^2 \equiv g^{KL} P_K P_L = M^2 \qquad (1)$$

(*positive curvature*: $g^{00} = -g^{11} = -g^{22} = -g^{33} = -g^{55} = 1$)

$$p_0^2 - p_1^2 - p_2^2 - p_3^2 - p_5^2 \equiv g^{KL} P_K P_L = -M^2 \qquad (2)$$

(*negative curvature*: $g^{00} = -g^{11} = -g^{22} = -g^{33} = -g^{55} = 1$)

$$K, L = 0,1,2,3,5$$

It is natural that QFT based on momentum representation of the form (1)-(2) must predict new physical phenomena at energies $E \geq M$. In principle, the parameter M may turn out to be close the Planck mass

$M_p = \sqrt{\hbar c / k} \approx 10^{19}\ GeV$. Then, the new scheme should include quantum gravity.

The standard QFT corresponds to the "small" 4-momentum approximation $\left|p_0\right|, \left|\vec{p}\right| << M$ and $p^5 = g^{55} p_5 \cong M$ which formally can be performed by letting $M \to \infty$ ("flat limit"). The formulation of QFT with fundamental mass discussed in this paper is based on the quantum version of the de Sitter equation (2), i.e. on the five-dimensional field equation

$$\left[\frac{\partial^2}{\partial x^\mu \partial x_\mu} - \frac{\partial^2}{\partial x_5^2} - \frac{M^2 c^2}{\hbar^2}\right]\Phi(x, x^5) = 0 \qquad (3)$$

$$\mu = 0, 1, 2, 3$$

All the fields independently of their tensor dimension must obey (3) since similar universality was inherent in the "classical" prototype of (3)- de Sitter p-space (2). As applied to scalar, spinor, vector and other fields we shall write down the five-dimensional wave function $\Phi(x,x^5)$ in the form $\phi(x, x^5), \psi_\alpha(x, x^5)$ and $A_\mu(x, x^5)$. The decision (3) in view of the relevant Cauchy problem, which is correctness on x^5, looks like:

$$\Phi(x, x^5) \leftrightarrow \begin{pmatrix} \Phi(x,0) \\ \partial\ \Phi(x,0) / \partial x^5. \end{pmatrix} = \begin{pmatrix} \Phi(x) \\ \partial\ \Phi(x,0)/\partial\ x^5. \end{pmatrix} \equiv \begin{pmatrix} \Phi(x) \\ \chi(x) \end{pmatrix} \qquad (4)$$

In other words, the statement that to each field in the 5-space there corresponds its wave function $\Phi(x, x^5)$ obeying (3), implies that each of these fields in the usual space-time is described by the wave function with a doubled number of components. Then, it is natural to assume that the initial date (4) obey the Lagrangian equations of motion following from the action principle

$$S = \int d^4 x L\left[\Phi(x,0), \frac{\partial\ \Phi(x,\ 0)}{\partial\ x^5}\right] \qquad (5)$$

A key role in the approach developed belongs to the five-dimensional configuration representation. Being four-dimensional in its essence the theory admits a specific local lagrangian formulation in which the dependence of fields on an auxiliary fifth coordinate is local too. Internal symmetry's in this formalism generate gauge transformations localized in the same five-dimensional configuration space.

3. Calculations

Let's consider simple examples of spontaneous breaking of various symmetries for the scalar theory with a fundamental mass. The real scalar field, whose Lagrangian can be obtained from the beneath expression:

$$L(x,M)=\frac{1}{2}\left[\left[\frac{\partial\,\Phi(x)}{\partial x_n}\right]^2+m^2\Phi^2(x)+M^2\left[\chi(x)-\cos\mu\,\Phi(x)\right]^2\right] \tag{6}$$

Using (4), and it can be expressed as follows:

$$L=\frac{1}{2}\left(\frac{\partial\varphi(x)}{\partial x_\mu}\right)^2-\frac{1}{2}m^2\varphi^2(x)-\frac{M^2}{2}\left(\chi(x)-\cos\mu\varphi(x)\right)^2-\chi(x)U(\varphi(x)) \tag{7}$$

Here $\cos\mu\equiv\sqrt{1-\frac{m^2}{M^2}}$ where m - mass of particles, described by fields φ, U (φ)-an unknown function characterizing interactions among these particles.

Is it possible to select the interaction L_{int} between the fields $\varphi(x)$ and $\chi(x)$ in order that under the exclusion of the field $\chi(x)$, the Higgs potential is appropriate to the field $\varphi(x)$?

The free Lagrangian is invariant relatively the transformations $\varphi\to-\varphi$ and $\chi\to-\chi$. It is necessary to require that $U(-\varphi)=-U(\varphi)$, i.e. $U(\varphi)$-an odd function of φ, an action for (7) will be written as:

$$S=\int\{\frac{1}{2}[(\frac{\partial\varphi}{\partial x_\mu})^2-m^2\varphi^2-M^2(\chi-\cos\mu\varphi)^2]+\chi(x)U(\varphi)\}d\varphi \tag{8}$$

Taking a derivative of (8) on χ we obtain:

$$\chi=\cos\mu\varphi+\frac{U(\varphi)}{M^2} \tag{9}$$

Substituting (9) to (7), we have:

$$L_{tot}(\varphi)=\frac{1}{2}[(\frac{\partial\varphi}{\partial x_\mu})^2-m^2\varphi^2+\frac{U^2(\varphi)}{M^2}+2U(\varphi)\cos\mu\varphi] \tag{10}$$

that is invariant relatively $\varphi\to-\varphi$.

We know from spontaneous breaking of the discrete symmetry for the usual scalar field, that the Higgs potential will have a view:

$$V(\varphi)=-\frac{1}{2}m^2\varphi^2+\frac{1}{4}\lambda^2\,\varphi^4 \tag{11}$$

where λ-a mass less constant, characterizing interactions among particles.

Let's find a form of the function $U(\varphi)$, in order for the Higgs potential to figurate in (10). Let's consider the Lagrangian (10) under $m \to im$, then $\cos\mu = \sqrt{1-\frac{m^2}{M^2}} \to ch\mu' = \sqrt{1+\frac{m^2}{M^2}}$

The potential energy (11) will have a view:

$$V(\varphi) = \frac{1}{2}m^2\varphi^2 - \frac{U^2}{2M^2} - U(\varphi)ch\mu\varphi \qquad (12)$$

Comparing (12) and (11) for $U(\varphi)$ we have two different roots (real and imaginary) under $\varphi^2 < \frac{2M^2ch^2\mu}{\lambda^2}$ and $U = -M^2ch\mu\varphi$ under $\varphi^2 = \frac{2M^2ch^2\mu}{\lambda^2}$. This results in this that

$$L_{tot}(\varphi)_{Higgs} = L^0_{\max imon}(\varphi), \text{ i.e. } L^0_{\max imon}(\varphi)\ \frac{1}{2}(\frac{\partial\varphi}{\partial x_\mu})^2 - \frac{1}{2}M^2\varphi^2 \qquad (13)$$

Now let's consider a case when $L_{tot}(\varphi) = -\frac{\lambda^2}{4}\varphi^2\chi^2$. Under $m \to i\,m$, the Lagrangian (7) will have a view:

$$L_{tot}(\varphi) = \frac{1}{2}[(\frac{\partial\varphi}{\partial x_\mu})^2 - M^2sh^2\mu'\varphi^2 - M^2(\chi - ch\mu'\varphi)^2 - \frac{\lambda^2}{2}\varphi^2\chi^2] \qquad (14)$$

Taking a derivative of (14) on χ we obtain: $\chi = \frac{M^2ch\mu'\varphi}{M^2 + \frac{\lambda^2\varphi^2}{2}}$

$$L_{tot}(\varphi) = \frac{1}{2}\left[(\frac{\partial\varphi}{\partial x_\mu})^2 + M^2sh^2\mu'\varphi^2 - \frac{\lambda^2}{2}\varphi^2(\frac{\lambda^2\varphi^2}{2M^2}+1)\frac{M^4ch^2\mu'\varphi^2}{(M^2+\frac{\lambda^2\varphi^2}{2})^2}\right] \qquad (15)$$

This is one of the Higgs' generalizations on a fundamental mass. We will obtain the usual Higgs' Lagrangian from (15) under M $\to\infty$:

$$\lim_{M\to\infty} L_{tot}(\varphi) = \frac{1}{2}\left[(\frac{\partial\varphi}{\partial x_\mu})^2 + m^2\varphi^2 - \frac{\lambda^2\varphi^4}{2}\right] \qquad (16)$$

If taking into account in (11) the strong connection ($\lambda \to \infty$) then we come to a Lagrangian:

$$L_{tot}(\varphi) = \frac{1}{2}(\frac{\partial \varphi}{\partial x_\mu})^2 - \frac{M^2\varphi^2}{2}, i.\ e. \quad L_{tot}(\varphi)_{Higgs} = L^0_{Maximon}(\varphi)$$

Spontaneous breaking of the global U (1)-symmetry results in:

$$L_{tot} = \left|\frac{\partial \varphi}{\partial x}\right|^2 - m^2|\varphi|^2 - M^2|\chi - \cos\mu\varphi|^2 - \frac{\lambda^2}{2}|\chi|^2|\varphi|^2 = \\ = \left|\frac{\partial \varphi}{\partial x}\right|^2 - M^2|\varphi|^2 - M^2|\chi|^2 + M^2\cos\mu\left|\chi\bar{\varphi} + \varphi\bar{\chi}\right| - \frac{\lambda^2}{2}|\chi|^2|\varphi|^2 \tag{17}$$

under $m \to i\,m$, then

$$L_{tot}(x) = \left|\frac{\partial \varphi}{\partial x}\right|^2 - M^2|\varphi|^2 - M^2|\chi|^2 + M^2 ch\mu'\left|\chi\,\bar{\varphi} + \overline{\varphi\,\chi}\right| - \frac{\lambda^2}{2}|\chi|^2|\varphi|^2 \tag{18}$$

This Lagrangian differs from (17) by a sign before m^2, but it is still invariant relatively the group of global transformations:

$$\varphi(x) \to \varphi(x) = e^{ig\varepsilon}\varphi(x), \qquad \varphi^*(x) \to \varphi^*(x) = e^{ig\varepsilon}\varphi^*(x) \\ \chi \to \chi'(x) = e^{ig\varepsilon}\chi(x), \qquad \chi^*(x) = e^{ig\varepsilon}\chi^*(x) \tag{19}$$

Taking the derivative of L_{tot} (x) on χ and $\bar{\chi}$, we will find the equation of motion for $\bar{\chi}$ and χ respectively $-M^2\bar{\chi} + M^2 ch\mu'\bar{\varphi} - \frac{\lambda^2}{2}|\varphi|^2\bar{\chi} = 0$ and

$$-M^2\bar{\chi} + M^2 ch\mu'\bar{\varphi} - \frac{\lambda^2}{2}|\varphi|^2\chi = 0$$

From here we get: $\bar{\chi} = \dfrac{ch\mu'\bar{\varphi}}{1 + \dfrac{\lambda^2}{2M^2|\varphi|^2}} \qquad \chi = \dfrac{ch\mu'\bar{\varphi}}{1 + \dfrac{\lambda^2}{2M^2|\varphi|^2}}$

$$L_{tot}(x) = \left|\frac{\partial \varphi^2}{\partial x}\right| - V(\varphi) \tag{20}$$

where V (φ)-Higgs potential V (φ)=M^2 $|\varphi|^2 - \frac{M^2 ch^2 \mu' |\varphi|^2}{1+\frac{\lambda^2}{2M^2}|\varphi|^2}$ under

$|\varphi|^2 = \frac{2M^2}{\lambda^2}(ch\mu'-1)$ has its minimum $V_{min}(\varphi)=--\frac{2M^4}{\lambda^2}(ch\mu'-1)^2$. In the flat limit M $\to\infty$, (20) will have a usual view. If we write $V|\varphi| = V_{\min}(\varphi)$, then

$$V_{New}(|\varphi|) = \frac{\lambda^2}{2}\frac{\left[|\varphi|^2 - \frac{h^2}{2}\right]^2}{1+\frac{\lambda^2}{2M^2}|\varphi|^2} \tag{21}$$

where $\frac{h^2}{2} = \frac{2M^2}{\lambda^2}(ch\mu'-1)$ under $M \to \infty$ equals $\frac{m^2}{\lambda^2}$. Finally, we obtain

$$L_{tot}(x) = \left|\frac{\partial\varphi}{\partial x}\right|^2 - \frac{\lambda^2}{2}\frac{\left[|\varphi|^2 - \frac{h^2}{2}\right]^2}{1+\frac{\lambda^2}{2M^2}|\varphi|^2} \tag{22}$$

The system, described by the Lagrangian (18), has the spontaneous broken *U (1)*-symmetry. Now a point is not appropriate to the minimum of energy $\varphi(x) = \bar{\varphi}^*(x) = 0$, but any point on a circle

of the radius $R = \sqrt{2}\frac{M^2}{\lambda}\sqrt{ch\mu'-1}$. Let's write $\varphi(x)$ in a view of the real and imaginary parts. As a stable vacuum, we can choose any state, lying on a circle of the radius of *R*, i.e. all the states are equivalent due to in variation relatively transformations (19). Let's pick out the magnitude of a gauge phase to be *β=0,* identical for the whole world, and let's write φ in a view

$$\varphi(x) = \frac{1}{\sqrt{2}}(h + \varphi_1(x) + i\varphi_2(x)) \tag{23}$$

Substituting (23) into (22), we obtain

$$L_{tot}(\varphi) \Rightarrow L_{tot}(\varphi_1, \varphi_2) =$$

$$= \frac{1}{2}\left(\frac{\partial\varphi_1(x)}{\partial x_\mu}\right)^2 + \frac{1}{2}\left(\frac{\partial\varphi_2(x)}{\partial x_\mu}\right)^2 - \frac{\lambda^2}{8}\frac{\left[\varphi_1^2 + 2h\varphi_2^2\right]^2}{1+\frac{\lambda^2}{16M^2}\left[\left(h+\varphi_1\right)^2 + \varphi_2^2\right]} \tag{24}$$

The Goldstone scalar mass less particle φ_2 has appeared as a result of the spontaneous breaking of the symmetry, and a real scalar particle with a mass

$$m_1 = \frac{\lambda h}{\left(1+\frac{\lambda^2 h^2}{16M^2}\right)^{1/2}} \tag{25}$$

Under $M\to\infty$ from (25) we have $m_1 = \sqrt{2m}$. If we consider the real scalar particle as a maximon, then from (40) we obtain: $m_{1\max simon} = \frac{2M}{\left(\sqrt{2}+1.25\right)^{1/2}}$

Acknowledgements

The authors are sincerely grateful to R.M.Ibadov, V.G.Kadyshevsky, M.M.Musakhanov and B.S.Yuldashev for useful arguing of outcomes, constant attention and help with a spelling of the given work.

References

1. Markov M.A. Supplement of the Progress of Theoretical Physics, Commemoration Issue for 30th Anniversary of Meson Theory by Dr.H.Yukawa, 1965, p.85; Markov M.A. Preprint INR, P-0207, 1981; P-0286, 1983; Markov M.A., Mukhanov V.F. Preprint INR, P-0331, 1984.
2. Kadyshevsky V.G. Preprint JINR, Dubna, P2-84-753, 1984; Kadyshevsky V.G., Nuclear Physics, B141, p.477, 1978; Kadyshevsky V.G. Particles and Nuclei, II, i.1, 1980, p.5.
3. Chizhov M.V., Donkov A.D., Ibadov R.M., Kadyshevsky V.G. and Mateev M.D. Nuovo Cimento, v.87A, N 3, p.350, 1985; v.87A, p.373, 1985; Ibadov R.M., Kadyshevsky V.G. Int. Symp. On Selected Topics in Statistical Mechanics Dubna-1989 world Scientific, p.131-156, 1989; Ibadov R.M. Proceeding Int. Conf." Probl. of Theor. Phys. and Solid State Phys.", Buchara 1997, p.22-23; Ibadov R.M., Kadyshevsky V.G. Abstracts of The Second Uzbekistan conference "Modern problems of Nuclear Physics". Samarkand 1997, p.187; Ibadov R.M., Ibadova U.R., Ravshanova D.R. and Umidullaev Sh.U. "On Quantum Field Theory with Fundamental mass" In Proc. International School-Seminar "Structure of Particles and Nuclei and their Interactions" Tashkent, Oct.1997, Dubna 1998, JINR, p.139-141; Ibadov R.M. and Ibadova U.R. http://menu2001.phys.gwu.edu/menu2001/abstracts/rust2.ps. (USA, 2001); Ibadov R.M., Ibadova, and Ravshanova D.R. http://pheno.physics.wisc.edu/pheno01/ravshanova.pdf. (USA, 2001).

ABOUT TOTAL KINETIC ENERGY DISTRIBUTION BETWEEN FRAGMENTS OF BINARY FISSION

[1)]Khugaev A.V., [1)]Koblik Yu.N., [1)]Pikul V.P., [2)]Ioannou P., [2)]Dimovasili E.

[1)]Institute of Nuclear Physics, Tashkent, Uzbekistan
[2)]University of Athens, Athens, Grecee

At the investigation of binary fission reactions one of the main characteristic of process is Total Kinetic Energy (TKE) of fission fragments and it distribution between them. From the values of these characteristics it is possible to extract the information about structure of fission fragments in the break up point of initial fissionable nuclear system. In our work TKE dependence from the deformation parameters of shape and density distribution of charge in the fission fragments are investigated.

From the consideration of fission process, produced by thermal neutrons: thermal neutron + target nucleus $\rightarrow$ fragment1+fragment2, we can to write, in the scisson point, from the conservation rules for the energy and moment following simple expressions:

$$m_n c^2 + \frac{2\pi^2\hbar^2}{m_n\lambda^2} + B_0 + \frac{\hbar^2 J_0(J_0+1)}{2I_0} = \\ = B_1 + B_2 + U_{12} + \frac{\hbar^2 J_1(J_1+1)}{2I_1} + \frac{\hbar^2 J_2(J_2+1)}{2I_2} + \frac{\hbar^2 L(L+1)}{2I_{12}} \\ |J_1 + J_2 - J_0 - \frac{1}{2}| \le L \le |J_1 + J_2 + J_0 + \frac{1}{2}| \qquad (1)$$

here L is relative moment of fission fragments, B_0, B_1, B_2 - correspond to the binding energy of considering nuclei, I_0, I_1, I_2 are their own moments of inertia and I_{12} is relative moment of inertia for the fragments of fission. Then, for the central collision with thermal neutron, in the Lab. system (target nucleus is in a rest), we can to write:

$$E_{TKE} = \left(1 + \frac{M_1}{M_2}\right)\varepsilon_1 - \frac{2\pi\hbar c}{\lambda}\frac{M_1}{M_2}\cos\vartheta_1\sqrt{\frac{2\varepsilon_1}{M_1c^2}} + \frac{1}{2M_2c^2}\left(\frac{2\pi\hbar c}{\lambda}\right)^2 \qquad (2)$$

where ε_1, ϑ_1 and λ are known values from the experimental data. ε_1 is kinetic energy of fission fragment, ϑ_1 is angle between directions of motion for the neutron and fission fragment in the Lab. system and λ is the wave length for the thermal neutron. From the last expression we can to fined TKE value for the fission fragments. After that we have set of equations, expressing the dependence of E_{TKE} through deformation parameters and density distributions for masses and charges of fission fragments:

$$E_{TKE} = U_{12} + \frac{\hbar^2 L(L+1)}{2\mu x_0^2}, \quad \mu = \frac{M_1 M_2}{M_1 + M_2}$$

$$\mathrm{E_{TKE}} = (\mathrm{m_n c^2} + \mathrm{B_0} - \mathrm{B_1} - \mathrm{B_2}) + \frac{\hbar^2 \mathrm{J_0(J_0+1)}}{2\mathrm{I_0}} - \frac{\hbar^2 \mathrm{J_1(J_1+1)}}{2\mathrm{I_1}} - \frac{\hbar^2 \mathrm{J_2(J_2+1)}}{2\mathrm{I_2}} + \frac{2\pi^2\hbar^2}{\mathrm{m_n}\lambda^2} \tag{3}$$

here U_{12} is potential energy of fission fragments, M_1 and M_2 are their masses and x_0 is the distance between c.m. of them. These last two equations show us the dependence of TKE value from the parameters of fission fragments I_0, I_1, I_2 and U_{12}, which are some functions from shape of nuclei (deformation) and distributions of charges and masses. Therefore from the knowledge of TKE value we can to investigate the shape, mass and charge distribution of fission fragments from the some model parametrisations and to calculate them from the comparison with E_{TKE}.

Some model suppositions

Let's to consider for the fission fragments two ellipsoids with aksial symmetry and parameters of a_1, c_1 for the first ellipsoid and a_2, c_2 for the second (see Fig.1).

From the conservation rule for the volume and charge of two considering fission fragments and in the suggestion, that the density of charge in the fission fragments is constant ρ_1 and ρ_2 we have :

$$ez_1 = \frac{4}{3}\pi a_1^2 c_1 \rho_1, \quad ez_2 = \frac{4}{3}\pi a_2^2 c_2 \rho_2$$

here z_1 and z_2 are charges for the fission fragments and for the c_1 and c_2 we also have, that:

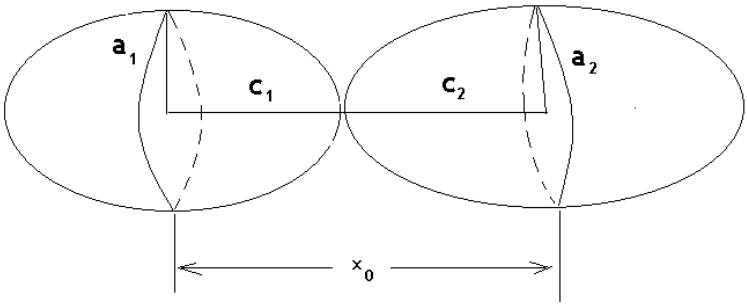


Fig1. Initial configuration of fission fragments in the scisson point.

$$c_1 = \frac{A_1 r_0^3}{a_1^2}, \quad c_2 = \frac{A_2 r_0^3}{a_2^2}, \quad x_0 = c_1 + c_2 + \delta, \quad A_0 = A_1 + A_2,$$

$$z_0 = z_1 + z_2, \quad r_0 \approx 1.2 \text{ fm}.$$

Here A_1, A_2 are atomic number of fission fragments. Then we can to write for deformation parametres a_1 and a_2 following set of equations:

$$\begin{cases} E_{TKE} = \left(\frac{3}{4\pi}\right)^2 \frac{z_1 z_2 e^2}{A_1 A_2 r_0^6} \Phi(a_1, a_2, x_0) + \frac{\hbar^2 L(L+1)}{2\mu x_0^2}, \mu = \frac{M_1 M_2}{M_1 + M_2} \\ E_{TKE} = \left(m_n c^2 + B_0 - B_1 - B_2\right) + \\ + \frac{\hbar^2}{2}\left[\frac{J_0(J_0+1)}{I_0} - \frac{5}{2}\left(\frac{J_1(J_1+1)}{a_1^2 e z_1} + \frac{J_2(J_2+1)}{a_2^2 e z_2}\right)\right] + \frac{2\pi^2(\hbar c)^2}{m_n c^2 \lambda^2} \end{cases} \tag{4}$$

where for the function $\Phi(a_1, a_2, x_0)$ we have:

$$\Phi(a_1,a_2,x_0) = \int_0^{2\pi} d\varphi \int_{-c_1}^{c_1} dz \int_0^{a_1\sqrt{1-\left(\frac{z}{c_1}\right)^2}} r dr \int_0^{2\pi} d\varphi' \int_{x_0-c_2}^{x_0+c_2} dz' \cdot \int_0^{a_2\sqrt{1-\left(\frac{z'-x_0}{c_2}\right)^2}} \frac{r' dr'}{\sqrt{r^2 + r'^2 - 2rr'\cos(\varphi-\varphi') + (z-z')^2}}$$

Therefore from the set of equations (4) we can to extract the information about hemiaxis for the ellipsoids of fission fragments. Of course, that all these relations are valid only in the framework of our model agreements: here we take distributions of charges constant and their shapes are ellipsoidal with rotation symmetry along axis c_1 and c_2. The set of equations can be solved using some numerical iteration. For the start of iteration procedure we can to take values:

$$x_0 = c_1 + c_2; \quad a_1 = r_0 \sqrt[3]{A_1}; \quad a_2 = r_0 \sqrt[3]{A_2}; \quad \delta = 0$$

Conclusion

Our approach is based on the well known liquid drop model. Many features of nuclear binary fission it is possible to explain within such simple approaches [1,2]. In our work we suggested some simple parametres of shapes and distributions of charges for fission fragments. Additional assumption is, that we neglected nuclear forces in scission point. In future we plane to describe products of binary fission reactions such as ^{239,241}Pu+n. For the densities of charge distribution we will take Fermi like distributions ore the shell model densities distributions for fission fragments [3]. In our work we simply present the possibility to extract some additional information about shape and charge density distribution for fission fragments.

Acknowledgments. One of the author A.V. thanks Dr. A. Nasirov for the fruitfull discussions and strong support on the way to clarify some difficult places of understanding fission nature.

References

1. W.I. Swiatecki and I.R. Nix, Nuclear Physics, v.71, 1965, p.1
2. S.V. Radionov,F.A. Ivanyuk, V.M. Kolomietz, A.G. Magner, Sov.J. Nucl.Phys. v.65,2002,p856
3. A.K. Nasirov, private communication

ALPHA-PARTICLE STATES AND α-CONDENSATE IN NUCLEAR MATTER

Gnilozub I.A.[1], *Kurgalin S.D.*[2] *and Tchuvil'sky Yu.M.*[1]

[1]Moscow, Russia;
[2]Voronezsh, Russia

Abstract. The theory of alpha-particle states of nuclei based on the microscopic Hamiltonian of broken SU(3) symmetry commutative with the antisymmetrizer is presented. The problem of α-condensed nuclear matter of normal density is discussed in light of the theory.

1. Introduction

Recently keen interest in the problem of alpha-particle (AP) condensate in nuclear matter takes place [1]. Both general properties of the condensate and possibility of its existence are disputable. The basic line of theoretical investigation is search for α-condensed matter at very low densities (less or about 1/5 of normal) of nuclear matter. The main test on the condensed nuclear states is the strong coupling of such states with α + nucleus channel (open or closed) populated in elastic α-scattering from nuclei, radiative capture, α -transfer reactions etc. So it is reasonable to treat the problem of α-condensate in connection with AP states. Wide experimental evidence on these states have been obtained up to now [2,3] for even-even (2s-1d)-shell nuclei both with N=Z and N=Z+2. Except near-magic regions of nuclei more than hundred levels in a spectrum of each researched nucleus (^{22}Ne, ^{32}S, ^{36}Ar, etc.) are observed.

The microscopic theory of α-particle states of nuclei is presented in the paper at hand. The theory allows one to make rather definite conclusions concerning α-condensate in nuclear matter.

2. Properties of the α -particle spectra. Obvious consequences

First of all let us discuss pronounced features of α -particle spectra known from Refs. [2,3] and some another papers.. Each spectrum is characterized by the following:

1.There is a great number of AP states for nonmagic nucleus. To explain their density using two-body model for ^{32}S as an example one needs a nuclear potential with normal depth and of about 15 fm as wide. So the resonances being strongly coupled with AP channel are nevertheless far from two-body type.

2.Although level density for any angular momentum L is high, but for the nuclei from the middle of (2s-1d)-shell it is about one order of magnitude less than total. In one and the same energy region only the small part of nuclear levels turns out to

be visible and the most part of them is not populated. The selectivity of α -particle scattering (and another mentioned reactions) is strong.
3.A-dependence of level density is strong and irregular. Spectra of nuclei irrelevant to magic or magic core+alpha types are much more dense than those fall in this category.

3. Basic formalism

Mentioned above properties places the rigid constraints on the theory. The desired model should contain the description of two-body asymptotics, and the spectra of the resonance states, and the coupling between them. For the sake of brevity we limit ourselves by short review of the methods involved. Let us consider (2s-1d)-shell N=Z-even nucleus. AP asymptotic state is antisymmetrized product of the cluster Ψ_{α}, core $\Psi_{(A-4)}$ and relative motion $\phi_E^L(\rho)$ wave functions:

$$\Psi_{as} = \hat{A}\left(\Psi_{\alpha} \Psi_{(A-4)} \phi_E^L(\rho) \right), \quad (1)$$

where $\hat{A}$ is the antisymmetrizer. Ground states of (A-4) target nucleus is well described in the Elliott model [4,5] and so the wave functions (WFs) are characterized by spin S=0 and isospin T=0, angular momentum and total spin L=J=0, Young frame $[f_c]=[4^{(A-4)/4}]$, Elliott symbol of SU(3)-symmetry $(\lambda\mu)$. The global Wigner SU(4) symmetry of the state is determined by the product of the Young frames of APs [4] and the core$[f_c]$ and consequently takes the sole value [f] = $[4^{A/4}]$. Another global quantum numbers (S,T,L) fulfill the ordinary selection rules.
Since the WF of the α --particle is SU(3)-scalar the global SU(3) Elliott symbol of the state is determined by the product $(\lambda\mu) \subset (\lambda_c\ \mu_c) \times (n0)$ where the last representation is related to the WF of the relative motion. The value n is determinate due to the possibility to expand the two-body continuum WF of the relative motion $\phi_E^L(\rho)$ onto the series of harmonic oscillator WFs $\phi_{nL}(\rho)$ where n is the principal quantum number (QN) of the oscillator functions. As a result a WF of the relative motion is characterized by the infinite number of the Elliott symbols (n0). With increasing of n the density of resonance states grows rapidly and so such resonances turn out to be overlapping and, consequently, invisible. By this way the components of asymptotic WF turn out to be written in the Elliott model also.
The basic hypothesis of the model is the existence of AP resonances describing by the same QNs [f], $(\lambda\mu)$, L, S, T as main components of WFs of asymptotic channels, strong coupling of discussed resonances and channels, and weak coupling of channels with another nuclear states.

Naturally all partial QNs of asymptotic state are not conserved because the antisymmetrizer is pitiless terminator of partial quantities at short distances.
Phenomenological argument in favor of the hypothesis is that for magic core (λ_c μ_c)=(00) and so ($\lambda\mu$) takes the sole value (n0) while in opposite case the list of ($\lambda\mu$) is wide. If one would exclude ($\lambda\mu$) -conservation requirement there would be too much states in the both cases.
Such resonances are to be the eigenstates of the Hamiltonian. To conserve Elliott SU(3) symbols Hamiltonian must be constructed by the number of the commuting invariant operators of SU(3) group and the related subgroups:

$$H = H_{osc.} + f_1(\hat{L}\hat{L}^2) + \\ + f_2(QQ) + f_3((Q \otimes Q)Q) + f_4(Q(\hat{L} \otimes \hat{L})), \quad (2)$$

where $H_{osc.}$ - the oscillator Hamiltonian, $\hat{L}$ - the operator of angular momentum, Q-quadrupol operator (see Ref.[5]). In some respects the approach is the extension of Elliott SU(3) model [4,5] on alpha-particle states developing it by incorporating of the Q^3, $Q\hat{L}^2$ terms into the model Hamiltonian. It may be written through the Casimir operators being typical Hamiltonian of broken symmetry.
It should be noticed that very similar (but containing operators associated with the subspaces i.e. not global in part) Hamiltonian is used for the same purposes in the semimicroscopic algebraic cluster model [6-8].
If in Eq.2 one uses the linear combination of commutative SU(3) invariants, the eigenvalues of the Hamiltonian are easily expressed through the QNs ($\lambda\mu$), L and Ω - the eigenvalue of Bargman operator $\hat{\Omega}$. So the proposed model incorporates the Hamiltonian and the WFs written through the nucleon variables. Consequently it is purely microscopic model.
The WFs of the resonances at first glance do not manifest a cluster structure which is defined in analogy with Eq.1. Where is a connection? To make it visible the multicluster generalization of two-body Wildermuth-Kannelopulos (see [9]) identity is built. It is possible to write translationally-invariant shell model WF in the form:

$$\Psi_A \equiv A\left(\prod_{i=1}^{k} \Psi_i \cdot N^{-1/2} \Psi_{rel.} \Delta \right) \quad (3)$$

here Ψ_A is the A-nucleon WF of the multicluster system, Ψ_i - the WF of a cluster i, $\Psi_{rel.}$ is the WF of the relative motion of k clusters in the SU(3) scheme, $\hat{N}$ - the (multicluster) overlap kernel of the resonating group model and Δ

denotes the global (characterizing the whole system) QNs. If one uses the alpha-particles as the clusters (constituents) than $\Delta \equiv$ {[f]=[4^{A/4}], (λμ), L, S=0, T=0, J=L, δ}, where δ denotes complementary QNs. Discussed above AP resonances are characterizing by the same QNs. Hamiltonian built by Casimir operators results by one and the same spectrum both in the full space of antisymmetrized A-nucleon WFs and in the space of the WFs of the relative motion of AP $\Psi_{rel.}$ (exchange matrix elements are equal to zero), so APs can be consider as structureless constituents. The only difference between the spectra is that some states contained in the space of the WFs of the relative motion turn out to be forbidden by Pauli principle in the full space and some another states there turn out to be multiple.

So the list of alpha-particle states is limited by, first, Pauli restrictions and, second, prescription of basic hypothesis of the model requiring coincidence of their QNs with asymptotic ones.

The final list of multiplicities of allowed Elliott symbols and spins for the ^{22}Ne nucleus is presented in tabl.1.

Table 1. Classification of the alpha-particle levels of the lower bands of ^{22}Ne nucleus.

(λμ)	n=8	n=9	n=10	L^{π}	n=8	n=9	n=10
(82)	1	0	0	0^+	3	0	99
(63)	1	0	0	1^-	0	10	0
(44)	2	0	0	2^+	7	0	164
(11 1)	0	1	0	3^-	0	19	0
(92)	0	2	0	4^+	10	0	239
(73)	0	3	0	5^-	0	23	0
(54)	0	4	0	6^+	8	0	239
(14 0)	0	0	3	7^-	0	19	0
(12 1)	0	0	3	8^+	5	0	194
(10 2)	0	0	21	9^-	0	12	0
(83)	0	0	30	10^+	0	0	119
(64)	0	0	45				

Finally a N=Z-even nuclear system behaves as a system of k stable α-particles (k=Z/2). Consequently in the proposed model an α-particle resonance is multicluster α-particle state.

If one describes a core nucleus by use of the wave function of Elliott type than the asymptotic state is the state of such nature also.

Another choice of the partition of the WF of a system is not valid because in this case the antisymmetrizer turns out to be the origin of channel coupling. There is one exclusion. Partition conserves validity if more heavy magic constituent (^{16}O,

^{40}Ca) is involved. However qualitative properties of ^{20}Ne spectrum testify that multi-alpha model of the states is preferable.
So precisely solvable mathematical model of cluster stability is built.
It should be noticed that the microscopic model allows one to determine the expressions of the spectroscopic factors of α-particles in the states under discussion.

4.Alpha-particle condensate in nuclei

So the states of nuclei generated by the SU(3) Hamiltonian and populated in the discussed above reactions manifest in these processes the properties of nuclear matter, condensed to multi-alpha-particle states. Internal structure of α-particles, exchange effects, nucleon degrees of freedom turn out to be visible for another entrance or outgoing channel only.
The picture of the process looks like the following: α-particles are penetrating one each other, interaction and nucleon exchange resulted by disintegration (loss of individuality) of the α-particles. Instead of that all the properties of multi-alpha-particle system are conserved and the memory about asymptotic α-particle channel turns out to be absolute (in analogy with elastic time-dependent Hartry-Fock picture). Nucleon dynamics determined by the Hamiltonian is the origin of stability of α-particle states.. And what is more this stability takes place at normal nuclear density.
So the nucleon system described by the Hamiltonian (2) and "α-particle" boundary conditions behaves as α-particle matter. All nucleons turn out to be condensed to α-particles. Peculiar kind of α-particle shell model is valid for the WF $\Psi_{rel.}$.
However mentioned above selection rules appearing due to Pauli principle put the limits on the number of α-particles placed on one α-level. Indeed, level with principal QN of the alpha-particle center of mass motion n_α=0 is completed by one, next (n_α=4) – by three, next (n_α=8) – by six α-particles etc. Intermediate values of n_α appears only if lower levels is not completed. So Pauli principle prevent condensation of a large number of α-particles on one level. Properties of alpha-condensate are essentially distinguished from ordinary Bose condensate.

5. Conclusion

1.The microscopic SU(3) theory of α-particle and states of light nuclei is developed. It is rather general since it allows to investigate arbitrary characteristics of the discussed states such as spectroscopic factors (reduced widths), B(E2)-probabilities, inelastic scattering ones etc.
2.The approach seems to be very natural since a lot of qualitative properties of α-particle systems appear automatically in it.

3.The properties of alpha -particle spectra (level densities and their variation from nucleus to nucleus, shapes of rotational bands etc.) are well reproduced in the model.
4. The point of the theory is precisely solvable model of cluster stability. The Hamiltonian of the model generates the properties of A-nucleon system completely reduced to the properties of A/4-α-particle one, i.e. the system behaves as α-condensed matter.
5.Pauli principle acting in A-nucleon system prevents condensation of a large number of α-particles on one level. So α-condensation is more complicated subject than ordinary Bose one.

Acknowledgements
Work supported by RFBR, grant No 00-02-16683.

References

1. A.Toshaki, H.Horiuchi, P.Schuk, G.Ropke. Phys.Rev.Lett. 87 (2001) 192501.
2. M. Brenner. 1997 et al Proc. 2nd Latinamerican Conference on Nucl. and Heavy Ion Phys. Caracas, Sept. 1-5 1997.
3. V.Z. Goldberg et al. 1997. Yad.Fiz. (Phys. At. Nucl.) 63 (1997) 573**.**
4. J.P. Elliott. Proc.Roy.Soc. A245 (1958) 128; 562.
5. M. Harvey. Adv.Nucl.Phys. 1 (1968) 67.
6. J. Cseh, G. Levai, W. Scheid, J. Smidt. Revista Mexicana de Fisica 41 Supplemento (1995) 109.
7. J. Cseh, G. Levai, A.Algora, P.O.Hess, K.Kato. Proceedings of the 174. WE-Heraeus Seminar on New Ideas on Clustering in Nuclear and Atomic Physics eds N. Cindro and W. Scheid Rauischholtzhausen (Germany) 9-13 June, 1997, Editrice Compository, Bologna 1997 p. 921.
8. G. Levai, J. Cseh, P. Van Isacker, W. Scheid. Ibid, p. 927.
9. K. Wildermuth, T. Kannelopulos. Nucl.Phys. 9 (1958) 449.

ANGULAR DEPENDENCE OF A TWO-PROTONS CORRELATION FUNCTION IN p+A AND d+A INTERACTIONS AT 3 AGeV

S.V. Afanasiev, Yu.S. Anisimov, V.K. Bondarev, D.K. Driablov, A.Yu. Isupov, V.I. Ivanov, A.G. Litvinenko, A.I. Malakhov, I.I. Migulina, V.N. Penev, A.Yu. Starikov, O.A. Titov

The SCAN experiment at the JINR Nuclotron has investigated p+A and d+A reactions at 3 AGeV. The azimuthal dependence of two-proton formation at high p_T was studied in a search for the reaction mechanism. The report includes the experimental results on the angular dependence of two-proton correlations. Protons, emitted in an angle interval between $90^0 \div 120^0$ in the laboratory system, were analyzed. The dependence on charge multiplicity and kinematic variables is discussed.

I. Introduction

Interest in the study of high-energy nucleus-nucleus interactions has recently increased. The formation of cumulative particles is one of the most interesting nuclear effects [1].

Cumulative particle production is the process in which the yield of secondary particles from an inelastic interaction is beyond the kinematic limits for a free-nucleon interaction. Cumulative hadron production in the kinematically forbidden region implies the existence of an object heavier than one nucleon inside the nucleus. Some models [2] consider these objects as nuclear density fluctuation products referred as fluctuons. Cumulative hadron production is accompanied by a high-momentum transfer to nuclei. Under such conditions, there appears the possibility to study nuclear structure at internuclear distances smaller than 1 Fm [3]. The investigation of cumulative production can also provide an insight into collective nuclear phenomena, for instance, phase transition in nuclear matter. Therefore, cumulative hadrons provide information on the properties of nuclear matter and not on those of the specific nucleus.

It is important to answer the question whether the fluctuon is a density system of correlated nucleons or a structure with significantly different properties. Thus, within the framework of quark models, the experimental data indicate that the fluction structure functuon is different from the nucleon one. A direct measurement of space-time properties of these objects can help in studies.

The intrinsic features of cumulative particle production can be better understood if correlated pair products are investigated. Studying a such reaction, one has to bear in mind that the projectile may collide with fluctuons inside the nucleus multiply. The number of intranuclear interactions was estimated in [4]

from the analysis of angular correlations using the 4-momentum conservation law. The quantities **r** and **n** where found to follow a simple reaction: $\mathbf{n}\cdot\mathbf{r}^{-3}$ =const. This relation implies a constant density of fluctuons inside the interaction region.

The most preferable way of such studies is to detect two cumulative protons with a small relative momentum. The yield of protons is more intensive, and the experiment can be performed for a reasonable time. The sensitivity of two-proton correlations to the space-time extension of nuclear reactions was noted by many authors. The measurement of two-proton correlations was used along with the pion HBT data as a probe of space-time properties of heavy ion collisions. A prominent "div+peak" structure in the proton correlation function is due to the interplay of the strong and Coulomb interactions along with the effects of quantum statistic. The proton source is typically assumed to be a chaotic source with a gaussian profile that emits protons instantaneously [5]. As shown for a simple static chaotic source [6,7], the height of the correlation peak approximately scales inversely with the source volume.

The experiments were performed at JINR using an internal 3 GeV/nucleon beam of up to 10^{10} nuclei/burst. The particles product from the C and W targets were detected at 90-120^0 in the laboratory system. The time-of-flight method (TOF), the amplitude of signals and coordinates were used to identify of secondary particles. All information was obtained by scintillation counters.

II. Experimental technique

The internal target chamber [8] and the SCAN-detectors [9] are shown in fig.1. The chamber consists of a 30 cm diameter cylinder made of iron with a 0.5 mm-thick wall and 20 mm-thick end-covers. The targets are placed in the beam every cycle of the accelerator by remote control. The fibers of carbon (8mkm) and tungsten (10mkm) are used as targets.

All the detectors were outside the scattering chamber. The multiplicity array H_M consisted of 32 plastic scintillator paddles. The paddles 5 mm thick were arranged

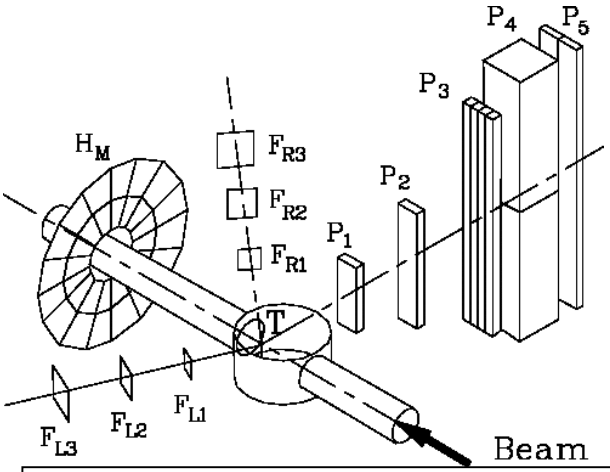


Fig.1 Schematic diagram of the internal target chamber, multiplicity array, scintillation telescope and monitors.

in two concentric azimuthal rings covering laboratory polar angles of $17.6^0 \div 47^0$. The rings comprised 16 paddles each covering 15 of azimuth. Each paddle was connected to a 3 cm photomultiplier tube (FEU-85) by an air light guide.

The TOF-E detector system was developed to measure stopped particles up to a proton energy of 240 MeV. The TOF system includes P_1 (20x100x3mm^3), P_2 (30x140x3mm^3) scintillation counters and 4-strip scintillation array P_3. Each strip is a bar of 35x20x1000 mm^3 coupled to two photomultipliers (FEU-87). The plastic scintillators of a large 200x600x200 mm^3 volume connected to 12cm-photomultipliers XP2041 were developed for E counters (P_4). The last layer (P_5 counters) is a rejection detector. Positioned at the back of the P_4, it was employed to improve the edge field of the spectrometer.

The detector array (P_3) allowed one to select up to two tracks and to reconstruct primary energy, angle emission and the type of particles. The particle mass reconstructed with these values (Fig.2) was used to select two-proton events Fig.3. The energies of secondary protons were corrected for degradation in the target chamber wall and the air gap upstream the target-chamber.

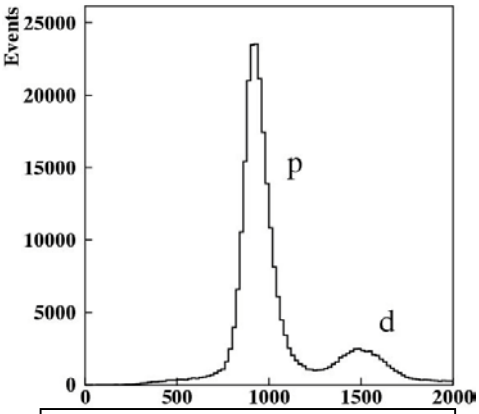


Fig.2 Reconstructed mass of secondary particles.

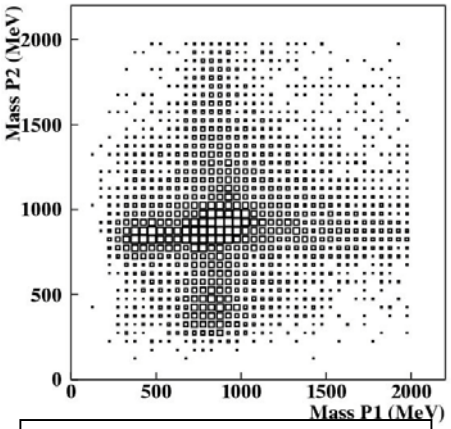


Fig.3 Two-dimensional plot of the recon-stricted masses.

Two monitor telescopes were attached to the scattering chamber symmetric to the beam in the horizontal plane at an angle of 14^0. Their purpose was to monitor charged particles from the target. The monitor telescopes were used as a check of beam intensities.

III. Experimental results

The two-proton correlation function was measured on a beam of relativistic deuterons and protons. For a second the accelerated particles were kept by a magnetic field of the accelerator. The target was moved into a primary beam every cycle of the accelerator. The target velocity was fixed so that the counting rate of the detectors did not exceed 10^6 of pulses per second. The typical intensity was $1\text{-}2\cdot10^5$ pulses per second.

The measurements were carried out sequentially. The angle was varied by a rotational displacement of the detectors relative to the target. The exposure was performed at an angle of 120^0, 103^0 and 90^0.

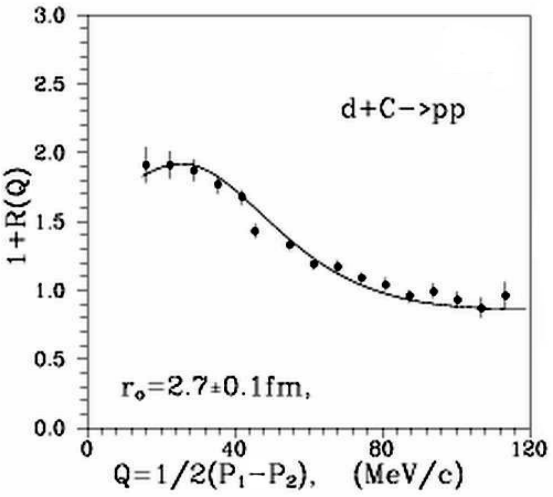


Fig.4 Two-proton correlation function constructed for the d+C reaction.

As a result of the preliminary analysis, the events were selected when both registered particles were classified as protons. For this purpose, we used the reconstructed effective mass, figs.2 and 3. The particles whose mass was over a range of 0.7÷1.2 GeV were considered as protons.

The experimental two proton correlated function R(q) is determined from the coincidence yield $Y(p_1,p_2)$, and the single-proton yields $Y(p_1)$,$Y(p_2)$

$$\sum Y(p_1,p_2)=C[1+R(q)]\sum Y(p_1)Y(p_2)$$

Here, p_1 and p_2 are the laboratory momenta of two protons and $q=1/2|p_1-p_2|$ is the relative momentum of a proton pair. The normalization constant C is determined from the requirement $R(q)\approx0$ at large q.

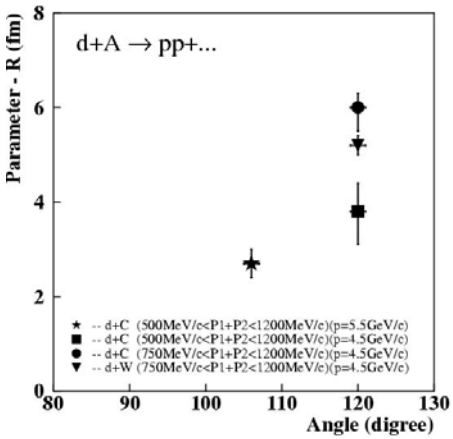


Fig.5 Radii obtained for the d+A reactions.

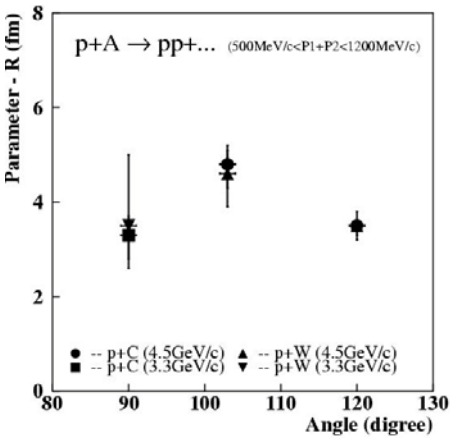


Fig.6 Radii obtained for the p+A reactions.

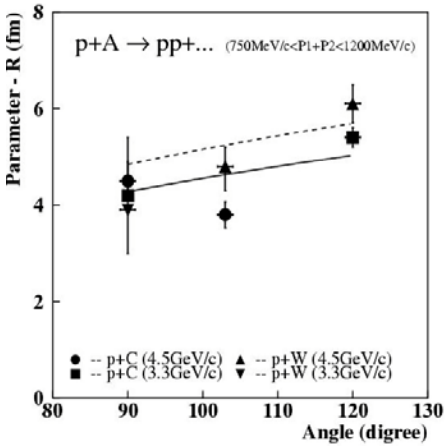


Fig.7 Radii obtained for the p+A reactions at p1+p2>700

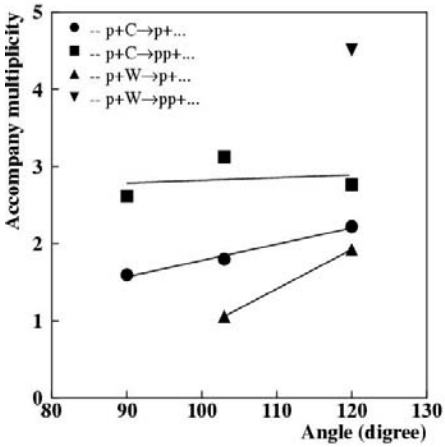


Fig.8 Mean charged multiplicity as a function of angle and

The function R (q) was under constructed in a momentum range of 0<q<200 Mev/c with a step of 20 MeV/c. The obtained points was fitted by the method published in [10]. A similar way was used to analyze all the data (fig.4). As seen from the figures, an increase in the source radius with increasing the

measurement angle is observed in all cases. At the same time, the type of initial particle has no influence on the source radius. The data for primary beams of deuterons (fig.5) and protons (fig.6) practically coincide.

To determine the dependence R(q) on the energy of secondary particles, the events were selected where the summed momentum of two protons was large then 700 MeV/c. This selection does not influence of the final result for the data collected at angles of 90^0 and 103^0. At an angle of 120^0, the source of a large size corresponds to faster protons, fig.7. Such a behaviour is characteristic both of the p+A and d+A reaction. There is no convincing explanation of this phenomenon. As a working hypothesis, one can assume that the particles emitted at an angle 120^0 go a large path inside the nucleus. The probability of elastic scattering on nucleons increases and may format pairs of slow particles emitted from the common point. As a result of such processes, we obtain the diminution of the effective radius.

Using the data for fast protons, we can consider the tube model. In this case, secondary particles should be radiated along the primary particle trajectory. It can be presented as the cylinder of radius r and length L. Generally speaking, L is averaged over all the volume of the nucleus if the impact parameter is not fixed. And as a first approximation, the tube length can be estimated as: $<L> =4/3R$, where R is the nucleus radius. Assuming that interactions happen sequentially, one can calculate mean time between two collisions: $t = <L>/\beta$ for a primary particle. From here it follows that the effective radius R(p,p), we measure in the experiment, should increase with increasing the measurement angle and this increase can be presented as follows: $R(p,p)=<L>/\beta_A\sqrt{(\beta_A^2+\beta_B^2-2\beta_A\beta_B\cos(\Theta))}$, where β_A is the velocity of an initial particle, β_B- the velocity of a secondary particle and Θ- the measurement angle.

In our measurements on carbon and tungsten nuclei, $<\beta_B>=0.37$ when averaging over all the range of momenta, $<\beta_B> =0.45$ for summed momenta P > 700 MeV/c and $\beta_A=0.98$. We fitted the data using these values. The fits are presented in fig.7. We obtained $R(p,p)=3.89\pm0.24$ Fm for the carbon target and $R(p,p)=4.4\pm0.47$ Fm for the tungsten target.

The angular dependence is observed in the behaviour of the charged multiplicity accompanying the proton pair, fig.8. The increase of multiplicity with increasing the measurement angle is seen well. Taking into account that the increase of multiplicity is directly related to decreasing the impact parameter, one can conclude that large emission angle corresponds to more central collisions.

IV. Conclusions

We have measured the correlation function of two protons emitted at different angles (90^0, 103^0,120^0) in p+C(W) and d+C(W) reactions. It was fixed what radii were practically a constant for protons with summed momentum over a

range of 500÷1200 MeV/c slowly growing with increasing the measurement angle for protons with summed momentum over a range of 700÷1200 MeV/c. The radius of the emission zone was found to be insensitive to the type of primary particles (for primary protons and deuterons) It should be marked that the accompanying multiplicity measured in the forward direction has a small angular dependence and increases sensitive to two particle emission in the backward direction.

References

1. V.S.Stavinskiy – Part.Nuclei, 1979, 10, p.945
2. A.V.Efremov - Part.Nuclei, 1982, 13, p.613
3. S.V.Bojarinov et al. - Sov. J. Nucl. Phys.,55,1992, p.917
4. P.V.Degtyarenko – Z.Phys. A 350, p 263
5. W. Bauer, C.Gelbke - Ann. Rev. Nucl. Part. Sci. 1992, 42:77-100, p.77
6. G.I.Kopylov, M.I.Podgorecky - Sov. J. Nucl. Phys. - 18, 1973, p.656
7. G.I.Kopylov - Phys.Lett., 1974, 50B, p.472
8. Malakhov A.I. et al. - Nucl. Instr. Meth. .A., 2000, N.2. - p.320
9. S.V.Afanasiev et al. - JINR Rap. Comm. No.5(91)-98, p.25.
10. P.Lednicky, V.L.Luboshic - Sov. J. Nucl. Phys.,35,1982, p.770

DEFINITION OF THE MASS OF BOUND STATE

M. Dineykhan, Zh. Baizhanova, A. Jahanshir, S.K. Sakhyev

Al-Farabi Kazakh National University, Almaty, Kazakhstan

Abstract: Definition of nonperturbative corrections to Hamiltonian of interaction according to the basis investigation of the asymptotically behaviour of the loop function of scalar particles in the external electromagnet field. The constituent masses of the bound state are analytically determined. It is shown that the constituent masses of the system differ from the masses of free particles. Are calculated the additives, bonded with the Thomas precession.

1 Introduction

Great efforts have been made to understand how bound state arise in the formalism of quantum field theory (QFT) and to work out effective methods to calculate all characteristics of these bound states, especially their masses. The analysis of a bound state is simplest when constituent particles can be considered to be nonrelativistic, i.e. when they travel at speeds considerably less than "c". The theoretical criterion is that the coupling constant should be weak and masses of intermediate particles (photon in QED, mesons in nuclear physics, gluons in QCD) should be small in comparison with masses of constituents [1]. New importance to the bound state physics was given by the development of QCD, the modern theory of strong interactions. It was realized that all hadrons, once through to be the elementary building blocks of matter, are themselves atom-like bound states of elementary quarks bound by the color forces. The other powerful stimulus for further development of the bound state theory is provided by the spectacular experimental progress in precise measurements of atomic energy levels. It suffices to mention that the relative uncertainly of measurement of the frequency of the 1S-2S transition in hydrogen was reduced during the last decade by three orders of magnitude from $3\cdot10^{-10}$ [2] to $3{,}4\cdot10^{-13}$ [3]. The relative uncertainly in measurement of the muonium hyperfine splitting was reduced recently by the factor 3 from $3.6\cdot10^{-8}$ [4] to $1.2\cdot10^{-8}$ [5].

Thus, the definition relativistic corrections to the energy spectrum as a atomic and hadronic structures is one of the important problems for toddies.

Corrections in atomic physics can be classified as relativistic, radiation and bonded by return. Numerous experimental and theoretical works are dedicated to the evaluation of these corrections (in detail see in [6]). At the present time the technical achievements of experimental studies make it possible to obtain the ions of heavy elements with one electron. In this case the coupling constant $(z\alpha)$ of

electromagnetic interaction becomes the order of one, so that electromagnetic interactions become strong and the calculation of relativistic corrections becomes necessary. However, the theoretical models, intended for describing the relativistic corrections to the spectrum, are limited to the lowest order on the coupling constant $(z\alpha)$ (details see in [6]).

We will consider this problem, according to the asymptotic behaviour of the loop function in the scalar electrodynamic field. The mass of the bound state analytical is calculated with Coulomb interaction. The result supplement very well with the result of others authors.

2 Formulations of the problem

We determine the representation of this loop in a form of functional integral and investigate its asymptotic bihaviour for large distance. The polarization loop functions for the scalar particles in a quantum gauge field we can write in the form:

$$\Pi(x-y)=\left\langle G_{m1}(x,y|A)G^{*}_{m2}(y,x|A)\right\rangle_{A} \tag{2.1}$$

where making averaging over the gauge field $A_{\alpha}(x)$. The Green function for a scalar particle in an external gauge field $A_{\alpha}(x)$ is defined by the equation:

$$\left[\left(i\frac{\partial}{\partial x_a}+\frac{g}{c\hbar}A_a(x)\right)^2+\frac{c^2m^2}{\hbar^2}\right]G(x,y|A)=\delta(x-y) \tag{2.2}$$

where m is the mass of our scalar particles and g is a coupling constant. The propagator $D_{\alpha\beta}(x-y)$ of the vector field $A_{\alpha}(x)$ has a form:

$$D_{\alpha\beta}(x-y)=\left\langle A_{\alpha}(x)A_{\beta}(y)\right\rangle_{A}=\delta_{\alpha\beta}D(x-y) \tag{2.3}$$

The mass of the bound state systems defined through $\Pi(x-y)$ loop function in the following way:

$$M=-\lim_{|x-y|\to\infty}\frac{\ln\Pi(x-y)}{|x-y|}\ . \tag{2.4}$$

The calculation details are given in paper [7]. For the mass of bound state system we get:

$$M=\sqrt{m_1^2-2\mu^2E'(\mu)}+\sqrt{m_2^2-2\mu^2E'(\mu)}+\mu E'(\mu)+E(\mu) \tag{2.5}$$

and the parameter μ is determined by the equation:

$$\frac{1}{\mu}=\frac{1}{\mu_1}+\frac{1}{\mu_2}=\frac{1}{\sqrt{m_1^2-2\mu^2E'(\mu)}}+\frac{1}{\sqrt{m_2^2-2\mu^2E'(\mu)}} \tag{2.6}$$

and where used notation $E'(\mu)=\frac{\partial E(\mu)}{\partial\mu}$. Parameters μ_1 and μ_2 we should consider as a constituent mass. According to (2.5) for the calculation of the mass spectrum bound state system, before we need to determine the quantity $E(\mu)$. The quantity $E(\mu)$ should be considered as a eigenvalue of the effective Hamiltonian.

In the paper [7] for the nonrelativistic case we obtainedfor the effective Hamiltonian:

$$H=\frac{1}{2\mu}\vec{P}^2+V(r) \tag{2.7}$$

where $V(r)$ is the effective interaction potential and for the Coulomb interaction equals:

$$V(r)=-\frac{\alpha_s}{r}. \tag{2.8}$$

3-Mass spectrum of Coulomb systems

According to (2.5) for determining the mass of the bound state systems first of all we shall determine the eigenvalues of the Hamiltonian with Coulomb potential. For this aim we consider following Shrodinger equation :

$$[\frac{p^2}{2\mu}-\frac{ze^2}{r}]\Psi=E\Psi \tag{3.1}$$

From this equation we find the energy spectrum of Coulomb potential:

$$E(\mu)=-\frac{\mu}{2n^2}.z^2.\alpha^2 \tag{3.2}$$

where $\alpha=e^2/4\pi$ - is the coupling constant of electromagnetic interaction.

Let us to determine the mass spectrum of atomic system with masses $m_1=m_n$ is the mass of nuclei and $m_1=m_e$ is the mass of electron. Usually, the mass of nuclei is consider as limit $m_n\to\infty$, and in this case for the binder energy we have:

$$E_{bin} = M - m_{\pi} \tag{3.3}$$

where it is the bound state energy.
After some simplification from (11) for the consistuent mass we get:

$$\mu = \frac{m_e}{\sqrt{1 - \frac{z^2\alpha^2}{\mu^2}}} \tag{3.4}$$

and for the binding energy:

$$\mathrm{E}_{bin} = m_e\sqrt{1 - \frac{z^2\alpha^2}{n^2}} \tag{3.5}$$

Our results are given in the table 1 and also show in the results of Ref. [8]. Which obtained into frameworks of the perturbation theory.

Table 1. The energy spectrum for the Coulomb system with units n=2, l=2, z=1 and m_e=1

α	Perturbation Theor. [8]	Our.
0.0155522	0.999969769	0.999964766
0.1425460	0.997452	0.997457
0.2599358	0.99147	0.99152
0.3566678	0.9838	0.9840
0.4359255	0.75	0.976
0.5	0.967	0.9682

4 Define the mass of π -atom

In this section we calculated the mass and binding energy of π-atom. After some analogycal calculations, which represented in above, for the mass we have:

$$M = m_{\pi}\sqrt{4 - \frac{\alpha^2}{n^2}}\ ; \tag{4.1}$$

and for binding energy:

$$\mathrm{E}_{bin} = \frac{M - 2m_{\pi}}{m} = m_{\pi}\left[\sqrt{4 - \frac{\alpha^2}{n^2}} - 2\right]. \tag{4.2}$$

The different values of coupling constant determined the binding energy and mass for π -atom. Our results are given in table 2.

Table 2. The energy spectrum for the π -atom with units n=2, l=1, z=1 and m_π =1

α	E_{bin}	M
0.0155522	-0.0000604687	1.999939531
0.1425460	-o.0050863082	1.994913692
0.2599358	-0.016963596	1.983036404
0.3566678	-0.03205994	1.96794006
0.4359255	-0.0480858	1.951914178
0.5	-0.063508326	1.936491673

References

1. W.Greiner and Y.Reinhart, Quantum Electrodynamics , Springer-Verleg, Berlin. N.Y, 1992.
2. M.G. Boshier, et al., phys.rev.A40 p.6169(1989)
3. Th. Udem, et. al., phys. Rev. Lett, 7-9 p.2646(1947)
4. F.G. Mriam, et. al., phys. Rev. Lett, 49 p.943(1982)
5. W. Liu, et. al., phys. Rev. Lets, 82 p.711(1999)
6. M.I. Efimov, H. Grotch, V.A. Shelyuto, Phys. Rep., 342 p. 63-261 (2001)
7. M. Dineykhan, D.S. Ashimov, A. Jahanshir, S.K. Sakhyev; “On the structure of the Hamiltonian of QCD string” in II Eurasian Conference, Almaty 2002.
8. N.Braumbilla and A.Vairo, phys. Lett. **B359**, p. 133(1995);

DETERMINATION OF DYNAMICAL QUADRUPOLE DEFORMATION OF NUCLEI AT NUCLEAR CAPTURES OF HEAVY IONS

[1]Khugaev A.V., [1]Koblik Yu.N., [1]Pikul V.P., [2]Jovliev U., [2]Nasirov A.K., [2]Muminov A.I., [2]Pavly K.V., [2]Poliak Yu.V., [2]Vdovkin P.O.

[1]Institute of Nuclear Physics, Uzbekistan, Tashkent
[2]Department of Heavy Ion Physics, Uzbekistan, Tashkent

The cross sections for nuclear captures at heavy ions collision strongly depend from the deformation parameters of colliding nuclei. In this work we investigate the quadrupole deformation parameter β behaviour for both nuclei from the collision dynamics. Here we present the method of solution for the β deformation equition at the heavy ions collision.

The dynamic of nuclear processes at heavy ions collision strongly depend from the behaviour of nucleus – nuclear potential for interacting nuclei. For the description of this interacting potential it is necessary to investigate dependence of quadrupole deformation parameter β. Here the main difficulties is, that in the differential equation for β deformation, the coefficients of equition also dependend from the deformation and this dependence is nonlinear. In this work we present the method of solution for the β deformation equition using decomposition of solution and coefficients of differential equitions by the small parameter ε. In this way we solve this problem and split the solution by the two parts. The first part will be devoted to the case of strong nuclear friction, and second to the weak.

Part 1. Strong nuclear friction: $\gamma_0 > \omega$

From the previouse, the main difficulties at the solution of this problem is nontrivial time dependence of β coefficient in the equation for β deformation [1]:

$$\beta'' + 2\gamma(R)\beta' + \omega^2\beta = F(R) \tag{1}$$

$$R = R_0(1 + \beta Y_{20}(\vartheta)), \qquad Y_{20}(\vartheta) = \sqrt{\frac{5}{16\pi}}(3\cos^2\vartheta - 1)$$

here γ(R) is nuclear friction, $\gamma(R)$, $F(R)$ are defined as in the paper [1] and ϑ - is angle between axis of colliding nuclei. Direct numerical solution of this problem is difficult by the reason of very complicate expressions for the $\gamma(R)$ and $F(R)$

functions and it suggest using of iteration methods, which are sometimes numerically unstable and has a bad convergence.

Therefore it is interesting to investigate this problem in the approach of a small parameter ε for the deformation coefficient β. In further we follows to the ideas, based on the paper [2]. In our work we estimate the value β up to first order by ε, however it is easy to see, that it is possible to do for any given order by ε. We write thesolution of equation (1) in the form:

$$\beta(t) = \beta_0(t) + \varepsilon\beta_1(t) \tag{2}$$

To expanding coefficients of equation $\gamma(R)$ and $F(R)$ by the parameter ε, we have:

$$\begin{cases} \gamma(R) = \gamma(R_0) + \dfrac{\partial\gamma}{\partial R}\Big|_{R_0} \cdot R_0 Y_{20}(\vartheta)\beta' \Delta t + o(\Delta t^2) \\ F(R) = F(R_0) + \dfrac{\partial F}{\partial R}\Big|_{R_0} \cdot R_0 Y_{20}(\vartheta)\beta' \Delta t + o(\Delta t^2) \end{cases}$$

and after introducing:

$$\gamma_0 = \gamma(R_0), \gamma_1 = \frac{\partial\gamma}{\partial R}\Big|_{R0} \cdot R_0 Y_{20}(\theta), F_0 = F(R_0), F_1 = \frac{\partial F}{\partial R}\Big|_{R0} \cdot R_0 Y_{20}(\theta)$$

in the assumption that $\Delta t = \varepsilon \ll 1$, we have following decompositions by the parameter ε:

$$\begin{cases} \gamma(R) = \gamma_0 + \gamma_1(\beta_0' + \beta_1'\varepsilon) + o(\Delta t^2) \\ F(R) = F_0 + F_1(\beta_0' + \beta_1'\varepsilon) + o(\Delta t^2) \end{cases}$$

For the first approximation we can to write, that:

$$\begin{cases} \gamma(R) = \gamma_0 + \varepsilon\gamma_1\beta_0' \\ F(R) = F_0 + F_1\beta_0'\varepsilon \end{cases} \tag{3}$$

and then the initial equation will be written as:

$$(\beta_0 + \varepsilon\beta_1)'' + 2(\gamma_0 + \varepsilon\beta_0')(\beta_0 + \varepsilon\beta_1)' + \omega^2(\beta_0 + \varepsilon\beta_1) = F_0 + \varepsilon F_1\beta_0'$$

here in the 1-st order approximation we have relations:

$$\begin{cases} \beta_0'' + 2\gamma_0\beta_0' + \omega^2\beta_0 = F_0 \\ \beta_1'' + 2\gamma_0\beta_1' + \omega^2\beta_1 = F_1\beta_0' - 2\gamma_1\beta_{0^2}' \end{cases} \tag{4}$$

The solution of first equation (4) it is possible to find by the ordinary way, using variable: $y = \beta_0 - \dfrac{F_0}{\omega^2} \rightarrow y'' + 2\gamma_0 y' + \omega^2 y = 0$ and then for the characteristic

equation: $\lambda_{1,2} = -\gamma_0 \pm g_0, g_0 = \sqrt{\lambda_0^2 - \omega^2}$. After all these simple transformations we have for $\beta_0(t)$:

$$\beta_0 = \left(F_0/\omega^2\right) + e^{-\gamma_0 t}\left[Ae^{g_0 t} + Be^{-g_0 t}\right] \tag{5}$$

and then, using $\beta_0(t)$ solution, we can easily define solution for the $\beta_1(t)$ function from the second equation of system (4). Actually, let's rewrite β_0 and β_0' function in the form:

$$\beta_0(t) = F_0/\omega^2 + Ae^{g_1 t} + Be^{g_2 t}, \beta_0'(t) = g_1 Ae^{g_1 t} + g_2 Be^{g_2 t}$$

where $g_1 = g_0 - \gamma_0$, $g_2 = -(g_0 + \gamma_0)$, from where:

$$\begin{cases} \beta_0' = c_1 e^{g_1 t} + c_2 e^{g_2 t} \\ \beta_0'^2 = c_1^2 e^{2_{g1^t}} + 2c_1 c_2 e^{(g_1+g_2)t} + c_2^2 e^{2g_2 t} \end{cases}$$

with new denotes: $c_1 = g_1 A$, $c_2 = g_2 B$. After that, the equation for β_1 will be rewritten by the following way:

$$\beta_1'' + 2\gamma_0\beta_1' + \omega^2\beta_1 = F_1 c_1 e^{g_1 t} + F_2 c_2 e^{g_2 t} -$$
$$-2\gamma_1 c_1^2 e^{2g_1 t} - 4\gamma_1 c_1 c_2 e^{(g_1+g_2)t} - 2\gamma_1 c_2^2 e^{2g_2 t}$$

Using new notations:

$$c_{11} = F_1 c_1, c_{12} = F_2 c_2, c_{13} = -2\gamma_1 c_1^2, c_{14} = -4\gamma_1 c_1 c_2, c_{15} = -2\gamma_1 c_2^2$$
$$g_{11} = g_1, g_{12} = g_2, g_{13} = 2g_1, g_{14} = g_1 + g_2, g_{15} = 2g_2$$

the equation for β_1 it is possible to rewrite as:

$$\beta_1'' + 2\gamma_0\beta_1' + \omega^2\beta_1 = \sum_{i=1}^{5} c_{1i} e^{g_{1i} t} \tag{6}$$

Solution of this equation we can to present as simple superposition:

$$\beta_1 = \sum_{i=1}^{5} \beta_{1i} \tag{7}$$

where β_{1i} satisfies to the equation:

$$\beta_1'' + 2\gamma_0\beta_1' + \omega^2\beta_1 = c_{1i} e^{g1it} \tag{8}$$

Then for the general solution of homogeneous equation we have: $\beta_{1i,h} = A_{1i} e^{g_1 t} + B_{1i} e^{g_2 t}$

Particular solution for the inhomogeneous equation we can to present as: $\beta_{1i,n} = B_i e^{g_{1i}t}$. Then it is easy to find B_i, from the direct substitution in the initial differential equation:

$$B_i = \frac{c_{1i}}{g_{1i}^2 + 2\gamma_0 g_{1i} + \omega^2} \tag{9}$$

from where we can to write general solution β_{1i}

$$\beta_{1i} = A_{1i} e^{g_1 t} + B_{1i} e^{g_2 t} + B_i e^{g_{1i} t} \tag{10}$$

and then for β_1:

$$\beta_1 = A_0 e^{g_1 t} + B_0 e^{g_2 t} + \sum_{i=1}^{5} B_i e^{g_{1i} t} \tag{11}$$

Finally, the solution for β we can to present as:

$$\beta = \beta_0 + \varepsilon\beta_1 = \frac{F_0}{\omega^2} + A_0 e^{g_1 t} + B_0 e^{g_2 t} + \varepsilon \sum_{i=1}^{5} B_i e^{g_{1i} t} \tag{12}$$

Solution analyse. Initial conditions

For the obtaining solution, for the numerical realization it is necessary to calculate following values:

1. γ_0, γ_1 (subroutines $\gamma\ (R_0)$, $\gamma_1(R_0, t, \theta)$)
   F_0, F_1 (subroutines $F_0(R_0)$, $F_1(R_0, t, \theta)$)
2. $g_0, g_1, g_2 (g_0 = \sqrt{\gamma_0^2 - \omega^2}$, $g_1 = g_0 - \gamma_0$, $g_2 = -(g_1 + \gamma_0))$
3. From the initial conditions for β_0 value, we can to define *A* and *B* constants and then:

$$c_1 = g_1 A, \qquad c_2 = g_2 B, \quad c_{11} = F_1 c_1, \quad c_{12} = F_2 c_2, \qquad c_{13} = -2\gamma_1 c_1^2$$

$$c_{14} = -4\gamma_1 c_1 c_2, \quad c_{15} = -2\gamma_1 c_2^2$$

$$g_{11} = g_1, \quad g_{12} = g_2, \quad g_{13} = 2g_1, \quad g_{14} = g_1 + g_2, \quad g_{15} = 2g_2$$

4. B_i coefficients calculation:

$$B_i = \frac{c_{1i}}{g_{1i}^2 + 2\gamma_0 g_{1i} + \omega^2}, \qquad i = 1,...,5$$

5. From the initial conditions we extract A_0 and B_0 coefficients, and then for the fixed value *t*:

$$\beta(t) = \frac{F_0}{\omega^2} + A_0 e^{g_1 t} + B_0 e^{g_2 t} + \varepsilon \sum_{i=1}^{5} B_i e^{g_{1i} t}$$

Less well defined place in this calculation is the determination of constants: A_0, B_0, A, B. In this work we still suggest following assumption: for an initial position t = 0 we suggest that interacting nuclei are still without strong deformation, that mean: $R = R_0(1 + \beta Y_{20}(\theta)) \equiv R_0$, and we have at $t = 0, \beta(t=0) = 0 \rightarrow \beta(t) = \beta_0(t) + \varepsilon\beta_1(t)$ and:

$$\beta_0(0) = 0,\ \beta_0' = 0, \text{ for 0 - order approximation}$$

$$\beta_1(0) = 0,\ \beta_1' = 0, \text{ for 1 - order approximation}$$

If we also suggest that exist some initial deformation without interaction between ions (nuclei are deformed from the beginning), then in the general case, for the arbitrary order of approximation by ε we have:

$$\beta_0(0) = \beta_0 - const,,\ \beta_0'\big|_{t=0} = 0, \text{ for 0 - order approximation}$$

$$\beta_1(0) = 0,\ \beta_0'\big|_{t=0} = 0, \text{ for 1 - order approximation}$$

… … …

$$\beta_i(0) = 0,\ \beta_i'\big|_{t=0} = 0, \text{ for i - order approximation}$$

From the last condition, up to i - th order approximation we have, that: $\beta_0(0) = \beta_0$, $\beta_0'\big|_{t=0} = 0$. This last relationship is equivalent to the following condition:

$$\begin{cases} A = \dfrac{1+\gamma_0}{2}(\beta_0 - \dfrac{F_0}{\omega^2}) \\ B = \dfrac{1-\gamma_0}{2}(\beta_0 - \dfrac{F_0}{\omega^2}) \end{cases} \tag{13}$$

and by the analogy for the β_1 coefficient at t = 0, we have: $\beta_1(0) = 0$, $\beta_1'\big|_{t=0} = 0$

that correspond for β coefficient: $\beta\big|_{t=o} = \beta_0$, $\beta'\big|_{t=0} = 0$, from where we can to write:

$$\begin{cases} B_0 = \dfrac{1}{g_1 - g_2}\left[g_1(\beta_0 - \dfrac{F_0}{\omega^2}) + \varepsilon \sum_{i=1}^{5} B_i(g_{1i} - g_1) \right] \\ A_0 = \beta_0 - \dfrac{F_0}{\omega^2} - \varepsilon \sum_{i=1}^{5} B_i - B_0 \end{cases}$$

Part 2. Weak nuclear friction: $\gamma_0 < \omega$

In this case also the solution of equation (1) we will try to find by the same way, as in the previous section. We want only to stress, that in the decomposition of $\gamma(R)$ and *F(R)* functions around R_0, R_0 can be any current

$$\gamma(R) = \gamma_0 + \gamma_1 \beta' \Delta t + o(\Delta t^2)$$
$$F(R) = F_0 + F_1 \beta' \Delta t + o(\Delta t^2)$$

value of *R,* which was determined in previous interval of time. It mean, that for the $t = t_0 + \Delta t$, *R* correspond to the time *t* and R_0 to the time t_0. In the case, if the nuclei orientation is fixed, during all time of interaction, we have the same decompositions as in the previous section:

Here also for $\Delta t = \varepsilon << 1$, we can to present the solution of β as: $\beta = \beta_0 + \varepsilon\beta_1$. Then, as in the previous section, we can to write for β_0 and β_1 in the same form with (4):

$$\begin{cases} \beta_0'' + 2\gamma_0 \beta_0' + \omega^2 \beta_0 = F_0 \\ \beta_1'' + 2\gamma_0 \beta_1' + \omega^2 \beta_1 = F_1 \beta_0' - 2\gamma_1 \beta_0'^2 \end{cases}$$

First equation of this system we can to rewrite in the form: $y'' + 2\gamma_0 y' + \omega^2 y = 0$

Where from the characteristic equation: $\lambda_{1,2} = -\gamma_0 \pm \sqrt{\gamma_0^2 - \omega^2}$. Here we introduced the variable $y = \beta_0 - \frac{F_0}{\omega^2}$. In our case $\gamma_0 - \omega$ <0, physically it means a small influence of nuclear friction. Introducing new variables: $\lambda_{1,2} = -\gamma_0 \pm ig_0$, $g_0 = \sqrt{\omega^2 - \gamma_0^2}$ we can to present the solution of last differential equation in the form:

$$y = e^{-\gamma_0 t}[(c_1 + c_2)\cos(g_0 t) + i(c_1 - c_2)\sin(g_0 t)]$$

Taking only real part of this solution with suggestion, that at the $t = t_0$, $\beta_0 = 0$ we have finally in general case:

$$\beta_0 = \frac{F_0}{\omega^2}(1 - e^{-\gamma_0 t}\cos(g_0 t))$$

Then, knowing β_0, the β_1 solution we can to rewrite as:

$$\beta_1''+2\gamma_0\beta_1'+\omega^2\beta_1=\frac{F_0F_1}{\omega}e^{-\gamma_0 t}\sin(g_0t+\varphi_0)-$$
$$-\frac{\gamma_1F_0^2}{\omega^2}e^{-2\gamma_0 t}+\frac{\gamma_1F_0^2}{\omega^2}e^{-2\gamma_0 t}\cos 2(g_0t+\varphi_0)$$

$$y''-2\gamma_0y'+\omega^2y=\frac{F_0F_1}{\omega}e^{\gamma_0 t}\sin(g_0t+\varphi_0)-\frac{\gamma_1F_0^2}{\omega^2}+\frac{\gamma_1F_0^2}{\omega^2}\cos 2(g_0t+\varphi_0)$$

here $\varphi_0=arctg\left(\frac{\gamma_0}{g_0}\right)$. After introducing intermediate variable $y:\beta_1=y\cdot e^{-2\gamma_0 t}$ we have this equation in the form:

For the solution of this equation will be convenient to rewrite it by the following way:

$$\ddot{y}_1-2\gamma_0\dot{y}_1+\omega^2y_1=Ae^{\gamma_0\tau}\sin(g_0\tau)+B\cos(2g_0\tau) \qquad (14)$$

Here we introduced new notations and variables:

$$y_1=y+\frac{\gamma_1F_0^2}{\omega^4},\tau=t+\frac{\varphi_0}{g_0},B=\frac{\gamma_1F_0^2}{\omega^2},A=\frac{F_0F_1}{\omega}e^{-\gamma_0\frac{\varphi_0}{g_0}},\dot{y}=\frac{dy}{d\tau}$$

Solution for the y_1 we can to present in the form $y_1=z_0+z_1+z_2$, where z_0 is the general solution of homogeneous equation for y_1 and z_1, z_2 are particular solutions of inhomogeneous equation with right hand sides $Ae^{\gamma_0 t}\sin(g_0\tau)$ and $B\cos(2g_0\tau)$ respectively.

1). General solution z_0. For the homogeneous equation (14) it is easy to write real part of solution in the form: $z_0=c_0e^{\gamma_0\tau}\cos(g_0\tau)$, where c_0 is arbitrary constant, which will be defined from the boundary or initial conditions.

2). Particular solution z_1. In this case we have inhomogeneous equation:

$$\ddot{z}_1-2\gamma_0\dot{z}_1+\omega^2z_1=Ae^{\gamma_0\tau}\sin(g_0\tau)$$

Introducing variable z as $z_1 = A \cdot z \cdot e^{\gamma_0 \tau}$ we can to write: $\ddot{z} + g_0^2 z = \sin(g_0 \tau)$. And for solution: $z = -\frac{\tau}{2g_0}\cos(g_0\tau)$. Then for z_1 we have: $z_1 = -\frac{A\tau}{2g_0} e^{\gamma_0 \tau}\cos(g_0\tau)$

3). Particular solution z_2. In this case we also have inhomogeneous equation for variable z_2:

$$\ddot{z}_2 - 2\gamma_0 \dot{z}_2 + \omega^2 z_2 = B \cdot \cos(2g_0\tau)$$

Introducing variable z as $z_2 = Re(z)$, where $z = B_1 \cdot e^{2ig_0\tau}$, we can to write it by the following way: $\ddot{z} - 2\gamma_0 \dot{z} + \omega^2 z = B \cdot e^{2i(g_0\tau)}$ For this equation it is easily to write solution in the form:

$$z_2 = \frac{B}{\omega^2}(B_R \cdot \cos(2g_0\tau) - B_I \cdot \sin(2g_0\tau))$$

$$B_R = \frac{\omega^2 - 4g_0^2}{\omega^2 + 8g_0^2}, B_I = \frac{4\gamma_0 g_0}{\omega^2 + 8g_0^2}$$

Then we can to write final solution for the second equation of (14) as:

$$\beta_1 = \left\{(c_0 - \frac{A\tau}{2g_0})^{\gamma_0\tau}\cos(g_0\tau) + \frac{B}{\omega^2}(B_R\cos(2g_0\tau) - B_I\sin(2g_0\tau)) - \frac{\gamma_1 F_0^2}{\omega^4}\right\} e^{-2\gamma_0\tau}$$

From the condition, that at $t = 0, \beta_1 = 0$ we have:

$$c_0 = \frac{A\varphi_0}{2g_0^2} + \left[\frac{\gamma_1 F_0^2}{\omega^4} - \frac{B}{\omega^2}(B_R\cos(2\varphi_0) - B_I\sin(2\varphi_0))\right] e^{-\gamma_0 \frac{\varphi 0}{g 0}}$$

And knowing solutions for the β_0 and β_1 we can to write final result as:

$$\beta(t) = \frac{F_0}{\omega^2}(1 - e^{-\gamma_0 t}\cos(g_0 t)) +$$

$$+ \varepsilon\left\{(c_0 - \frac{A\tau}{2g_0})e^{\gamma_0\tau}\cos(g_0\tau) + \frac{B}{\omega^2}(B_R\cos(2g_0\tau) - B_I\sin(2g_0\tau)) - \frac{\gamma_1 F_0^2}{\omega^4}\right\} e^{-2\gamma_0\tau}$$

The β_0 dependence from the time t and frequency ω is shown in the Fig.1.

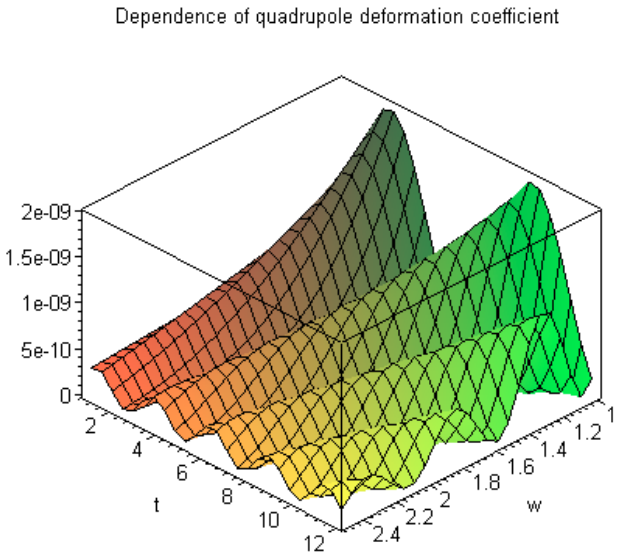


Fig. 1. Dependence of quadrupole deformation coefficient with arbitrary units for t and W axis.

This work was supported by the STCU Foundation (under grant UZB – 45).

References

1. N.V. Antonenko, E.A. Cherepanov, A.K. Nasirov, V.P. Permjakov and V.V. Volkov, Physics Letters B319, (1993); Phys.Rev., C51 (1995), p.2635;
2. N. Kriloff and N. Bogoliuboff, "Introduction to non - linear mechanics ", Prineston, 1947, 106 pages.

DIAGRAM METHODS IN NUCLEAR REACTION THEORY

Blokhintsev L.D.

Skobeltsyn Institute of Nuclear Physics, Lomonosov Moscow State University, Moscow, Russia

Nowadays diagram methods are extensively used not only in elementary particle physics, but in nuclear physics as well. The subject matter of this paper is related to nuclear reactions at low and intermediate energies when one can use non-relativistic kinematics. In that case a distinction should be made between four-dimensional and three-dimensional diagrams. Four-dimensional non-relativistic diagrams are usual Feynman diagrams, in which an individual non-relativistic propagator $(E_i - \vec{k}_i^2 / 2m_i + i0)^{-1}$ corresponds to each virtual particle i and integration over 4-momentum corresponds to each closed contour. On the other hand, in three-dimensional diagrams, a propagator $(E - H_0 + i0)^{-1}$ and integration over 3-momentum correspond to each intermediate state, E and H_0 being the total energy and the free Hamiltonian of the system, respectively. Note that if one considers processes in a three-body system, then four-dimensional diagrams can be reduced to three-dimensional ones by performing trivial integrations over energy variables. For four- (or more) body systems the one-to-one correspondence between four- and three-dimensional diagrams does not exist.

In what follows several aspects of using Feynman diagram formalism in nuclear reaction theory at low and intermediate energies are considered.

1. <u>Extrapolation of differential cross sections to the pole position</u>. Consider the $A + x \to B + y$ reaction where composite bound systems A and y can be represented as $A = B + c,\ y = x + c,$ c being a nucleon or a cluster. The amplitude of this reaction has a pole in $z = \cos\theta$ at $z = z_0,\ z_0$ lying in the unphysical region $|z_0| > 1$ (θ is the c.m. scattering angle). This pole corresponds to the diagram of Fig.1.

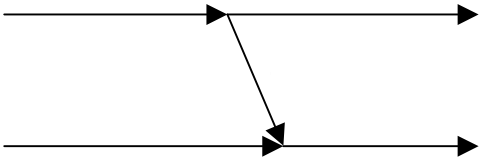


Fig.1

The differential cross section of the reaction has a pole of the second order and can be written as

$$\sigma(z) = a_0 /(z - z_0)^2 + a_1 /(z - z_0) + a_2(z) \quad (1)$$

Consider a quantity $\varphi(z) = (z - z_0)^2 \sigma(z)$. At $z = z_0$ one has $\varphi(z_0) = a_0$. a_0 can be expressed in terms of the product squared $G_{ABc}^2 G_{yxc}^2$ of the vertex constants corresponding to the vertices of the diagram in Fig.1. The vertex constant G_{ABc} is the on-shell matrix element of the virtual $A \to B + c$ process. It is an important nuclear characteristic related directly to the asymptotic normalization coefficient of the wave function of the A nucleus in the $B + c$ channel. To find a_0, $\varphi(z)$ is written as $\varphi(z) = \sum_{i=1}^{N} c_i R_i(z)$ where $R_i(z)$ are some known polynomials, for example, the Hermite polynomials. Coefficients c_i are fitted to experimental values of $\varphi(z)$ in the physical region $-1 \le z \le 1$. Then $\varphi(z)$ is extrapolated to the pole position by putting $z = z_0$. The method under discussion allows one to extract the valuable information on asymptotic normalization coefficients of bound-state nuclear wave functions. It is of interest to extend that method to the case of singularities other than a pole one, in particular, to logarithmic singularities due to triangle Feynman diagrams.

2. <u>Derivation of the generalized folding potential</u>. The four-dimensional covariant formalism of non-relativistic Feynman diagrams is used for the derivation of the general expression for the generalized folding potential (GFP), describing the interaction of a particle with a composite system (say, a nucleus) [1]. The input, which is required to construct the GFP, is the same as that for the standard folding potential (SFP). This input includes the potentials of the pair interaction of the incoming particle with the constituents (nucleons or clusters) of the composite system as well as the inner wave function of this system. The GFP corresponds to the amplitude of the triangle Feynman diagram containing three vertices: i) the vertex of the virtual decay of the target nucleus into constituents; ii) the vertex of the reverse process of the virtual synthesis of the nucleus and iii) the vertex describing the above-mentioned pair interaction. In the simple case that target A consists of two constituents b and c, the GFP is the sum of two terms, one of which is represented in Fig.2. The second term is obtained from Fig.2 by the substitution $b \leftrightarrow c$.

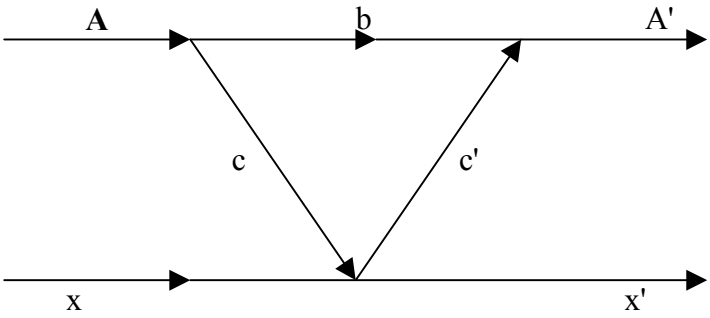


Fig.2

In Fig.2 particles x and x' are on energy shell and A and A' are off shell. The potential thus obtained is non-local and energy-dependent. It becomes complex above the inelastic threshold. As distinct from the SFP, the GFP, being inserted into the Schrödinger or Lippmann-Schwinger equations, leads to the solutions accounting for the contribution not only from the elastic channel but from inelastic channels as well. The difference between the SFP and the GFP is due to the different way of going off energy shell. On shell, the expression for the GFP goes over into that for the SFP. This property implies, in particular, that, within the first Born approximation, the scattering amplitudes corresponding to the GFP and the SFP coincide.

The results described above can easily be extended to the case of the double-folding potential. In that case the expression for the GFP is written as a product of the amplitudes of two diagrams of the type of Fig.2.

3. <u>Asymptotic behavior of bound state wave functions</u>. Consider a non-relativistic composite bound system a, say, a nucleus, which can be divided into two subsystems (fragments) b and c. Define the overlap integral (OI) $I(\vec{r})$ for the virtual process $a \to b + c$

$$I(\vec{r}) = \int \Psi_b^+(\tau_b)\Psi_c^+(\tau_c)\Psi_a(\tau_a, \tau_b, \tau_c)\, d\tau_b\, d\tau_c, \qquad (2)$$

where $\Psi_i(\tau_i)$ is the internal wave function of the system i. For brevity we neglect the long-range Coulomb interaction and consider spinless systems a, b and c, hence $I(\vec{r}) = I(r)$, r being the distance between b and c. In the general case the results given below are valid for radial OI's $I_{ls}(r)$ corresponding to specific values of a channel orbital momentum l and channel spin s [2]. For a wide class of processes, main contributions to their amplitudes come from the values of OI's at large r. In particular, the asymptotics of OI's

determines the cross sections for certain reactions, which are of interest for nuclear astrophysics [3]. Relating the OI by a Fourier transform to the form factor $G(q)$ for the $a \to b + c$ vertex (q being the relative momentum of b and c fragments) and making use of the Cauchy theorem, one obtains the asymptotic form of $I(r)$ as [4]

$$I(r) = c_0 e^{-\kappa r} / r + c_1 e^{-\kappa_1 r} / r^p, \quad r \to \infty, \tag{3}$$

where c_0 and c_1 are some constants, κ is related to the binding energy in the $a \to b + c$ vertex, $\kappa = \kappa_{abc}$, $\kappa_{ijk} = \sqrt{2\mu_{jk}(m_j + m_k - m_i)}$, $\mu_{jk} = m_j m_k /(m_j + m_k)$, m_i is a mass of a particle i, $i\kappa_1$ is the position of the singularity of $G(q)$ in the complex q plane nearest to the physical region $q \geq 0$ and $p > 1$ is determined by the type of this singularity. The first term in Eq.(2) corresponds to the usually adopted "normal" asymptotics of the OI. If the system a consists of three or more constituents, then, as a rule, $i\kappa_1$ is a proper singularity of one of triangle Feynman diagrams of the type of Fig.3 where b, c, d, e and f are certain fragments, into which the composite system a can be divided.

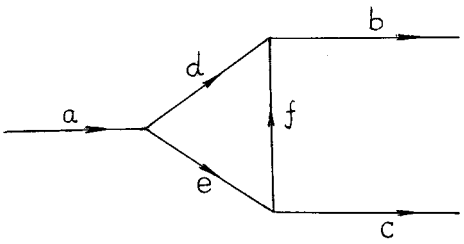


Fig.3

For such a diagram $\kappa_1 = (m_b / m_d)(\kappa_{ade} + \kappa_{bdf})$ [4,5] and $p = 2$. Apart from that diagram, one may consider generalized triangle diagrams, which are obtained from Fig.3 by substituting two or more inner lines for lines d, e or f. According to the general theory of the singularities of Feynman diagrams [6], the position $i\kappa_1$ of the singularity of such a diagram is obtained from that of an

ordinary triangle diagram by the substitution of the corresponding sums of masses for the masses of d, e and f. If the total number of inner lines in a generalized triangle diagram is n, then in Eq.(3) the exponent $p=(3n-5)/2$. The examples of generalized triangle diagrams are shown in Fig.4 ($n=4,\ p=7/2$) and Fig.5 $(n=5,\ p=5)$.

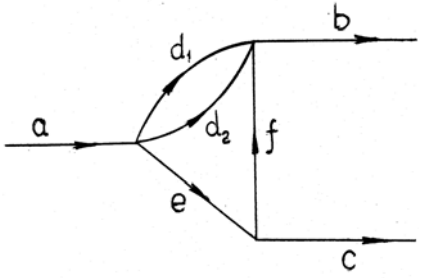


Fig.4

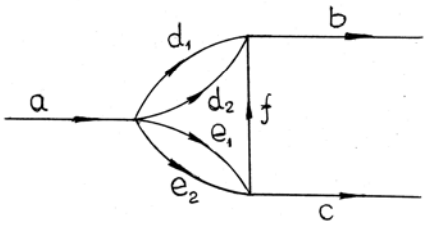


Fig.5

It is possible that $\kappa_1 < \kappa$; in that case the asymptotics of $I(r)$ is determined by the second ("anomalous") term in Eq.(2).

The typical examples of the anomalous asymptotics of the OI $(\kappa_1 < \kappa)$ are as follows: $^{16}O \to {}^{13}N + {}^{3}H$ and $^{20}Ne \to {}^{17}O + {}^{3}He$ (Fig.3), $^{9}Be \to {}^{6}Li + {}^{3}H$ and $^{12}C \to {}^{9}Be + {}^{3}He$ (Fig.4), and $^{16}O \to {}^{9}Be + {}^{7}Be$ (Fig.5).

4. <u>Tensor interaction in the</u> $d\alpha$ <u>system</u>. There exists a long-standing problem of describing tensor interaction in the $d\alpha$ system. In particular, calculations of the ^{6}Li quadrupole moment Q within various versions of a three-body model ($n,\ p,\ \alpha$) results in large positive values ($Q_{theor} \approx 4 \div 6$ mb), whereas the experimental value is small negative ($Q_{\exp} = -0.82$ mb) [7]. Note that other characteristics of ^{6}Li are well described by three-body models. The preliminary results [8] show that the problem under discussion could be solved by allowing for the exchange $d\alpha$ potential, which is described by the diagram of deuteron transfer (see Fig.6).

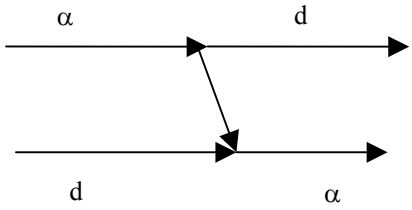


Fig.6

Within this approach, the tensor part of the exchange potential is due to the D state admixture in the dd-channel of the α particle wave function. The $d\alpha$ potential, which is generated by the diagram of Fig.6, is non-local and energy-dependent. It leads to the large negative contribution to Q. It is worth noting that this potential can be included into three-body Faddeev calculations of ^{6}Li by the procedure analogous to the inclusion of three-body forces.

This work was supported by the Russian Foundation for Basic Research under the project No. 01-02-16621.

References

1. L.D.Blokhintsev. 52th Int. Conf. on Nucl. Spectroscopy and Nucl. Structure. Abstracts. P.258. Moscow, 2002.
2. L.D.Blokhintsev, O.Dias, D.Kh.Muminova and R.Yarmukhamedov, Vestnik Mos. Univ., No.4, 32 (2000).
3. A.M.Mukhamedzhanov et al., Phys. Rev. **C51**, 3472 (1995).
4. L.D.Blokhintsev, Izv. Akad. Nauk, ser. fiz., **65**, 74 (2001).
5. L.D.Blokhintsev, E.I.Dolinsky and V.S.Popov, Nucl. Phys. **40**, 117 (1963).
6. L.D.Landau, Nucl. Phys. **13**, 181 (1959).
7. V.I.Kukulin et al., Nucl. Phys. **A586**, 151 (1995).
8. L.D.Blokhintsev, V.I.Kukulin and V.N.Pomerantsev (in press).

DISPLAYING OF FORMATION OF ATOMIC CLUSTERS IN RADIOACTIVE LUTETIUM OXIDE FILMS

V.M. Kartashov, A.G. Troitskaya

Institute of Nuclear Physics, National Nuclear Center of Kazakhstan, Almaty

We earlier reported [1] the results of our investigations of the electronic spectra structure of radioactive lutetium oxide films on the magnetic β-spectrometer $\pi\sqrt{2}$ with the momentum resolution 0.04 -0.1 %. The researches were conducted many times during ≈ 15 years, and a lot of the date has resulted us in the conclusion about possible formation of toroidal structures in these films. Briefly our experimental data, their dynamic features and suppositions about gears, stipulating them, are tabulated (table 1).

It is impossible to consider a radioactive oxide layer, deposited on platinum foil support, having the electric potential of its foil support on all its depth because of its high dielectric properties. There is the potential gradient (≈ 10^6 - 10^7 V/cm) on its depth because of constant outflow of electrons from its surface.

In the Lu fraction three long-lived activities decaying with formation of atoms Yb were contained: ^{174m}Lu ($T_{1/2}$=142 days), ^{174g}Lu ($T_{1/2}$=1200 days) and ^{173}Lu ($T_{1/2}$=500 days). As the average of the nuclei which have decayed during Δt is equal $N_0 \cdot \lambda \cdot \Delta t$, where N_0 – the initial number of the nuclei, the interval $\Delta t_2 = t_2 - t_1$, for which the number of decayed nuclei equals to one for the interval $\Delta t_1 = t_1 - t_0$, is determined by expression $\Delta t_1/(1-\lambda \cdot \Delta t_1)$, therefore, the indicated activities should stop to introduce the contribution to the cluster formation accordingly through 200, 1740 and 720 days. As a whole these crude estimates are not refuted by our results, but the manifest deviations from the exponential time function were watched also.

The absence of special instrumentation for research of time processes was indemnified by application of a way of graphic deduction of the spectra which were taken with different time intervals. It presented the special requirements to detection equivalent (on energy) points on spectrum lines and - thereby - to a system of energy reference marks. As a result of application of this processing techniques of spectra it was possible to show, in particular, a discontinuity of energy losses of electrons and to determine values of these losses as lying in limits from few tens electron volt up to several keV. The non single-stage of these losses was also showed.

From the literature it is known, that for growth of a large cluster (consisting from hundreds and thousand atoms) the apposition of large units of atoms is characteristic. The clusters can organize new stable frames which are not having of analogues in well-known existing systems, apparently, - and toroids.

Our experiment included in itself also giving a potential, accelerating for electrons, to the metallic foil support. In this case we received a capability to watch the auto emission electron part and the low-energy Auger electrons.

Figure 1 illustrates the most low-energy part of electronic radiation studied in our experiment under the submission of accelerating displacement in 10 kV to the platinum foil support.

In fig. 1 (as well as in two subsequent figures 2 and 3) on the abscissa axis the values f - frequency of the proton resonance (Hz) in the sensor of measurement of a magnetic field on the eqilibrium orbit of the spectrometer – are marked. For our spectrometer in the broad range

$f / Br = 83.75\ (1) + 4.5\ (4) \cdot 10^{-7} f$, where Br corresponds to this frequency.

On the axis of ordinates the numbers of impulses are plotted in the logarithmic scale (as the range of their values in this area is very great).

The strongest line of the LMN-series of Cu is conditioned by the source holder material and by our spectrometer design. This line has appeared very useful for the energy calibration of this part of the spectrum.

The analysis of the threshold relation and behavior (in time) of the M_4NN and M_5NN Auger electron intensities have resulted us in the conclusion that the greatest contribution to structure formations of these oxide films is introduced by the electrons of M_4-, M_5- and N-sub-shells of ytterbium atoms (being formed as the result of radioactive decay of the lutetium fraction with half-times from 140 to 1200 days).

The auto emission electron spectrum testifies to composite scission of M4 and M5 stationary states of the atom. It is possible to offer as the explanation a quantum flat rotator.

If the particle orbit encompasses the solenoid with a magnetic flux Φ, energy condition of a rotator $E_m = h^2(m - \Phi/\Phi_0)^2/(8\pi^2 m_e R_0^2)$, where m_e – electron mass, R_0 – an electron orbit radius, m – a magnetic quantum number, a $\Phi_0 = hc/e$ – a quantum of magnetic flux. At a quantum flow $\Phi = n\Phi_0$ (n – integer) and the energy spectrum does not differ from a spectrum without the solenoid.

The behavior (in time) of the experimental auto emission electron spectrum responds the supposition, that the main contribution to formation of the solenoid is introduced by N-electrons, and M_4-, M_5-electrons are gyrated around it.

The reduced in figure 2 segment of the conversion radiation is taken, when the radiation source became so faint, that a development of process of clustering became improbable and the part of the spectrum between lines of electrons of internal conversion should be explained by else causes.

The existence of a correlation, dependent on a spin, in differential cross sections of processes of scattering is doubtless. For this reason the idea of separation of a beam of charged particles on polarizations in the storage device at the expense of interplay of a spin with external fields is discussed [2].

Table 1. The most typical features of our experimental results and their possible explanations

Our experimental data	Dynamic features of our experimental data	The suspected mechanism
Conversion lines of composite structure: main and displaced towards smaller energies (hundreds of eV).	Time function.	Formation of clusters from Lu atoms or Lu_2O_3 moleculas at electrolysis deposition.
Heightened quantity M4- and M5-Auger-electrons (in tens time as contrasted to their decay part) with threshold relation to the supplied potential). Display of the interference pattern in the electronic spectrum correlated with the transition multipolarity).	Time function.	Originating of nanostructure in the form of a toroid. Display of Aharonov-Bohm effect.
Scission of electronic lines of the auto emission spectrum.	Time function.	M4 and M5- electrons revolve on the toroid "winding". Display of the picture of a quantum rotator and toroid scission.
Availability of asymmetrical sattelite lines in the electronic spectrum (They find out multipolar relation).	Time function.	Formation of toroids with an opposite direction of toroid moments in unlike clusters. Interplay of spins of the ordered electrons with an external electromagnetic field.
Observation of orientation effects at registration of electrons in the spectrometer.	Time function. Energy relation of threshold nature	Formation of the structure, chanelling the ordered electrons which are pulled out from "traps", in the gap between the toroids. Spin correction of their focusing by the magnetic field of the spectrometer.

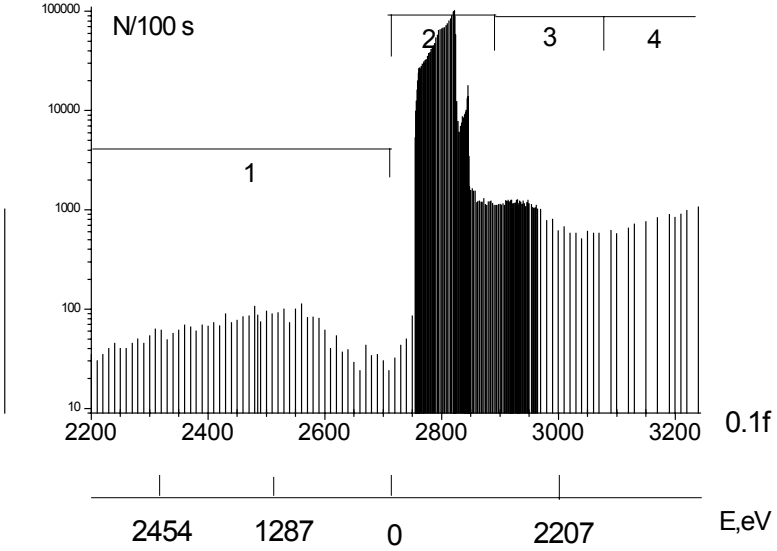


Fig. 1. The spectrum of electron rays of the Lu_2O_3 radioactive film near the 0-energy

1 – The auto-emission spectrum
2 – M_5, M_4-components of auger-transitions in Yb and the LMN-line of Cu
3 – M_3-, M_2- and M_1-components of auger-transitions in Yb
4 – The beginning of the L-series of the auger-spectrum

The interference pattern of electrons scattered by virtue of Aharonov-Bohm effect demonstrates that the solenoid magnetic flux varies. But it is known that if the current in a winding of a toroidal solenoid grows linearly, there is a dipole static electrical field around it [3]. Maybe just this circumstance is the explanation of the appearance of the satellite peaks on the right from the main peak in the spectrum of internal conversion electrons (fig. 3). The appearance of peaks on the left from the main peak (and farther from it) is possible to consider as conditioned by existence of more composite toroidal structure, for example, toroidal quadrupole type one.

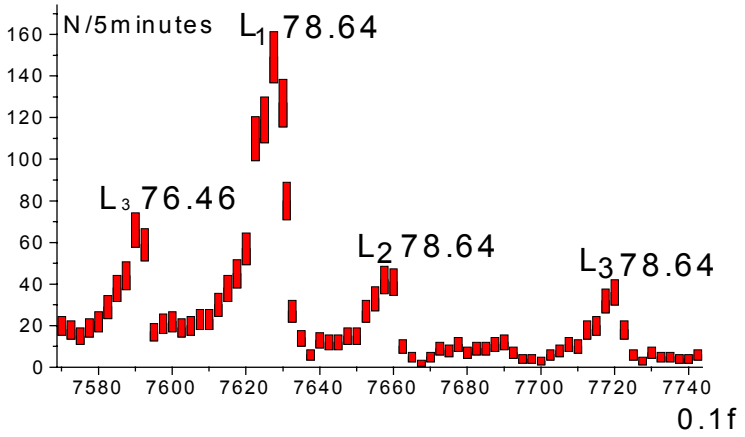


Fig. 2. The area of L-conversion lines of the 76.46 keV transition in ^{174}Yb and 78.64 keV transition in ^{173}Yb.
From L $_2$ 78.64 to L $_3$ 78.64 the electron interference spectrum is visible.

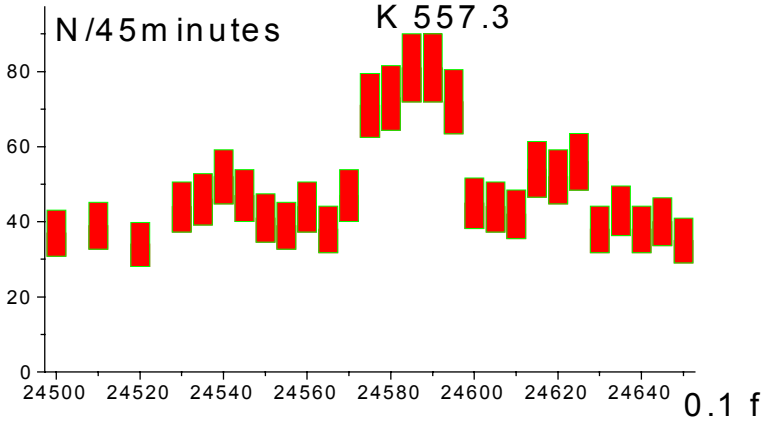


Fig. 3. The line of K-conversion of the 557.3 keV transition in ^{173}Yb and its satellite peaks

Because of a smallness of mass the electron already at energy 100 keV has velocity v, equal half of velocity of light (c), and at energy 600 keV $\beta = v/c = 0.9$. The large values β for electrons (as the particles with the internal moment) cause necessity of the count of relativistic effects, for example, at calculation of their pathways of motions in electromagnetic fields. At the expense of interplay of a spin with an external electromagnetic field there is a additional force of Lorentz

$$\vec{f} = \frac{eg}{2m}\vec{s}\,\frac{\partial \vec{B}}{\partial \vec{r}} + \frac{e(g-1)}{2m}\left(\frac{d}{dt}[\vec{E}\times\vec{s}] - \vec{s}[\vec{v}\times\frac{\partial \vec{E}}{\partial \vec{v}}]\right),$$

where $\vec{B}$ и $\vec{E}$ – external magnetic and electrical fields,
e, m, $\vec{s}$ и $\vec{v}$ – charge, mass, spin and speed of a fragment,
g – gyromagnetic ratio [2].

Perhaps, just the veering in this "backlash" of fields about each dipole, sufficient for the termination of mutual approach of dipoles at close range and inhibition of electrons, is the non-linear response of medium between two toroidal dipoles. The toroidal interplay with degenerate states of "rotator" does the scission observe. Under our date the value of the dipole toroidal moment of quadrupole components can be evaluated as $T_1 \approx 10^9 \mu_N$ fm. This estimation demonstrates comparability of our experimental value to the date for some oxides of magnetic piezoelectrics and magnetoelectrics [3]. It is possible also to consider the connection of our results with the fraction quantum Hall effect.

Bound states of charged particles in a homogeneous magnetic field, in which one the thin solenoid with a magnetic flux Φ is placed, by virtue of effect Aharonov-Bohm extra split on degenerate levels shifted concerning the Landau levels on value, conditioned by a fractional part of quanta of a magnetic flux in the solenoid. These levels respond quantum orbits encompassing the solenoid. For this reason in theory of fractional quantum Hall effect such system as an electron with the affixed solenoid permitting to explain a series of the experimental facts is considered. And it allows to guess a capability of analogies between this phenomenon and processes, considering by us.

References

1. Kartashov V.M., Troitskaya A.G. Abstracts I. Eurasia Conference on Nuclear Science and its Application. Izmir-Turkey, 2000, p.516.
2. Pomeranskii A.A., Sen′kov R.A., Khriplovich I.B., Physics-Uspekhi, 45 N 7, 2002, p.1129.
3. Bukina E.N., Dubovik V.M., Technical Physics, v. 71, N 2, 2001, p.1.

EFFECT OF PHOTON INTERACTION DEPTH IN THE DETERMINATION OF ABSOLUTE EFFICIENCY OF HPGe DETECTOR FOR LIQUID VOLUME SOUCE

Demirel, H[a]., Yücel H[a]., Çetiner M.A[a]. , Çetiner B.[a]., Yurtseven İ[a]., Demircioğlu B., Karadeniz, H.[a] and Özmen A[b].

Ankara Nuclear Research and Training Center, 06100 Beþevler, Ankara, Turkey
[a] Gazi University, Faculty of Science and Art, Physics Department, Ankara, Turkey

Abstract

For practical measuring purposes in high pure Ge detectors, some useful semiempirical approaches are often used to calculate the peak efficiency (absolute efficiency) for any source-to-detector distance *(d)* if the efficiency has been measured at one known distance *(d_1)*. In all approaches considered, normally, one begins an experimental efficiency calibration for single measuring geometry at a distance *(d_1)*, and then derives the efficiency for any other arbitrary distance *(d)*, from the relation

$$\frac{\in(d)}{\in(d_1)} = \frac{\Omega(d)}{\Omega(d_1)}$$

where $\in$ denotes the detector efficiency for any gamma ray energy and Ω is solid angle that is subtended by detector to the source position. However, this relation is only valid when the distances used in the relation was corrected for the effective photon interaction depth for any gamma-ray energy (Debertin and Helmer, 1988;Yücel et al.1996) since the efficiency ratio, $\in(d)/\in(d_1)$, is not equal to the inverse ratio, d_1^2/d^2. In the present work, the photon interaction depths depending upon gamma- ray energies in the range of about 50-2000 keV for point gamma sources (^{241}Am, ^{137}Cs, ^{60}Co, ^{133}Ba and ^{152}Eu) and a liquid volume (cylindrical) source containing ^{57}Co, ^{88}Y, ^{113}Sn, ^{137}Cs, ^{109}Cd, ^{139}Ce and ^{60}Co radionuclides were measured. Then, the calculation of the peak efficiency of a p-type HPGe detector is experimentally tested for both point and the extended (cylindrical) liquid source at various distances from the surface of the end cap of the detector by introduction of the effective photon interaction for any gamma-ray energy.

1. Introduction

In the last forty years γ-ray spectrometer with germanium detector is one of the fundamental instruments in experimental nuclear physics. Experimental work with γ-ray semiconductor detectors requires very often accurate knowledge of the

detector efficiency. Many efforts on the measurement of the efficiency of Ge detectors of various sizes and configurations have been discussed at some conferences (Debertin et al., 1976; Hirshfeld et al., 1976). An excellent review of the attempts at calculating detector efficiencies is given in a recent book by Debertin and Helmer (1988). "Although detector efficiencies must, in the end, be measured, it is useful to consider what information can be obtained from various related calculations." So begins the section on detector efficiency calculations in that book. Nonetheless, there are many obvious incentives for calculating efficiency (or greatly reducing the calibration effort), rather than laboriously measuring it (Gunnik, 1990). For practical measuring purposes, some useful semi empirical approaches are often used to calculate the efficiency for any source-to-detector distance if the efficiency has been measured at one known distance. In all approaches considered, normally, one begins an experimental efficiency calibration for single measuring at a distance d_1, and derives the efficiency for any other arbitrary distance d, form the relation

$$\frac{\in(d)}{\in(d_1)} = \frac{\Omega(d)}{\Omega(d_1)} \tag{1}$$

Where d and d_1 are distances measured from the surface of the end cap of detector to the radioactive source, $\in(d)$ is the efficiency of the detector at d, $\in(d_1)$ is the efficiency of the detector at d_1, and Ω is solid angle that is subtended by detector at the source position.

The exact expression for the solid angle for a point source is

$$\Omega(d) = 2\pi\left(1 - \frac{d}{\sqrt{d^2 + R^2}}\right) \tag{2}$$

Where R is the radius of a right circular cylindrical detector and d is distance of point-source positioned on the symmetry axis of a detector. Equation (1) assumes the validity of the concept of geometry independent intrinsic detector efficiency. As long as d and d_1 are large in comparison with the detector radius R, or if $d \approx d_1$, this concept may be acceptable. However, this relation is not acceptable approximation especially for thicker detectors because of the coincidence summing effects that play an important role on the counts in the full-energy peaks at low source-to-detector distances (Debertin and Schötzig, 1979).

For thicker detectors, where photon interactions do not only occur at the surface, but are distributed over the detector volume, the detection efficiency for a point source is proportional to the solid–angle Ω which varies approximately as $1/d^2$. Of course, the detector is never, and the source is seldom, a point. However, the single point-to-point distance implied by Eqn (1) is determined by using semi empirical model that, for calculating purposes, reduces the detector volume to an equivalent point (a point B shown in Fig. 1). It is a point where all γ-ray interactions are

considered to occur. That is the efficiency at a distance d_1 divided by the efficiency at a distance d is not equal the inverse ratio of the squares of distances

$$\frac{\in(d)}{\in(d_1)} \neq \frac{d_1^2}{d^2} \tag{3}$$

If the concept of an imaginary point of detection is located at a distance d_e (E_γ) behind the real detector surface as marked point B in the detector shown in Fig. 1, the equality of Eqn (3) can be obtained with replacing the distance d by the sum of $d_s+d_w+d_c+d_e(E_\gamma)$. Hence it is then possible to make use of Eqn (1) with $\frac{\Omega(d)}{\Omega(d_1)}$ equal to $\frac{d_1^2}{d^2}$.

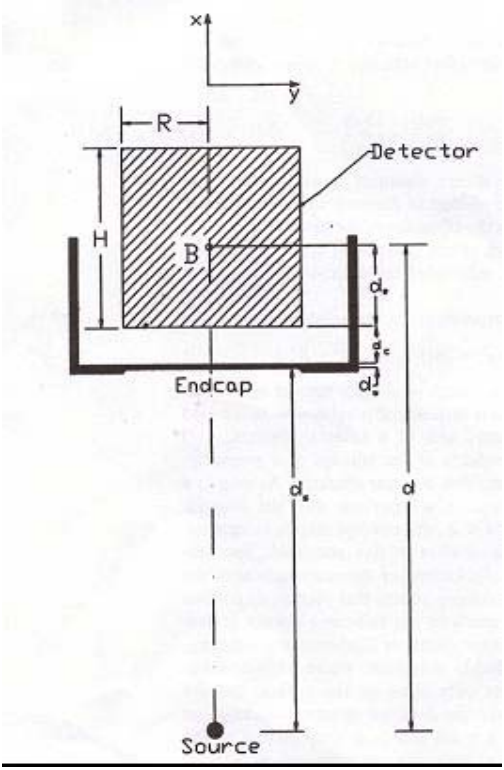


Fig. 1. A schematic measuring geometry of a Ge detector with a point source

The calculations on effective photon interaction depth is based on an equivalent point-detector concept suggested by Notea (1971). Although the concept of an effective interaction depth for thicker detectors is questionable, it is still an applicable approximation in most practical cases. Therefore, some functions which have a semi empirical character can be useful to determine the effective interaction depth of γ-rays in the Ge detectors.

In the present study, semi-empirical functions which relates the given γ-ray energy and the effective interaction depth in Ge is used to fit the measured interaction depth values for point sources and volume sources. The present concept involves that a given fraction of the total photon interactions for a particular energy of γ-ray distributed over the detector has occurred in a distance within the detector described from the real surface of the detector to any imaginary point. In the study, we have tested the concept of effective interaction depth depending on the gamma-energy for an extended source (a cylndiric ampoule) containing radioactive standards (^{57}Co, ^{88}Y, ^{113}Sn, ^{137}Cs, ^{109}Cd, ^{139}Ce and ^{60}Co) because the real samples to be measured are rarely point sources, but in general, they are the extended sources in practice. The measurements for the determination of photon interaction depths have been carried out in a high purity germanium detector.

2. Experimental

The γ-ray spectrometer consists of one high purity Ge detector with a charge-sensitive preamplifier, a linear amplifier, an analog-to-digital converter (ADC) and a Canberra series 35+ MCA with 4096 channel. The commercially available HpGe detector in this investigation is the closed ended coaxial p-type Ge crystal with active volume of approx. 57 cm^3. The detector configuration and characteristics as specified by manufacturer are given in Table 1. The γ reference point source set and a calibrated standard solution used are obtained from the Amersham Int. Ltd. and Isotope Products Inc., respectively. The calibrated point sources (^{241}Am, ^{133}Ba, ^{152}Eu, ^{137}Cs, ^{60}Co, ^{22}Na) provide a sufficient number of full energy peaks for this investigation. The standard solution in a 5 ml ampoule contains the radionuclides, ^{57}Co, ^{88}Y, ^{113}Sn, ^{137}Cs, ^{109}Cd, ^{139}Ce and ^{60}Co. The activities of the present calibrated sources are known to be accurate less than 3%. The standard point sources are encased in a thin plastic holder.

The peak count rates were measured at various source-to-detector distances and different photon energies. The distance, *d*, from the source to the detector endcap was altered from 8 to 21 cm for the different γ-emitters used. Since the activities of the sources used in experiments are not too high, the pile-up losses (random summing) from the full-energy peak counts are negligible. Also, there is no problem from point of view of dead-time correction since MCA works in the live-time mode, the analyzer corrects its dead-time losses. The full-energy peak areas obtained from the ^{133}Ba and ^{152}Eu measurements may some losses because of the coincidence summing effects on the spectra of multi energy γ-ray emitters

(Debertin and Schötzig, 1979). Although the coincidence summing losses may occur in the peak counts obtained from especially ^{133}Ba and ^{152}Eu sources at closer distances. The measurements with ^{133}Ba and ^{152}Eu were also carried out at a distance of 8 cm below the nominal value of 10 cm. The counting time for each measurement predetermined was 30 min but some spectra were collected at different counting times in the range of 10-20 min. The counting time is high enough to ensure good statistical quality of the data. The count rate measurements at each selected distance were repeated five times to improve the statistical precision. Thus the mean values of the measured count rates were used in the calculations. The series 35+ MCA interfaced to a PC for the transfer of γ-ray spectra. The number of counts under each full-energy peak were evaluated by a software, and then divided these counts by the counting time to calculate the count rate. The variation in the full-energy peak areas is estimated to be less than 0.5%.

Table 1.Detector Specifications and performance data

Description	
Detector model	Canberra AL-30-C
Relative Efficiency*	12,4%
Energy Resolution (FWHM)** (keV)	1,96
Peak-to-compton ratio	42,1:1
Detector geometry	Closed-ended-coaxial
Detector material	p-type Ge
Diameter, D (cm)	4,5
Length, H (cm)	3,6
Active area facing window (cm^2)	15,9
Window material and thickness, d_w (mm)	Al, 0,5
Distance from the window, d_c (mm)	5
Crystat and dewar configuration	Vertical Dipstick Canberra Standard 7500

3. Results and discussion

The various plots of $N^{-1/2}$as a function of the distance d_s are obtained for different photon energies by using the mean peak count rates measured independently in detector. The plots of $N^{-1/2}$ are shown in Fig.2 for the point sources ^{241}Am, ^{137}Cs, ^{22}Na and ^{60}Co, and the multi energy point sources in Fig.3 for ^{133}Ba, and in Fig. 4 for ^{152}Eu. In addition a plot of $N^{-1/2}$ is shown for a liquid volume source containing the radionuclides, ^{57}Co, ^{88}Y, ^{113}Sn, ^{137}Cs, ^{109}Cd, ^{139}Ce and ^{60}Co in Fig. 5. The effective interaction depth d_e is determined by plotting the root of the reciprocal count rates $N^{-1/2}$ against the source-detector endcap distance (d_s) at the particular energy of γ-ray, and extrapolating the line to obtain the zero of $N^{-1/2}$ The

experimental points are fitted by linear least squares method. The experimental and the calculated points are in good agreement.

The regression constants obtained are order of 0.999. If the effective interaction radius $r_e(E_\gamma)$ is neglected, the intercept of the line on the d_s axis at $-(d_c + d_w + d_e(E_\gamma))$, the quantity of interest. Since the distance ($d_c + d_w = 5.5$ *mm*) is known as the detector specification $d_e(E_\gamma)$ in given Table 1 $d_e(E_\gamma)$ is easily calculated from the intercept value of the line for a γ-ray of a particular energy. Thus, the γ-ray energies and respective the interaction depths for the detector used are given in Table 2 for all point sources and in given Table 3 for a volume source, respectively.

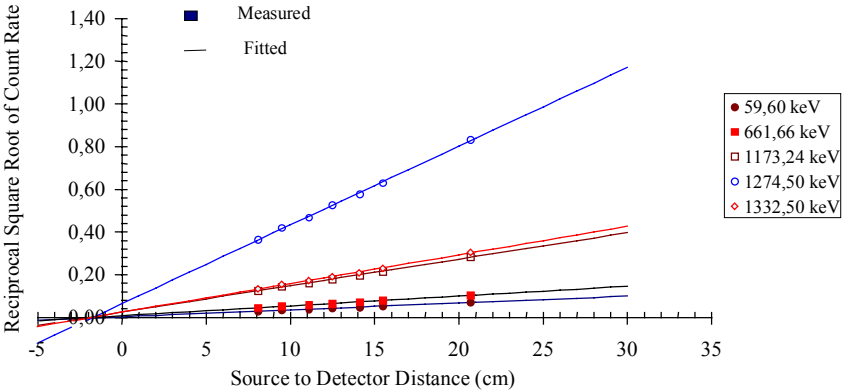


Fig. 2. Plot of Square Root of Reciprocal Count Rates for ^{241}Am, ^{137}Cs, ^{22}Na, ^{60}Co Point Sources

The dependence of $d_e(E_\gamma)$ on the photon energy obtained for the high purity Ge detector is shown in Fig. 6 for the point sources ^{241}Am, ^{137}Cs, ^{22}Na and ^{60}Co and the multi energy point sources in Fig.7 for ^{133}Ba, and ^{152}Eu and is shown in Fig. 8 for a liquid volume source.

The absolute efficiency is calculated by taking the ratio of the measured activity for that particular γ-ray and given geometry to the stated activity of the calibrated source. The absolute efficiencies at 9,5 cm, at 15,4 cm and at 20,7 cm as a function of γ-ray energy for Ge detectors is shown in Fig 9 for point sources and in Fig. 10 for a volume source. The experimental and the calculated values for the absolute efficiencies at these distance are also given in Table 4 for point source geometry and in Table 5 for a cylindiric volume source**.** For the absolute efficiency curve for

a volume source, the acceptable fit is obtained although the fit in the low energy region (50-90 keV) is not done as can be seen in Fig 9 due to the lack of experimental points, especially in the energy range.
The measured and calculated absolute efficiencies give in Table 4 agree within 0.1 to 7% when effective interaction depths were taken into account in Eq. 3 for two different distances of at d_1=9,5 cm and d =15,4 cm. The validation of Eq. 3 introducing interaction depths for a volume source given in table 5 is obtained by 0,1 to 7,6%, assuming that all photons are emitted from the source at its half height. Besides, the experimental interaction depths for point sources and a volume source can be approximated well using Least Square Methods (LSQ) by the following function;

$$d_e(E_\gamma) = a(1 - e^{b(E_\gamma + c)})$$

Where the coefficients, a,b and c are determined by LSQ method, and E_γ was chosen in MeV and d_e in cm. It is apparent that the curves shown in Figures 6, 7 and 8 exhibit the same behaviour. The curves increase with increasing gamma ray and level out at higher energies of photons.

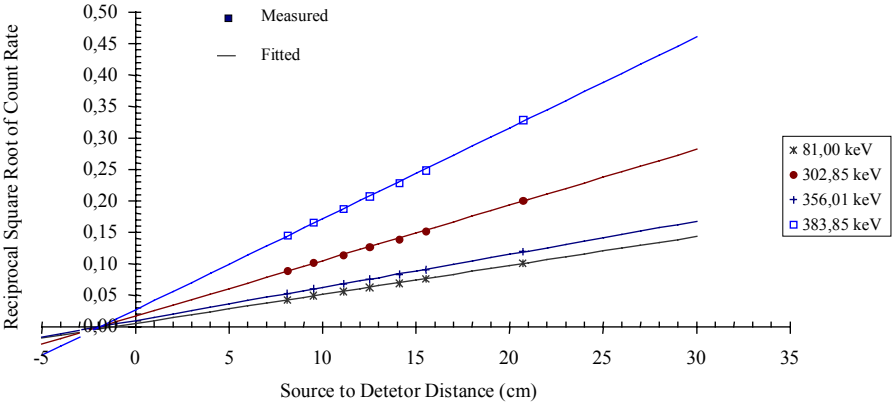


Fig. 3 Plot of Square Root of Reciprocal Count Rates for a ^{133}Ba Point Source

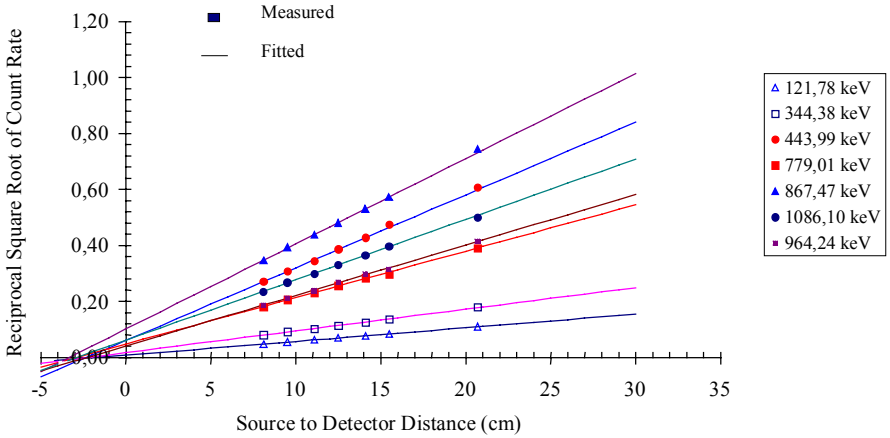


Fig. 4. Plot of Square Root of Reciprocal Count Rates for a ^{152}Eu Point Source

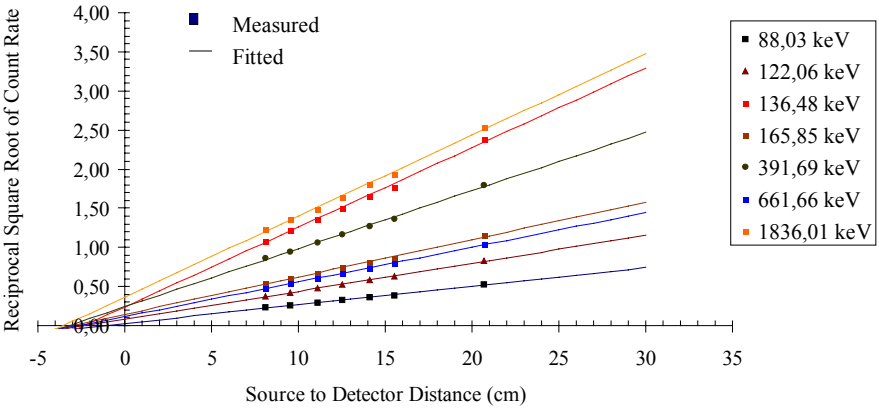


Fig. 5 Plot of Square root of Reciprocal Count Rates for a Volume Source

Conclusion

The well established procedures for the efficiency calibration of Ge-detector spectrometers appeared in the literature, however, an attempt was made to show that a semi empirical function relating the particular energy of γ-ray and effective interaction depth in Ge can facilitate the achievement of absolute efficiency calibration of a coaxial Ge detector without the necessity of much laboriously calibration effort. If an experimentalist determines the absolute efficiency at a distance, e.g at 10 cm by a calibrated source, then these values can be used to determine the efficiencies at any sample to detector distance by using the effective interaction depths.

Table 2. Photon Interaction Depth for all point sources

Nuclide	Photon Energies	Interaction Depth (mm)
Am-241	59,60	9,15
Cs-137	661,66	17,26
Co-60	1.173,24	19,85
Co-60	1.332,50	18,00
Na-22	1.274,50	17,43
Ba-133	81,00	11,43
	302,00	18,80
	356,00	19,12
	384,00	19,02
Eu-152	121,78	16,58
	344,32	21,48
	411,17	22,07
	443,99	23,09
	779,01	28,56
	867,47	33,11
	964,24	22,52
	1.086,10	28,41
	1.112,30	31,37
	1.299,50	36,43
	1.408,30	22,35

Table 3. Photon Interaction depth for volume sources

Nuclide	Photon Energies	Interaction Depth (mm)
^{109}Cd	88,03	11,69
^{57}Co	122,06	21,97
^{57}Co	136,48	23,41
^{139}Cd	165,85	30,29
^{113}Sn	391,69	32,23
^{137}Cs	661,66	26,13
^{88}Y	898,02	32,56
^{60}Co	1173,24	28,16
^{60}Co	1332,50	29,39
^{88}Y	1836,01	35,14

Table 4. The Measured and Calculated Efficiencies for Foint Sources

	Measured efficiency(x10^{-3})						
Energy (keV)	$\in_1$ (9,5 cm)	$\in_2$ (15,4 cm)	$\in_3$ (20,7 cm)	Interaction Depth (cm)	($\in_1/\in_2$) (meas.)	($\in_1/\in_2$) (calc.)	%Bias
59,60	5,43	2,27	1,23	0,92	2,40	2,37	-1,3
81,00	7,97	3,41	1,91	1,14	2,34	2,33	-0,2
121,78	7,26	3,23	1,83	1,66	2,24	2,26	0,8
302,85	3,34	1,49	0,86	1,88	2,24	2,23	-0,3
344,32	2,82	1,29	0,74	2,15	2,19	2,20	0,6
356,01	2,80	1,25	0,72	1,91	2,24	2,23	-0,5
383,85	2,64	1,18	0,67	1,90	2,25	2,23	-0,7
661,66	1,50	0,66	0,38	1,73	2,28	2,25	-1,1
779,01	1,15	0,56	0,32	2,86	2,07	2,12	2,7
867,47	0,98	0,46	0,36	3,31	2,12	2,08	-2,2
964,24	0,97	0,44	0,25	2,25	2,19	2,19	0,1
1.086,10	0,88	0,44	0,33	2,84	1,98	2,12	6,6
1.112,30	0,84	0,38	0,22	3,14	2,19	2,10	-4,6
1.173,24	0,83	0,37	0,22	1,99	2,24	2,22	-1,0
1.299,50	0,67	0,35	0,19	3,64	1,90	2,05	7,0
1.274,50	0,75	0,33	0,19	1,74	2,25	2,25	0,0
1.332,50	0,73	0,33	0,19	1,80	2,24	2,24	0,3
1.408,30	0,62	0,29	0,16	2,23	2,17	2,19	0,8

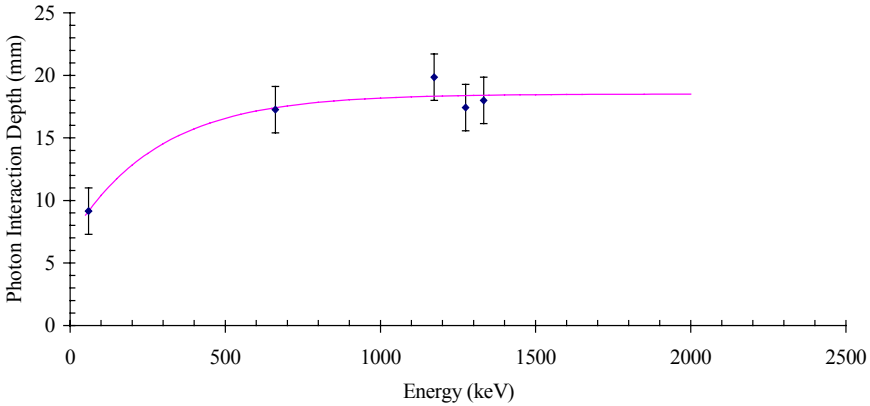


Fig. 6 Effective Photon Interaction Depth for ^{241}Am, ^{137}Cs, ^{22}Na and ^{60}Co Point Sources

Table 5. The Measured and Calculated Efficiencies for Foint Sources

	Measured efficiency(x10^{-3})						
Energy (keV)	$\in_1$ (9,5 cm)	$\in_2$ (15,4 cm)	$\in_3$ (20,7 cm)	Interaction Depth (cm)	$(\in_1/\in_2)$ (meas.)	$(\in_1/\in_2)$ (calc.)	%Bias
88,03	5,20	2,20	1,19	1,17	2,36	2,33	-1,5
122,06	5,04	2,23	1,28	2,20	2,25	2,20	-2,6
136,48	4,85	2,23	1,25	2,34	2,18	2,18	0,1
165,85	4,40	2,02	1,17	3,03	2,18	2,11	-3,3
391,69	1,92	0,86	0,51	3,22	2,23	2,09	-6,9
661,66	1,08	0,51	0,29	2,61	2,13	2,15	0,8
898,02	0,78	0,37	0,21	3,26	2,13	2,08	-2,2
1.173,24	0,62	0,29	0,17	2,82	2,13	2,13	0,0
1.332,50	0,53	0,25	0,15	2,94	2,13	2,11	-0,6
1.836,01	0,40	0,18	0,11	3,51	2,22	2,06	-7,6

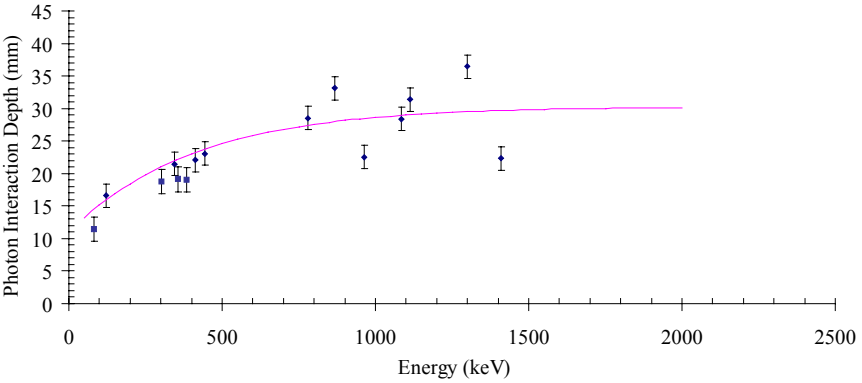


Fig. 7 Effective Photon Interaction Depth for ^{152}Eu and ^{133}Ba Point Sources

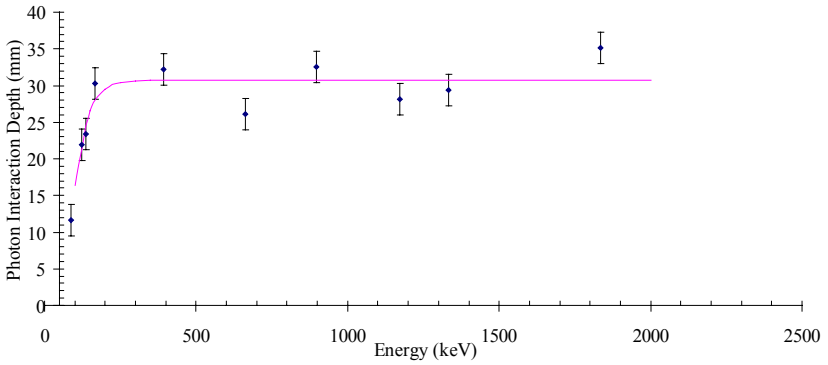


Fig. 8 Effective Photon Interaction Depth For Volume Source

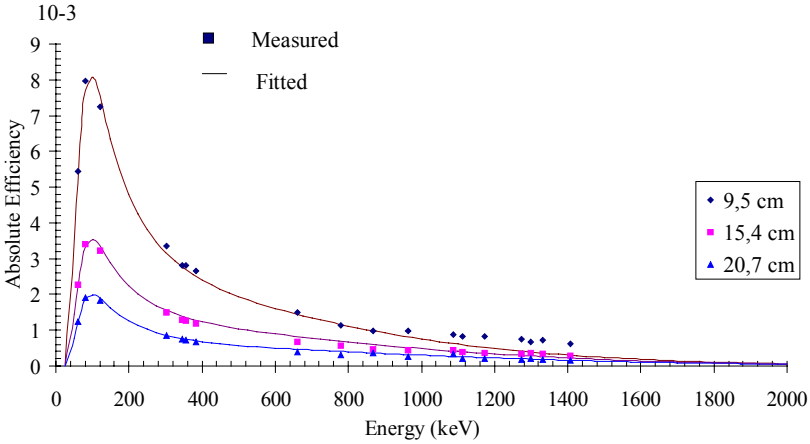


Fig. 9 Absolute Efficiency for point sources

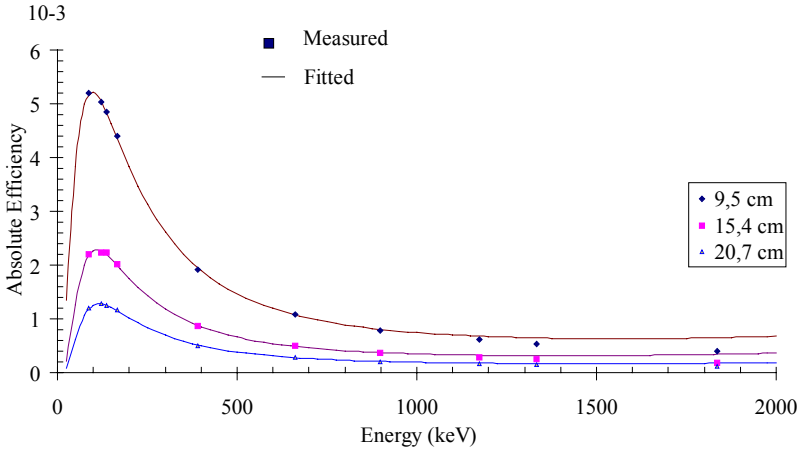


Fig. 10 Absolute Efficiency for a Volume Source

References

1. Cline J. E. (1979) A tecnique of γ-ray detector absolute efficiency calibration for extended sources. In Proc. Am. Nucl. Soc. Topical Conf. Computers Activat. Analysis γ-ray Spectros. CONF-780421, p.185 Mayaguez Puerto Rico.
2. Crisler D. F., Jarmer J. J. and Eldridge H. B. (1971) A method for absolute calibration of Ge(Li) detectors using effective interaction depth. Nucl. Instrum. Meth. 94, 285.
3. Debertin K. and Helmer R.G. (1988) γ-and X-ray spectrometry with semi conductor Detectors. Elsevier, New York.
4. Debertin K. and Schötzig U. (1979) Coincidence summing corrections in Ge(Li) –specrometry at low source-to-detector distances. Nucl. Instrum. Meth. 158,471.
5. Debertin K., Schötzig U., Walz K. F., and WeiB H. H., (1976) Efficiency Calibration of semi conductor spectrometers –techniques and accuracies. In Proc. ERDA Symp. X-Ray and γ-Ray Sources Applic. Ann Arbor, MI. (edited by Griffin H.C.), CONF-760539 p.59 National Technical Information Service, Springfield, VA.
6. Gunnik R. (1990) New Method for calibrating a Ge detector by using only zero to four efficiency points. Nucl. Instrum. Meth. Phys. Res. A299,372
7. Helmer R. G. (1982) Efficiency Calibration of a Ge detector for 30-2800 keV γ-rays. Nucl. Instrum. Meth. 199,521
8. Hirsfield A. T., Hoppes D. D and Schima F. J. (1976) Germanium detector efficiency calibration with NBS standards. In Proc. ERDA Symp. X-Ray and γ-Ray Sources Applic. Ann Arbor, MI. (edited by Griffin H.C.), CONF-760539 p.90 National Technical Information Service, Springfield, VA.
9. Notea A. (1971) The Ge(Li) spectrometer as a point detector. Nucl. Instrum. Meth. 91, 513
10. Rieppo R. (1987) The efficiencies of different photon detectors. A review covering work done between 1975 and 1985. Appl. Radiat. Isot. 38,1.
11. Yücel H., Cetiner M. A., Demirel H., (1996) Dependence of Photon Interaction Depth on Linear Attenuation Coefficient in High Pure Germanium Detectors. Appl. Radiat. Isot Vol 47, No. 5/6 pp. 535-541

ELASTIC AND INELASTIC DIFFRACTION INTERACTIONS OF NUCLEONS AND LIGHT NUCLEI AT INTERMEDIATE AND HIGH ENERGIES
(Review of the theoretical results and experimental data)

Ye.I. Ismatov[1], K.A. Kuterbekov[2], Sh.Kh. Djuraev[3], Sh.F. Esanniyazov[3], S.B. Strigina[1], M.I. Fazylov[1]

[1)] Institute of Nuclear Physics, Uzbekistan Academy of Science, Uzbekistan
[2)] Institute of Nuclear Physics, NC, Republic of Kazakhstan
[3)] Termez State University, Uzbekistan

I. Diffraction scattering of light nuclei

The elastic and inelastic scattering of nucleons and light nuclei on nuclei at intermediate and high energies has been studied for a long time. The scattering at such energies has diffraction character and Glauber-Sitenko diffraction multiple scattering theory (GSDMST) [1-6] is successfully applied to analyze the processes. The main assumptions underlying GSDMST are enumerated and the general structure of amplitudes and cross-sections of scattering is analyzed. The way is shown for calculation of cross-section of elastic and inelastic nucleus-nucleus scattering with using the condition of completeness of wave functions in the final state. In terms of GSDMST the amplitude of elastic nucleus-nucleus scattering may be written as

$$F_{el}^{A_1A_2}(q)=\frac{ik}{2\pi}\int d\vec{\rho}e^{i\vec{q}\vec{\rho}}\left|\psi_{A_1}\left(r_1,r_2...r_{A_1}\right)\right|^2\times$$
$$\times\left|\psi_{A_2}\left(\vec{\tilde{r}}_1,\vec{\tilde{r}}_2...\vec{\tilde{r}}_{A_1}\right)\right|^2\omega\left(\vec{\rho};\{s_1\};\{s_2\}\right)\prod_{i=1}^{A_1}d^3r_i\prod_{k=1}^{A_2}d^3r_k \qquad (1)$$

where the profile function

$$\omega\left(\vec{\rho};\{s_1\};\{s_2\}\right)=1-\prod_{i=1}^{A_1}\prod_{k=1}^{A_2}\left[1-\omega_{ik}\left(\vec{\rho}+\vec{s}_{1i}+\vec{s}_{2k}\right)\right] \qquad (2)$$

$\vec{r}_i$ and $\vec{r}_k$ are nucleon radius-vectors of nuclei A_1 and A_2, $\vec{s}_i$ and $\vec{s}_k$ - are their projections on impact parameter planes.

Nucleus ^{6}Li. Study of ^{6}Li structure showed for sure, that the most of experimental data cannot be explained within the framework of the plain shell model. Dynamic base of calculations is the Glauber-Sitenko theory of multiply

scattering (GSDMST) [1-4], which is used successfully for description of interaction between high-energy particles with nuclei. We will calculate the amplitude of scattering of particles by ^{6}Li nuclei assuming that nucleons are in its mass center. In this case the amplitude of elastic scattering of particles on nuclei ^{6}Li is the same as that of nucleons on the nuclei [10-13]. Then instead of (1) and (3) we can accept the following amplitude:

$$F_{e\ell}\left(\vec{k},\vec{q}\right)=\frac{ik}{2\pi}\int d\vec{\rho}\;\; e^{i\vec{q}\vec{\rho}}\omega\left(\vec{\rho}\right), \tag{3}$$

where the profile function in the case of the target nuclei transition from the ground state $|0>$ to an excited state $|f>$

$$\omega\left(\vec{\rho}\right)=<\left|\left[1-\prod_{j=1}^{A}\left(1-\omega\left(\vec{\rho}-\vec{\rho}_j\right)\right)\right]\right|0>. \tag{4}$$

Elastic scattering. Using methods described in [7,10], the final expression for the amplitude of elastic scattering is the following

$$\left(\frac{d\sigma}{d\Omega}\right)_{e\ell}=\left|F_{0\to 0}\left(k,q\right)\right|^2 \tag{5}$$

Inelastic scattering. Expression for amplitude of inelastic scattering for ^{6}Li with excitation to 3^+T=0 (2.18 MeV) state is obtained in the same way as that for elastic scattering. The only but substantial difference is, that there is the spherical function $Y_{2M}(x_5)$ under the integral in (11). Using it's concrete form [7,10], it is not difficult to obtain an amplitude of the transition into states M= 0, ±1, ±2.

The angular distributions of protons at elastic and inelastic scattering on nuclei were calculated by the expressions:

$$\left(\frac{d\sigma}{d\Omega}\right)_{3^+T=0}=\sum_{\mu}\;\left|F_{00\to 2M}\left(k,q\right)\right|^2 \tag{6}$$

Figures 1 and 2 show that the cluster model is in good agreement with the experimental data [7,14].

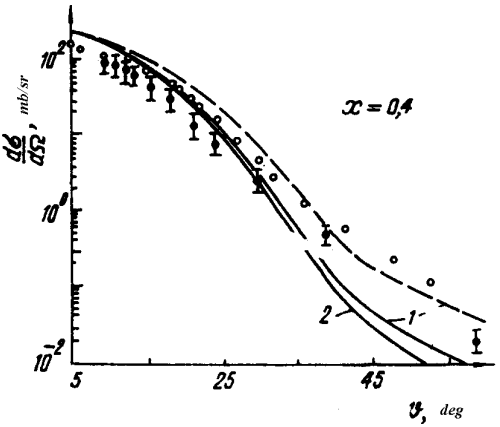


Fig. 1. Differential cross-section of elastic scattering of the protons at nuclei ^{6}Li on two cluster model (c.m.)

$$1 - P_0(R) = 1 - 8/9\,\beta R^2$$

$$2 - P_0(R) = 1 - 8/9\,\alpha_1 R^2$$

Numeric calculations by formula (6). The dashed curve – the shell model limiting (x=y=1). The dots are experimental data [14] for the energy E=152 MeV (light dots) and E=185 MeV (dark dots).

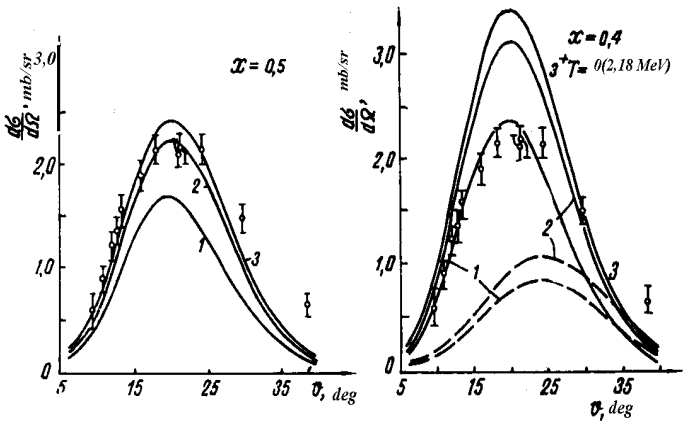


Fig. 2. Differential cross section of elastic scattering of protons with E=185 MeV at nuclei ^{6}Li in two cluster model (c.m.) Numeric calculations by formula (7).

$$1 - P_0(R) = 1 - 8/9\,\beta R^2$$

$$2 - P_0(R) = 1 - 8/9\,\alpha_1 R^2$$

The dashed curve – the shell model limiting (x=y=1). The dots are experimental data.

^{7}Li nucleus. Associative effects in nuclei ^{7}Li are pronounced not so well as in ^{6}Li, the most of the experimental data cannot be explained in the framework of the simple shell model. Moreover, the one-parameter shell model does not explain satisfactorily the inelastic form-factor at any value of the oscillator parameter. The most proper model, taking into account the discrepancy between the wave functions of ^{7}Li and that of shell model, is the cluster model. It gives good correlation between the data on elastic and inelastic scattering at the same values of wave function's parameters.

The differential cross-section of elastic scattering is determined by

$$\left(\frac{d\sigma}{d\Omega}\right)_{ynp} = \sum_{MM'=-1}^{1}\left|F_{1M\to 1M'}(kq)\right|^2 = \\ = \frac{1}{3}\left\{2\left[\left|F_{11}(kq)\right|^2 + \left|F_{1-1}(k,q)\right|^2\right] + \left|F_{00}(k,q)\right|^2\right\} \tag{7}$$

The amplitude of inelastic scattering with excitation of the 7/2 $^-$ T=1/2 (4.63 MeV) state is calculated in the same way as that of elastic scattering. The only difference is that the function Y_{2M} should be under the integral instead of the spherical function Y^*_{LM}. Using its concrete form, it is not difficult to obtain all the amplitudes of the transition. Because of symmetry it turns out, that only 6 of 21 transitions 1M$\to$3M′ should be considered.

The differential cross-section of inelastic scattering has the form [7,20]:

$$\left(\frac{d\sigma}{d\Omega}\right)_{7/2^- T=\frac{1}{2}} = \frac{1}{3}\sum_{M=-1}^{1}\sum_{M=-3}^{1}\left|F_{1M\to 1M'}(kq)\right|^2 = \\ = \frac{1}{3}\left\{\left|F_{00}(k,q)\right|^2 + 2\left[\left|F_{13}(q,k)\right|^2 + \left|F_{11}(k,q)\right|^2 + \right.\right. \\ \left.\left. + \left|F_{1,-1}(q,k)\right|^2 + \left|F_{1,-3}(q,k)\right|^2 + \left|F_{02}(q,k)\right|^2\right]\right\}. \tag{8}$$

The angular distributions of protons at elastic and inelastic scattering on ^{7}Li nuclei were calculated with the expression (9) and (10). As it is seen at figure 3, the cluster model agrees well with the experimental data [16-18].

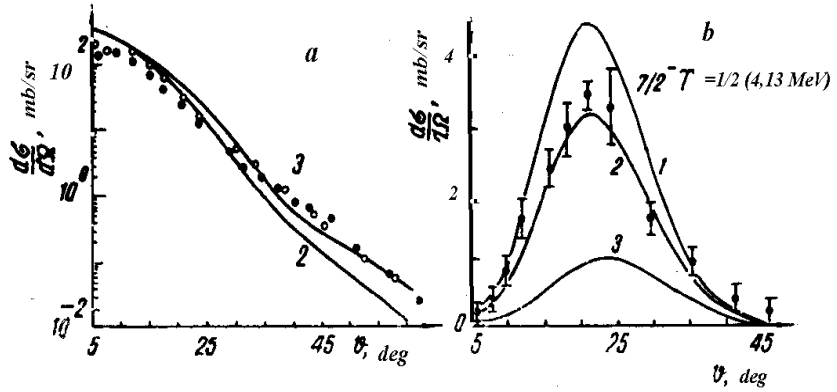


Fig. 3. Differential cross-sections of elastic and inelastic scattering of protons with E=185 MeV on nuclei ^{7}Li (c.m.) in two cluster model
1 and 2 calculations by formulae (6) according to x-0,4 and 0,5. 3-shell model limiting (x=y=1). The dots are experimental data for the energy E=152 MeV (light dots) [15] and E=185 MeV (dark dots) [16,17].

Nucleus ^{12}C. The cross-sections of nucleon and light nuclei scattering on ^{12}C nuclei is described in the framework of the Glauber-Sitenko theory of diffraction nuclear reactions. The wave function of ^{12}C nuclei is presented as a determinant composed of one-particle functions $\Phi_{jm}(r,\sigma)\,\tau_\gamma$, that are eigen functions of square total moment $\hat{j}^2$ of a nucleon and it's projection on Z-axis, and also square isospin $\hat{t}^2$ of nucleon and it's projection on Z-axis.

Taking the wave function from [7,10] as that of ground state of ^{12}C nuclei, the amplitude of elastic scattering of protons and α-particles on ^{12}C nuclei will be in the following form

$$F_{0\to 0}(q)=\frac{ik}{2\pi}\exp\left[q^2<r^2>/104\int d\vec{\rho}e^{i\vec{q}\vec{\rho}}\cdot\right.$$
$$\cdot\left\{1-N_0^2\int d\vec{r}_1\ldots d\vec{r}_{12}\cdot\exp\left(-\frac{1}{a^2}\sum_j r_j^2\right)\cdot\right. \tag{9}$$
$$\left.\left.\cdot\Psi_s\left[1+\frac{1}{20a^4}\sum_M(-1)^M Q_{-M}^2 Q_M^2+\ldots\right]\cdot\prod_{j=1}^{12}\left(1-\gamma_j\right)\right\}\right.$$

These functions are antisymmetrized over all arguments. Antisymmetrization of ψ_s-function over all coordinates is not necessary, because the operators are not dependent on spin and isospin of particles.

The differential cross-sections of elastic scattering of protons and α-particles on ^{12}C nuclei are calculated with the expression (11) and shown in Fig.4.

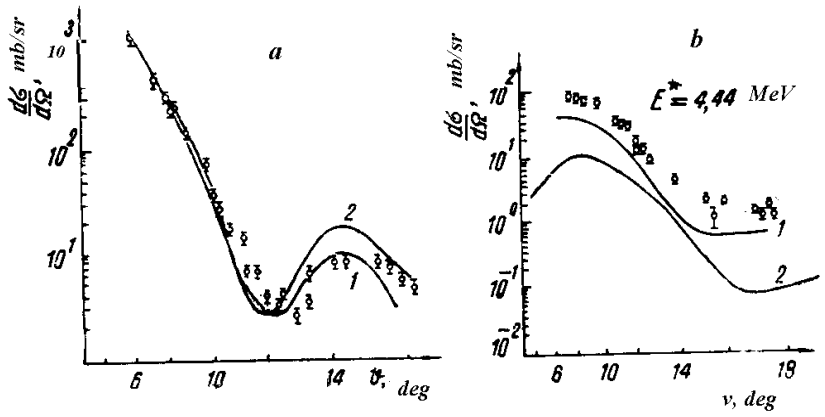


Fig.4. Differential cross-section of elastic and inelastic scattering of protons with energy E=1 GeV on nuclei ^{12}C (The solid curve is obtained at $<r^2>1/2 = 2.29$fm). Numerical calculations by formulae (9) and (10).

1 - The deformed nucleus ($\varepsilon = 1{,}35$)

2 - The spherical symmetrical nucleus ($\varepsilon = 1$). The dots are the experimental data.

Taking the wave functions Φ_0 and Φ_{2M} from [7,10], we obtain the amplitude of inelastic protons with excitation of 2′ level of ^{12}C:

$$F_{00\to 2M}(q) = \frac{N_0 N_{2M}}{2a^2}\left(\frac{ik}{2\pi}\right)\exp\left[q^2 < r^2 > /104\right]\cdot$$
$$\cdot \int d\vec{\rho} e^{i\vec{q}\vec{\rho}} \cdot \int d\vec{r}_1 ... d\vec{r}_{12} \Psi_s^2(\vec{r}_1 ... \vec{r}_2)\cdot$$
$$\cdot \exp\left(-\frac{1}{a^2}\sum_j r_j^2\right)\cdot\{(Q_{2M} + ...)\cdot \tag{10}$$
$$\cdot\left(1 + \frac{1}{40a^4}\sum_M (-1)^M Q_M^2 Q_{-M}^2 + ...\right)\Big\}\cdot \sum_{j=1}^{12}(1-\gamma_j).$$

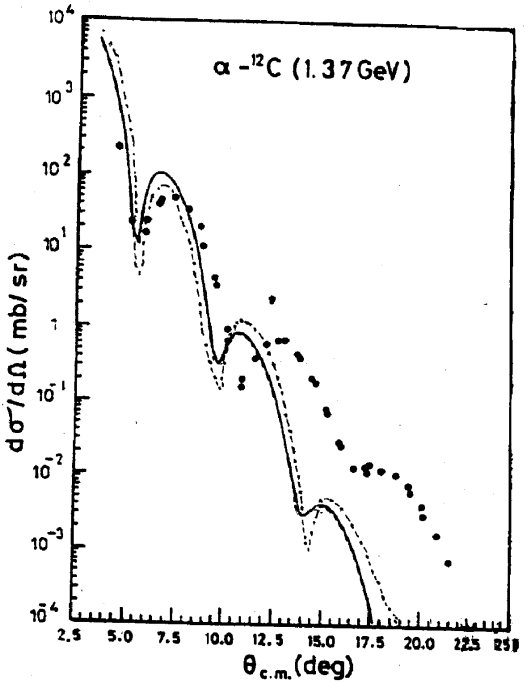


Fig. 5.

Differential cross-section of elastic scattering for the α - ^{12}C reaction at 1,37 GeV. The dashed curve is obtained by formula (27). The solid curve is obtained with phase variation [γ^2 = 2(GeV/c)$^{-2}$] from the work [9].
The dots are the experimental data [19].

The differential cross-sections of inelastic scattering of 1 GeV-protons on ^{12}C nuclei are calculated with the expression (28) and shown in Fig.4b. The parameters of nucleus and nucleon-nucleon amplitude are the same as those for the elastic scattering. The cross-section calculated in this way is better than that in [21,22], however it is not in a good agreement with the experimental values.

The results on the elastic scattering of α-particles, ^{12}C and ^{40}Ca at the energies of 1.37, 1.44, 1.503, 2.4 GeV, calculated by us with the help of the cluster model within the framework of the GSDMST, were compared to the corresponding experimental data [19] and the theoretical results in [9]. For comparing our approach with the calculations in [9], the figure 5 shows calculated and experimental [19] values of the diffraction cross-section of the elastic scattering of α-particle on ^{12}C nuclei at the energy E_α= 1.37 GeV. Thus, it is seen, that our calculations are almost coincide with the results of [9] and describe correctly the character of angular distributions of α-particles.

II. Diffraction interaction taking into account nucleon

In the given chapter the method of profile function calculation via phase shifts is developed. It is calculated in quasi-classic approximation from the hadron-nucleus interaction potential. It is performed without introduction of adjustable parameter [1-5]. The method used in the work describes the experimental angular distributions of deuterons on the nuclei at intermediate energies of incident particles. It is found that the cross-sections are sensitive to the parameters of nucleon-nucleus interactions. This fact can be used to make more precise conclusions on model understanding of the nuclei structure and the nuclear processes mechanisms. [6-7]. The differential cross-sections of deuterons elastic scattering by means of correct consideration of Coulomb interaction in diffraction approximation were calculated.

It is well known that the nucleons scattering amplitude can be determined by the Fourier representation of profile function

$$\omega(\rho) = 1 - \exp[2i\delta(\rho)], \tag{1}$$

where ρ is the impact parameter, δ(ρ) is scattering phase.

$$\delta(\rho, E) = k\left\{\int_{b(V_N)}^{\infty} d\vec{r}\sqrt{1-\rho^2/r^2 - 2\mu V_N(\vec{r},E)/k^2} - \int_{b(0)}^{\infty} d\vec{r}\sqrt{1-\rho^2/r^2}\right\}. \tag{2}$$

E, k, μ are relative energy, wave number of a scattering particle, reduced mass, respectively, b(k) and b(0) are the roots of real parts of integrand. $V_N(\vec{r},E)$ in (2) is the Woods-Saxon potential

$$V_N(r,E) = -\frac{V(E) + iW(E)}{1 + \exp(\frac{r-R}{\Delta})}, \tag{3}$$

where V(E), W(E) are parameter and potential, obtained from the experimental data. $R = r_0\sqrt[3]{A}$, Δ – is the parameter of the diffuse border of the nucleus's surface.

When $V_N(\vec{r},E) << E$ the formula (2) can be rewritten as follows

$$\delta(\rho, E) = -\frac{1}{v}\int d\vec{s}\{\mathrm{Re}\, V_N(r,E) + i\,\mathrm{Im}\, V_N(r,E)\}, \tag{4}$$

v is the relative velocity of nucleon and the target-nucleus, $s = \sqrt{r^2 - \rho^2}$.

In the relativistic energies region one can have the following expression using the theory of multiple scattering (not taking into account nucleon correlations)

$$V_N(r,E) = -\frac{2\pi}{E+M} f(0)\rho_N(2), \tag{5}$$

where $f(0)=k\sigma_t(i+\gamma)/4\pi$ is the amplitude of the nucleon-nucleon scattering on the zero angle, $\sigma_t = \sigma_t(E)$ is the total cross-section on nucleon-nucleon interaction, M is the nucleon's mass, $\rho_N(r)$ is the density distribution in target-nuclei. The σ_t and γ are determined experimentally. Normally in calculations the cross-section distribution in the nucleon plane is chosen to be as

$$\rho_N(r) = \rho_{N0}\left(1+\exp\left(\frac{(r-R)}{\Delta}\right)\right)^{-\xi} \tag{6}$$

using these assumptions for the amplitude of elastic scattering at intermediate energies on the deuterons nuclei one can have (not taking into account Coulomb interaction)

$$F(q) = ik\left\{2\exp\left(-q^2/32\lambda\right)\int_0^\infty d\rho\rho\omega(\rho)J_0(q\rho) - \right. \tag{7}$$

$$\left. -\frac{4\lambda}{\pi}\int_0^\infty d\rho_1\rho_1\omega(\rho_1)\int_0^\infty d\rho_2\omega_2(\rho_2)\int_0^\pi d\varphi_{21}\exp\left(-2\lambda\,|\,\vec{\rho}_1-\vec{\rho}_2\,|^2\right)J_0\left(\frac{q}{2}\,|\,\vec{\rho}_1+\vec{\rho}_2\,|\right)\right\}$$

where $q = |\vec{k}-\vec{k}'|$ is the transferred momentum, $\vec{k}(\vec{k}')$ are the wave vectors of the incident and scattered deuterons, φ_{21} is the angle between $\vec{\rho}_1$ and $\vec{\rho}_2$ vectors, $\omega_1(\rho_1)$ and $\omega_2(\rho_2)$ are the profile functions. If one should consider elastic diffraction scattering of the weakly bound cluster nuclei on nuclei then in the region of tenth of MeV it is necessary to take into account Coulomb interaction with the target-nuclei.

Then instead of (7) one can have the following expression:

$$F(\vec{q}) = F_1(\vec{q}) + F_2(\vec{q}) + F_{12}(\vec{q}) = \frac{k}{k_1}f(\vec{q})\Phi_0(-\vec{q}/2) + \frac{k}{k_2}f_2(\vec{q})\Phi_0(-\vec{q}/2) + \tag{8}$$

$$+\frac{ik}{2\pi\vec{k}_1\vec{k}_2}\int d^{(2)}\vec{g}f_1(\vec{q}/2+\vec{g})f_2(\vec{q}/2-\vec{g})\Phi_0(\vec{g})$$

where $q = |\vec{k}-\vec{k}'|$ is the transferred momentum, $\vec{k}(\vec{k}')$ is the wave vectors of the incident(scattered) deuteron k_i and $f_i(\vec{q})$, $q=1,2$ are the wave numbers of deuteron clusters (1-st neutron, 2-nd proton) and cluster-nuclear amplitude is as follows

$$f_i(\vec{q}) = \frac{ik}{2\pi}\int d\vec{\rho}_j\exp\left(i\vec{q}\vec{\rho}_j\right)\omega_j(\rho_j) \tag{8a}$$

where $\vec{\rho}_j$ is the vector of the impact parameter of j-cluster, $\omega_j(\rho_j)$ are the corresponding profile functions which can be presented in the following way for the dark diffuseless nucleus:

$$\omega_1(\rho_1)=\begin{cases}1, & \rho_1 < R\\ 0, & \rho_1 > R\end{cases}$$
$$\omega_2(\rho_2)=\begin{cases}1, & \rho_2 \le R\\ 1-\exp[2i\eta(\rho_2)], & \rho_2 > R\end{cases} \quad . \tag{8b}$$

$R=r_0(1+A^{1/3})$ is the radius of cluster-nuclear interaction, $\eta(\rho_2)$ is the Coulomb scattering phase, which can be defined in the diffraction approximation via $\eta(\rho_2)=n_2\ln(k_2\rho_2)$, $n_2=z\alpha\mu_2/k_2$ is the Sommerfeld parameter, z is the charge number of the nucleus, α is the fine structure constant, $\mu_2=Mm_2/(M+m_2)$ is the reduced mass of proton and target-nucleus. The deuteron form-factor in (9) is expressed as follows:

$$\Phi_0(\vec{q})=d^{(3)}\vec{r}\,\varphi_0^2(\vec{r})\exp[\mu\vec{q}\cdot\vec{r}j], \tag{8c}$$

where $\varphi_0(r)$ is the internal wave function of deuteron.

$$F(\vec{q})=G(\vec{q})+g^{(1)}(\vec{q})+g^{(2)}(\vec{q}) \tag{9}$$

where $G(\vec{q})$ is the term in the amplitude $F(\vec{q})$ not taking into account the Coulomb effects.

$$G(\vec{q})=ik\left[\Phi_0(\vec{q}/2)+\Phi_0(-\vec{q}/2)\right]\frac{RJ_1(qR)}{q}-$$
$$-\frac{R^2}{2\pi}\int d^{(2)}\vec{g}\,\Phi_0(\vec{g})\frac{J_1(|\vec{q}/2-\vec{g}|)}{|\vec{q}/2-\vec{g}|}\cdot\frac{J_1(|\vec{q}/2+\vec{g}|)}{|\vec{q}/2+\vec{g}|} \tag{10}$$

$g^{(1)}(\vec{q})$ and $g^{(2)}(\vec{q})$ in (9) are the terms of $F(\vec{q})$, which are responsible for single and double scattering of clusters with Coulomb interaction taken into account:

$$g^{(1)}(\vec{q})=-n\frac{2k}{q^2}\Phi_0(\vec{q}/2)\left[J_0(qR)+in\int_R^\infty d\rho\frac{J_0(q\rho)}{\rho}\exp\{2i[\eta_2(\rho)-\eta_2(R)]\}\right] \tag{11}$$

$$g^{(2)}(\vec{q})=\int d^{(2)}\vec{g}H(\vec{g},\vec{q}),$$
$$H(\vec{g},\vec{q})=n\frac{kR}{\pi}\Phi_0(\vec{g})\left[\frac{J_1(|\vec{q}/2-\vec{g}/R|)}{|\vec{q}/2-\vec{g}|}\frac{1}{|\vec{q}/2-\vec{g}|^2}\cdot\right. \tag{12}$$
$$\left.\cdot J_0(|\vec{q}/2+\vec{g}/R|)+2in\int_R^\infty d\rho\frac{J_0(|\vec{q}/2+\vec{g}|\rho)}{\rho}\exp\{-2i\eta_2(\rho)-\eta_2(R)\}\right.$$

It is easy to notice that expression (12) is logarithmically divergent at $\vec{g} = -\vec{q}/2$. Also, the integrals by momenta in nuclear diffraction are the double integrals and the integration plane is perpendicular to the momentum $\vec{k}$. It is considered that the transferred momentum $\vec{q} = \vec{k} - \vec{k}'$ where $\vec{k}'$ is the momentum of the diffracted particle is placed in the integration plane, i.e. $\vec{q}\vec{k} = 0$. Such approximation is negligible for the short-range nuclear interaction. But if one takes into account the simultaneous scattering of clusters from the incident complex particle with added Coulomb interaction between neutron-target leads to logarithmic divergence of some double momentum integrals which was originally shown by Akhiezer and Sitenko [4].

Therefore, it is possible to get rid off the mentioned divergences if one takes into account that the transferred momentum $\vec{q}$, as it is known from kinematics, is indeed only approximately perpendicular to the momentum $\vec{k}$. Even if the $q_z \equiv \vec{q}\vec{k} - k = 2k\sin^2(\theta/2) \approx (k/2)\theta^2$ component, where θ, the angle between k and k' vectors (scattering angle) is small comparatively to $q = 2k\sin^2(\theta/2) \approx k\theta$. However, its account leads to the convergent integrals, in general, for any number of charged clusters since, for instance, the arguments of the amplitude $f_1(\vec{q}/2 - \vec{g})$ and $f_2(\vec{q}/2 + \vec{g})$ in the expression (8) does not become equal to zero at any $\vec{q}$ when $q_z \neq 0$.

If the incident complex particle (e.g. deuteron, ^{11}Li and ^{11}Be nuclei) has only one charged cluster then it is possible to consider as before that the $\vec{q}$ vector is perpendicular to the $\vec{k}$ ($\vec{q}\,\vec{k} = 0$) vector. However, to deal with the divergences caused by the consideration of Coulomb interaction it is necessary to transfer from double integration by $\vec{g}$ in (7), (10) and (12) to triple integration. This can be done by using the following model approach: the double integral $\int d^{(2)}H(\vec{g},\vec{q})$ can be represented via one-dimensional δ-function $\delta(\vec{g})$ as triple integral $\int d^{(3)}\vec{g}\,\delta(\vec{q}_z)H(\vec{g},\vec{q})$ and then $\delta(g_z)$ can be substituted by more realistic g_z distribution (with efficiency of $g_z \sim \overline{\lambda}$) [4].

The ratios were calculated. Consider the processes of the elastic deuterons scattering using the above-mentioned expressions.

$$\sigma/\sigma_R \equiv \sigma(\theta)/\sigma_R(\theta) \tag{13}$$

where $\sigma(\theta) = \left|F(\vec{q})\right|^2, \sigma_R = \sigma_R(\theta)$is Rutherford cross-section. They showed satisfactory agreement with the experimental data on the elastic scattering of deuterons at the energies of 0.7GeV on ^{40}Ca nuclei. σ(θ) calculation was done by using the cluster-nuclear profile functions which are determined by the formulae (1), (4), (5), (6) and at ξ=2. Figure 6a corresponds to γ=Ref(0)/Imf(0), and figure 1b to γ=0.37. The angular dependencies of σ/σ_R for deuterons elastically scattered by ^{68}Zn and ^{208}Pb nuclei at energies of 80 MeV are presented on Figure2. Dotted line correspond to case in which Coulomb interactions are not considered, dashed-dotted line represents data with $g^{(1)}(q)$ taken into account, and the solid line stands for the case with $g^{(1)}(q)$ and $g^{(2)}(q)$ taken into account simultaneously.

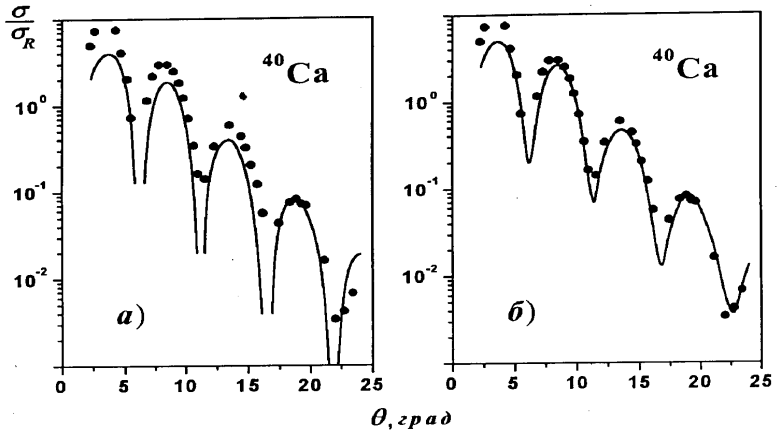


Fig. 6. Angular dependence of σ/σ_R ratio for the inelastic scattering of deuterons at energy of 0.7 GeV by ^{40}Ca nuclei.

The influence of the structure and diffusity of the target-nuclei's surface on the scattering cross-sections was studied. The angular dependencies of the cross-sections are in satisfactory agreement with experiment in the range of both first and the secondary diffraction maximums. The experimental data was kindly presented by the authors of [1-3]. We hope that the method developed in this work, which was effective enough for description of differential cross-section of the elastic scattering of deuterons, can successfully describe elastic scattering of weakly bound nuclei on spinless nuclei such as ^{28}Si and ^{12}C.

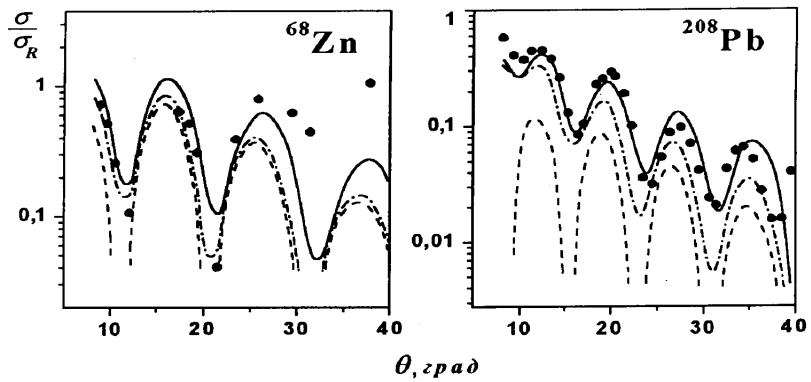


Fig. 7. Angular dependence of σ/σ_R ratio for the elastic scattering of deuterons at energy of 80 MeV by ^{68}Zn and ^{208}Pb. The dashed line is for the case when the Coulomb interaction is not taken into account, dashed-dotted line takes into account $g^{(1)}(q)$, the solid line takes into account $g^{(1)}(q)$ and $g^{(2)}(q)$.

In the work [4] the general formalism to describe the diffraction elastic scattering and diffraction fission of weakly bound double-cluster nuclei on the spinless nuclei with Coulomb interaction taken into account, simultaneous scattering of clusters, their spin-orbit interaction with the nuclei-target and diffuse edges of nucleus. The calculations of the differential cross-sections were carried out for complex nuclei at intermediate energies of the radioactive exotic ions of ^{11}Li and ^{11}Be having large neutron halo. Differential cross-section of the elastic scattering of ^{11}Li ions on the spinless nucleus can be expressed via $G^z(\vec{q})$ and $H_0^z(\vec{q})$ in the coordinate system with the z-axis along the $\vec{k} \times \vec{k}'$ vector in the following way:

$$\sigma_{el}(\theta) = (kR^2)^2 \left(|G_0^z|^2 + \frac{5}{4} |H_0^z|^2 \right) \tag{14}$$

The elastic scattering differential cross-sections of ^{11}Be on the spinless nucleus in the same coordinate system can be expressed as follows:

$$\sigma_{el}(\theta) = (kR^2)^2 \left(|G_0^z|^2 + \frac{1}{4} |H_0^z|^2 \right) \tag{15}$$

Figure 8 shows the results of the differential cross-section calculations (14) of the elastic scattering of ^{11}Li ions at the energy of 29 MeV/nucleon on ^{28}Si nuclei together with the experimental angular distribution measured in [9,10]. In the calculations the parameter γ, characterizing the intensity of the spin-orbital interaction appeared to be equal to 0.2 fm^2. The dashed line on the Figure 8

presents the calculation of the cross-section (14) when the charges of the colliding particles are neglected, i.e. the scattering is in the purely nuclear field. Dotted line represents the calculations including the Coulomb effects in case of transition to the three-dimensional integration using the finite by g_z distribution defined by the following expression:

$$P_1(g_z) = \frac{1}{\sqrt{8\pi\lambda}} \exp\left(\frac{g_z^2}{8\lambda}\right), \quad \lim_{\lambda\to 0} P_1(g_z) = \delta(g_z) \tag{16}$$

the solid line on this figure was calculated for the case taking into account the Coulomb interaction q_z=0.

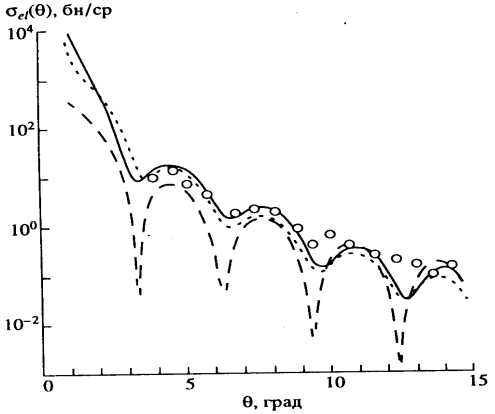


Fig.8. The angular distribution of the ratio σ/σ_R for the elastic scattering of ^{11}Li ions at the energy of 29 MeV/nucleon on ^{28}Si nuclei [4,9,10].

III. Application of the quark model of nuclei for the inelastic diffraction scattering

According to the quark model of nucleus the wave function of the nucleus can be presented as the system of interacting colourless three-quark cluster-nucleons. Both in bound or in unbound nuclear systems, i.e. in the nuclei, at the collision of different particles and nuclei with nuclei complex multi-quark systems can appear. First of all these are the 6q, 9q and 12q systems which are the overlap of two, three or of larger number of nucleons.

It is obvious to expect that in the ground and weakly excited states of the nuclei such overlaps are some small additions to the ground state Ψ(AN) (without overlap) in the complete phase of the nucleus's function.[1-6].

$$\Psi = \alpha\Psi(AN) + \beta\Psi(3Aq), \tag{1}$$

i.e. in this case $|\beta|^2 << 1$, $|\alpha|^2 \approx 1$.

Consider the most simple two-nucleon system – deuteron. The ground state of deuteron is the weakly bound state of two three-quark cluster – proton *p* and neutron *n* with weight $|\alpha|^2$ close to one, as well as small six-quark state with small

weight $|\beta|^2<<1$. Therefore, the corresponding wave function of deuteron Ψd, as in the general case (a), can be presented in the following way:

$$|d\rangle \equiv \Psi_d = \alpha\Psi(AN) + \beta\Psi(3Aq) \quad (2)$$

The external part of Ψ(pn), the total wave function of deuteron (2), in the non-relativistic case can be presented in antisymmetrized way from different variables [1]

$$\Psi(pn) = e^{-\frac{i}{\hbar}\vec{p}\vec{R}_d}\hat{a}\left\{\varphi_n(\vec{\xi}_1,\vec{\xi}_2)\psi_c^n\varphi_p(\vec{\eta}_1,\vec{\eta}_2)\psi_c^p\varphi_0(\vec{r})\chi_{1M_s}Z_{00}\right\} \quad (3)$$

Let us, now, compose the antisymmetric wave function of the six-quark state in the deuteron Ψ(6q), which is in the (2). The wave function can be expressed in the factorized way [1]

$$\Psi(6q) = e^{\frac{i}{\hbar}\vec{P}\vec{R}}\varphi_{6q}(\vec{\rho},\vec{\xi}_1,\vec{\xi}_2,\vec{\eta}_1,\vec{\eta}_2)\Psi_{cst} \quad (4)$$

The full title of the functions in (3) and (4) can be found in [1]. In terms of the shell model the internal wave function of deuteron can be rewrite as follows:

$$\Psi(6q) = |\, s^6[6]_\chi[2^3]_C[42]_S[3^2]_T \,|\left|[1^6]_{\chi CST}\right\rangle \quad (5)$$

The considered six-quark model of deuteron has two electric parameters. They are structure parameter Ω and the probability of the six-quark states in deuteron $|\beta|^2$. It follows from the experimental data that $\Omega\approx 25\text{fm}^{-2}$ and $|\beta|^2\approx 2\%$. Within the oscillation quark model we have studied the differential cross-section of the elastic scattering of electrons. Since $|\beta|^2<<1$ then in the region of relatively small transferred momenta $q\leq 3$ fm^{-1}. It is possible to provide calculations with one external (nucleon) function of deuteron. Good agreement with the corresponding experiment can be reached in such approximation.

In the last experiments on the electrons scattering by nuclei with high momenta transfer $q\geq 5\text{fm}^{-1}$ it was observed that the electron can penetrate into the bulk of nuclei as deep as $q\leq 0.2$fm, where the quark structure of the nuclear matter can be observed. Figures 9 and 10 show the calculated dependencies of the deuteron form-factors $A(q^2)$ and $B(q^2)$ at high momenta transfer with the six-quark states of deuteron taken into account [3]. It is important to note that the form-factors $A(q^2)$ and $B(q^2)$ are related to the structure of deuteron and are in the differential cross-section of the elastic scattering of electrons on deuterons.

$$\frac{d\sigma}{d\Omega} = \frac{\sigma_M(\theta)}{1+\frac{2k}{M_d}\sin\frac{\theta}{2}}\left\{A(q^2)+B(q^2)tg\frac{\theta}{2}\right\}, \quad (6)$$

where θ and k are the scattering angle and momentum of the electron, M_d is the mass of deuteron ($\hbar=c=1$), $\sigma_M(\theta)$ is the cross-section of Mott for the electron scattering on the point-like charge.

Consideration of the six-quark component in the deuteron wave function give a possibility for better description of the other properties of deuteron and the processes in which it takes part. in particular, photo-fission of deuteron at γ-quanta energies of ~1GeV, protons distribution over the momentum in the deuterons and nuclei collision reactions, which are produced in the reactions under the small angles. Figure 11 shows the comparison with experiment. The calculated dependencies of the differential cross-sections of the unpolarised deuterons fission process with momentum of deuterons of 8.9 GeV/c on the carbon nuclei are presented [4]. The wave function of neutron-proton system, here, was calculated for the Parisian NN-potential. The bold line corresponds to the consideration of six-quark state in deuteron; dashed-dotted line is for the case in which this state is not taken into account.

One can see from the figure that in the wide range of proton momenta values ($200 \le P_p \le 450$MeV/c) is described well by the corresponding to the experimental data, if one takes into account 6q-component in the wave function of deuteron.

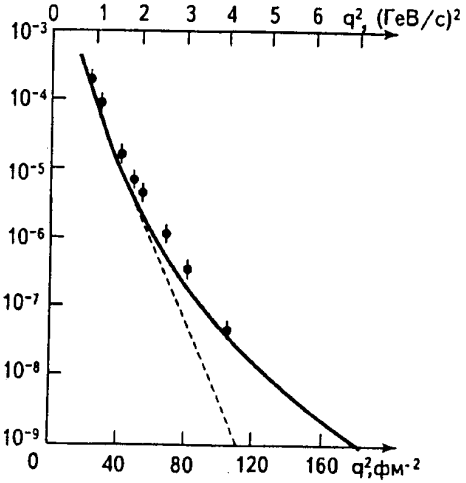


Fig.9. Dependence of the deuteron form-factor $A(q^2)$ on the transferred by electron momentum squared q^2.

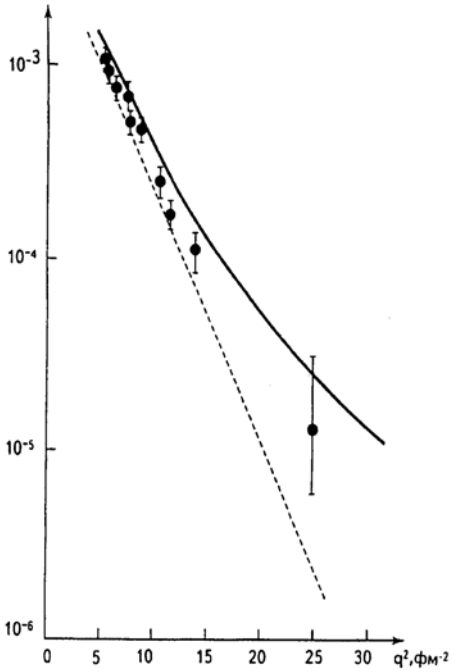


Fig. 10. Dependence of the deuteron form-factor $B(q^2)$ on the transferred by electron momentum squared q^2.

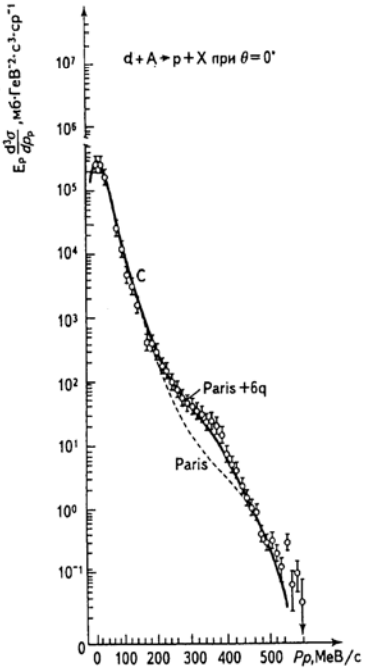


Fig. 11. Differential cross-section of the deuteron's fission on the ^{12}C nuclei depending on the proton's momentum.

References I

1. R.J.Glauber «High energy collision theory» Lect.Theor. Phys., p. 315-414. (1959).
2. A.I.Akhiezer, A.G.Sitenko // Phys.Rev., v.106, p. 1236 (1957).
3. A.G.Sitenko «Theory of nuclear reaction»// Energoatomizdat, 353 p. (1983).
4. A.G.Sitenko, Ye.I.Ismatov, W.K.Tartakovsky.// Phys.Atom.Nuc., v. 5, p.573 (1967).
5. G.G.Arushanov, Ye.I.Ismatov «Elastic and inelastic diffraction nuclear interaction» // Tashkent «FAN», 283 p. (1988).
6. Ye.I.Ismatov, Sh.Kh.Djuraev, A.V.Khugaev «Phenomenological theory interaction nucleons and nicleus»// Tashkent «FAN», 296 p. (1994).

7. Ye.I.Ismatov «Theory of the diffraction process» // Tashkent «FAN», 176 p. (1978).
8. Yu.A.Berezhnov, V.Yu.Korda // Phys.Atom.Nuc., v. 62, No 11, (1999).
9. M.M.El-Gogary, A.S.Shalaby, M.Y.M.Hasson// Phys.Rev.C., v.58, No 6, p. 3513. (1998).
10. I.M.Dozenko, A.D.Fursa // Phys.Atom.Nuc., v. 17, p. 770-783, (1973).
11. A.G.Sitenko, A.D.Polozov, M.W.Ewlanov.// Preprint ITP-73-161. P.Kiev, 25 p. (1973).
12. A.G.Sitenko, A.D.Fursa, I.M.Dozenko // Ukr.Phys. J., v.16, p.881 (1971).
13. A.G.Sitenko, A.D.Fursa// Ukr.Phys. J., v. 17, p. 110 (1972).
14. B.M.Golowin, I.M.Rozanova // Preprint P-2861, JINR, Dubna, (1966).
15. A.Johanson, U.Svanberg, P.E.Hodgson //Akk.för.Fys. v.19, p.541 (1961); v.20, p.643 (1962)
16. C.Rolland, B.Geoffrion et.al.// J. Phys., v.27, p.282 (1966).
17. D.Hasselgren, P.U. Renberg et.al.// Phys.Lett., v.9, p.116 (1964).
18. H.Palevsky.// Phys.Rev.Lett., v.18, p.1200 (1967).
19. S.M.Lenzi, A.Vilturi, P.Zardi.// Phys.Rev.C. 40, p.2114 (1989).
20. E.B.Lewshin, A.D.Fursa // Phys.Atom.Nuc. v. 21. № 3. P. 531. (1975).
21. R.H.Bassel, C.Wilkin // Phys.Rev.Lett. V. 18 p. 871 (1967).
22. R.H.Bassel, C.Wilkin // Phys.Rev.Lett. V. 174 p. 1179 (1968).
23. E.I.Ismatov, Sh.Kh.Djuraev, Sh.P.Esanniyazov, S.B.Strigina, B.K.Poluanov // Proceeding I EURASIAN Conference on Nuclear Science and its Application, vol. 2, 2000, Izmir, Turkey, p.871-878.
24. E.I.Ismatov, E.U.Turaev, Sh.Kh.Djuraev, Sh.P.Esanniyazov, B.K.Poluanov Elastic and inelastic nucleons scattering of intermediate and high energies on light cluster nuclei within the theory of multiple scattering // Abstracts of International conference on nuclear physics, 2000, Saint Petersburg, p. 455.

References II

1. V.K.Tartakovski, A.V.Furaev, V.I.Kovalchuk // Izvestiya RAN, seriya fizicheskaya, 2001, v. 65, № 5, pp. 792-797.
2. V.K.Tartakovski, A.V.Furaev, V.I.Kovalchuk // UFJ, 2001, v. 46, № 1, pp. 28-35; № 4, pp. 409-414.
3. V.K.Tartakovski, A.V.Furaev, V.I.Kovalchuk // Sbornik nauchnikh trudov, Scientific Centre «Institute for Nuclear Research» NASU, 2001, № 2(4), pp. 7-13.
4. M.V.Evlanov, A.M.Sokolov, V.K.Tartakovski // Yad.Fiz., 1996, v. 59, № 4, pp. 679-690.
5. Ye.I.Ismatov // Izvestiyta AN RU, seriya fizicheskaya, 1967, № 4, pp. 37-41.

6. Ye.I.Ismatov «Theory of diffraction nuclear processes» // Tashkent, «FAN», 1978, 178 p.
7. G.G.Arushanov, Ye.I.Ismatov «Elastic and inelastic diffraction interactions» // Tashkent, «FAN», 1988, 283 p.
8. B.S.Yuldashev, Ye.I.Ismatov, M.I.Fazylov // Doklady Akademii Nauk RU, 2002, №4.
9. Ann P et al. // Izv. RAN, seriya physicheskaya, 1993, v.57, p.127; 1994, v58 p.2
10. Lewitowicz et al.// Proc.Int School-Sem on Heavy Ion Physics, Dubna, Russia, 1993, v1, p.92.

References III

1. A.G.Sitenko, V.K.Tartakovski Teoriya yadra // Kiev, 'Libid', 2000, p.608.
2. L.B.Okun Leptons and quarks, Moscow, Nauka, 1990, p.346.
3. A.P.Kobushkin Electromagnetic form-factors of the deuteron at high transferred momenta// Yad.Fiz., 1978, v.28, ed2(8), pp. 495-509.
4. A.P.Kobushkin, V.P.Shelest Problemi reliativistskoi dinamiki kvarkov i kvarkovaya struktura deitrona // PhECHAYa, 1983, v.14, ed5, pp.1196-1192.
5. V.G.Neudachin, I.T.Obukhovski, Yu.F.Smirnov Kvarkovie konfiguratsii v legchaishikh yadrakh// PhECHAYa, 1984, v.15, ed6, pp.1165-1207.
6. V.V.Burov, V.K.Lukianov, A.I.Titov Mnogokvarkovie sistemi v yadernikh protsessakh// PhECHAYa, 1984, vol.15, ed 6, pp.1249-1295

ELASTIC NUCLEUS-NUCLEUS INTERACTION WITHIN THE DIFFRACTION THEORY OF MULTIPLE SCATTERING

B.S.Yuldashev[1)], Ye.I.Ismatov[1)], K.A.Kuterbekov[2)], Z.F.Fazylova[1)], M.I.Fazylov[1)]

[1)] Institute of Nuclear Physics, Academy of Sciences, Tashkent, Uzbekistan,
[2)] Institute of Nuclear Physics of the National Center of the Republic of Kazakhstan, Almaty

The transition from one particle scattering on nucleus to nucleus-nucleus scattering in eikonal approximation can be usually done trivially [1–6]. Similarly to the hadron-nucleus case, one can expect significant simplifications if it is assumed that nucleon distribution in nuclei is non-correlated and the weight functions $|\Phi_{A_1}|^2$ and $|\Phi_{A_2}|^2$ can be expressed in a factorized form. Averaging by one of the nuclei (to be precise by A_2 nucleus) and using the above assumptions, one can derive the elastic nucleus-nucleus scattering amplitude as follows:

$$F_{el}(q) = \frac{ik}{2\pi}\int d\vec{\rho} e^{i\vec{q}\vec{\rho}} \prod_{i=1}^{A} \rho(r_i) d\vec{r}_i [1 - (1 + \frac{x}{A_2})^{A_2} - \\ - \int \Omega_{A,N}(\rho - \tilde{s}, \{s\}) T_2(\tilde{s}) d\tilde{s}], \quad (1)$$

where the A_2 is the nucleus thickness function $T_2(\tilde{s})$ can be determined in regular way [1]

$$T_2(\tilde{s}) = A_2 \int d\tilde{z} \rho \sqrt{\tilde{s}^2 + \tilde{z}^2}\ .$$

The profile function (the interaction operator) is presented as follows:

$$\Omega_{A_1 N}(\vec{\rho} - \tilde{s}, \{s_i\}) = 1 - \prod_{i=1}^{A_1} (1 - \omega(\vec{\rho} - \tilde{s} - s_i))\ .$$

In case of nucleus-nucleus scattering the use of factorized expression for the A_2 nucleus squared absolute value of wave function allows one to simplify significantly the integration and calculations of the obtained results raised to the power of A_2. However, the further simplifications of the averaging procedure in (1) is impossible explicitly even if one assumes that $|\Psi_{A_1}|^2$ can be also presented in a factorized form. This is related to the following fact. The dependence of the averaged value of $exp_{A_1}[-\int \Omega_{A_1 N}(\vec{\rho} - \tilde{s}, \{s\}) T_2(\tilde{s}) d\tilde{s}]$ on S_i coordinate cannot be factorized. Therefore, if no another simplifying assumptions are used,

then the calculation of the amplitude $F^{el}_{A_1A_2}$ will require $3A_1$ times more numerical integration in comparison with those for hadron-nucleus scattering amplitude calculation. Therefore, in every certain case according to the physical conditions of the problem considered, the additional approximations are used. They allow us to simplify the averaging procedure of (1). In so-called zeroth approximation by the shadow effects of A_1 nucleus [1] for the nucleus-nucleus scattering amplitude one can have the following expression:

$$F^{el}_{A_1A_2}(q) = \frac{ik}{2\pi}\int d\vec{\rho}\exp(i\vec{q}\vec{b})[1- \\ -(\int \rho_{A_1}(\vec{r})d\vec{r}\exp[-\int \omega(\rho - s - \tilde{s})T_2(\tilde{s})d\tilde{s}])^{A_1}] \qquad (2)$$

Such approximation can be used to calculate the A_1A_2-scattering amplitudes of A_1 light nuclei scattering on heavy A_2 nuclei since, in this case, Born approximation terms are predominant in the amplitude of NA_2-scattering at small angles. If the Gaussian parameterization for nucleon-nucleon profile functions and the thickness approximation are used when their combinations with the thickness function of heavy target-nuclei are calculated one can simplify significantly the procedure of (1) and (2) calculation. In particular, it is possible to consider α-particle scattering on A_2 nucleus and parameterize its wave function with gaussian functions

$$|\Psi_\alpha(r_1 \ldots r_4)|^2 = \prod_{i=1}^{4}\left(\frac{\alpha}{\pi R^2}\right)^{3/2} e^{-r^2/R^2}$$

Then the amplitude of αA-scattering can be presented as follows:

$$F(q) = \frac{ik}{2\pi}\int d\vec{\rho}\, exp[i\vec{q}\vec{\rho}]\Omega(\rho) = ik\int \rho J_0(\vec{q}\rho)\Omega(\rho)d\rho \qquad (3)$$

where $\Omega(\rho) = \omega_0(\rho) + \omega_1(\rho) + \omega_2(\rho)$.

Hence, in the given range of momentum transfer $0<q<2f^{-1}$ αA-scattering amplitude calculation iteration procedure as a range expansion by the "power" of shadow effects in α-particle converges pretty fast. Also, the effects of threefold and fourfold screening are negligibly small, whereas the effects of the first screening must be taken into account in the first order only.

The possibility to use such procedure in analysis of more complex nuclei scattering on the nuclear targets requires detailed study. Apart from the slower convergence of the iteration procedure the other difficulties appear. They are related to the fact that it is impossible to parameterize with gaussian function the single particle densities of more complex nuclei than α-particle. To consider scattering of more complex nuclei on complex nuclei it is preferable to use the method of rigid incident nucleus [1,8]. It is convenient to use it because the scattering amplitude can be presented in the simple form. In case of the nucleus-nucleus scattering

problem this statement can be formulated as follows: if the scattered nucleus A_1 is very compact, then one can expect that the following expression can be a good approximation to the exact amplitude of A_1A_2-scattering:

$$F^{rigid}_{A_1A_2}(q) = \frac{ik}{2\pi}\int d\vec{\rho} e^{i\vec{q}\vec{\rho}}(1 - exp\{-\int\prod_{i=1}^{A_1} d\vec{r}_i \mid \psi_{A_1}(\vec{r}_1 \ldots \vec{r}_A)\mid^2 \Omega_{A_1N}(\vec{\rho} - \vec{s}; \{s\})T_{A_2}(\vec{s})d\vec{s}\}) \quad (4)$$

But, the $\int\prod_{i=1}^{A_1} d\vec{r}_i \mid \Psi_{A_1}(r_1 \ldots r_A)\mid^2 \Omega_{A_1N}(\vec{\rho} - \vec{s}; \{s\})$ value is the profile function of the $\Omega_{A_1N}(\vec{\rho} - \vec{s})$ NA_1–scattering amplitude. Therefore, in the rigid incident nucleus approximation, the expression of the A_1A_2-scattering is similar to that of the hadron-nucleus amplitude in the optical approximation except of one thing. The profile function of the elementary act is replaced by the A_1N-scattering profile function. This fact together with the relatively simple calculation technique makes the discussed approximation very convenient primarily for the qualitative analysis of the nucleus-nucleus scattering characteristics. The comparison of the model predictions with experimental data from the works [see 6,9,10-12] concerning the elastic α-^{12}C and α-^{40}Ca scattering at energies of 1.37 GeV as well as α-α scattering at the momenta of incident α-particle of 4.32 GeV/c and 5.07 GeV/c showed that the model describes the experimental data well and they are in good agreement with the theoretical results [7]. The dependences of the differential cross-sections on the momentum transfer and the angle are presented on the figures. For large scattering angles the model of rigid incident nucleus leads to a significant overestimation in the value of scattering cross-sections. It is not always convenient to compare the results of the range of validity of the model and its precision determination with the experiment as in many experiments the general normalization of the measured cross-sections is not defined. In case of α-nuclear scattering the very good fact allowing one to obtain such inner-self-consistent estimation of the rigid incident nucleus approximation is the possibility to approximate the nucleons distribution in α-particle with gaussian function with good precision. Therefore, for the gaussian parameterization in the wave function of α-particle the amplitude of αA-scattering in the optical approximation by the atomic number of the target-nucleus can be presented as follows:

$$F_{\alpha A}(q) = \frac{ik}{2\pi}\int d\rho\, exp(i\vec{q}\vec{\rho})[1 - < exp\{-\int d\vec{s}\,\Omega_{\alpha N}(\rho - \vec{s}, \{s\})T(\vec{s})\} >_{C.M.}] \quad (5)$$

the C.M index denotes averaging over the distribution in which the center of mass effects are not eliminated. It is also possible to average over the uncorrelated distribution.

One can show that the amplitude calculation in the rigid incident nucleus approximation may be reduced to the single integration:

$$(F_{\alpha N}(q))_i = ik[K(q)]^{i-1}\int_0^{\infty}\rho d\rho J_0(q\rho)[1-exp\,\Phi_i(\rho)] \qquad (6)$$

where K(q) and $\Phi_i(\rho)$ are defined in [3]. This model leads to sensible results for the αA-scattering cross-sections in the range of values of momentum transfer $0<q<q_{min}$ (q_{min} is the position of the first diffractional minimum of the αA-scattering cross-section). It is exactly in this range the elastic scattering cross-section dominates over the quasi-elastic cross-section and determines the value of the experimentally observed effect. The analysis of αA-scattering cross-section's sensitivity in this region to the variations of calculated physical values – the total cross-sections of NN-interaction σ_{NN}^{tot}, the ratio of the real and imaginary parts of the NN-scattering amplitude, the slope parameter ***B*** of differential scattering cross-section, which is the measure of the NN-interaction radius, and other parameters determining the value of αA-scattering slope parameter, must be conducted by the procedure not requiring a lot of integration. Besides, in the rigid incident nucleus model, it is relatively simple to estimate the role of various effects of reciprocal screening of nucleons in α-particle and the convergence rate of the iteration procedure when the amplitude is expanded in series by the power of the shadow effects. The analysis of the results discovers the following: the precision of the both approximations becomes better at transition from light to heavy target-nuclei in the whole momentum transfer region; the precision of the rigid incident nucleus approximation becomes worse with momentum transfer growth almost after the first diffractional minimum; the precision of zeroth radius approximation of the NN-interaction weakly depends on the transfer momentum, however, one can observe slight growth in precision. It is important that the accuracy of the both approximations in the region of diffractional cone is the value of the order of 20 – 30%, which significantly exceeds that of observed in the experiment.

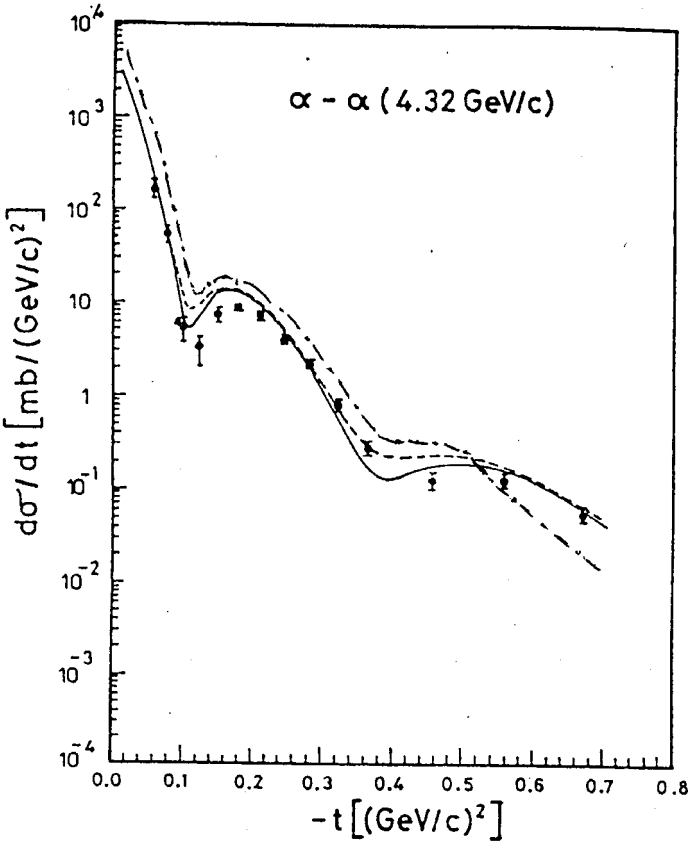


Fig. 1. Elastic differential cross-section for (α-α) reaction at incident particle momentum of 4.32 GeV/c. The dashed curve is constant phase result ($\gamma^2=0$). The solid curve is obtained with phase variation [$\gamma^2=2(\text{Gev/c})^{-2}$] [7]. The dashed-dotted curve is the result of present work. The dots are experimental data [11,12].

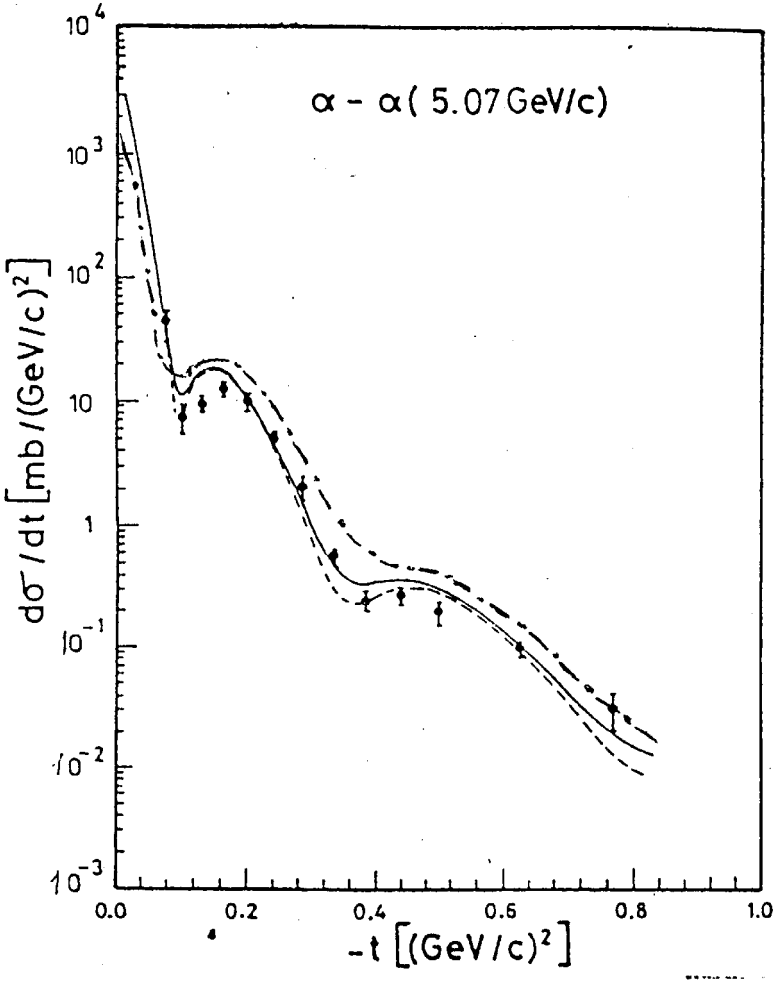


Fig. 2. Elastic differential cross-section for (α-α) reaction at incident particle momentum of 5.07 GeV/c. The dashed curve is constant phase result (γ^2=0). The solid curve is obtained with phase variation [γ^2=3(Gev/c)$^{-2}$] [7]. The dashed-dotted curve is the result of present work. The dots are experimental data [11,12].

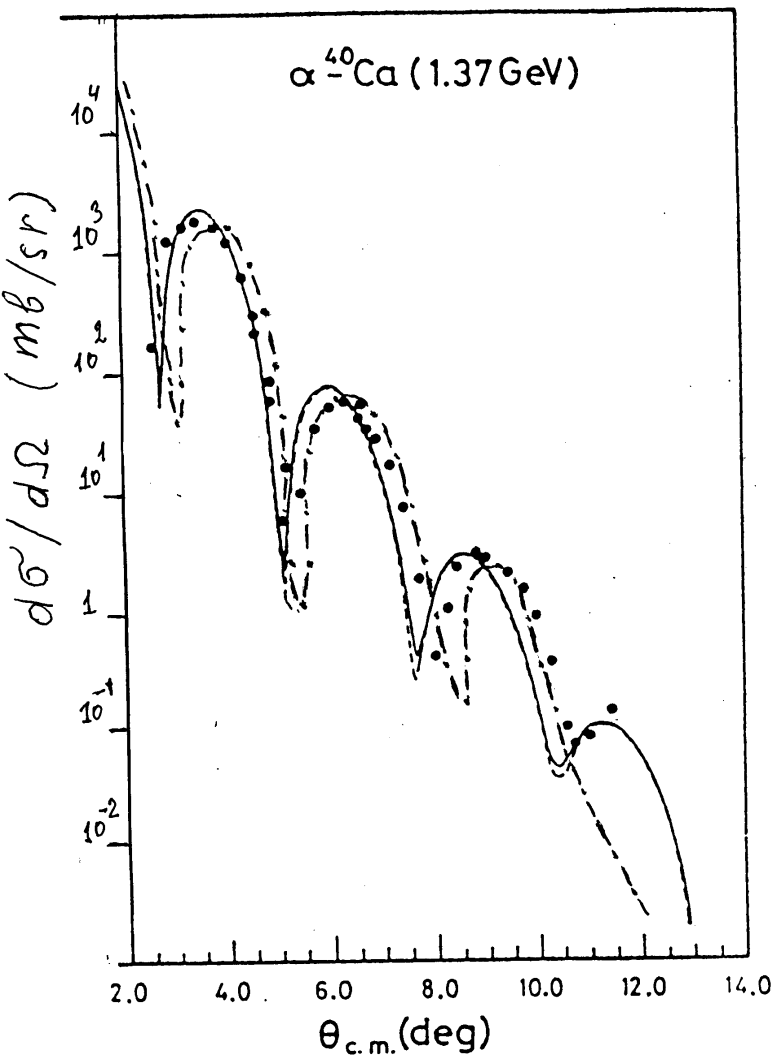


Fig 3. Elastic differential cross-section for α-^{40}Ca reaction at 1.37 GeV. The dashed curve is constant phase result (γ^2=0). The solid curve is obtained with phase variation [γ^2=-2(Gev/c)$^{-2}$] [7]. The dashed-dotted curve is the result of present work. The dots are experimental data [see 9,10].

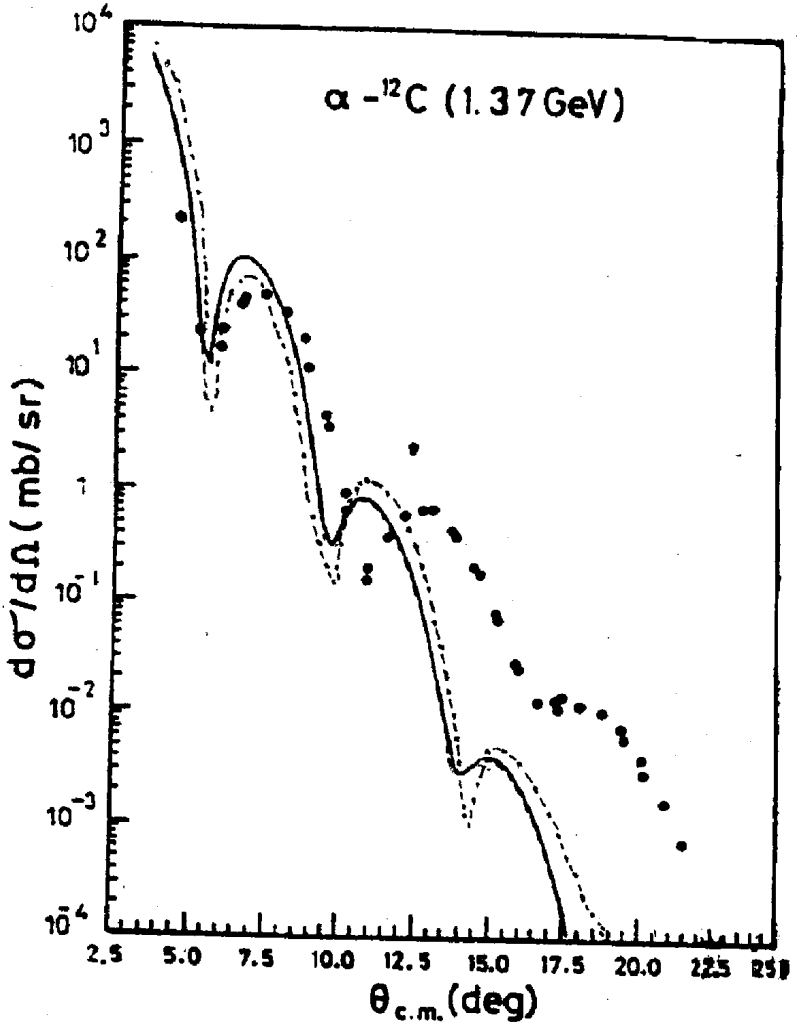


Fig 4. Elastic differential cross-section for α-^{12}C reaction at 1.37 GeV. The dashed curve is constant phase result (γ^2=0). The solid curve is obtained with phase variation [γ^2=-2(Gev/c)$^{-2}$] [7]. The dashed-dotted curve is the result of present work. The dots are experimental data [see 9,10].

References

1. A.G.Sitenko, Teoriya yadernix reaktsiy, Moscow, Energoatomizdat, 1983, p.352
2. O.G.Sitenko, V.K.Tartakovskiy, "Teoriya yadra", Kiev, 2000 'Libid'.
3. R.J.Glauber, Lectures in theoretical Phys., ed. W.E.Britten et al., Interscience, New-York, **1,** 315, 1959
4. V.Franco, R.J.Glauber /Phys.Rev. 142, 1195(1966)
5. G.G.Arushanov, Ye.I.Ismatov "Elastic and inelastic diffraction nuclear interaction" Tashkent, "FAN", 1988, p.283
6. Ye.I.Ismatov "Theory of the diffraction nuclear processes", Tashkent, "FAN", 1978
7. M.M.El-Gogary, A.S.Solaby, M.J.Hassan //Phys.Rev. 1998, V.58, p.6, 3513-3522
8. Ye.I.Ismatov, Sh.Kh.Djuraev, Sh.P.Essaniazov, S.B.Strigina, B.K.Paluanov "Proceeding of the Eurasian Conference on Nuclear Science and ITS application", Izmir, Turkey, 2000, V.2, p.871-878
9. G.D.Alhazov et al., Nucl.Phys, A280, 365(1977)
10. S.M.Lenzi, A.Vitturi and F.Zardi, Phys.Rev, **C40**, 2114, 1989
11. F.L.Fabri et al., Nucl.Phys., **A338**, 421(1980)
12. L.Satta et al., Phys.Lett., **139B**, 263(1984)

ELASTIC SCATTERING OF PROTONS ON ^{8}Li NUCLEUS IN INVERSE KINEMATICS

M.A. Zhusupov, E.T. Ibraeva, O. Imambekov[*]*, A.B. Sanfirova*

Institute Nuclear Physics NNC RK, Almaty, Kazakhstan
Al-Farabi Kazakh State National University, Almaty, Kazakhstan

Within the framework of Glauber-Sitenko diffraction theory, the differential cross section of proton elastic scattering on ^{8}Li nucleus has been calculated in inverse kinematics at energies of E_{8Li}=0.2 and 1 GeV/nucleon. The nuclear wave function has been used in αtn-model. Sensitivity of the calculated characteristics to model wave functions and to the contribution of double scattering in Ω operator has been analyzed. A comparison with differential cross sections of proton scattering on other Li isotopes has been carried out.

Progress in accelerating facilities and possibility of radioactive nuclei acceleration have given the new prospect for investigation in nuclear physics both in the investigation of nuclear structure and studying the nuclear reaction mechanism. Recently, the investigation of exotic nuclei (proton- and neutron- rich nuclei) such light elements as Li, Be, B is of the increased interest. The reason for it lies in the fact that we can observe the following unknown effects: irregularities of proton and neutron densities (halo), the new deformation regions and new types of the collective excitations at low energies (the soft dipole resonance), irregularities in the shell filling.

At small and intermediate energies the different spectroscopic data (halo and core radii, binding energy, width of energy levels) and numerical information about spatial matter distribution in nuclei can be obtained from the experiments for radioactive nuclei scattering on stable target correspondingly.

Theoretical studying the mentioned processes is realized within the framework of Glauber multiply scattering theory which allows to describe with high accuracy proton-nuclear scattering and to extract information from the measured magnitudes. In the present paper the proton elastic scattering on ^{8}Li in inverse kinematics is studied. The inverse kinematics means that a beam of radioactive nuclei is scattered on a stable hydrogen target. Proton as a target has an advantage during the interaction since it is stable and mechanism of proton-nucleus scattering is quite simple.

The ^{8}Li nucleus chosen is interest of both as one neutron halo nuclei and for nuclear astrophysics. It has been synthesised in the ^{7}Li(n,γ)^{8}Li reaction after inhomogeneous Big Bang. Our imagination of the Universe evolution can change in dependence of this reaction rate.

The up-date wave functions (WF) of ^{8}Li are calculated in three-body αtn-models with the realistic potentials of intercluster interactions. The spectrum of low lying nuclear levels is studied and one stresses the importance of low lying resonance determination for understanding the reaction mechanism of radioactive capture [1].

The effect of ^{7}Li strong deformation and dynamical core polarisation and its excitation are considered together [2]. The wave function of this nucleus has been calculated in the work [3] where it was shown that such a model well describes the main spectroscopic characteristics of the nucleus: root-mean square radius, binding energy, locations of low lying energy levels, magnetic momentum and also total cross section and the ^{7}Li(n,γ)^{8}Li reaction rate at a wide energy region. This wave function has been used in our paper.

Within the Glauber-Sitenko multiply scattering theory, the differential cross section of elastic p^{8}Li- scattering has been calculated. The first and the second multiplicities of scattering on nucleons and clusters of the nucleus were taking into account in Ω multiply scattering operator. Sensitivity of the differential cross section both to the different wave functions of the target-nucleus and to the parameters of the elementary amplitudes and sensitivity to the scattering multiplicities at several beam energies has been investigated. Comparison with the differential cross sections of elastic p^{6}Li- and p^{7}Li scattering has been carried out.

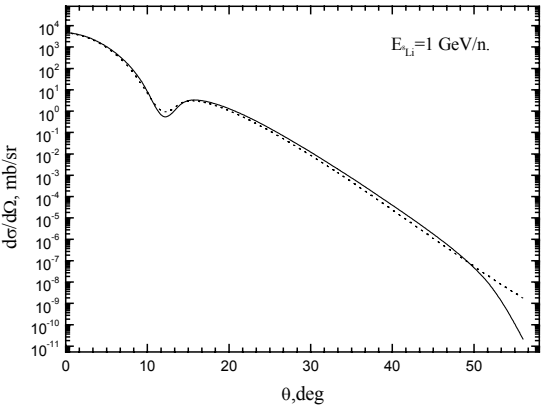


Fig.1. DCS of proton elastic scattering on ^{8}Li nucleus in dependence on different WF: solid curve is a calculation with the WF in model 1, dot curve is in the model 2.

Dependence of DCS on the ^{8}Li various model WF calculated with the different potentials of intercluster interaction is shown in fig.1. For both models αn- and tn-potentials were taken in the Gauss form and they were splitted by parity of orbital momentum. The difference of these models are in the αt-potential: in model 1, it is the Gauss one in Buck form which well describes binding energy and the ^{7}Li spectroscopic characteristics; in model 2, it is a standard potential in Wood-Saxon form. These potentials contain the spin-orbital splitting and they adjust low energy dependence of elastic scattering phases. Both curves (dot and dash curves in the models 1 and 2

correspondingly) coincides that is the WF calculated with both different potentials are similar.

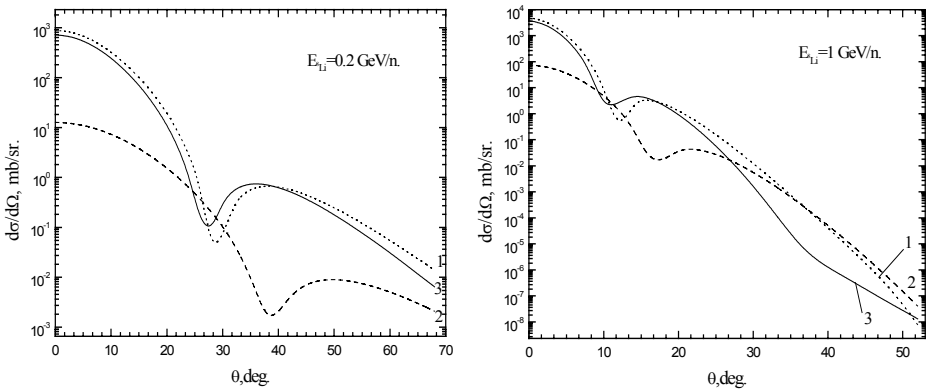


Fig.2. Contribution of different scattering multiplicities to DCS at the following energies: *a*-E_{8Li}=0.2 and *b*-E_{8Li}=1 GeV/nucleon. Curves 1,2,3 are calculation of single, double scattering and their sum correspondingly.

In fig.2, the contributions of different scattering multiplicities into DCS are shown at the following energies of ^{8}Li nucleus: E=0.2 (*a*) and 1 GeV/n (*b*). In case of proton interaction with α- and t- clusters and valence nucleon, the Ω Glauber multiple scattering operator may be written as:

$$\Omega_{^8Li} = \Omega_\alpha + \Omega_t + \Omega_n - \Omega_\alpha\Omega_t - \Omega_\alpha\Omega_n - \Omega_t\Omega_n + \Omega_\alpha\Omega_t\Omega_n . \qquad (1)$$

Curve 1 stands for single scattering (that is approximation of optical limit), i. e. DCS is computed with the first three terms of formula (1). Curve 2 stands for double scattering (DCS calculation with the following three terms of formula (1)). Curve 3 stands for their sum. The thrice scattering, the last term of formula (1), is not taken into account since its contribution is by about several factors of ten smaller even than double scattering contribution [4]. It is shown in fig. *b* that rescattering contribution is not significant at small scattering angles ($\theta<10^0$), but as curve 2 falls down much slower than curve 1, their contribution into the total cross section appears in the region of curve 1 minimum and large scattering angles ($\theta>30^0$).

In fig.3, there is shown more detailed contribution of various terms to the single scattering DCS. Curve 1 stands for contribution of the (α+t) clusters, curve 2 stands for the neutron contribution, curve 3 stands for their sum (this curve is similar to curve 1 in fig.2*b*). Not having interpreted this result as scattering on core and halo, one points out the following: the contribution of scattering on (α+t)

clusters is by one order greater than the calculation of scattering on nucleon. It may be explained by a significant deference of the total cross sections in case of the pα- and pn- elementary collisions (σ_{tot}=12.7 fm^2, σ_{pn}=4.4 fm^2 [5]) which determine DCS value at zero scattering angle (optical theorem). The conclusion of that the core size is more important for DCS description than halo one has been formulated. Such a conclusion has been made in the work [6] during the discussion of various reaction mechanisms with halo nuclei and a new information derived from the measured characteristics. The approval of core size importance has been confirmed by our calculations.

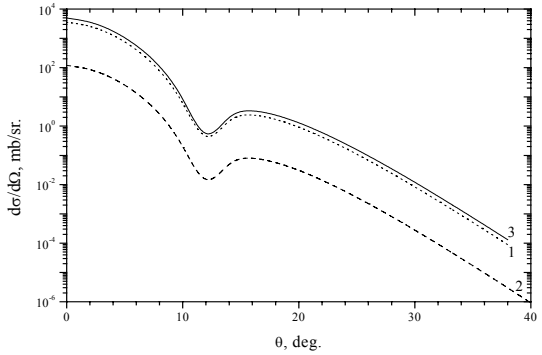


Fig.3. DCS at energy of E=1 GeV/nucleon. Curves 1,2,3 are scattering on (α+t) cluster, neutron and their sum correspondingly.

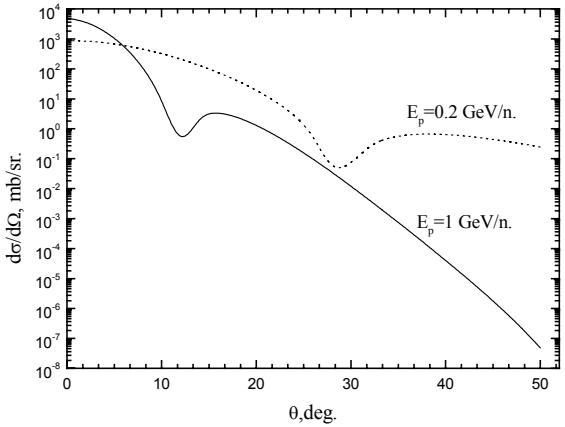


Fig.4. DCS of elastic scattering at various energies of the incident beam: solid curve stands for E_{8Li} =1 GeV/nucleon, dot curve stands for E_{8Li}=0.2 GeV/nucleon.

Fig.4 shows DCS dependence on energy of the incident nucleus and it demonstrates the following regularities: as energy increases, the diffraction minimum shifts to the region of smaller scattering angles and for $\theta=0^0$ cross section absolute slightly rises. According to the optical theorem, cross section at zero angle is determined by value of σ_{tot} and the latter increases as energy goes up.

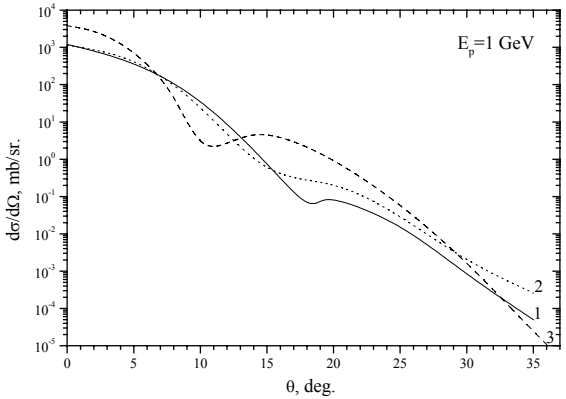


Fig.5. DCS of proton elastic scattering on the Li isotopes at energy of E=1 GeV. Curves 1,2,3 correspond to scattering on ^{6}Li, ^{7}Li and ^{8}Li nuclei.

In fig.5, there are shown DCS for scattering on Li isotopes at energy of E=1 GeV. Calculation of DCS on the ^{6}Li (WF in αnp-model) and ^{7}Li (WF in αt-model) nuclei is taken from the work [4]. There is the following regularity in behavior of DCS: as A (nucleon number) rises, the diffraction minimum shifts to the region of small scattering angles (it is localized at $\theta\sim18^0$, 15^0 and 11^0 for ^{6}Li, ^{7}Li and ^{8}Li nuclei correspondingly) and it appears more for nuclei A=6 and 8 and less for nuclei with A=7.

The first effect is evident.: as a number of nucleons goes up, the scattering multiplicities increases and the minimum (caused by the interference of different scattering multiplicities) shifts into the region of small scattering angles. This regularity is properly seen in the all papers beginning from Glauber [7]. The second effect is connected with deformation of nuclei (it is numerically determined by quadrupole momentum): as the nucleus is deformed more, the diffraction minimum fills up higher. Since the ^{7}Li quadrupole momentum is maximum (Q=4.0 fm^2), therefore its cross section does not have the sharply determined minimum and it has a bend. The minimum is filled up by quadrupole component contribution.

References

1. Csoto A. // arxiv: nucl-th/9908081. 1999. V2. P.1.
2. Grigorenko L.V., Danilin B. V. // Phys. ReV. C. 1998. V. 57. № 5. P. 1.
3. Zhusupov M.A., Sagindukov Sh. Sh., Sahiev S.K. // Izv. Rus.Acad. Science. Ser.fiz. 2001. V.65. №5. P.714.
4. Shusupov M.A., Ibraeva E.T. // EPAN. 2001. V. 31. P. 1427.
5. Ibraeva E.T., Sanfirova A.B., Prmantaeva B. // Dep. KazGosINTI № 8599-Ka99. 1999. P. 17.
6. Zhukov M., Parfenova Yu., Vaagen J.S. // Yad.Fiz. 2002. V.65. №4. P.779.
7. Глаубер Р.Г.// UFN. 1971. V. 103. №4. P. 641.

ENERGY DEPENDENCE OF MACROSCOPIC AND SEMI-MICROSCOPIC POTENTIAL PARAMETERS FOR ALPHA-PARTICLES IN THE RANGE OF ENERGIES 20 - 80 MeV

[1]K.A. Kuterbekov, [1]T.K. Zholdybayev, [1]B.M. Sadykov, [1]A. Mukhambetzhan
[2]Yu. E. Penionzhkevich, [2]I.N. Kukhtina

[1]Institute of Nuclear Physics of National Nuclear Center RK, 480082, Almaty, Kazakhstan
[2]Joint Institute for Nuclear Research, Dubna, Moscow region, Russia

Global energy dependences of optical potential for α-particles with energies up to 80 MeV have been received. A Woods-Saxon form-factor for macroscopic potential has been used and recommendations from works of M. Nolte, H. Machner, J. Bojowald about global dependences at energies higher than 80 MeV and L.W. Put and A.M.J. Paans about geometry of optical potential have been taken into account. Energy dependence of the semi-microscopic α-particle potential parameters have been investigated for the first time. In general, a good description of elastic and inelastic differential and total reaction cross sections for different nuclei using the revealed global parameters has been received within the framework of macroscopic and semi-microscopic approaches.

1. Introduction

Macroscopic and semi-microscopic analyses of angular distributions of differential cross sections (ADDS) for α-particle scatterings are the important source of information about matter distribution in nuclides and properties of the potential of nucleus-nucleus interaction.

Optical potential (OP) parameters of α-particle interaction with nuclei at low and intermediate energies received from the analysis of ADDS of elastic scattering within the framework of optical model (OM) are exposed to considerable ambiguities and require reliable estimations [1, 2]. It is very important for receiving of detailed information about nuclear structure (parameters of deformation lengths, ratio of neutron and proton components, etc.) in the framework of up-to-date potential approaches (OM, methods of coupled channels and distorted waves). Global optical potential on the basis of data on elastic scattering of ^{90}Zr has been received in the work [3] for α-particles at energy above 80 MeV. At that the recommendations about parameter geometry OP and its dependencies upon energy received by Put and Paans has been used [4]. Up to present time there were no successful global potentials because of increase of strong absorption with energy up to 80 MeV. Effects of strong absorption lead to two types of OP ambiguities. It is discrete ambiguities often shown through depth

value of real part of potential corresponding to changes necessary for conditions of phase equivalence [5]. Continuous ambiguities forming potential family characterized by equal behavior near nuclear surface exists for each of discrete parameter number. Pointed ambiguities of OP need a search of physical situations that could restrict them.

Differential and total reaction cross sections with energy above 80 MeV for nuclei from A=12 – 124 have been calculated and their systematic analysis has been carried out firstly within the framework of the double folding model [6] on the basis of full M3Y-effective interaction and nucleon densities calculated for all collided nuclei by the method of density functional.

Inclusion in analysis together with ADDS of elastic scattering and values of total reaction cross sections allows limiting ambiguities of OP parameters since data on differential and total reaction cross sections are the main nuclear values received from OM. Theoretical model pretended to full description of data must render both experimental ADDS and total reaction cross sections with the same number of entering parameters. Nowadays there are not many works where analysis has two these values simultaneously in one model. Choice of optimal parameters of macroscopic OP and folding model [6] further allows receiving reliable information about structure of excited state of investigated nuclear.

This work firstly proposes the global energy dependence of parameters of macroscopic OM and semi-microscopic folding model (SFM) for α-particles in weakly studied energy range.

2. Experimental data for global analysis

We selected and compiled the initial experimental material including results of our work [7-13] and literature sources for building of desired global dependence of potential parameters of α-particle interaction.

The main characteristics of experimental conditions when ADDS have been received are shown in table 1. Information published in corresponding works [4, 7-10, 11] are shown for literature data.

Experimental ADDS from works [10,12,13] including into analysis have been received at isochronous cyclotron U-150M using the registration system and identification of reaction products on the complex base CAMAC-PC/AT [14].

Table 1. Main characteristics of the experiment on elastic scattering of α-particles

Nuc-leus	E_α, MeV	Target		Angular diapason (deg., c.m.)	Reference
		thickness (mg/cm^2)	Composition (%)		
For energy dependence					
^{90}Zr	21.0	0. 730	97.0	48-177	[7]
^{90}Zr	23.4	0. 730	97.0	48-177	[7]
^{90}Zr	25.0	0. 730	97.0	48-177	[7]
^{90}Zr	31.0	1.0	98.0	10-98	[8]
^{90}Zr	35.4 35.4	0.520 0.855	97.65 97.67	10-100 6-47	[9]
^{90}Zr	40.0±0.2 40.0±0.5	0.84-2.47 2.13±0.08	97.6 95.0	5-175 10-70	[4] [10]
^{90}Zr	50.1±0.5	2.13±0.08	95.0	15-80	[10]
^{90}Zr	59.1±0.3	0.84 –2.47	97.6	5-175	[4]
^{90}Zr	65.0	5.0-8.5	95.0	10-76	[11]
^{90}Zr	79.5±0.4	0.84 –2.47	97.6	5-175	[4]
^{90}Zr	99.5±0.5	0.84 –2.47	97.6	5-175	[4]

3. Data analysis and global dependence of potential parameters

3.1. Macroscopic optical model analysis

Complex optical potential $U(\vec{r})$ with Woods-Saxon form-factor for real and imaginary parts in the case of α-particles scattering has a standard form:

$$U(\vec{r}) = V(1+\exp\frac{r-R_V}{a_V})^{-1} + iW(1+\exp\frac{r-R_W}{a_W})^{-1} + V_C(r)\,. \qquad (1)$$

In this formalities OP is characterized by six parameters: depths of real V and imaginary W of particles, their corresponding to radial parameters R_v and R_w and diffuseness parameters a_v and a_w at the nucleus periphery. $V_c(r)$ corresponds to Coulomb potential of uniformly charged sphere with radius $R_c=1.25\,A^{1/3}$ fm.

Experimental ADDS of elastic scattering of α-particles in present work were analyzed within the framework of deformed OM potential using code SPI-GENOA [15]. Potential parameters met to optimal correspondence of experimental and theoretical cross section values were found by minimization of the following value

$$\chi^2 = \frac{1}{N}\sum_{i=1}^{N}[\frac{\sigma^T(\theta_i)-\sigma^E(\theta_i)}{\Delta\sigma^E(\theta_i)}]^2\,, \qquad (2)$$

where N- number of experimental points in angular distribution, σ^{T} and σ^{E}- calculated and measured value of differential cross section of scattering at angle of θ_i, and $\Delta\sigma^{E}$- value uncertainty $\sigma^{E}(\theta_i)$.

Optimal OP parameters were selected in such way, in order to reach the best agreement within the framework of joint analysis ADDS scattering and data on total reaction cross sections, description of "transparency effect" [7,16] for nuclei with A=90 and tendency of value change of volume integral J_R^P from real part [2].

In concluding part of the present work the optimal OP parameters received by us keeping above mentioned criterions were described using the following expressions for all six OP parameters:

$$V(A,Z,E_\alpha)=a_0+a_1ZA^{-1/3}+a_2E_\alpha\ ,\quad W(A,Z,E_\alpha)=b_0+b_1A^{1/3}+b_2E_\alpha\ , \tag{3}$$

$$r_V=c_0+c_1A^{1/3}+c_2E_\alpha\ ,\quad r_W=d_0+d_1A^{1/3}+d_2E_\alpha\ , \tag{4}$$

$$a_V=e_0+e_1A^{1/3}+e_2E_\alpha\ ,\quad a_W=f_0+f_1A^{1/3}+f_2E_\alpha\ . \tag{5}$$

We can note that expressions (3) for depth dependence of real and imaginary part of OP are similar to the part which was received by Nolte and Machner [3] for α-particles with energy above 80 MeV and F.G. Perey [17] for nucleons. Term which is proportional to $Z/A^{1/3}$ was adopted by F.G. Perey [17] for effect calculation appeared due to Coulomb repulsion: average coulomb potential on nuclear surface is proportional to Z/R and, correspondingly, to the value $Z/A^{1/3}$. A linear dependence from nucleus radius and energy E_α of incident particles was adopted for the depth of imaginary part of potential in the case of α- particles.

3.1.1. Energy dependence

The analysis of 12 experimental ADDS of elastic scattering of α-particles with energies from 21 to 99.5 MeV at nucleus ^{90}Zr was carried out in order to build energy constituent of global dependence of parameters OP with energy below 80 MeV. Taking into consideration the fact, that global dependence of OP with energy above 80 MeV is built on the basis of data for ^{90}Zr in work [3], the choice of the investigation object is very successful what increases essentially the value of this work in which the community of approach is kept (and possibility of result unification) at global dependence building with energy below and above 80 MeV.

We found optimal values of OP for each ADDS at different energies using recommendations from [3,4] for search of energy dependence of OP parameters of α-nuclear interaction. We began the analysis of data family from 12 ADDS from energy of α-particles 99.5 – 79.5 MeV (above 80 MeV) in order to provide overlap in energy diapason with works [3,4]**.** The values recommended in [3] are adopted as starting parameters of OP. One can note that the less energy of incident α-particles the worse parameters OP from [3] describe experimental ADDS (depending upon E_α) with decrease of energy of incident α-particles (below 80

MeV). It was found in work [4] that geometry of optical potential for ^{90}Zr is almost constant at α-particles energy above 80 MeV (effect of Put – Paans). However, it becomes reliant on E_α with more low energies. We have studied energy dependence of geometric parameters OP with energies of α-particles below 80 MeV. Because of discrete ambiguity of OP the one of main difficulties at building of such dependencies is mutual parameter influence on each other (V and R_v, W и R_w: increase of one parameter results in decrease of another). For liquidation of such ambiguities we used recommendations of Hodgson and others [18].

We applied the method of two-phase adjustment of OP parameters: firstly we varied depth values V, W and diffuseness parameters a_v, a_w, and then values of OP radii r_v , r_w. A number of partial waves we took into account reached 35-75 depending on mass of nucleus-target and energy of α-particles. Optimal values of OP parameters received in present work are shown in table 2. Then the independent selection of "physically" significant potentials was carried out: one of such possibilities is use as value criterion of volume integral from real part OP which sharply changes its values at transition from one family to another because of discrete ambiguity. It is set [2] that value of volume integral J_R^P , related to a number of interacted nucleon pares i.e. $J_R^P = J_R / 4A$ is value of the same order for different types of charged particles and there are potential families with the same value J_R^P ~(330-370) MeV•fm^3 for protons, deuterons, ^{3}He-ions and α-particles scattered at the same nuclei. Holding this point of view, we were choosing OP parameters according to change tendency J_R^P [4]: its value must change weakly with energy E_α.

Table 2. Optimal values of parameters OP for α-particles at nucleus ^{90}Zr .

E_α, MeV	**V**, MeV	r_v, fm	a_v, fm	**W**, MeV	r_w, fm	a_w, MeV	χ^2/N	$J_R/4A$, MeV•fm^3
21	272.52	1.245	0.582	15.426	1.570	0.316	3.74	609
23.4	161.08	1,245	0.649	11.458	1.570	0.452	3.82	368
25	159.48	1.245	0.648	10.884	1.569	0.583	2.80	365
31	196.86	1,248	0.707	22.272	1.571	0.501	3.41	464
35.4	144.97	1.246	0.757	19.361	1.574	0.577	5.26	347
40	145.16	1.245	0.729	12.983	1.624	0.819	24.48	343
50.1	144.99	1,245	0.760	14.504	1,567	0.583	28.06	347
59.1	144.13	1.245	0.805	18.550	1.570	0.510	6.49	351
65	143.73	1.247	0.827	22.231	1.572	0.632	5.92	355
79.5	140.58	1.245	0.857	19.437	1.570	0.692	8.25	350
99.5	134.31	1.244	0.832	20.714	1.570	0.636	8.82	330

Fig. 1 presents the analysis results of ADDS of α-particle elastic scattering for various energies at ^{90}Zr at optimal values of obtained OP parameters. One can see good correspondence with experimental data in wide angular range.

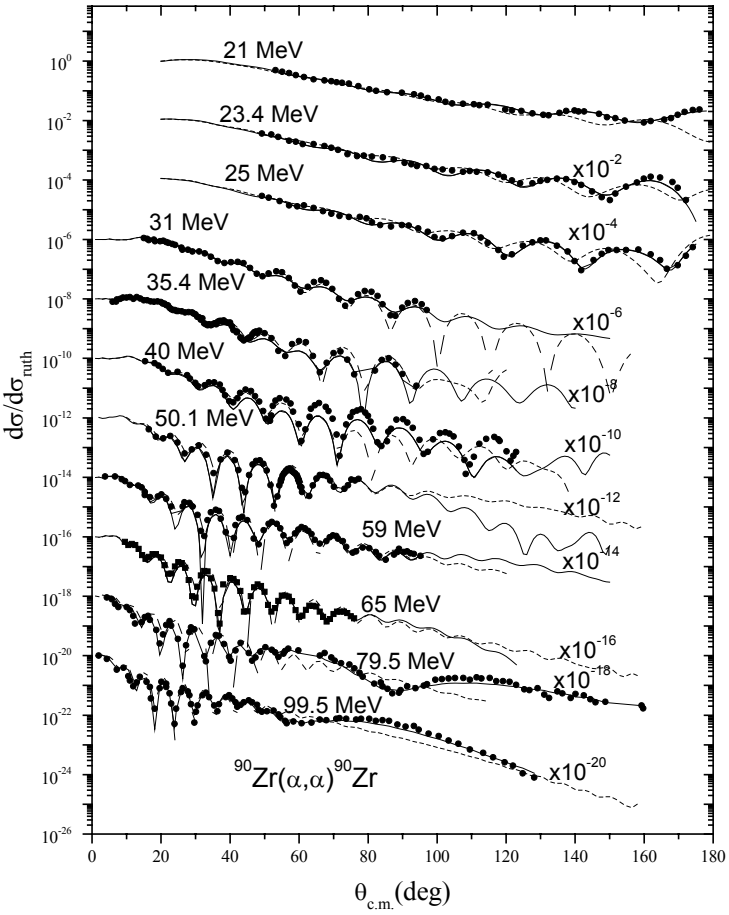


Fig. 1. Angular distributions of differential cross sections of elastic scattering for α–particles at ^{90}Zr. Points – experimental data, solid lines – macroscopic OM, dash lines – semi-microscopic folding-model.

We also tested other variants of adjustments (namely: firstly variation of V and W depth at other fixed parameters; secondly, changing radial parameters

with fixed depths and diffusenesses and then changing diffusenesses with fixation of the rest OP parameters and, finally, leaving all 6 OP parameters simultaneously). But as a result of these actions there were large scattering values and it was not possible to obtain any dependencies, so the method of adjustments mentioned above is more acceptable.

We used values of total reaction cross sections σ_R with energies of α-particles up to 80 MeV as an additional criterion for selection of optimal OP parameters that are calculated using the code SPI-GENOA [15]. The figure 2 shows that received calculated values σ_R at nucleus ^{90}Zr at optimal and global parameters OP reproduce the measured values of total reaction cross section and tendency of their change with increase of α-particles energy what confirms the reality of theoretical cross sections calculated using the approach described above.

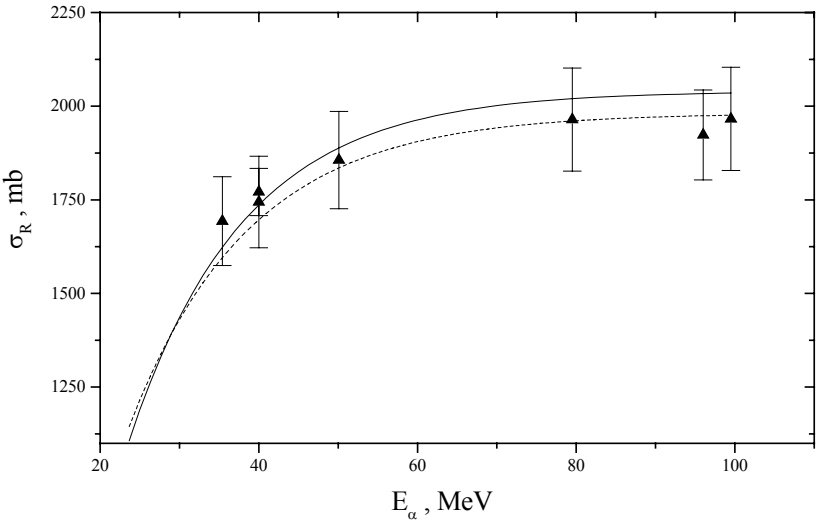


Fig. 2. Total reaction cross sections for α-particles at nucleus ^{90}Zr. Experimental data (open triangles) are taken from [10] and other published sources. Theoretical values of total reaction cross sections are shown for macroscopic OP by solid line, for semi-microscopic model by dash line.

We investigated possibilities for "transparency effect" description for nuclei with A=90 [7,16] using the received global parameters. A pronounced minimum at energy ~ 23 MeV [7,16] is observed in excitation function at

scattering of α-particles at nucleus ^{90}Zr at angle of 176^0 in c.m. Figure 3 presents a satisfactory description of indicated effect on an example of ^{90}Zr using received global OP parameters.

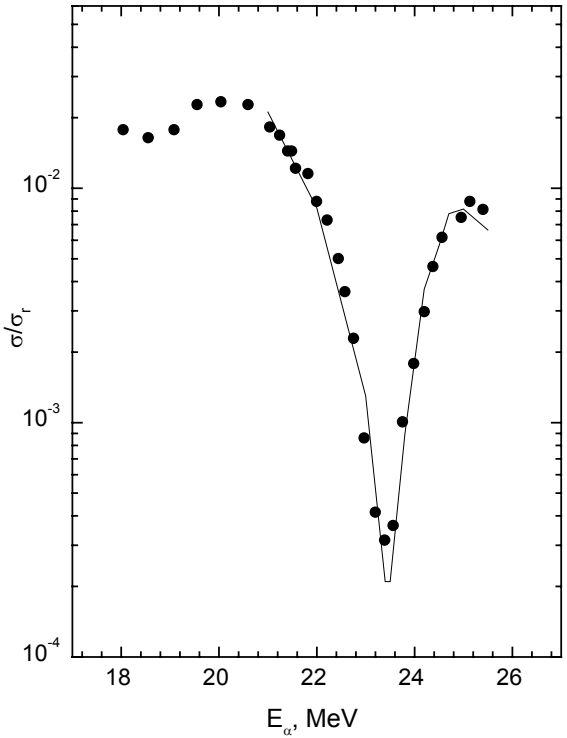


Fig.3. "Transparency" effect at ^{90}Zr with energies of α-particles 18 - 26 MeV. Experimental data - points [7] and theoretical values on macroscopic OM- solid curve.

After selection by the method of the least squares the linear dependencies of OP parameters from E_α (firm lines at fig.4) were received in the following form:

$$V=160.229-0.260\bullet E_\alpha\,,\ W=8.109+0.138\bullet E_\alpha\,, \quad (6)$$

$$a_v=0.621+0.0026\bullet E_\alpha\,,\ a_w=0.544+0.0012\bullet E_\alpha\,, \quad (7)$$

where values V, W, E_α are in MeV, and diffuseness parameters a_v and a_w – in fm. Radial parameters r_v and r_w showed weak change with energy E_α: r_v =1.2456±0.0004 fm и r_w =1.5704±0.0018 fm. For comparison dash lines on Fig. 4 present global dependencies at energies $E_\alpha > 80$ MeV from [3].

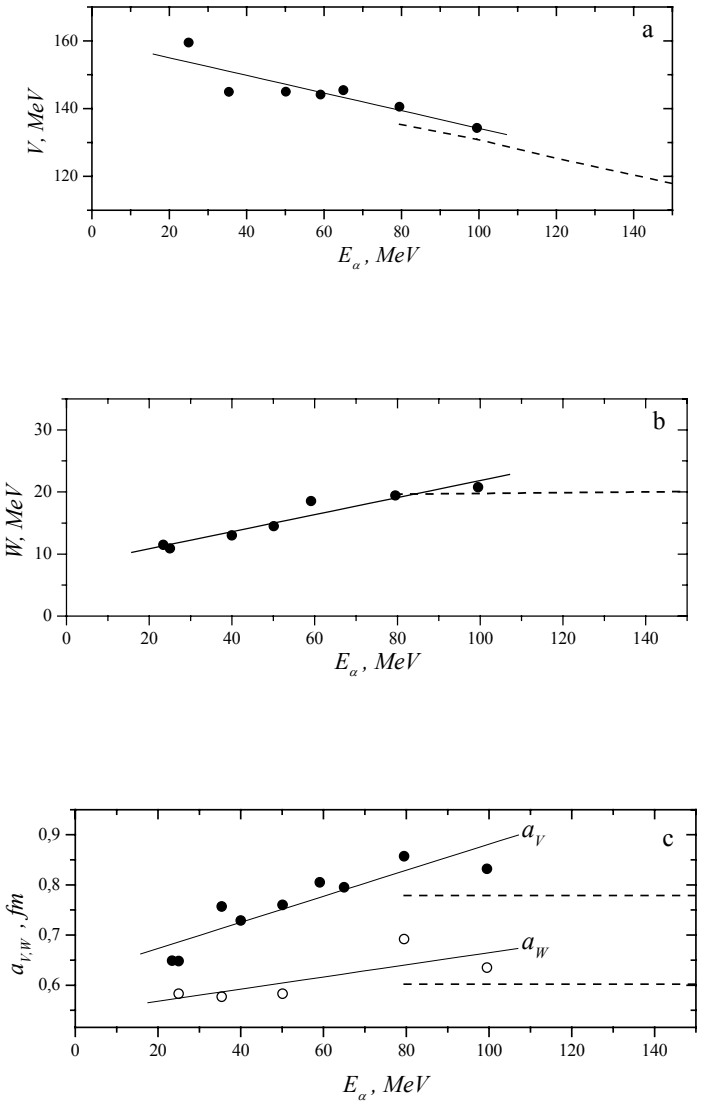


Fig. 4. Energy dependence of macroscopic OP-parameters: a – depth of real part; b – depth of imaginary part; c - radii r_v and r_w; d - diffusenesses a_v and a_w. Solid lines – global dependencies received in the present work; dash lines – in [3].

3.2. Global semi-microscopic data analysis

Semi-microscopic optical potential $U(R)$ is built within the framework of folding-model on the basis of full M3Y-effective interaction and nucleon densities calculated under the method of density matrix functional [6]. Interaction potential of two collided nuclei in the first order on effective forces can be presented as:

$$U(R) = U^E(R) + U^D(R), \tag{8}$$

where $U^D(R)$ – "direct" potential of double folding model [1]:

$$U^D(R) = \iint \rho^{(1)}(r_1) V^D(s)\ \rho^{(2)}(r_2) dr_1\, dr_2\,. \tag{9}$$

The term $V^D(s)$ in expression (8) is a direct component of effective interaction ($s = r_2 - r_1 + R$), $\rho^{(i)}(r_i)$ are densities of collided nuclei (i =1, 2). Such calculation scheme of "exchange" potential $U^E(R)$ is described in [6]. The effects of one-nuclide exchange, which are described in formality of density matrix [19] give the main contribution in it:

$$U^{EX}(R) = \iint \rho^{(1)}(r_1, r_1 + s) V_{EX}(s)\ \rho^{(2)}(r_2, r_2 - s) \exp(ik(R)\, s/\eta)\, dr_1\, dr_2\,, \tag{10}$$

where $V_{EX}(s)$ – exchange part of effective nucleon-nucleon forces, $\rho^{(i)}(r, r')$, $(i=1, 2)$ – density matrix of collided nuclei with mass numbers A_1 and A_2, $k(R)$ – local impulse of relative movement of nuclei determined by the ratio

$$k^2(R) = (2m\eta/h^2)[E - U(R) - V_c(R)]. \tag{11}$$

Here $\eta = A_1 A_2 / (A_1 + A_2)$, $s = r_2 - r_1 + R$, E – energy in the center-of-mass system of and $V_c(R)$ – Coulomb potential. Thus, net potential depends upon energy because of effects of one-nucleon exchange. Initial data for calculation of potentials are effective nucleon-nucleon forces and proton and neutron densities of collided nuclei.

Full optical potential SFM besides real part should include the imaginary part responsible for incident particle absorption in inelastic channels. In our case we built potential of absorption depended on calculated real part in the form [20]:

$$W(R) = i\,[N_w U(R) - \varphi_w\, R\, dU(R)/dR], \tag{12}$$

where $U(R)$ – potential of double folding (8) and N_w and φ_w – parameters that characterize volume and surface parts of absorption potential, correspondingly. A surface term imitating the contribution of dynamic polarized potential is introduced in the real part of the potential [21]. Full optical potential SFM has the following form:

$$U_t(R) = U(R) - \varphi_v\, dU(R)/dR + i\,[N_w U(R) - \varphi_w\, dU(R)/dR], \tag{13}$$

where φ_v, N_w, φ_w are varying parameters.

At calculation of ADDS of inelastic scattering the form-factor of inelastic transition has a form $\varphi_L \dfrac{dU_t(R)}{dR}$ [22].

In frameworks of SFM we have carried out global (energy and mass) analysis of the same experimental data (as well as at investigation a macroscopic OM) in explored region of α-particles energies for the nuclei with A=12-124.

Theoretical cross sections of elastic scattering are calculated under the modified version of the program ECIS-88 [23] (ECIS-PM), in which semimicroscopic potentials are constructed as in the formula (13). The adjustment theoretical ADDS of elastic scattering and values σ_R to experimental data was carried out by a variation of parameters φ_v , N_w, φ_w. One should mention that at the joint analysis of differential and total reaction cross sections the SFM parameters are determined uniquely.

In the present work the nucleon densities for α-particles were calculated in Gaussian representation with root-mean-square radius 1.57 fm [3], and for nucleus - targets the densities were calculated by the density-functional method [19].

In fig. 1 and 2 (dashed lines) the results of calculations ADDS for elastic scattering and total reaction cross sections on SFM on the ^{90}Zr nucleus at energies of α-particles 21- 99.5 MeV are presented. Good agreement of theoretical calculations with experimental data is obtained. The optimum values of the obtained SFM parameters are presented in the table 3; errors are 1%. Tendencies of the SFM parameters change with energy E_α are presented in fig. 5.

Table 3. Parameters of semimicroscopic potential of α-particles interaction, volume integrals J_V in ($\bullet 10^3$ MeV$\bullet$fm^3) and root-mean-square radii r_{sfm} in fm for folding potentials on ^{90}Zr at different energies of α-particles.

E_α, MeV	φ_v	N_W	φ_w	J_V	$<r^2_{sfm}>^{1/2}$
21	0.010	0.10	0.010	-129.3	4.989
23.4	0.020	0.10	0.010	-128.7	4.990
25	0.020	0.10	0.010	-128.4	4.990
31	0.017	0.18	0	-127.3	4.990
35.4	0.050	0.10	0	-126.5	4.991
40	0.045	0.12	0.012	-125.7	4.992
50.1	0.052	0.11	0.010	-123.9	4.993
59.1	0	0.25	0.015	-122.3	4.994
65	0	0.18	0.025	-121.3	4.994
79.5	0	0.26	0.030	-118.9	4.996
99.5	-0.020	0.35	0.032	-115.7	4.999

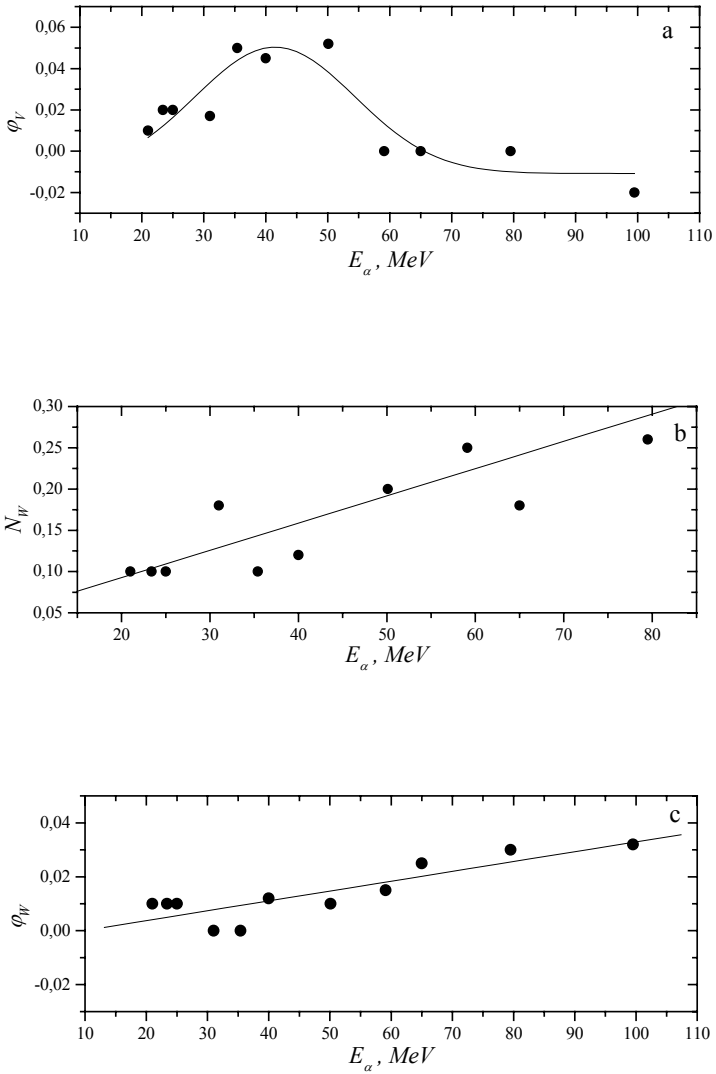


Fig. 5. Energy dependence for parameters of SFM potential: points - optimum values, solid lines – approximation a) by the Gaussian dependence for the parameter φ_v ; b), c) by a linear dependence for the parameters N_W and φ_w .

From Tab. 3 one can see that φ_v parameter increases with energy increase of scattering α-particles in energy range up to 50 MeV, further its value is equal to 0 and, further, becomes negative at energy 99.5 MeV. The N_W parameter increase slowly with energy. The φ_w parameter decreases to 0 at energy 31 and 34.5 MeV, and further increases for 1.6 times at energies 40-99.5 MeV. Due to non-linearity of φ_v -parameter we have described it with Gaussian dependence from E_α (see fig. 5a):

$$\varphi_v = -0.0108 + 0.0612 \bullet exp(-0.003 \bullet (E_\alpha - 41.485)^2) \ . \qquad (14)$$

Analytical approximation of N_W and φ_w parameters by the linear dependence (fig. 5 b,c) from energy E_α by the least square method is in the following form:

$$N_W = 0.0234 + 0.0030 \bullet E_\alpha \ ; \quad \varphi_w = -0.0036 + 0.0004 \bullet E_\alpha \ . \qquad (15)$$

From the table 4 one can see that the volume integral J_v is decreases on an absolute value with increase of E_α at fixed A. The magnitudes of root-mean-square radii (tab. 3) of folding-potentials with increase of α-particles energy for given A =90 vary insignificantly.

4. Results and discussion

Within the framework of a macroscopic OM and semimicroscopic model a good description of differential and total reaction cross section, tendencies of a volume integral of a real part magnitude change, effect of "transparency" (for the nuclei with A=90) with α-particles involved in the energy range up to 80 MeV at the investigated nuclei were obtained. We have verified how the obtained global potential describes experimental ADDS of inelastic scattering for α-particles. At testing of global dependencies of the parameters for macroscopic OP and SFM approaches, quite satisfactory description of ADDS for inelastic scattering with excitation of low lying collective states of the nuclei is obtained. In fig. 6 on an example of the nucleus ^{124}Sn the analysis of ADDS for inelastic scattering of 50.5 MeV α-particles is carried out within the framework of a method of coupled channels (MCC) by ECIS-PM and distorted waves (DWBA) by the code DWUK [24].

From the performed analysis it was established, that the macroscopic OM and the SFM approach provide us with good enough shape and magnitude of differential and total cross sections at nuclei with A=12-124 in forward area of angles at all energies of α-particles. For large angles and light nuclei the correspondence was not reached, what can be probably explained by the contribution to elastic scattering of exchange mechanisms resulted in back scattering. With mass number A increase the correspondence of the theory and experiment is essentially improved.

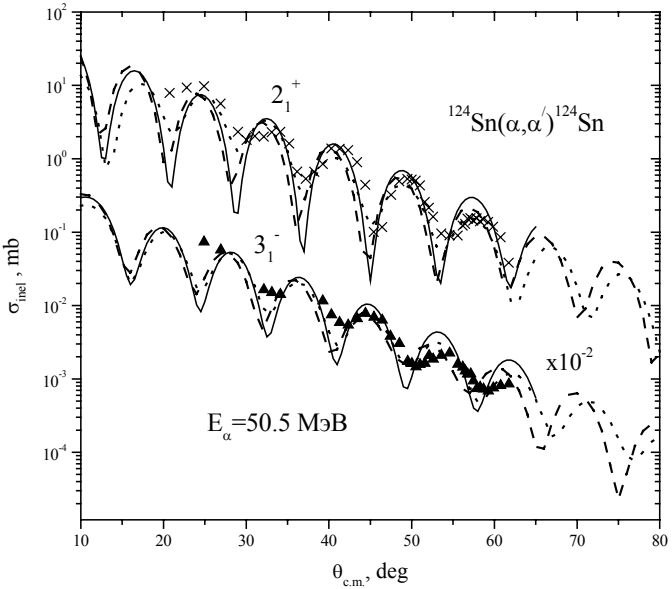


Fig. 6. Angular distribution of inelastic scattering of α-particles on the nuclei ^{124}Sn (points - experiment, solid curve – semimicroscopic folding model, dot line - macroscopic analysis on MCC for 2_1^+ and 3_1^- states, dash line - DWBA) at E_α = (50.5±0.5) MeV.

On the basis of the systematic analysis of experimental data we have received energy of global dependencies of macroscopic OP for α-particles in the range of energies up to 80 MeV. After cross-linking and adjustment of dependencies (6)-(7) the following values for coefficients in the formulas (3) - (5) particular are obtained (table 4).

Table 4. Coefficients for global parameters of macroscopic OP for α-particles with energy up to 80 MeV.

a_0	110.500±5.041	b_0	19.578±4.527	c_0	1.241±0.006
a_1	5.177±0.398	b_1	-2.202±1.077	c_1	0.00066±0.00080
a_2	-0.260±0.064	b_2	0.138±0.018	c_2	0
d_0	1.564±0.007	e_0	0.697±0.051	f_0	0.643±0.096
d_1	0.00109±0.0009	e_1	-0.014±0.010	f_1	-0.022±0.021
d_2	0	e_2	0.0026±0.0005	f_2	0.0012±0.0006

5. Conclusion

In the present paper the global energy dependencies of parameters for macroscopic OM and semimicroscopic folding-model for α-particles in the energy range up to 80 MeV for a wide class of the nuclei are obtained for the first time. For their build-up the joint analysis of a set of experimental data (ADDS of scattering, total reaction cross sections, tendency of the volume integral changes, etc.) is carried out, what will allow to restrict ambiguities in determination of parameters in the indicated energy region. One should mention, that identification and localization of the potential parameters for complex particles, in an acceptable approximation, can be carried out with using the above-stated criteria. Unity of our approach with the same used in [3, 4] and possibility to join together the data and reconstruct the global dependencies below and higher 80 MeV considerably strengthens value of the present work.

The work is performed with partial support of RFBR, Project 00-01 - 00617.

References

1. G.R. Satchler , *Direct Nuclear Reactions* (Oxford University Press, Oxford, 1983). P.E. Hodson, Rep. of Progress in Physics. **34**, 756 (1971).
2. R.Barret, D.Jackson, Razmery i Structura jader (Naukova dumka, Kiev, 1981). R.C. Barrett and D.F. Jackson, *Nuclear Sizes and Structure* (Oxford University Press, Oxford, 1977).
3. M. Nolte, H. Machner, J. Bojowald , Phys. Rev. C **36**, 1312 (1987).
4. L.W. Put and A.M.J. Paans, Nucl. Phys. A **291**, 93 (1977).
5. R.M.Drisko, G.R.Satchler, R.M.Bassel, Phys.Lett. **5**, 347 (1963).
6. O.M. Knyazkov, I.N. Kukhtina, S.A. Fayans, Physics of Particles and Nuclei. **30**, 870 (1999). O.M. Knyazkov, I.N. Kukhtina, S.A. Fayans, Physics of Particles and Nuclei. **28**, 1061 (1997).
7. M.Wit, J.Schiele, and K.A. Eberhard, Phys.Rev. C **12**, 1447 (1975).
8. E.J. Martens and A. M. Bernstein, Nucl. Phys. A **117**, 241 (1968).
9. D. Rychel, R. Gyufko, B. van Kruchten, *et al.*, Z. Phys. A **326**, 455 (1987). B.J. Lund, N.P.T. Bateman, S. Utku, *et al.*, Phys. Rev. C **51**, 635 (1995).
10. A.Duisebaev, K.A.Kuterbekov, I.N.Kukhtina i dr., Preprint № P6-2001-223, JINR (Dubna 2001); (prinjata k pechati v zhurnal Yadernaja fizika, 2002).
11. C.R. Bingham, M.L. Halbert, R.H. Bassel, Phys. Rev. **148**, 1174 (1966).
12. N.Burtebaev, A. Duisebaev, G.N.Ivanov i dr., Preprint 88-01, INP (Alma-Ata, 1988); N.N.Pavlova, C.J.Aisina, K.A.Kuterbekov i dr., Preprint INP (Alma-Ata, 1990); K.A.Kuterbekov, C.J.Aisina, N.N.Pavlova, i dr., Preprint INP (Alma-Ata, 1991).

13. K.A.Kuterbekov, A. Duisebaev, N.Burtebaev, Izv. RAN. Ser. Fiz.59, 112 (1995)
14. A. Duisebaev, B.A. Duisebaev, K.M.Ismailov i dr., Izv. Ministerstva Obrazovanija i Nauki Respubliki Kazakhstan, NAN RK. Ser. Fiz.-mat., №2, 103 (2002).
15. F. Perey. SPI-GENOA an optical model search code (unpubl.). NBI version by B.S. Nillson. (1976).
16. F. Michel, G. Reidemeister, S. Ohkubo, International conference "Clustering Phenomena in Nuclear Physics", June 14-17, 2000, St.-Peterburg. 2000. P.30.
17. F.G. Perey, Phys. Rev. 131, 745 (1963).
18. P.E. Hodgson. Opticheskaja model. Moskva. Atomizdat, 1966, 232s. J.S. Nodvik, D.S. Saxon, Phys. Rev. 117, 1539 (1960).
19. D.B.Bolotov,O.M.Knyazkov, I.N. Kukhtina i dr., Yad. Fiz. 63,1631 (2000).
20. I. Tanihata, T. Kobayashi, O. Yamakawa et al., Phys. Lett. B 206, 592 (1988).
21. C.M. Perey and F.G. Perey, At.Data and Nucl.Data Tables 17, 1 (1976).
22. R.B. Firesrone, Table of Isotopes, Eighth Edition (A. Wiley-Interscience Publication JOHN WILEY & SONS, New York, 1999, Update).
23. A. Ingemarson, J. Nyberg, P.U. Renberg et al., Nucl.Phys. A 676, 3 (2000).
24. P.D. Kunz, Computer program DWUCK4 (unpubl.).

FROM STORAGE ION TRAP TO EFFECTIVE ACCUMULATOR-COLLAIDER OF ACCELERATED FUSIONING HYDROGEN NUCLEI

N.I. Tarantin

Flerov Laboratory of Nuclear Reactions, JINR, Dubna, 141980 Russia

There are a methods of electronuclear neutron generation with help of the height energy accelerator of the charged particles for transmutation of the radioactive nuclei and for production energy. As alternative of these methods some proposal for a low-energy-consumption electronuclear generation of the neutrons in reaction of vacuum collisions of two hydrogen ion beams, namely in the phenomenal reaction $^{2}H + ^{3}H = ^{4}He + n$ having a very large resonance cross section (5.0 b) at very low energy (63.0 keV in the centre-of-mass frame). is consider [1]. Confinement, accumulation and colliding of the accelerated ions take place in crossed magnetic field of a solenoid and electrostatic of three dimensional field using in mass spectrometric storage ion trap of the short-lived radioactive nuclei.

It is considered head-on-head and side by side collisions of accelerated molecular hydrogen ions at equal kinetic energy 126 keV .

The acceleration of deuterium and tritium ions up to the needed energy at large electric current of the beam is produced by linear static accelerator of direct operation using a new tecnique of electrostatic quasi-quadrupole alternating focusing [2], analogous to known RFQ focusing.

The large electric current of hydrogen ions can be produced in a special gas-discharge ion source [3] with the high perveance of the bombarding electron flux contracted by the end fringing magnetic field of a solenoid.

The proposed device allows to create at ion currents of 10 A (the ion current density is 0.1 A/cm^2) a continuos neutron flux, for example, for the transmutation of fission fragments
and minor actinides, with intensity of 10^{19} s^{-1}. This device can be also used as a driver of a subcritical nuclear fission reactor with the coefficient of neutron multiplication k=0.975 for production of 20 GW of commercial electric power.

References

1. N.I. Tarantin // III Scientific Seminar in Memory of V.P. Sarantsev. Dubna, 22-23 September 1999. P. 180 (in Russian). Dubna D9-2000-69.
2. N.I. Tarantin // Announcement of Invention, N 99108653, 5.05.99, Russian Agency for Patents and Trade Marks. 2001, N4. (in Russian).
3. N.I. Tarantin // International Symposium Space Charge Effects in Formation of Intense Low Energy Beams. Dubna, Russia, February 15-17, 1999, P. 135.

HIGH-EFFECTIVE POSITION-TIME SPECTROMETER IN ACTUAL MEASUREMENTS OF LOW INTENSITY REGIONS OF ELECTRON SPECTRA

M.I. Babenkov , *V.S. Zhdanov*

Institute of Nuclear Physics of Kazakhstan National Nuclear Center, Almaty

The improvement of charged particles spectrometer efficiency is maintained in two basis directions. One of them is connected with searching of new configurations of electric and magnetic fields or their combination having the best focusing properties. For the recent years it has been advanced moderately. In the other direction the possibilities possessed by spectrometers of existed types (in particular, some of them have focal planes) are used. The use in such spectrometers of unequipotential sources of a large area or multichannel registration allows to speed up many times the spectral information set without any noticeable resolution deterioration. The device efficiency can be increased in first case by not less than one order of magnitude, in second case - more than two orders. Unfortunately it is impossible to combine an unequipotential source with a multichannel (position) registration because the condition of electrostatic compensation of the source width can not be realized for wide energy range simultaneously.

A magnetic position-time spectrometer is proposed in [1], where not only electron coordinates in focal plane are measured by position-sensitive detector but places of their birth in beta source plane of a large area are fixed using another position-sensitive detector, situated behind it, by quick effect, accompanying radioactive decay. Position-sensitive detectors on basis of microchannel plates are used, prototype of which is position-sensitive detector from [2]. For the first time it is succeeded in position-time spectrometer to combine beta source of a large area with multichannel registration for a wide energy interval.

First of all on the example of the simplest spectrometer with transverse uniform magnetic field the fixation of a place of electron flight from the source plane opening some new possibilities is discussed. In the given case it is possible to measure coordinates in the dispersion direction only. Let's see fig. 1, which presents simplified scheme of position-time spectrometer with single-channel registration. We can note that in non-relativistic case all trajectories of electrons in cross uniform magnetic field are isochronous. On the narrow inlet window of a detector placed at $2\rho_0$ distance from the middle of the source of a large area the electrons are focused whose energy depending on their place of production is defined by the relation:

$$E = E_0 + \Delta E = E_0 + (1 + \frac{\mu}{\mu + E_0}) E_0 \frac{x}{4\rho_0} \quad ,$$

where $\mu = m_0 c^2$, x is the distance from the place of electron production to the source middle line, ρ_0 is the radius of equilibrium orbit for electron with E_0 energy. The energy interval value $2\Delta E_{\max}$ simultaneously measured by the device is defined by the source width and device dispersion. In order to record a spectrum it is sufficient by a signal of position-sensitive detector 1 at whose inlet window a source is placed to determine the place x of production of electron fallen in detector 2. It can be realized by a coincidence unit 5 whose operating allows the further analysis and information record from position-sensitive detector 1. A signal from position-sensitive detector 1 received by coincidence unit 5 is retarded by delay line 4 for τ time equal to the time of the electron passage from the source to the detector along central trajectories.

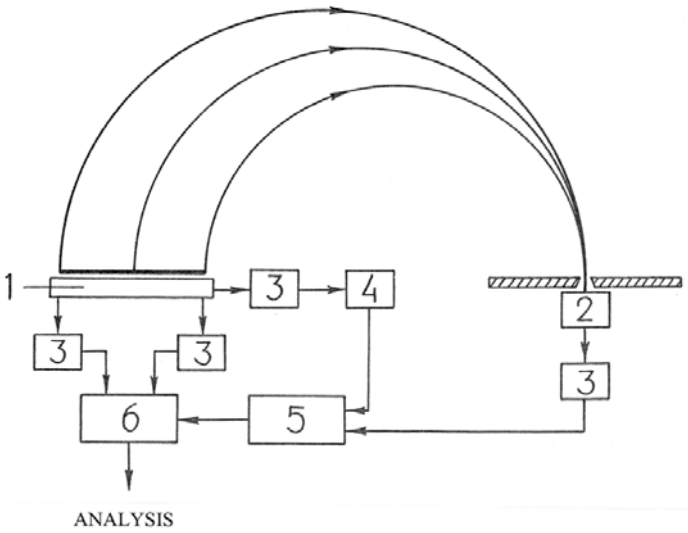


Fig. 1. Simplified scheme of position-time spectrometer with single-channel registration. 1 – position-sensitive detector with radioactive source of large area at entrance window, 2 – fast detector, 3 – amplifier-shaper, 4 – delay line, 5 – coincidence unit, 6 – time-amplitude converter.

The role of coincidence unite 5 is not limited to the identification electron flown out from the given place of a source. Trajectories of electrons, which do not

coincide with central ones, differ from the last ones on the length that leads to some spread of flight time of such electrons in relation to flight time τ. Thus, if detectors 1 and 2 allow to realize sufficiently small resolving time in the coincidence unite then coincidence unit 5 will begin to function as an aperture diaphragm – so-called "electron" diaphragming. It is easy to show that in case of such diaphragming the value of divergence angle of registered beam of electrons in middle, normal to magnetic field direction, plane in non-relativistic approximation does not depend upon electron energy and is given only by resolution time $\Delta\tau$ of coincidence unit 5. It is necessary to mention that at mechanical diaphragming of this angle any variant of allocation of limited entrance diaphragm has its disadvantages [3].

Further development of the proposed scheme consists in the simultaneous use of multichannel detector with the registration of decay place of nuclei on source backing. A position-sensitive detector is also used as a multichannel detector. The width of its sensitive part should be several times more than that of the position-sensitive detector in the source plane. Let's see the fig. 2, which presents the simplified scheme of position-time spectrometer with multichannel registration.

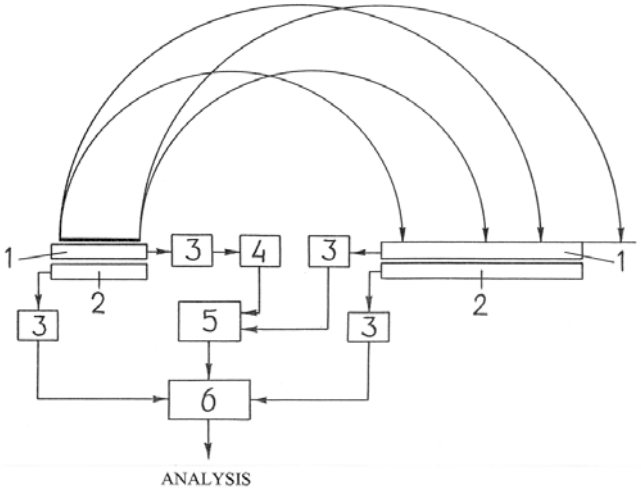


Fig. 2. Simplified scheme of position-time spectrometer with multichannel registration. 1 – position-sensitive detector, 2 – delay line of detector, 3 – amplifier-shaper, 4 – delay line, 5 – coincidence unit, 6 – time-amplitude converter.

We can see that electron beams not fully incident on right position-sensitive detector will be registered with lesser intensity that is easy to take into account.

This inconvenience is compensated by that for the device function with two position-sensitive detectors any additional electron equipment is not necessary. Value of apparatus characteristics starting from average characteristics of position-sensitive detectors on basis of microchannel plates gives an apparatus resolution defined practically only by aberrations on level of 0.1% on energy, which at the ends of the registered energy interval in 10% differs by lesser than 1%. The $\Delta\tau$ resolving time value of a coincidence unite for acceptable divergence angles of electron beam is ~ 1 ns.

Owing to both detectors engaging on coincidence the relation of effect/background is sharply improved. In the case of investigations of weak effects the values of this relation for traditional beta-spectrometer i.e. for spectrometer with position-sensitive detector only in focal detector plane and for position-time beta-spectrometer are connected by the following way [4]:

$$\frac{(effect/background)_{position-time}}{(effect/background)_{traditional}} \approx \frac{1}{2\cdot\Delta\tau\cdot I} \quad ,$$

where $\Delta\tau$ is resolving time of position-time beta-spectrometer coincidence unit, I is beta-source activity. $\Delta\tau \approx 1$ ns was received above. Let $I \le 10^7$ s^{-1}, then the last ratio will give $\ge 10^2$ value. The received value is the strongest estimation for position-time spectrometer as the background growth didn't take into account in traditional spectrometer because of a source presence in the chamber and first of all its activity is taken rather large (usually there are used considerably weaker sources). Thus, for position-time spectrometer ratio value of effect/background on low intensity regions of electron spectra is better in two orders at the minimum.

At some complication of mathematical apparatus it is received that high characteristics of position-time spectrometer remain for energy interval ~5% also at magnetic field, providing double focusing. Owing to double focusing the advantage in efficiency of measurements will make one more order of magnitude [5].

The performed high-effective precision position-time beta-spectrometer is supported to use first of all in measurements of low intensity regions of electron spectra, which are important for fundamental physics development.

First of all this is valuation of electron antineutrino mass $m_{\tilde{\nu}_e}$, one of the most exact and rather cheap method on the form of tritium beta-spectrum in the region of boundary energy. Here last time there was problem of nonphysical negative values of $m^2_{\tilde{\nu}_e}$, caused most probably by unknown "systematical" errors. For resolving this problem the use of principally different high-effective precision beta-spectrometers in measurements possessed improved background qualities can play the definite role. The position-time spectrometer relates to a number of such apparatus, which provides considerably best background conditions at very large

efficiency of carrying out of tritium beta-spectrum form measurement in the region of boundary energy with acceptable high resolution. The use of position-time spectrometer for tritium beta-spectrum measurement [6] is based on condition that decay place of tritium nucleus on the surface of beta-source can be set according to electron irradiation appeared at Auger relaxation of the system of daughter helium ion – surface of metallic backing of a source taking place for 10^{-14} s. There are some examples on fig. 3. An important advantage of position-time beta-spectrometer is possibility to measure simultaneously spectrum of final states of daughter helium ion on beta-source backing

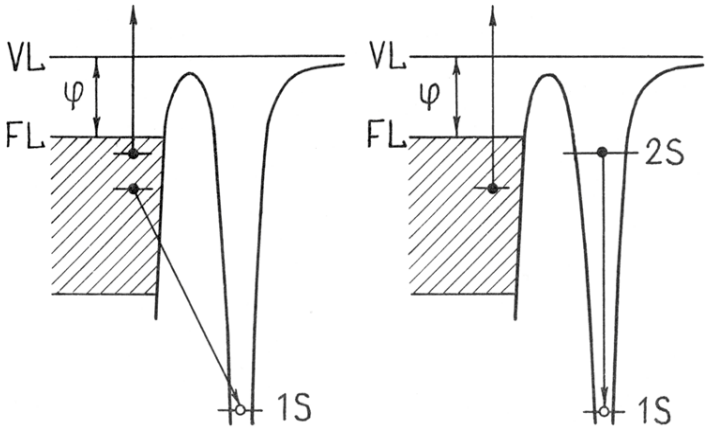


Fig. 3. Examples of nonradiative processes of Auger relaxation at interaction of ions in main and metastable states with metal surface taking place for ~ 10^{-14} s. FL – Fermi level, VL – vacuum level, φ - work of electron exit from metal.

Generally, the presented information allows to hope on receiving of mass estimation of electron antineutrino $m_{\tilde{\nu}_e}$ at least on the level of the best measurements. Finally, the essential difference of function principle of position-time spectrometer from function principle of other spectrometers used in tritium experiments can play the positive role in understanding of "systematical" errors mentioned above.

The spectral investigations of three-electron Auger transitions which allow to receive qualitative experimental information necessary for adequate understanding of electron-electron correlation in atom are also interesting. Intensity of these transitions is less on some orders than intensity of usual two-electron Auger transitions. A high effectiveness of measurement carrying out, excellent relation effect/background at effect tendency to zero and acceptable resolution

make the position-time spectrometer irreplaceable in measurements of three-electron Auger transitions spectra, for example LL MMM [7].

References

1. M.I. Babenkov, V.S. Zhdanov, S.A. Starodubov // Problems of Precision in Nuclear Spectroscopy. Vilnus. USSR. 1984, P.206-211 (in Russian).
2. M.I Babenkov, V.S. Zhdanov, S.A. Starodubov // Nucl. Instr. Meth. Phys. Res. 1986, V.252, P.83-86.
3. Alpha-, Beta- and Gamma-Ray Spectroscopy. Ed. K. Siegbahn. Amsterdam. North-Holland Publishing Company. 1965. V.1.
4. M.I. Babenkov, V.S. Zhdanov, V.Yu. Ryzhykh // Problems of Precision of Nuclear Spectroscopy. Vilnus. USSR. 1990, P.21-26 (in Russian).
5. M.I. Babenkov, V.S. Zhdanov, S.K. Lyubov // LI-th International Conference on Nuclear Spectroscopy and Nuclear Structure. Sarov. Russia. 2001, P.258 (in Russian).
6. M.I. Babenkov, V.S. Zhdanov // Problems of Precision of Nuclear Spectroscopy. Vilnus. USSR. 1990, P.27-31 (in Russian).
7. M.I. Babenkov, V.S. Zhdanov // XXXXV-th International Conference on Nuclear Spectroscopy and Nuclear Structure. Sankt-Peterburg. Russia. 1995, P.435 (in Russian).

HYDROGEN PLASMA ION SOURCE WITH SEPARATION OF IONS IN BEAM BY MASS COMPOSITION

L.M. Nazarenko, E.M. Yakushev, O.V. Stakhov, A.G. Mit',
A.K. Elengeev, N. Alkozhaev

Institute of Nuclear Physics, National Nuclear Centre, Almaty, Kazakhstan

Multi-purpose hydrogen plasma ion source with separation of ions in beam by mass composition was developed and produced.

The principal technical characteristics of ion source is following:

- *Ion energy – (10-50) keV*
- *Summary ion current after the focusing lens – 3 mA*
- *Current of the H_2^+ ions in the plane of detection – 130 mkA*
- *Instability of ion current during one hour of operation - ≤ 1%*

The ionic-optical scheme of the considered device has been presented in fig.1. Its basic parts are actually source of ions 1, ionic lens 2, magnetic prism 3, magnetic screens 4, ion collectors 5 and 6.

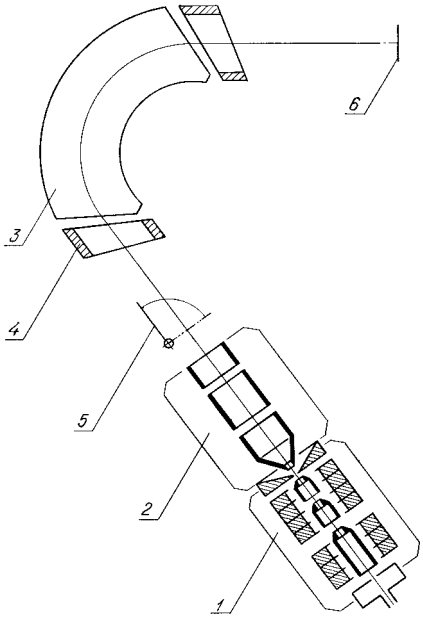


Fig. 1. Ion-optical scheme of hydrogen plasma ion source: 1 – duoplasmatron;
2 – ion lens; 3 – magnetic prism; 4 – magnetic screens; 5 and 6– ion collectors

Duoplasmotron with hollow cold cathode was chosen as a ion source [1,2]. Use of cold catode is preferable because of the greater resource of its continuous work in comparison with heated cathodes and absence of too complex system of compulsory cooling. We have created and approved on the testbed some its constructive variants to achieve parameters mentioned above. The design of duoplasmotron in the final variant is represented in fig.2.

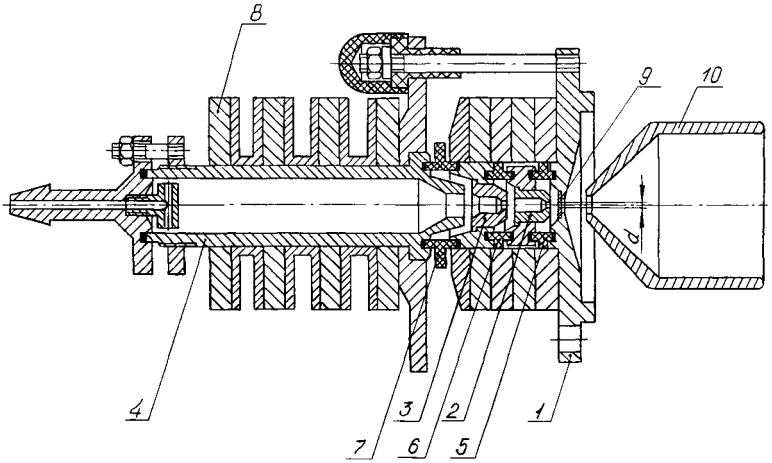


Fig. 2. Duoplasmotron with hollow cold cathode

Details of the duoplasmotron forming the electric field (anode 1, additional anode 2 compressing electrode 3 and hollow cathode 4) are divided by rings 5,6 and 7 from teflon. The same rings together with linings from vacuum rubber such as "witon" (they are not shown in figure) serve for compression of the chamber – working volume of duoplasmotron. The longitudinal magnetic field in duoplasmotron is created by permanent magnets 8.

The potential difference between the anode and hollow cathode about (600-800)V is applied at switching of ion source. The plasma discharge appeared in chamber duoplasmotron generates ions of gas, whose filling is realised from the side of the hollow cathode from special box through leak valve. The extraction of positive ions from plasma is realized through the aperture in the molybdenum inset 9 of anode with the help of the extractor 10 which is also electrode of ion lens.

Focusing of the ions beam is realized by axial-symmetric three-electrode lens (fig. 3).

The basic constructive elements of ionic lens are the electrode-extractor 1, the middle electrode 2 which creates the braking electrostatic field and the electrode 3 which has the same potential as electrode 1, high-voltage isolators 4 and 5, forming the vacuum chamber of lens, the cover 6 to which plasmatron fastens and the screen 7 interfering pollution of isolator 4 by products of burning of

plasma. The cover 6 fastens to isolator 4 and is condensed by a rubber lining with the help of the clamping ring 8 and of some fixing details.

Fractionating of ions by mass composition occurs in the wedge similar magnetic prism 3 [3] (fig. 1).

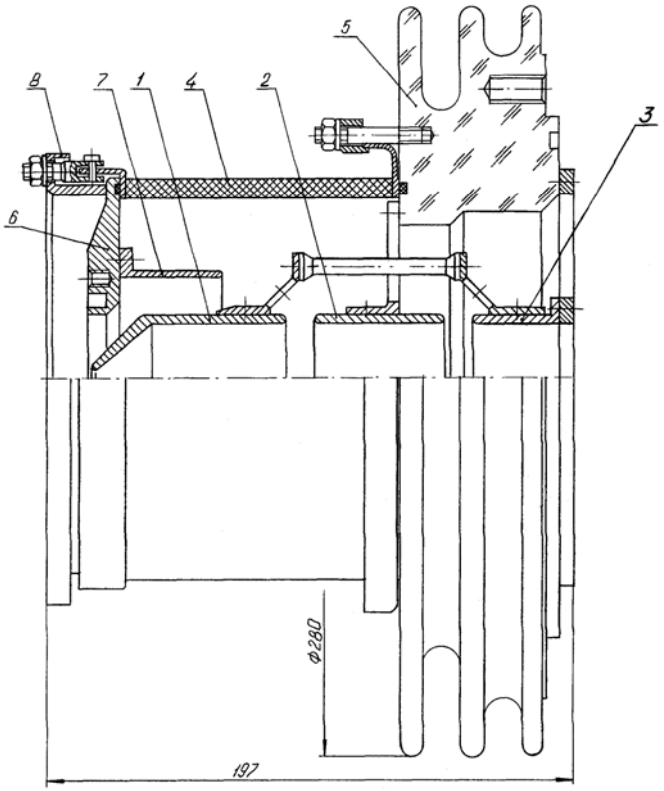


Fig. 3. Ion focusing lens

The circuit developed specially for the given source of ions, includes:

- high-voltage source (0-7) kV with the dividing transformer for excitation and burning of the plasma;
- high-voltage source (10-30) kV for beam focusing;
- high-voltage source (10-50) kV with the converter for formation and acceleration of an ion beam.

Testing of ion source have shown the significant dependence of ion current magnitude and its qualitative composition from a choice of values of varying

parameters: discharge current, vacuum in the chamber of duoplasmatron, accelerating potential, potential on a middle electrode of the lens, and also sizes of the emission aperture of anode, accelerating interval between anode and electrode - extractor, and entrance aperture in this electrode .

The example of recording of ion current is shown in figure 4.

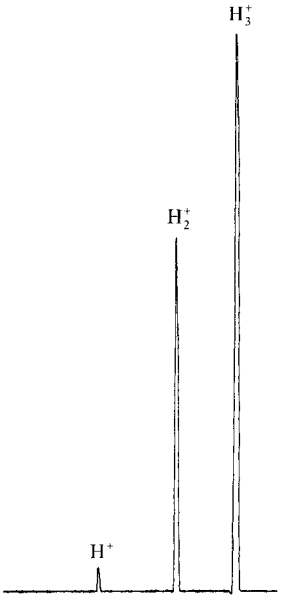


Fig.4. Spectrum of ions hydrogen
H^+ - 8 mkA;
H^+_2 - 130 mkA;
H^+_3 - 180 mkA

It is necessary to pay attention to significant prevalence molecular components of ions of hydrogen in comparison with proton component. Ion source is supposed to use in the installation for definition of tritium concentration in hydrogen containing objects of an environment [4]. It can find application for varies investigations connected with using of high- current monomolecular ion beams of comparatively low energy and in installations of ionic implantation as well.

References

1. V.T. Barchenko, S.N. Zagranichnii, A.Yu. Sokolovskii// Izv.LETI. Issue 303. L. LETI, 1982. P.42-47.
2. A. Forrester. Large ion beams. M.: Mir, 1992.
3. B.M. Kelman, I.V. Rodnikova, L.M. Sekunova. Statical mass-spektrometers. A-ata: Nauka, 1985.
4. E.M. Yakushev, L.M. Nasarenko. Methods of mass-spectral definition of tritium contents in hydrogen and device for its realization. Patent of Republic Kasahkstan N 8046 from 12 March 1969.

HYPOTHESIS OF FUNDAMENTAL MASS AND CONCRETE EXPERIMENTAL CONSEQUENCES AT ULTRAHIGH ENERGIES

Ibadov R.M.

Department of Theoretical Physics and Computer Sciences,
Samarkand State University, Samarkand, 703004, Uzbekistan

Abstract

In the present work researches on revealing of some experimental consequences of new Quantum Field Theory (QFT) with Fundamental Mass (FM) M in calculations of processes of the second order are carried out.

1. Introduction

The article is a prolongation of V.G. Kadyshevsky and his co-workers' research [1-11] about formulation and physical interpretation of Quantum Field Theory (QFT) with new universal parameter - Fundamental Mass M. This fundamental mass and corresponding to it fundamental length $\ell = \hbar / Mc$ possible are called to play so main role in the physical theory as Planck's constant $\hbar$, speed of light c or Newtonian gravitational constant κ and to represent as a characteristic scale in the field of ultrahigh energies.

The Fundamental Mass fixes a new universal scale of theory in the high-energy region. The standard QFT is recovered in the "flat limit". Could the advanced theory be free from ultra-violet disperse? At the present moment we still do not have answer to this question at issue, however we can calculate effective sections of some processes in wood approach and estimate the contribution of fundamental mass.

2. Hypothesis about fundamental mass

The idea about presence of new universal constant dimension of weight or lengths in nature, which would fix the certain scale in the field of high energies (or on small space-time distances) was discussed in the literature in the most various contexts for many times.

One of known is quantization of space-time-direction in QFT, based on a hypothesis about discrete to structure space-time world in the field of small scales. The linear size of "quantum-space" is interpreted as a new universal constant of the theory - fundamental (also elementary, minimal) length ℓ. From the point of view of the given approach the limiting case $\ell = 0$ answers to standard QFT.

This hypothesis about quantization of space-time is based only on theoretical arguments. The most popular of them is existence in standard QFT so-

called ultraviolet divergence, i.e. indefinitely big quantities, appearing as a result of direct application of QFT equations in the field of very small space-time distances, or, that is equivalent, in the field of very high energies and impulses. These divergences do not appear at all if very small distances to expel from the theory from the very beginning. It can be reached, for example, by replacement of continuous space-time to four-dimensional lattice, to which nodules discrete values of coordinates and time answer. However for disposal from divergences in this case it is necessary to pay very high price: in the theory there is no relativistic invariance, standard laws of conservation of energy, impulse, the moment of quantity of movement are broken.

The parameter such as fundamental length ℓ (or fundamental mass M) certainly arose in the so-called not local variants QFT also aimed to disposal of the theory from ultraviolet divergences. Many researchers have appreciated the difficult problem of construction of internally consistent not local field theory. Despite of the certain successes, this direction has not left frameworks of the phenomenological approach as form-factors, overwhelming divergences, in not local theories are necessary to take from the skilled data.

As we know, however, that the most important realistic field theories - QED, quantum chromodynamics, Salam-Veinberg-Glashow model etc., belong to a class so-called renormalizability theories in which existence of divergences does not prevent to the realization of quantitative calculations with any degree of accuracy. Successes of these theories in the description of experimental data available for today are not argument against existence of fundamental length ℓ. They testify only that the modern high-energy physics still far will defend from that boundary behind which can will be shown new geometrical properties of space - time. Experimental detection of the new fundamental scale testifying to existence specific atoms of space - time, would mean, that in knowledge of a nature the new step, commensurable on the value with opening quantum properties of a matter is made. According to the modern data if the constant ℓ also exists then she submits to restriction $\ell \le 10^{-19}$ cm. This boundary still extremely far will defend from " Planck lengths " $\ell \ge 10^{-33}$ cm, determining spatial scales of effects of quantum gravitation. And, certainly, it is impossible to exclude, that in process of overcoming an enormous interval $10^{-19} \ge \ell \ge 10^{-33}$ cm will be open the new physical phenomena and laws, associate with new in " scale of a nature " - fundamental length ℓ

In the following section we briefly shall state main idea construction and substantiation QFT with fundamental weight, in five-measured configuration representation [1-16].

3. QFT with FM

Here we will cite briefly the major ideas of quantum field theory (QFT), in which the four-dimensional momentum space is a constant curvature space with a large radius M [1,9,11]. A key role in the developing approach belongs to the five-dimensional configuration representation. Being four-dimensional in its essence the theory admits a specific local Lagrangian formulation in which the dependence of fields on auxiliary fifth coordinate is local too. Internal symmetries in this formalism generate gauge transformations localized in the same five-dimensional configuration space. The de Sitter space has a constant curvature. Depending on its sign there are two possibilities

$$p_0^2 - p_1^2 - p_2^2 - p_5^2 \equiv g^{KL} P_K P_L = M^2 \qquad (1)$$

$$K, L = 0,1,2,3,5$$

(positive curvature: $g^{00} = -g^{11} = -g^{22} = -g^{33} = -g^{55} = 1$)

$$p_0^2 - p_1^2 - p_2^2 - p_3^2 - p_5^2 \equiv g^{KL} P_K P_L = -M^2 \qquad (2)$$

(negative curvature: $g^{00} = -g^{11} = -g^{22} = -g^{33} = -g^{55} = 1$)

It is natural that QFT based on momentum representation of the form (1)-(2) must predict new physical phenomena at energies $E \geq M$. In principle, the parameter M may turn out to be close the Planck mass $M_p = \sqrt{\hbar c / k} \approx 10^{19}\ GeV$. Then, the new scheme should include quantum gravity.

The standard QFT corresponds to the "small" 4-momentum approximation $|p_0|, |\vec{p}| << M$ and $p^5 = g^{55} p_5 \cong M$ which formally can be performed by letting $M \to \infty$ ("flat limit"). The formulation of QFT with fundamental mass discussed in this paper is based on the quantum version of the de Sitter equation (2), i.e. on the five-dimensional field equation [9]

$$\left[\frac{\partial^2}{\partial x^\mu \partial x_\mu} - \frac{\partial^2}{\partial x_5^2} - \frac{M^2 c^2}{\hbar^2} \right] \Phi(x, x^5) = 0 \qquad (3)$$

$$\mu = 0, 1, 2, 3$$

All fields independently of their tensor dimension must obey (3) since similar universality was inherent in the "classical" prototype of (3)- de Sitter p-space (2). As applied to scalar, spinor, vector and other fields we shall write down the five-dimensional wave function $\Phi(x, x^5)$ in the form $\phi(x, x^5), \psi_\alpha(x, x^5)$ and

$A_\mu(x,x^5)$. The decision (3) in view of the relevant Cauchy problem, which is correctness on x^5, looks like:

$$\Phi(x,x^5)\leftrightarrow\begin{pmatrix}\Phi(x,0)\\ \partial\Phi(x,0)/\partial\, x^5\end{pmatrix}\equiv\begin{pmatrix}\Phi(x)\\ \chi(x)\end{pmatrix} \tag{4}$$

In other words, the statement that to each field in the 5-space there corresponds its wave function $\Phi(x, x^5)$ obeying (3), implies that each of these fields in the usual space-time is described by the wave function with a doubled number of components. Then, it is natural to assume that the initial date (4) obey the Lagrangian equations of motion following from the action principle

We arrive at the complete action of the free Dirac field in our approach in the configuration 5-space

$$S=\frac{1}{2}\int d^4x\Big\{\overline{\Psi}(x,x^5)(i\hat{\partial}+M)(\frac{-i}{M}\frac{\partial}{\partial x^5}\Psi(x,x^5))+(\overline{\frac{-i}{M}\frac{\partial}{\partial x^5}\Psi(x,x^5)})(i\hat{\partial}+M)\Psi(x,x^5)-$$

$$+(\overline{\frac{-i}{M}\frac{\partial}{\partial x^5}\Psi(x,x^5)})(\frac{-i}{M}\frac{\partial}{\partial x^5}\Psi(x,x^5)-\overline{\Psi}(x,x^5)[M+\frac{(i\hat{\partial})^2}{M^2}]\Psi(x,x^2)\Big\}, \tag{5}$$

where the spinor field $\Psi(x,x^5)$ satisfies (3). On a basis (4) we have: $\Psi(x,0)\equiv\Psi(x)$, $\frac{-i}{M}\frac{\partial}{\partial x^5}\Psi(x,0)\equiv\chi(x)$. The same procedure we applied in the spinor cases, leads to following total action integral of the electromagnetic field in QFT with the fundamental mass

$$S=-\frac{1}{4}\int d^4x\left\{F_{KL}(x,x^5)F^{KL}(x,-x^5)+2\left|\frac{\partial A^\mu(x,x^5)}{\partial x^\mu}-iMA_5(x,x^5)-\frac{\partial A_5(x,x^5)}{\partial x^5}\right|^2\right\} \tag{6}$$

where $F_{KL}(x,x^5)=\frac{\partial}{\partial x^K}(e^{-iMx^5}A_L(x,x^5))-\frac{\partial}{\partial x^L}(e^{-iMx^5}A_K(x,x^5))$ and $A_L(x,x^5)$ - 5-tensor and 5-potential of the electromagnetic field.

The Lagrangian density in (6) is not pure local expression in the 5-space configuration but a quantity invariant under local gauge transformation of the 5-potential

$$e^{-iMx^5}A_K(x,x^5)\to e^{-iMx^5}A_K(x,x^5)-\frac{\partial}{\partial x^K}(e^{-iMx^5}\Lambda(x,x^5))$$

where the function $\Lambda(x,x^5)$, like $A_K(x,x^5)$, obeys (3). Naturally, $\frac{\partial S}{\partial x^5}=0$ as usual. It is to be pointed out that "natural" field variables in (6) are thought to be not $A_K(x,x^5)$ but $e^{-iMx^5}A_K(x,x^5)$ which in the flat limit $M\to\infty$ are independent of x^5. A key role in the developing approach belongs to the five-dimensional configuration representation. Being four-dimensional in its essence the theory admits a specific local lagrangian formulation in which the dependence of fields on an auxiliary fifth coordinate is local too. Internal symmetry's in this formalism generate gauge transformations localized in the same five-dimensional configuration space.

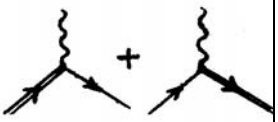
4. **Concrete experimental consequences at ultrahigh energies**

In the field theory standard procedure of calculation of any value representing interest from the point of physics view, is based on Feynman rules. The effective application of these rules substantially simplifies calculations. The most important in Feynman rules are expressions for propagator and tops describing structure of the theory. We especially would like to emphasize that any reorganization of the base of field theory first of all is a call to quantum electrodynamics as predictions of QED excellent be coordinated to a number of high precisions experiments. Therefore the hypothesis about fundamental mass at the beginning should be considered with reference to QED. The requirement of gauge invariance of quantum electrodynamics with fundamental mass results in appearing of new interactions which intensity is defined by parameter fundamental mass. Characteristic feature of these interactions is obvious P-and CP- symmetry breaking, and also not preservation of helicity at high-energy. Our calculations show, that the basic test revealing distinction between standard and new QED, processes with the polarized particles serve. Therefore we shall consider processes in view of particles polarization. We shall reveal some experimental consequences of the hypothesis about fundamental mass at high-energy.

On basis of new Lagrangian QED, containing fundamental mass M, we research section and asymmetry of $e^-+e^-\to e^-+e^-$, $e^-+e^+\to e^-+e^+$, $e^-+e^+\to\mu^-+\mu^+$ processes, in view of particles polarization. In comparison with usual *QED* new Lagrangian contains of additional members which in diagram technique should be compared new tops (look the table).

The single directed line $\overset{p}{\longrightarrow}$ is put here in conformity to field $\varphi(p)$, and double $\overset{p}{\Longrightarrow}$ - to field $\chi(p)$.

Table. New tops in QFT with FM.

Top	The factor in a matrix element	Element of the diagram
Usual electrodynamics top	$e\gamma^n$	
New electrodynamics tops	$e(q+p)_n\gamma^5$	
New electrodynamics tops	$-\frac{\alpha}{\pi}\gamma^5\delta_{nm}$	

A). Section of process $e^-e^- \to e^-e^-$. In the given process the diagrams represented on fig.1.give the contribution

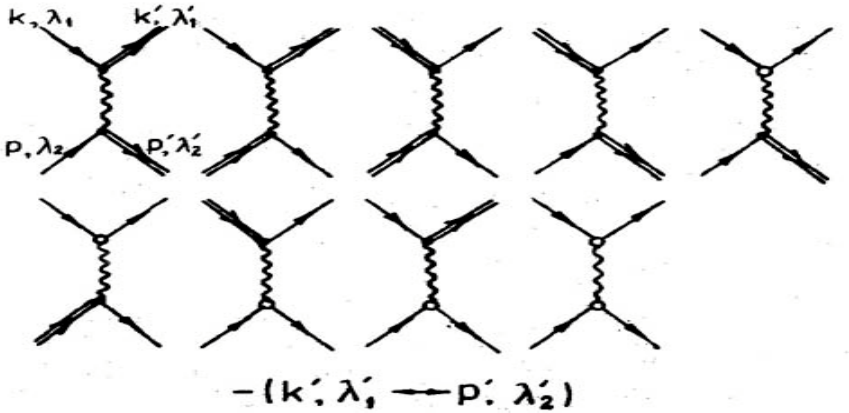


Fig.1. Diagrams of $e^-e^- \to e^-e^-$ process on basis of QED with FM:

In ultrarelativistic limit $E^2 >> m^2$ we receive differential section of electron dispersion with initial polarizations λ_1 and λ_2 to electrons with final polarizations $\lambda_1^{'}$, $\lambda_2^{'}$:

$$\left[\frac{d\sigma}{d\Omega}\right]^{e^-e^-\to e^-e^-}_{\lambda_1\lambda_2\to\lambda_1'\lambda_2'} = \left[\frac{d\sigma_0}{d\Omega}\right]^{e^-e^-\to e^-e^-}_{\lambda_1\lambda_2\to\lambda_1'\lambda_2'} + \frac{1}{M^2}\frac{\alpha^2}{32E^2}\left\{\left[1-\lambda_1\lambda_2\lambda_1'\lambda_2'\right]s\left[\frac{u}{t}+\frac{t}{u}-2\right]+\right.$$
$$+\left[\left(1+\lambda_1\lambda_1'\right)\left(1+\lambda_2\lambda_2'\right)-\left(\lambda_1+\lambda_1'\right)\left(\lambda_2+\lambda_2'\right)\right]\frac{(t-s)u}{4t}+$$
$$+\left.\left[\left(1+\lambda_1\lambda_2'\right)\left(1+\lambda_2\lambda_1'\right)-\left(\lambda_1+\lambda_2'\right)\left(\lambda_2+\lambda_1'\right)\right]\frac{(u-s)t}{4u}\right\}+ \quad (7)$$
$$+\frac{1}{M^4}\frac{\alpha^2}{(32)^2E^2}\left\{\left(1-\lambda_1\lambda_1'\right)\left(1-\lambda_2\lambda_2'\right)(s-u)^2+\left(1-\lambda_1\lambda_2\right)\left(1-\lambda_2'\lambda_1'\right)(s-t)^2+\right.$$
$$\left.+\left[\left(1+\lambda_1\lambda_2\right)\left(1+\lambda_1'\lambda_2'\right)-\left(\lambda_1+\lambda_2\right)\left(\lambda_1'+\lambda_2'\right)\right](s-u)(s-t)\right\}$$

where

$$\left[\frac{d\sigma_0}{d\Omega}\right]^{e^-e^-\to e^-e^-}_{\lambda_1\lambda_2\to\lambda_1'\lambda_2'} = \frac{\alpha^2}{32E^2}\left\{\left(1+\lambda_1\lambda_1'\right)\left(1+\lambda_2\lambda_2'\right)\frac{u^3-s^3}{ut^2}+\right.$$
$$+\left(\lambda_1+\lambda_1'\right)\left(\lambda_2+\lambda_2'\right)\frac{s^3+u^3}{ut^2}+\left(1-\lambda_1\lambda_2'\right)\left(1+\lambda_1\lambda_1'\right)\frac{t^3-u^3}{tu^2}- \quad (8)$$
$$\left.-\left(\lambda_1+\lambda_2'\right)\left(\lambda_2+\lambda_1'\right)\frac{t^3+u^3}{ts^2}\right\}$$

s, t and u - invariant Mandelstam variables.

B). Section of annihilation process $e^-e^+\to e^-e^+$**.** From the formula (7) it is easy to receive differential section of process $e^-e^+\to e^-e^+$

$$\left[\frac{d\sigma}{d\Omega}\right]^{e^-e^+\to e^-e^+}_{\lambda_1\lambda_2\to\lambda_1'\lambda_2'} = \left[\frac{d\sigma_0}{d\Omega}\right]^{e^-e^+\to e^-e^+}_{\lambda_1\lambda_2\to\lambda_1'\lambda_2'} + \frac{1}{M^2}\frac{\alpha^2}{32E^2}\left\{\left[1-\lambda_1\lambda_2\lambda_2'\lambda_1'\lambda_2'\right]u\left[\frac{s}{t}+\frac{t}{s}-2\right]+\right.$$
$$+\left[\left(1+\lambda_1\lambda_1'\right)\left(1+\lambda_2\lambda_2'\right)+\left(\lambda_1+\lambda_1'\right)\left(\lambda_2+\lambda_2'\right)\right]\frac{(t-u)s}{4t}+$$
$$+\left.\left[\left(1+\lambda_1\lambda_2'\right)\left(1+\lambda_2\lambda_1'\right)-\left(\lambda_1+\lambda_2'\right)\left(\lambda_2+\lambda_1'\right)\right]\frac{(s-u)t}{4s}\right\}+ \quad (9)$$
$$+\frac{1}{M^4}\frac{\alpha^2}{(32)^2E^2}\left\{\left(1-\lambda_1\lambda_1'\right)\left(1-\lambda_2\lambda_2'\right)(u-s)^2+\left(1+\lambda_1\lambda_2\right)\left(1+\lambda_2'\lambda_1'\right)(u-t)^2+\right.$$
$$\left.+\left[\left(1+\lambda_1\lambda_2\right)\left(1+\lambda_1'\lambda_2'\right)-\left(\lambda_1+\lambda_2\right)\left(\lambda_1'+\lambda_2'\right)\right](u-s)(u-t)\right\}$$

where

$$\left[\frac{d\sigma_0}{d\Omega}\right]^{e^-e^+\to e^-e^+}_{\lambda_1\lambda_2\to\lambda_1'\lambda_2'} = \frac{\alpha^2}{32E^2}\left\{(1+\lambda_1\lambda_1')(1+\lambda_2\lambda_2')\frac{s^3-u^3}{st^2} + \right.$$

$$+(\lambda_1+\lambda_1')(\lambda_2+\lambda_2')\frac{s^3+u^3}{st^2} + (1-\lambda_1\lambda_2')(1-\lambda_1\lambda_1')\frac{t^3-u^3}{ts^2} - \quad (10)$$

$$\left. -(\lambda_1-\lambda_2')(\lambda_2-\lambda_1')\frac{t^3+u^3}{ts^2}\right\}$$

Asymmetry combination

$$A=\frac{\left(\sin^8\frac{\theta}{2}+\cos^8\frac{\theta}{2}\right)\left(\frac{d\sigma}{d\Omega}\right)_{\lambda_1=\lambda_2}-\left(\frac{d\sigma}{d\Omega}\right)_{\lambda_1=-\lambda_2}}{\left(\sin^8\frac{\theta}{2}+\cos^8\frac{\theta}{2}\right)\left(\frac{d\sigma}{d\Omega}\right)_{\lambda_1=\lambda_2}+\left(\frac{d\sigma}{d\Omega}\right)_{\lambda_1=-\lambda_2}} \quad (11)$$

is differ from zero in usual quantum electrodynamics due to radiating corrections but decreases at high E^2 as $\frac{\alpha m^2}{E^4}\ln\frac{E^2}{m^2}$.

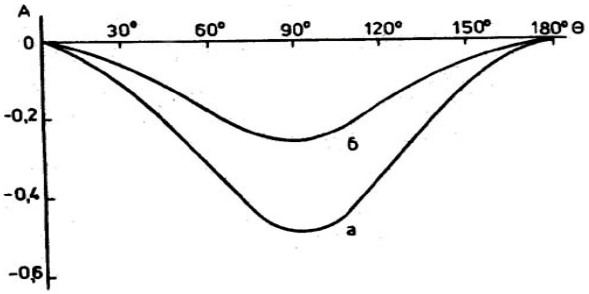


Fig 2. Dependence A on a scattering angle Θ.

Radiating corrections on projected electron-positron accelerators on clashing beams will be slighting small, and the basic contribution to A size will give new interaction, depending on fundamental mass (fig.2. $a-M=300\ Gev;\ b-M=500\ Gev$).

C). Section of annihilation process $e^-e^+\to\mu^-\mu^+$

Considering still that $E^2>>m^2$, we find

$$\left[\frac{d\sigma}{d\Omega}\right]^{e^-e^+\to\mu^-\mu^+}_{\lambda_1\lambda_2\mapsto\lambda_1'\lambda_2'} = \left[\frac{d\sigma_0}{d\Omega}\right]^{e^-e^+\to\mu^-\mu^+}_{\lambda_1\lambda_2\mapsto\lambda_1'\lambda_2'} + \frac{1}{M^2}\frac{\alpha^2}{32E^2}\left[1-\lambda_1\lambda_2\lambda_1'\lambda_2'\right]\frac{ut}{s} + \frac{1}{M^4}\frac{\alpha^2}{(32)^2E^2}(1+\lambda_1\lambda_2)(1+\lambda_1'\lambda_2')(u-t)^2, \quad (12)$$

where

$$\left[\frac{d\sigma_0}{d\Omega}\right]^{e^-e^+\to\mu^-\mu^+}_{\lambda_1\lambda_2\mapsto\lambda_1'\lambda_2'} = \frac{\alpha^2}{32E^2}\left\{(1-\lambda_1\lambda_2)(1-\lambda_1'\lambda_2')\frac{u^2+t^2}{s^2} + (\lambda_1-\lambda_2)(\lambda_1'-\lambda_2')\frac{u^2-t^2}{s^2}\right\}$$

If helicities of beginning particles are identical $\lambda_1 = \lambda_2$, process of annihilation in usual QED follows the account of radiating corrections and section decreases with energy of colliding particles. However in our case we have $(\sigma_{tot})^{e^+e^-\to\mu^+\mu^-} = \frac{\pi}{3}\frac{\sigma}{M^2}$.

On the basis of new QFT containing of fundamental mass M sections and asymmetry of processes $e^- + e^- \to e^- + e^-$, $e^- + e^+ \to e^- + e^+$ and $e^- + e^+ \to \mu^- + \mu^+$ are investigated in view of polarization of particles. Research of differential section and also asymmetry shows that in the new circuit there are the effects caused by existence of fundamental mass. New interaction does not keep spirally. In the theory P-and CP-symmetry breakings caused by existence of electric dipole moments (EDM) $d = e\ell/2$ at easy charged particles in particular τ- lepton take place. Therefore experimental detection of EDM at electron, μ-mesons and τ- lepton would have extremely important value for the developed approach.

5. My Creator, Mighty Lord, I am begging You: You created everything, including different constants and, may be, You also created fundamental mass- M ? If You did not create it, it won't be difficult for You to create it. Please, allow some day the participants of Eurasian conferences to discover fundamental mass- M and, therefore, to prove the hypothesis of my teacher V.G. Kadyshevsky. Please grant to organizational of "II Eurasian

Conference Nuclear Science and Its Application" happiness and luck in their noble work.

Acknowledgements

The authors are sincerely grateful to Kadyshevsky V.G., Musakhanov M.M. and

Yuldashev B.S. for useful arguings of outcomes and constant attention

References

1. Kadyshevsky V.G. Nuclear Physics, B141, p.477, 1978; Kadyshevsky V.G. Particles and Nuclei, II, i.1, 1980, p.5; Kadyshevsky V.G., Mateev M.D. Phys.Lett., 106B, 1980, p.5.
2. Donkov A.D., Ibadov R.M., Kadyshevsky V.G., Mateev M.D. and Chizhov M.V. Some experimental consequences of a hypothesis about fundamental length // Izvestiya AN USSR, Series Physics. –1982. - т.46, N 9, P.1772.
3. Ibadov R.M., Chizhov M.V. Application of quantum electrodynamics with In the fundamental length to high power process // Izvestiya AN UZSR, Series Physics and Mathematics –1983. - N 5, P.38.
4. Ibadov R.M., Deep elastic scattering of Electron in Nucleons and Fundamental lengths // Izvestiya AN UZSR, Series Physics and Mathematics - 1984.- N 3, P.44.
5. Chizhov M.V., Donkov A.D., Ibadov R.M., Kadyshevsky V.G. and Mateev M.D. Quantum Field Theory and a New Universal High Energy Scale. Dirac Fields.// Nuovo Cimento.- 1985. - V.87A, No.3, P.350.
6. Chizhov M.V., Donkov A.D., Ibadov R.M., Kadyshevsky V.G. and Mateev M.D. Quantum Field Theory and a New Universal High Energy Scale. Gauge Vector Fields// Nuovo Cimento. – 1985. - V.87A, No.4, P.375.
7. Ibadov R.M., Kadyshevsky V.G About transformations of supersymmetry in Theories of a Field with Fundamental Mass // Preprint JINR.-1986- P2-86-835, Dubna, 4 P.
8. Ibadov R.M., Kadyshevsky V.G. The new point of view on auxiliary fields in supersymmetric models// Works of VIII International Meeting on problems of the Quantum Theory of a Field. Alushta. -1988.- Dubna, D2-87-798, P.141.
9. Ibadov R.M., Kadyshevsky V.G. New formulation of Quantum field theory with Fundamental mass// Proceedings 5th International Symposium on Selected Topics in Statistical Mechanics, Dubna –1989 -, world Scientific, P.131-156.
10. Fursaev D.V., Kadyshevsky V.G., Ibadov R.M. The Rotation Invariant gauge Model with the compact momentum space.// Proceedings of the 25th International Conference on High Energy Physics, Singapore – 1990 - world Scientific, P.928.

11. Ibadov R.M., Kadyshevsky V.G. Abstracts of The Second Uzbekistan conference "Modern problems of Nuclear Physics". Samarkand 1997 , p.187;
12. Ibadov R.M., Ibadova U.R., Ravshanova D.R., Umidullaev Sh.U. On Quantum Field Theory with Fundamental mass// in Proc. of the International Scholl-Seminar “Structure of Particles and Nuclei and Their Interactions “. Humson.–1998.- Dubna, P.139-142.
13. Ibadov R.M., Ravshanova D.R. Stochastic Quantization and Fundamental Mass// Abstr. of the third International conf. «Modern Problems of Nuclear Physics», Bukhara.- 1999. - P.153.
14. R.M. Ibadov and U.R. Ibadova “Quantum field theory with a new universal scale - fundamental mass in the field of superhigh energies and some experimental consequences” http://menu2001.phys.gwu.edu/menu2001/abstracts/rust2.ps. (USA 2001).
15. Umida Ibadova, Rustam Ibadov and Rashid Artikov “Spontaneous breaking of symmetry and fundamental mass” http://pheno.physics.wisc.edu/pheno01/ibadova.pdf. (USA 2001).
16. Rustam M.Ibadov, Umida R.Ibadova, and Dilbar R.Ravshanova “Concept of Stochastic Quantization of the Abelian Fields and Fundamental Mass” http://pheno.physics.wisc.edu/pheno01/ravshanova.pdf. (USA 2001).

INFLUENCE OF HIGHER ORDER ABERRATIONS ON THE RESOLUTION ABILITY OF MIRROR OBJECTIVE FREE FROM THE THIRD ORDER SPHERICAL ABERRATION

S. B. Bimurzaev, G. S. Serikbaeva and E. M. Yakushev

Institute of Nuclear Physics, National Nuclear Center, Almaty, Kazakhstan

Abstract: The settlement formulas for spherical aberration factors of the axis symmetrical electrostatic electronic mirror are derived. A technique of excluding from subintegral expressions of high order derivatives of the potential axial distribution in mirror systems is presented. The conditions for spherical aberration elimination in a three-electrode axis symmetrical mirror consisting of coaxial cylinders of equal diameter are found. For such (found) conditions (the mirrors) the aberration spherical factor of the fifth order for mirror objective is calculated along with its limiting resolution by means of direct numerical calculation of the exact equations of trajectories. The calculations show that the considered electrostatic mirror objective does not concede the best objectives with magnetic lens.

It is presented a functional diagram for transmission electron microscope with dark-field image with an electrostatic electron mirror as the objective.

Key words: spherical aberration factor, electrostatic electron mirror, and electrostatic mirror objective glass, electron microscope.

Introduction

Resolution of a transmission electron microscope is limited by spherical aberration (of the third order) of its objective - electronic lens [1]. Since spherical aberration of axis symmetrical electron lenses cannot be essentially eliminated, search for various aberration correctors of electronic lenses are in progress, in particular, on the basis of application of electrostatic electronic mirrors [2-3]. However, utilization of such correctors essentially complicates the electron-optical scheme of the objective which, besides an objective lens, should include not only an electrostatic mirror, but also a magnetic system for parting of the incident and reflected beams.

Use of electrostatic mirrors as correctors, as is described in [2-3], is connected with the generally accepted opinion that the sign of spherical aberration factor for electron mirrors is opposite to the sign of the spherical aberration factor for electron lenses, and, on the other hand, with the necessity to correct the resulted enlarged image [4] due to a small scale of an electron mirror [5]. However, as it is shown in [6-7], in electron mirrors there can exist areas, where spherical aberration factor can be both positive and negative continuously passing through zero.

In the present work the class of axis-symmetrical electronic mirrors with eliminated spherical aberration of the third order is calculated, and also the opportunity of use such mirrors as an objective in transmission electron microscope instead of an electron lens is discussed.

Formulas for the spherical aberration factor

Let us introduce a cylindrical coordinate system r, ψ, z, which axis z coincides with an optical axis of a mirror. Then the third order spherical aberration factor $C_s^{(3)}$ given in a subject plane $z = z_0$, combined with the focal plane $z = z_f$ of the mirror, can be written down as:

$$C_s^{(3)} = J_1 + J_2 + J_3 + \alpha, \tag{1}$$

where

$$J_1 = \frac{1}{(4p_0')^4\sqrt{\Phi_0}}\int_{z_u}^{z}\frac{1}{\sqrt{\Phi}}\left\{\begin{array}{l}\dfrac{p^3}{2}\left[\dfrac{\Phi''-\Phi_u''-\Phi_u'''(z-z_u)}{\Phi^2}\right]\left[\dfrac{3}{2}\Phi'^2 p-\Phi(4\Phi' p'+\Phi'' p)\right]+\\ +\dfrac{p^4-1}{2\Phi}\Phi_u'''\Phi'+32pp''(\Phi p'^2+\dfrac{1}{4}\Phi'' p^2)\end{array}\right\}dz\,, \tag{2}$$

$$J_2 = \frac{1}{(16p_0'g_0')^2\sqrt{\Phi_0}}\int_{z_u}^{z}\left\{\begin{array}{l}\dfrac{1}{\sqrt{\Phi}}\left(\dfrac{\Phi_u''-\Phi''}{\Phi}\right)\left(\Phi_u'+\dfrac{5}{2}\Phi' pq\right)\Phi' pq+\\ +\left(\dfrac{\Phi''-\Phi_u''}{\sqrt{\Phi}}+\dfrac{\Phi_u''}{\sqrt{\Phi_0}}\right)\left[2pq\left(\Phi_u'+\dfrac{5}{2}\Phi' pq\right)\right]'+\\ +64g\left[2p''\left(\sqrt{\Phi}p'g'+\dfrac{1}{4}\Phi'' pq\right)+q''\left(\Phi p'^2+\dfrac{1}{4}\Phi'' p^2\right)\right]\end{array}\right\}dz, \tag{3}$$

$$J_3 = \frac{1}{(4g_0')^4\sqrt{\Phi_0}}\int_{z_u}^{z}\left[\frac{7}{2}(\Phi''-\Phi_u'')\left(q^4\Phi'\sqrt{\Phi}\right)'+32\sqrt{\Phi}qq''\left(\Phi g'^2+\frac{1}{4}\Phi'' g^2\right)\right]dz\,, \tag{4}$$

$$\alpha = \left(\frac{3}{2}+\frac{7\Phi_u''}{16p_0'g_0'\sqrt{\Phi_0}}\right)\frac{\Phi_u'}{16p_0'g_0'\sqrt{\Phi_0}}-\frac{\Phi_u'''}{(4p_0')^4\Phi_0}\,. \tag{5}$$

Here $\Phi = \Phi(z)$ - axial distribution of electrostatic potential, $p = p(z)$ and $g = g(z)$ - linearly independent partial solutions of the equation

$$\Phi r'' + \frac{\Phi' r'}{2} + \frac{\Phi'' r}{4} = 0\,, \tag{6}$$

and p - analytical function, $g = q\sqrt{\Phi}$, where $q = q(z)$ - also analytical function satisfying the equation

$$\Phi q'' + \frac{3}{2}\Phi' q' + \frac{3}{4}\Phi'' q = 0. \qquad (7)$$

Primes designate differentiation by z; subscript "0" denotes values in the object plane $z = z_0$, and "u" - in the point of turn of the mirror $z = z_u$.

For clarity it is accepted that functions p and q satisfy the following initial conditions:

$$p_u = q_u = 1, \qquad p_u' = q_u' = -\frac{\Phi_u''}{2\Phi_u'}. \qquad (8)$$

The given formulas for spherical aberration factor differ from the formulas in [8] by elimination of the derivatives $\Phi'''(z)$ and $\Phi'^{v}(z)$ from axial distribution of potential. It is necessary to note, that the procedure of excluding derivatives of highest orders from subintegral expressions in mirror systems though is carried out, as usual, by integration by parts, however because of presence of special point $z = z_u$, where $\Phi_u = 0, \quad \Phi_u' \neq 0$, differs a little from similar procedures used at calculation of electron lenses. Apparently, due to this, but not because of time as the independent variable, the authors of [3] were not able to decrease orders of the derivatives in the final formulas. In mirror systems the subintegral functions proportional to $\Phi^{(n)}(z)$, should be transformed as follows:

$$F(z)\Phi^{(n)}(z) \to F'(z)\left(\Phi^{(n-1)}(z) - \Phi^{(n-1)}{}_u\right). \qquad (9)$$

Three-electrode aspherical electrn mirrors

As shown in [9], in two-electrode axis symmetrical mirror made of coaxial cylinders of equal diameter, the sign of the spherical aberration factor is opposite to the sign of the spherical aberration factor of electronic lenses. However, there were no cases revealed that reduce to zero the spherical aberration factor (located near focal plane). In order to obtain aspherical (free of spherical aberration of the third order) mirror systems, the given work investigated a three-electrode axis-symmetrical mirror also made of three coaxial cylinders of an equal diameter (fig.1). Such mirror can be considered as a leans-mirror system, where a gap between the first and second electrodes serves as an electron lens, and a gap between the second and third electrodes - electronic mirror. Axial distribution of electrostatic potential for the examined mirror is in the form [10]

$$\Phi(z) = \frac{1}{2}\left[\left(V_1 + V_3\right) + \sum_{i=1}^{2}\left(V_{i+1} - V_i\right)U(z - z_i)\right], \qquad (10)$$

where

$$U(z) = sign(z)\left[1 - \sum_{k=1}^{\infty} \frac{\exp(-2\alpha_k |z|/d)}{\prod_{m=1}^{\infty}\left(1-\alpha_k^2/\alpha_m^2\right)_{k\neq m}}\right]. \qquad (11)$$

Here V_1, V_2 и V_3 - potentials at the electrodes, z_i - coordinate of a middle for the i th gap between the electrodes, α_k, α_m - roots of the zero order Bessel function, d - diameter of the cylinder.

Calculation of a mirror was made as follows. For the given values of length of the second electrode l there was a ratio of potentials at electrodes of the system ensuring conditions for elimination of the third order spherical aberration. In order to find partial solutions of the equations (6)-(7) taking into account initial conditions (8) the technique of Runge Gutta of the fourth order is used. From the variety of possible ways for elimination of spherical aberration the cases of large magnification are picked out, when the subject plane located in free-of-the-field space, is near the mirror focal plane $z = z_f$. For the cases of large magnification the spherical aberration factor of the fifth order $C_s^{(5)}$ is calculated by direct numerical calculation of the exact equations of trajectories. The results are given in table. 1, where $z = z_b$ - location of the mirror top. Thus, the dimensions are given in terms of d and electrical values are in terms of potential of the first electrode V_1. It is accepted, that the positive direction of an axis z coincides with a direction of a incident beam, and the origin is in middle of the first gap.

It can be shown that for the aspherical systems near gauss image plane there is also a certain plane in which the radius of point dispersion circle is minimal. In the mirror with eliminated spherical aberration of third order the distance between the best focusing plane $z = z_M$ and the gauss image plane $z = z_G$ and radius ρ of the least section circle of a beam in this plane are determined by the equality:

$$z_M - z_G = \frac{5R}{16\alpha}, \qquad \rho = \frac{1}{16}R, \qquad (12)$$

Where α - aperture of a beam, $R = C_s^{(5)}\alpha^5$ - radius of dispersion of a beam of the fifth order in the plane of gauss image.

The schematic course of trajectories in a mirror with eliminated spherical aberration for $l = 0.4$, $V2 = -0.07$, $V3 = -0.319$, is given at the fig.1. (Scale on an axis r is increased for n times.)

Table 1. Three-electrode axially symmetric mirror with removed spherical aberration.

l	V_2	$-V_3$	$-z_f$	z_b	$-10^{-3} * C_s^{(5)}$
0.4	-0.050	0.358	1.84	0.561	72.9
	-0.055	0.347	1.52	0.568	30.7
	-0.060	0.337	1.28	0.575	15.1
	-0.065	0.328	1.10	0.581	8.27
	-0.070	0.319	0.964	0.587	4.96
	-0.075	0.311	0.854	0.592	3.95
	-0.080	0.304	0.766	0.597	2.24
	-0.085	0.298	0.695	0.600	1.59
	-0.090	0.293	0.637	0.603	1.22
0.5	0.010	0.369	2.70	0.673	430
	0.005	0.349	1.84	0.690	78.2
	0.000	0.327	1.30	0.710	20.1
	-0.005	0.304	0.923	0.733	6.38
	-0.010	0.282	0.652	0.761	2.64
0.6	0.035	0.368	3.07	0.812	512
	0.030	0.334	1.73	0.848	67.6
	0.025	0.285	0.865	0.917	11.3

Conclusion

The received results allow to hope for significant increase of resolution and sensitivity of electrostatic electron microscope using as its objective an electronic mirror free of spherical aberration of the third order instead of an electron lens. The electron-optical scheme of transition electron microscope for a dark-field image with mirror objective is shown at fig.2. At that the optical axis of the mirror coincides with the main axis of the electronic microscope and the object plane is located close to the focal plane of the mirror. Electronic microscope operates as follows. Generated by a lighting system 1 electronic beam 2 falls on an object under investigation 3 located on a little table at some angle to the main optical axis of the microscope. At appropriate choice of this angle only those electrons, which due to interaction with the object have deviated from the initial way will pass through the hole of the aperture diaphragm 6. This diaphragm will stop another part of the electrons that did not undergo interaction with the object. Rejected from initial pass electrons 4, having reflected from an electrostatic electron mirror – objective 5, will create a magnified aberration-free image of the object at the intermediate screen 7. Further devices of supervision and image

registration 8 will create the magnified image of this intermediate image on a plane of the screen 9.

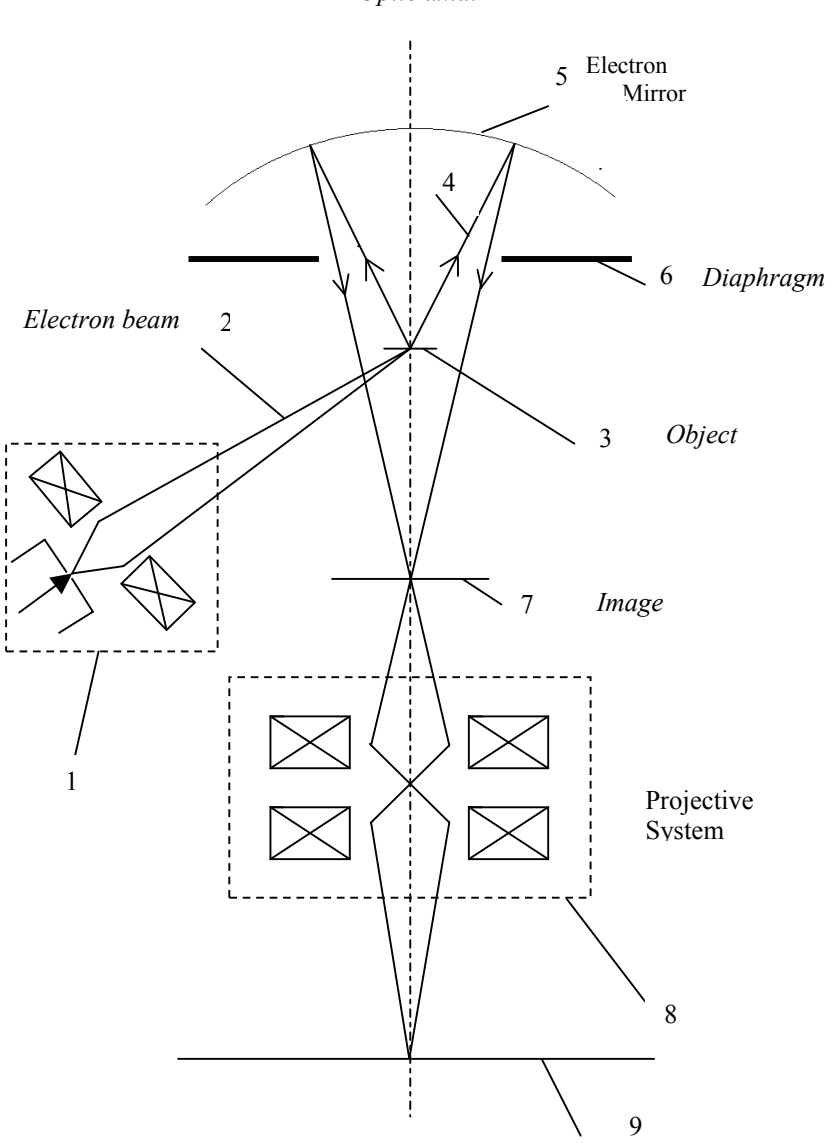


Fig.2. Electron microscope with mirror lens.

References

1. P.W. Hawkes and E.Kasper. (1989). *Principles of Electron Optics* (Academic, New York).
2. G.F. Rempfer. (1990). A theoretical study of the hyperbolic electron mirror as a correcting element for spherical and chromatic aberration in electron optics. *J. Appl. Phys*. **67**(10): 6027.
3. D. Preikszas and H. Rose. (1997). Correction properties of electron mirrors. *J. Electron microscopy*. **46**(1): 1.
4. R.M.Henkelman and F.P.Ottensmayer. (1974). *J. Phys*. E7, 176.
5. E.G. Ramberg. (1949). *J. Appl. Phys*. **20**:183.
6. S.B. Bimurzaev. (1976). Telescope electrostatic system with zero spherical aberration. *Zh. Tech. Fiz*. **46**(11): 2292.
7. S.B. Bimurzaev. (1976). Elimination of spherical aberration from a telescopic electrostatic system. *Zh. Tech. Fiz*. **46**(7): 1580.
8. E.M. Yakushev and L.M. Sekunova. (1986). Theory of Electron Mirrors and Cathode Lenses. *Adv. Electronics and Electron Physics*. **68**: 337.
9. L.M. Sekunova. (1977). Параксиальные свойства и аберрации двухэлектродного осесимметричного зеркала. *Zh. Tech. Fiz*. 47, 2030.
10. B.V. Bobykin, Yu.A. Nevinniy, E.M. Yakushev. (1975). Двухтрубчатый электронно-оптический элемент для предварительного ускорения медленных электронов в бета-спектрометрии. *Zh. Tech. Fiz***. 45**(11): 2368.
11. Патент Республики Казахстан №2000/0259.1. (2000). Электронный микроскоп. (The Republic of Kazakhstan Patent No. 2000/0259.1. (2000) Electron microscope)

INVESTIGATION of SPACE – TIME-OF-FLIGHT FOCUSING PROPERTIES of TWO –DIMENSIONAL ELECTRONIC MIRRORS with CURVILINEAR AXIAL TRAJECTORY

S.B. Bimurzaev, Z.D. Iskakova and N.S. Sarsenbaeva[1]

Institute of Nuclear Physics of Kazakhstani National Nuclear Center,
[1]Kazakh National University, Almaty, Kazakhstan.

Abstract: Equations of motion for two–dimensional electron mirrors with curvilinear axial trajectory have been reduced to a form similar for such mirrors with a rectilinear axial trajectory by introduction of effective potentials. On the basis of this analogy the general expressions to within sizes of the second order, describing time-of-flight and equations of trajectory in a middle plane in two–dimensional electron mirrors with curvilinear axial trajectory are received. The space and time-of-flight focusing conditions are determined along with conditions for elimination of some kinds of aberrations. By numerical calculations the conditions for stigmatic focusing and elimination of spherical aberration of the second order in two and three-electrode mirror electrostatic power analyzers are found; the electrodes there are pairs of parallel plates separated with linear gaps. The time-of-flight focusing conditions up to the second order for a three-electrode plain mirror are also found.

Key words: effective potential, 2-D electron mirrors with curvilinear axial trajectory, stigmatic spatial focusing, time-of-flight focusing, power dispersion, mass dispersion, three-electrode plain mirror.

1. Introduction

Investigation methods for time-of-flight focusing properties of mirror systems with a rectilinear axial trajectory are well developed [1,2]. This technique can be generalized as well for the systems with curvilinear axial trajectory, if one of spatial coordinates is cyclic. In this case by introduction of effective potentials the task with curvilinear axial trajectory can be reduced to a task with a rectilinear axial trajectory.

The present work is devoted to determination of time-of-flight and equation of trajectory in a middle plane of two–dimensional electron mirrors with curvilinear axial trajectory by the method of effective potentials, and also to investigation with numerical methods of properties of space and time-of-flight focusing for a wide class of such systems, in which pairs of parallel plates separated with linear gaps serve as electrodes.

2. Equation of motion

Let us introduce a Cartesian coordinate system x, y, z having combined z axis with an optical axis of a mirror, axis x with a direction, in which the field does not vary, and plane xz with an average plane of a field. Then the equations of motion for a particle with charge e and mass m will be written down in the form

$$\dot{x} = \sigma\sqrt{-\frac{2e}{m}(\varphi+\varepsilon)}\sin(\vartheta+\Delta\vartheta)\cos\gamma = const, \tag{1}$$

$$\ddot{y} = -\frac{e}{m}\frac{\partial\varphi}{\partial y}, \tag{2}$$

$$\dot{x}^2 + \dot{y}^2 + \dot{z}^2 = -\frac{2e}{m}\left(\varphi+\varepsilon\right), \tag{3}$$

Here $\varphi = \varphi(y,z)$ - electrostatic potential, ε - complete energy of a particle expressed in terms of potential, γ - inclination angle of a trajectory to the middle plane, xz, ϑ - angle between the axial trajectory (laying in the middle plane) and axis z, $\Delta\vartheta$ - angular dispersion, σ - sign multiplier that describes direction of a particle's motion along an axis, and the dots designate, as usual, the time differentiation. We shall define potential so that it is equal to zero in that place, where the energy of central (driven on an axial trajectory with $\varepsilon = 0$) particle is equal to zero.

Decomposing (1) on small parameters ε, $\Delta\vartheta$, γ and limiting our considerations with values of not more than the second order trifle, we re-write (2) - (3) in the form

$$\ddot{y} = -\frac{e}{m}\frac{\partial\varphi^*}{\partial y}, \tag{4}$$

$$\dot{y}^2 + \dot{z}^2 = -\frac{2e}{m}\left(\varphi^* + \varepsilon^*\right). \tag{5}$$

Here

$$\varphi^* = \varphi - \varphi_0\sin^2\vartheta_0, \tag{6}$$

- effective potential, and

$$\varepsilon^* = \varepsilon - \varphi_0\sin^2\vartheta_0\left(2\delta+\delta^2\right), \tag{7}$$

where

$$\delta = \frac{1}{2}\left[\frac{\varepsilon}{\varphi_0} + 2ctg\vartheta_0\Delta\vartheta_0 + \frac{\varepsilon}{\varphi_0}ctg\vartheta_0\Delta\vartheta_0 - \frac{1}{4}\left(\frac{\varepsilon}{\varphi_0}\right)^2 - \Delta\vartheta_0^2 - \gamma_0^2\right], \tag{8}$$

- have the same meaning as ε in units of effective potential. Hereinafter the subscript "0" denotes values in the initial plane $z = z_0$.

Equations (4) and (5) that describe particle motion in a vertical plane yz are different from the corresponding equations for mirrors with a direct optical axis [2] only by the fact that they have instead of φ and ε their effective values. Hence, the conclusions following from them will be similar. Therefore, we shall below limit our considerations by consideration of motion of particles in the middle plane, which we shall consider located horizontally.

3. The time of flight

According to [2] time-of-flight *t* of a particle from an initial plane $z = z_0$ to an arbitrary plane $z = const$ is equal to

$$t = T + \Delta t, \tag{9}$$

where

$$T = -\frac{1}{v_0}\left(z - z_t^{(0)}\right) \tag{10}$$

- time-of-flight of a central particle,

$$\Delta t = \frac{1}{v_0}\left[\sum_{k=1}^{2}\left(\frac{\varepsilon^*}{\Phi_0}\right)^k D_{t\varepsilon}^{(k)} + T_1 y_0'^2 + T_2 y_1' y_0 + T_3 y_0^2\right] \tag{11}$$

total time-of-flight aberration up to the second order, inclusive. Here $\Phi = \varphi^*(0, z)$ axial distribution of effective potential,

$$D_{t\varepsilon}^{(k)} = (-1)^{k+1}\frac{(2k-1)!!}{(2k)!!}(z - z_t^{(k)}) \tag{12}$$

- factor of time-of-flight chromatic aberration of k - order, and T_1, T_2 and T_3 - the factors of time-of-flight geometrical aberration of the second order [2].

Values $z_t^{(0)}$ and $z_t^{(k)}$, as it follows from (10) and (12), are effective subject plane and plane of time-of-flight focusing by energy of k -order and are defined by the ratio

$$z_t^{(j)} = 2z_T^{(j)} - z_0, \quad (j = 0,1,...,k) \tag{13}$$

where $z_T^{(j)}$ - the functions of axial distribution of potential [2] only. One should note that the values $z_T^{(1)}$ and $z_T^{(2)}$ define position of reference planes for time-of-flight focusing of the first and second orders, accordingly.

4. Time-of-Flight Focusing

As one can see from (12) when the following condition is satisfied

$$z = z_t^{(k)} \, (k = 1,2,...) \tag{14}$$

time of flight focusing on k - order energy can be reached in the mirror.

At overlapping $z = z_t^{(1)}$ and $z = z_t^{(2)}$ planes, i.e. when the con dition is satisfied

$$z_T^{(1)} = z_T^{(2)} = z_T, \tag{15}$$

the following from (13), it can be achieved in a mirror the time-of-flight focusing on energy up to the second order inclusive.

Taking into account (14) one can re-write (10) in the form

$$T = T_0 - \frac{1}{\upsilon_0}(z - z_t^{(1)}), \tag{16}$$

where T_0 - a time interval the central particle passes from the initial plane up to the main plane $z_t^{(1)}$ [1] of time-of-flight focusing:

$$T_0 = \frac{1}{\upsilon_0}(z_T^{(0)} - z_T^{(1)}). \tag{17}$$

This time interval we call a temporary interval of focusing. Dependence of the temporary interval of focusing on a particle mass defines the rate of time-of-flight mass dispersion of a mirror:

$$D_{tm} = m\frac{\partial T_0}{\partial m} = \frac{1}{2}T_0. \tag{18}$$

Effective drift distance of a mirror is also defined by a temporary interval of focusing:

$$L = \upsilon_0 T_0 = z_T^{(0)} - z_T^{(1)}. \tag{19}$$

5. Equation of a trajectory in the middle plane

As one can see from (1), the trajectory of a particle in the middle plane is a linear function of time. Then, taking into account (7) - (8) and (10) - (12) equation of trajectory can be written down in the form

$$x = X + \Delta x, \tag{20}$$

where

$$X = x_0 - tg\vartheta_0 \left(z - z_x \right) \tag{21}$$

- equation of a paraxial trajectory,

$$\Delta x = K_\vartheta \Delta\vartheta_0 + K_\varepsilon \frac{\varepsilon}{\Phi_0} + K_{\vartheta\vartheta} \Delta\vartheta_0^2 + K_{\vartheta\varepsilon} \frac{\varepsilon}{\Phi_0} \Delta\vartheta_0 + K_{\varepsilon\varepsilon} \left(\frac{\varepsilon}{\Phi_0} \right)^2 + \tag{22}$$

$$K_1 y_0'^2 + K_2 y_0' y_0 + K_3 y_0^2$$

- total spatial aberration.

Here K_ϑ and K_ε - factors of the first order aberrations, $K_{\vartheta\vartheta}, K_{\vartheta\varepsilon}, K_{\varepsilon\varepsilon}, K_{\gamma\gamma}, K_{x1}, K_{x2},$ и K_{x3} - factors of the second order aberrations, and

$$K_\vartheta = \left(1 + tg^2\vartheta_0\right)\left(z - z_\vartheta\right), \tag{23}$$

$$K_\varepsilon = -\frac{L}{2}\sin 2\vartheta_0, \tag{24}$$

$$K_{\vartheta\vartheta} = \frac{tg\vartheta_0}{2}\left(1 + 3tg^2\vartheta_0\right)\left(z - z_{\vartheta\vartheta}\right), \tag{25}$$

$$K_{\vartheta\varepsilon} = -\sin^2\vartheta_0 \left(z - z_{\vartheta\varepsilon}\right), \tag{26}$$

$$K_{\varepsilon\varepsilon} = \frac{1}{8}\sin 2\vartheta_0 \cos^2\vartheta_0 \left(L + 3(z_T^{(1)} - z_T^{(2)})\right), \tag{27}$$

$$K_1 = -tg\vartheta_0 \left(z - z_y\right), \tag{28}$$

$$K_2 = -tg\vartheta_0 T_2, \tag{29}$$

$$K_3 = -tg\vartheta_0 T_3. \tag{30}$$

Here

$$z_x = 2z_u^* - z_0, \tag{31}$$

$$z_\vartheta = 2z_\vartheta^* - z_0, \tag{32}$$

$$z_{\vartheta\vartheta} = 2z_{\vartheta\vartheta}^* - z_0, \tag{33}$$

$$z_{\vartheta\varepsilon} = 2z_{\vartheta\varepsilon}^* - z_0, \tag{34}$$

$$z_y = 2z_y^* - z_0, \tag{35}$$

where

$$z_u^* = z_T^{(0)}, \tag{36}$$

$$z_\vartheta^* = \frac{z_T^{(0)} + z_T^{(1)} tg^2 \vartheta_0}{1 + tg^2 \vartheta_0}, \tag{37}$$

$$z_{\vartheta\vartheta}^* = -\frac{z_T^{(0)} - 2z_T^{(1)} - 3z_T^{(2)} tg^2 \vartheta_0}{1 + 3tg^2 \vartheta_0}, \tag{38}$$

$$z_{\vartheta_\varepsilon}^* = -\frac{1}{2}\frac{(z_T^{(0)} - z_T^{(1)}) + (z_T^{(1)} - 3z_T^{(2)}) tg^2 \vartheta_0}{tg^2 \vartheta_0}, \tag{39}$$

$$z_y^* = z_u^* - T_1 / \cos^2 \vartheta_0. \tag{40}$$

As it follows from (21), (23), (25) and (28), the values $z_u^*, z_\vartheta^*, z_{\vartheta\vartheta}^*$ and z_y^* define the location of an effective plane of reflection and reference planes of space focusing in the middle plane of the mirror.

6. Spatial focusing

The spatial focusing condition in the middle plane, as it is seen from (22), is defined by the equation:

$$K_\vartheta = 0. \tag{41}$$

A root of this equation, hence, a plane coordinate of gauss image for an average plane, is the value $z = z_\vartheta$.

Solving equality (32) together with the equation of the image for a vertical plane yz [1]

$$\frac{1}{z_0 - z_c} + \frac{1}{z - z_c} = \frac{2}{R}, \tag{42}$$

Where $R = z_b - z_c$ - radius of a mirror, and z_c and z_b - location its center and top; one can obtain a condition of stigmatic focusing:

$$z_{1,2} = z_\vartheta^* \pm \sqrt{(z_\vartheta^* - z_c)(z_\vartheta^* - z_b)}. \tag{43}$$

In the plain of gauss image the equalities (19) and (21) can be written down in the form

$$L = \frac{1}{\sin^2 \vartheta_0}\left(z_u^* - z_\vartheta^*\right), \tag{44}$$

$$X = x_0 + 2Ltg\vartheta_0 \sin^2 \vartheta_0. \tag{45}$$

From all aberrations of the second order the greatest interest represents spherical aberration, determined by the factors $K_{\vartheta\vartheta}$ and K_1. The condition of their simultaneous equality to zero at stigmatic focusing (43), i.e. space focusing up to the second order inclusive, is determined by a ratio:

$$z = z_{\vartheta}^{*} = z_{\vartheta\vartheta}^{*} = z_{y}^{*}. \tag{46}$$

7. Spatial time-of-flight focusing

Let us determine locations of interconjugated planes, in which space and time of flight focusing can be simultaneously realized.

At first, we shall define it for a vertical plane. Solving together (13) and (42), one can get a condition of space time-of-flight focusing of the first order:

$$z_{1,2} = z_T^{(1)} \pm \sqrt{(z_T^{(1)} - z_c)(z_T^{(1)} - z_b)}\,. \tag{47}$$

At simultaneous satisfaction of conditions (19) and (47) in a mirror the time-of-flight focusing can be achieved up to the second order including with spatial focusing in a vertical plane.

In the middle plane the condition of spatial time-of-flight focusing is determined by the equality

$$z_T^{(0)} = z_T^{(1)}, \tag{48}$$

followed from (13), (32) and (37). It means, that in the middle plane the spatial time-of-flight focusing is impossible, except for a trivial case $L = 0$ (18).

8. Calculations

Two-dimensional electron mirrors are calculated, with pairs of parallel plates, serving as electrodes, separated by linear gaps *d* (Fig. 1). The axial distribution of effective potential for three-electrode system is described by the expression [3]:

$$\Phi(z) = V_1^{*} + \frac{2}{\pi}\sum_{i=1}^{2}\left(V_{i+1}^{*} - V_1^{*}\right)U\left(z - z_i\right). \tag{49}$$

Here z_i - coordinate z of the middle of i^{th} gap between the electrodes,

$$U(z) = arctg\exp(\pi z)/d\,, \tag{50}$$

and V_1^{*}, V_2^{*} and V_3^{*} - effective potentials at first, second and third electrodes accordingly, which are connected to potentials on electrodes V_1, V_2 and V_3 by the ratio

$$V_i^* = V_i - V_1 \sin^2 \vartheta_0 . \quad (i = 1,2,3). \tag{51}$$

Results of the calculation are submitted in the tables 1-3. In tab. 1 two data groups, determining condition for stigmatic focusing in a two-electrode mirror are given. The data relate to the 1st group when $z_\vartheta^* = z_c$, and to the 2nd - $z_\vartheta^* = z_b$. The second group of data is of interest since an object and its image are out of the mirror field. The conditions for elimination of spherical aberration of the second order in a three-electrode mirror at stigmatic focusing for a case $z_\vartheta^* = z_b$ are submitted in tab. 2. One should note that these data correspond well to the data received by the other method [4]. In tab. 3 the conditions of time-of-flight focusing up to the second order inclusive in a three-electrode plain mirror are presented. The characteristics of the plain flat mirror is that the mode of vertical focusing is picked up so, that the incident parallel beam remains parallel after reflection by the mirror. The considered mode is of great interest at development of time-of-flight mass spectrometers, in which the plain mirror plays a role of a reflector of ions, and their spatial focusing is carried out by electronic lenses.

TABLE I. Two-Electrode Mirrors Creating a Stigmatic Image of an Object

Group	ϑ_0, deg.	φ_2	z_u	z_u^*	$-z_\vartheta^*$	$z_{\vartheta\vartheta}^*$	z_y^*	m_y
	20	-0.0226	0.485	1.95	0.096	4.72	5.59	-1
	25	-0.0147	0.374	1.53	0.266	3.21	3.39	-1
	30	0.0212	0.304	1.30	0.467	3.03	3.54	-1
	35	0.0894	0.262	1.17	0.710	3.32	4.93	-1
1	40	0.183	0.238	1.10	0.991	3.79	7.98	-1
	45	0.293	0.223	1.06	1.29	4.29	13.6	-1
	50	0.409	0.214	1.04	1.60	4.76	23.1	-1
	55	0.526	0.208	1.02	1.91	5.17	39.2	-1
	60	0.638	0.204	1.01	2.20	5.51	66.3	-1
	20	0.0508	0.703	3.06	2.94	113	6.05	1
	25	0.112	0.681	2.93	5.31	159	13.5	1
	30	0.188	0.671	2.87	8.13	207	30.2	1
	35	0.272	0.666	2.84	11.3	251	62.1	1
2	40	0.363	0.663	2.83	14.7	290	118	1
	45	0.457	0.661	2.82	18.1	324	210	1
	50	0.551	0.660	2.81	21.6	352	360	1
	55	0.642	0.659	2.80	25.0	375	603	1
	60	0.728	0.658	2.80	28.2	395	1010	1

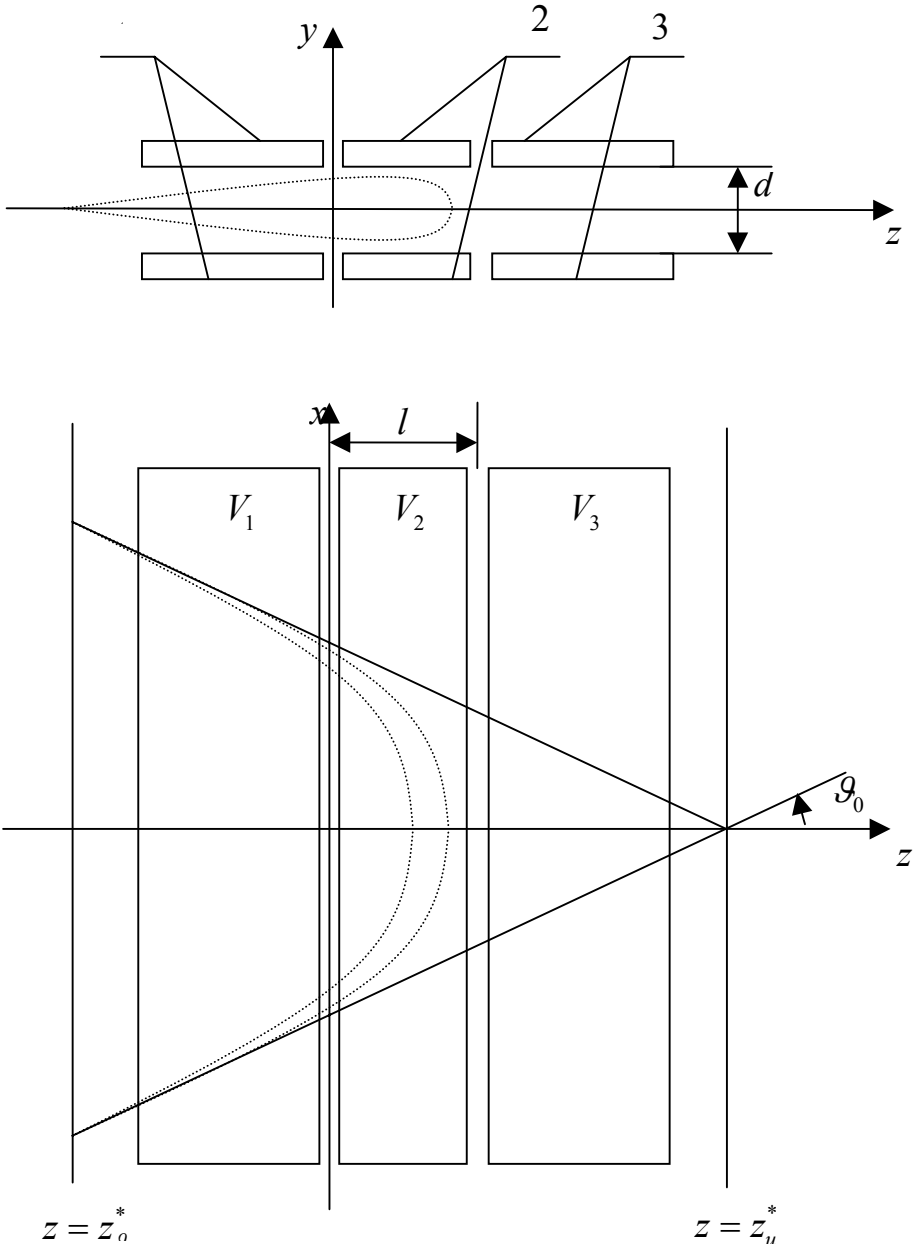


Figure 1. A tree-electrode mirror with parallel electrode plates in two projections. 1-3, the mirror electrodes; $z = z_u^*$, the effective plane of reflection.

TABLE II. Three-Electrode Mirrors Creating a Stigmatic Image of an Object while Elimination Second-Order Spherical Aberrations

ϑ_0, deg.	l	V_2	V_3	z_u	z_u^*	$-z_\vartheta^*$
25	1.20	0.214	0.106	1.15	4.73	2.46
30	1.19	0.284	0.173	1.11	4.46	3.94
35	1.18	0.361	0.255	1.10	4.34	5.71
40	1.18	0.442	0.346	1.10	4.28	7.70
45	1.17	0.525	0.441	1.09	4.22	9.72
50	1.17	0.608	0.538	1.09	4.22	11.9

TABLE III. Time-of-flight focusing up to the 2nd order in three – electrode mirror

l	V_2^*	$-V_3^*$	z_u	z_u^*	L
1.1	0.0251 0.114	0.139 0.262	0.942 0.971	3.69 3.10	28.1 8.66
1.2	0.0548 0.115	0.140 0.249	1.08 1.07	4.10 3.43	22.0 8.09
1.3	0.702 0.115	0.152 0.248	1.18 1.15	4.34 3.72	16.2 6.75

References

1. E.M. Yakushev and L.M. Sekunova. // Adv. Electronics and Electron Physics. 68: 337. (1986).
2. S.B.Bimurzaev , R.S.Bimurzaeva , B.T.Sarkeev. R & E. №11. 36: 2186. (1991).
3. Glikman L.G., E.M. Yakushev. JTF, 37: 2097. (1967).
4. S.P.Karetskaya, L.G.Glikman, L.G.Beizina and Yu. V.Goloskokov. // Adv. Electronics and Electron Physics. 89: 391. (1994).

INVESTIGATION OF PARTICLE CORRELATIONS BY THE METHOD OF DEFINITION OF RAPIDITY INTERVALS DENSITY IN INELASTIC COLLISIONS OF NUCLEI

E.G. Boos, M. Izbasarov, N.N. Zastrozhnova

Institute of Physics and Technology, MES RK, Almaty, Kazakhstan

Abstract

In this work the new method of the multiparticle correlations has been proposed. *CC* and *CTa* - interactions at 4.2 A GeV/c have been analysed. It is shown that the experimental data (*CC* - interactions) are well agree with predictions of cascade model. However, for *CTa* - interactions considerable distinction from a model predictions is observed.

The research of multiparticle correlations has the important value to study the multiple particle production processes, proceeding in small phase volume. In the present paper the new technique is developed which uses the information on filled quasi-rapidity intervals [1]. Carbon - carbon (*C-C*) and carbon – tantalum (*C-Ta*) interactions with high multiplicity at momentum 4,2 GeV/c have been analysed on the basis of this new technique.

As a variable for the analysis quasi-rapidity $y = \frac{1}{2} \ln [(p+p_{11}) / (p- p_{11})]$ is used, where p and p_{11}- total and longitudinal momenta of secondary particles.

We designate the rapidity interval restricted by i- th and (i+k) -th particle as $G_k = y_{i+k} - y_i$ and enter concept "density" of intervals ε_k

$$\varepsilon_k = \frac{k}{G_k}$$

In the indicated interval $k+1$ particles and k non-filled rapidity intervals are available.

For events with fixed number of secondary charged particles (n) average density of rapidity intervals $<\varepsilon_k^n>$ for every k

$$<\varepsilon_k^n> = \frac{\sum_{i=1}^{n-k} \varepsilon_k^i}{n-k}$$

and average density on all events (N)

$$< \varepsilon_k > \; = \; \frac{\sum_{i=1}^{N} < \varepsilon_k^n >_i}{N}$$

were determined.
The a probability density of a normal distribution

$$P\left(< \varepsilon_k^n > \right) = \frac{1}{\sqrt{2\pi}\ \sigma_k} \exp \left[\frac{\left(< \varepsilon_k^n > - < \varepsilon_k > \right)^2}{2\,\sigma_k^2} \right]$$

where

$$\sigma_k^2 = \frac{\sum_{N=1}^{N} \left(< \varepsilon_k^n > - < \varepsilon_k > \right)^2}{N}$$

were defined for each k hypothesis.
Then we obtain a probability density

$$W = \prod_{k=1}^{n-1} P(< \varepsilon_k^n >)$$

for each event.

The distributions of a log of the accumulated probability densities *LnW* for various fixed numbers of secondary charged particles in CC and *CTa* - interactions are represented in a fig.1. For considered types of nuclei collisions the calculations on cascade model [2] are also given. It is seen, that for carbon - carbon collisions (Fig. 1a) the experimental data are well agree with predictions of cascade model (solid line). However, for *CTa* - interactions (fig. 1б) with growth of multiplicity noticeable distinction of experimental data from a model predictions is observed. Obviously, it may be connected with the fact that in inelastic collisions of heavy nuclei at large multiplicities the role of secondary charged particles correlation is more essential.

The dependence of average density $< \varepsilon >$ from number of non-filled rapidity intervals k for various fixed numbers of secondary charged particles is show in fig.2. From a figure it is seen, that at *k=1* the average density for *CC* and *CTa* - interactions is high, and with increase of multiplicity it grows. It especially is very noticeably for *CTa* - interactions. Here calculation data for cascade model are also shown.

The experimental data (*CC* - interaction) are not bad coincided with predictions of model, but for *CTa* - interactions with growth of multiplicity some difference is observed.

At $k \geq 2$ dependences of average density $<\varepsilon>$ from k is identical for *CC* and *CTa* - interactions. The model also shows the similar dependence.

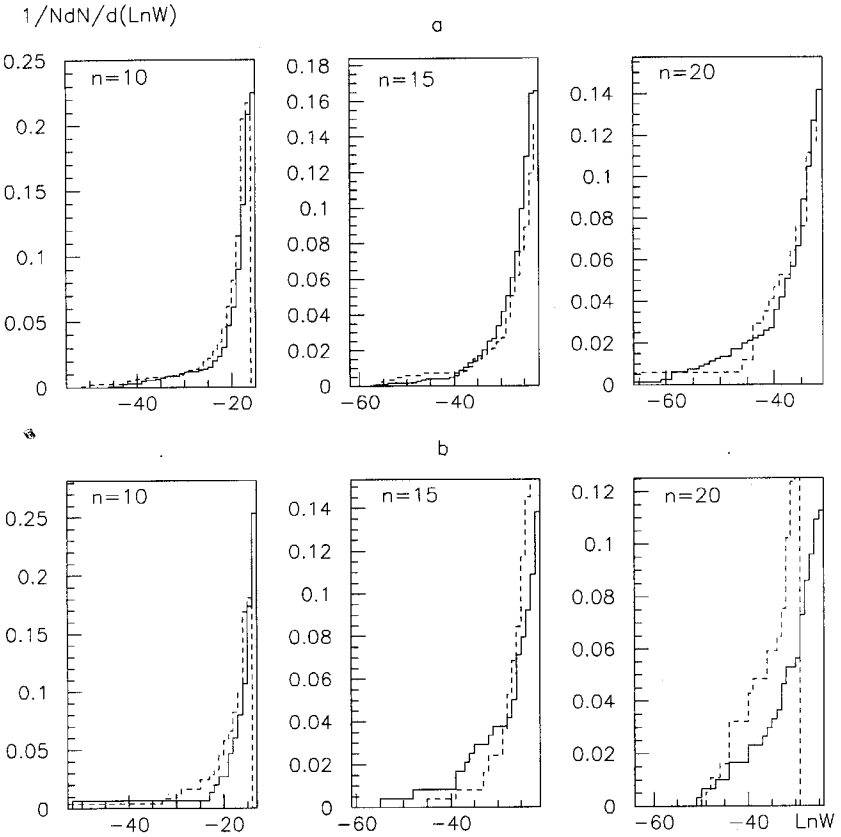
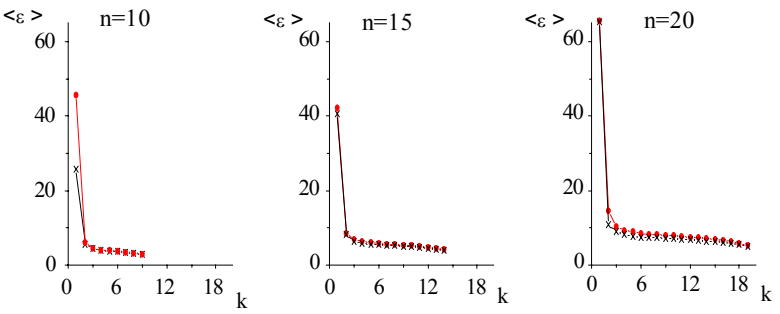


Fig.1. The distributions of a log of the accumulated probability densities *LnW* for various fixed numbers of secondary charged particles.
Solid line - predictions of cascade model.
a) *CC* - interactions at 4.2 A GeV/c
b) *CTa* - interactions at 4.2 A GeV/c

CC



CTa

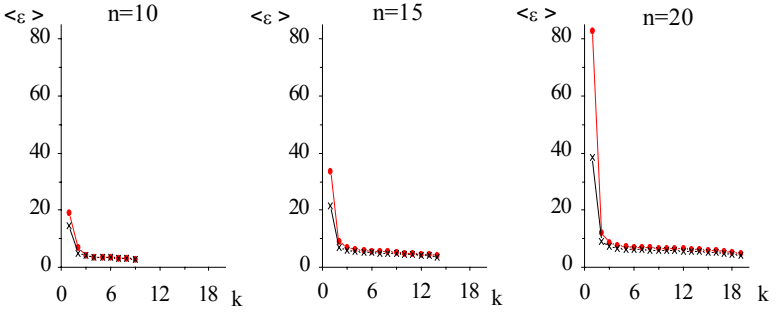


Fig.2. The dependence of average density $<\varepsilon>$ from number of non-filled rapidity intervals k for various fixed numbers of secondary charged particles.
• – the experimental data; **x** – predictions cascade model.
a) *CC* – interactions at 4.2 A GeV/c
b) *CTa* – interactions at 4.2 A GeV/c

References

1. E.G. Boos et al. - Zeitschrift fur Phyzik. A351, p. 209-215, 1995.
2. K.K. Gudima, V.D. Toneev – Nucl. Phys, т.27, with. 658-677,1978, Nucl. Phys., V.A400, p.173, 1983.

MASS DEPENDENCE OF MACROSCOPIC AND SEMI-MICROSCOPIC POTENTIAL PARAMETERS FOR ALPHA-PARTICLES IN THE RANGE OF ENERGIES 20 - 80 MeV

[1]K.A. Kuterbekov, [1]T.K. Zholdybayev, [1]B.M. Sadykov, [1]A. Mukhambetzhan, [2]Yu. E. Penionzhkevich, [2]I.N. Kukhtina

[1]Institute of Nuclear Physics of National Nuclear Center RK, Almaty, Kazakhstan
[2]Joint Institute for Nuclear Research, Dubna, Moscow region, Russia

Global mass dependences of optical potential for α-particles with energies up to 80 MeV have been received. A Woods-Saxon form-factor for macroscopic potential has been used and recommendations from works of M. Nolte, H. Machner, J. Bojowald about global dependences at energies higher than 80 MeV and L.W. Put and A.M.J. Paans about geometry of optical potential have been taken into account. Energy and mass dependences of the semi-microscopic α-particle potential parameters have been investigated for the first time. In general, a good description of elastic and inelastic differential and total reaction cross sections for different nuclei using the revealed global parameters has been received within the framework of macroscopic and semi-microscopic approaches.

I. Introduction

Macroscopic and semi-microscopic analyses of angular distributions of differential cross sections (ADDS) for α-particle scatterings are the important source of information about matter distribution in nuclides and properties of the potential of nucleus-nucleus interaction.

Optical potential (OP) parameters of α-particle interaction with nuclei at low and intermediate energies received from the analysis of ADDS of elastic scattering within the framework of optical model (OM) are exposed to considerable ambiguities and require reliable estimations [1, 2]. It is very important for receiving of detailed information about nuclear structure (parameters of deformation lengths, ratio of neutron and proton components, etc.) in the framework of up-to-date potential approaches (OM, methods of coupled channels and distorted waves). Global optical potential on the basis of data on elastic scattering of ^{90}Zr has been received in the work [3] for α-particles at energy above 80 MeV. At that the recommendations about parameter geometry OP and its dependencies upon energy received by Put and Paans has been used [4]. Up to present time there were no successful global potentials because of increase of strong absorption with energy up to 80 MeV. Effects of strong absorption lead to two types of OP ambiguities. It is discrete ambiguities often shown through depth value of real part of potential corresponding to changes necessary for conditions of

phase equivalence [5]. Continuous ambiguities forming potential family characterized by equal behavior near nuclear surface exists for each of discrete parameter number. Pointed ambiguities of OP need a search of physical situations that could restrict them.

Differential and total reaction cross sections with energy above 80 MeV for nuclei from A=12 – 124 have been calculated and their systematic analysis has been carried out firstly within the framework of the double folding model [6] on the basis of full M3Y-effective interaction and nucleon densities calculated for all collided nuclei by the method of density functional.

Inclusion in analysis together with ADDS of elastic scattering and values of total reaction cross sections allows limiting ambiguities of OP parameters since data on differential and total reaction cross sections are the main nuclear values received from OM. Theoretical model pretended to full description of data must render both experimental ADDS and total reaction cross sections with the same number of entering parameters. Nowadays there are not many works where analysis has two these values simultaneously in one model. Choice of optimal parameters of macroscopic OP and folding model [6] further allows receiving reliable information about structure of excited state of investigated nuclear.

This work firstly proposes the global mass dependence of parameters of macroscopic OM and semi-microscopic folding model (SFM) for α-particles in weakly studied energy range.

2. Experimental data for global analysis

We selected and compiled the initial experimental material including results of our work [7-13] and literature sources for building of desired global dependence of potential parameters of α-particle interaction.

The main characteristics of experimental conditions when ADDS have been received are shown in table 1. Information published in corresponding works [4, 7-10, 11] are shown for literature data.

Experimental ADDS from works [10,12,13] including into analysis have been received at isochronous cyclotron U-150M using the registration system and identification of reaction products on the complex base CAMAC-PC/AT [14].

In works [10,12,13] the systematic error in scattering ADDS is connected mainly with uncertainties: target thickness (4-6%), solid angle of spectrometer (1%), calibration of current integrator and did not exceed 10%. Statistic error of analyzed data comprises 1-5% and only in some cases (in minimums of ADDS at large angles) reaches 6-15%. All used targets produced by the method of thermal evaporation are self-bearing. Target thickness has been defined according to α-particle energy loss of radioactive source ^{241}Am-^{243}Am-^{244}Cm and ^{239}Pu. Errors of absolute values of cross sections in scattering ADDS in published data [4, 7-10, 11] comprise 5-10%.

Experimental values of total reaction cross sections σ_R which errors comprised 4-7% in investigated energy are taken from work [10] and other sources.

Table 1. Main characteristics of the experiment on elastic scattering of α-particles

Nuc-leus	E_α, MeV	Target		Angular diapason (deg., c.m.)	Reference
		thickness (mg/cm^2)	Compositi on (%)		
For mass A-dependence					
^{12}C	50.5±0.5	1.1-2.0	98.9	13-173	[12]
^{24}Mg	50.5±0.5	1.0-3.2	99.1	12-172	[12]
^{28}Si	50.5±0.5	0.59 –0.76	92.17	11-171	[12]
^{48}Ti	50.5±0.5	4.5±0.08	99.2	24-64	[12]
^{50}Ti	50.5±0.5	3.15±0.08	83.2	32-84	[13]
^{58}Ni	50.5±0.5	0.56	99.5	20-65	[12]
^{68}Zn	50.5±0.5	3.48±0.08	91.2	16-76	[12]
^{70}Zn	50.5±0.5	3.10±0.08	95.0	16-66	[12]
^{90}Zr	50.1±0.5	2.13±0.08	95.0	16-75	[10]
^{94}Zr	50.1±0.5	2.60±0.08	91.2	12-75	[10]
^{120}Sn	50.5±0.5	2.20±0.08	99.2	10-63	[12]
^{124}Sn	50.5±0.5	2.00±0.08	95.1	10-65	[12]

3. Data analysis and global dependence of potential parameters

3.1. Macroscopic optical model analysis

Complex optical potential $U(\vec{r})$ with Woods-Saxon form-factor for real and imaginary parts in the case of α-particles scattering has a standard form:

$$U(\vec{r}) = V(1+\exp\frac{r-R_V}{a_V})^{-1} + iW(1+\exp\frac{r-R_W}{a_W})^{-1} + V_C(r). \qquad (1)$$

In this formalities OP is characterized by six parameters: depths of real V and imaginary W of particles, their corresponding to radial parameters R_v and R_w and diffuseness parameters a_v and a_w at the nucleus periphery. $V_c(r)$ corresponds to Coulomb potential of uniformly charged sphere with radius $R_c=1.25\ A^{1/3}$ fm.

Experimental ADDS of elastic scattering of α-particles in present work were analyzed within the framework of deformed OM potential using code SPI-GENOA [15]. Potential parameters met to optimal correspondence of experimental

and theoretical cross section values were found by minimization of the following value

$$\chi^2 = \frac{1}{N}\sum_{i=1}^{N}\left[\frac{\sigma^T(\theta_i)-\sigma^E(\theta_i)}{\Delta\sigma^E(\theta_i)}\right]^2 , \qquad (2)$$

where N- number of experimental points in angular distribution, σ^{T} and σ^{E}- calculated and measured value of differential cross section of scattering at angle of θ_i, and $\Delta\sigma^{E}$- value uncertainty $\sigma^{E}(\theta_i)$.

Optimal OP parameters were selected in such way, in order to reach the best agreement within the framework of joint analysis ADDS scattering and data on total reaction cross sections, description of "transparency effect" [7,16] for nuclei with A=90 and tendency of value change of volume integral J_R^P from real part [2].

In concluding part of the present work the optimal OP parameters received by us keeping above mentioned criterions were described using the following expressions for all six OP parameters:

$$V(A,Z,E_\alpha)=a_0+a_1ZA^{-1/3}+a_2E_\alpha \ , \quad W(A,Z,E_\alpha)=b_0+b_1A^{1/3}+b_2E_\alpha \ , \qquad (3)$$

$$r_V= c_0+c_1A^{1/3}+c_2E_\alpha \ , \quad r_W= d_0+d_1A^{1/3}+d_2E_\alpha \ , \qquad (4)$$

$$a_V= e_0+e_1A^{1/3}+e_2E_\alpha \ , \quad a_W= f_0+f_1A^{1/3}+f_2E_\alpha \ . \qquad (5)$$

We can note that expressions (3) for depth dependence of real and imaginary part of OP are similar to the part which was received by Nolte and Machner [3] for α- particles with energy above 80 MeV and F.G. Perey [17] for nucleons. Term which is proportional to $Z/A^{1/3}$ was adopted by F.G. Perey [17] for effect calculation appeared due to Coulomb repulsion: average coulomb potential on nuclear surface is proportional to Z/R and, correspondingly, to the value $Z/A^{1/3}$. A linear dependence from nucleus radius and energy E_α of incident particles was adopted for the depth of imaginary part of potential in the case of α- particles.

3.1.2. Mass dependence

There were studied mass dependence of OP parameters for α-particles with energy ~ 50 MeV at nuclei ^{12}C, ^{24}Mg, ^{28}Si, ^{48,50}Ti, ^{58}Ni, ^{68,70}Zn, ^{90,94}Zr, ^{120,124}Sn in the energy range up to 80 MeV on the basis of experimental data [10, 12, 13], received in the Institute of Nuclear Physics NNC RK.

Used algorithm of the OP parameters adjustment was the same as at investigation of energy dependence. The received values of optimal parameters of macroscopic OP are presented in table 3.

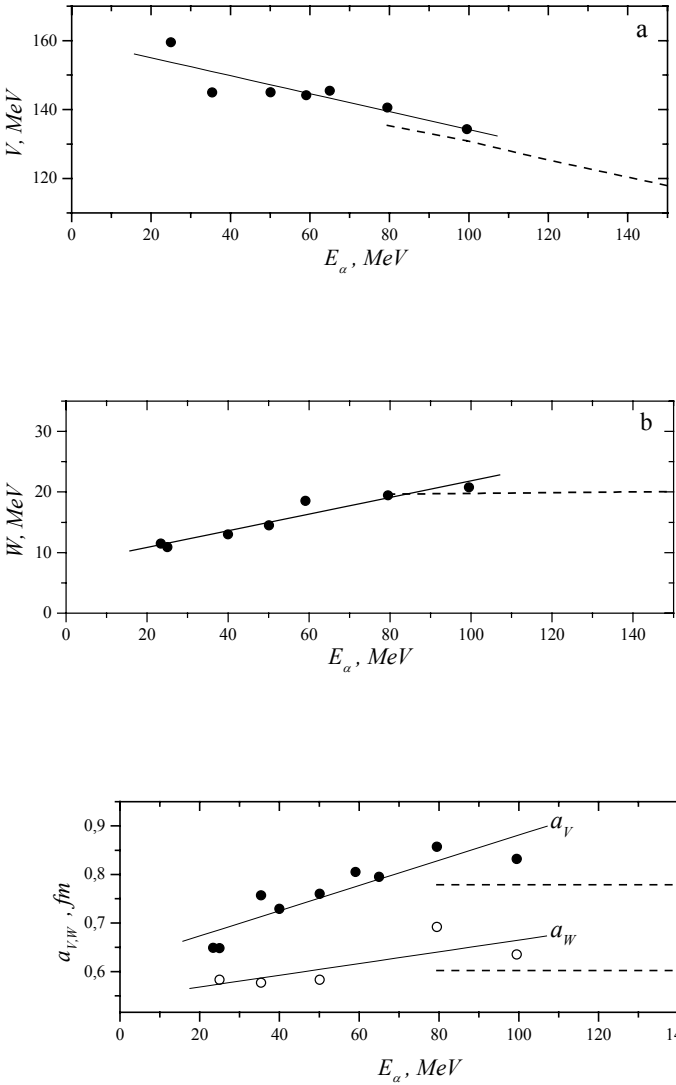


Fig. 1. Energy dependence of macroscopic OP-parameters: *a* – depth of real part; *b* – depth of imaginary part; *c* - radii r_v and r_w; *d* - diffusenesses a_v and a_w. Solid lines – global dependencies received in the present work; dash lines – in [3].

Table 2. Optimal values of OP parameters for different nuclei at E_α = 50.5 MeV.

Nuc-leus	V, *MeV*	r_v, *fm*	a_v, *fm*	W, *MeV*	r_w, *fm*	a_w, *fm*	χ^2/N	$J_r/4A$, MeV•fm^3
^{12}C	108.40	1.228	0.747	20.064	1.551	0.688	28.40	357
^{24}Mg	111.85	1.256	0.776	24.138	1.578	0.591	25.94	330
^{28}Si	118.80	1.247	0.808	19.018	1.570	0.716	14.81	350
^{48}Ti	123.62	1.246	0.806	24.925	1.571	0.559	14.16	329
^{50}Ti	128.24	1.245	0.766	18.804	1.570	0.643	3.82	330
^{58}Ni	140.78	1.247	0.760	17.492	1.571	0.650	4.12	356
^{68}Zn	163.73	1.246	0.776	29.685	1.572	0.509	16.42	408
^{70}Zn	130.97	1.245	0.824	23.106	1.580	0.601	17.61	332
^{90}Zr	144.13	1.245	0.805	18.550	1.570	0.510	6.49	351
^{94}Zr	135.93	1.246	0.782	16.623	1.573	0.628	8.30	327
^{120}Sn	147.88	1.245	0.750	15.841	1.570	0.580	2.66	343
^{124}Sn	142.79	1.245	0.763	15.144	1.570	0.658	2.65	331

Fig. 2 shows satisfactory description of experimental ADDS of elastic scattering for α-particles with energy 50.5 MeV at nuclei with A=12-124. It is seen from the value analysis χ^2/N (table 2) that they increase with decrease of mass number A. This evidences that the adopted geometry or dependence of OP parameters is worse with larger a target nucleus differs in mass from ^{90}Zr, in particular at nucleus ^{12}C. A number of experimental and theoretic investigations of scatterings at light nuclei [18] show that there is an anomalous growth of cross sections at the large angles in ADDS of elastic scattering at nucleus ^{12}C in investigated energy range. This effect cannot be explained within the framework of standard OM as it is caused by other mechanisms including mechanism of alpha-cluster exchange between incident particle and target nucleus. So, during the analysis of experimental ADDS we paid a special attention to quality of data analysis for angles up to 90^0, where the potential scattering is the main mechanism.

Changing tendency of experimental values on total reaction cross sections σ_R from mass number A in investigated field of energies of α-particles is well described by the received number of parameters for macroscopic OP (fig.3). Since no measured data on σ_R at $E_\alpha \sim 50$ MeV we have used for testing its mass dependence the experimental values σ_R obtained in [10] and other published sources at energies 40 MeV [19] and 69.6 MeV [20]. Fig. 3 shows that the theoretical dependencies of σ_R are in satisfactory correspondence with the mentioned experimental values.

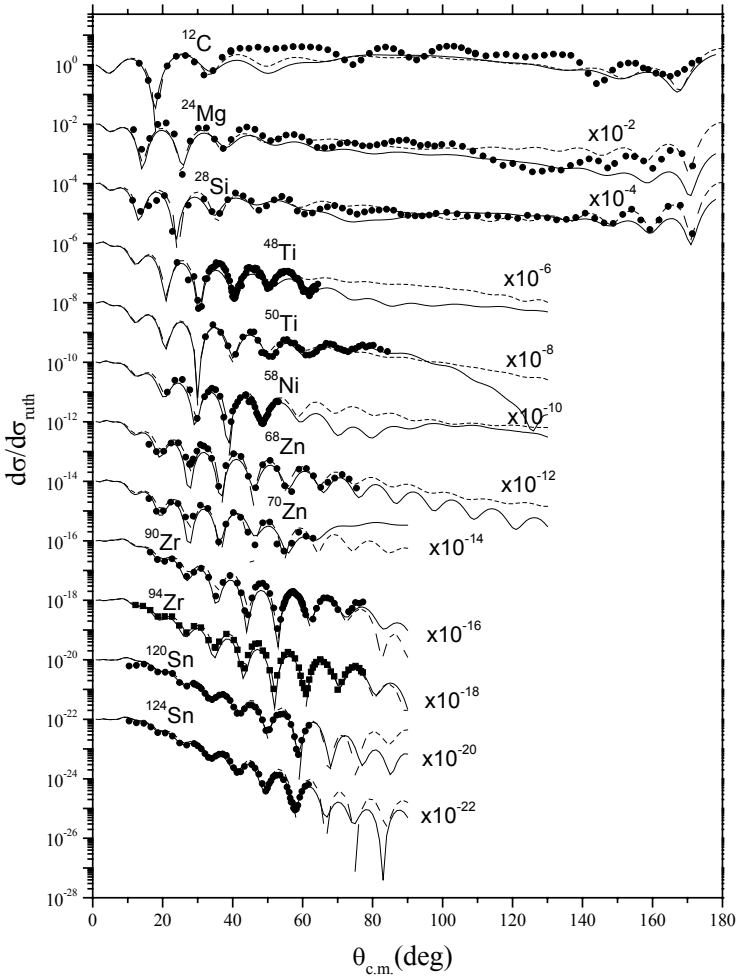


Fig. 2. Angular distributions of differential cross-sections of elastic scattering for α–particles with $E_\alpha \sim 50$ MeV at nuclei A=12-124. Points – experimental data, solid lines – macroscopic OM, dash lines – semi-microscopic folding-model.

Use as a selection criterion of OP value of volume integral J_R^P showed (table2) that its value changes weakly for different mass numbers at $E_\alpha \sim 50$ MeV being in the interval $J_R^P \sim (330\text{-}360)$ MeV•fm^3.

The received (based on data from table 2) global mass dependence of OP parameters at $E_\alpha = 50.5$ MeV is approximated by linear dependence (fig. 4). They can be analytically presented in the following form:

$$V=93.838+5.177\bullet Z\bullet A^{-1/3},\ W=28.122-2.202\bullet A^{1/3}, \quad (6)$$

$$r_v=1.241+0.00066\bullet A^{1/3},\ r_w=1.563+0.0011\bullet A^{1/3}, \quad (7)$$

$$a_v=0.840-0.0141\bullet A^{1/3},\ a_w=0.705-0.0222\bullet A^{1/3}. \quad (8)$$

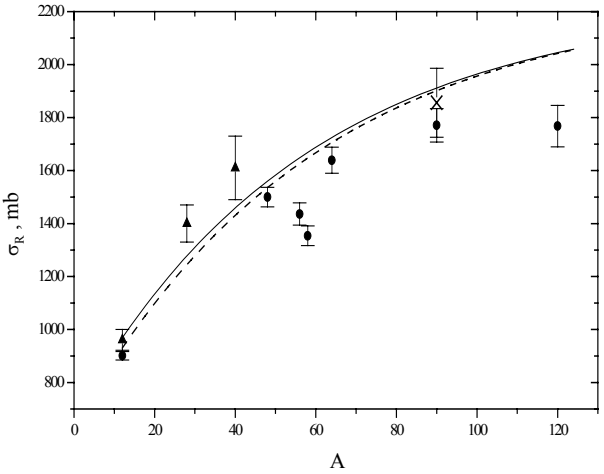


Fig. 3. Total reaction cross sections for α–particles with $E_\alpha \sim 50$ MeV at nuclei A=12-124. Experimental data: crosses denote sections for 50.1 MeV [10], circles – 40 MeV [19], triangles – 69.6 MeV [20]. Theoretical values of total reaction cross sections are shown for macroscopic OP by the solid line, for semi-microscopic model – by the dash line.

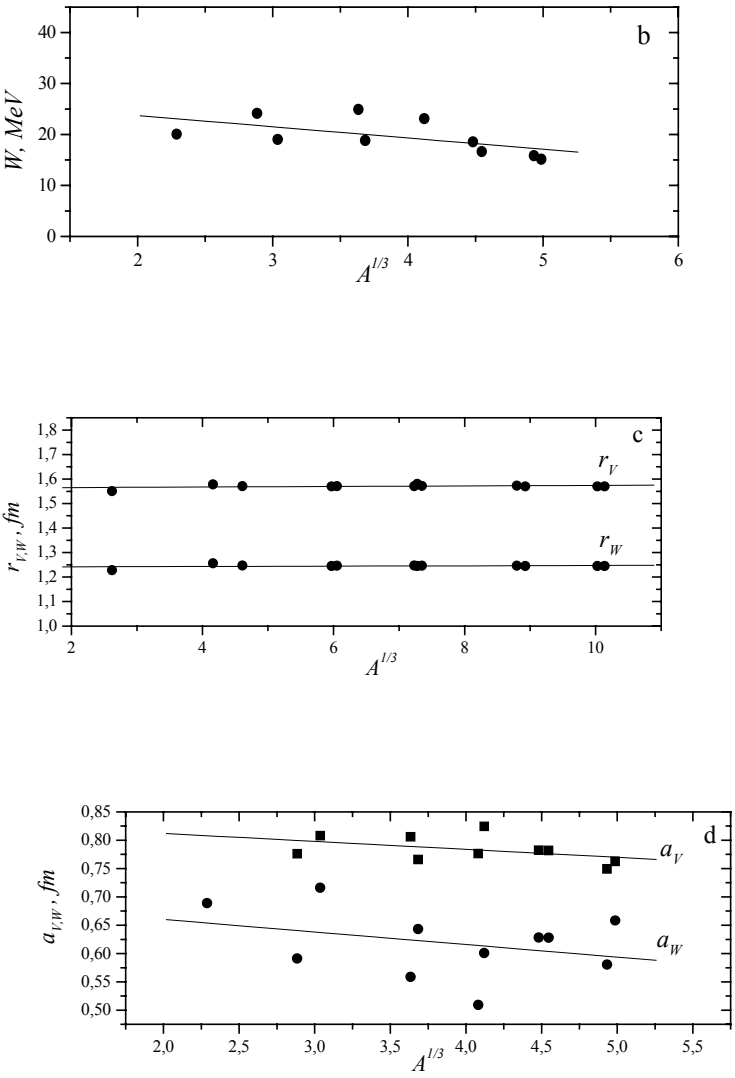


Fig. 4. Mass dependence of parameters OP: *a* – depth of real part; *b* – depth of imaginary part; *c* - radiuses r_v and r_w ; *d* - diffusenesses a_v and a_w. Firm lines – global dependencies received in the present work.

3.2. Global semi-microscopic data analysis

Semi-microscopic optical potential $U(R)$ is built within the framework of folding-model on the basis of full M3Y-effective interaction and nucleon densities calculated under the method of density matrix functional [6]. Interaction potential of two collided nuclei in the first order on effective forces can be presented as:

$$U(R) = U^E(R) + U^D(R), \quad (9)$$

where $U^D(R)$ – "direct" potential of double folding model [1]:

$$U^D(R) = \iint \rho^{(1)}(r_1) V^D(s)\ \rho^{(2)}(r_2) dr_1\, dr_2\,. \quad (10)$$

The term $V^D(s)$ in expression (9) is a direct component of effective interaction $(s = r_2 - r_1 + R)$, $\rho^{(i)}(r_i)$ are densities of collided nuclei (i =1, 2). Such calculation scheme of "exchange" potential $U^E(R)$ is described in [6]. The effects of one-nuclide exchange, which are described in formality of density matrix [21] give the main contribution in it:

$$U^{EX}(R) = \iint \rho^{(1)}(r_1, r_1 + s) V_{EX}(s)\ \rho^{(2)}(r_2, r_2 - s) \exp(ik(R)\, s/\eta)\, dr_1\, dr_2\,, \quad (11)$$

where $V_{EX}(s)$ – exchange part of effective nucleon-nucleon forces, $\rho^{(i)}(r, r')$, $(i=1, 2)$ – density matrix of collided nuclei with mass numbers A_1 and A_2, $k(R)$ – local impulse of relative movement of nuclei determined by the ratio

$$k^2(R) = (2m\eta/\hbar^2)[E - U(R) - V_c(R)]. \quad (12)$$

Here $\eta = A_1 A_2 / (A_1 + A_2)$, $s = r_2 - r_1 + R$, E – energy in the center-of-mass system of and $V_c(R)$ – Coulomb potential. Thus, net potential depends upon energy because of effects of one-nucleon exchange. Initial data for calculation of potentials are effective nucleon-nucleon forces and proton and neutron densities of collided nuclei.

Full optical potential SFM besides real part should include the imaginary part responsible for incident particle absorption in inelastic channels. In our case we built potential of absorption depended on calculated real part in the form [22]:

$$W(R) = i\,[N_w U(R) - \varphi_w\, R\, dU(R)/dR]\,, \quad (13)$$

where $U(R)$ – potential of double folding (8) and N_w and φ_w – parameters that characterize volume and surface parts of absorption potential, correspondingly. A surface term imitating the contribution of dynamic polarized potential is introduced in the real part of the potential [23]. Full optical potential SFM has the following form:

$$U_t(R) = U(R) - \varphi_v\, dU(R)/dR + i\,[N_w U(R) - \varphi_w\, dU(R)/dR]\,, \quad (14)$$

where φ_v, N_w, φ_w are varying parameters.

At calculation of ADDS of inelastic scattering the form-factor of inelastic transition has a form $\varphi_L \dfrac{dU_t(R)}{dR}$ [23].

In frameworks of SFM we have carried out global mass analysis of the same experimental data (as well as at investigation a macroscopic OM) in explored region of α-particles energies for the nuclei with A=12-124.

Theoretical cross sections of elastic scattering are calculated under the modified version of the program ECIS-88 [24] (ECIS-PM), in which semimicroscopic potentials are constructed as in the formula (14). The adjustment theoretical ADDS of elastic scattering and values σ_R to experimental data was carried out by a variation of parameters φ_v , N_w, φ_w. One should mention that at the joint analysis of differential and total reaction cross sections the SFM parameters are determined uniquely.

In the present work the nucleon densities for α-particles were calculated in Gaussian representation with root-mean-square radius 1.57 fm [3], and for nucleus - targets the densities were calculated by the density-functional method [21].

At examination of mass dependence of parameters SFM for α-particles with energy 50.5 MeV a good agreement between theoretical and experimental ADDS of elastic scattering and total reaction cross sections on the nuclei with A=12-124 (fig. 2-3) is obtained. It once again confirms reliability of the theoretical sections calculated using discussed above semimicroscopic approach. From fig. 2 it is possible to see, that the more light nuclei - target, the theoretical sections to experimental ADDS are worse adjusted. Thus, in a region of angles up to 60 degrees the theoretical sections, as a rule, well describe the experimental data. We have revealed that the values of adjusted SFM parameters in the angular range to 30 deg. influence slightly to the theoretical curve since at small angles the section value, mainly, is determined by the contribution from the real part of the total full microscopic potential (14). In the angular diapason 30-60 deg. the experimental elastic scattering ADDS and values for total reaction cross-sections are described well only with adjustment of all SFM parameters. The discrepancy of theoretical and experimental ADDS at larger angles, in particular on the ^{12}C nucleus, apparently means that other reaction mechanisms begin to play an essential role.

In table 3 the root-mean-square radii for a density distribution of protons, neutrons and matter, and also their difference Δr_{np} for nuclei-targets are presented. It shows, that for the nuclei ^{12}C, ^{24}Mg and ^{28}Si the magnitude of densities distribution radii for protons exceed the same for neutron, and for the remaining nuclei (A=48 -124) – visa versa, except for the nucleus ^{58}Ni.

Table 3. Root-mean-square radii (in fm) of neutron, proton and matter density distributions, and also the difference $\Delta r_{np}=\langle r_n^2\rangle^{1/2} - \langle r_p^2\rangle^{1/2}$ at E_α= 50.5 MeV.

Nucleus	$\langle r^2_n\rangle^{1/2}$ *fm*	$\langle r^2_p\rangle^{1/2}$ *fm*	$\langle r^2_m\rangle^{1/2}$ *fm*	Δr_{np} *fm*
^{12}C	2.39	2.41	2.40	-0.02
^{24}Mg	2.84	2.86	2.85	-0.02
^{28}Si	2.95	2.98	2.97	-0.03
^{48}Ti	3.41	3.37	3.39	0.04
^{50}Ti	3.45	3.38	3.42	0.07
^{58}Ni	3.67	3.67	3.67	0.00
^{68}Zn	3.87	3.81	3.84	0.06
^{70}Zn	3.97	3.86	3.93	0.11
^{90}Zr	4.26	4.19	4.23	0.07
^{94}Zr	4.37	4.24	4.31	0.13
^{120}Sn	4.71	4.59	4.66	0.12
^{124}Sn	4.77	4.61	4.70	0.16

In the table 4 the integrated characteristics of 50.5 MeV α-particles interaction potentials for isotopes with A=12-124 in the frameworks SFM is presented: J_V - volume integrals, $\langle r^2_{sfm}\rangle^{1/2}$ - root-mean-square radii of the folding-potentials.

Table 4. SFM parameters, volume integral J_V in ($\bullet 10^3$ MeV$\bullet$fm^3) and root-mean-square radii r_{sfm} in fm for folding-potentials for the nuclei with A=12-124 at E_α=50.5 MeV.

Nucleus	φ_v	N_W	φ_w	J_V	$\langle r^2_{sfm}\rangle^{1/2}$
^{12}C	0	0.37	0	-17.36	3.45
^{24}Mg	0	0.27	0.012	-30.82	3.77
^{28}Si	0	0.26	0.010	-41.16	3.99
^{48}Ti	0	0.25	0	-60.40	4.27
^{50}Ti	0	0.26	0.021	-62.75	4.30
^{58}Ni	-0.011	0.22	0.012	-80.13	4.50
^{68}Zn	-0.015	0.21	0.022	-93.95	4.69
^{70}Zn	-0.010	0.24	0.023	-96.69	4.73
^{90}Zr	0.052	0.11	0.010	-123.9	4.99
^{94}Zr	0.053	0.13	0.010	-129.6	5.07
^{120}Sn	0.051	0.104	0.007	-165.2	5.39
^{124}Sn	0.051	0.13	0.007	-170.5	5.44

From the table 4 one can see, that the volume integral J_V increases by its absolute value with increase of mass number at fixed energy E_α of an incident α-particle. The magnitudes of root-mean-square radii (tab. 4) of folding-potentials also are increased with increase of A at energy E_α =50.5 MeV.

It is established, that between the SFM parameters there are no noticeable correlation and the submitted sets (table 4) of parameters for each of the nuclei–targets are optimal. Errors for SFM parameters are 1 %. Parameter φ_v influences phase shifts in ADDS to the right or to the left depending on its sign. The tendencies of the parameter φ_v modification with increase of a mass number of a nucleus - target are as follows (fig.5): for nuclei-targets with A = 12-50 values of this parameter are equal to zero, i.e. there is no phase shift. For nucleus-targets with A= 58-70 values of the parameter φ_v are negative, i.e. without introduction of the parameter φ_v the theoretical curve would be moved to the right from the experimental points. For moderate heavy nuclei (A=90-124) the magnitude φ_v is, on the contrary, positive and shifts the curve to the left. If observe the dependence of an imaginary part of a potential, one could conclude that the parameter N_w, gradually decreases with growth of mass number, and the value of parameter φ_W , first, grows with increase of A, reaches a maximum at A=70, and then monotonically decreases. Since the dependence of φ_v -parameter on mass number at fixed energy E_α =50.5 MeV is quite complex, fig.5a presents interpolation of its optimal values. Analytical approximation of the parameters N_w and φ_W by a linear dependence of mass number A (fig. 5 b,c) by the least square method has the following form:

$$N_W = 0.3469 - 0.0021 \bullet A \;\; ; \;\; \varphi_w = -0.01030 + 0.00001 \bullet A \; . \qquad (15)$$

The absence of experimental ADDS of scattering and values of total reaction cross section on the nuclei with A>124 at E_α =50.5 MeV has not allowed to trace a course of dependence of SFM parameters from a mass number for nucleus – targets beyond this region.

4. Results and discussion

Within the framework of a macroscopic OM and semimicroscopic model a good description of differential and total reaction cross section, tendencies of a volume integral of a real part magnitude change, effect of "transparency" (for the nuclei with A=90) with α-particles involved in the energy range up to 80 MeV at the investigated nuclei were obtained. We have verified how the obtained global potential describes experimental ADDS of inelastic scattering for α-particles.

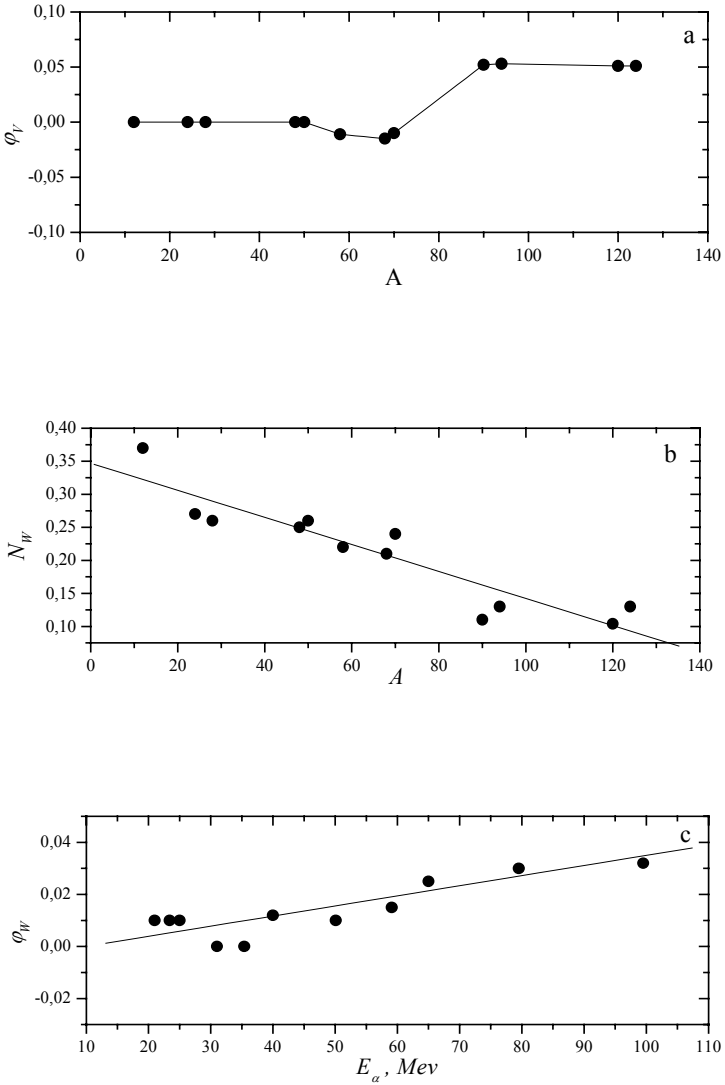


Fig.5. Mass dependence of the SFM potential parameters: points - optimal values, solid lines - approximation by a linear fit.

At testing of global dependencies of the parameters for macroscopic OP and SFM approaches, quite satisfactory description of ADDS for inelastic scattering with excitation of low lying collective states of the nuclei is obtained. In fig. 6 on an example of the nucleus ^{124}Sn the analysis of ADDS for inelastic scattering of 50.5 MeV α-particles is carried out within the framework of a method of coupled channels (MCC) by ECIS-PM and distorted waves (DWBA) by the code DWUK4 [25].

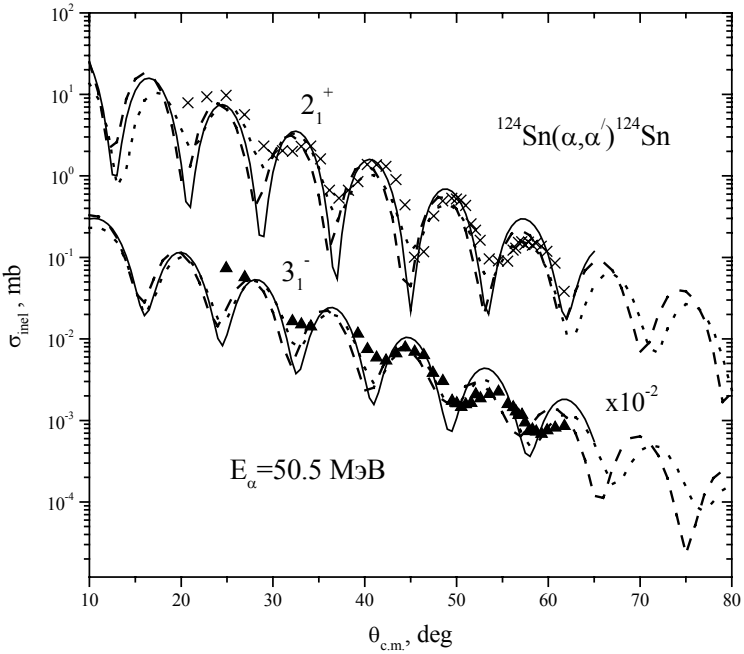


Fig. 6. Angular distribution of inelastic scattering of α-particles on the nuclei ^{124}Sn (points - experiment, solid curve – semimicroscopic folding model, dot line - macroscopic analysis on MCC for 2_1^+ and 3_1^- states, dash line - DWBA) at $E_α$ = (50.5±0.5) MeV.

From the performed analysis it was established, that the macroscopic OM and the SFM approach provide us with good enough shape and magnitude of differential and total cross sections at nuclei with A=12-124 in forward area of angles at all energies of α-particles. For large angles and light nuclei the correspondence was not reached, what can be probably explained by the

contribution to elastic scattering of exchange mechanisms resulted in back scattering. With mass number A increase the correspondence of the theory and experiment is essentially improved.

On the basis of the systematic analysis of experimental data we have received energy and mass components of global dependencies of macroscopic OP for α-particles in the range of energies up to 80 MeV. After cross-linking and adjustment of dependencies (8) - (10) the following values for coefficients in the formulas (3) - (5) particular are obtained (table 5).

Table 5. Coefficients for global parameters of macroscopic OP for α-particles with energy up to 80 MeV.

a_0	110.500±5.041	b_0	19.578±4.527	c_0	1.241±0.006
a_1	5.177±0.398	b_1	-2.202±1.077	c_1	0.00066±0.00080
a_2	-0.260±0.064	b_2	0.138±0.018	c_2	0
d_0	1.564±0.007	e_0	0.697±0.051	f_0	0.643±0.096
d_1	0.00109±0.0009	e_1	-0.014±0.010	f_1	-0.022±0.021
d_2	0	e_2	0.0026±0.0005	f_2	0.0012±0.0006

5. Conclusion

In the present paper the global mass dependencies of parameters for macroscopic OM and semimicroscopic folding-model for α-particles in the energy range up to 80 MeV for a wide class of the nuclei are obtained for the first time. For their build-up the joint analysis of a set of experimental data (ADDS of scattering, total reaction cross sections, tendency of the volume integral changes, etc.) is carried out, what will allow to restrict ambiguities in determination of parameters in the indicated energy region. One should mention, that identification and localization of the potential parameters for complex particles, in an acceptable approximation, can be carried out with using the above-stated criteria. Unity of our approach with the same used in [3, 4] and possibility to join together the data and reconstruct the global dependencies below and higher 80 MeV considerably strengthens value of the present work.

The work is performed with partial support of RFBR, Project 00-01 - 00617.

References

1. G.R. Satchler , *Direct Nuclear Reactions* (Oxford University Press, Oxford, 1983). P.E. Hodson, Rep. of Progress in Physics. **34**, 756 (1971).
2. R.Barret, D.Jackson, Razmery i Structura jader (Naukova dumka, Kiev, 1981). R.C. Barrett and D.F. Jackson, *Nuclear Sizes and Structure* (Oxford University Press, Oxford, 1977).

3. M. Nolte, H. Machner, J. Bojowald , Phys. Rev. C **36**, 1312 (1987).
4. L.W. Put and A.M.J. Paans, Nucl. Phys. A **291**, 93 (1977).
5. R.M.Drisko, G.R.Satchler, R.M.Bassel, Phys.Lett. **5**, 347 (1963).
6. O.M. Knyazkov, I.N. Kukhtina, S.A. Fayans, Physics of Particles and Nuclei. **30**, 870 (1999).
   O.M. Knyazkov, I.N. Kukhtina, S.A. Fayans, Physics of Particles and Nuclei. **28**, 1061 (1997).
7. M.Wit, J.Schiele, and K.A. Eberhard, Phys.Rev. C **12**, 1447 (1975).
8. E.J. Martens and A. M. Bernstein, Nucl. Phys. A **117**, 241 (1968).
9. D. Rychel, R. Gyufko, B. van Kruchten, *et al.*, Z. Phys. A **326**, 455 (1987).
   B.J. Lund, N.P.T. Bateman, S. Utku, *et al.*, Phys. Rev. C **51**, 635 (1995).
10. A.Duisebaev, K.A.Kuterbekov, I.N.Kukhtina i dr., Preprint № P6-2001-223, JINR (Dubna 2001); (prinjata k pechati v zhurnal Yadernaja fizika, 2002).
11. C.R. Bingham, M.L. Halbert, R.H. Bassel, Phys. Rev. **148**, 1174 (1966).
12. N.Burtebaev, A. Duisebaev, G.N.Ivanov i dr., Preprint 88-01, INP (Alma-Ata, 1988);
    N.N.Pavlova, C.J.Aisina, K.A.Kuterbekov i dr., Preprint INP (Alma-Ata, 1990);
    K.A.Kuterbekov, C.J.Aisina, N.N.Pavlova, i dr., Preprint INP (Alma-Ata, 1991).
13. K.A.Kuterbekov, A. Duisebaev, N.Burtebaev, Izv. RAN. Ser. Fiz.59, 112 (1995)
14. A. Duisebaev, B.A. Duisebaev, K.M.Ismailov i dr., Izv. Ministerstva Obrazovanija i Nauki Respubliki Kazakhstan, NAN RK. Ser. Fiz.-mat., №2, 103 (2002).
15. F. Perey. SPI-GENOA an optical model search code (unpubl.). NBI version by B.S. Nillson. (1976).
16. F. Michel, G. Reidemeister, S. Ohkubo, International conference "Clustering Phenomena in Nuclear Physics", June 14-17, 2000, St.-Peterburg. 2000. P.30.
17. F.G. Perey, Phys. Rev. 131, 745 (1963).
18. J.C. Correli, E. Bleuler and J. Tandem, Phys.Rev. 1959. V.116. P.1184.
19. I.B.Teplov, N.S.Zelenskaja, B.M.Lebedev i dr., Fiz.Elem.Chastits At.Yadra. 1977. T.8,Vyp.4. S.769-816 .
20. A.K. Ghaudhuri, D.N. Basu, B. Sinha, Nucl. Phys. A 439, 415 (1985).
21. S.A. Fayans, O.M. Knyazkov, I.N. Kuchtina et al., Phys. Lett. B357, 509 (1995).
22. D.B.Bolotov,O.M.Knyazkov, I.N. Kukhtina i dr., Yad. Fiz. 63,1631 (2000).
23. I. Tanihata, T. Kobayashi, O. Yamakawa et al., Phys. Lett. B 206, 592 (1988).
    R.B. Firesrone, Table of Isotopes, Eighth Edition (A. Wiley-Interscience Publication JOHN WILEY & SONS, New York, 1999, Update).
24. A. Ingemarson, J. Nyberg, P.U. Renberg et al., Nucl.Phys. A 676, 3 (2000).
25. P.D. Kunz, Computer program DWUCK4 (unpubl.).

MASS SPECTROMETER WITH TWO ION SOURCES

L.G. Glickman, A.G. Mit'

Institute of Nuclear Physics, National Nuclear Center, Almaty, Kazakhstan

The modern mass spectrometer is complicated device, and its creation is connected with using of the modern achievements of the ion optics, technique of high vacuum, electronics, information processing etc. It is highly important to use most fully the possibilities of this device. In many cases they are determined by the type of ion source. Depending on tasks decided with help of mass spectrometer it is optimal the use of either ion source. It is necessary to change the ion source when you go over to the other class of tasks and it takes you much time to adjust the ion source every time and make agree it with mass analyzer too.

Statical mass spectrometer with mid-plane near which ions are moving is considered in this article. Two ion sources are used; their exit slits are perpendicular to the mid-plane. The simple method of the replacement of the source is offered. Two concave transaxial mirrors are used for this aim [1]. The field of each mirror is symmetric relative to the axis, which is perpendicular to the mid-plane. In a transaxial mirror the planes that contain the symmetry axis of the field and perpendicular to rectilinear sections of the axial trajectory in the object and image spaces are always principal [1]. In the principal plane, independently of the field distribution in a mirror, dispersion on energy and the coefficient of the second-order spherical aberration, related to the angle of beam divergence in the mid-plane, are equal to zero. When an image forms in the principal plane and it is stigmatic, the second-order spherical aberration is eliminated completely in two directions of focusing.

Each electrode of the considered mirrors is composed of a pair of identical plates, located symmetrically with respect to the mid-plane. This plane contains the axial trajectory of a charged particle beam. The plates of the neighbor electrodes are separated by curvilinear slits. Their projections onto the mid-plane represent sections of concentric rings. The typical feature of the mirrors considered is the fact that the field decreases rapidly and smoothly, when the distance from the slits separating the neighbor electrode plates increases. At a certain distance from the slits, it has practically no effect on the trajectory form. With correctly chosen electrode sizes the scattering field effect on a trajectory form does not manifest itself.

The mid-plane used two-electrodes concave transaxial mirror coincides with the mid-plane of the device. The exit slit of each source is located in the principal plane of the object space. The principal planes of the image space of the both mirrors coincide. The images of the exit slits of the sources are in these planes and

coincide too. We use the mirrors making stigmatic images with the magnification one to one, in which the dispersion on energy and the spherical aberrations of the second order are equal to zero. These images are the object on which the ion-optical system of the mass spectrometer is tuned. When you choose one from two ion sources it is enough to switch the corresponding mirror.

In figure 1 one of possible variants of described system is schematically submitted. Electrodes 1 and 2 form the first mirror for which a subject is the output slit 5 of the ion source. Electrodes 3 and 4 form the second mirror for which a subject is the output slit 6 of the second ion source. The slit 7 in which there are images of slits 5 and 6 created by mirrors is a subject for the mass-analyzer to which the system from two mirrors and two sources is connected. The deflection angle of a beam of ions in each of mirror is equal to 90^0, that is a special case from lines of its values resulted in table 2 [2]. On constructive and technological reasons it is more preferable.

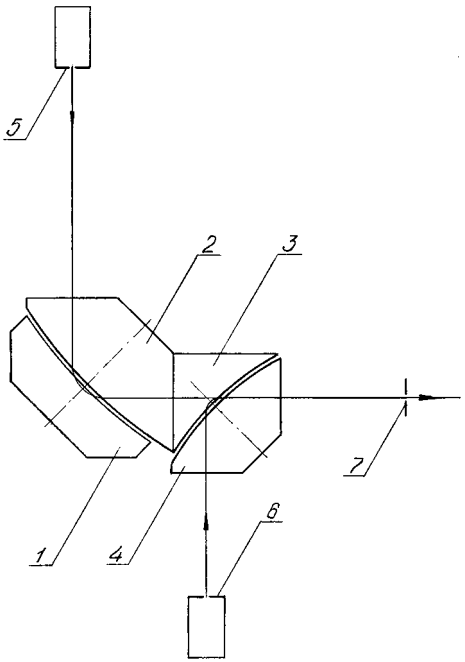


Fig.1. Ion-optical schema of system with two ion mirrors and two ion sources

Apparently from fig. 1 the beam of ions deflected by the first mirror before to get in the slit 7, passes through area occupied with the second mirror. The design of a mirror, each electrodes of which consists of two plates located symmetrically

concerning the mid plane and is placed from each other on distance d = (8-12) mm for real systems, allows to pass an ion beam without handicaps provided that the potential on its electrodes is equal to zero.

Radii of curvature of the slits dividing electrodes of mirrors, are equal: R_1=50d - for the first mirror and R_2=30d – for the second one. In the operating time of corresponding mirrors on electrode 1 potential $V_1 = 0.5\ \varphi_1$ is given, on electrode 3 – potential $V_2 = 0.7\varphi_2$ (φ_1 and φ_2 - accelerating potentials ion sources). Electrodes 2 and 4 earthed. It is accepted, that for earthed electrodes the potential is equal to zero.

The given system can be organically entered in many static mass-spectrometers. The variant of possible modernization before produced mass-spectrometer MI-1201 is shown in fig. 2.

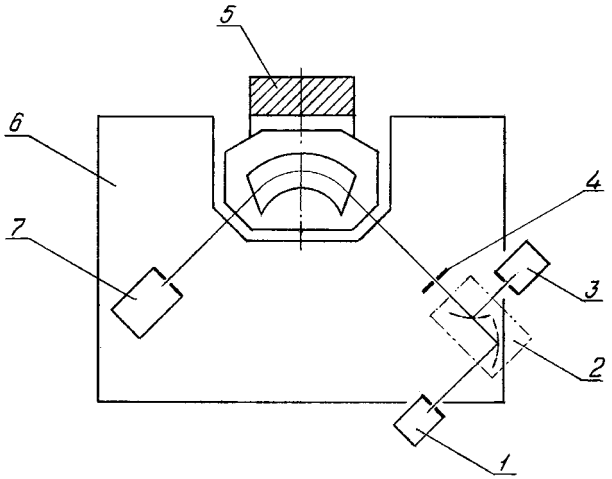


Fig. 2. Ion-optical schema of mass-spectrometer with two ion sources: 1,3 – ion sources; 2 – block of ion mirrors; 4 – enter slit of mass- analyser; 5 – magnet; 6 – basic plate of mass-spectrometer; 7 - detector

The system from two ion mirrors and two ion sources, one of which, for example, may be gas, the other -solid-state will allow to solve more operatively many practical tasks meeting in analytical mass - spectrometry.

References

1. S.P. Karetskaya, L.G. Glickman, L.G. Beizina, Yu.V. Goloskokov. Mirror-Bank Energy Analysers. Advances in Electronics and Eletron Physics. (1994), vol.89, p.391-480.
2. L.G. Beizina, S.P. Karetskaya. Zh. Tekh. Fiz. 1987, vol.57, N10, p.1972-1977.

MAXIMAL HEAT LOADING OF THE ELECTROSTATIC DEFLECTOR'S SEPTUM AT THE CYCLOTRON

A. Arzumanov, A. Borissenko

Institute of Nuclear Physics, Almaty, Kazakhstan

Abstract

An electrostatic deflector is used for extraction of accelerated particles at the isochronous cyclotron U-150 (Institute of Nuclear Physics, Almaty, Kazakhstan). Efficiency of beam extraction depends on the set of factors. Decisive is heat state of the septum and essentially beam extraction is limited by beam power dissipation in the deflector. Due to works carried on for radioisotopes production, determination of septum's maximal heat loading and optimization of the septum's geometry become a decisive factor. Maximal heat loading of deflector's septum and it's dependence on septum's geometry and thermal-physical properties of septum's material are presented in the paper as result of numerical calculation. The obtained results are discussed.

Isochronous cyclotron U-150 in the Institute of Nuclear Physics (National Nuclear Center, Republic of Kazakhstan) is used both for scientific and applied research. External and internal beam is used for irradiation. A 110°-long electrostatic deflector with plane and hyperbolic shape of electrodes for deflection and focusing of accelerated beam is used. An operating voltage of the deflector is equal to 70 kV. At present time some work related to production of radioisotopes at the cyclotron is performed. Such irradiation, especially radioisotope production, needs the use of maximal intensity of beam. This value is limited in some cases by heat power, which the deflector withstands. In this connection a computer modeling of heat transfer processes in ground plate of deflector – septum – was performed. Accelerated beam entering deflector's field encounters the septum. Power dissipation takes place in the face part of the septum.

The calculations can be combined in the following parts:

- Dependence of temperature distribution in septum, made of copper, determined thickness and with determined volume density of heat sources;
- Dependence of temperature distribution in septum, made of tungsten, determined thickness and with the same volume density of heat sources; comparison with results of above calculations;
- Temperature distribution in septum, made of copper, with cut, comparison with results of above calculations.

Calculated model of septum represents a plate, cooled with water. The thickness of septum is equal to L mm, the height – 2 cm, the length – 16 cm. The

schematic view of the septum is shown in fig 1. Heat sources caused by stopping of 30 MeV protons are represented in a gray color. Volume density of heat sources is equal to 34965 W/cm^3. It corresponds to surface current density – 233.1 μA/cm^2 and produces heat flow – 6993 W/cm^2. Coefficient of heat transfer by water is equal to 2.3 W/cm^{2}K.

Numerical integration of 3-D equation of heat conductivity $\nabla^2 T + \frac{q_V}{\lambda} = 0$ (where T (°C) – temperature, q_V (W/cm^3) – volume density of heat sources, λ (W/cmK) – heat conductivity of septum's material) in technique of finite differences was performed.

Heat flow of 6990 W/cm^2 can provoke a boiling of water in cooling tube. In the frame of this model it is assumed that the temperature of cooled surface under boiling is equal to temperature of saturated water at pressure 5 bars – 160°C.

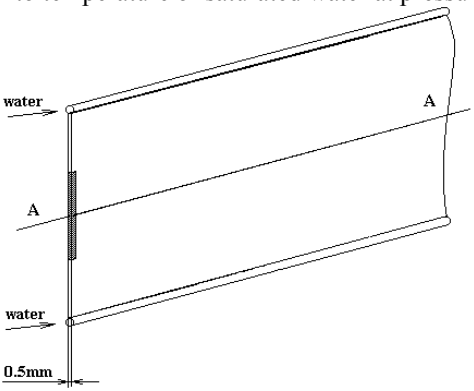
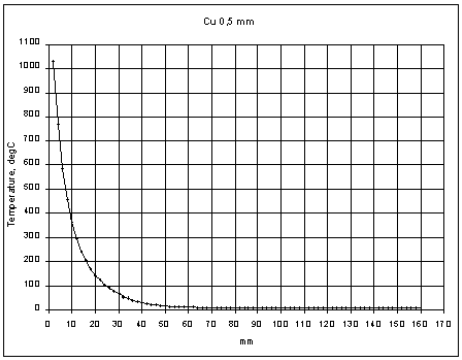
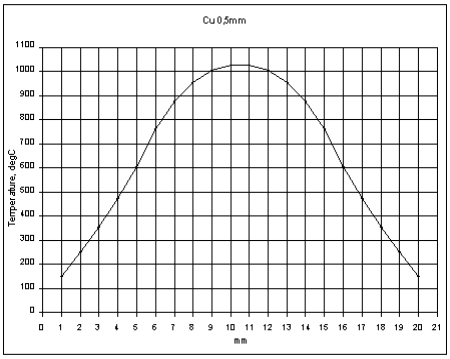


Fig.1. Schematic view of the septum.

Results of calculations of the Cu septum (thickness of 0.5 mm, 1 mm, 2 mm) with the same density of heat sources gave the same temperature distribution in volume of the septum, with maximal temperature in 0.5 mm thickness – 1028°C, 1 mm thickness – 1030°C, 2 mm thickness – 1031°C. The septum with increasing thickness (from 0.5 mm to 2 mm on the 10 cm length) was calculated. However, the result was the similar to above results. Such increasing of the thickness does not make any sense for improving of heat transfer, since the main temperature fall takes place on the length of 5 cm. There is not any opportunity to change the increasing of septum's thickness due to conditions of accelerated beam passing in deflector. It is shown in fig 2: typical temperature distribution in the septum along the A-A line (a) and across the septum in the line with heat sources from one cooled edge to another (b).



a) Temperature distribution in the septum along the A-A line.



b) Temperature distribution across the septum in the line with heat sources from one cooled edge to another (the region of heat sources – from 6-th mm to 15-th).

Fig 2. Typical temperature distribution in the septum, made of copper, thickness of 0.5mm, 1mm and 2mm and with increasing thickness (from 0.5mm to 2mm) (volume density of heat sources – 34965 W/cm^3).

In a similar manner there were done calculations of heat transfer in the septum, made of tungsten, 0.5 mm, 1 mm and 2 mm thickness. Volume density of heat sources was the same. Tungsten has lower heat conductivity with comparison to copper, but it has higher melting point. The calculations showed the same type of temperature distribution. And this volume density of heat sources is a "critical" one for tungsten too; the maximal temperature in the septum reaches 3000°C. Gradual change of septum's thickness does not improve the heat transfer. The typical for all cases temperature distribution in septum, made of tungsten, along the A-A line is shown in fig 3.

The heat transfer by irradiation was not taken into account in the calculations. Although it can be sufficient at such temperature, a reliable junction between the septum and cooling tube can be the most important thing to ensure the withstandability of the septum. Some experiments with septums, made of copper and made of tungsten, showed the advantage of operation with copper.

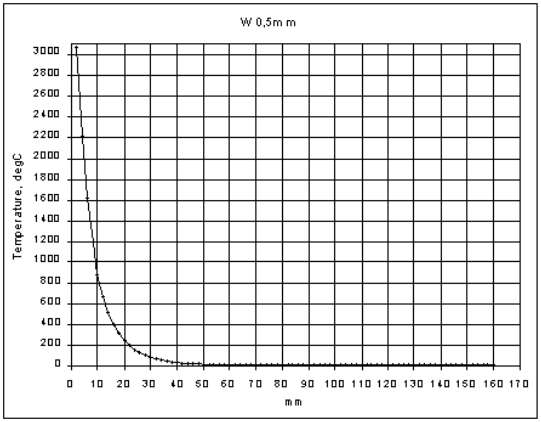


Fig 3. Typical temperature distribution in the septum made of tungsten.

An effective improvement of heat transfer in the septum is a cut in the range of heat sources, made for decreasing of surface density of heat flow. The schematic view of the septum with cut is shown in fig 4. Heat sources are represented in a gray color. The temperature distribution in the 0.5 mm Cu septum at the same heat power as in the 0.5 mm Cu septum without cut is shown in fig 5.

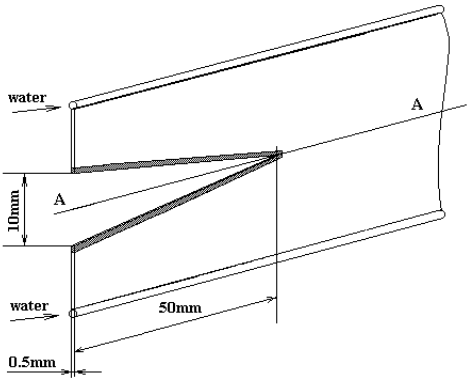


Fig 4. Schematic view of the septum with cut.

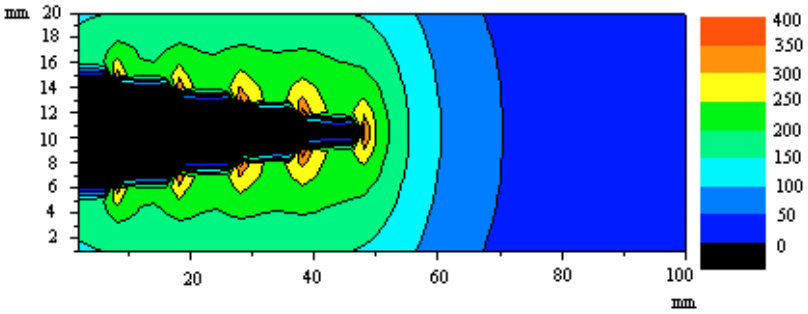


Fig 5. The picture of temperature distribution in the 0.5 mm Cu septum with cut (heat power is the same as in the 0.5 mm Cu septum without cut, 350W)

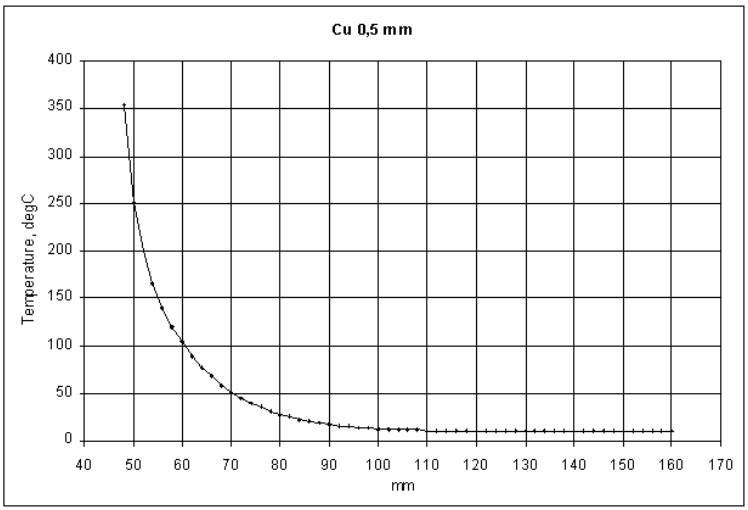


Fig 6. Temperature distribution in the septum along the A-A line.

As it is seen in fig 5 and 6, the maximal temperature (378°C) is quite low here. Temperature, close to melting point, can be reached at heat power 4 times higher.

All above results are presented in table 1.

Table 1. Maximal heat power and maximal temperature in the septum of electrostatic deflector, made of copper and made of tungsten (deflected particles are 30 MeV protons).

	i, μA/cm^2	I, μA	q, W/cm^2	Q, W	T_{max}
Cu 0.5 mm	233.1	11.655	6993	350	1028
Cu 1 mm	233.1	23.31	6993	699.3	1030
Cu 2mm	233.1	46.62	6993	1398.6	1031
Cu 0.5 mm – 2 mm (chamfer)	233.1	11.655	6993	350	1021
W 0.5 mm	233.1	11.655	6993	350	3059
W 1 mm	233.1	23.31	6993	699.3	3059
W 2 mm	233.1	46.62	6993	1398.6	3060
W 0.5 mm – 2 mm (chamfer)	233.1	11.655	6993	350	3036
Cu 0.5 mm (slit)	23.31	11.655	699.3	350	378
Cu 0.5 mm (slit)	93.24	46.62	2779.2	1398.6	1080

Performed computer-aided heat transfer modeling allows to determine following peculiarities of heat transfer in the septum:

1. Septum material must enable a reliable junction with cooling tube.
2. Thickness of septum must be small enough and is to be determined only by mechanical durability of the design.
3. Effective technique for improving of heat transfer is cut in the septum in the region of power deposition. Dimensions of the cut are determined by its influence on the electric field of the deflector.

MEASUREMENT OF ABSOLUTE GAMMA RAY EMISSION PROBABILITY OF 1001 keV FROM THE DECAY OF ^{234m}Pa

Çetiner B.[*], *Karadeniz H.*[*], *Yücel H.*[*], *Özgür İ.*[**], *Çetiner M.A.*[*] *and Özmen A*[***]

* Ankara Nuclear and Research Training Center, Beşevler, Ankara, Turkey
** Osmangazi University, Faculty of Science and Art, Physics Dept., Eskişehir, Turkey
*** Gazi University, Faculty of Science and Art, Physics Department, Ankara, Turkey

Abstract

In recent years, the 1001 keV gamma ray emission from ^{234m}Pa as an analytical peak is commonly used in the direct gamma ray spectrometric measurements of ^{238}U content. ^{234m}Pa is the second daughter of ^{238}U and rapidly reaches secular equilibrium with parent nucleus. This "clean" peak is well resolved by high purity Ge detectors and gives more accurate indication of uranium content without requiring any self attenuation correction.

Several experimental results for the absolute emission probability of the 1001 keV gamma ray of ^{234m}Pa have resulted in doubts concerning the old recommended value of 0.59±0.01% obtained by following a radiochemical separation method. Therefore, this old value is now obsolete and a newly value of 0.835±0.004% is recommended. In this study the gamma-ray spectrometric measurements for the determination of the absolute emission probability of the 1001 keV gamma ray of ^{234m}Pa were carried out using the powdered uranium samples. A new experimental value of 0.861±0.015% for the absolute gamma ray emission probability for the 1001 keV gamma ray of ^{234m}Pa has been obtained. The present measured value agrees within 2.5 to 4% with the most recent experimental results appeared in the literature and the newly recommended value of the absolute emission probability for the 1001 keV gamma-ray of ^{234m}Pa. However, it is different from the latest experimental value of 0.92±0.02%, obtained by Anilkumar et al. (1999).

1. Introduction

With the introduction of the high-resolution gamma ray spectrometry with the high purity Ge detectors having the larger crystal volumes(i.e. with the higher detection efficiency), the gamma-ray emission probabilities (absolute and relative) as one of nuclear parameters for various radionuclides have been studied extensively resulting in a new and more precise results[1,2]. The decay data obtained accurately from these studies are necessary for the quantitative assessments of

radionuclides, for example, for the determination of concentrations of those contained in the samples by employing the gamma ray spectrometric method.

The naturally occurring isotope, ^{238}U, a radioactive primordial elements such as thorium and potassium is one of the obvious and most important sources of radioactivity in the environment. The measurements of primordial nuclides in areas of igneous geology, in nuclear wastes and in environmental samples are often carried out by high-resolution gamma-ray detectors. Since ^{238}U isotope directly emits only very weak gamma rays which are at 49.55 keV (0.064%) and at 113.5 (0.010%) shown in Fig.1, it is possible, however, to measure the emission of gamma rays from of a daughter nuclide which is in radioactive equilibrium with the ^{238}U parent.

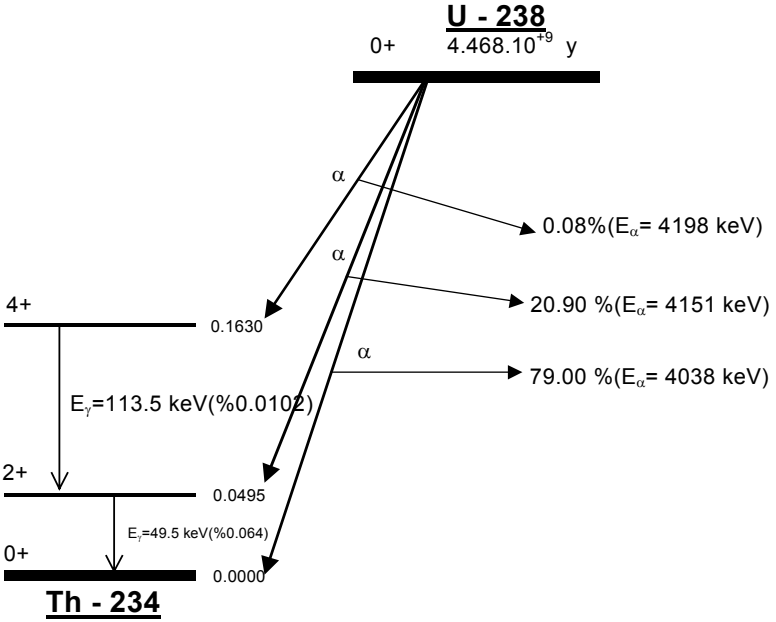


Fig 1. Decay scheme of ^{238}U

This condition is fulfilled by one of the first three daughters of ^{238}U, viz. ^{234}Th (24.1 d), ^{234m}Pa(1.17 m) and ^{234g}Pa(6.70 h) because of very short-lived compared with ^{238}U(4.468x10^9 y). For example, the necessary time for the radioactive equilibrium for the ^{234Th} with ^{238}U parent is attained about 168 days. The partial decay scheme for the first three daughters of ^{238}U chain is shown in Fig.2.

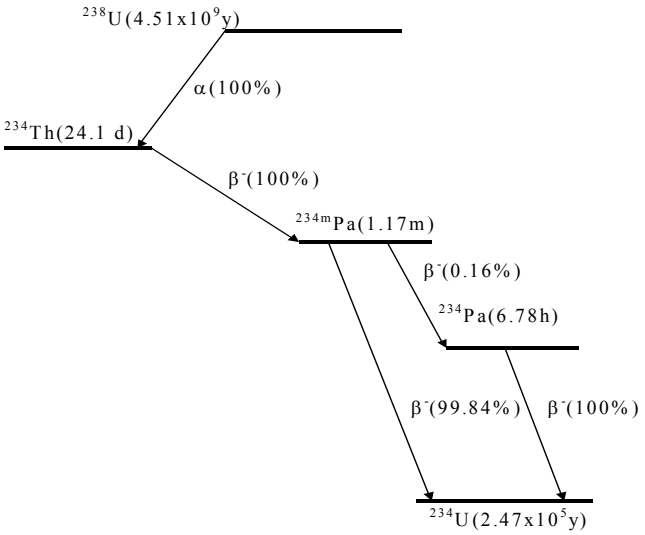


Fig. 2. Decay scheme for ^{238}U-^{234}Th-$^{234, 234m}$Pa-^{234}U chain

On the other hand, in many cases, this equilibrium state in natural system may not reach, especially for a daughter such as ^{210}Pb, ^{214}Pb, ^{214}Bi etc. from the uranium decay series that is quite far down the decay chain. Therefore, recent gamma-ray spectrometry measurements have focused on determining the ^{234Th} and ^{234m}Pa in which they are secular equilibrium with ^{238}U in the samples. However, since the 63.3 keV peak of ^{234Th} includes contributions from the 63.9 keV(0.023%) emission from ^{231}Th , the 63.9 keV(0.255%) emission from ^{232}Th and the 62.9 keV(0.018%) emission from ^{234Th}, a recent study concerning the measurements of uranium concentrations in the samples emphasizes the use of 1001 keV peak of ^{234m}Pa, which is a "clean" peak well resolved by HpGe detectors[3]. The 1001 keV peak of ^{234m} Pa in equilibrium with ^{234g}Pa, ^{234}Th and ^{238}U can also be selected for the uranium analysis since it does not include any contribution from any other gamma emissions and does not have any interference with other peaks in the high energy region even if the samples contain high amounts of thorium. Thus, this analytical peak gives more accurate indication of uranium concentration in the samples without requiring any gamma ray self-attenuation correction or with a negligible self attenuation correction factor because the 1001 keV gamma-ray is in high-energy region in the observed gamma-ray the spectrum. However, the problem in quantifying this radionuclide on the basis of its decay parameters in the gamma-ray spectrometric measurements is that the discrepancy among the recent absolute

emission probabilities (P_γ) measured for the 1001 keV line of ^{234m} Pa can reach more than 15%.

The P_γ value for the 1001 keV line of ^{234m}Pa first produced by Bijornholm and Nielsen [4] who measured the disintegration rates from the beta particles and gamma-ray spectra of ^{234m}Pa in equilibrium with ^{234g}Pa(6.70 h) and the parent, ^{234} Th (24.1 d) . This single datum, which was a value of 0.59±0.01%, generated in the 1960s was extremely important for the P_γ of the 1001 keV gamma-ray transition of ^{234m}Pa following internal conversion, and it was adopted in the evaluations carried out in the past.

Scot and Marlow[1] have investigated the P_γ of the 1001 keV gamma line of ^{234m}Pa by using uranium solution and they obtained a value of 0.839±0.005%. Siemon et al.[5] have also obtained a value of 0.845±0.021% for the P_γ of this gamma-ray using one-year old thin depleted uranium metal foils for analysis, adopting a method based on measurement of absolute activity ^{234m}Pa in equilibrium with ^{238}U. Anilkumar et al.[6] have recently obtained a value of 0.92±0.02% for the P_γ of 1001 keV gamma ray of ^{234m}Pa using samples of different origin and history by fundamental parameter method. This last value is different from the other previously quoted experimental values.

Several measurements of the P_γ of the 1001 keV gamma-ray of ^{234m}Pa have resulted in doubts concerning earlier recommended decay data as a value of 0.59±0.01%. Therefore all previously known gamma-ray probabilities (absolute and relative) in the decay of ^{234m}Pa have been examined and evaluated to obtain a new and more precise values for the gamma-ray emissions from ^{234m}Pa by Nzuruba [7]. He suggested that the evaluated value of 0.835±0.004% at 1001.025 keV from the ^{234m}Pa is more precise than the value of 0.837±0.012% currently in adoption.

In the present study we have observed that there are only six experimental results for the P_γ of 1001 keV line of ^{234m}Pa in the literature survey and the discrepancy among the few experimental results for the 1001 keV gamma line seems to be high. So, the gamma-ray spectrometric measurements for determination of the P_γ of 1001 keV line of ^{234m}Pa were carried out using powder uraniumtrioxide (U_3O_8) samples by the method based on measurement of absolute activity of ^{234m}Pa in equilibrium with the parent ^{238}U.

2. Experimental

Gamma-ray spectrometric measurements have been performed, in turn, using two different high pure Ge detectors manufactured by Canberra Inc. One of the HPGe detectors used is a p-type crystal with active volume of approx. 57 cm^3 with a relative efficiency of 12.4%. The other is a n-type crystal with active volume of approx. 100 cm^3 with a relative efficiency of 22.6%. The full energy peak

efficiency as a function of gamma-ray energy for each Ge detector was determined using the powder radioactive standard source containing a mixture of ^{109}Cd, ^{57}Co, ^{123m}Te, ^{151}Cr, ^{113}Sn, ^{89}Sr, ^{137}Cs, ^{60}Co, and ^{88}Y radionuclides, obtained from Isotope Products Laboratories, traceable to NIST. The measured efficiency data were fitted to an efficiency function of the form:

$$\varepsilon_P = \exp\left[a_0 + \sum_{i=1}^{6} a_i \cdot \ln^i\left(E_\gamma\right)\right] \quad (1)$$

where, ε_p is the full energy peak efficiency at a given gamma ray energy E_γ and a_0, a_i (for i= 1 to 6) are regression constants . The uncertainties on the detector efficiencies are about 2% in the range of 50 to 2000 keV gamma ray energy. Then, only a small amount, about 1.5 to 8 g, of dried and powdered samples are filled into the polystyrene tubes with 1 mm wall thickness. The samples were filled to same height to ensure identical counting geometry. The counting time for each run predetermined was high enough to ensure good statistical quality of data, and the counting times chosen for runs varied between 80,000 s and 210,000 s. A schematic diagram of the counting system used is shown in Fig 3.

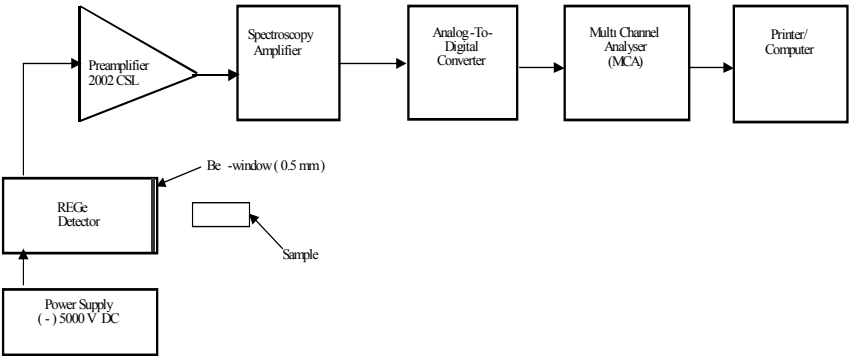


Fig. 3. Block diagram of gamma counting system with a REGe detector

The samples were coaxially positioned with the detector in a given distance. The measurements were repeated three to ten times to improve statistical precision. Thus, the mean values of the measured count rates were used in the calculations. The net sample count rate for each measurement was obtained after background subtraction of the peak area. The emission probability, P_γ is calculated as follows:

$$P_\gamma = \frac{\lfloor N_p / t_c \rfloor}{A \cdot \varepsilon_p} \cdot F_g \tag{2}$$

where, N_p: the net counts under photopeak, t_c: the measuring time, A: sample activity (Bq) and F_g: gamma ray attenuation factor and ε_p is the full energy peak efficiency at a given gamma ray energy E_γ.
The correction factor for gamma-ray self attenuation, F_g has been taken into account by the following equation:

$$F_g = \frac{\mu x}{1 - e^{-\mu x}} \tag{3}$$

where, μ (cm^{-1}) is the linear attenuation coefficient of U_3O_8 and x (cm) is total sample thickness. Mass attenuation coefficients, μ/ρ ($cm^2.g^{-1}$) were taken from XCOM database of Berger and Hubbell[8]. The estimated values of F_g for 1001 keV gamm ray in U_3O_8 samples are small however, they found in the range of 1.0015 to 1.0032 for 1001 keV gamma ray, depending on sample size.

3. Results and Discussion

The measured absolute gamma-ray emission probability, P_γ for the 1001 keV gamma-ray emission from ^{234}Pa, together with previous experimental results and evaluated values are given Table 1.
The present value is the weighted average of the results obtained by using two Ge detectors. Main sources of uncertainty of the absolute emission probability measurement are statistical error (<0.2-0.3%), efficiency of REGe or HPGe (1.5-2.0%), sample activity (0.1%), systematic error (0.5%). Final combined uncertainty of the measured value of the P_γ for 1001 keV from ^{234m}Pa is estimated within 1.2 to2.1%.

The present experimental value agrees within 2.5 to 4 % with the measurements of Scott and Marlow[1], Moss[2], Gunnink and Tinney[10], and the most recent evaluated value of 1001 keV from ^{234m}Pa by Nzuruba[7]. However, there existed a discrepancy between the present value and the result of Anilkumar et al.[6] by 7%. The measurement of Anilkumar et al.[6] seems to be unrealistically larger than our measurement and other recent experimental results given in Table 1, and is different from the newly recommended value of 0.835±0.004% by 9.2%.

Table 1. Comparison of the present result with other studies for the absolute gamma ray emission probability of 1001 keV gamma-ray of ^{234m}Pa.

Year	Data type	Reference	Gamma-ray emission probability, P_γ(%)	Relative Bias (%)
2002	Experimental	This work	0.861±0.015	-
1999	Experimental	Anilkumar et al. [6]	0.92±0.02	-6.85
1999	Evaluated	Nzuruba [7]	0.835±0.004	+3.02
1990	Experimental	Scott and Marlow [1]	0.839±0.005	2.55
1986	Experimental	Moss [2]	0.834±0.007	+3.13
1986	Evaluated	Browne and Firestone's TRI [9]	0.65	+24.51
1971	Experimental	Gunnink and Tinney[10]	0.828±0.008	+3.83
1963	Experimental	Bjornholm and Nielson[4]	0.59±0.10	+31.47

References

1. Scott, H. L. and Marlow, K. W., Nucl. Inst. And Methd. Phys. Res. A 286, (1990) 549.
2. Moss, C. E., Radiat Eff. 94 (1986) 81.
3. Yücel, H., Çetiner, M. A. and Demirel, H., Nucl. Instrum and Meth. Phys. Res. A 413 (1998)74.
4. Bijornholm and Nielsen, O. B., The decay of 1.14 min isomer of ^{234}Pa (UX_2), Nucl. Phys. 42, 642.
5. Siemon, K., Esterlund, J. Van Aarle, Knaack, M., Appl. Radiat. Isotopes 43(1992) 873
6. Anilkumar,S., Krishnan, Narayani, Abani, M.C., Appl. Radiat. Isotopes 51(1999) 725.
7. Nzuruba A. C., Nucl. Instrum and Methd. Phys. Res. A 424 (1999) 425-443.
8. Berger, M. J., Hubbell, J. H.: XCOM Photon Cross Sections Database, NBSIR 87-3597,1987.
9. Browne, E. and Firestone, R.B., Table of Radioactive Isotopes (Wiley, New York, 1986).
10. Gunnink, R. and Tinney, J. F., Lawrence Radiation Laboratory Report No. UCRL-51086, Appendix C (1971).

MEASUREMENT OF MASS DISTRIBUTIONS OF FISSION FRAGMENTS ^{235}U INDUCED BY THERMAL NEUTRONS IN ASYMMETRIC AREA

U. Jovliev, Yu.N. Koblik, A.V. Khugaev, A.I. Muminov, A.K. Nasirov, K.V. Pavliy, V.P. Pikul, Yu.V. Polyak

Institute of nuclear physics, Tashkent, Uzbekistan

The mass yields of fission fragments ^{235}U induced by thermal neutrons for A=145-160 and E_k=50-75 MeV with the help of mass spectrometer are measured. The thin structure is found out at A=150, 153 and E_k=50-60 MeV. The received results have the good consent with predictions of model of double nuclear system.

The complete understanding of dynamics suffices and mechanism of process of fission of nucleuses is not achieved yet. It is determined first of all by that the nuclear fission represents one of the most complex nuclear transformations connected to deep redistribution of mass and a charge of a compound nucleus, formation of the strongly deformed and exited splinters having high spin and energy of excitation, sufficient for emission of several neutrons and about ten γ-quantum. The second essential circumstance is that in the majority of experiments the nuclear division is studied in conditions, when it is impossible to receive the complete information reflecting dynamics of fissionable nucleuses. The process of fission nucleuses allows to receive nucleuses in unusual condition described is abnormal by high deformation and large surplus of neutrons, that opens opportunities of research of such properties of nucleuses, which are inaccessible to study by other ways (collective movement with large amplitude, force functions of β-decay, viscosity and friction of a nuclear matter etc.).

The definition of mass yields of fission fragments as functions of their mass, kinetic energy and charge is the important task for the analysis of process of division. We carry out measurements of mass and power distributions of the unslowed fission products of ^{235}U in area, where there are not enough of experimental data, namely in area for A = 150 -160 and E_k = 50 - 75 МэВ. Measurements were carried out with the help of electromagnetic mass spectrometer of the unslowed of fission products. It is on the horizontal channel nuclear reactor ВВР-SM of Institute of Nuclear Physics of Academy Sciences of Republic Uzbekistan /1/. The accuracy of measurement of kinetic energy of fission products makes 0.02 %, mass - 0.06%.

Mass distributions of fission products of ^{235}U induced by thermal neutrons are resulted on fig.1. Ones carried out with different kinetic energy ($E_к$ = 55, 60, 65, 70 and 75 MeV) heavy group fission fragments /2/. In a range $E_к$ = 55-60 MeV the structure is displayed with A=146, that, most likely, is

connected to large probability of formation of complementary light fragments with A= 88-90. The contour diagrams of the shell corrections designed on Wilkins /3/ show, that there are areas with the minimal potential energy not only with small deformations for magic numbers Z = 50 and N-50, 82, but also for N = 66, 88 and Z = 40, 44 with large deformations $\beta = 0{,}6 \div 0{,}7$.

For the given $E_к$ of a heavy group fission fragments were complete kinetic energy TKE of complementary fragments, determined on formula:

$$TKE=E_k(A_0/(A_0 - A_h - \nu_h)) \quad (1)$$

where A_0 - mass number of a divided nucleus, $E_к$ - kinetic energy of a heavy fragment, A_h - mass number of a heavy fragments, ν_h – number of neutrons from heavy fragment, determined under the formula:

$$\nu_h = 0{,}531\nu + 0{,}062\,(A_h - 143) \quad (2)$$

where ν - average number of neutrons from a fissionable nucleus (in case of fission ^{235}U induced by thermal neutrons n = 2.35).

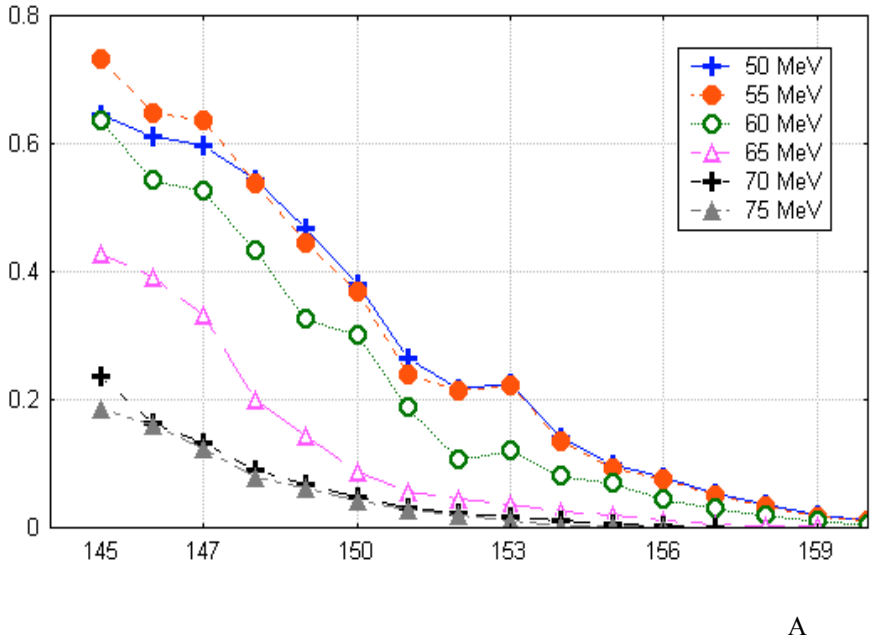


Рис.1. Mass distributions of fission fragments ^{235}U induced by thermal neutrons for E_k= 55 - 75 MeV.

For the same meanings TKE the accounts of distances center to center of

ellipses were carried out in a scission point under the formula:

$$D = K\frac{Z^2 R_a}{TKE\left(1+R_a\right)^2} \tag{3}$$

where Z - charge of a fissionable nucleus, R_a - mass relations A_h/A_l, K= 1.44 MeV*fm / $(e0)^2$.

Parameter of deformation simultaneously was calculated

$$\beta = 1.05\frac{c_i - a_i}{\sqrt[3]{a_i^{\,2} c_i}} \tag{4}$$

where c_i and a_i - large and small axes of ellipse.

According to work /3/ the mass yields of fission fragments ^{235}U induced by thermal neutrons were calculated depending on distance centre to centre of fission fragments in a point of scission and the contour diagrams for the different mass relations are constructed. On these contour diagrams the meanings of distances D for different meanings TKE (fig.2) were put. The rather close correlation between the mass yields, measured by us, and calculated on model of Willkins /3/ is observed. The contour diagrams of dependences shell corrections /3/ from parameters of deformation β also show large probability of formation of pairs fission fragments with deformation β= 0,6 - 0,7. To each meaning TKE there corresponds a set of meanings of parameters of deformation β of each fission fragment. The particular importance of these parameters are determined by structure of a nucleus. The fission fragments have in a scission point such meanings β, which correspond to minima of potential energy. The situation of these minima depends first of all on number of protons and neutrons in a nucleus and in a smaller degree from energy of excitation and angular moment of a nucleus. These factors also determine kinetic energy of fission fragments and her dispersion with various distributions on mass and charge, and also their dependence on properties of a fissionable nucleus.

The potential energy Q of a compound nucleus (AH, AL) in a saddle point can be received from the half-empirical mass formulas /4 /, and also from the tables of power balance of reaction of fission Milton /5/. Knowing TKE, it is possible to find of energy excitation of fission fragments and form of a nucleus in a scission point . The model representations give the form of a nucleus in a saddle point. Hence, it is possible to receive change of the form of a nucleus with motion from a saddle point to a scission point and to reveal the factors influencing to dynamics of process fission (for example, force of friction).

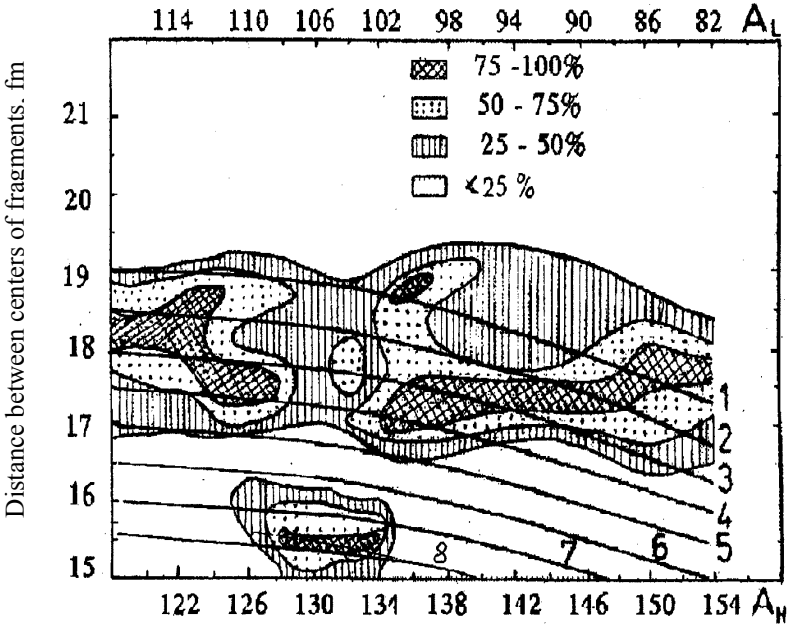


Рис.2. The contour diagrams of mass yields of fission fragments ^{235}U induced by thermal neutrons depending on distance centre to centre in a scission point . Curve 1-8 - distance with the fixed meanings TKE: 1-160 MeV, 2-165 MeV, 3-170 MeV, 4-175 MeV, 5-180 MeV, 6-185 MeV, 7-190 MeV, 8-195 MeV.

The nuclear-physical researches with heavy ions low energies have opened two new objects of the nuclear microcosm - nuclear molecules and double nuclear systems /2 /. It is supposed, that after complete dissipation of kinetic energy of collision the nuclear complex - double nuclear system (DNS) is formed. Such system differs from nuclear molecules by instability of the condition, changing in time by transfer nucleons from one nucleus to other. These changes carry a statistical property and proceed on set of trajectories in (Z, A) - space of nucleuses, forming this system. By major feature of double nuclear system is the preservation of individuality of nucleuses, included in it, that is caused by shell structure of these nucleuses. Nucleons are transferred from more heavy to an easy nucleus, the system with the minimal superficial energy will not be generated yet. The compound nucleus from a saddle point up to a scission point can be considered as double nuclear system existing till 10^{-16} s. The accounts of mass

yields of fission fragments executed within the framework of model DNS (fig.3), have shown the good consent with experimental data for a case of superasymmetric fission of a nucleus ^{235}U.

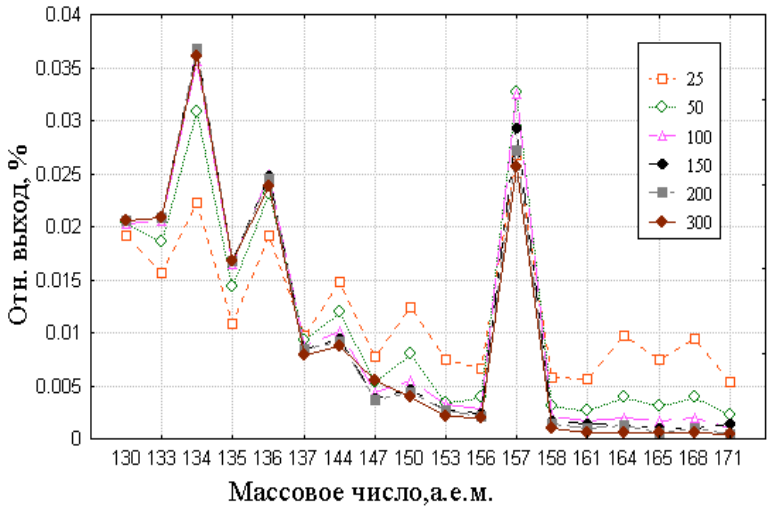


Рис.3. The mass yields of fission fragments nucleuses ^{235}U induced by thermal neutrons designed on model DNS (in a figure times of release from a saddle point to a scission point $x10^{-19}$ s).

This work was supported by STCU (Grant Uzb-45).

References

1. Koblik Y.N., Pikul V.P., Yuldashev B.S. Proc. 4-th Intern. Conf. " Modern Problems of Nuclear Physics ", Tashkent, 2001, p.102-103.
2. Volkov V.V. et al. Phys. Rev. C, v.51, 1995, p.2635.
3. Wilkins B.D., Steinberg E.P., Chasman R.R. "Scission point model of nuclear fission based on deformed shell effects" .Phys. Rev. C., 1976, v.14, № .5, p.1832.
4. Кравцов В.А. Masses of atoms and binding energy of nucleuses. // М.: Атомиздат, 1974, 340с.
5. Milton Y.C.. Fission energy tables and an application to nuclear division. // Berkley, 1965. California, 1962, 76 p.

MEASUREMENT OF THERMAL NEUTRON CROSS SECTION AND RESONANCE INTEGRAL FOR $^{139}La(n,\gamma)^{140}La$ REACTION BY ACTIVATION METHOD USING CADMIUM RATIOS

Yücel, H.[*], *Karadağ, M.*[**], *Çetiner, M.A.*[*], *Tan, M.*[**] *And Özmen, A.*[**]

* Ankara Nuclear Research and Training Center (ANRTC), 06100 Beşevler, Ankara, Turkey

** Gazi University, Gazi Education Faculty, Art and Science Faculty, Physics Department, 06500 Teknikokullar, Ankara, Turkey

Abstract

Thermal neutron cross section and resonance integral for the $^{139}La(n,\gamma)^{140}La$ reaction was measured by the activation method. The experimental samples with and without a cylindrical Cd shield case in 1 mm wall thickness were irradiated in an isotropic neutron field of the ^{241}Am-Be neutron source. The extent of the non-ideality of the epithermal neutron spectrum(i.e., α- shaping factor for $1/E^{1+\alpha}$ epithermal distribution) at the sample irradiation position was experimentally determined by the two-detector(Au and W foils) method, and it was found to be 0.560±0.002. The induced activities in the samples were measured by high resolution γ-ray spectrometry with a calibrated n-type Ge detector. Thermal neutron cross section for 2200 m/s neutrons and resonance integral for the $^{139}La(n,\gamma)^{140}La$ reaction has been obtained relative to the reference values, σ_0=13.3±0.1 b and I_0=14.0±0.3 b for the $^{55}Mn(n,\gamma)^{56}Mn$ reaction as a single comparator. The results corrected for gamma attenuation, thermal neutron and resonance neutron self-shielding effects and the effect of α- shaping factor on the resonance integral value of the (n,γ) reactions. For the conversion of the measured infinite dilution resonance integral, $I(\alpha)$ to the I_0 for 1/E ideal epithermal neutron spectrum, the concept of effective resonance energy, $\overline{E}_r$ described by De Corte for the Ryves' method[1] has been used. By defining Cd cut-off energy 0.55 eV, the results obtained were: σ_0=9.27 ± 0.37 b and I_0=12.16 ± 0.60 b for the $^{139}La(n,\gamma)^{140}La$ reaction. These results are discussed and compared with previous measurements and the evaluated data in JEF-2.2, IAEA and JENDL-3.2. Thermal neutron cross section for $^{139}La(n,\gamma)^{140}La$ reaction is in good agreement with the recent measurements. There existed the discrepancies between present results and some of old experimental data for thermal cross section and resonance integral for this reaction is within about 6-40%.

1. Introduction

A knowledge of thermal neutron cross-section and resonance integral cross-section for lanthanum (La), which is as a rare earth element from the lanthanides is important for thermal or epithermal neutron activation analysis. Both resonance integrals and thermal cross sections are required in the theoretical and experimental studies concerning in experimental reactor physics and in checking nuclear resonance parameters within the interaction of neutrons with matter. For most isotopes a wide range of reported values exists, so that often a resonance integral is not known within 20%, making it of little practical use[1]. It is also apparent the uncertainties quoted for many measurements are poorly defined and unrealistically small. The measured thermal neutron cross-sections for $^{139}La(n,\gamma)^{140}La$ reaction in the literature are usually consistency, but some of old experimental thermal neutron cross-sections and resonance integrals for this reaction differ about 6-30% from each other due to the known problems such as the separation of the response of the nuclide to be activated to intermediate neutrons, much larger self-shielding for epithermal(intermediate energy) neutrons (from cadmium cut-off energy 0.55 eV to about 0.1 MeV), and the perturbation of the response corresponding to the resonance peak by the contribution of the 1/v region of thermal neutron cross section. As the required precision of measurements increases, it becomes desirable to provide more consistent resonance integral data.

Methods of measurement for thermal cross section for thermal neutrons and the resonance integral for epithermal neutrons are the pile reactivity and the activation technique[2] The first method implies reactivity measurements with a reactor oscillator, while the second method implies foil activations to compare cadmium ratios for foils of the materials of interest to cadmium ratio of foils of a reference material, for which usually gold (σ_0=98.65 ± 0.09 b, I_0=1550 ± 28 b) is employed [3]. Since there are sufficient number of internationally accepted accurate values for the thermal neutron cross section (known to ± 0.75%) and resonance integral (known to ± 2%) for $^{55}Mn(n,\gamma)^{56}Mn$, we have used Mn monitor instead of standard Au monitor. In addition, .the $^{55}Mn(n,\gamma)^{56}Mn$ reaction can be chosen as a suitable monitor in this experiment because the value of the resonance integral for $^{55}Mn(n,\gamma)^{56}Mn$ monitor reaction is in the same order with that for $^{139}La(n,\gamma)^{140}La$ and the characteristic-prominent resonances in the epithermal region for ^{55}Mn and ^{139}La are far from 0.55 eV cadmium cut-off energy, which is in a cylindrical Cd box (height/diameter=2) with a wall thickness of 1mm, according to the definition of E.A.N.D.C[4].

The purpose of this study is to measure the thermal neutron cross section and resonance integral for the $^{139}La(n,\gamma)^{140}La$ reaction by an activation technique using cadmium ratios, relative to a single standard material, manganese in an isotropic neutron field by ^{241}Am-Be neutron source.

2. Experimental

In the present measurements, the oxide forms of the elements(La and Mn) were diluted by more 90% using Al_2O_3 with low absorption cross section(σ_a= 0.23 b) so as to minimize errors due to neutron self shielding effect. Then the samples were irradiated in an isotropic neutron field of the three 592 GBq ^{241}Am-Be neutron sources. The geometrical configuration of the neutron sources immersed in paraffin moderator shielded with lead as a neutron irradiation unit, installed at Ankara Nuclear Research and Training Center (ANRTC), is shown in Fig 1. The oxide forms of the analytical grade samples to be activated were filled in the polystyrene tubes (height/diameter ≈2) with 1 mm wall thickness. They were exposed to the neutrons in a fixed position in the irradiation hole(labeled no.1 in Fig1) of very large volume compared to the sample volume. Therefore, the effect of thermal fluence depression at the irradiation site has been neglected. The extent of non-ideality of epithermal neutron spectrum at the sample irradiation position were determined by using analytical grade-20 μm-thin Au and W foils.

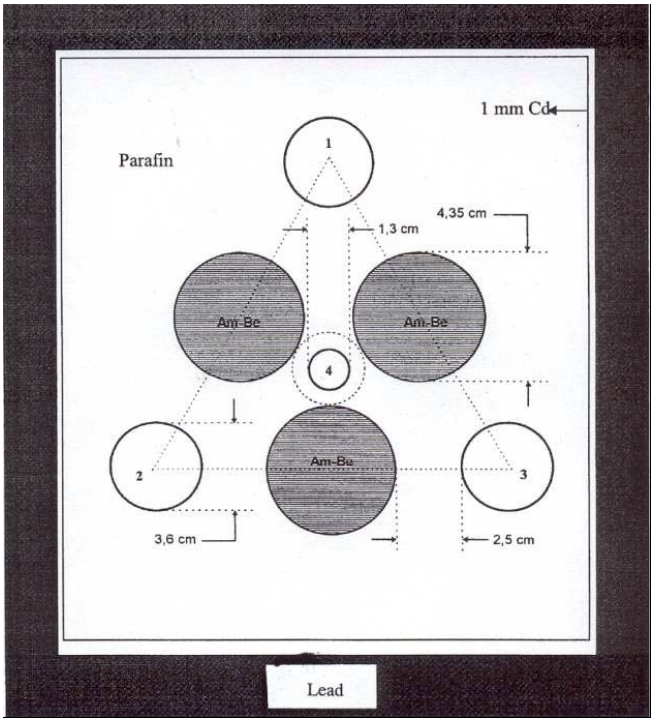


Fig.1 Cross sectional view of 3x592 GBq Am-Be source configuration
Sample irradiation positions in Fig.1 are numbered by Circles 1, 2, 3 and 4.

The irradiations of the samples were carried out within and without a cylindrical cadmium shield case. The 10 diluted samples for each element, Mn and La are individually prepared from the fresh stocks. Each set of 5 samples of MnO_2 and La_2O_3 were irradiated with and without Cd case for the Cd-ratio determinations. The irradiation times for the (n,γ) reactions of ^{55}Mn and ^{139}La were chosen for a period of three to six half lives, yielding enough activity to be measured in a γ-ray counting system. The suitable waiting times were employed to minimize dead time losses and. Dead times were typically less than 0.5 %. The counting times predetermined between 50,000 s and 100,000 s for each measurement was high enough to ensure good statistical quality of data.

The detector used in the measurements was a n-type germanium (REGe) with Be-window and total active volume of 100 cm^3 manufactured by Canberra, Inc. The measured resolution of the Ge detector was 1.80 keV for 1332.5 keV (^{60}Co) and 0.97 keV for 122 keV (^{57}Co) and its relative efficiency was 22.6%. The detector was shielded by lead lined copper sheets on all sides. The absolute photopeak gamma-ray efficiency as a function of energy for the REGe detector in a given sample geometry was determined using the powder radioactive standard containing a mixture of ^{109}Cd, ^{57}Co, ^{123m}Te, ^{51}Cr, ^{113}Sn, ^{85}Sr, ^{137}Cs, ^{60}Co and ^{88}Y radionuclides, obtained from Isotope Products Laboratories Inc. traceable to NIST.

Nuclear decay data, taken from NUDAT database [5], used for determination of the radioactivities and used in the cross section measurements and of the epithermal neutron fluence shaping factor for the neutron irradiation position are given Table 1.

Table 1. Nuclear decay data used for the determination of the radioactivities for the fluence rate, α-epithermal neutron fluence shaping factor and cross section measurements.

Nuclear reaction	Half-life	Detected γ-ray	
		Energy *(keV)*	*Intensity (%)*
^{55}Mn(n,γ)^{56}Mn	2.5789 h	846.754	98.9
^{139}La(n,γ)^{140}La	1.6781 d	487.021	45.5
		1596.21	95.4
^{186}W(n,γ)^{187}W	23.72 h	479.550	21.8
		685.73	27.3
^{197}Au(n,γ)^{198}Au	2.69517 d	411.80203	95.58

3. Neutron fluence rate determination

Using the irradiation data for a monitor sample such as Mn or Au, the equivalent 2200 m/s thermal neutron fluence rate can easily be determined by the formula:

$$\Phi_0 = \frac{1}{g\sigma_0 G_{th}}\left(R_s - R_{s,Cd}F_{Cd}\right) \tag{1}$$

where R_s is the reaction rate per atom, for an isotope exposed to a mixed thermal and epithermal neutron field(i.e., bare irradiation, $R_{s,Cd}$ is the reaction rate per atom produced within Cd shield case, F_{Cd} is a correction factor, which accounts for the transmission of epithermal neutrons through 1 mm cadmium, and can be taken to be unity, and also g is the Westcott factor, and can also be taken unity for this study because g(20 °C) is 1.0004 for ^{55}Mn and 1.00 for^{139}La [6], G_{th} is thermal neutron self shielding factor.

The reaction rate per atom, R_s and $R_{s,Cd}$ can be calculated by the following equation:

$$\mathrm{R_s \text{ or } R_{s.Cd}} = \frac{(\mathrm{A_{sp} \text{ or } A_{sp,e}})\,\mathrm{F_g\,M}}{\theta\,\mathrm{N_A}\;\gamma\;\varepsilon_p} \tag{2}$$

where A_{sp} and $A_{sp,e}$ denote the specific activities obtained after a bare and Cd covered isotope irradiation, and they can be determined as follows:

$$\mathrm{A_{sp} \text{ or } A_{sp,e}} = \frac{\mathrm{N_p}/\mathrm{t_m}}{\mathrm{w\,S\,D\,C}} \tag{3}$$

where the nuclear parameters in Eq.2 and in Eq.3 are:

N_p net number of counts under the full-energy peak collected during measuring time, t_m,

w weight of irradiated element,

S $= 1-e^{-\lambda t_{irr}}$, saturation factor with λ=decay constant, t_{irr} = irradiation time,

D $= e^{-\lambda t_d}$ decay factor; t_d = decay time,

C $= \frac{1-e^{-\lambda t_m}}{\lambda t_m}$, measurement factor correcting for decay during the measuring time, t_m,

M atomic weight,

θ isotopic abundance,

N_A Avogadro's number,

γ absolute gamma-ray emission probability,

ε_p full-energy peak detection efficiency,

F_g correction factor for gamma ray attenuation.

The correction factor for gamma ray attenuation in the sample at a given gamma ray energy at a fixed geometry for the case of a cylinder, coaxially positioned with the detector, is given by:

$$F_g = \frac{1 - e^{-\mu \rho x}}{\mu \rho x} \tag{4}$$

where μ is the total mass attenuation coefficient (cm^2/g) for the compounds used, taken from XCOM photon cross sections database of Berger and Hubbel [7], ρ is the density of sample (g/cm^3) and x is the sample thickness (cm).

The measured thermal and epithermal fluence rates of the used irradiation hole(labeled as No.1 in Fig.1) of the 3x592 GBq ^{241}Am-Be neutron source, are given in Table 2.

Table 2. The results for the thermal and epithermal fluence rates of the used irradiation hole of the 3x592 GBq ^{241}Am-Be neutron source

No	*Thermal neutron fluence rate, Φ_0 ($n.cm^{-2}s^{-1}$) x 10^4*	Epithermal neutron fluence rate, Φ_e ($n.cm^{-2}s^{-1}$) x 10^3	*Thermal to epithermal fluence ratio, $f=\Phi_0/\Phi_e$*
1	1.60 ± 0.07	1.45 ± 0.05	11.03 ± 0.61
2	1.59 ± 0.08	1.43 ± 0.05	11.12 ± 0.68
3	1.54 ± 0.13	1.46 ± 0.06	10.55 ± 0.99
4	1.56 ± 0.12	1.48 ± 0.06	10.54 ± 0.92
Average	1.57 ± 0.21	1.46 ± 0.11	10.81 ± 1.63

4. Determination of thermal neutron cross section by using a single standard material

In the present work, the thermal neutron cross section for the reaction ^{139}La(n,γ)^{140}La has been determined relative to that for the ^{55}Mn(n,γ)^{56}Mn monitor reaction. The thermal neutron cross section, $\sigma_{0,x}$ for the (n,γ) reaction of interest with respect to Eq.1, is calculated as:

$$\sigma_{o,x} = \frac{\left(R_s - R_{s,Cd}\right)_x}{\left(R_s - R_{s,Cd}\right)_{Mn}} \cdot \frac{\left(G_{th}\, g\right)_{Mn}}{\left(G_{th}\, g\right)_x} \cdot \sigma_{o.Mn} \tag{5}$$

where x corresponds to La. The reaction rates R_s and $R_{s,Cd}$ for ^{55}Mn monitor and ^{139}La isotope are determined from Eq.2, after a bare and Cd covered sample irradiations.The thermal neutron self shielding factors G_{th}, given in Table 4, have been calculated for the relevant reactions according to the self shielding correction procedure described in section 7.1.

5. α- shape factor determination in the 1/E $^{1+\alpha}$epithermal ^{241}Am-Be source-neutron spectrum

The extent of non-ideality of epithermal fluence shape, α-factor at the sample irradiation position of the used irradiation hole of the ^{241}Am-Be neutron sources

immersed in paraffin, was experimentally determined by using the dual monitor method suggested by De Corte et al [8,9], using the measured Cd ratios, R obtained from $^{197}Au(n,\gamma)^{198}Au$ and $^{186}W(n,\gamma)^{187}W$ reactions, in which 20 μm thin Au and W foils were used.

$$\frac{(R-1)_{Au}}{(R-1)_{W}} = \frac{\left[\left(\frac{I_0}{\sigma_0}\right)_{W} - 0.426\right]\left(\overline{E}_{r,W}\right)^{-\alpha} + \frac{0.426}{(2\alpha+1)E_{Cd}^{\alpha}}}{\left[\left(\frac{I_0}{\sigma_0}\right)_{Au} - 0.426\right]\left(\overline{E}_{r,Au}\right)^{-\alpha} + \frac{0.426}{(2\alpha+1)E_{Cd}^{\alpha}}} \tag{6}$$

The reference values of I_0/σ_0 for ^{197}Au and ^{186}W are used [9]. α-epithermal neutron spectrum shape factor is found to be 0.560 ± 0.002 for the sample irradiation position(labeled no.1 in Fig 1.) by solving Eq. 7 graphically, by means of a computer.

6. Determination of resonance integral cross section

In an ideal 1/E epithermal neutron spectrum, the resonance integral cross section, I_0 including 1/v tail of thermal neutron spectrum, tabulated in literature is defined by the following relation:

$$I_0 = \int_{E_{Cd}=0{\cdot}55eV}^{\infty} \frac{\sigma(E)}{E}\, dE \tag{7}$$

where σ(E), is the cross section as a function of energy E, E_{Cd} is the cadmium cut-off energy. It has been shown by De Corte et al. [8] that the resonance integral definition I_0 according to Eq.7 is not valid in a non-ideal, real epithermal neutron spectrum and that such a deviating epithermal neutron fluence distribution can be in most cases approximated by $\Phi_e(E) \sim 1/E^{1+\alpha}$ which is epithermal neutron flux per unit $(E^{-\alpha}/-\alpha)\cdot 1eV^{\alpha}$ of neutron energy interval. Accordingly, a resonance integral $I_0(\alpha)$ replacing by Eq.7 for a $1/E^{1+\alpha}$ real epithermal spectrum is defined as [8-10]:

$$I_0(\alpha) = \int_{E_{Cd}}^{\infty} \frac{\sigma(E)\,(1eV)^{\alpha}}{E^{1+\alpha}}\, dE \tag{8}$$

where α is an energy independent correction factor for spectrum shape, which can be positive or negative, depending on the irradiation system configuration (moderator material, geometry of irradiation site, etc.), $I_0(\alpha)$ is the resonance integral, which should be used in the calculation of the epithermal activation in a particular irradiation position, characterized by α, and the term $(1\ eV)^{\alpha} \equiv 1$ is omitted.

It has been shown that the relationship between I_0, as tabulated in literature, and $I_0(\alpha)$ for the conversion is given by [9]:

$$I_0(\alpha) = (1eV)^{\alpha}\left[\frac{I_0 - 0.426\,\sigma_0}{(\bar{E}_r)^{\alpha}} + \frac{0.426\,\sigma_0}{(2\alpha+1)(E_{Cd})^{\alpha}}\right] \tag{9}$$

where $\bar{E}_r$, effective resonance energy (eV), as defined and tabulated by Moens et al.[11], and the term $(I_0\text{-}0.426\sigma_0)$ represent the reduced resonance integral, i.e. with the 1/v tail subtracted. The Eq.9 is only valid for E_{Cd} = 0.55 eV, since $0.426=2(E_0/E_{Cd})^{1/2}$ with E_0=0.025 eV and E_{Cd} = 0.55 eV. The values of effective resonance energy, $\bar{E}_r$ are 412 eV for ^{55}Mn and 76.8 eV for ^{139}La [11]

In a mixed thermal and $1/E^{1+\alpha}$ epithermal neutron field, the ratio of the epithermal neutron fluence rate per unit of $(E^{-\alpha}/\text{-}\alpha)$ interval to thermal neutron fluence rate can be written as:

$$f = \frac{\Phi_0}{\Phi_e} = [R-1]\,\frac{I_0(\alpha)}{g\sigma_0}\,\frac{G_{epi}}{G_{th}} \tag{10}$$

where R is the cadmium ratio at the irradiation position, defined by $R=(A_{sp}/A_{sp,e})$, using specific activities without Cd and with Cd.

The measured $I_0(\alpha)$ value for the $^{139}La(n,\gamma)^{140}La$ reaction has been determined relative to that for the $^{55}Mn(n,\gamma)^{56}Mn$ reaction as a standard by the following relation:

$$I_0(\alpha)_x = I_0(\alpha)_{Mn}\,\frac{g_x\,\sigma_{0,x}}{g_{Mn}\,\sigma_{0,Mn}}\,\frac{(R-1)_{Mn}}{(R-1)_x}\left(\frac{G_{epi}}{G_{th}}\right)_{Mn}\left(\frac{G_{th}}{G_{epi}}\right)_x \tag{11}$$

In the determination of resonance integral $I_0(\alpha)_x$, for any isotope under study from Eq. 11, the estimated thermal and epithermal self shielding factors, G_{th} and G_{epi} given in Table 4 and in Table 6, and reference values of $\sigma_{0,Mn}$, $I_{0,Mn}$, g_{Mn} are used. Then, the obtained $I_0(\alpha)$ values were converted to I_0 by using Eq.9, and the results are given in Table 8.

7. Neutron self-shielding correction factors

7.1. Thermal neutron self-shielding correction factor

The magnitude of the fluence correction with sufficient precision can be evaluated by making appropriate assumptions:(1) neutrons are considered to be in a Maxwellian distribution with a velocity of 2200 m/s, (2) the neutron fluence can be treated being isotropic. Hence, a neutron self shielding factor, G for a sample is defined as follows:

$$G = \frac{\Phi_{av}}{\Phi_0} \tag{12}$$

where, Φ_{av} is an average fluence rate in the sample and will be always less than Φ_0 which is the incident fluence. The magnitude of self shielding factor depends on the size and shape of the sample. The thermal neutron self-shielding factor G_{th} for a finite cylinder of radius R and length L in an isotropic neutron field can be

calculated in conjunction with macroscopic absorption cross section $\Sigma_a=n\sigma_a$ as follows:[12, 13, 14]:

$$G_{th}=\frac{R\cdot G_{slab}+L\cdot G_{\inf\, cyl}}{R+L} \tag{13}$$

where G_{slab} and $G_{inf\ cyl}$ are the self-shielding factors for a slab and an infinite cylinder, respectively.
For a slab:

$$G_{slab}\cong 1-\frac{\tau}{2}\left[0.9228+\ln\frac{1}{\tau}\right] \tag{14}$$

For an infinite cylinder with radius R:

$$G_{\inf\, cyl}\cong 1-\frac{4}{3}\tau \tag{15}$$

with $\tau = N\sigma t$, where N= atom density(atoms/cm^3), t=slab thickness(cm) or t=R cylinder radius and σ=average thermal neutron cross section. The sample shape parameter , τ for a cylinder with a sample volume(V), and its surface area(S), is defined as

$$\tau=\frac{2V}{S}\Sigma_a=\frac{R\cdot L}{R+L}\Sigma_a \tag{16}$$

The composition weighted macroscopic cross section, Σ_a can be related to the known constituents of a sample and it can be calculated using the tabulated elemental values given in Table 3 by following relation:

$$\Sigma_a=\frac{\sqrt{\pi}}{2}\sum_i N_i\sigma_{0i} \tag{17}$$

where Σ_a is total macroscopic absorption cross-section of the compound or mixture (Maxwellian average),
N_i is number of absorbing nuclides per cm^3 of ith component in the compound or mixture, and σ_{0i} is absorption cross section with 2200 m/s neutron velocity for the ith component.
Since the neutrons from the isotopic neutron sources at the room temperature, T_0=20.43 ^oC for irradiation purposes were used instead of reactor neutrons, the averaged absorption macroscopic cross section would become independent of neutron temperature. However, the effect of neutron scattering in the sample has been taken into account by applying the necessary correction for this effect given by the following formula [12,13]:

$$G_{th}^{*}=\frac{G_{th}}{1-\frac{\Sigma_s}{\Sigma_t}\left(1-G_{th}\right)} \tag{18}$$

where G^*_{th} is the thermal self-shielding factor corrected for scattering, $\Sigma_t=\Sigma_a+\Sigma_s$, Σ_s are total and scattering macroscopic cross-sections, respectively. The thermal neutron self-shielding factors, G^*_{th} , including the scattering effect for Mn and La were calculated from Eq 18. Typical values of G^*_{th} for the samples investigated are given in Table 4.

Table 3. Absorption, scattering and total microscopic cross sections for thermal neutrons, and atomic weights for elements of interest

Element	*Atomic Weight, M (g/mol)*	*Microscopic cross sections (b)*		
		Absorption, σ_a	*Scattering, σ_s*	*Total, σ_t*
$_8$O	15.9994	$1.9\ 10^{-4}$	3.78	3.780
$_{25}$Mn	54.9380	13.41	2.17	15.58
$_{57}$La	138.905	8.93	10.13	19.06

Table 4. The calculated thermal neutron self shielding factors for MnO_2, and La_2O_3.

	Samples used	
	MnO_2	*La_2O_3*
Molecular weight, W ($g.mol^{-1}$)	86.9368	325.8092
Mass of the irradiated sample, m(g)*	0.035	0.047
Thermal self shielding factor, G_{th} from Eq.13	0.9978	0.9989
Thermal self shielding factor including scattering, G^*_{th} from Eq.18	0.9988	0.9996

*A typical value for an example irradiation.

7.2 Epithermal neutron self shielding correction factor

The epithermal neutron self-shielding factor, G_{epi} is defined by

$$G_{epi}=\frac{I_{eff}}{I_o} \tag{19}$$

where I_0, I_{eff} are the infinitely diluted resonance integral and the effective resonance integral, respectively. I_{eff} can be calculated by using the sum of symmetric Breit-Wigner line shape arising from the various resonances, as follows [15]:

$$I_{eff}=I_{1/v}+\frac{\pi}{2}\sum_i\left(\frac{\Gamma_\gamma}{E_r}\right)_i\frac{\sigma(E_{ri})}{\sqrt{1+2Nd\sigma(E_{ri})}} \tag{20}$$

and similarly, I_0 can also be calculated as follows :

$$I_0=I_{1/v}+\frac{\pi}{2}\sum_i\left(\frac{\Gamma_\gamma}{E_r}\right)_i\sigma(E_{ri}) \tag{21}$$

where,

E_{ri} i^{th} neutron resonance energy,

$\Gamma_{\gamma i}$ the probability per unit time interval for the compound nucleus to de-excitate by emitting one or more photons for i^{th} resonance,

$\sigma(E_{ri})$ total cross-section at maximum of i^{th} resonance,

N number of absorbing nuclides per cm^3 and,

d mean chord length (=2V/S), where, V, S denote volume and total surface of cylinder, respectively,

$I_{1/v}$ 1/v contribution (=0.43 σ_0 for E_{Cd}=0.55 eV for cylinder box with 1 mm wall thickness).

The epithermal neutron self-shielding factors, G_{epi} for the cylindrical sample geometry were calculated by using the characteristic resonance parameters given in Table 5 ,and material constants given in Table 6.

Table 5. Some characteristic resonance parameters of main resonances for ^{55}Mn and ^{139}La [16].

Nuc-lide	*Resonance Energy E_r(eV)*	*Radiative width of the resonance, Γ_γ(eV)*	*Total width of the resonance, Γ (eV)*	*Cross section at the resonance energy, $\sigma(E_r)$ (b)*
^{55}Mn	337.3	0.31	22.3	3287
	1099	0.31	15.7	1439
	2327	0.34	395	675.7
^{139}La	72.30	0.054	0.088	6251
	617.2	0.031	0.057	1118
	875.4	0.023	0.044	799.6
	962.9	0.030	0.049	485.5
	1179	0.051	2.163	958.8

Table 6. Calculated epithermal neutron self-shielding factors.

Element	*Sample*	*Sample mass, m (g)*	*Target nuclide*	*Abundance θ (%)*	*Number of nuclides per cm^3, $N x10^{20}$ (cm^{-3})*	*Epithermal neutron self shielding factor♠, G_{epi}*
Mn	MnO_2	0.035	^{55}Mn	100	2.058	0.916
La	La_2O_3	0.047	^{139}La	99.909	1.535	0.848

♠: These values are for the specified sample amounts.

8. Results and discussion

The thermal neutron cross section for the $^{139}La(n,\gamma)^{140}La$ reaction has been obtained relative to the reference cross section value of 13.3 ± 0.1 b of $^{55}Mn(n,\gamma)^{56}Mn$ reaction. The experimental uncertainties for the ^{139}La and ^{55}Mn are given in Table 7. The main sources of the uncertainties are due to statistical errors (0.38-0.39%), detection efficiencies (2.52-2.75%) and other errors including some corrections. The data obtained with different irradiation and counting times of activation samples were relatively close to each other, and the difference of the results is within about 1.2% for La. There existed a consistency among the measured data.

The obtained thermal cross section value for $^{139}La(n,\gamma)^{140}La$ reaction is σ_0=9.27 ± 0.37 b given in Table 8 and compared with experimental and evaluated data. The present result for thermal cross section for the $^{139}La(n,\gamma)^{140}La$ reaction is in good agreement with the measurements of Holden [17] and Heft [15], and is close to within 1 to 5% with the values obtained by Gleason [18], Ryves [19], Mughabghab et al. [3], De Corte et al. [20] and Kafala et al. [21], but disagrees with the measurements of Steinnes [22] and Lyon [23] by 14.4-17.2. The present value agrees within 3-4% with the evaluated values of JENDL-3.2[16], IAEA[24] and BNL[25].

The value of resonance integral for the $^{139}La(n,\gamma)^{140}La$ reaction has been obtained relative to the reference value of 14.0 ± 0.3 for the $^{55}Mn(n,\gamma)^{56}Mn$ reaction by assuming the cadmium cut-off energy of 0.55 eV The obtained result for the resonance integral cross section for the $^{139}La(n,\gamma)^{140}La$ reaction is 12.16 ± 0.60 b and this value disagrees with the measurements of Ryves[19], Harris et al. [26] and Alian [27] by 6-40.6%. However, the present result agrees well the recently reported value obtained by Holden[17] by 0.13%, assuming Cd cut-off energy of 0.50 eV. The precision of the present measurement is higher than that of Holden[17]'s result, but the precision of the result obtained by Kafala et al.[21] is two times better than those of the results in the surveyed literature, given in Table 8.

In conclusion, the present results for the $^{139}La(n,\gamma)^{140}La$ reaction obtained by the activation method show that the thermal neutron cross section and the resonance integral for the isotopes can be determined with sufficient accuracy by using small amounts of powder samples similar to the foils, when the necessary corrections are made for the results. Manganese having the good nuclear parameters can be used a standard material in the activation method instead of ideal monitor- gold employed in the analysis of the most reactions.

Table 7. Experimental uncertainties for the thermal neutron cross section and resonance integral cross section measurements.

Thermal neutron cross section measurements		
Uncertainties due to	*Uncertainties (%)*	
	$^{139}La(n,\gamma)^{140}La$	$^{55}Mn(n,\gamma)^{56}Mn$
Statistical error*	0.38	0.39
Detection efficiency,	2.52	2.75
Mass of sample	0.01	0.01
Half-life	0.018	0.004
Isotopic abundance	0.0005	---
Branching ratio	1.13	0.30
Self-shielding factor	0.01	0.01
g-factor	< 0.05	< 0.05
Monitor thermal neutron cross section [9,8]	--	0.75
Total error (in quadrature)	2.79	2.89

Resonance integral cross section measurements		
Uncertainties due to	*Uncertainties (%)*	
	$^{139}La(n,\gamma)^{140}La$	$^{55}Mn(n,\gamma)^{56}Mn$
Cadmium ratio	1.58	1.60
Self-shielding factor	0.60	0.20
g-factor	< 0.05	< 0.05
Reference thermal neutron cross section	0.448	0.75
Monitor resonance integral cross section [5, 21]	--	2.14
α-shape parameter	0.89	1.20
--	--	--
Total error(in quadrature)	1.96	4.56

*Errors are based on counting statistics of ± 1.65 σ(at 90 % confidence level)

Table 8. Thermal neutron cross section and resonance integral cross section for $^{139}La(n,\gamma)^{140}La$ reaction.

Year	*References*	*Thermal neutron cross section, σ_0 (b)*	*Resonance integral cross section, I_0 (b)*	*Cadmium cut-off energy, E_{Cd} (eV)*
	This Work	9.27 ± 0.37	12.16 ± 0.60	0.55
1999	Holden [17]	9.2 ± 0.2	12 ± 1	0.50
1997	Kafala et al. [21]	9.67 ± 0.30	11.6 ± 0.2	0.55
1997	JENDL-3.2 [16]	8.930	11.8	0.50
1989	De Corte et al. [20]	9.43 ± 0.09	11.6	---
1987	IAEA [24]	8.93 ± 0.04	12.2 ± 0.8	---
1981	Mughabghab et al. [3]	8.93 ± 0.04	11.8 ± 0.8	0.50
1978	Heft [10]	9.18 ± 0.05	12.6 ± 0.6	0.50
1978	Takiue [28]	8.63 ± 0.34	---	---
1975	Gleason [18]	9.15 ± 0.25	12.5 ± 0.4	0.50
1975	Steinnes [22]	11.2 ± 0.5	---	0.50
1974	V.D.Linden et al. [29]	11.6 ± 0.7	---	0.55
1973	BNL [25]	9.0 ± 0.3	12.2 ± 0.6	0.50
1973	Alian [27]	---	17.1	0.50
1972	Steinnes [30]	---	11.8 ± 1.2	0.50
1971	Ryves [19]	9.03 ± 0.33	11.4 ± 0.8	0.50
1971	De Corte [31]	---	11.0	0.50
1968	Orvini [32]	---	10.8 ± 1.1	0.55
1967	Brien [33]	9.5 ± 0.5	11.2 ± 0.6	0.54
1960	Lyon [23]	8.10	---	---
1957	Cummins [34]	9.1 ± 0.2	---	---
1951	Pomerance [35]	8.8 ± 0.44	---	---
1951	Benoist [36]	8.35 ± 0.10	---	---
1950	Harris et al. [26]	---	13.2	0.50

References

1. Ryves,T.B and Zieba, K.J. J.: Phys: Math., Nucl. Gen., **7**(18), 2318 (1974).
2. Neutron fluence measurements, Technical report series no: 107, IAEA, Vienna, 1970.
3. Mughabghab, et al.: *Neutron Cross Section from Neutron Resonance Parameters and Thermal Cross Sections*, Academic Press, New York, 1981.
4. Goldstein, H., et al.: Recommended definitions for resonance integral cross section, Report E.A.N.D.C., 12, 1961.

5. Nuclear Data Retrieval, http://www.nndc.bnl.gov (NuDat).
6. El. Nimr, T., et al.: J. Radioanal. Chem., **67**(2), 421 (1981).
7. Berger, M. J., Hubbell, J. H.: XCOM Photon Cross Sections Database, NBSIR 87-3597,1987.
8. De Corte, F., et al.: J. Radioanal. Chem., **52**(2), 305 (1979).
9. De Corte, F., et al.: J. Radioanal. Chem., **52**(2), 295 (1979).
10. Heft, R. E.: A consistent set of nuclear-parameter values for absolute instrumental neutron activation analysis, Conf. on Computers In Activ. Analysis, Mayaguez, Puerto Rico, 1978, p. 495.
11. Moens, L., et al.: J. Radioanal. Chem., **52**(2), 379 (1979).
12. Gilat, J., Gurfinkel, Y.: Nucleonics, **21**(8), 143 (1963).
13. Fleming, R. F.: Int. J. Appl. Radiat. Isot., **33**, 1263 (1982).
14. Shakir, N. S., Jervis, R. E.: J.: Radioanal. Nucl. Chem., **248**(1), 61 (2001).
15. Beckurts, K., Wirtz, K.: *Neutron Physics*, Springer, Berlin, 1964
16. Fukahori, T., et al.: *JENDL-3.2*, JAERI-Data/Code 97-044, 1997.
17. Holden, N. E.: Neutron scattering and absorption properties (revised 1996) In: *CRC Handbook of Chemistry and Physics* (D. R. Lide, ed.), 79 th ed., CRC Press, New York 1999.
18. Gleason, G.: Radiochem. and Radioanal. Letters, **23**, 317 (1975).
19. Ryves, T. B.: J. Nucl. Energy, **25**, 129 (1971).
20. De Corte, F., et al. : Radioanal. Nucl. Chem., **133**, 43 (1989).
21. Kafala, S. I., et al.: J. Radioanal. Nucl. Chem., **215**(2), 193 (1997).
22. Steinnes, E. : J. Inorg. Nucl. Chem., **37**, 1591 (1975).
23. Lyon, W. S.: Nucl. Sci. Eng., **8**, 378 (1960).
24. Handbook of nuclear activation data, Tech. Rept. series no: 273, IAEA, Vienna, 1987.
25. Neutron cross-sections, BNL-325, 3rd ed., Vol.1, 1973.
26. Harris, S. P., et al.: Phys. Rev., **79**, 11 (1950).
27. Alian, A., et al. : Radioanal. Chem., **15**, 535 (1973).
28. Takiue, M., Ishikawa, H.: Nucl. Instrum. Methods in Physics Res., **148**(1), 157 (1978).
29. Van Der Linden, R., et al.: J. Radioanal. Chem., **20**, 695 (1974).
30. Steinnes, E. : J. Inorg. Nucl. Chem., **34**, 2699 (1972).
31. De Corte, F., et al. : Radioanal. Chem., **9**, 9 (1971).
32. Orvini, E., et al. : J. Inorg. Nucl. Chem., **30**, 1353 (1968).
33. Brien, H. A., et al.: J. Inorg. Nucl. Chem., **29**, 584 (1967).
34. Cummins, J. D.: A.E.R.E. Harwell Reports, 2333, 1957.
35. Pomerance, H.: Thermal neutron capture cross sections, Phys. Rev., **83**, 641 (1951).
36. Benoist, P., et al.: Journal de Physique, **12**, 584 (1951).

MEASUREMENT OF TIME STRUCTURE AND THE INTERNAL BEAM INTENSITY AT THE CYCLOTRON

A. Arzumanov, M. Gorkovets, V. Koptev

Institute of Nuclear Physics, Almaty, 480082, Kazakhstan

Abstract.

During last years the application of the cyclotron has been increased essentially. More high beam quality and more operative tuning of the cyclotron were needed.

To obtain current information on beam acceleration at the cyclotron six inductive pick up probes were mounted in the dee. These probes make possible to determine the phase of the ion beam and phase wide on the different radii. Simultaneously internal beam intensity is determined with these probes.

In the article design of the pick up probes and the results of beam parameters measurement are presented. The accuracy of phase measurement is equal to 0.35° and measurement of the time duration of the ions bunch is equal to 0.5 ns.

The variable energy isochronous cyclotron U-150M had been put into operation in 1972. Different modes of operation are based on the magnetic field measurements and calculations of beam dynamic performed at that time. Two probes were mounted in the cyclotron for diagnostic of internal beam: first one is located between dees in the direction of resonators (it can be moved along the radius), second one is located behind the exit channel. These probes cannot give full information about ion acceleration process from the center to the final radius.

In connection with new irradiation works demanding more bombarding accuracy inside the vacuum tank of the cyclotron it is necessary to optimize the process of acceleration mode. In order to get phase information along the cyclotron radius six pickup probes have been mounted in the right cyclotron's dee. The probes are located along the radius at points: 31 cm, 38 cm, 45 cm, 52 cm, 58 cm and 65 cm. The accuracy of probe mounting is equal to ± 0,5 cm.

Phase probes

6 identical pickups are made as parts of a strip line (fig.1.).

The probe's iterative impedance is equal to Z=50 Ohm, bandpass – 1 GHz, ripple – 3 db. The design of probe allows to mount it on the lower surface of the right dee. The probes are connected with measurement devices by equal length coaxial cable. Difference of cables' electrical size is not more than ± 50 psec, or it is equal to 5′ (in phase degree) at 30 MeV protons mode.

Scheme of measurement of the beam phase is shown in the fig.2.

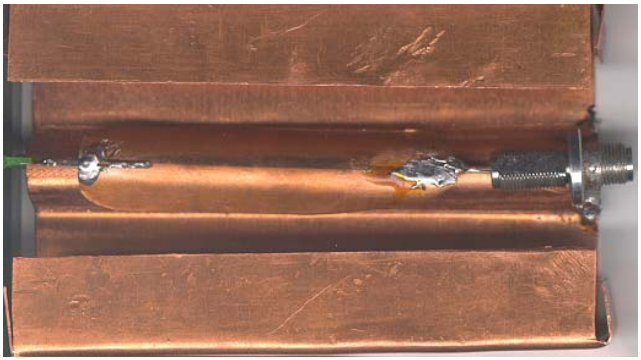


Fig.1. Phase probe.

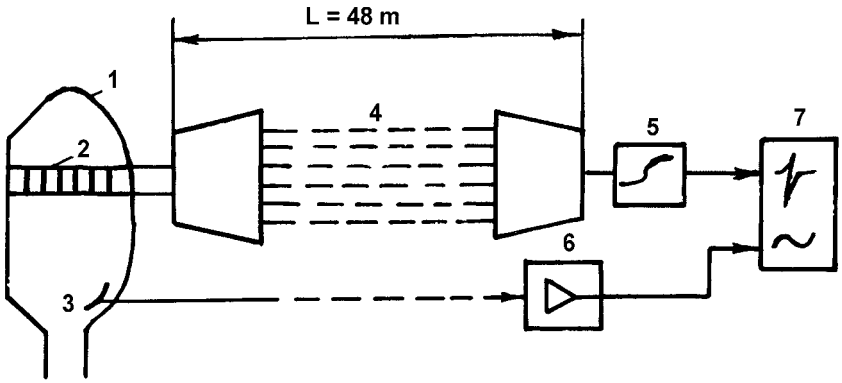


Fig.2. Scheme of phase beam measurement.
1 – dee, 2 – pickups, 3 – probe of accelerating voltage, 4 – feeders,
5 – filter (0 – 21 MHz), 6 – amplifier with delay, 7 – measurement device.

In order to get real phase information multiplexers and commutators were excepted. The oscilloscope TDS-380 with a time step of 20 psec was used as a measuring instrument. Output voltage of one pickup and accelerating voltage probe are shown in the fig.3. The accuracy of phase measurement is equal to 0.35°.

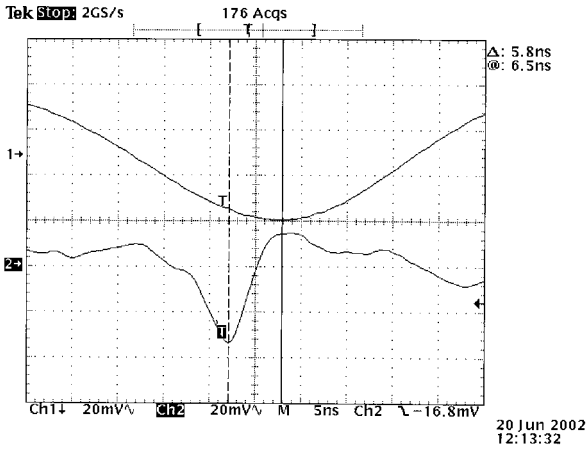


Fig.3. Measured signals of pickup (2) and accelerating voltage probe (1).

Measurements

Measurements of the accelerated ion beam phase were carried out at the 22 MeV protons mode of operation (f=15.7 MHz, U_{left}/U_{right}=45/43 kV, I= 20 μA of the internal beam). The sinusoidal signal of accelerating voltage probe fed one channel of the oscilloscope while signals of pickups fed second channel by turns. Since the signal of accelerating voltage has a stable phase and amplitude, it was used as reference signal. As a calibration method was chosen an accelerating zero phase for the first pickup. It means that the peak of a pulse from the 1-st pickup marked by the cursor was combined by means of delay line with the maximum amplitude of accelerating voltage, marked also by the cursor. In fig.4 it is shown the beam phase changes relative to accelerating rf-voltage along the cyclotron radius.

Dependence of average magnetic field vs. radius determines beam phase change. For example, in fig 5 dependence of average magnetic field vs. radius for 30 MeV protons mode is shown. According to this field the beam phase changes, as it is shown in fig 6. One can distinctly see isochronous acceleration in the range of 30 cm – 54 cm. The measured phase change (fig 7) reflects the field configuration in the experiment.

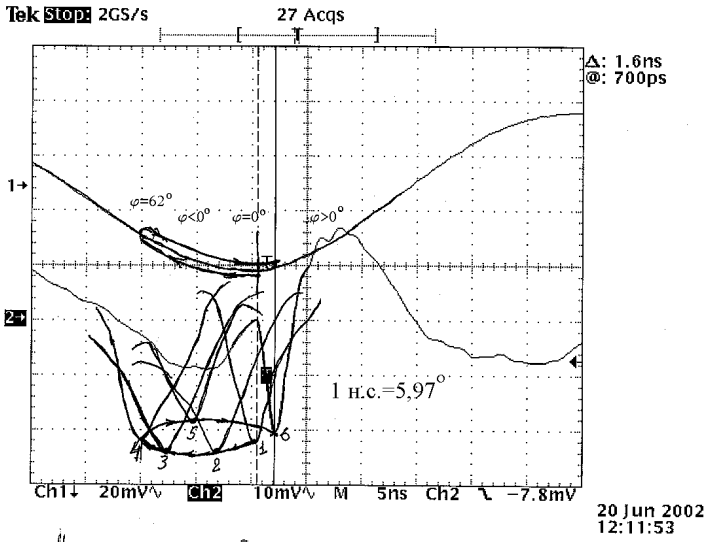


Fig.4. Change of phase as pickups' output voltage and the projection of pickups' signals to the reference one.

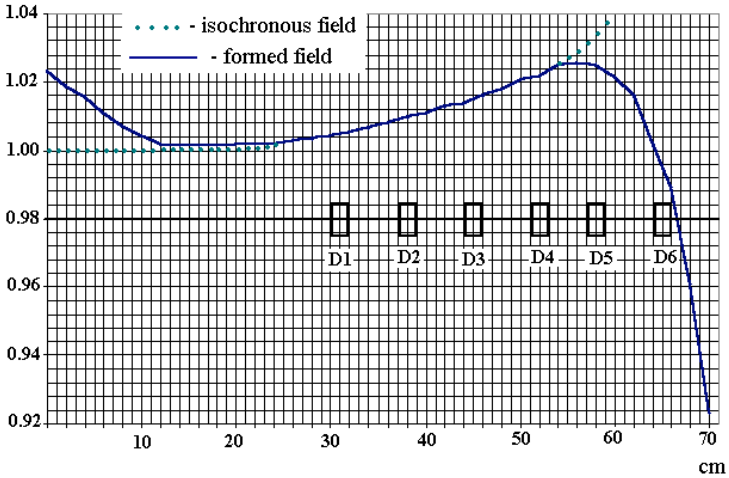


Fig.5. Dependence of average magnetic field of 30 MeV protons mode versus radius. D1, D2, D3, D4, D5, D6 – pickup probes.

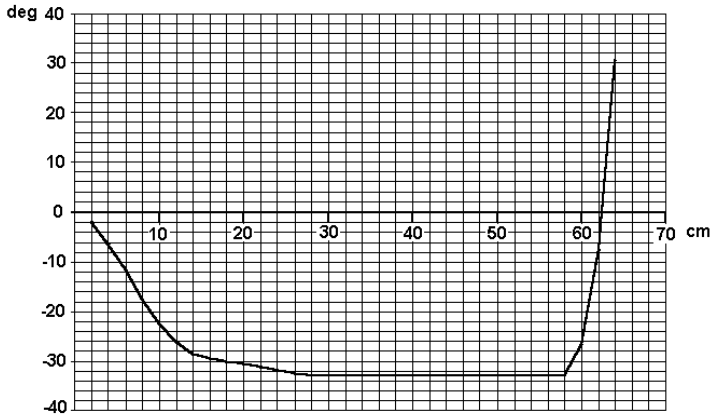


Fig.6. Dependence of RF phase versus radius.

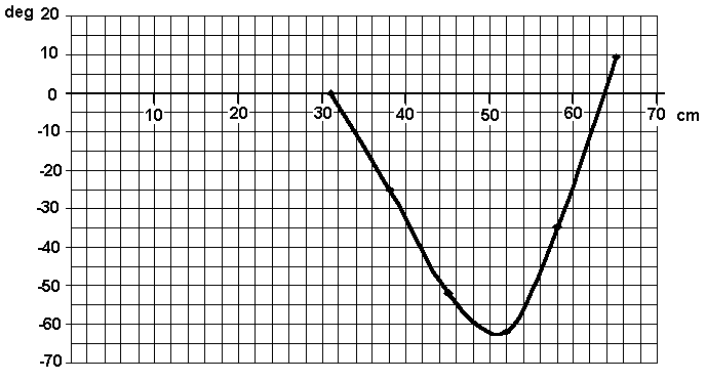


Fig.7.Dependence of measured beam phase versus radius.

Conclusion

Pickup probes, mounted in dees, give information about the beam phase change along radius in accordance with formed magnetic field of operational mode. In order to provide optimal cyclotron operation it is necessary to create a control system of pickups more than 6. It will allow to correct isochronous field to given mode and increase internal and external beam parameters.

References

1. Arzumanov A.A., Butishev V.N. et.al. Status of the Alma- Ata Isochronous Cyclotron. –10-th Int. Conf. Cycl. and their Appl., East Lansing (USA), 1984, pp. 476-482.

MEASUREMENTS OF GROUND, FIRST EXCITED-STATE ENERGY AND WIDTH OF ^{5}He VIA d-^{7}Li REACTION

[1]Baykal Adnan, [1]Tarcan Gökçe, [1]Reyhancan Iskender Atilla and [2]Erduran M. Nizamettin

[1]Çekmece Nuclear Research and Training Centre, Department of Physics, P.O.Box.1, Atatürk Airport, TR-34831, Istanbul-TURKEY
[2]University of Istanbul, Faculty of Science, Department of Physics, Vezneciler 34459 Istanbul-TURKEY

Abstract

The reaction products from d-^{7}Li were studied using a 150 keV deuteron beam from SAMES J-15 accelerator at Çekmece Nuclear Research and Training Centre (ÇNAEM). The target was obtained by evaporating natural LiF (800μg/cm^2) onto Aluminium backing (1500μg/cm^2). Two silicon surface barrier detectors (SSB) were chosen in order to detect all the alpha-particles produced in the reaction and they were placed on the opposite side respect to the beam. The alpha-alpha coincidence technique was employed and energy signals from SSB#2 detector placed on 83.5^0 are gated with 6.7 - 8.2 MeV interval of energy signals from SSB#1 placed on 90^0 . Coincidence spectra obtained were corrected for the energy loss in the target. The coincidence spectra were then unfolded and alpha lines belonging to the ground and first excited states of ^{5}He were then identified.

1. Introduction

Up to now, the ground state width of ^{5}He is measured by a few laboratories. Measured values are range of 0.525 and 1.36 MeV [1]. In last measured data [2], the values of excitation energy and width are 0.80±0.02 MeV and 0.65±0.02 MeV for ground state via ^{3}H(d,γ)^{5}He reaction respectively.

Although first excited state of ^{5}He is also measured by a lot of laboratories, there are discrepancies between reported values[3]. These values are range 1.97-5.2 MeV and 1.5-7 MeV for excitation energy and width of first excited state respectively. Evaluated values for ground state width, energy of the first excited state and state width are 0.6±0.02 MeV, 4.0±1.0 MeV 4.0±1.0 MeV respectively [4].

2. Experimental Set-up

The scattering reaction chamber is a cylinder shape of 25.4 cm diameter, 10 cm height and has vacuum 10^{-6}torr. It is coupled SAMES J-15 low energy ion accelerator (E_d=150keV). Two silicon surface barrier detectors (SSB) are chosen in order to detect all the alpha particles produced in the reaction and they are placed

on the opposite side respect to the beam. First one (SSB#1) is fixed at 90° and the other one (SSB#2) has changeable angular movement (0-360 degrees) (Figure 1). Both of the detectors have collimators of 8 mm in diameter and 10 mm in length. The specifications of SSB detectors are energy resolution <14 keV and depletion layer 300μm.

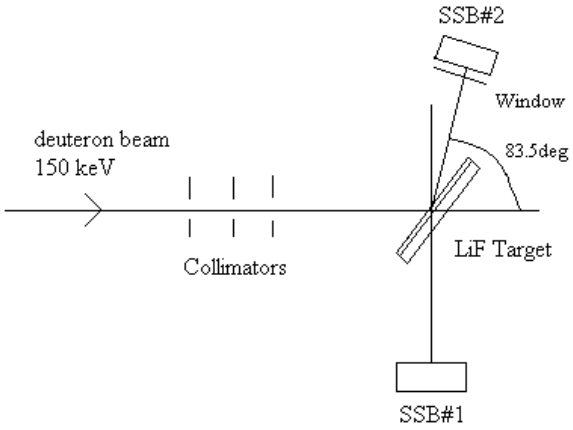


Figure 1. Experimental Setup

Unanalysed deuteron beam (76% atomic and 24% molecular) before Li target passes through the three separate collimators of 18 cm length and 3 mm diameter. Li target is placed 45° with respect to the beam. Due to the deuteron scattering on the target, the SSB#2 detector faced to the Li target has a window made of Aluminum-Mylar of 850 μg /cm^2. SSB#1 has no such a window because it is placed opposite side respect to the beam and behind the Li target.

Thin Li targets are produced with coating LiF (800μg/cm^2) on the Aluminum substrate (1500μg/cm^2) by evaporation method in the vacuum chamber (~10^{-4}Torr). During the irradiation, deuteron current is measured 10 μA on the target. Experimental set-up is shown Figure 1 and electronic setup is also seen Fig.2.

3. Kinematics of Reaction

d-Li reaction is formed three different channels. These channels are direct reaction ^{7}Li(d,αα)n, disintegration of ^{5}He via ^{7}Li(d,α) ^{5}He(α)n and disintegration of ^{8}Be via ^{7}Li(d,n)^{8}Be(α)^{4}He.

The contribution of disintegration of ^{5}He is higher than other two reactions in estimated spectra, the sum of contributions of other two reactions are also less than 10% [5]. Using direct reaction kinematics formula [5], energy diagram of α_1 and α_2 particles is obtained as shown Figure 3 (Dalitz Diagram) for a

given bombarding energy E_d = 150 keV and two angles of detection angles $\theta_1 = 90^o$, θ_2 = 60,75,83.5, 90 and 95 degrees.

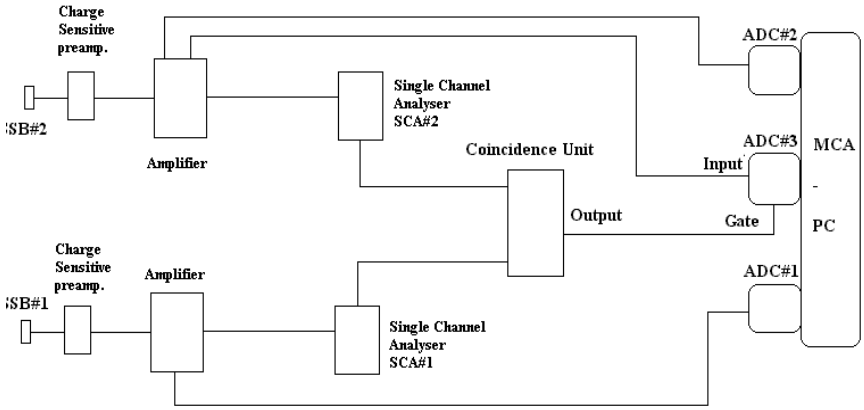


Figure 2. Block diagram of electronics

When knowing the energy of alpha particles detected by coincidence spectra from SSB detectors experimentally, corresponding the ground and first excited states of ^{5}He nucleus (J^π =3/2$^-$, 1/2$^-$ respectively) and the ground and excited states of ^{8}Be nucleus (0$^+$, 2$^+$ and 4$^+$ respectively) can be found with help of this diagram. At the same time, energies of alpha particles which are found by changing E_x excitation energy of ^{5}He nucleus (E_x (^{5}He)=0 - 9 MeV) are shown at Fig. 4.

4. Analysis and Results

The charge particle energy spectra collected from SSB#1 (θ_1=90^0) and SSB#2 (θ_2=83.5^0) detector are shown in Figure5. At the same time, in this spectra, Coincidence spectra is taken at SSB#2 detector for θ_2=83.5^0 (0-13 MeV) gated by consecutive energy window of the SSB#2 detector for θ_1=90^0 over the energy range 6.7-8.2 MeV.

Energy calibration for SSB#1 is made with help of mixed alpha source (5.142, 5.484, 5.808 MeV at Pu-239, Am-241, Cm-244 respectively), protons from the reaction ^{2}H (d,p)^{3}H and alphas from the reaction ^{6}Li(d,α)^{4}He. The reactions ^{2}H (d,p)^{3}H, ^{6}Li(d,α)^{4}He and ^{6}Li(d,p)^{7}Li are used for energy calibration of SSB#2 detector.

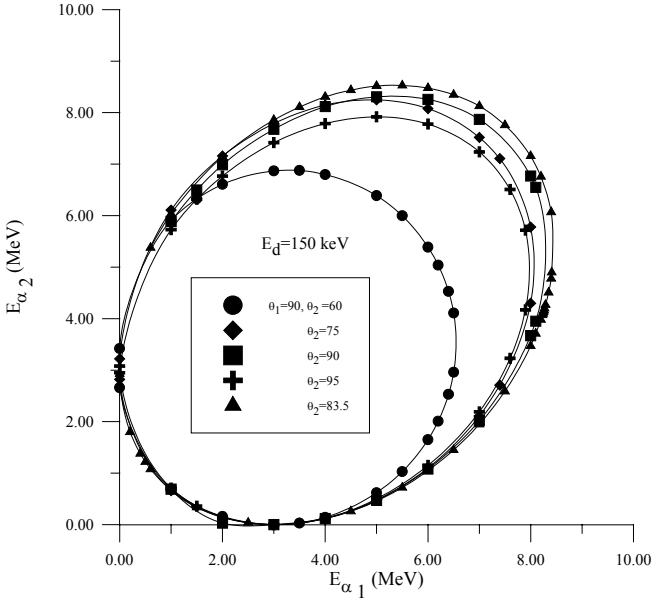


Figure 3. Dalitz Diagram

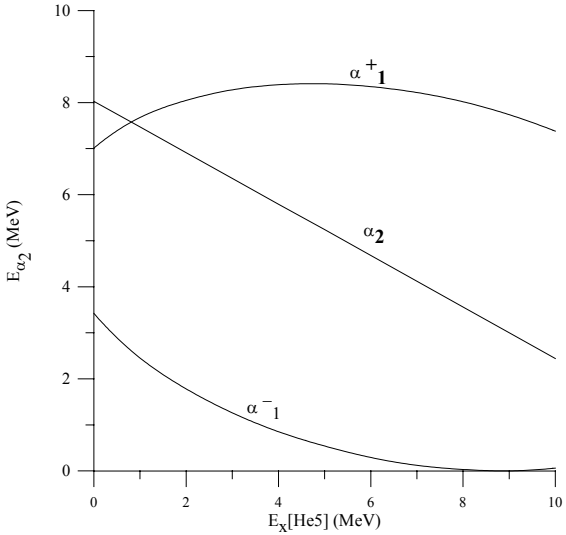


Figure 4. Energetics of ^{5}He formation

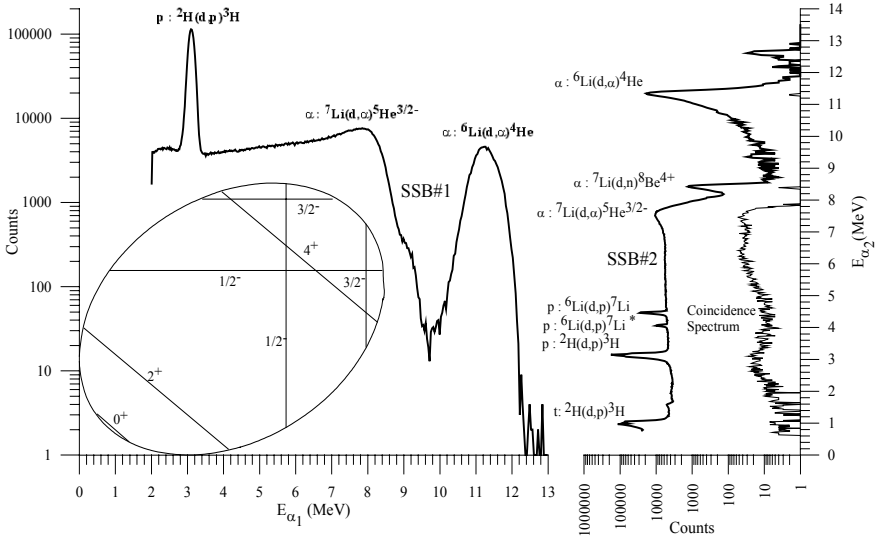


Figure 5. Alpha energy and Coincidence Spectrum

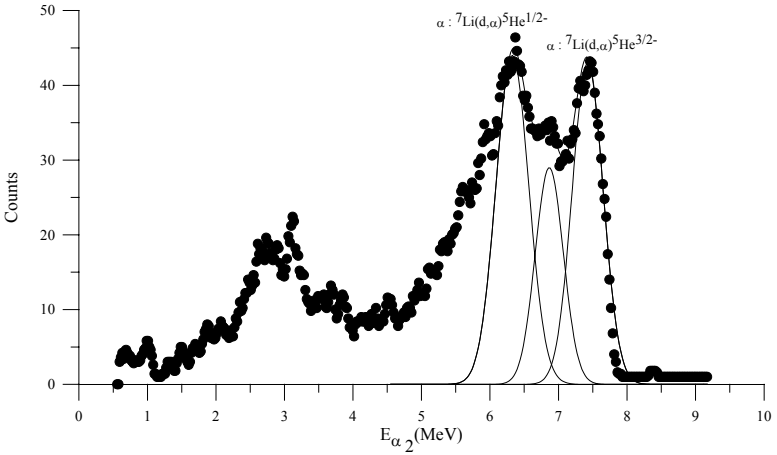


Figure 6. Smoothed Coincidence Spectrum

Because the SSB#1 detector is behind the Li target and Aluminum foil in front of SSB#2 detector is used for eliminating noise (deuteron scattering), energy loss for charge particles must be corrected. Coincidence spectrum is smoothed for analyzing by 5-point zeroth order smooting method (Figure 6). The calculated energy values for the ground and first excited states of ^{5}He using Figure 4 are shown below.

$E_x(^5He^{3/2-}) = 1.0\pm0.4$ MeV, $\Gamma(^5He^{3/2-}) = 0.5\pm0.2$ MeV
$E_x(^5He^{1/2-}) = 3.0\pm0.5$ MeV, $\Gamma(^5He^{1/2-}) = 0.6\pm0.2$ MeV

5. Discussion

The alpha energies of the ground and first excited states of ^{5}He are measured at the coincidence spectrum well. Measured alpha energy values are fitted with theoretical Dalitz Diagrams for the ground and first excited states of ^{5}He nucleus. Uncertainties of the width and energy values are higher than other literature data, because the data collection time is not enough for a good statistics during the data taking, although the time is 131000 sec and so long. Additionally, the $^7Li(d,\alpha)^5He$ reaction cross section for 150 keV deuteron energy is so low (0.15 mb). If the reaction experiment is done with analyzed 300 keV deuterons, because of higher reaction cross section (1.5 mb) [6], we can get a good counting statistics.

References

1. M.J. Balbes, G. Feldman, L.H. Kramer and H.R. Weller, Phys. Rev. C, Vol. 43, Num. 1, (1991), 343-346.
2. V.D. Efros and H. Oberhummer: Physical Review C, Vol. 54, Num. 3, (1966), 1485-1487.
3. N. Arena et al.: Journal of the Physical Society of Japan Vol. 60.No.1, (1991), 100-106.
4. F. Ajzenberg-Selove: Nuclear Physics. A 490. (1988). 1- .
5. P.A. Assimakopoulos, N.H. Gangs and S. Kossionides : Nuclear Physics 81, (1966), 305-321.
6. M. Manalis and J.E. Henkel. Physical Reviev. Vol. 136. Number 6B. (1964), B 1741-B1743.

MULTIPLE PRODUCTION OF PARTICLES IN ANTIPROTON - PROTON ANNIHILATION AT MOMENTUM 22.4 GeV/c

Boos E.G., Temiraliev T., Pokrovsky N.S., Samoilov V.V.

Institute of Physics and Technology MES RK, Almaty, Kazakhstan

The main information on the mechanism of particle generation in antiproton - proton annihilation at high energies (E_0>10 GeV) was gained by indirect methods [1-3]. For the first time in paper [4] at primary momentum 22.4 GeV/c the annihilation and non-annihilation antiproton - proton interactions were divided individually. It has allowed to analyse in details the mechanism of particle generation of particles in antiproton - proton annihilation. The unexpected result was obtained in [5] that in the annihilation channel the equal quantity (on three the average) of π^0, π^+, π^- - mesons was produced and the production on the average of three π^0 - mesons in each multiplicity was observed. This result has stimulated the analysis of effective mass distributions in antiproton - proton annihilation events.

In a Fig. 1 the data on $(\pi^+\pi^-)$ effective mass distributions in two-prong inclusive reactions for the annihilation class (Fig. 1a) and for events with a neutron - antineutron pair in finite state (Fig. 1b) are represented.

From comparison of Fig. 1a) and Fig. 1b) it follows, that, firstly, effective mass distribution of meson pairs from the non-annihilation channel is essentially limited in the region of $M_{eff.}$ about 1 GeV/c^2 and is breaked at $M_{eff.}$ $(\pi^+\pi^-)$ > 1.5 GeV/c^2, while about half of all annihilation type events are concentrated in region $M_{eff.}$ $(\pi^+\pi^-)$ > 1 GeV/c^2, and the effective masses up to 4 GeV/c^2 are observed ; secondly, in annihilation events the manifestation of three peaks is visible in a spectrum of $(\pi^+\pi^-)$ masses, the first peak in region M $(\pi^+\pi^-)$ = 0.525 GeV/c2 apparently is connected to kinematics of particle production, and the subsequent two peaks (statistical security of which leaves for two standard deviations) in M $(\pi^+\pi^-)$ = 0.775 and 1.225 GeV/c^2 mass distributions indicate on the production of ρ and f_2 resonances. In M $(\pi^+\pi^-)$ distribution the irregularities are not observed in the mass region of ρ and f_2 resonances in reaction $\tilde{p}p \to n\tilde{n}\pi^+\pi^- X^0$. These new results definitely testifies that in annihilation channels meson resonances essentially appear unlike

the non-annihilation channels, where the pions in the main have an isobaric origin.

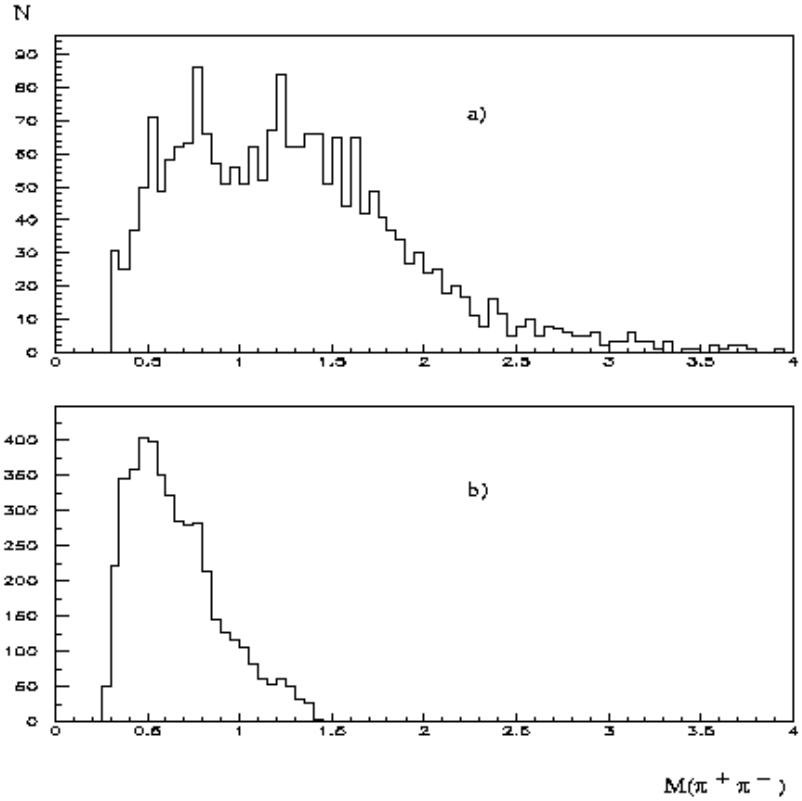


Fig. 1. Effective mass $M(\pi^+\pi^-)$ distributions:

a) $M(\pi^+\pi^-)$ in reaction $\tilde{p}p \to \pi^+\pi^- x^0$;

b) $M(\pi^+\pi^-)$ in reaction $\tilde{p}p \to n\tilde{n}\,\pi^+\pi^- x^0$;

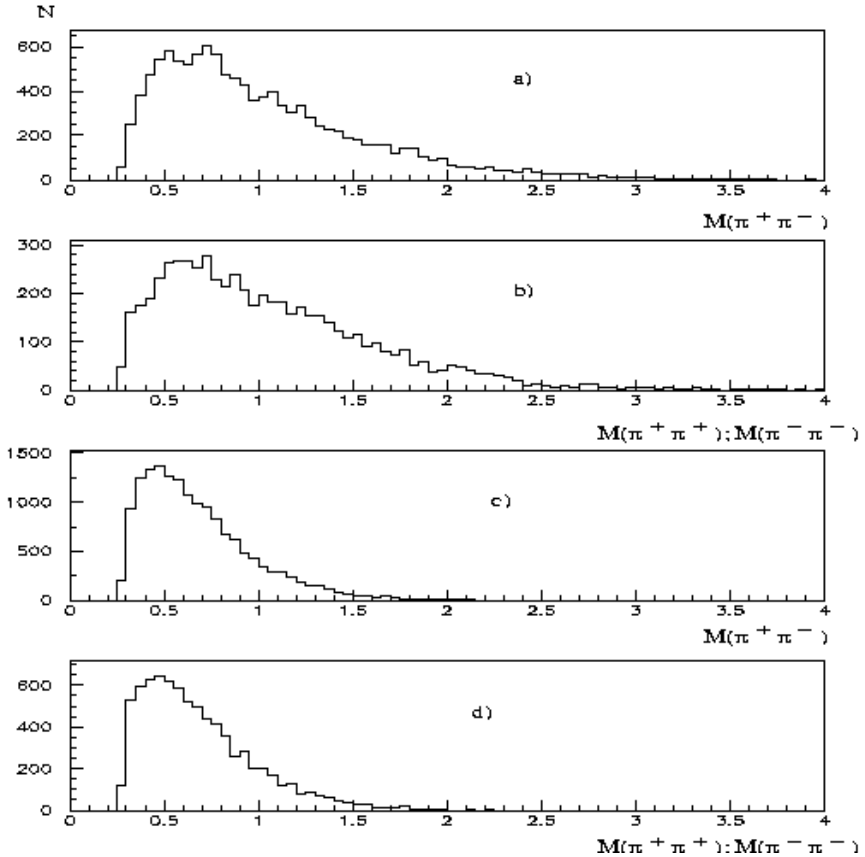


Fig. 2. Two-pion effective mass distributions:

a) – $M(\pi^+\pi^-)$ and b) – $M(\pi^+\pi^+)+ M(\pi^-\pi^-)$ in reaction $\tilde{p}p \to \pi^+\pi^+\pi^-\pi^- x^0$;

c)– $M(\pi^+\pi^-)$ and d) – $M(\pi^+\pi^+)+ M(\pi^-\pi^-)$ in reaction $\tilde{p}p \to n\tilde{n}\,\pi^+\pi^+\pi^-\pi^- x^0$;

The similar picture is seen in two-pion effective mass distributions in semi-inclusive reactions with 4 charged pions in final state (Fig. 2). From Fig. 2a the same tendency as in the previous case, follows, though the manifestation of pion resonances in M $(\pi^+\pi^-)$ system "is covered" a little with combinatorial factor, and nevertheless effective masses of two pions in reaction with two nucleones (Fig. 2c) are limited to area 2 GeV/c^2, while in annihilation events they are extended up to 3,6 GeV/c^2.

On summary distribution of wittingly non-resonance sets $(\pi^+\pi^+)$ and $(\pi^-\pi^-)$ (Fig. 2b; 2d) any significant peaks do not appear, though the shift of mass spectrum in area of smaller values (< 2 GeV) for non-annihilation events is saved (Fig. 2d).

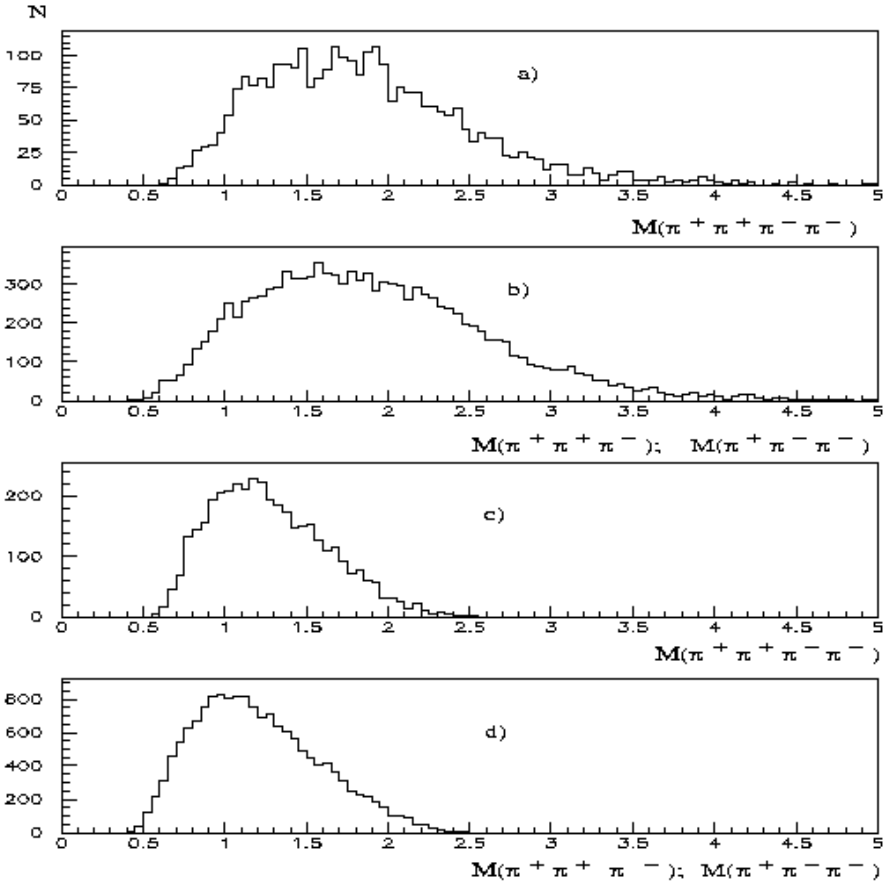


Fig. 3. Effective mass distributions for three and four mesons:
a) – *M(4π)* and b) – *M(3π)* - in reaction $\tilde{p}p \to 2\pi^+ 2\pi^- X^0$;
c) – *M(4π)* and d) – *M(3π)* - in reaction $\tilde{p}p \to n\tilde{n} 2\pi^+ 2\pi^- X^0$.

For four-particle neutral sets $(2\pi^+ 2\pi^-)$ the similar general picture (Fig.3a, Fig. 3c) is seen: the candidates in decays from resonances can be ρ (1450), ρ (1700) and f_2 (2010). In three-particle modes $(2\pi^{\pm}\pi^{\mp})$ (Fig. 3b) there are no such bumps in mass spectrum, but more wide $M_{eff.}$ distribution up to 5 GeV/c^2 is saved, in contrary with the events of non- annihilation type (Fig. 3d).

The indications are obtained that the abundant production of vector ρ and f_2 meson resonances in annihilation type reactions is observed. It can indicate on more complex, than simply statistical, annihilation mechanism. The detected effects are essential for understanding of mechanism of nucleon-antinucleon pair annihilation and require further theoretical explanation .

The authors are grateful to "Ludmila" collaboration for collective processing and accumulation of the primary data.

References

1. Raja R. // Phys. Rev., 1977, v. D16, p. 142.
2. Ward C.P. et al. // Nucl. Phys., 1979, v. B153, p. 299.
3. Boos E.G., Temiraliev T. et al. // YaF, 1996, v. 59, N3, p. 491.
4. Boos E.G., Temiraliev T. et al. // Izvestia MON NAN RK, 2000, N2, p. 35
5. Boos E.G., Temiraliev T. et al // Proc. 3 International Conference Nuclear and Radiation Physics, Almaty, 2001, p.179-189.

NEW DATA ON THE ANOMALOUSLY DELAYED PARTICLES IN CORE REGION OF THE ABOVE-THE-KNEE EXTENSIVE AIR SHOWERS

V.P. Antonova[2], A.P. Chubenko[1], A.S. Baigubekov[4], S.V. Kryukov[2], A.I. Kupchishin[5], V.V. Oskomov[5], T.Ch. Sadykov[4], A.L. Shepetov[1], L.I. Vildanova[3], N.N. Zastrozhnova[4]

[1]P N Lebedev Physical Institute of RAS, Russia, [2]Ionosphere Institute, Almaty, Kazakhstan, [3]Tian-Shan Mountain Cosmic Ray Station, Almaty, Kazakhstan, [4]Physical and Technical Institute, [5]Al-Faraby Kazakh State University

Abstract

Investigation of the particles delayed for some hundreds of microseconds found in the EAS which belong to the above-the-knee region of primary cosmic ray spectrum is continuing at Tien-Shan mountain station of P.N. Lebedev Physical Institute [1]. To check the reliability of our previous results and to study the attenuation of anomalous EAS component in the atmosphere a new registration point at the height 1700 m a.s.l. has been created which consists of a neutron monitor and a detector of EAS electrons and γ–quanta. The data obtained confirm the fact of the existence of peculiar events in the common flow of registered showers which have the anomalously prolonged time distributions both of the EAS hadron and e/γ -component.

Introduction

The fact that the overwhelming majority of elementary particles constituting an extensive air shower (EAS) do have relativistic energies and, moving with a speed near to that of light, do intersect the shower installation of usual sizes during some nanoseconds is a commonplace of the modern cosmic ray physics. Accordingly, all installations which have been used so far for the investigation of nuclear interaction of extra high energy cosmic rays (ionization calorimeters, scintillation detectors, Cherenkov and Geiger counters) have a registration time with characteristic duration of the order of some microseconds. Nevertheless, the experiments being carried out in last years at Tien-Shan mountain station of P.N. Lebedev Physical Institute give a reason for a principal change in our views on the passage of EAS particles through the atmosphere.

Since the early 90-th a modified 18NM64 type neutron supermonitor has been operating as a part of Tien-Shan complex installation for EAS studies. Time distribution measurements of the secondary thermal neutrons born by the EAS hadrons were held on this monitor during 1993-99 [2]. It has been found that in the core region of EAS with the size $N_e>10^6$ (i.e. above the knee of primary cosmic ray

spectrum) peculiar neutron signals are observed which are delayed for 300–500 mcs relative to the common shower front.

To study this unusual phenomenon a special measurement run with a small-sized neutron counters SNM18 was carried out. Because a their small size these counters have a 10 times lower neutron registration efficiency than the SNM15 type counters commonly used inside the NM64 monitor. The low registration efficiency reduces the neutron count and, consequently, the influence of statistical losses on the measured neutron intensities. The data obtained have shown, that in the events with extra high neutron multiplicity (which is the total number of neutrons being registered by a monitor unit), M>1000, the experimental time dependence of neutron intensity deviates drastically from the standard exponential distribution which corresponds to the simple diffusion process of thermal neutrons inside the monitor and agrees well with the experimental distribution at lower multiplicities. Moreover, a secondary neutron intensity maximum appears in the time distribution at high multiplicities whose location on the time axis is some hundreds microseconds later than the moment of EAS front passage.

The further analysis with the use of the data from shower installation of the Tien-Shan station has shown that practically all the events having the value of neutron multiplicity M above 1000 are accompanied by the EAS with the size $N_e>10^6$. The share of these events in the total shower flux is 5–10% at $N_e\geq10^6$, 40–50% at $N_e\geq10^7$ and nearly 100% at $N_e\geq10^8$. Hence, some unusual EAS component capable to generate neutrons inside a neutron monitor and delayed for hundreds of microseconds is supposed to exist in EAS born by primary cosmic particles having the energy above 10^{16} eV.

To specify more exactly the properties of the effect discovered an investigation of the electron-photon component of the EAS accompanying the anomalous neutron events was made. For this purpose our neutron monitor was supplemented with a detector of charged particles based on the SI5G type proportional counters capable to measure intensities of the shower electrons in the time range –300–4800 mcs relative to the moment of the EAS front passage. The use of SI5G counters is due by their relatively low sensitivity for the γ-quanta and neutrons.

It was found that the resulting time distributions of the intensity of EAS charged particles are quite analogous to those of neutron signals. Charged particles intensity exceeds 10^5 s^{-1} in the events with M>1000 which is 50 times higher than the background level; its maximum being delayed for 500–1000 mcs relative to the shower front.

Summarising our results we have concluded that:

- the phenomenon talked about has a clear threshold nature: it is observed only in the EAS having a sufficiently large size ($N_e>10^6$) and only in the core region of these showers (not farther than 10 m from the shower's axis);

- the share of anomalous events increases with the increase of shower size (from 10% at $N_e \sim 10^6$ up to 100% at $N_e \sim 10^8$).
- observation of the delayed time distributions of particle intensity is not a consequence of methodical distortions in our measurements but must have some physical reason;

Therefore, the question arises what could be the reason of the peculiarities in time distributions of particle intensity being observed in the events with M>1000. One obvious answer is the appearance of some abnormally delayed, probably hadronic component in the showers of sufficiently large sizes. Another, exotically for the same extent, explanation could be the chain process of lead nuclei fusion inside the monitor being triggered by the shower particles. This process must have an energetic threshold since it is observed only in relatively small percentage of EAS with $N_e > 10^6$. It is doubtfully enough that such a process could be initiated by usual hadrons; one have to suppose the existence of some exotic particles in EAS for it's explanation.

To clear up the mechanism of the phenomenon of the delayed intensity distributions one needs to execute an experiment with ionization-neutron calorimeter (INCA) which could ascertain the nature of anomalously delayed particles of the hadronic and electromagnetic components being born in the vicinity of the EAS axis. To reach this purpose the following tasks are planned to be solved at Tien-Shan mountain station in the nearest years:

- to study the amplitude of the effect of delayed time distributions of particle intensity at various depths of the lead absorber;
- to define the dependence of the lateral size of the shower core region where this effect is observed on the total EAS particle number N_e;
- to study the influence of the atmosphere depth on the generation probability of the EAS with delayed intensity distributions;
- to clear up the connection between the anomalously delayed particles of the hadronic and electromagnetic origin;
- to specify more exactly the dependence of the events with delayed intensity distributions on the shower size N_e;
- to define where — in the atmosphere or inside an experimental installation — the generation of anomalously delayed particles takes place;
- to determine the necessary corrections for the models of EAS passage through the atmosphere and their interaction with an experimental installation taking into account the process of delayed particles generation;
- to define the coordinates of the EAS with delayed particle distributions on the celestial sphere.

Intermediate detection point

To verify the reliability of our earlier results and to study the attenuation of the anomalously delayed EAS component in the atmosphere a new shower particles detection point is created in 2001 year at the Intermediate station which is

placed at the height 1700 m a.s.l. and 14 km apart from the Tien-Shan mountain station. On the analogy of our Tien-Shan installation, this detection point includes a neutron monitor and a detector of EAS charged particles.

The neutron monitor of the Intermediate station consists of two identical units 1x1 m^2 in size. Each unit consists of the following main parts:

1. 6 proportional boron counters of the SNM-8 type having the sizes 3.5x100 cm^2 which permit to register the thermal neutrons thanks to reaction $B^{10}(n,a)Li^7$. The counters are placed inside a 2.5 cm thick paraffin cylinders destined to slow down the evaporation neutrons until the thermal energies ($\sim 10^{-2}$ eV).
2. A 5 cm thick lead generator sheet which is used as a target for high energy comic ray hadrons. Interacting with the lead nuclei the latter generate evaporation neutrons having the energies up to 10 MeV.
3. A 30 cm thick outer paraffin reflector screening the monitor's interior from the slow neutrons coming from outside.

For the registration of the EAS electromagnetic component a SI5G counters based detector is used. This detector overlaps the space above the neutron monitor and has a 6 m^2 sensitive area. To decrease the registration dead time the SI5G counters are operating in proportional regime quite so as the electron- and γ-detectors of the Tien-Shan station. The pulse amplitudes do not exceed 0.05–0.1 V for this regime, 100–200 times lower as those observed in Geiger-Mueller mode. The dead time of SI5G counters in our conditions is 8-10 mcs only and their registration efficiency is inferior to that of the counters operating in Geiger regime.

Pulse intensities from each neutron counter and from the detector of electromagnetic component are measured separately in 85 subsequent time intervals having duration 60 mcs each. Zero point of the time scale in each event coincides with the moment of the passage of relativistic shower particles through the monitor and proportional counters.

Below are presented preliminary results obtained in the measurements held in the Winter season 2001–02 at the new detection point of Intermediate station.

Experimental data

Fig.1 shows the neutron multiplicity spectra, i.e. probability distributions of the total number of pulses obtained from the neutron counters of the monitors at the heights 3340 m a.s.l. (Tien-Shan mountain station) and 1700 m a.s.l. (Intermediate station). It is obvious, that in the multiplicity range $M>100$ the difference between the cosmic ray interaction intensities being observed at these two levels achieves two order of amplitude. This is the consequence of the difference in atmospheric depth resulting in additional attenuation of primary cosmic ray particles flow at the level of Intermediate station.

Time distributions of the neutron signal intensities being registered from the neutron monitor of the Intermediate station in various diapasons of the total

neutron multiplicity M are shown in Fig.2. Since the neutron multiplicity M is connected with the energy deposit of the hadronic component in the monitor and the latter, in it's turn — with the size and the core distance of the accompanying EAS, the selection of the neutron events accordingly to the value of M is equivalent to the selection of the EAS which belong to various ranges of the shower size N_e whose axes travel in the nearest vicinity (of the order of 2–3 m) of the monitor.

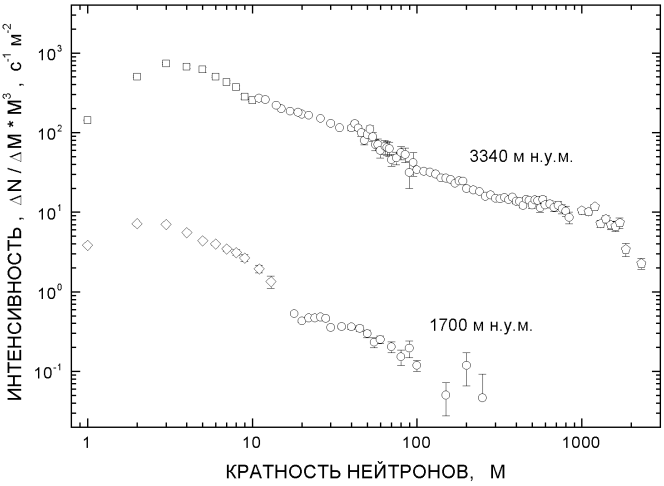


Fig.1. Neutron multiplicity spectra measured at various depths in the atmosphere.

As it is seen from Fig.2, in the events with a low neutron multiplicity values the time dependence of the neutron intensity may be well described by a sum of two exponents correspondingly to the diffusion process of the thermal neutrons in two layers of light substance inside the monitor: in the inner paraffin cylinders surrounding each neutron counter particularly (the exponent with the shorter life time value) and in the common outer reflector which covers a monitor unit from the outside (the exponent with longer life time). In the events which belong to the range of higher multiplicities (approximately M>70–100) a significant difference is observed between the experimental neutron intensity distributions and those predicted by the simple diffusion model; the maximum of experimental intensity distribution being displaced from the moment of EAS front passage to 100–200 mcs. It is the same phenomenon which was observed earlier at Tien-Shan station and was the reason for the hypothesis about the existence of abnormally delayed particles in EAS.

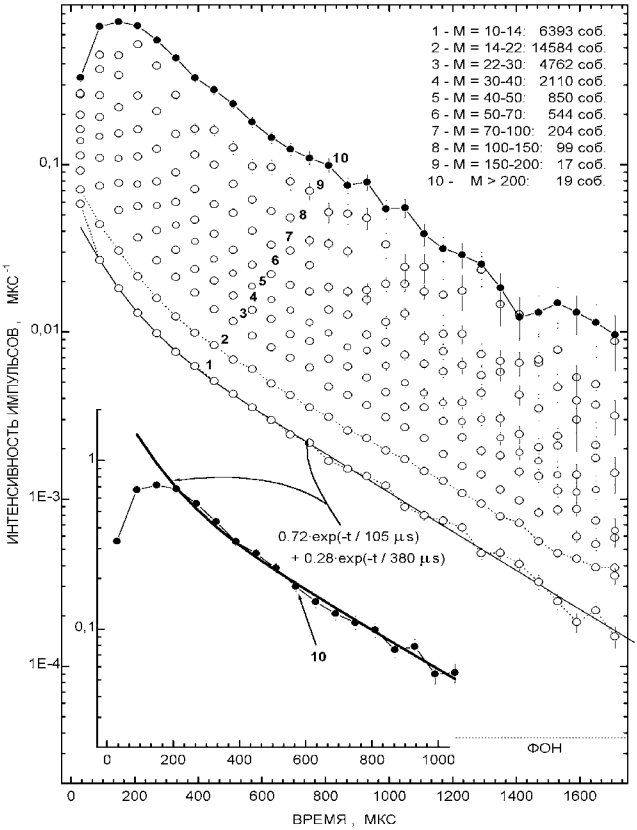


Fig.2. Time distributions of the intensity of neutron signals being registered at the Intermediate station. The smooth exponential curve corresponds to the diffusion process of the thermal neutrons in the monitor.

Fig.3 demonstrates the time distributions of the signals from the EAS electromagnetic component detector. To avoid the overlapping of the neighbouring curves pulse intensities registered in the events which belong to the N-th neutron multiplicity range are multiplied by the 3^{N-1} coefficient, dotted lines marking the background level for each curve.

We can see that in the low multiplicity events any signal is absent everywhere except the short excess in the moment of EAS front passage. In the events having high M values the shape of the time distributions is qualitatively different: together with the short intensity outburst around zero time moment a broad secondary maximum is seen delayed for some hundreds of microseconds.

The pulse intensity during the secondary maximum remains an order of the amplitude higher than the corresponding background level. The same picture has been observed earlier both at Tien-Shan station and in experiments carried out by the other groups.

Therefore, the data obtained at the Intermediate station do confirm the existence of the anomalously delayed time distribution effect.

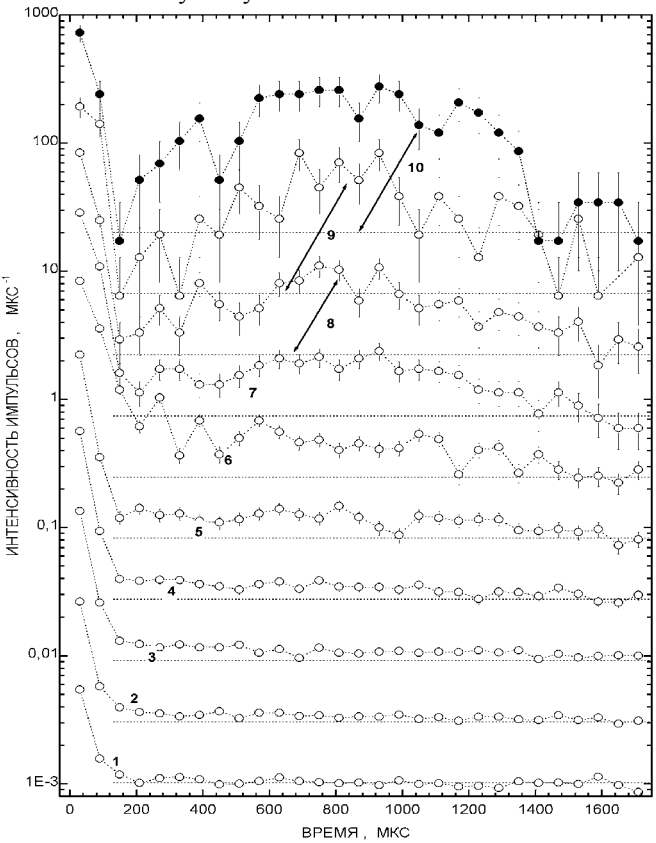


Fig.3. Time distributions of the intensity of neutron signals being registered at the Intermediate station. Multiplicity range numbers and events count are the same as in Fig.2. Dotted lines mark the position of background level for each curve.

References

1. V.P.Antonova, A.P.Chubenko, S.V. Kryukov et al. // Journal of Physics G: Nuclear and Particle Physics, v.28, 2, 2002, p. 251-266.
2. V.P.Antonova, A.P.Chubenko, M.M. Kokobaev et al. // Nuclear Physics B (Proc. Suppl.) 75A, 1999, p. 333-335.

ON THE PROPERTIES AND APPLICATIONS OF RELATIVISTIC DUFFIN-KEMMER-PETIAU EQUATION

I. Boztosun and F. Taskin, [1]N. Burtebayev

Department of Physics, Erciyes University, Kayseri 38039 Turkey
[1]Institute of Nuclear Physics, Almaty, Republic of Kazakstan

Abstract
In view of recent interest in the use of the Duffin-Kemmer-Petiau relativistic equation, we consider some of its properties which are needed for practical calculations. We also address the unresolved problem of the spinless DKP bosons in a central .eld and derive the system of first-order coupled differential radial equations which enable the energy eigenvalues as well as full wavefunctions to be evaluated. We then show how those .rst order coupled differential equations can be reduced to the second order Schrodinger type equation which the solutions are well known. As an example, we calculate the eigen-energies and wavefunctions of a pion in the finite and infinite square-well potentials using relativistic Duffin-Kemmer-Petiau equation.

1 Introduction

In the conventional relativistic approach, the interaction of S=0 and S=1 hadrons with different nuclei has been described by the second-order Klein-Gordon (KG) equation for S=0 and Proca equation for S=1 particles [1, 2, 4]. It has been well known that it is very difficult to tackle these second-order equations in time and space mathematically and to obtain the physics behind them. Therefore, considerable interest in recent years has been devoted to examine the interactions of S=0 and S=1 hadrons with nuclei by using the first-order relativistic Duffin-Kemmer-Petiau (DKP) equation [1, 2, 3], which is very similar to the first-order relativistic Dirac equation.

The Dirac-like DKP equation is not new and dates back to the 1930s [1, 2]. Historically, the loss of interest in the DKP stems from the equivalence of the DKP approach to the KG and Proca descriptions in on-shell situations [10, 11], in addition to the greater algebraic complexity of the DKP formulation.

As part of larger programme to study the interactions of spinless mesons with nuclei within the DKP approach, this paper is devoted to study of some selected properties and applications of the DKP equation.

Unlike earlier studies, the DKP is approached here from the perspective of relativistic single-particle wave mechanics with an emphasis on features needed for practical calculations.

In the next section, we first introduce the properties of DKP wave equation and then consider the DKP current for which we introduce the Gordon decomposition so as to make its physical interpretation transparent. Following this, we show the solution of DKP equation for a free particle. Finally, at the end of this section, we discuss the DKP propagator in order to describe the scattering process. Section 3 is devoted to the DKP formalism and the derivation of the first order coupled differential equations. Using these equations, we show the applications in section 4. Here, section 4.1 shows the free particle solution, sections 4.2 and 4.3 show the application of this formalism to the study of a pion in the finite and infinite square-well potentials for DKP to calculate the DKP spherical waves. We also discuss some general properties of the full DKP wavefunction and derive the set of first-order coupled differential equations which determine all the DKP radial wavefunctions. Finally, we give our summary and conclusions in section 5.

2 Properties of the DKP equation

2.1 Definition

The first-order relativistic DKP equation for a free S=0 or 1 particle of mass m is given as;

$$(i\beta^{\mu}\partial_{\mu} - m)\psi = 0 \tag{1}$$

where the internal variables β^{μ} (μ = 0; 1; 2; 3) satisfy the commutation relation

$$\beta^{\mu}\beta^{\nu}\beta^{\lambda} + \beta^{\lambda}\beta^{\nu}\beta^{\mu} = g^{\mu\nu}\beta^{\lambda} + g^{\nu\lambda}\beta^{\mu} \tag{2}$$

The β^{μ} matrices do not have an inverse and generate a ring consistently with integer spin algebra [12] The DKP algebra matrices β^{μ} have three irreducible representations: a one-dimensional representation which is trivial, a five-dimensional representation associated with spinless particles and ten-dimensional one relevant to vector bosons [12]. Explicitly, in the five-dimensional representation, the β^{μ} are 5x5 matrices given by

$$\beta^{0} = \begin{pmatrix} \Theta & 0 \\ 0 & 0 \end{pmatrix}, \quad \beta^{i} = \begin{pmatrix} 0 & p^{i} \\ -p_{T}^{i} & 0 \end{pmatrix} \tag{3}$$

where

$$\Theta = \begin{pmatrix} 0 & 1 \\ 1 & 0 \end{pmatrix}, \quad \rho^{1} = \begin{pmatrix} -1 & 0 & 0 \\ 0 & 0 & 0 \end{pmatrix} \tag{4}$$

$$\rho^{2} = \begin{pmatrix} 0 & -1 & 0 \\ 0 & 0 & 0 \end{pmatrix}, \quad \rho^{3} = \begin{pmatrix} 0 & 0 & -1 \\ 0 & 0 & 0 \end{pmatrix} \tag{5}$$

while ρ_T designates the matrix transform of ρ. The dynamical state ψ of a spinless boson is five-component spinor whereas it has ten-component for S=1 particles.

2.2 Adjoint equation and conserved current

The adjoint DKP equation obtained from equations (1) and (2) takes the form

$$i\partial_\mu \overline{\psi}\beta^\mu + m\overline{\psi} = 0 \tag{6}$$

with $\overline{\psi} = \psi + \eta^0$ as the adjoint spinor for which $\eta^0 = 2\beta^{0^2} - 1$. The continuity equation one gets from equations (1) and (6),

$$\partial_\mu(\overline{\psi}\beta^\mu\psi) = 0 \tag{7}$$

implies that $\overline{\psi}\beta^\mu\psi$ is the four-vector current density $(\rho = \overline{\psi}\beta^0\psi, j = \overline{\psi}\beta\psi)$. In order to exhibit the physical content of this DKP current, one can perform a Gordon decomposition. Writing the current as

$$j^\mu = \overline{\psi}\beta^\mu\psi = \frac{1}{2m}(\overline{\psi}\beta^\mu\psi - \partial_\nu\overline{\psi}\beta^\nu\beta^\mu\psi) \tag{8}$$

and using equations (1), (2) and (6) while separating the $\nu = \mu$ terms from the $\nu \neq \mu$ ones yields

$$j^\mu = j^\mu_{\nu=\mu} + j^\mu_{\nu\neq\mu} \tag{9}$$

where

$$j^\mu_{\nu=\mu} \equiv j^\mu_{conv} = \frac{1}{2m}(\overline{\psi}(\partial^\mu\psi) - (\partial^\mu\overline{\psi})\psi) \tag{10}$$

$$\rho_{conv} = \frac{i}{2m}\left\{\overline{\psi}\frac{\partial\psi}{\partial t} - \frac{\partial\overline{\psi}}{\partial t}\right\}, \quad j_{conv} = \frac{i}{2m}\left\{\overline{\psi}(\nabla\psi) - (\nabla\overline{\psi})\psi\right\},$$

and

$$j^\mu_{\nu\neq\mu} \equiv j^\mu_{\text{int}} = \frac{1}{2m}\partial_\mu(\overline{\psi}\left|\beta^\mu, \beta^\nu\right|\psi) \tag{11}$$

$$p_{\text{int}} = \frac{i}{2m}\nabla(\overline{\psi}\left[\beta^0, \beta\right]\psi),$$

$$j_{\text{int}} = \frac{+i}{2m}\left\{-\frac{\partial}{\partial t}(\overline{\psi}\left[\beta^0,\beta\right]\psi) - \nabla\wedge\overline{\psi}(\beta\wedge\beta)\psi\right\},$$

The $j^\mu_{\nu=\mu}$ current does not have any β matrix and the corresponding expressions for p and j are formally identical to those in the Schrodinger theory. This is the

convection component of the DKP current $\overline{\psi}\beta^{\mu}\psi$. The other component, $(j^{\mu}_{\nu\neq\mu} \equiv (\rho_{\text{int}}, j_{\text{int}}))$, is associated to some internal motion since it involves average values of combinations of the internal variables β^{μ}. We suggest in a study of a DKP particle in an electromagnetic field [13] that $\overline{\psi}(\beta^{\mu}, \beta^{\nu})\psi$ and $\overline{\psi}(\beta \wedge \beta)\psi$ are associated with a polarization density P and a magnetization density M, respectively, in such a way that $\rho_{\text{int}} = -\nabla.P$ and $j_{\text{int}} = \dfrac{\partial P}{\partial t} + \nabla \wedge M$.

2.3 Solution of the DKP equation for a free S=0 particle

If one seeks stationary solutions such as $\psi(r) = u(k)e^{-i(Et-k.r)} = u(k)e^{-ik.x}$, the free DKP equation can be express as

$$(k - m)u(k) = 0 \tag{12}$$

where $k = \beta^{\mu}k_{\mu}$ and u(k) is a 5-component DKP spinor independent of x . In Hamiltonian form, it can be shown from equations (1) and (2) to be

$$Hu = (\delta.k + \beta^0 m)u = Eu \tag{13}$$

with $\delta = \left[\beta^0, \beta\right]$. Written in matrix form, the Hamiltonian reads

$$Hu = \begin{pmatrix} 0 & m & 0 & 0 & 0 \\ m & 0 & -k_1 & -k_2 & -k_3 \\ 0 & -k_1 & 0 & 0 & 0 \\ 0 & -k_2 & 0 & 0 & 0 \\ 0 & -k_3 & 0 & 0 & 0 \end{pmatrix} u = Eu \tag{14}$$

Its eigen-energies consist of the usual Dirac values $\pm\sqrt{k^2 + m^2}$ as well as a three-fold degenerate 0 eigenvalue. The 0 eigenvalue solution is unexpected for this massive spinless particle. An usual feature also manifests itself in the spin states of the particle. From the transformation properties of the DKP wavefunction under rotations [11], the spin operator can be expressed as

$$S_k = i\left[\beta^l, \beta^m\right] = ie_{kim}\beta^l\beta^m \qquad (k, l, m \quad \text{cyclic}) \tag{15}$$

More explicitly,

$$S_k = \begin{pmatrix} 0 & 0 \\ 0 & s_k \end{pmatrix} \tag{16}$$

where S_k are usual 3x3 spin-one matrices. The eigenstates of S^2 consist of a doubly degenerate 0 eigenvalue together with a peculiar three-fold degenerate 2 eigenvalue. This spin-one solution is also present as an eigenstate of S_3 and helicity operator $S.\hat{k}$. If one considers the commutation relation of the Hamiltonian with the orbital angular momentum, one finds

$$[H, L] = -i(\delta \wedge k) \tag{17}$$

instead of 0. This implies that there is some missing angular momentum. Since

$$[H, S] = -i(\delta \wedge k) \tag{18}$$

it is only the total angular momentum (J = L + S) which is conserved, i.e.

$$[H; J] = 0 \tag{19}$$

just as Dirac case, the Hamiltonian of this free spinless boson commutes with the helicity operator, i.e.

$$[H, S.k] = 0 \qquad \left(\hat{k} = \frac{k}{k}\right) \tag{20}$$

It is should be noted, however, that these unusual states are not measurable since the expectation values of S^2, S_3 and $S.\hat{k}$ are zero in all DKP spin states. Whereas the Dirac spinors are 4-component vectors reflecting the $2(2 \times \frac{1}{2} + 1) = 4$ degrees of freedom, the DKP spinor for spinless bosons has 5 components for only 2 degrees of freedom. The three lower components of the DKP spinor, which reflect the presence of these extra degrees of freedom, were defined as redundant components in earlier work [14, 15]. In the context of pion-nucleus interactions, we propose a physically more appealing interpretation of this massless spin-one object coupled to the spinless DKP bosons as the space part of the pionic axial current [16].

2.4 The DKP propagator

In order to calculate the scattering processes in the DKP theory one needs to specify the DKP propagator. In analogy with the non-relativistic definition, the free relativistic DKP propagator can be defined to satisfy a Green's function equation

$$(i\beta^{\mu}\partial'_{\mu} - m)G_{DKP}(x'-x) = \delta^4(x'-x) \tag{21}$$

$G_{DKP}(x'-x)$ accounts for the wave product at $x' \equiv (t', r')$ by unit source at $x \equiv (t, r)$. Inserting the

Fourier transform of $G_{DKP}(x'-x)$ into equation (21) gives

$$\int \frac{d^4k}{(2\pi)^4}(i\beta^\mu \partial'_\mu - m)e^{-ik(x'-x)}G_{DKP}(k) = \int \frac{d^4k}{(2\pi)^4}e^{-ik.(x'-x)} \tag{22}$$

and therefore the free particle propagator is

$$G_{DKP}(k) = \frac{1}{k-m} = \frac{1}{k^2-m^2}(k+\frac{k^2}{m}) \tag{23}$$

G_{DKP} is a 5x5 matrix for S=0 whereas it is a 10x10 matrix for S=1. It is singular at $k^2 = m^2$ $(k_0 = \pm\sqrt{k^2+m^2})$. Imposing the appropriate boundary conditions on $G_{DKP}(x'-x)$, i.e. such that the positive energy DKP particle propagates forward in time and the negative energy DKP particle propagates backward in time, one gets

$$G_{DKP}(x'-x) = \frac{-i}{(2\pi)^3} \text{ x}$$

$$\text{x}\int \frac{dk}{2E}((k+\frac{k^2}{m})e^{-ik(x'-x)}\Theta(t'-t) + (-k+\frac{k^2}{m})e^{ik.(x'-x)}\Theta(t-t') \tag{24}$$

with $\Theta(t'-t)$ being the unit step function. If one denotes by u(k) the normalized particle spinor of equation (12) and by v (k) spinor of the anti-particle, then

$$u(k)\bar{u}(k) = k+\frac{k^2}{m} \quad \text{and } u(k)\bar{v}(k) = -k+\frac{k^2}{m} \tag{25}$$

in which case the free propagator can be written

$$G_{DKP}(x'-x) = -i\int \frac{dk}{(2\pi)^3}\frac{m}{E}(\wedge_+ e^{ik.(x'-x)}\Theta(t'-t) + \wedge_- e^{ik.(x'-x)}\Theta(t-t')) \tag{26}$$

where $\wedge_+ = u\bar{u}/2m (\wedge_- = v\bar{v}/2m)$ is the positive (negative) energy projection operator. For time-independent scattering problems, the free Green's function in coordinate representation is

$$G_{DKP}(r,r') = \left\langle r\left|\frac{1}{k=m}\right|r'\right\rangle = \int \frac{dk}{(2\pi)^3}\frac{e^{ik.(r-r')}}{k^2-m^2+ie}(k+\frac{k^2}{m}) \tag{27}$$

A lengthy but otherwise straightforward calculation yields, in the asymptotic limit,

$$\lim_{r\to\infty} G_{DKP}(r,r') = \left(k'+\frac{k'^2}{m}\right)\frac{e^{ikr}}{4\pi r}e^{-ik'.r'} = -2m\frac{e^{ikr}}{4\pi r}e^{-ik'.r'}\wedge(k') \tag{28}$$

Note that $k' \cong kr$. $G_{DKP}(r,r')$ appears in the product of the usual free Green's function with the positive-energy DKP projection operator.

3 Formalism

The central interaction is assumed to be the sum of a Lorentz scalar (U_s) and a time-like vector (U_v^0) potential. The stationary states of the DKP particle in this case are determined by solving

$$(\beta.kc + mc^2 + U_S + \beta^0 U_v^0)\psi(r) = \beta^0 E\psi(r) \tag{29}$$

where the file component DKP spinor

$$\psi(r) = \begin{pmatrix} \psi_{upper} \\ i\psi_{lower} \end{pmatrix} \quad \text{with} \quad \psi_{upper} = \begin{pmatrix} \Phi \\ \varphi \end{pmatrix} \quad \text{and} \quad \psi_{lower} = \begin{pmatrix} A_1 \\ A_2 \\ A_3 \end{pmatrix} \tag{30}$$

Equation (29) cannot be expressed in the Hamiltonian form as in the free-particle case. It can be rewritten, in a suggestive way, as

$$\begin{cases} ip.kc\psi_{lower} = \left[(E - U_v^0)\varphi - (mc^2 + U_S)\right]\psi_{upper} \\ p_T.kc\psi_{upper} = i(mc^2 + U_S)\psi_{lower} \end{cases} \tag{31}$$

which is a form somewhat analogously the one often used for the Dirac equation. Using the de.nition of [17], the second equation which couples ψ_{upper} and ψ_{lower} without involving the energy (or the time derivative in general) is known as a subsidiary condition of the firs kind. More explicitly, equation (29) is

$$\begin{cases} (mc^2 + U_S)\phi = (E - U_v^0)\varphi + \hbar c\nabla.A \\ \hbar c\nabla\phi = (mc^2 + U_S)A \\ (mc^2 + U_S)\varphi = (E - U_v^0)\phi \end{cases} \tag{32}$$

where A is a vector (A_1;A_2;A_3).

In all eigenvalues of (29), the total angular momentum J = L + S, that is,

$$J = \begin{pmatrix} L & 0 \\ 0 & L + s \end{pmatrix} \tag{33}$$

which commute with β^0, is a component of the motion, i.e.

$$\frac{d}{dt}\left(\overline{\psi}\beta^0 J\psi\right) = 0 \tag{34}$$

Thus for a DKP boson in a central potential, one can construct a simultaneous eigenfunction of equation (29), J^2 and J_3 with corresponding eigenvalues denoted E, J(J + 1) and M.

Since the five-component wavefunction ψ is simultaneously an eigenfunction of L^2 and L_3

$$J^2\begin{pmatrix}\psi_{upper}\\ \psi_{lower}\end{pmatrix}=\begin{pmatrix}L^2\psi_{upper}\\ (L+s)^2\psi_{lower}\end{pmatrix}=J(J+1)\begin{pmatrix}\psi_{upper}\\ \psi_{lower}\end{pmatrix} \tag{35}$$

$$J_3\begin{pmatrix}\psi_{upper}\\ \psi_{lower}\end{pmatrix}=\begin{pmatrix}L_3\psi_{upper}\\ (L_3+s_3)^2\psi_{lower}\end{pmatrix}=M\begin{pmatrix}\psi_{upper}\\ \psi_{lower}\end{pmatrix} \tag{36}$$

The full DKP spinor ψ is not an eigenstate of L^2 which is not a constant of motion. However, L^2 is equal to J^2 when it acts separately on ψ_{upper} so that any eigenfunction ψ_{upper} of J^2 is also an eigenfunction of L^2. If the eigenvalue of L^2 acting on ψ_{upper} is $l_{up}(l_{up}+1)$ then $l_{up} = J$ On the other hand, this does not hold for ψ_{lower}.

The most general eigensolution of equation(29) is therefore

$$\psi_{JM}=\begin{pmatrix}f_{nJ}(r)Y_{JM}(\Omega)\\ g_{nJ}(r)Y_{LM}(\Omega)\\ i\sum{}_L h_{nJL}(r)Y^M_{JL1}(\Omega)\end{pmatrix} \tag{37}$$

where $Y_{JM}(\Omega)$ is the spherical harmonics of order J and $Y^M_{JL1}(\Omega)$ standards for the normalized vector spherical harmonics [18]

$$Y^M_{JL1}(\Omega)=\sum{}_{\lambda,\mu}\left\langle JM\middle|L\lambda 1\mu\right\rangle Y_{L\lambda}(\Omega)\chi_{1\lambda} \tag{38}$$

inserting $\psi_{LM}(r)$ as given in equation (37) into equation (32) while using the properties of vector spherical harmonics [19] below

$$\nabla.(f_{nJ}(r)Y^M_{J,J+1,1})=-\left(\frac{J+1}{2J+1}\right)^{\frac{1}{2}}\left(\frac{df(r)}{dr}+\frac{J+2}{r}f(r)\right)Y_{JM} \tag{39}$$

$$\nabla.(f_{nJ}(r)Y^M_{J,J,1})=0 \tag{40}$$

$$\nabla.(f_{nJ}(r)Y^M_{J,J-1,1})=\left(\frac{J}{2J+1}\right)^{\frac{1}{2}}\left(\frac{df(r)}{dr}-\frac{J-1}{r}f(r)\right)Y_{JM} \tag{41}$$

$$\frac{r}{r}Y_{JM}=-\left(\frac{J+1}{2J+1}\right)^{\frac{1}{2}}Y^M_{J,J+1,1}+\left(\frac{J}{2J+1}\right)^{\frac{1}{2}}Y^M_{J,J-1,1} \tag{42}$$

$$\nabla Y_{JM} = \left(\frac{J+1}{2J+1}\right)^{\frac{1}{2}} \frac{J}{r} Y^{M}_{J,J+1,1} + \left(\frac{J}{2J+1}\right)^{\frac{1}{2}} \frac{J+1}{r} Y^{M}_{J,J-1,1} \tag{43}$$

the spin-angular functions drop out and one gets the following set of .rst-order coupled radial differential equations

$$(E - U^{0}_{\nu}) f_{nJ} = (mc^2 + U_S) g_{nJ} \tag{44}$$

$$\hbar c\left(\frac{df_{nJ}}{dr} - \frac{J}{r} f_{nJ}\right) = -\frac{1}{\alpha_J}(mc^2 + U_S) h_{nJJ+1} \tag{45}$$

$$\hbar c\left(\frac{df_{nJ}}{dr} + \frac{J+1}{r} f_{nJ}\right) = \frac{1}{\xi_J}(mc^2 + U_S) h_{nJJ-1} \tag{46}$$

$$-\alpha_J\left(\frac{dh_{nJJ+1}}{dr} + \frac{J+1}{r} h_{nJJ+1}\right) + \xi_J\left(\frac{dh_{nJJ-1}}{dr} - \frac{J-1}{r} h_{nJJ-1}\right)$$

$$= \frac{1}{\hbar c}((mc^2 + U_S) f_{nJ} - (E - U^{0}_{\nu}) g_{nJ}) \tag{47}$$

with $\alpha_J = \sqrt{(J+1)/(2J+1)}$ and . $\xi_J = \sqrt{J/(2J+1)}$ .If one redefines the radial functions in such a way that

$$f_{nJ}(r) = \frac{F(r)}{r} \qquad g_{nJ}(r) = \frac{G(r)}{r} \qquad h_{nJJ\pm1} = \frac{H_{\pm1}(r)}{r} \tag{48}$$

then the system of radial differential equations becomes

$$(E - U^{0}_{\nu}) F(r) = (mc^2 + U_S) G(r) \tag{49}$$

$$\hbar c\left(\frac{dF(r)}{dr} - \frac{J}{r} F(r)\right) = -\frac{1}{\alpha_J}(mc^2 + U_S) H_1(r) \tag{50}$$

$$\hbar c\left(\frac{dF(r)}{dr} + \frac{J+1}{r} F(r)\right) = \frac{1}{\xi_J}(mc^2 + U_S) H_{-1}(r) \tag{51}$$

$$-\alpha_J\left(\frac{dH_1(r)}{dr} + \frac{J+1}{r} H_1(r)\right) + \xi_J\left(\frac{dH_{-1}(r)}{dr} - \frac{J-1}{r} H_{-1}(r)\right)$$

$$= \frac{1}{\hbar c}((mc^2 + U_S)F(r) - (E - U_v^0)G(r)) \tag{52}$$

Whereas this system of radial equations is particular to the assumed Lorentz scalar-vector potential, the method developed here can be used for interactions of any Lorentz type provided they are spherical symmetric. The nature of the coupling between the differential equations reflects the extent to which the assumed interaction mixed the different components of the DKP spinor between themselves. The radial wavefunctions in equation (37) are constrained in such a way that the full DKP spinor must satisfy the normalization condition

$$\int \overline{\psi}_{JM}(r)\beta^0\psi_{LM}(r)dr = 1 \tag{53}$$

(a non-covariant normalization is chosen here) in which case using the orthonormalization properties of spherical harmonics yields

$$\int_0^\infty \mathrm{Re}\left[F^*(r)G(r)\right]dr = \frac{1}{2} \tag{54}$$

This constraint differs significantly from the traditional KG normalization condition.

Finally, to fully specify the DKP wavefunction its parity needs to be de.ned. The parity operator is $\Pi = \eta^0 P^{(0)}$ where $\eta^0 = 2\beta^{0^2} - 1$, explicitly

$$\eta^0 = \begin{pmatrix} 1 & 0 & 0 & 0 & 0 \\ 0 & 1 & 0 & 0 & 0 \\ 0 & 0 & -1 & 0 & 0 \\ 0 & 0 & 0 & -1 & 0 \\ 0 & 0 & 0 & 0 & -1 \end{pmatrix} \tag{55}$$

and $P^{(0)}$ is the `orbital parity' operator (i.e. $P^{(0)}\phi(r) = \phi(-r)$). The parity of Y_{JM} is $(-1)^J$ and the

parity of the irrotational fields $Y^M_{J,J+1,1}$ and $Y^M_{J,J-1,1}$ is $(-1)^{J+1}$ so that

$$\Pi\psi_{JM}(r) = \eta^0 P^{(0)}\psi_{JM}(r) = \begin{pmatrix} -P^{(0)}\psi_{upper} \\ P^{(0)}\psi_{lower}(r) \end{pmatrix} = (-1)^J \psi_{JM}(r) \tag{56}$$

Even though the two upper components and three lower ones have opposite parities, $\psi_{JM}(r)$ has a well defined parity of $(-1)^J$.

4 Applications

4.1 Free particle

As a first application of the preceding formulation. We assume $U_S = U_V^0 = 0$, in which case the stationary solutions with well defined angular momentum and parity are the free DKP spherical waves. Using $U_S = U_v = 0$ in equations (49), (50), (51) and (52) the corresponding system of differential equations to be satisfied by the radial wavefunctions becomes

$$EF = mc^2 G \tag{57}$$

$$\hbar c\left(\frac{dF}{dr} - \frac{J}{r}F\right) = -\frac{1}{\alpha_J} mc^2 H_1 \tag{58}$$

$$\hbar c\left(\frac{dF}{dr} + \frac{J+1}{r}F\right) = \frac{1}{\xi_J} mc^2 H_{-1} \tag{59}$$

$$-\alpha_J\left(\frac{dH_1}{dr} + \frac{J+1}{r}H_1\right) + \xi_J\left(\frac{dH_{-1}}{dr} - \frac{J-1}{r}H_{-1}\right) = \frac{1}{\hbar c}(mc^2 F - EG) \tag{60}$$

Eliminating G, H_1 and H_{-1} in favor of F, we obtain the second order differential equation

$$\left(\frac{d^2}{dr^2} - \frac{J(J+1)}{r^2} + \frac{(E^2 - m^2c^4)}{(\hbar c)^2}\right)F(r) = 0 \tag{61}$$

this equation is the free radial Schrodinger equation if E^2-m^2c^4 were replaced by $2mc^2e$, being the nonrelativistic energy. Equation (43) therefore verifies the consistency of the system of coupled differential equations (49), (50), (51) and (52).

For any positive value of E^2-m^2c^4, (43) has only one regular solution. Introducing $kc = \sqrt{E^2 - m^2c^4}\left(|E| \geq mc^2\right)$ and $p = kr/\hbar$, regular solution is

$$F(p) = NpJ_J(p) \tag{62}$$

where J_J is the Bessel function of order J and N is a normalization constant. Using (62) together with known properties of the Bessel functions, the remaining radial wavefunctions are found to be

$$G(p) = N\frac{E}{mc^2} pJ_J(p) \tag{63}$$

$$H_1(p) = N\alpha_J \frac{k}{mc} pJ_{J+1}(p) \tag{64}$$

$$H_{-1}(p) = N\xi_J \frac{k}{mc} pJ_{J-1}(p) \tag{65}$$

4.2 Finite Square Well

As a second example, we consider the bound state of a spinless charged pionic atom (π^-) in a following scaler finite square well potential $(V_V^0 = 0)$. Unlike pionic atoms found in nature, it assumed here that there is no nuclear interaction involved and the atomic nucleus is treated as a point charge Z_e.

$$V(r) = \begin{cases} -V_0 & for 0 < r \le R \\ 0 & for > R \end{cases} \tag{66}$$

where $V_0 = \frac{Z_1 Z_2 e^2}{4\pi\varepsilon_0 R}$ and R is given as $R = R_0 A^{1/3}$ with R_0 = 1.2 and A is the number of the nucleons in $^{209}_{83}Bi$. Outside the square well (r > R), the solutions are the same as free particle solution as given by equations 62, 63, 64 and 65. Inside the well where V (r) =-V_0, the equations can be written as:

$$EF = (mc^2 - V_0)G \tag{67}$$

$$\hbar c\left(\frac{dF}{dr} - \frac{J}{r}F\right) = -\frac{1}{\alpha_J}(mc^2 - V_0)H_1 \tag{68}$$

$$\hbar c\left(\frac{dF}{dr} + \frac{J+1}{r}F\right) = \frac{1}{\xi_J}(mc^2 - V_0)H_{-1} \tag{69}$$

$$-\alpha_J\left(\frac{dH_1}{dr} + \frac{J+1}{r}H_1\right) + \xi_J\left(\frac{dH_{-1}}{dr} - \frac{J-1}{r}H_{-1}\right) = \frac{1}{\hbar c}((mc^2 - V_0)F - EG) \tag{70}$$

If we take G, H_1 and H_{-1} from equations (67), (68) and (69) and plug them into the equation (70), we get following second-order Schrodinger type differential equation.

$$\left(\frac{d^2}{dr^2}-\frac{J(J+1)}{r^2}+\frac{(E^2-(mc^2-V_0)^2}{\hbar^2c^2}\right)F(r)=0 \tag{71}$$

by defining

$$k=\frac{1}{\hbar c}\sqrt{E^2-(mc^2-V_0)^2} \tag{72}$$

We finally obtain

$$\left(\frac{d^2}{dr^2}-\frac{J(J+1)}{r^2}+k^2r^2\right)F(r)=0 \tag{73}$$

The solution of this equation is similar to equation 62 with k defined as in equation 72. Equation (73) appears as the radial KG equation for a point charge in a finite square-well potential [20]. We give the normalized full DKP wave functions in figure 1. These solutions are in very good agreement with the KG solution [20].

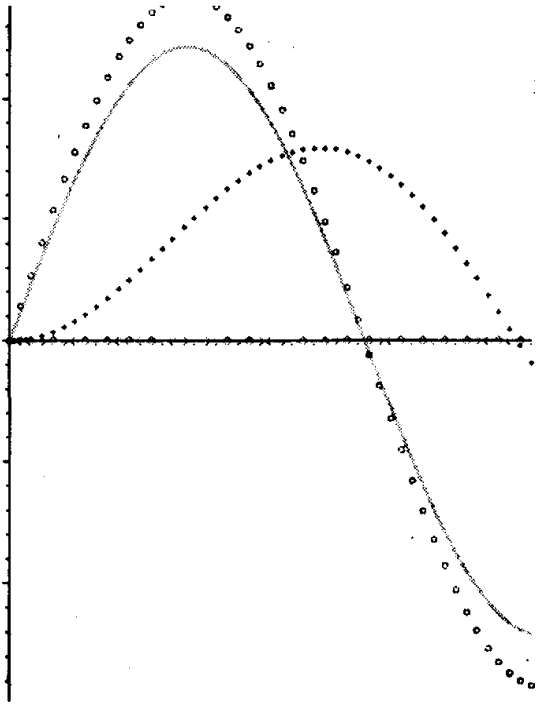


Figure 1: Finite square well wave functions where, F is given by solid line, G by circle, H_1 by cross and , H_{-1} by diamond.

4.3 Infinite Square Well

Finally, we consider the behavior of the same pionic atom in the following infinite square well.

$$V(r)=\begin{cases}0 & for 0<r\le R\\ \infty & for>R\end{cases} \tag{74}$$

$$EF=(mc^2)G \tag{75}$$

$$\hbar c\left(\frac{dF}{dr}-\frac{J}{r}F\right)=-\frac{1}{\alpha_J}(mc^2)H_1 \tag{76}$$

$$\hbar c\left(\frac{dF}{dr}+\frac{J+1}{r}F\right)=\frac{1}{\xi_J}(mc^2)H_{-1} \tag{77}$$

$$-\alpha_J\left(\frac{dH_1}{dr}+\frac{J+1}{r}H_1\right)+\xi_J\left(\frac{dH_{-1}}{dr}-\frac{J-1}{r}H_{-1}\right)=\frac{1}{\hbar c}(mc^2F-EG) \tag{78}$$

As in the case of free particle and finite square well solutions, we take G, H_1 and H_{-1} from equations (75), (76) and (77) and plug them into the equation (78), we obtain following second-order Schrodinger type differential equation.

$$\left(\frac{d^2}{dr^2}-\frac{J(J+1)}{r^2}+\frac{E^2-m^2c^4}{\hbar^2c^2}\right)F(r)=0 \tag{79}$$

by taking

$$k=\frac{1}{\hbar c}\sqrt{E^2-m^2c^4} \tag{80}$$

We obtain

$$\left(\frac{d^2}{dr^2}-\frac{J(J+1)}{r^2}+k^2r^2\right)F(r)=0 \tag{81}$$

Inside the infinite square well, the solution is exactly the same as the free particle solution. These solutions are also in agreement with the KG solution [20]. We give the normalized full DKP wave functions in figure 2.

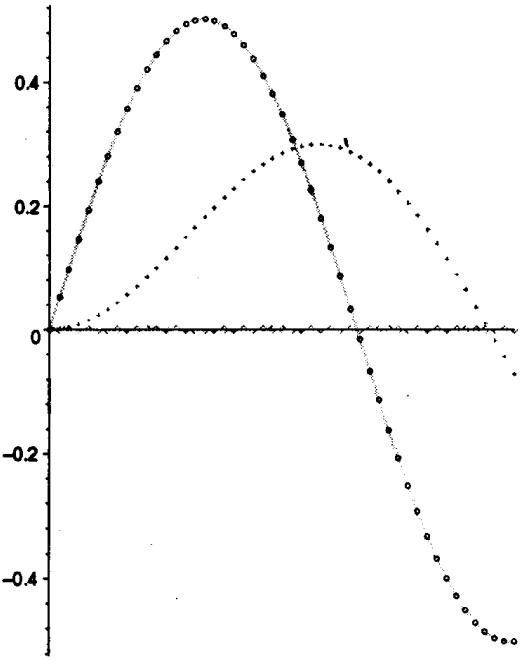


Figure 2: Infinite square well wave functions where, F is given by solid line, G by circle, H_1 by cross and , H_{-1} by diamond.

5 Summary and Conclusion

We have considered the properties and applications of the relativistic Duffin-Kemmer-Petiau equation. In the introduction, we explained the reason why we choose to use DKP equation to describe a relativistic S=0 particle. In the following sections, we first introduced the properties of DKP wave equation and then consider the DKP current for which we introduced the Gordon decomposition so as to make its physical interpretation transparent. By following this, we have shown the solution of DKP equation for a free particle and finally, at the end of the section, we have discussed the DKP propagator in order to describe 10 the scattering process. We have discussed the DKP formalism and the derivation of the first order coupled differential equations and using these equations, we have made some applications of the relativistic DKP equation for a pion in the finite and infinite square-well potentials.

It is clearly shown that the DKP approach outlined in this paper is an alternative approach to KG and Proca equations to describe the S=0 and S=1 particles. This approach is very convenient to be used for the examination of such particles. Although it seems very complicated mathematically, we have explicitly shown that it could be reduced to the second-order Schrodinger type differential equation,

which the solutions are very well know. We have also shown that the DKP solutions of the potentials considered are in perfect agreement with the KG solutions [20].

References

1. Y. Nedjadi and R. C. Barrett 1993 J. Nucl. Phys. G. 19 87
2. G. KAalbermann 1986 Phys. Rev. C 34 2240
3. B. C. Clark, S. Hama, G. KAalbermann, R. L. Mercer and L. Ray Phys. Rev. Lett. 55 592
4. R. E. Kozack, B. C. Clark, S. Hama, V. K. Mishra, R. L. Mercer and L. Ray 1989 Phys. Rev. C 40 2181
5. M. D. Scadron 1979 Advanced Quantum Theory Springer-Valey
6. G. Petiau 1936 Acad. R. Belg. Cl. Sci. Mem. Collect. 16 No. 2
7. N. Kemmer 1938 Proc. R. Soc. 166 127, 1939 Proc. R. Soc. A 173 91
8. R. J. Du±n 1938 Phys. Rev. 54 1114
9. R. A. Karajcik and M. M. Nieto 1977 Am. Journ. Phys. 45 818
10. E. Fischbach, M. M. Nieto and C. K. Scott 1972 Prog. Theo. Phys. 48 574
11. R. A. Karajcik and M. M. Nieto 1974 Phys. Rev. D 10 4049
12. E. Fischbach, M. M. Nieto and C. K. Scott 1973 Journ. Math. Phys.14 1760, 1974 Phys. Rev. 15 60
13. Y. Nedjadi and R. C. Barrett 1994 J. Math. Phys. A 27 4301
14. W. Heitler 1943 Proc. Irish. Acad. 49 1
15. R. A. Karajcik and M. M. Nieto 1975 Phys. Rev. D 11 1442
16. Y. Nedjadi and R. C. Barrett 1998 J. Math. Phys. A 31 3867, Y. Nedjadi and R. C. Barrett 1998 J. Math. Phys. A 31 6717
17. C. G. Koutroulos 1991 Physics Essays 4 228
18. A. S. Davydov 1976 Quantum Mechanics Pergamon Press
19. E. H. Hill 1954 Am. Journ. Phys. 22 211
20. W. Grenier 2000 Relativistic Quantum Mechanics Springer-Verlag Press

ON THE STRUCTURE OF THE HAMILTONIAN OF QCD STRING

M. Dineykhan, D.S. Ashimov, A. Jahanshir, S.K. Sakhyev

al-Farabi Kazakh National University, Almaty, Kazakhstan

Abstract – On the basic of investigation the asymptotic bihaviour of the polarization loop for the scalar particles in the external gauge field determined the nonperturbative corrections to the Hamiltonian. The constituent mass composition particle in the bound state is analytically derived. Shown, that the constituent mass of composition particles is differ to the mass of particles in free states.

1. Introduction

The development of idea of gauge invariance has reduced in creation QCD, which describes interaction of color objects. Gross, Welczek [1] and Politzer [2] have shown, that a coupling constant of quark – gluon interaction on small distances are small, and will increase with growth of space scale. In the present time it is confirmed in the analyses of many experimental data, in particular of deeply inelastic electronic scattering on protons and neutrons. The force of interaction between quarks on small distances agreement with Coulomb low in an electrodynamics, and for large distances should satisfy the confinement of quarks. Thus, the interaction of quarks depending on a distance transition from a phase confinement to deconfinement. Most satisfying to this condition is phenomenological potential model of quarks [3]. However, phenomenological potential model of quarks does not follow from to basic principle of QCD.

The last three decades the theorists try to obtain the interaction Hamiltonian quarks, which satisfied of confinement and deconfinement conditions of constituent particles, proceeding from a basic principle QCD. In the present moment exist a set of potential models of quarks, which are constructed proceeding from the various physical suggestions. These models describe physics of hadrons consisting only from heavy quarks. However, when considering the properties of hadrons consisting from light quarks take into account of a relativistic character of interactions, is required. In the present time not have the account of a relativistic character of interaction within the framework of a phenomenological model of quarks. On the other hand well known that the bound state problems with the strong coupling constant of interaction is pure relativistic effect and are solved only within the framework of a quantum field theory.

In relativistic quantum field theory, bound states are identified by the occurrence of poles of corresponding amplitudes with appropriate quantum numbers. These poles have a nonperturbative character, so that they can arise as a result of a nonperturbative rearrangement of series over a coupling constant. The

investigation of nonperturbative properties was done by establishing integral equations among amplitudes. One should say that these equations, having absolutely general form, in reality can be used when the kernels contain contributions of the lowest Feynman diagrams only. The Bethe-Salpeter equation is the most important integral equation of this type.

Thus, at the definition of a nonperturbative corrections in the standard QFT usually face with a solution of an integral equation with the arbitrary kernels. The determination of an exact solution of such equation is impossible. When studying the structure and formation of mechanism of bound state is necessary to account the internal structure of object. Thus the interaction between of the components of bound state is carried out by exchanging of nonlocal current. In paper [4] assume that the interaction between components of bound state is nonlocality and very well described the bosonization mechanism of color objects and obtained results agree with experimental data. However, authors of these papers studied the bosonization mechanism of system consisting only the heavy quarks. Thus the studying of hadronization mechanism, hadrons consisting of light quarks and three-quark are represented great interest.

In this paper we will study this problem on the basis of investigation of asymptotic bihaviour of the loop function for the scalar particles and determined the structure of interaction Hamiltonian with nonperturbative corrections.

2. Determination of the mass spectrum of bound state system

We shall consider the interactions of the two charged scalar particles in the external gauge field. Our approach is based on the investigation of the polarization loop operator of scalar particles in a quantum gauge field. We introduce the representation of this loop in a form of functional integral and investigate its asymptotic bihaviour for large distance. The polarization loop functions for the scalar particles in a quantum gauge field we can write in the form:

$$\Pi(x-y)=\left\langle G_{m1}(x,y|A)G^{*}_{m2}(y,x|A)\right\rangle_{A} \tag{2.1}$$

where making averaging over the gauge field $A_{\alpha}(x)$. The Green function for a scalar particle in an external gauge field $A_{\alpha}(x)$ is defined by the equation:

$$\left[\left(i\frac{\partial}{\partial x_a}+\frac{g}{c\hbar}A_a(x)\right)^2+\frac{c^2m^2}{\hbar^2}\right]G(x,y|A)=\delta(x-y) \tag{2.2}$$

where m is the mass of our scalar particles and g is a coupling constant. When averaging over the gauge field $A_{\alpha}(x)$ we limited only by the lowest order (two point Gausses a correlator) and is define by the relation:

$$\left\langle \exp\left\{ i\int dx A_\alpha(x) J_\alpha(x)\right\}\right\rangle_A = \exp\left\{ -\frac{1}{2}\int\int dx dy J_\alpha(x) D_{\alpha\beta}(x-y) J_\beta(y)\right\} \quad (2.3)$$

where $J_\alpha(x)$ is a real current. The propagator $D_{\alpha\beta}(x-y)$ of the vector field $A_\alpha(x)$ has a form:

$$D_{\alpha\beta}(x-y) = \left\langle A_\alpha(x) A_\beta(y)\right\rangle_A = \delta_{\alpha\beta} D(x-y) \quad (2.4)$$

For the determination of the loop function represented in (2.1), the solution of (2.1) can be representing in the form of the following functional integral [5]:

$$G(x,y|A) = \int_0^\infty \frac{ds}{(4s\pi)^2} \exp\left\{ -sm^2 - \frac{(x-y)^2}{4s}\right\} d\sigma_\beta \exp\left\{ ig\int_0^s d\xi \frac{\partial Z_\alpha(\xi)}{\partial \xi} A_\alpha(\xi)\right\} \quad (2.5)$$

here used the notations:

$$\begin{aligned} Z_\alpha(\xi) &= (x-y)_\alpha \xi + y_\alpha - 2\sqrt{s} B_\alpha(\xi); \\ d\sigma_\beta &= N\delta B_\beta \exp\left\{ -1/2 \int_0^1 d\xi \dot{B}^2(\xi)\right\} \end{aligned} \quad (2.6)$$

and with a normalization: $B_\alpha(0) = B_\alpha(1) = 0; \qquad \int d\sigma_\beta = 1$

Substituting (2.5) into (2.1) and to carry out averaging over the gauge field $A_\alpha(x)$, for the loop function we have (same calculation details see in Ref. [5]):

$$\Pi(x) = \int_0^\infty \int_0^\infty \frac{d\mu_1 d\mu_2}{\left(8x\pi^2\right)^2} \exp\left\{ -\frac{1}{2}|x|\left(\frac{m_1^2}{\mu_1} + \mu_1\right) - \frac{|x|}{2}\left(\frac{m_2^2}{\mu_2} + \mu_2\right)\right\} \cdot J(\mu_1, \mu_2) \quad (2.7)$$

here

$$\begin{aligned} J(\mu_1,\mu_2) = N_1 N_2 \iint \delta r_1 \delta r_2 \exp\left\{ -\frac{1}{2}\int_0^x d\tau \left(\mu_1 \dot{r}_1^{\,2}(\tau) + \mu_2 \dot{r}_2^{\,2}(\tau)\right)\right\} \cdot \\ \cdot \exp\left\{ -W_{1,1} + 2W_{1,2} - W_{2,2}\right\} \end{aligned} \quad (2.8)$$

and introduced the notation:

$$W_{i,j} = \frac{g^2}{2}(-1)^{i+j} \cdot \int_0^x \int_0^x d\tau_1 d\tau_2 \dot{Z}_\alpha^{(i)}(\tau_1) D_{\alpha\beta}\left(Z^{(i)}(\tau_1) - Z^{(j)}(\tau_2)\right) \dot{Z}_\beta^{(j)}(\tau_2) \quad (2.9)$$

The functional integral $J(\mu_1, \mu_2)$ looks like the Feynman [6] path integral in nonrealistivic quantum mechanics for the four-dimensional motion of the two particles with masses μ_1 and μ_2. The interaction of these particles is defined by the nonlocal functional represented in (2.9) which contains potential

and nonpotential interaction. The mass of the bound state systems defined through $\Pi(x-y)$ loop function in the following way:

$$M = -\lim_{|x-y|\to\infty} \frac{\ln \Pi(x-y)}{|x-y|} \tag{2.10}$$

One of the basic problems of description the formulation dynamics of bound state systems is the determination of the mass of this system. From (2.10) we see, that if we find the loop functions then we can define the mass bound state system. However, we can not calculate the functional integrals represented in (2.7) and (2.8) in the general case. According to (2.10) we must define the asymptotic bihaviour loop function at the large distances. Now, in the limit $|x-y| \to \infty$ the functional integral represented in (2.8) we can define in the following way:

$$\lim_{|x|\to\infty} J(\mu_1, \mu_2) = \exp\{-xE(\mu_1, \mu_2)\} \tag{2.11}$$

here $E(\mu)$ is the quantity dependence only on the parameters μ_1, μ_2 and also the coupling constant g. In the this approximation, the functional integral represented in (2.7) for the limit $|x-y| \to \infty$ calculated by the sadil point methods, and after some transformations we can get for the mass bound state systems:

$$M = \sqrt{m_1^2 - 2\mu^2 E'(\mu)} + \sqrt{m_2^2 - 2\mu^2 E'(\mu)} + \mu E'(\mu) + E(\mu) \tag{2.12}$$

and the parameter μ is determined by the equation:

$$\frac{1}{\mu} = \frac{1}{\mu_1} + \frac{1}{\mu_2} = \frac{1}{\sqrt{m_1^2 - 2\mu^2 E'(\mu)}} + \frac{1}{\sqrt{m_2^2 - 2\mu^2 E'(\mu)}} \tag{2.13}$$

and where used notation $E''(\mu) = \dfrac{\partial E(\mu)}{\partial \mu}$. When determined the mass spectrum of a relativistic bound state the constituent mass component is usually introduced which differ from a mass of an initial particle. In particular, when determine the of a mass spectrum of hadrons consisting from quarks, then the mass of valent and current quarks is usually introduced which differ among themselves. On the other hand, if the bound states consist of two gluons, the mass of constituent gluon, according to (2.13), is not equal to zero. In this case, two - gluon bound states it is possible to identify with pomeron, which widely used for describing of mechanism of the nonelastic scattering of particles.

3. Formulation of the problem

According to (2.12) for the calculation of the mass spectrum bound state system, before we need to determine the quantity $E(\mu)$. From (2.8) we see that if

in the framework of the some approximation we can represent the function $W_{i,j}$, which shown in (2.9), as a effective potential of the system, then the quantity $E(\mu)$ should be considered as a eigenvalue of the effective Hamiltonian with this potential.

Let us restore the parameters $\hbar$ and c in (2.8), then for the function $J(\mu_1, \mu_2)$ we have:

$$J(\mu_1,\mu_2) = N_1 N_2 \iint \delta r_1 \delta r_2 \exp\left\{-\frac{1}{2}\int_0^x d\tau \begin{pmatrix} \mu_1(\dot{\vec{r}}^2{}_1(\tau) + \dot{r}_1^{(4)})^2(\tau)) \\ +\mu_2(\dot{\vec{r}}_2^2(\tau) + \dot{r}_2^{(4)})^2(\tau) \end{pmatrix}\right\}. \qquad (3.1)$$

$$\cdot \exp\{-W_{1,1} + 2W_{1,2} - W_{2,2}\}$$

where: $\delta r_j = \delta\vec{r}_j \cdot \delta r_j^{(4)} \qquad j = 1,2$

$$W_{i,j} = \int_0^x \int_0^x d\tau_1 d\tau_2 (-1)^{i+j} \left(\vec{n} + \frac{1}{c}\dot{\vec{r}}_i(\tau)\right)\left(\vec{n} + \frac{1}{c}\dot{\vec{r}}_j(j)\right) \cdot \int \frac{d\vec{q}}{(2\pi)^3} \int_{-\infty}^{\infty} \frac{ds}{2\pi} * \qquad (3.2)$$

$$* \tilde{D}\left(\vec{q}^{\,2} + \frac{s^2}{c^2}\right) \frac{g^2}{2} \exp\left\{is(\tau_1 - \tau_2) + \frac{is}{c}\begin{bmatrix} r_i^{(4)}(\tau_1) - \\ - r_j^{(4)}(\tau_2) \end{bmatrix} + i\vec{q}\begin{bmatrix} \vec{r}_i(\tau_1) - \\ - \vec{r}_j(\tau_2) \end{bmatrix}\right\}$$

In the paper [7] considered the limit $|x - y| \to \infty$, i.e. in the nonrelativistic case get:

$$H = \frac{1}{2\mu}\vec{P}^2 + V(r)$$

where $V(r)$ is the effective interaction potential and for the Coulomb interaction equals:

$$V(r) = -\frac{\alpha_s}{r}$$

In the given paper we consider the case c$<\infty$. When considered any relativistic corrections in the framework of the standard methods is the limited usually lowest order of the values $\frac{v}{c}$, but in the our approach the infinite series obtained in the order of the values $\frac{v}{c}$, is summarized.

From (2.1) and (2.5) we see, that the representation for the loop functions is equivalent to the Wilson-loop path integral representation the confinement of quarks and gluons is satisfied via area low. In the other hand when averaging over

the gauge field $A_\alpha(x)$ we limited only by the lowest order, i.e. two point correlators. But in the general case we must take into account many point correlators, in the particularly for four point correlators, in the coordinate space this is corresponding to the confinement potentials. Therefore, the contributions of many point correlators is should be approximated by the confinement potential. Take into account the contributions many point correlators through confinement potential the loop function represented in (2.8) can be rewrite in the form:

$$\Pi(x)=\int_0^\infty\int_0^\infty \frac{d\mu_1 d\mu_2}{\left(8x\pi^2\right)^2}\exp\left\{-\frac{x}{2}\left(\frac{m_1^2}{\mu_1}+\mu_1\right)-\frac{x}{2}\left(\frac{m_2^2}{\mu_2}+\mu_2\right)\right\}\cdot J_\mu(\mu_1,\mu_2)e^{-S_{\min}} \qquad (3.5)$$

where $S_{\min}=\sigma\cdot r$ is the minimal area; and σ is the string tension; and $J(\mu_1,\mu_2)$ is shown in (3.1). Thus, the main problem of this paper is define of the effective potential representation for the function $W_{i,j}$ in (3.1).

4. Definitions of the nonperturbative correction to the interaction Hamiltonian

Now we shall begin the definition of a structure of a Hamiltonian of interaction. Interactions between composite particles are carried out changing of gauge fields, therefore the propagator can be represented in standard way:

$$\widetilde{D}\left(\vec{q}^{\,2}+\frac{s^2}{c^2}\right)\approx\frac{1}{\vec{q}^{\,2}+\frac{s^2}{c^2}}=\int_0^\infty dx\cdot\exp\left\{-x\left(\vec{q}^{\,2}+\frac{s^2}{c^2}\right)\right\} \qquad (3.1)$$

Then, after integration on $d\vec{q}$ from (2.16) we have for the interaction potential:

$$W_{i,j}=\frac{1}{2}g^2(-1)^{i+j}\int_0^t\int_0^t d\tau_1 d\tau_2\int_{-\infty}^\infty\frac{ds}{2\pi}\int_0^\infty dx\left(2\sqrt{\pi x}\right)^3\cdot\exp\left\{-\frac{\vec{r}^{\,2}}{4x}\right\}*$$
$$*\sum_{k=0}^\infty\sum_{n=0}^k\frac{(-1)^{n+k}}{n!(k-n)!}\cdot x^n r^{(4)(k-n)}\left(\frac{is}{c}\right)^{n+k}\exp\{is\tau\}\cdot\Xi \qquad (3.2)$$

Where the following notations used:

$$\tau=(\tau_1-\tau_2);\qquad \vec{r}=\vec{r}_i(\tau_1)-\vec{r}_j(\tau_2);\qquad r^{(4)}=r_i^{(4)}(\tau_1)-r_j^{(4)}(\tau_2);$$
$$\Xi=1+\frac{\vec{n}}{c}\left(\dot{\vec{r}}_i(\tau_1)+\dot{\vec{r}}_j(\tau_2)\right)+\frac{\dot{\vec{r}}_i(\tau_1)\dot{\vec{r}}_j(\tau_2)}{c^2} \qquad (3.3)$$

Here τ_1 and τ_2 - is considered as proper time quarks 1 and 2, respectively. We suppose that in initial moment quark rest and interact among themselves only by chromoelectric field. In this case we have $\Xi = 1$. On the other hand, we consider that $r^{(4)}$ - Euclidean time is connected with τ - proper time quarks as follows: $r^{(4)} = c(\tau_1 - \tau_2) \equiv c\tau$. Then, taking into account (3.3), and making integration on the variables ds, after some simplifications from (3.2) is obtained:

$$W_{i,j} = \frac{g^2}{8\pi}(-1)^{i+j}\int_0^t\int_0^t d\tau_1 d\tau_2 \frac{\delta(\tau_1-\tau_2)}{\left|\vec{r}_i(\tau_1)-\vec{r}_j(\tau_2)\right|} + \frac{g^2}{8\pi} * \\ * \sum_{k=1}^{\infty}\frac{(-1)^k}{(2k)!c^{2k}}\int_0^t d\tau \frac{\partial^{2k}}{\partial\tau^{2k}}\left(\left|\vec{r}_i(\tau_1)-\vec{r}_j(\tau_2)\right|^{2k-1}\right) = W_{i,j}^{(1)} + W_{i,j}^{(2)} \tag{3.4}$$

Every term in (3.4) we shall consider separately. The first term $W_{i,j}^{(1)}$ - corresponds to the contribution of one gluon exchanging, and $i = j$ determines a renormalization of a mass operators:

$$-W_{1,1}^{(1)} + 2W_{1,2}^{(12)} - W_{2.2}^{(1)} = \int_0^t d\tau\left(-\frac{\alpha_s}{r(\tau)} + V(0)\right) \tag{3.5}$$

where

$$\vec{r}(\tau) = \vec{r}_1(\tau_1) - \vec{r}_2(\tau_2); \qquad V(0) = \alpha_s\int\frac{d\vec{k}}{(2\pi)^2}\frac{1}{\vec{k}^2} \tag{3.6}$$

and $V(0)$ - correspond a usual renormalization of mass operator in a nonrelativistic limit, and further we shall consider as a constant. From (3.4) we see, that the function $W_{i,j}^{(2)}$ gives only crossing term, and diagonal term is equal to zero. Parameter τ - we shall consider as proper time of the quarks. Then variables $v(\tau)$

$$\vec{v}(\tau) = \frac{\partial}{\partial\tau}(\vec{r}(\tau)) \tag{3.7}$$

consider as a velocity of relative motion of quarks. First of all, we shall consider the case, when the velocity of quarks is constant: $\frac{\partial\vec{v}(\tau)}{\partial\tau} = 0$. The nonperturbative corrections to the interaction Hamiltonian in this case is obtained, and the calculation details are given in the Appendix A. Then taking into account (3.5), (3.6) and (A5), from (3.4) for a Hamiltonian of bound state system we have:

$$H = H_0 + \Delta H_{nonper} \tag{3.8}$$

where

$$H_0 = \frac{1}{2\mu}\vec{p}^{\,2} - \frac{\alpha_s}{r} + r\sigma + V(0); \qquad \Delta H_{nonper} = \frac{\alpha_s}{r}\left[\frac{1}{\sqrt{1+\frac{l(l+1)}{r^2}}} - 1\right] \tag{3.9}$$

Thus, we have received the nonperturbative corrections to the interaction of Hamiltonian, which connected with a relativistic nature of a system. From (3.9) we see, that the nonperturbative component gives orbital-excited state, i.e. the nonperturbative component is connected to driving quarks rather from each other, therefore in a nonrelativistic limit ($c \to \infty$) this interaction is absent. Thus nonperturbative component is connected to a relativistic nature of a system.

Appendix A

Let as give some details of summarization of following series:

$$I = \sum_{k=1}^{\infty} \frac{(-1)^k}{(2k)!\,c^{2k}} \cdot \frac{\partial^{2k}}{\partial \tau^{2k}} r^{2k-1}, \tag{A.1}$$

where $r = |\vec{r}|$. For this purpose we shall calculate of differentials a radius vector:

$$\vec{v} = \frac{\partial \vec{r}}{\partial \tau}; \qquad \frac{\partial r}{\partial \tau} = (\vec{n}\cdot\vec{v}); \qquad \vec{n} = \frac{\vec{r}}{r}; \qquad \vec{v} = \frac{\partial \vec{M}}{\partial \tau} = 0 \tag{A.2}$$

In this approximation for various values k is obtained:

$$\begin{aligned} &k = 1; && \frac{\partial^2 r}{\partial \tau^2} = \frac{[\vec{r},\vec{v}]^2}{r^3} = \frac{\hat{l}^2}{r^3} \\ &k = 2 && \frac{\partial^4 r}{\partial \tau^4} = \frac{9\hat{l}^4}{r^5} \\ &\cdots \\ &k = n && \frac{\partial^{2n}}{\partial \tau^{2n}} r^{2n-1} = \frac{\hat{l}^{2n}}{r^{2n+1}} \prod_{j=1}^{n} (2j-1)^2 \end{aligned} \tag{A.3}$$

$\hat{l} = [\vec{r},\vec{v}]$ is operator orbital moment of two-body system. Using relations with single masses:

$$\prod_{j=1}^{k}(2j-1) = \left[\frac{(2k-1)!}{2^{k-1}(k-1)!}\right]^2 = \frac{\Gamma^2(2k)}{\Gamma^2(k)2^{k-1}}; \qquad \Gamma(2k) = \frac{2^{2k-1}}{\sqrt{\pi}}\Gamma(k)\Gamma\left(k+\tfrac{1}{2}\right) \tag{A.4}$$

And taking into account (A.3) for an initial series (A.1) we have:

$$I = \frac{1}{\sqrt{\pi r}} \sum_{k=1}^{\infty} \frac{(-1)^k A^k}{k!} \cdot \int_0^{\infty} dx \frac{x^k}{\sqrt{x}} e^{-x} = \frac{1}{\sqrt{\pi r}} \cdot \int_0^{\infty} \frac{dx}{\sqrt{x}} e^{-x} \left(e^{-Ax} - 1\right) =$$

$$= \frac{1}{r} \left[\frac{1}{\sqrt{1 + \frac{l(l+1)}{r^2}}} - 1 \right] \quad ; \qquad A = \frac{\hat{l}^2}{c^2 r^2} . \tag{A.5}$$

Thus, we summarized series obtained on degrees $\left(\frac{v}{c}\right)^2$ at $\dot{v} = 0$.

References

1. D.J.Gross, P, Wilezek. Phys. Rev. Lett.30p.l343 (1973) Phys. Rev. D8, p.3633 (1973)
2. H.D.Politzer, Phys. R.ev. Lett., 30p.1346 (1973)
3. E.Eichten et al., Phys. Rev. Lett., 34,369 (1975) D.Gromes, Nucl. Phys. B131,80 (1977) J.L.Richardson, Phys. Lett.82B, 272 (1979) C.Quigg. And J.L.Rosner, Phys. Rept.56,167 (1979) A.Martin, Phys. Lett.lOOB, 511 (1981)
4. G.V. Efimov, S.N. Nedelko, Phys. Rev. D51, p. 176 (1995); Phys. Rev. D54, p. 4483 (1996)
5. M. Dineykhan, G.V. Efimov and Kh. Namsrai, Fortsh. Phys., 39, p. 259-318 (1991);] M. Dineykhan, G.V. Efimov, Sacharov Conf. 1, Proceed., Mos. V. 2, p. 963-969 (1991).
6. R.P. Feynman and A.P. Hibbs, Quantum Mechanics and Path Integrals, New York McGraw-Hill 1965.

PREDICTION OF CATASTROFE THEORY FOR HEAVY IONS COLLISION AT HIGH ENERGIES

Kuchin I.A.

Almaty, Kazakhstan

The new approach to studying a fragmentation of massive nucleus phenomenon is offered. It is shown, that the fragmentation is a typical object for catastrofe theory, and the mass spectrum of its products is similar to chemical composition of cosmic rays.

Introduction. Last years in relativistic nuclear physics the small boom around the processes of fragmentation of massive nucleus in collisions at high energies is observed. The limiting fragmentation of explosive type, a multifragmentation is found out, a number of new models and approaches to studying this interesting phenomenon is offered: a thermal fragmentation, claster disintegration, method of topological characteristics etc. (see, for example, [1,2]). In the USA a new collaider for massive relativistic ions (RHIC) with energy 130 GeV/nucleon is started. The main theme of all this activity – investigating the question of existence of a new condition of substance - of a quark – gluon plasma. (QGP). Doubts in possibility of preparation such compact, strongly compressed and termalisated conditions during short-term interaction of nucleus (as against stationary conditions of the graviting star medium) are proved and well-known [3]. At the same time at sufficient temperature other phase transformations are theoretically possible also: in hadron gas or in $\pi -$ condensate. It looks like a crisis of a problematics coming.

The new approach: the basic idea and method. The purpose of the present work is to show that we do not have necessity to reduce all problems to a question of warming nucleus up. The termalisation role may be carried out by the stochastisation of confinement dynamics which, naturally, develops in nucleus at nonequilibrium collision action. Phase transformations may occur not only as a result of overbarrier transitions of termalisated particles, but also due to downturn of of the most potential barrier height as a result of nucleons creep at loss of stability by the last. And, simultaneously with decomposition of parent nucleus it may be carried out recombination of fragments and formation of daughter nucleus. It is interesting to find out qualitative features of processes in the stochastic script. As a research method it is offered to use representations of the dynamic systems (DS) theory, in particular, the applied theory of catastrofe [4].

From dynamical stochastisation to many-dimensional catastrophes. F.G.Lepehin apparently was one of the first who has turned a close attention that

scattering of heavy ions begins on large distances by Coulomb interaction [5]. Even before occurrence on a stage of nuclear forces kinetic energy of a nucleus decreases, passing in potential, and the nucleus of a target is accelerated aside. But nucleus is not such a solid body and all can not be limited to change of direction of its movement as a whole. In a nucleus the recharge of nucleons and rearrangement of positions between neutrons and protons begins. To the moment of nuclear forces inclusion the nucleus already is in slightly polarized and dissociated condition, that in turn results in far-reaching consequences [6].

The chaos is understood in DS theory as hashing of phase space (PS). Mathematilally hashing is carried out by operations of stretching and compression of PS (baker transformations or Smale's horseshoe). Therefore the geometrical picture of chaos is a folded relief of many-dimensional PS. Chaotization develops in a direction of increase of number folds as as their magnitude. During scattering of nucleus the condition of chaos formation is provided automatically as at fast flight of nucleus the compression of medium is replaced by stretching, and stretching - with compression.

Dynamic consequences of a folded relief are studied in the catastrophe theory (CT). The term catastrophe should not be understood dramatically. It designates only rapid and spasmodic character of system transition from one physical condition to another, qualitatively distinct from the first. Phase transitions of the first or second type are concerned to catastrophes in thermodynamics. But it is catasrophe of the lowest order, with small number of maxima and minima of potential function *V (x)*. In general CT is an effective device for studying many-dimensional nonlinear processes in the distributed mediums when the opportunity of their adequate description in terms of simple models with small number of variables and controling parameters is excluded. For example, in climatology.

Multiplicity of phase transitions. Earlier [7] we already showed an opportunity of the explanation of compound objects (nucleons) collision within the framework of representations of nonlinear optics as scattering of coherent beams of particles-constituetnts on each other. It was shown, that P_{st} -the stationary solution of the Focker – Planck equation for such problems is expressed through potential of phase transition of the second type (as in the theory of superconductivity by Ginzburg-Landau):

$$V_{st} = \frac{1}{n+1}\left[(2(1-\frac{k_1}{\gamma\gamma_1})|p_1|)A^2 + (k_1^2/\gamma\gamma_1)A^4 \right] = \alpha A^4 + \beta A^2, \quad (1)$$

where n - volume (number) of radiative modes, k_1 - a degree of radiation phases alignment, γ_1 - a constant of absorption of external radiation, γ - volume stoks and fonon modes, and A- amplitude of radiation. This potential as function of a variable A has one maximum at A = 0 (for a case $|p_1|$ less than some threshold

value $\gamma\gamma_1 / k_1$) and two minima (for $|p_1|$ is more then $\gamma\gamma_1 / k_1$) (Fig. 1). In the catastrophe theory [4] this transition is described by catastrophe of assembly of a kind

$$V(x; a, b) = 1/4\, x^4 + 1/2a\, x^2 + bx, \qquad (2)$$

where numerical factors get out so that the appropriate manifold of catastrophe *M*, determined by the equation of a type

$$\frac{d}{dx} V(x; a, b) = x^3 + ax + b = 0$$

would have the elementary kind. Comparing (1) and (2), we see, that to constant factors *a* and *b* of universal C*T* (in a case when there is a possibility of the parallel phenomenological analysis of the phenomenon) the certain functions describing action of the concrete mechanism of process, having threshold character . In applied C*T* there is an accepted principle, that transition of the probe particle from one potential hole in another is made or as a result of change of the general form of a relief (a principle of the maximal delay), or due to own noise (thermal) movement of a particle and skipping it through a potential barrier at the constant general form of a hole (Maxwell's principle) so after all the condition of system will be determined by a global minimum of potential function. (See Fig. 2)

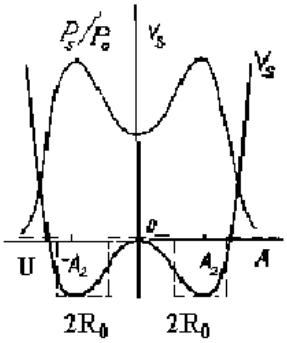


Fig. 1. Catastrofe of assembly or phase transition of II type [5.] V_s - a curve of the generalized potential; P_s/P_0 the ratio of the stationary solution to a normalizing constant. Minima of potential function corresponds to maxima of the stationary solution. A dotted line below - approximation of a minimum by a smooth curve rectangular hole.

Extending this theory on the case of massive ions collision, we should take into account a possibility of strong interaction of system components on small distances. It is the easiest to make it, approximating minima by potential function *V (x, c)* rectangular holes from fermi -gas model in nuclear physics. (Fig. 1). The

theory is necessary to reveal general holistic nature of process - to find dynamic connection between channels of birth of fragments of different masses and a charge.

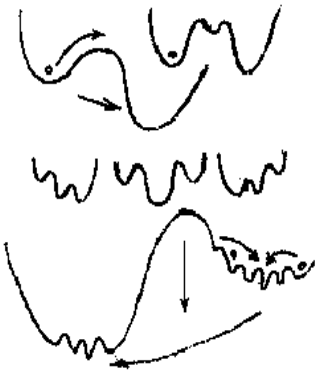


Fig 2. A variety of forms of a potential function *V (x, c)* relief in the theory of catastrophe [4].

Potential function. Central object of CT is potential function $V(x;c)$, which depends from *n* state variables (parameters of the order) *x* and *k* controlling parameters *c*. Studying of physical system is reduced to revealing and the subsequent analysis of equilibriums and local instabilities $V(x;c)$, and also critical values of the specified parameters on branches of stable equilibrium. Balance is defined by a condition $\frac{\partial V}{\partial x_i} = 0$, and local stability by $\frac{\partial^2 V}{\partial x_i \partial x_j} > 0$.

The fact of existence of a multifragmentation as the phenomena already speaks that in the nuclear medium formation of a great number of potential holes of the different sizes and forms is possible. Therefore we should head for catastrophies of high enough orders. Usually the applied CT is limited to discussion of the seven first catastrophes of Thoma. For definiteness we shall give a concrete kind of last two of them:

elliptic $V(x, y; a, b, c) = x^3 - 3xy^2 + a(x^2 + y^2) + bx + cy$ and

parabolic ombilic $V(x, y; a, b, c, d) = x^2 y + y^4 + ax^2 + by^2 + cx + dy$.

Here *x* and *y* designate active variables (parameters of order, function of a state), and letters *a, b, c, d* - passive variables (external or controlling parameters). On physical conditions of a problem momentums (rapidity) of secondary particles are

active variables , and energy of interaction, impact parameters, masses and diameters of colliding nucleus are controlling parameters.

As a $V(x;c)$ not any polynom of n - power may act. All catastrophes are formed by the general principle. In each of them there is a catastrophe germ submitted by members of the senior degrees of independent variables and other polynom part as a germ perturbation. The polynom of perturbation is formed so that at reception by variables of some increment $x \to x' + \Delta_1$, $y \to y' + \Delta_2$, the general view of multivariate perturbation function did not vary. This property is necessary for topologically important features *V (x, c)* did not disappear at displacement along an axis of coordinates in searches of local minima and maxima. From here it is visible, that a set of the fragments, observably on experience in concrete event, characterizes a potential function and carries the nontrivial topological information on a condition of a nuclear matter in the volume exceeding the volume of a concrete nucleus. The number of possible transitions – catastrophe depends on the number of external (control) parameters. They supervise the general states of investigated object. The more parameters, the more number of posible catastrophes. And conversely the greater number of phase transitions we are going to take into account, the greater number of variables and parameters is required to be put in the theory. If we consider the nucleus medium to be homogeneous it will be not possible explain the fact of multiple fragment birth - we simply do not collect necessary number of external parameters $V(x;c)$.

The main result, which follows from this theory for a fragmentation consists in the general form of an output curve of its products. This curve turns out the same kind as a spectrum of chemical elements prevalence in the Universe or of initial cosmic ray composition. Emphasized only processes of a limiting fragmentation are emphasized - a product of full nucleus desintegration and an initial state of multifragmentation (Fig. 3). The contribution of other elements is kept approximately at one level. And to minima of $V(x;c)$ the maxima of an output curve of reaction products correspond. From fig. 3 and 4 one can see, that in due course the data of various authors is tend to reduce the disorder and to gather at a level of a fragmentation curve from CT.

Similarity of spectra of nuclear transformations of different nature and direction (synthesis or desintegration), (fusion or fission) speaks that despite of a variety of concrete macroconditions - high temperatures and pressure in stars, the variety of concrete mechanisms of acceleration and braking (in collision) of particles in a wide range of energies in a rarefied space - at a microlevel as a matter of fact only two factors appear to be determining - a folded relief of phase space and strong interaction of nucleons on small distances.

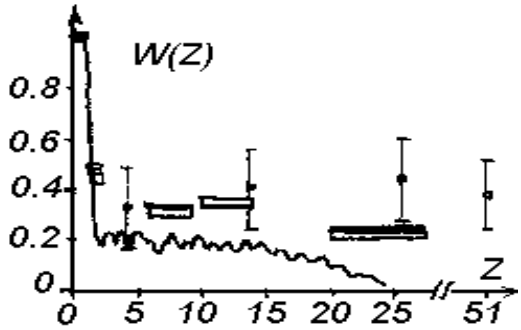


Fig. 3. A output curve for fragmentation products in *TK* on a background of the new data on chemical composition of cosmic ray. (All is normalized on unit): _ - ($E_0 = 10^{15}$-10^{16} eV) [8]; o - ($E_0 > 1$ TeV; Juliusson, 1975) [9]; ▒ - ($E_0 > 1$ TeV; Linsley T., 1983) [9].



Fig. 4. Prevalence of nuclear fragments in Nature [10]: (α) nuclear composition of cosmic ray (Kurnosova L.V. et all., 1967г.) and (β) prevalence of chemical elements in the Universe (Ginzburg V.L. et all , 1964).

The conclusion. So, the multifragmentation is a typically synergetical process, where chaotic dynamics on an input results in the organization of new structures (i.e.nucleus) on an output and the appropriate nonlinear theory is necessary for its adequate description with a big number of variables and control parameters. It's complete, holistic description at a level simple, low-dimentional models is impossible in principle. Models can be considered as original "conseptual maps" of interactions which purpose (assignment) is to effeclively lower the number of independent variables by accounting one factors and rough neglecting others. As a result - a uniform nature of the phenomenon is artificialy broken on a number of independent linear processes, each of which is considered independently contrary to their common nature.

It would be desirable to emphasize, that growing now interest to configurations SD of various nucleus [11] (in particular, to exotic nucleus),

objectively conducts to the statement of system-dynamic representations in nuclear physics, and through them to a new, deeper understanding of a nature of a fragmentation as a holistic process.

References

1. Karnauhov V.A. et all.// Nucl. Phys. (rus), 1999, V. 62, N2, P. 272.
2. Chestnov J.A., Sokolovsky B.Yu. // Izv. AS. ser.phys.(rus), 2002, V. 66, N.5, P. 685.
3. Chernavskaya O.D., Chernavsky D.S.// U.Fiz.Nauk, 1988, V.154, P. 497.
4. Gilmore R.// Applied catastrophe theory, V.1,2, M., 1984.
5. Lepehin F.G.// Workshop materials of collaboration EMU-01, April - May 2000r.
6. Kuchin I.A.// Works ICNRP 01, Almaty, June, 4-7, 2001, P. 234-242
7. Kuchin I.A.// Nonequlibrium and instability in evolution of dynamic structures in nature. Almaty, “Gylym” (rus), 1998, P.141-149.
8. Nikol'skij S.I.,Pavljuchenko V.P., Stamenov I.N.// Brief mess. in phys., Ph.Inst.RAS,1981, P. 49..
9. Ivanenko I.P. et al.// 5 th Intern. Symp. on VHECRI, Lodz, 1988, P.197-224.
10. Murzin V.S.// Physics of cosmic rays (rus). Mosc. State Univer., 1970, 285 P..
11. Yushkov A.V.// Particles and nuclei (rus), Dubna, 1993, V. 24**,** N2, P. 348-408.

PRODUCTION OF Pd-103 RADIONUCLIDE AT THE CYCLOTRON

A. Arzumanov, V. Berger, N. Gorodiskaya, A. Knyazev, Yu. Popov

Institute of Nuclear Physics, Almaty, Kazakhstan

Abstract

In the recent years prostate cancer, even when cured was accompanied by very high incontinency side effects as the surgery or external radiation treatment often caused significant damage to the surrounding organs.

Brachytherapy is a procedure by which the radioactive source, as small sized "seeds" or thin wires, is implanted within a cancerous tumor and the radiation treats the tumor from the inside, and it is rapidly developing over the few years.

This type of treatment has reduced side effects, requiring only mild intervention. One of the key radioisotopes used in brachytherapy is Palladium-103 with a half-life equal to 17 days.

In this paper results are presented on the technique of Pd-103 production by irradiation with protons at the cyclotron of Rh-103 foil with following thermodiffusion of radioactive impurity atoms to the metal surface and their extraction by dissolution of the irradiated foil in a mineral acid.

Up to now 70% yield of Pd-103 was obtained and purity of the extracted nuclide was no less than 99, 99%

I. Introduction

The number of patient suffering from prostate cancer treated by brachytherapy is increasing from year to year. Nowadays ^{125}I and ^{103}Pd are used for this technique with success[1)]. Palladium is offers advantage properties than Iodine such as short half-life, low energy and total cumulative dose delivery at a higher dose and is promising radioisotope for localized tumor treatment.

Production of carrier-free ^{103}Pd based on cyclotron irradiation of rhodium foil with protons via the reaction ^{103}Rh (p,n) ^{103}Pd and further separation of ^{103}Pd are considered.

Current commercial processes of irradiated materials processing consists, as a rule, of several stages:

- dissolution of irradiated material;
- extraction of desired nuclide;
- recovery of enriched material.

Methods of ion-exchange and extraction chromatography are mainly used for extraction of a radionuclide "carrier free"; these methods enable to achieve high rate of the desired isotope purification.

The only shortcoming of the methods is their methodological complexity due to multiple stages of chemical procedures.

There are several modifications of "dry" methods for radionuclide extraction, such as sublimation, dry distillation, thermochromatography, etc., that exclude the stage of irradiated material transformation to another chemical form. These methods are more express and less expensive in comparison with classic/standard methods of "wet" chemistry.

The main objective of the conducted investigations is study of the thermodiffusion method as one of the possible for cyclotron production of "career free" ^{103}Pd from rhodium.

II. Experimental techniques and evaluation of date

The core of the method is in thermal annealing of irradiated metallic matrix at temperatures below the melting temperature of the irradiated material during the time interval required for outcome of radioactive impurity atoms to the binding surface of the phase interface. The radioactive impurity atoms diffused to the metal surface are extracted by a chemical reagent chosen taking into consideration chemical properties of the elements to be separated.

The experiment was encouraged by the following:

♦ Metallic rhodium exists in two allotropic modifications with different crystal lattice structure. α-form of the rhodium allotropic modification is represented by a single cubic lattice with the edge parameter 9.211 Å. β-form has face-centered cubic lattice with the edge parameter 3.795 – 3.803 Å. At room temperature metallic rhodium consists of both form with the α-one prevailing [2,3]. Temperature of rhodium polymorphous transformation was determined by the measurements of rhodium differential emf using Kurnikov's pyrometer. Rhodium thermoelectromotive force decreases at temperature increase, and, at 1030 °C there is a bump change related to the polymorphous transformation of α-Rh to β-Rh. This makes it possible to look for possibility of one or several types of diffusion mechanisms for daughter radioactive atoms during the crystal lattice reconstruction in bulk metal and their concentration on surface at abrupt cooling.

♦ Metallic palladium, opposite to rhodium that is practically insoluble at normal conditions, is easily dissolvable in mineral acids. Significant difference in solubility in mineral acids of palladium and rhodium may be a basis for quick extraction of "carrier free" ^{103}Pd [4].

Objective of the first stage is qualitative validation of diffusion and extraction of palladium without calculations of the diffusion coefficients and investigation of the impurity atom re-dislocation mechanisms.

In the experiment, rhodium foils of the total thickness of 50 μm (> 99,9 % pure, Merck) were irradiated with the internal beam at the Almaty cyclotron U-150, 18 MeV protons at the 30 μA beam current during two hours. The range of

energy used for activation of Rh was taken from dates of cross-sections and target yield (MBq/μA) [5-8]. It was allowed to obtained high radionuclide purity of ^{103}Pd.

When irradiating targets with high intensity internal beam the target is inclined with respect to the beam axis at the angle of 18° in order to reduce beam power density on the target. Thin layer 0,5 mm thick of cooling water, flowing at a velocity of approximately 30 m/s along the target surface is employed to ensure necessary cooling of the target. Cooling water pressure is equal to 20 bar.

Measurements for ^{103}Pd activity were done using the X-lines as well as the E_γ=357.7 keV line by HPGe type of detector coupled to Canberra Accuspec boards and Genie 2000 acquisition/software.

Upon determination of activity the foils were placed into a tantalum container and subjected to thermal annealing in a cylinder vacuum furnace ($7\cdot10^{-3}$ mm Hg) at temperatures 1050, 1200, 1400 (± 10) ^{0}C during 30 minutes, hardened in water and treated with hot solution of 0.05 N hydrochloric acid. Experimental data of the repeated foil activity measurements were used for the ^{103}Pd yield calculation.

III. Results of experiment

The results of the experiment are shown in the Table1. The gamma-spectrum of Rhodium foil after EOB is represented in fig.1. In Fig.2 is shown gamma-spectrum of ^{103}Pd in 0.05 N hydrochloric acid.

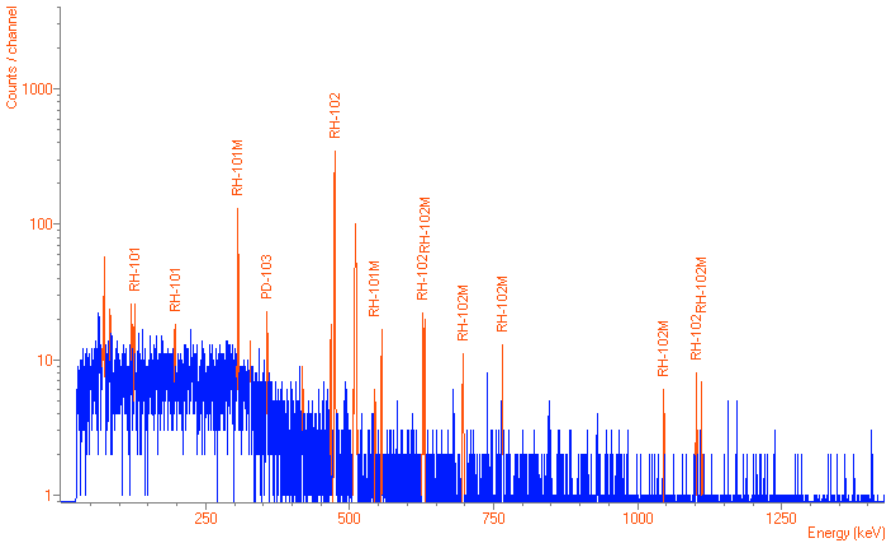


Fig.1. Gamma-spectrum of irradiated rhodium foil after EOB

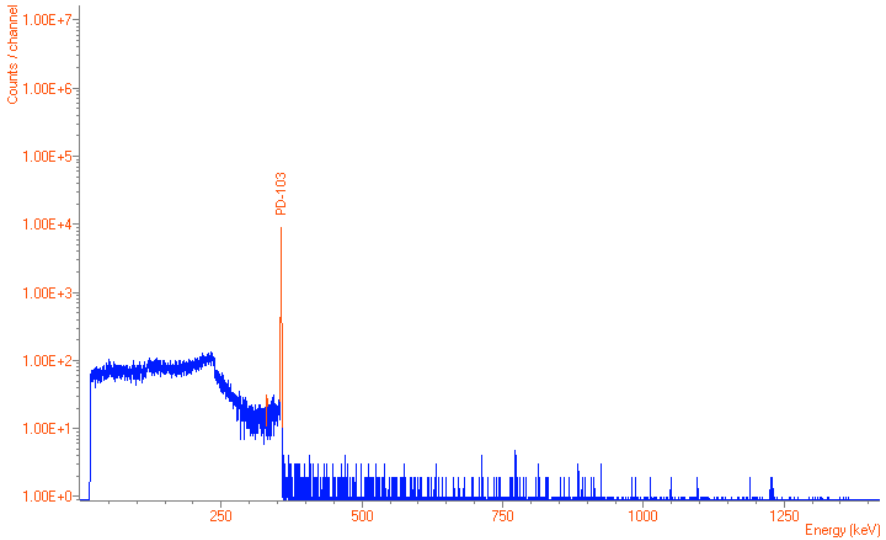


Fig.2 Gamma-spectrum of final product

Summary of the Palladium-103 production

Table 1

NN of foil	Activity of ^{103}Pd, kBq (before annealing)	T, ^{0}C	Activity of ^{103}Pd, kBq (after annealing)	Yield of ^{103}Pd, %
1	410	1050	330	19.5
2	297	1200	120	59.6
3	1250	1400	375	70

IV. Conclusion

In this work an attempt was undertaken to apply the thermodiffusion method as one of the possible for cyclotron production of "career free" ^{103}Pd from rhodium.

The experimental results have shown the following:

- At thermal treatment and further abrupt cooling of rhodium the daughter impurity atoms of palladium diffuse and concentrate on the metal surface;
- Diffusion rate increases with increase of temperature;
- When the metal is treated with lean solution of hydrochloric acid palladium is extracted without destruction of the main metal matrix;
- Purity of the extracted nuclide is not less than 99.99%.

So, as a result of the investigations it was revealed that the thermodiffusion method can be applied for extraction of Pd-103 from irradiated rhodium matrix.

For further experiments it is supposed to utilize an induction furnace that enables quick heating and cooling of the target material.

Acknowledgement

This study was financially supported by the IAEA for CRP research contract 11384. Prof. Dr. P. Van den Winkel (Vrije Universiteit Brussel) gracefully supplied the Rh-foil.

References

1. S. Nag, D. Beryer, J. Friedland etc., Int. J. Radiation Oncology Biol. Phys. 44 (1999) 789
2. I.A. Fedorov, "Rhodium", Science, Moscow (1966)
3. F.E. Beamish. The analytical chemistry of noble metals, Pergamon, p.1 (1966)
4. A.A. Rudnizki, R.S. Polyakova, I.I. Tyurin. Proc.sector of Pt, IOHN USSR, 29, 183 (1955)
5. A.Hermanne, M.Snock, A. Fenyvesi and L. Daraban, Nuclear Instrument and Method B 170 (2000) 133
6. P.P. Dmitriev, N.N. Krasnov and G.A. Molin, "Radionuclide yield in reactions with protons, deuterons, alpha particles and helium-3", INDC(CCP)-263/G+CN+SZ, Vienna (1986)
7. S. Takacs, F. Szelecsenyi etc., Nuclear Instrument and Method B 170 (2000) 133
8. "Charged-particle cross-section database for medical radioisotope production. Diagnostic radioisotopes and monitor reactions", IAEA-TECDOC-1211, IAEA, Vienna, 2001.

PROMPT GAMMA-RAY NEUTRON ACTIVATION ANALYSIS (PGNAA) SYSTEM BY USING A 740 GBq ^{241}Am-Be NEUTRON SOURCE

Çetiner M.A., Yücel H*., Demirbaş A*., Demirel H*., Bozkurt A*., Turhan Ş*. and Özmen A.***

* Ankara Nuclear Research and Training Center (ANRTC), 06100 Beşevler, Ankara, Turkey
** Gazi University, Art and Science Faculty, Physics Department, 06500 Teknikokullar, Ankara, Turkey

Abstract
A PGNAA system consisting of a 740 GBq ^{241}Am-Be neutron source and a gamma spectrometer with a n-type Ge (REGe) detector was installed at ANRTC to measure the prompt gamma-rays produced by the interactions of thermal neutrons in the samples for the analysis of light elements such as B, P, S and Cl, and some trace elements with large cross sections (Cd, Hg, Sm, Gd, etc.).
In the irradiation system, a 55 cm diameter cylinder tank filled with water moderator comprises the neutron source placed in a polypropylene tube that was coaxially positioned in the lead rings (internal diameter: 9 cm and outer diameter: 21 cm) in order to reduce the gamma rays emitted directly from the source such as 0.0596 MeV (^{241}Am) and 4.43 MeV (0.6 gamma per neutron) from the excited state of $^{13}C^{*}$ via the $^{9}Be(\alpha, n)^{12}C$ reaction in the source. The moderator tank was shielded with paraffin in all sides against fast neutrons. The thickness of paraffin at the front side of the tank is 28 cm and 18 cm at other sides. The neutron irradiation system was also shielded by using chevron lead bricks of 18 cm thickness. The background-prominent gamma rays, which is especially the 2.223 MeV gamma ray from the $^{1}H(n,\gamma)^{2}H$ reaction formed in hydrogenous materials used for neutron moderation was reduced remarkably in view of the permissible gamma dose for overall irradiation room. The neutrons thermalized in moderator travel through the hole with 6 cm diameter for sample irradiations. The detector was shielded with Li_2CO_3 powder against thermal neutrons to avoid radiation damage and surrounded by additional lead bricks to reduce gamma-background. The measurements are carried out for the efficiency calibration of the detector by using the standard sources. The features of the PGNAA system with an isotopic neutron source are described and its analysis capability is discussed in this paper.

1. Introduction

Over the last forty years, prompt gamma-ray neutron activation analysis (PGNAA) has been developed at many research institutes and applied in various fields, such as mineralogy, geology and biology [1-3]. The PGNAA is a complementary

technique to conventional-delayed neutron activation analysis method (i.e., INAA) and is characterized by its capability both for nondestructive multi-element analysis and for analyzing especially light elements such as H, B, C, N, P, S and Cl which are generally difficult to analyze by INAA [4]. In addition, some toxic elements such as Cd and Hg and the elements (Eu, Dy, Sm and Gd) having higher neutron absorption cross-section can be analysed by PGNAA. In principle, PGNAA is based on detection of capture gamma rays emitted within 10^{-14} to 10^{-12} s by target material while it is being irradiated with neutrons. Nuclei formed in neutron-capture reactions have excitation energies equal to the binding energy of the added neutron. The excitation energy is released by emission of gamma rays of which the energies range from about 100 keV to 10 MeV. Thus, the elemental concentration is retrieved for the identified elements in any matrix.

Thermal and cold neutron beams for PGNAA applications are usually extracted from the research reactors or obtained from the accelerator based sources. More than 30 PGNAA facilities with the fluence rate of 10^5 to 10^{10} n.cm^{-2}.s^{-1}, installed at reactors in the world, are widely used to determine elemental concentrations in various samples [5]. In recent years, a thermal neutron guide system at the 10 MW Budapest Research Reactor has been developed for the purposes: neutron capture γ-ray spectroscopy and its application, namely PGNAA facility [6,7]. A prompt gamma neutron activation analysis system at HANARO, a 30 MW research reactor in the Korea Atomic Energy Research Institute was designed to obtain a high thermal neutron flux ($1x10^8$ n.cm^{-2}.s^{-1}) with low background by employing a set of pyrolytic graphite crystals [8]. In addition to reactor-based PGNAA applications, a number of applications of this technique by using both isotopic neutron sources or portable neutron generators and accelerators are in use. The isotopic neutron sources for PGNAA are a much cheaper alternative with the added advantage of mobile application possibilities. In particular, PGNAA technique with the neutron sources such as ^{252}Cf and ^{241}Am-Be is used for on-line and in situ analysis in various fields such as industrial, mineral and oil exploration, etc [9]. Since, for example, ^{241}Am-Be neutron source has a long half life of 432.2(7) y, it gives a constant and stable neutron output for years. However, there are two main disadvantages of the use of isotopic neutron sources in PGNAA facilities. The first is the contribution of the gamma rays emitted from the source itself to the sample gamma-ray spectrum to be analyzed. For example, the 59.6 keV (34.6%) gamma ray and the other 334 gamma rays with weak intensities from the ^{241}Am, the Doppler broadened 4.43 MeV (0.6 gamma per neutron) from the excited state of $^{13}C^*$ via ^{9}Be(α,n)^{12}C reaction in all ^{9}Be(α,n) sources may interference with the analytical gamma-ray peaks from the elements of interest induced by (n,γ) reactions. The second disadvantage of isotopic sources is that their neutron output is low, for example, 2.2 x 10^6 n.s^{-1}.Ci^{-1} for ^{241}Am-Be source. However, they have high penetrable neutrons, the average neutron energy of ^{241}Am-Be source is 4.43 MeV, and its neutron energy distribution spans from 1 to 12.1 MeV [10].

Although the obtainable thermal neutron fluence rate from the isotopic neutron source for a PGNAA application is lower compared with that of reactor beam neutrons, it has still a potential analysis capability for some elements such as H, B. Since these elements don't emit any delayed gamma ray, they are difficult to analyze by INAA. Especially, boron analysis is very important for jeo-chemistry, mineralogy and biology. However, it seems more difficulty for the hydrogen analysis in samples by PGNAA with use of isotopic source because there exists the background of 2.223 MeV gamma ray from the $^{1}H(n,\gamma)^{2}H$ reaction formed in hydrogenous materials used for neutron moderation. On the other hand, PGNAA technique has a great advantage for the analysis of boron, cadmium, gadolinium, samarium, etc. The measurements used to detect boron are based on the detection of the 478 keV gamma rays following the reaction $^{10}B(n,\alpha)^{7}Li$. The isotopic abundance of ^{10}B in natural boron is 19.8% of weigh units[11]. The recoiling ^{7}Li nucleus, initially in an excited state, decays with 94% by Doppler broadened 478 keV prompt gamma ray. Thus the broadened boron peak is easy to identify in a prompt gamma-ray spectrum, because it is wider than other peaks. Similarly, using capture of a neutron by cadmium and gadolinium in $^{113}Cd(n,\gamma)^{114}Cd$, $^{157}Gd(n,\gamma)^{158}Gd$ and $^{149}Sm(n,\gamma)^{150}Sm$ reactions can decay to stable ground state by emitting the characteristic gamma-ray(s), mainly 558.3 keV for Cd and 181.9 keV for Gd and 333.9 keV for Sm, respectively. In this study a special interest is given to analyze the B, Cd, Gd and Sm with a larger thermal neutron cross section because especially the elements B and Cd have particular importance in practice.
In this paper, a description of a PGNAA system with a ^{241}Am-Be neutron source is given in detail, and the prompt gamma-ray spectra collected for boron and some elements are discussed related to performance of the PGNAA system in its future applications, especially the analysis of boron in the Turkish borate ore samples.

2. System Features

2.1 Irradiation facility

The PGNAA system with a 740 GBq ^{241}Am-Be neutron source, which is installed in a room at ANRTC, is shown in Fig.1. The physical dimensions of the irradiation unit are 132 cm(W) x 132 cm(L) x 103 cm(H).

In the irradiation unit, a 55 cm diameter cylinder polypropylene tank filled with water moderator comprises the neutron source placed in a polypropylene tube that was coaxially positioned in the geometrical center of lead rings with the thickness of 6 cm (internal diameter: 9 cm, outer diameter: 21 cm and total height: 33 cm).

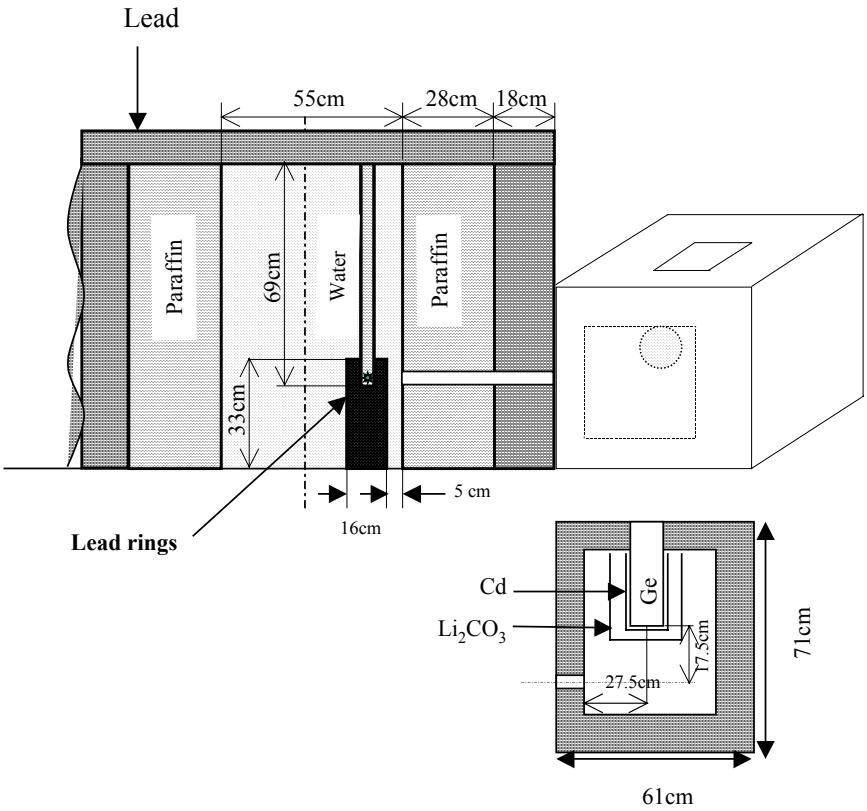


Fig. 1. A schematic diagram of PGNAA system with a 740 GBq ^{241}Am-Be neutron source

Thus, the gamma rays emitted directly from the source itself such as the photons with energy of 0.0596 MeV, 0.662 MeV (^{241}Am) and 4.43 MeV (0.6 gamma per neutron) from the excited state of $^{13}C^*$ via the $^{9}Be(\alpha,n)^{12}C$ reaction in the source was reduced substantially by using the lead rings placed in the cylinder tank. The moderator tank was additionally shielded with paraffin in all sides to prevent the detector sides from fast neutrons. The thickness of paraffin at the front side and other sides of the tank is 28 cm and 18 cm, respectively. Two surfaces of the neutron irradiation unit was also shielded by using chevron lead bricks in total thickness of 18 cm, and the other surfaces are back the concrete walls in the thickness of 1 to 2 m in a basement. The background-prominent gamma rays, which is especially the 2.223 MeV gamma ray from the $^{1}H(n,\gamma)^{2}H$ reaction with σ_a =0.332 b formed in hydrogenous materials used for neutron moderation was

reduced remarkably in view of the permissible gamma dose for overall irradiation room. The measured gamma dose rate is less than 40 μR/h and the estimated neutron dose rate is less than 1 mrem/h at working area. The neutrons thermalized in moderator travel through the hole with 6 cm diameter for sample irradiations. The detector was shielded with both natural lithium carbonate (Li_2CO_3) powder contained in a hollow wooden box (powder thickness: 5 cm at front of detector window, 1.5 cm on the sides of the Al end-cap of the detector) and 1 mm thick cadmium cap against thermal neutrons. The ^{6}Li nuclide(7.52% abundance in natural lithium) captures thermal neutrons by the reaction $^{6}Li(n,\alpha)^{3}H$ and no gamma is emitted. As well, the Cd shield case protects the detector against the thermal neutrons by the absorption reaction $^{113}Cd(n,\gamma)^{114}Cd$. However, Cd produces additional prompt gamma rays such as 559 keV and 651 keV, and it can become radioactive in time. Both the neutron shields encasing the detector end-cap are surrounded additionally by polyethylene bricks in 5 cm thickness to thermalize stray fast neutrons. These neutron shields can be removable from the end-cap. In case of Cd analysis, the metal-cylindiric Cd shield case with thickness of 1 mm can be removed from the end cap of Ge detector. However, only shield containing lithium carbonate is removed while boron is analysing. Finally, the detector assembly are surrounded by the chevron lead bricks with a 10 cm thick to reduce gamma-ray background at the detector site. By removing the cover made of lead bricks from the top side of detector shielding, the samples can be placed perpendicular to the hole in the front wall at the distance of 27.5 cm. These measures have not entirely removed backgrounds, but have reduced to acceptable the levels given in Table 1.

2.2 Gamma-ray detection system

The basic gamma-ray detection system consists of a n-type high purity germanium (REGe) detector with its own preamplifier with a side-looking type LN_2 dewar, a spectroscopy amplifier, a 8K ADC and a conventional Canberra 35^{+} type multichannel analyzer (MCA). The REGe detector has an relative efficiency of 22.6%, an energy resolution of 1.80 KeV at 1332.5 keV (^{60}Co) and of 0.97 keV at 122 keV (^{57}Co), and a peak-to-Compton ratio of 53.5:1. Data acquisition system allows the collection of only one type of the spectrum at a time because at present a single-input MCA is used.

3. Experimental

The energy and efficiency calibration of the gamma-ray spectrometer system is very important for both nuclear structure and analytical experiments. The efforts have been made to obtain accurate absolute efficiency calibration of the REGe detector used. In the energy range of 100 keV to 2500 keV, the absolute efficiencies were measured at two different sample geometries placed at a distance of 17.5 cm between sample and detector. The measured efficiencies for a tube (4

cm in diameter and 6 cm in height) and a 5 m*l* ampoule geometry are shown in Fig 3 and in Fig 4, respectively.

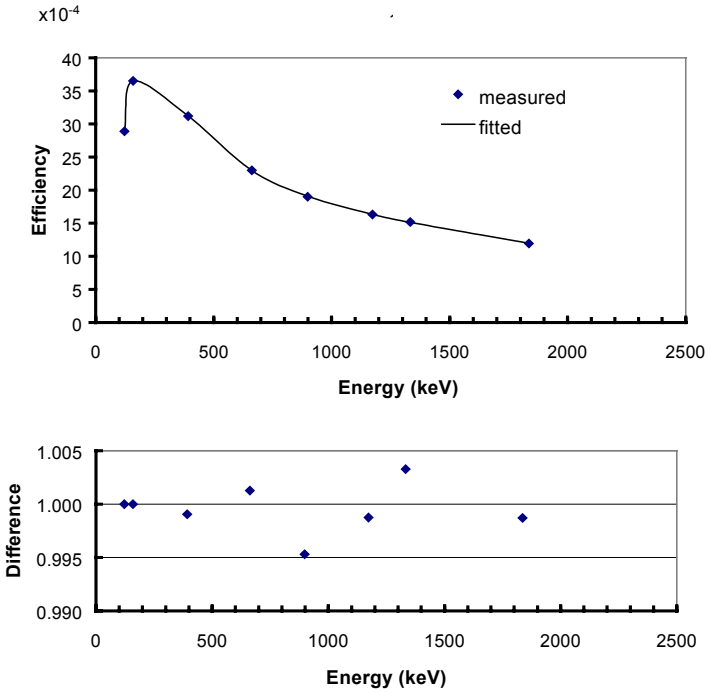


Fig. 3. Photopeak efficiency for REGe at a distance=17.5 cm with a vial (4 cm dia. and 6 cm height)

The experimental data are fitted to the functions using least square fitting method. The relative deviations between the experimental efficiencies and the calculated ones remained within 0.5- 5%. The efficiency calibrations have not yet completed for higher energy range of 2.5 MeV to 10 MeV.

The gamma-ray detection system is well shielded from gamma rays and neutrons to reduce the contunious background and the unwanted prompt gamma-rays from capture of neutron in the detector and structure materials during experiments and to prevent long-term activation and radiation damage of the detector. The REGe detector is mounted on the wooden table. The distance between sample and the front surface (detector window) of the detector is fixed 17.5 cm to eliminate the

coincidence summing losses and avoid the direct gamma-rays and neutrons that may expose the detector.

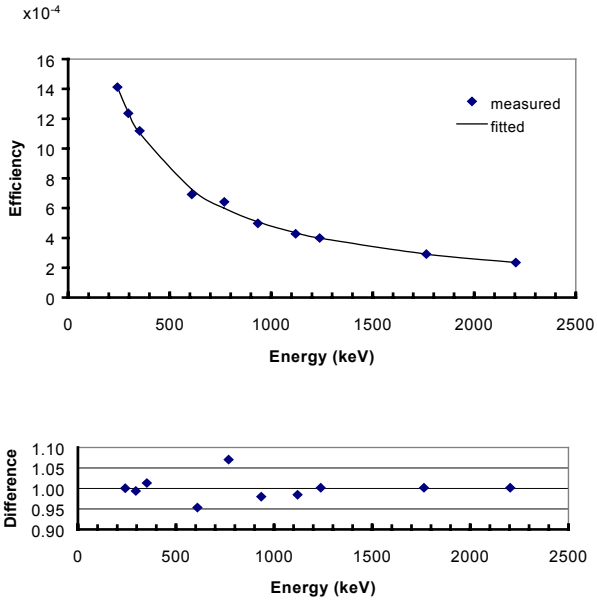


Fig. 4. Photopeak efficiency for REGe at a distance=17.5 cm with a 5 ml ampoule geometry

The singles gamma ray spectra from neutron capture are extremely complex. Hence, the analysis of prompt gamma ray spectra requires a high quality fitting computer code for data analysis. However, at present, automatic element identification on the basis of peak energies is not possible because of not available a built-in prompt gamma library. Therefore, the peak energies observed in the spectra are selected manually on the display of MCA by the analyst.

Since the most important drawback of the present technique is the high level of the background arising from various origins as shown in Fig. 2: Main background peaks are:

1. Neutron captures in the elements constitutive of the experimental set-up, essentially from H, C, Pb, Li and Cd. The 2.223 MeV gamma ray from hydrogen is observed as the most important peak in the spectra. The recoiling ^{7}Li nucleus, initially in an excited state, decays with 94% by Doppler broadened 478 keV

prompt gamma ray, and the $^{113}Cd(n,\gamma)^{114}Cd$ reaction in the neutron shield produces additionally the prompt gamma rays such as 559 keV and 651 keV.

2. The 4.43 MeV Doppler broadened gamma ray of $^{13}C^{*}$ via the $^{9}Be(\alpha,n)^{12}C$ reaction in the neutron source together with it single escape(3.92 MeV) and double escape(3.41 MeV) peaks, and

3. The high Compton scattering background due to the large number of gamma rays.

Table 1. The observed count rates for main gamma rays with their origin reactions

Reaction	**Energy (keV)**	**Count rate x10^{-2} (cps)**
$^{10}B(n,\alpha)^{7}Li$	478	2,07
Annihilation	511	6,86
$^{113}Cd(n,\gamma)^{114}Cd$	559	16,7
^{214}Bi(Ra series)	609,3	4,12
$^{113}Cd(n,\gamma)^{114}Cd$	651	3,52
$^{208}Pb(n,n'\gamma)$	806,2	1,51
^{214}Bi(Ra series)	1120,3	1,08
$^{1}H(n,\gamma)^{2}H$(DE)	1201	1,15
$^{1}H(n,\gamma)^{2}H$(SE)	1712	0,93
$^{1}H(n,\gamma)^{2}H$	2223,3	6,42

An experiment was carried out using the certified borate ore(SRM 1835) containing 18.739±0.115 %wt B_2O_3. The time for the background collection and the irradiation of the sample in this experiment was chosen 100 000 s. The collected spectra are shown in Fig.2 (a), the observed 478 keV peak is 2.54 times higher than that of background of 2.07 cps for $^{10}B(n,\alpha)^{7}Li$ reaction. After subtracting the background from the 478 keV peak, detection sensitivity for boron is estimated to be 115 cps/g-B The detection limit in the weight dimension is proportional to the square root of the background region of interest and inversely proportional to both the sensitivity and counting time. The detection limit for boron element is about 0.3-0.5 mg level for a counting time of 100 000 s using SRM 1835 borate ore. The lower detection limit can be achieved by extending the counting time and increasing thermal neutron fluence incident on the sample.

(a)

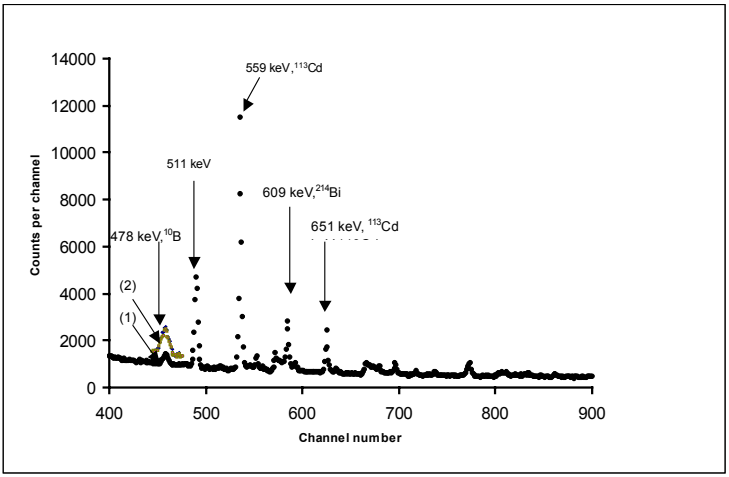


Fig.2(a). Prompt γ-ray spectrum(lower part)
(1) Background for 478 keV, (2) Borate ore (SRM 1835) containing 18.739±0.115 %wt. B_2O_3

(b)

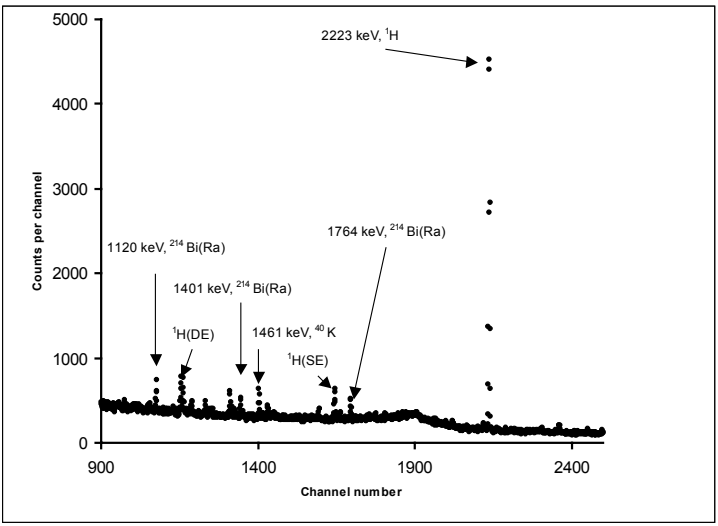


Fig. 2(b). Prompt γ-ray spectrum (upper part).

5. Conclusions

Since the estimated thermal neutron fluence rate of about order of 10^2 n.cm^{-2}.s^{-1} is very low, the expected sensitivity for the elements considered would be low. The detection limit for boron element is about 0.3-0.5 mg level for a counting time of 100 000 s using SRM 1835 borate ore. It is possible that a lower detection limit can be achieved by extending the counting time and increasing thermal neutron fluence incident on the sample. Therefore, the necessary modifications in the source-detector geometry will be made resulting in an increase in the thermal neutron fluence rate. In future, it is planned to built to enable a digital spectrum analyzer based on digital signal processing technique (DSA) or a data acquisition system This enables us an effective and fast data evaluation by using a gamma software.

References

1. Giarratano, J.C. and Shalek, R.J., Int. J. Applied Isotopes, 30 (1979) 423.
2. Hassah, A.H., El-Kady, A. and El-Azaby, B. Nucl. Instr. Methods, 192 (1982) 595.
3. Matsumato,T. and Aizawa O., Appl. Radiat. Isot., 41 No.9(1990)897
4. Acharya, R. N., Sudarshan, K., Nair, A. G. C., Scindia, Y. M., Goswami, A., Reddy, A. V. R. and Manohar, S. B., J.Radioanal. Nucl. Chem. 250, No.2(2001) 303.
5. Paul, R.L. and Lindstrom, R.M., J.Radioanal. Nucl. Chem. 243, No.1 (2000) 181.
6. Molnar, G.L and Lindstrom, R.M Nucl Methods in mineralogy and Geology:Techniques and Applications, Edited by Vertes et al., Plenum Press, New York, (1998) 145-163.
7. Molnar, G.L., Revay, Zs. Belgya and Firestone, R.B., Appl. Radiat. Isot., 53 (2000) 527.
8. Byun, S.H. and Choi, H.D, J.Radioanal. Nucl. Chem. 244, No.2(2000) 413.
9. Chung, C. and Tseng, Tzu-C., Nucl. Instr. Methods in Phys. Res. A267(1988)223.
10. Lorch, E.A., Int. J. Appl. Radiation Isotopes, 24(1973)588.
11. Tuli, J.K.,Nuclear Wallet Cards, National Nuclear Data Center, BNL, USA,(2000)

RADIAL AND LATITUDINAL GRADIENTS OF GALACTIC PROTONS

Ye. K. Kazkenov, A.A. Aitmuhambetov, R.R. Ashirov

Kokshetau State University, Republic of Kazakhstan, Kokshetau

Abstract

Our modulation model is implicated to study radial and latitudinal gradients of galactic protons intensity. Modulation parameters are justified and energy dependence of radial and latitudinal gradients is investigated. We note that to fit calculations to experimental data latitudinal transport of low energy galactic protons should be taken into account.

Introduction

Investigation of intensity gradients of galactic cosmic ray (GCR) plays a vital role for modulation theory. Analysis of cooperative work of IMP 8, Ulysses, Voyager 1 and 2, Pioneer 10 and 11 spacecraft allows to obtain information on intensity gradients for galactic hydrogen and helium in both inner and distant heliosphere. Experimental data are difficult to be given quantitative explanation. Radial gradients in cycle with positive polarity (A>0) are small both in inner and distant heliosphere, whereas ones in cycle with negative polarity (A<0) are large. *Ulysses* first fast latitude scan of high latitude regions of heliosphere revealed surprisingly low latitude variation of galactic protons intensity. In this work we examine idea of non-spherical heliosphere to explain such behavior of GCR distribution.

Model Description

GCRs intensity distribution is described by the Parker equation:

$$\frac{\partial f}{\partial t} = \frac{\partial}{\partial x_i} D_{ij} \frac{\partial f}{\partial x_j} - u_i \frac{\partial f}{\partial x_i} + \frac{R}{3} \frac{\partial u_i}{\partial x_i} \frac{\partial f}{\partial R} \tag{1}$$

where f is the GCRs distribution function and u is solar wind speed.

Here the following relation is used for the northern hemisphere:

$$\left.\begin{aligned} u_r &= 450(1 + 3 \cdot \cos^2 \theta)\ \mathrm{km \cdot s^{-1}}, \text{ for } \theta \geq \theta_0 = 60^0 \\ u_r &= u_r(\theta_0), \qquad\qquad \text{for } \theta < \theta_0 \end{aligned}\right\} \tag{2}$$

θ is a polar angle.

Diffusion tensor D_{ij} is present as:

$$D_{\parallel} = \frac{\lambda_{\parallel} V}{3}$$
$$D_{\perp} = \frac{1}{1+\left(\frac{\lambda_{\perp}}{\rho}\right)^2} \frac{\lambda_{\perp} V}{3} \qquad (3)$$
$$D_A = -\frac{1}{1+\left(\frac{\lambda_{\perp}}{\rho}\right)^2} \frac{\lambda_{\perp}^2 V}{3\rho}$$

according to Kazkenov (2001) and Webb et al.(2001).

Assuming azimuthal symmetry non-steady state Equation (1) was solved by means of Monte-Carlo techniques.

In (Kazkenov 2001) a simple model gave the following relations for $\lambda_{\parallel}$ and $\lambda_{\perp}$:

$$\left.\begin{aligned} \lambda_{\parallel} &= \frac{1}{150B} \frac{CR_0}{arctg^2 \frac{\alpha R_0}{R}} \\ \lambda_{\perp} &= \frac{1}{300B} \frac{R}{1+\frac{R}{2CR_0} arctg^2 \frac{\alpha R_0}{R}} \end{aligned}\right\} \qquad (4)$$

where R_0=7.5 GV is a parameter corresponding to characteristic dimension of fluctuations l=10^{12} sm, R is particle rigidity, B is the interplanetary magnetic field magnitude, α is a parameter depending on fluctuation magnitude and C is a normalizing factor.

In original work R_0 was taken to be of order 1 GV. Here it was however substituted to value of ~ 10 GV to support a flat profile of energy dependence of $\lambda_{\parallel}$. Value of C is examined in a range from 1 to 4 that corresponds to value of $\lambda_{\parallel}$ from 0.03 a.u. to 0.13 a. u. respectively. These values of C cover the most probable interval of GCRs mean free path magnitude (see e. g. Ragot 1999, Valdes-Galicia et al. 1988) and satisfy ratios of $\frac{\lambda_{\parallel}}{\lambda_{\perp}}$, calculated by Hedgecock (1975).

Results

On the basis of above described model we calculate galactic protons' intensity gradients in two successive minima (1987 and 1996 years).

In many works it was pointed out that intensity of GCR at the Earth's orbit and is radial evolution cannot be described involving the same set of kinetic coefficients (Moraal et al. 1979, Potgieter 1997, Kalinin and Krainev 2000).

Moraal et al (1979) have used classical expressions for D_{ij} and have found that in this case drift of galactic protons was too effective. Kalinin and Krainev (2000) tried to interpret radial dependence of GCR intensity by considering existence of electrostatic potential at the heliosphere boundary.

The main hypothesis of this contribution is that in solar minima with opposite magnetic polarity are characterized by different effective modulation region dimension. One can give physical explanation based on idea of non-spherical heliosphere.

GCR protons enter majorly the heliosphere at equatorial regions in A<0 cycle and hence effective modulation region is limited by little sphere on Fig. 1, GCRs' effective sources is located at equatorial region, while sinks are situated at polar regions of heliosphere due to drift motion of charged particles.

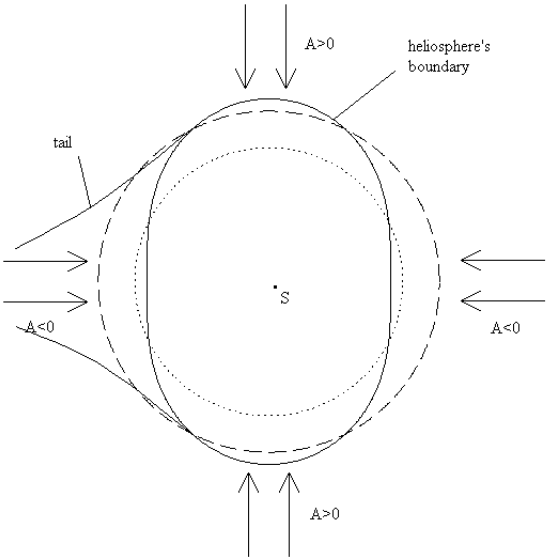


Fig. 1

After interplanetary magnetic field polarity reversal (in A>0 cycle) sources and sinks exchange each other and thereby effective dimension of modulation region is shaped by sphere larger than one in A<0 cycle.

Application of heliosphere's shape elongated in polar directions is confirmed by many researchers (see e.g. Exhargos and Moussas 2000; Baranov, Krasnobaev and Kulicovskii 1971), caused by interstellar wind affection on heliosphere. The non-spherical shape is the most probable due to anisotropy caused

by magnetic fields and latitude dependence of interplanetary magnetic field and solar wind speed. Idea of non-spherical heliosphere is mere, nevertheless the shape of the heliosphere is ussually assumed to be spherical.

We neglect influence of heliosphere's tail on GCRs distribution believing that such the effects is significant for GCRs with energy lower than 130-230 MeV.

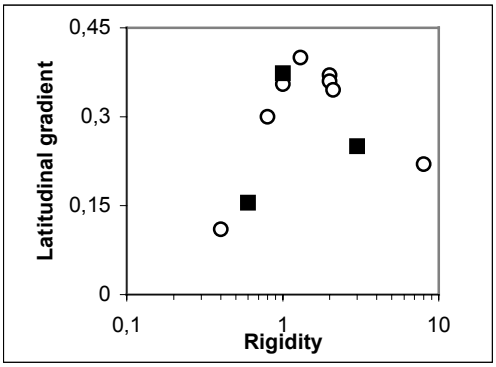


Fig. 2. A sample calculation of GCR latitudinal gradient as a function of rigidity.

Results of calculation of GCR latitudinal intensity gradients at r≈2 a.e. is presented on Fig. 2 for C=1 (black squares) in A>0 cycle. Experimental data (open circles) are taken from Burger, Potgieter and Heber (1999). One can see qualitative agreement between experimental data and calculations – a characteristic knee in graph for R=1 GV. For instance calculation gives somewhat low value of intensity gradient for R=0.6 GV. On Fig. 3 dependence of latitudinal gradient on magnitude of C is presented. The best coincidence succeeds for C≈2.

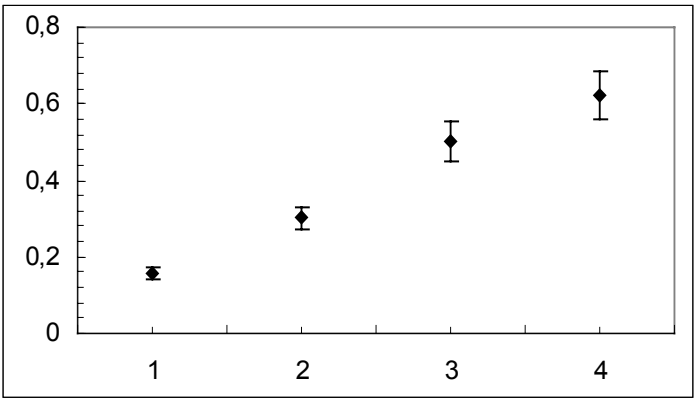


Fig. 3. Calculation of GCR latitudinal gradient as a function of C.

On Fig. 4 result of calculation of radial intensity gradients for A>0 cycle is presented. Experimental data are taken from Fujii and McDonald (1999). Easy to see that the best agreement is obtained for 2<C<3. Fig. 5 presents calculations of GCR intensity radial gradient as a function of particle rigidity in A>0 cycle. It's evident that radial intensity gradient has a peak as well as latitudinal gradients do in agreement with Burger and Hattingh (1998) calculation. Both of the calculation however agree only qualitatively with experimental data.

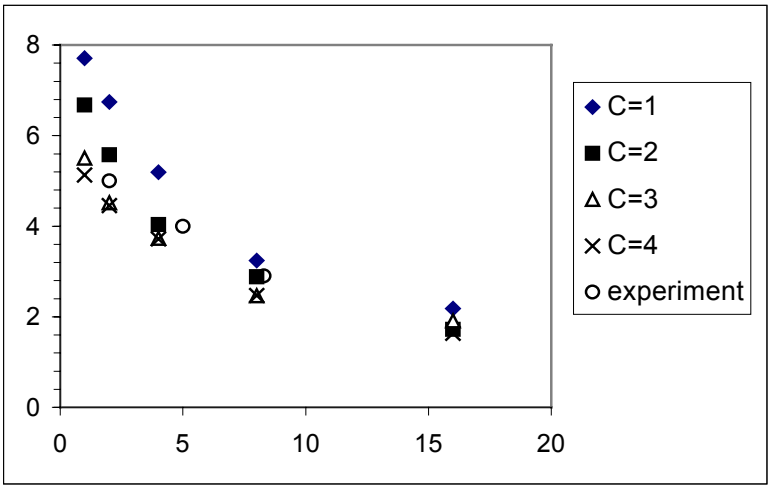


Fig. 4. Calculation of galactic protons intensity radial gradient at different distances as function of C.

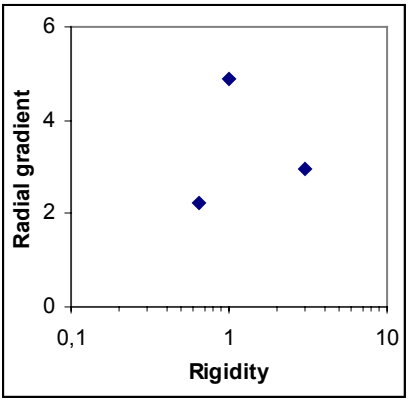


Fig. 5. Energy dependence of galactic protons intensity radial gradient.

Conclusion

Let's in conclusion remark:

i) anisotropy of interstellar medium, latitude dependence of interplanetary magnetic field and solar wind speed can be responsible for non-spherical shape of the heliosphere. It's considered that tail of the heliosphere caused by interstellar wind affection gives negligible contribution into GCR distribution with energy ≥ 100 MeV;

ii) qualitative correct rigidity (energy) dependence is obtained for latitude intensity gradient;

iii) the best agreement between experimental data and calculations of galactic protons latitude intensity gradients is reached for $C \approx 2$, whereas calculations of galactic protons radial intensity gradients coincide experimental data for $2<C<3$. A discrepancy might be removed by taking into account latitudinal component of interplanetary magnetic field that diminishes magnitude of latitudinal gradient of low energy GCR (Burger and Hattingh 2001);

iv) GCR intensity radial gradients in $A>0$ cycle also reveal a peaked profile in presentation as function of rigidity.

References

1. Baranov, V. B., Krasnobaev, K. V., and Kulicovskii, A. G.: 1971, *Soviet Phys.–Docl.*, **15**, 791.
2. Burger, R. A., and Hattingh, M.: 1998, *ApJ*, **505**, 244.
3. Burger, R. A., and Hattingh, M.: 2001, Proc. *27th ICRC (Hamburg)*, 3698.
4. Burger, R. A., Potgieter, M. S., and Heber, B.: 1999, Proc. *26th ICRC (Salt-Lake-City)*, **7**, (SH 3.3.02).
5. Fujii, Z., and McDonald, F. B.: 1999, Proc. *26th ICRC (Salt-Lake-City)*, **7**, (SH 3.3.03).
6. Kalinin, M. S., and Krainev, M. B.: 2000, Submitted to *Intern. J. of Geomagnetism and Aeronomy* (http://eos.wdcb.rssi.ru/gpo/2000/gai99338/gai99338.htm).
7. Kazkenov, Ye. K.: 2001, *Astronomy Letters*, **27**, 11, 732.
8. Moraal, H., Gleeson, L. J., and Webb, G. M.: 1979, Proc. *16th ICRC (Kyoto)*, **3**, 1.
9. Potgieter, M. S.: 1997, Proc. *25th ICRC (Durban)*, **2**, 1.
10. Ragot, B. R.: 1999, Proc. *26th ICRC (Salt-Lake-City)*, **7**, 86 (SH 3.1.24).
11. Valdes-Galicia, J. F. et al.: 1988, *Solar Phys.*, **117**, 135.
12. Webb, G. M., Kota, J., Zank, G. P., and Lu, J. Y.: 2001, Proc. *27th ICRC (Hamburg)*, 3326.

RADIATION ASPECTS ON THE EARTH'S SURFACE DURING SOLAR FLARES

Mansurov K.Zh., Aitmuhambetov A.A.

Kokshetau University, Abay st.76, Kokshetau 475000, Kazakstan

Abstract. In the paper the results of investigation of radiational situation in the space near the Earth at the different altitudes of the Earth atmosphere and at the ground level in dependence on geocoordinates and solar activity during 1957 - 1997 are presented. Radiation is due to the Galactic Cosmic Rays flux for different periods of the Solar activity. The radiation near ground level of the Earth for the last 500 years was calculated also using the data of the radioactive carbon ^{14}C intensity investigations.

Introduction

Now different components of the primary cosmic rays on a lage scales of cosmos, in the cosmic space near the Earth and on the boundary of the Earth's atmosphere have studied [1-3]. There are the results of measurements and theoretical calculations of the energy spectra, the angular distribution of different components of the secondary cosmic rays from ground level of the Earth up to the atmospheric boundary, and also the fluxes of direct and reverse albedo on the atmosphere boundary [4-8]. Total radiational doses at different levels of the Earth atmosphere and in the cosmic space near the Earth were calculated on the base of data of primary and secondary Galactic and solar radiation. It is shown that the maximum doses of radiation are at the altitudes of 16-19 km from the ground level of the Earth (60÷50 g/cm^2). Secondary cosmic emission maximum is at these altitudes as a function of geolatitude. It is also emphasized that when appring to as for aviation at altitudes more than 12 km flight during the 6-7 and more hours is undesirable [9-10].

It is necessary to point out that the contribution of the nuclei with $Z>2$ at energies E<1 GeV into the secondary fluxes of the different components of CR is small. Therefore it is possible that the nuclei with relatively are not taken into consideration $Z>2$ and $E>10^9$ eV as a rule when determining the doses what, it seems to us, is unjustified [9, 11, 12].

Equivalent dose rate is calculated in the case of biological object radiation. Its spectral composition is known from the formula:

$$P_i(x,R) = \sum_i \iint D_i(E) N_i[E,\Omega,x] dE d\Omega \qquad (1)$$

where $D_i(E)$ - is conventional specific equivalent dose Zv/cm^2/particle ; E - is the energy of i-sort particle radiation; $N(E,\Omega)$ - is the differential density of this

radiation flux at depth x. We noted $m(E,x,E',\theta)dE'd\Omega$ - to be the number of i-sort secondary particles with energies ($E',E'+dE'$) in angle $d\Omega$ at depth x, produced by a primary particle with energy E and isotropicaly falled on the atmosphere boundary. Then the intensity of i-sort particles is written down in the form:

$$N_i^R(E,x,\theta)=\sum_i N_i\left(E'\right)m_i(E',x,E,\theta)dE' \qquad (2)$$

In the case the equivalent dose rate

$$P_i(x,R)=\sum_i\int_{E_m}^{\infty}\int_{\Omega}^{\infty}N_i(E,x,\theta)D_i(E)dEd\Omega=\sum_i\int_{E_m}^{\infty}D_i(E)\int_{\Omega}d\Omega\int_{R}^{\infty}N_0(E')m(E',x,E,\theta)dE'dE=$$

$$=\sum_i\int_{R}^{\infty}N_0(E')\left\{\int_{\Omega}d\Omega\int_{E_m}^{\infty}D_i(E)m(E',x,E,\theta)dE\right\}dE'=\sum_i\int_{R}^{\infty}N_0(E')\mathrm{d}\Omega\Re(E',x)dE'$$

---

where $\Re_i(E',x)=\int_{\Omega}d\Omega\int_{E_m}D_i(E)m(E',x,E,\theta)dE$ - is integral of the equivalent dose rate from the incident particle with energy E.

It is noted that the dose rate may be calculated also from:

$$P_i(x,R)=\sum_i\int_{E_R}^{\infty}N_0(E')\Re(E',x)dE' \qquad (4)$$

where E_R - is the correspondent to the cut off rigidity energy R.
For the simplicity one can introduce the transition coefficient for dose rate:

$$W_p(R,\rangle\varepsilon,x)=P_i(x,R)/N_0(0,\rangle\varepsilon_m) \qquad (5)$$

where the numerator is given by (1) and denumerator - is the primary spectrum at the pole from single particle.
The coefficient (5) has dimension and it is the standartized rate of equivalent dose.
The CR spectrum for the Earth's orbit have been taken for the calculations in the form:

$$N(\varepsilon)=1{,}32\cdot10^4\,\varepsilon^{-2{,}65}\left(1-\frac{0{,}6}{\sqrt{E}}\right)\cdot\exp-\int_r^{r_0}\frac{U}{\chi}dr \qquad (6)$$

where E- is the total energy, U - the solar wind velocity, χ - the diffusion coefficient, r_0 - width of the modulation region.

The calculations shows that the modulation coefficient $K=\int_r^{r_0}\frac{U}{\chi}dr$ varies from the minima to the maxima of solar activity in range 0,3÷2,5.

Results

The calculated doses of irradiation by GCR at different altitudes of the Earth's atmosphere and their change in time presented below.

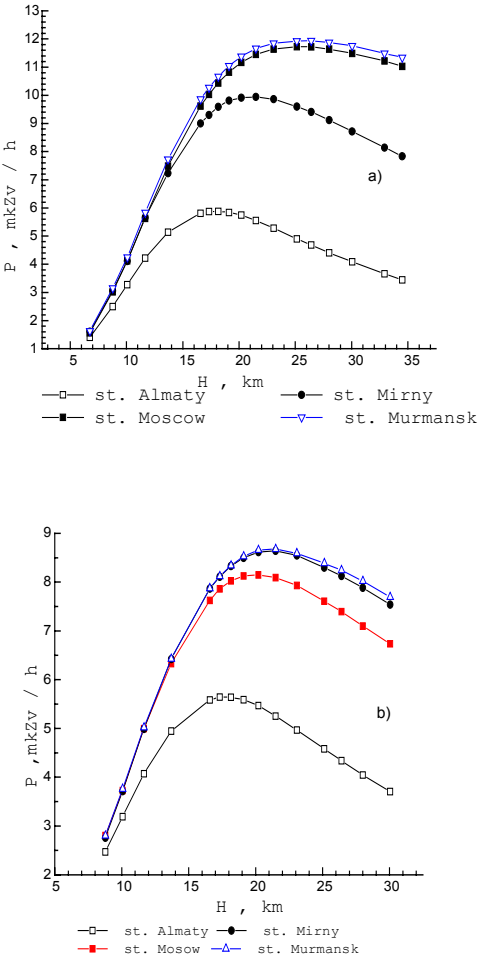


Figure 1. The doses of total ionization component at the different Earth atmospheric levels.

a) for the solar activity minimum

b) for the solar activity maximum.

Figure 1. shows the doses, calculated on the basis of the experimental data of measurements total ionization component of cosmic radiation connected with the different Earth atmospheric levels, for the solar activity minimum -fig.1.a. and for solar activity maximum - fig.1.b. and also for 4 stations of the Earth with geomagnetic cut off rigidity 6,61 GV (Almaty, $\lambda=43^0$ N, $\varphi\approx76^0$E), 2,39 GV (Moscow, $\lambda\approx55^0$ N, $\varphi\approx37^0$E), 0,5 GV (Murmansk, $\lambda\approx69^0$ N, $\varphi\approx33^0$E), 0,03 GV (Mirny, Antarctida, $\lambda\approx-66^0$ S, $\varphi\approx93^0$E). From fig.1. we can make a conclusion that the maximum of radiation is on 16-19 km height (at the altitude of cruiser flight of supersound planes), also we can notice, that the radiation over Almaty is almost twice less because of the high geomagnetic cut off rigidity, then in high latitude stations. We can stress that CIC CR includes p, $e^{\pm}$, $\mu^{\pm}$,γ, $\pi^{\pm}$ and doesn't include neutrons, which make a large contribution to the radiation doses.

Time modifications of the radiation doses on the different Earth atmospheric heights are shown in fig.2. From fig.2. we can make a conclusion, that in the solar activity minimums in high latitude stations the radiation doses on heights more than 12 km are 1,5 times more. This fact is also observed at middle latitude stations (Moscow), the difference between the radiation doses at minima and maxima equals to 35%, and in Almaty equals to 20%.

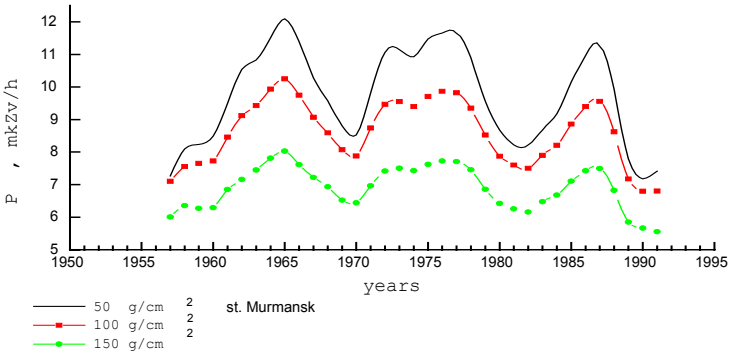


Fig.2. Time changes of the radiation doses at the different Earth atmospheric levels.

In fig. 3 the variations of radiocarbon ^{14}C and radiational doses within period 1000 to 1990 are shown. Calculations of radiational doses were carried out on the base of radiation intensity data through radioactive carbon ^{14}C [13-14]. It

seenos from fig. 3, that the variation of ^{14}C for more than 900 years have got two visible peaks in the minimum of Maunder minimum (1645-1715) of the Solar activity and in period after on 1950, when a number of nuclear weapon tests were made at the Earth's atmosphere. Fig. 3 also presents two maxima of the radiational doses at the same time as in the fig. 3.

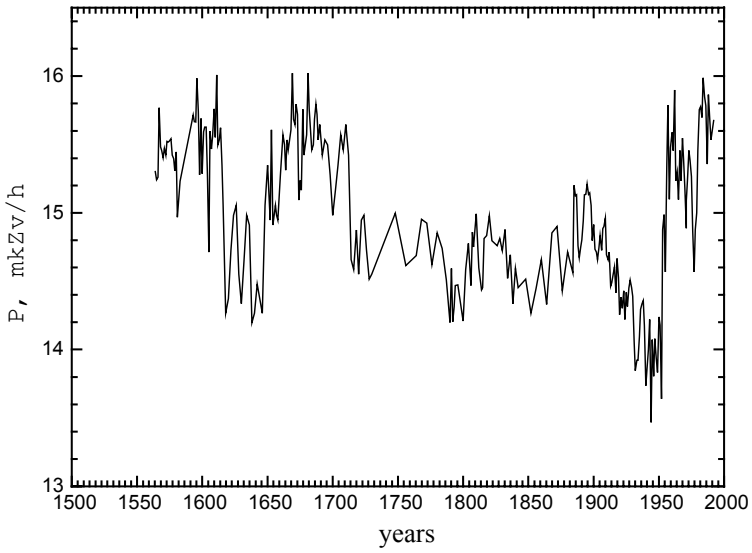


Figure 3. Radiation doses of C^{14} at the different period.

Thus the radiation dose variations for a long period in the Earth atmosphere are caused by natural and quaternary influences. In conclusion, using the obtained results of the work we can make the next conclusions:

- -the radiation doses are several times more than background doses (at the expense of GCR on the Earth surface) at the altitudes of the maximum of the second cosmic radiation of the Earth atmosphere - 16-19 km.
- -in high geomagnetic latitudes the radiation doses also exceed background doses in several times.
- -during the nuclear tests in the Earth's atmosphere the radioactive clouds at latitudes ~12-13 km which go ground the Earth two or three times were created.
- -it seems to us that these couds make a certain contribution to the ecological situation in the Earth atmosphere and on the surface.

From the above mentioned we can make a conclusion that aviation shouldn't flight at the altitudes more than 12 km, especially in high latitude and in the Solar activity minimum.

Reference

1. Ginzburc V.L., Syrovatski S.I., proucxojdenie kosmiheckix luchei., Izd, SA USSR,384, 1963.
2. Hayakava S., Physica kosmicheckix luchei., Izd, «Mir», Moscow, 701, 1973.
3. Murzin B.C. Vvedenie v physice kosmicheckix luchei., Izd. MGY, 320, 1988.
4. Bogomolov E.A., Romanov V.A., Stepanov S.V., Shulakova M.C., Preprint LFTI № 629. L., 41, 1979.
5. Jabs A., Nuovo cimento, A12, 565-578, 1972.
6. Daniel R., Stephens S., Rev. Geophys. Space Phys, 12, 233-258, 1971.
7. Freier P.S., Waddington C.J., J. Geophys. Space Phys., 12, 233-258, 1971.
8. Lockwood J.A., Hsieh L., Frilling L.A e.a., 15th ICRC, 4,192-196,1977
9. Barsukov O.A., Kolomeets E.V., Radiasionnie aspekti issledovania kosmicheskogo izluchenia v ctratosfere, Moscow, Energoatomizdat, 123, 1985.
10. Kolomeets E.V., et. al. Radiasionnaia opasnost poletov samoletov i drugix letatelnix apparatov, Izd.»Print», Almaty,257, 1997.
11. Barsucov O.A., Kolomeets E.V., Poteri i dozi iader kosmicheskogo proisxojdenie v atmosphere Zemli. In the printing.
12. Barannikov Y.I., et. al. J.kosmicheskaia biologia i aviakosmicheskaya medizina, 2,69-73, 1987.
13. 1Rasprostrnenie izotopov v okrujaiushei srede i astrofisisheskie yavlenie. The subject collected.Lenengrad, 1984.
14. Konstantinov A.N. et.al. Izv. AN. Ser. Phys.1997, V.61, N 6, p.1242-1248.

REACTIONS OF MASSIVE NUCLEI FOR HEAVY AND SUPERHEAVY ELEMENTS

G.Fazio[1], G.Giardina[1], A.Lamberto[1], A.I.Muminov[2], A.K.Nasirov[2♣], U.T.Yakhshiev[3], R.Palamara[1], R.Ruggeri[4]*

[1] INFN, Sezione di Catania, and Dipartimento di Fisica dell'Universita di Messina, Messina, Italy
[2] Heavy Ion Physics Department, INP, Tashkent, Uzbekistan
[3] Theoretical Physics Department, National University of Uzbekistan, Tashkent, Uzbekistan
[4] Dipartimento PAU dell'Universita di Reggio Calabria, Reggio Calabria, Italy

We study the effect of the entrance channel and the shell structure of reacting massive nuclei on the fusion mechanism leading to the formation of heavy and superheavy nuclei. Calculations performed in the framework of the dinuclear system model taking into account the nuclear shell effect and shape of colliding nuclei allow us to reach useful conclusions about the mechanism of the fusion-fission process that is in competition with the quasifission process, and the production of the evaporation residues.

We analyze the ^{40}Ar + ^{176}Hf and ^{48}Ca + ^{174}Yb reactions leading to ^{216,222}Th*; the ^{48}Ca + ^{248}Cm, ^{48}Ca + ^{243}Am and ^{48}Ca + ^{249}Cf reactions leading to the ^{296}116, ^{291}115 and ^{297}118 compound nuclei, respectively.

PACS: 25.70.Gh; 25.70.-z; 27.80.+w $190 \le A \le 219$; 27.90.+b $220 \le A$

I. Introduction

In this paper we analyse the importance of the entrance channel effect on the fusion-fission reaction mechanism in collisions of massive nuclei. The DNS concept [1] reveals the reason for the strong decrease in the fusion cross section for a massive system or for a symmetric entrance channel. In calculations of the excitation function of evaporation residues, the choice of suitable parameters allows a description of experimental data, but the peculiarity of the reaction mechanism of projectile-target pairs with different mass-asymmetry is still unclear. It is well known that it is difficult to measure fusion cross section, directly due to the fact that establishing the origin of fusion-fission reaction fragments is ambiguous.

* e-mail: fazio@nucleo.unime.it
♣ Also at Bogoliubov Laboratory of the Theoretical Physics, JINR, Dubna, Russia

Calculations based on the DNS-concept show [2,3] that entrance channel effects are important to describe the experimental data in the case of collisions of massive nuclei. It allows us to estimate decrease of fusion probability due to increase of quasifission process. In the present work, we consider a set of reactions leading to the formation of heavy ^{216,222}Th and superheavy (^{291}115, ^{296}116, ^{297}118) nuclei.

Due to the fact that calculation of the competition between complete fusion and quasifission process in the framework of the model under discussion includes the nuclear shell effect and shape of colliding nuclei allow us to reach useful conclusions about the mechanism of the fusion-fission process. Possibility of collisions of nuclei by different orientations of their axial symmetry axis is considered.

II. The model and calculation

According to the DNS concept, the complete fusion between heavy ions is a complete transfer of all the nucleons of the projectile (lighter) nucleus into the target (heaviest) nucleus forming compound nucleus of complete shape. Due to large inertia parameter of deformation the change of nuclear shape is not so large and the size of overlap region of nuclei is small: it is about 5-6% of the total volume. The nucleons of the interacting nuclei form a shell structure which is retained during interaction. Fusion is considered as a two stage process. The first step is overcoming the Coulomb barrier in motion along the axis connecting nuclear centers by nuclei at the incoming stage of collision, and formation of nuclear composite (molecular-like so-called dinuclear system). This stage is called capture. The second one is transformation of the DNS into more compact compound nucleus, overcoming the intrinsic barrier (B^*_{fus}) on the potential energy surface during evolution on mass (charge) asymmetry axis. In the DNS concept, the potential energy surface is built as a function of the mass (charge) asymmetry and relative distance between centers of nuclei forming DNS.

For light and intermediate nuclear systems or for heavy nuclear systems with larger mass asymmetry, this barrier is equal to zero and capture immediately leads to fusion. Therefore, in those cases, the fusion cross section is calculated in the framework of well known models [4-7].

The B^*_{fus} is determined by the difference between the maximum value of the driving potential $U(Z,A,R_m)$ and its value at the point corresponding to the initial charge asymmetry of the considered reaction. If the excitation energy of dinuclear system, $E^*_{DNS}=E_{c.m.}-V(R_m,l)$, is not enough to overcome B^*_{fus} then dinuclear system decays into two fragments, i.e. it undergoes to quasifission. Quasifission occurs due to motion along relative internuclear distance R and depends on the $V(R)$ nucleus-nucleus interaction potential. Thus, for quasifission, it

is necessary to overcome the barrier (B_{qf}) which is equal to the depth of well of *V(R)*.

In the DNS concept [9], the evaporation residue cross section is factorized as follows:

$$\sigma_{er}(E) = \sum_{l=0}^{l} (2l+1)\sigma_l^{fus}(E,l)W_{sur}(E,l).$$

Here, the effects connected with the entrance channel are included in the partial fusion cross section $\sigma_l^{fus}(E,l)$, which is defined by the expressions:

$$\sigma_l^{fus}(E,l) = \sigma_l^{capture}(E)P_{CN}(E,l)$$

$$\sigma_l^{capture}(E) = \frac{\lambda^2}{4\pi} P_l^{capture}(E),$$

where λ is the de Broglie wavelength of the entrance channel, P_{CN}(E,*l*) is a factor taking into account the decrease in the fusion probability due to break up of the DNS (quasifission); $P_l^{capture}(E)$ is the capture probability which depends on the collision dynamics and it is determined by the number of partial waves (l_d) leading to capture.

For a complete description of the method and for more details, see [2,3,8].

III. Comparison of DNS model results and experimental data

The role of the entrance channel in the formation of the compound nucleus and evaporation residues is the main focus of our interest. Experimental excitation functions of the evaporation residues measured in the ^{40}Ar+^{176}Hf [9,10] and ^{48}Ca + ^{174}Yb [11] reactions have been compared with the results of calculation in the framework of the method presented in Section II.

The experimental data reveal that the ER yield cross section for ^{40}Ar+^{176}Hf (I) [9,10] is smaller than for ^{48}Ca + ^{174}Yb (II) [11]. Because the capture and fusion cross sections of for the reaction (II) forming ^{222}Th* are higher than for (I) forming ^{216}Th*, even if the fusion factor P_{CN} (see Table I) for the reaction (II) is lower than for the (I). In fact, in our calculation we find that the Γ_n/Γ_f ratio is lower for the reaction (I) forming ^{216}Th* than for the Γ_n/Γ_f value of the reaction (II) forming ^{222}Th*. This because at each step of the de-excitation cascade of the compound nucleus, the neutron binding energy is about 1-2 MeV higher for the cascade of ^{216}Th* in respect to the cascade of ^{222}Th*. The ^{40}Ar + ^{176}Hf reaction has a larger charge asymmetry (η_z=(Z_2-Z_1)/(Z_1+Z_2)) in comparison with the ^{48}Ca + ^{174}Yb reaction (see Table I) leading to two isotopes of thorium. The height of B_{fus}^* in the way to fusion (that is in competition with quasifission) for the reaction (I) is smaller than for (II), joined with a higher value of the B_{qf} barrier (against

quasifission) with respect to the B_{qf} value for the (II) reaction. The way to fusion is longer for the DNS, which has a more mass symmetric configuration. In Figs.1a and 1b, the excitation functions of the capture and fusion calculated in the framework of the DNS for the two reactions are compared. The evaporation residue excitation functions, calculated in the framework of the advanced statistical model [8] for those reactions, are in good agreement with the experimental data (see Fig.1c).

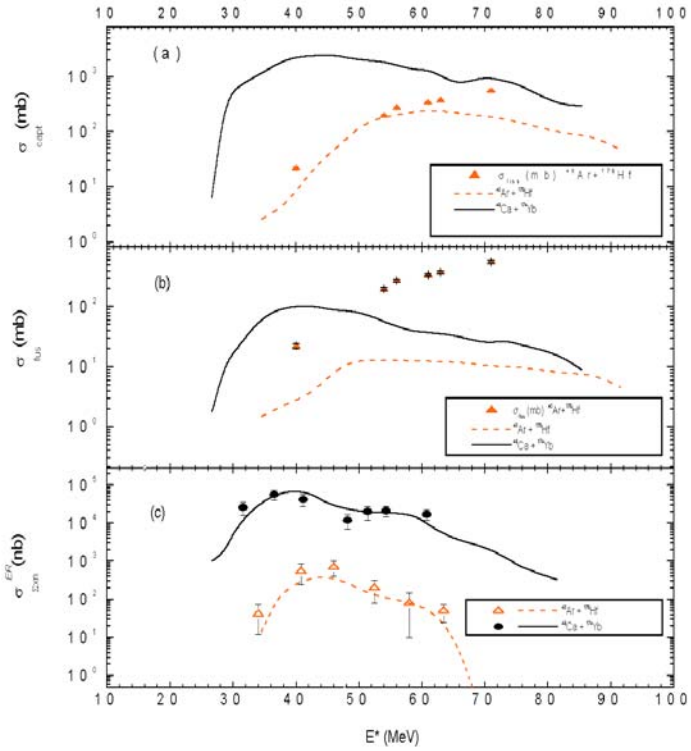


Fig.1. Comparison of the calculated capture (a), fusion (b) and evaporation residue (c) excitation functions as well as the measured excitation functions of evaporation residue (c) for the ^{40}Ar + ^{176}Hf reaction (dashed curve, open triangles [9,10], leading to the ^{216}Th* CN, and for the ^{48}Ca + ^{174}Yb reaction (full line, full points [11]. The solid triangles in (a) and (b) are the fission fragment excitation functions obtained from the measurements of the two symmetric mass fragments for the ^{40}Ar + ^{176}Hf reaction [10].

Table I. Charge asymmetry, intrinsic fusion B^*_{fus} and quasifission (B_{qf}) barriers, and the fusion factor (P_{CN}) for the reactions leading to the ^{216}Th* and ^{222}Th compound nuclei.

Reactions	η_z	B^*_{fus}, MeV	B_{qf}, MeV	P_{CN}
^{40}Ar + ^{176}Hf (I)	0.60	2.31	7.12	0.121
^{48}Ca + ^{174}Yb (II)	0.56	3.20	5.37	0.065

Comparison of the calculated fusion excitation function and the measured fission excitation function is intriguing when discussing the mechanism of fusion-fission reactions. This has been done for the ^{40}Ar + ^{176}Hf reaction (Fig.1b). In [10], the fission excitation function was obtained from the detection of reaction products of symmetric masses. It should be stressed that those products could be formed not only at the fission of a hot CN but at quasifission of DNS which lives long enough to reach mass equilibration in the subsequent re-separation process. Experimentally it is difficult to distinguish between fission of the compound nucleus and quasifission. In [2], the calculations showed that a contribution of quasifission is increased with beam energy above the fusion barrier. For this reason, the measured fission data in the ^{40}Ar + ^{176}Hf reaction [10] are closer to calculated capture cross section (Fig.1a) that is a sum of fusion and quasifission cross sections.

Therefore, the fact that the measured fission cross section is higher than the fusion cross section (Fig.1b) could be explained by the sizeable contribution of quasifission products to the measured fission data [10]. Appearance of difference between the measured fission and theoretical capture cross sections at energies higher than E^* = 55 MeV means that events of capture accompanied by the preequilibrium emission of neutrons, protons and α - particles from fragments were not taken into account in the model under consideration.

IV. The formation of the superheavy elements

A relevant problem to the synthesis of superheavy elements obtained by reactions with massive nuclei is to find out unambiguously the quasifission contribution in respect to the complete fusion contribution. The assumption about consideration of all the symmetric fragments having mass number in range $(A_1 + A_2)/2 \pm 20$ registrated in reactions with massive nuclei as the products of fusion-fission processes is questionable. Because the quasifission process contributes into the asymmetric fragments as well as to the more symmetric fragments. Moreover, the analysis of the fragment angular distribution and the kinetic energy distribution of fragments also does not allow one to find out unambiguously the contribution of quasifission as compared with the fusion-fission contribution.

In respect of the above-mentioned consideration, if we consider as an example the experimental data [12] obtained in the analysis of the ^{48}Ca + ^{248}Cm reaction leading to the ^{296}116 compound nucleus, we can note that our calculation of the capture cross section (full line in Fig.2) is in complete agreement with the experimental data for the production of all fragments (full squares), while the fusion cross section calculation (dashed line) is not in agreement with the data (open squares) for the symmetric mass fragments (*A/2*) when a large mass interval equal to ± 20 amu is assumed.

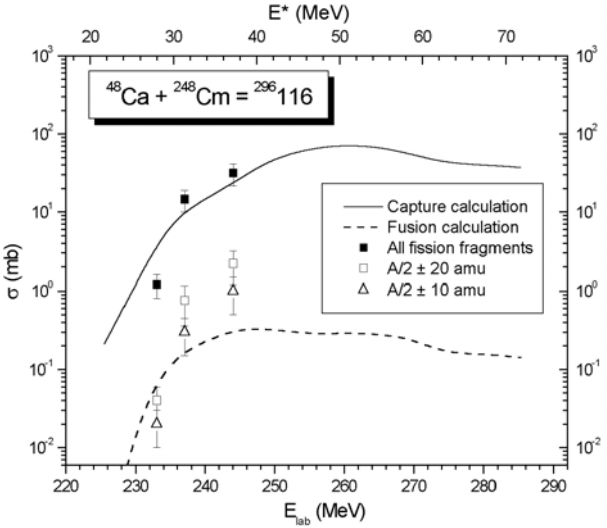


Fig.2. The capture and fusion cross section calculation, in comparison with the experimental data [12,13], for the ^{48}Ca + ^{248}Cm reaction leading to the ^{296}116 superheavy CN. The difference between the fusion calculation and more symmetric fragment yield (*A*/2 ± 10 amu) at higher excitation energy is related to the contribution of the quasifission process yielding more symmetric fragments.

Such a strong disagreement is connected with the contribution of the quasifission process in the range of the more symmetric fragments in which the contribution of the fusion-fission fragments is present. In fact, if one assumes for $\eth m$ an interval of ±10 amu (almost close to the $(A/2)^{1/2}$ value) for selecting the symmetric fragment events, the fusion calculation (dashed line) will appear approximately in agreement with the new selection of the experimental data (open triangles [13] in Fig.2. Of course, also in this last-mentioned case, there is an appreciable contribution of the quasifission process (or a contribution which cannot be neglected), in addition of the fusion-fission fragment formation. This is the

reason why the new selection of the experimental data of fragments still a little higher than the calculated fusion cross section at higher excitation energies. In our calculation, the capture and fusion cross sections for $^{296}116$ are related to the driving potential. They are characterized by the B^*_{fus} intrinsic fusion barrier of 4.48 MeV which depends on the shell structure of the reacting nuclei, and the B_{qf} quasifission barrier of 4.12 MeV. These values lead to the fusion factor P_{CN} of about 0.011.

In Fig.3 we also present the excitation functions of the evaporation residues obtained as a result of the 2-5 neutron emission from the $^{296}116$ compound nucleus. The maximum of the evaporation residue cross section for the 3n emission (ER_{3n}) is several pb, and it is almost 2 pb for the maximum of the 4n emission.

In addition, we present the result for the reaction induced by the ^{48}Ca beam (even-even nucleus at double shell closure) on the ^{243}Am target (odd-even nucleus) leading to the excited $^{291}115$ compound nucleus.

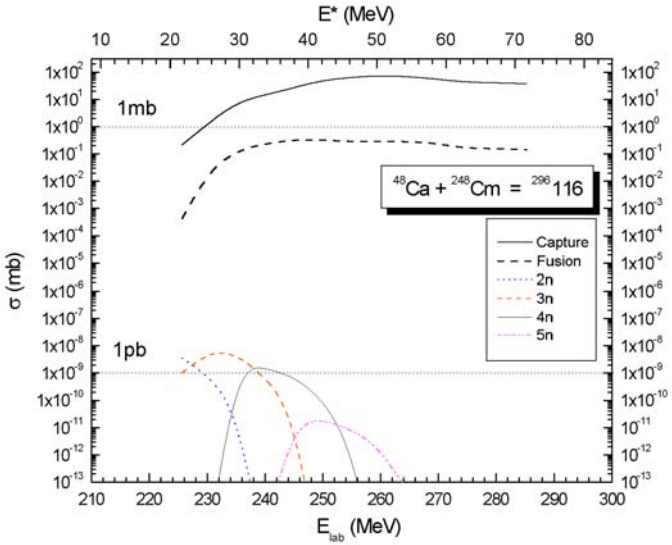


Fig.3. The excitation functions for the evaporation residue nuclei obtained from the $^{296}116$ CN after the (2-5) neutron emission, by the ^{48}Ca + ^{248}Cm reaction. In the figure, we also report the capture and fusion cross section calculation.

In our calculation, we found the value of about 3.2 MeV for the intrinsic fusion barrier B^*_{fus}, and the value of 1.5 MeV for the B_{qf} quasifission barrier. The conditions of the entrance channel lead to a competition between the complete fusion and quasifission determining by the fusion factor P_{CN} of about 0.12.

In Fig.4, we present the capture and fusion cross sections as well as the excitation functions of the evaporation residues after the emission of 2-5 neutrons from the $^{291}115$ compound nucleus. As one can see, the maximum value of the fusion cross is about 1.7 mb at E^*= 28 MeV, and the maximum value for the ER_{3n} is about 5 pb. We also find that the maximum value of ER is about 24 pb at E^* of about 17.5 MeV.

The present reaction forming the $^{291}115$ compound nucleus appears to have a good yield of residues also in respect to the formation of $^{294}114$ and $^{296}116$ found in the experiments performed at the Flerov Laboratory of JINR Dubna.

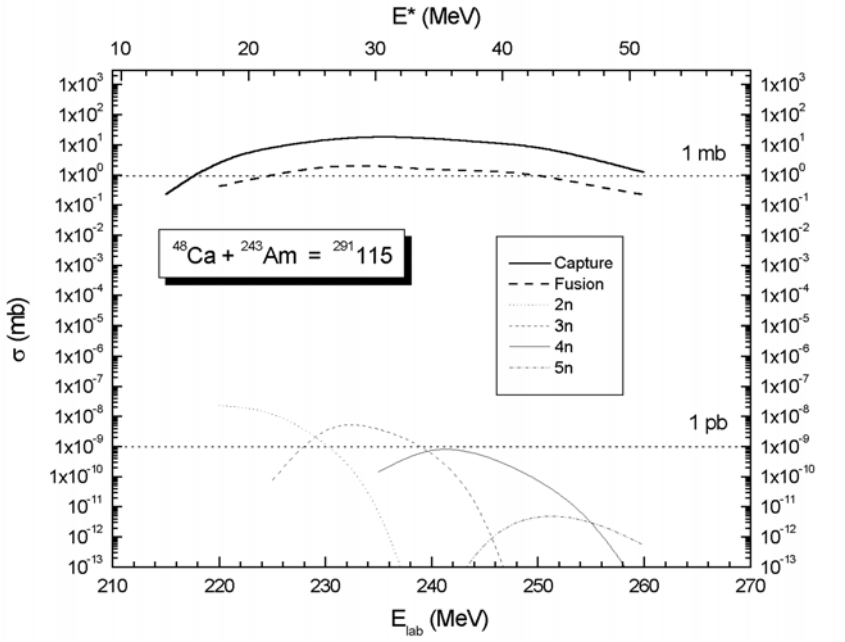


Fig.4. The excitation functions for the evaporation residue nuclei obtained from the $^{291}115$ CN after the (2-5) neutron emission, by the ^{48}Ca + ^{243}Am reaction. In the figure, we also report the capture and fusion cross section calculation.

We also present our calculations for the ^{48}Ca + ^{249}Cf reaction (Fig.5), leading to the $^{297}118$ compound nucleus, to evaluate the fusion cross section and the excitation functions for the evaporation residue nuclei obtained as a result of the x (2-5) neutron emission from the compound nucleus. For this reaction, we obtain the intrinsic fusion barrier B^*_{fus} of about 9 MeV, the quasifission barrier B_{qf} of about 4.5 MeV, and the fusion factor P_{CN} of about 0.132.

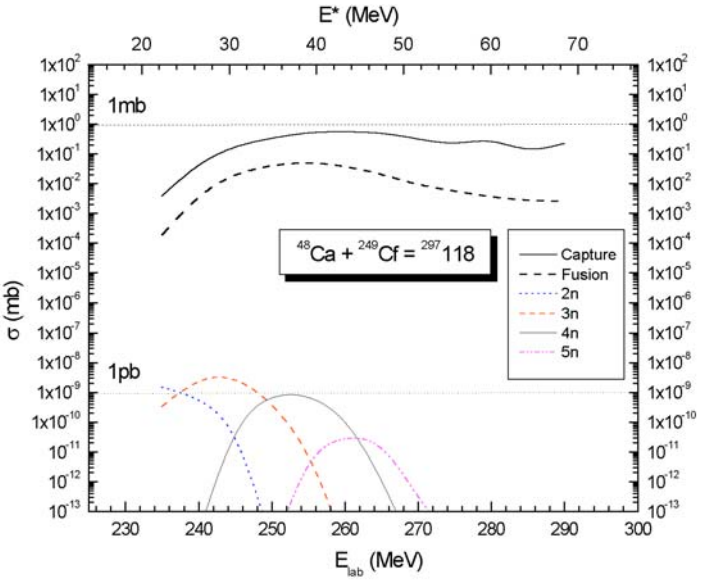


Fig.5. As Fig.3 but for the ^{297}118 superheavy CN obtained by the ^{48}Ca + ^{249}Cf reaction. The capture, fusion and evaporate residue cross sections are lower than the ones respectively obtained for the ^{296}116 CN by the ^{48}Ca + ^{248}Cm reaction.

In Fig.5, we show the capture cross section (lower than 1 mb) and the fusion cross section (with a maximum value of about 50 μb) versus the beam energy. For the evaporation residue cross section, we find the maximum values of about 3.5 pb for the 3n channel, and about 0.8-0.9 pb for the 4n channel.

By comparing the results of the two last-mentioned reactions, namely ^{48}Ca + ^{248}Cm, ^{249}Cf (leading to the ^{296}116 and ^{297}118 compound nuclei, respectively), one can make a conclusion that the complete fusion decreases, as does the evaporation residue nuclei $ER_{3n,4n}$ in the case of the ^{297}118 nucleus formation.

Conclusions

The role of the entrance channel in fusion-fission reactions was studied to account for the difference between the experimental data and results of calculations. The combined dynamical and statistical models based on the DNS approach were used to estimate the excitation functions of quasifission, fusion, and formation of evaporation residues in fusion reactions with massive nuclei. The capture stage was calculated using the dynamical model. At calculation of the fusion stage by the statistical approach, the competition of complete fusion with

quasifission was taken into account. The fusion excitation functions calculated in this way were used to estimate the survival probability of the formed compound nucleus relative to fission in the framework of the advanced statistical model for the de-excitation cascade. In calculations of the excitation function for capture, fusion and evaporation residues, we used such quantities as potential energy surface, driving potential, spin distributions and survival probability of compound nucleus, which are responsible for the mechanism of fusion-fission processes.

The results of the calculations in the framework of the DNS concept and advanced statistical model for evaporation residue cross sections for the sum of *x*n-channel contributions have been compared with the experimental data measured in the ^{40}Ar + ^{176}Af and ^{48}Ca + ^{174}Yb leading to the ^{216,222}Th* CN.

Having analyzed the ^{48}Ca + ^{248}Cm reaction, we note that the quasifission process also contributes into the symmetric fragment formation at higher E^{*} excitation energies.

For the considered reactions leading to superheavy elements, the ^{48}Ca + ^{243}Am reaction gives an appreciable rate of the evaporation residue cross section, while for the other two investigated reactions, increasing Z of superheavy elements from 116 to 118 (obtained by the synthesis of nuclear reactions), the respective cross sections (capture, fusion and evaporation residue nuclei) decrease.

Acknowledgements

This work was performed partially under the financial support of the RFBR (Grant No. 99-02-16447) and INTAS (Grant No. 991-1344). Authors (A.I.M and A.K.N.) are grateful to the STCU Uzb-45, Uzbekistan State Scientific-Technical Committee (Grant No. 7/2000) and Fund of Uzbek Academy of Science for Support of Basic Research (No. 45-00) for partial support. A.K.N. would like to express his gratitude for the warm hospitality during his stay at the University of Messina (Italy). A.K.N. is also grateful to the Fondazione Bonino-Pulejo (FBP) of Messina for the support received in the collaboration with the Messina group.

References

1. V.V. Volkov, N.V. Antonenko, E.A. Cherepanov, A.K. Nasirov, V.P. Permjakov, Phys. Lett. B319, 425 (1993); Phys. Rev. C51, 2635 (1995).
2. G. Giardina, F. Hanappe, A.I. Muminov, A.K. Nasirov, L. Stuttgé, Nucl. Phys. A671, 165 (2000).
3. G. Giardina, S. Hofmann, A.I. Muminov, A.K. Nasirov, Eur. Phys. J. A8, 205 (2000).
4. W.J. Swiatecki, Phys. Scr., 24, 113 (1981); Nucl. Phys. A376, 275 (1982).
5. K.T.R. Davies, A.J. Sierk, J.R. Nix, Phys. Rev. C28, 679 (1983).
6. P. Frobrich, Phys. Rep. 116, 337 (1984); Phys. Lett. B215, 36 (1988).

7. J.P. Blocki, H. Feldmeier, W.J. Swiatecki, Nucl. Phys. A459, 145 (1986).
8. A. D'Arrigo, G. Giardina, M. Herman, A.V. Ignatyuk, A. Taccone, J. Phys. G20, 365 (1994).
9. D. Vermeulen, H.-G. Clerc, C.-C. Sahm, K.-H. Schmidt, J.G. Keller, G. Munzenberg, W. Reis-dorf, Z. Phys. A318, 157 (1984).
10. H.-G. Clerc, J.G. Keller, C.-C. Sahm, K.-H. Schmidt, H. Schulte, D. Vermeulen, Nucl. Phys. A 419, 571 (1984).
11. R.N. Sagajdak. JINR (p.60, Dubna 2000).
12. M.G. Itkis, et al., Proc. of the International Conference on Nuclear Physics at Border Lines, May 21-24, 2001 Lipari (Messina), Italy, eds. G. Fazio, G. Giardina, F. Hanappe, G. Imme, N. Rowley. World Scientific, Singapore, p.146-156, 2002.
13. E. Kozulin, private communication.

REGENERATION OF ENRICHED ^{98}Mo FROM WASTE ^{99m}Tc GENERATORS

S. Khujaev, N.A. Mirzaeva,U.T. Ashrapov, L.B. Nushtaeva, M. Berdieva

Institute of Nuclear Physics of Uzbekistan Academy Sciences

At Institute of Nuclear Physics the production of ^{99m}Tc generator is based on application of molybdenum trioxide enriched in ^{98}Mo, which irradiated by neutron in nuclear reactor to produce of the parent ^{99}Mo radionuclide [1].In last time the sharp rise of the level of prices for enriched isotope of ^{98}Mo resulted in the increase in cost of production expences. This circumstance caused the study to be started of regeneration conditions for enriched ^{98}Mo and its reuse in ^{99m}Tc generator production.

The specific activity of the parent ^{99}Mo radionuclide reaches to 5 Curie/g after activation of target material of ^{98}Mo by thermal neutrons. The mass of activated ^{99}Mo in the principal mass of target material ^{98}Mo is 10^{-5} g. There is a lot of the waste aluminium oxide with sorbed ^{98}Mo in the manufacture as the ^{99m}Tc generator is returned after its application.

The problem of ^{98}Mo regeneration from the waste generators includes the study of conditions of its desorption from sorbent phase, the purification from possible impurities, the conversion of product in goods state ($^{98}MoO_3$) and analysis of the ready product.

The laboratory investigations were carried out using the chromatographic columns with aluminium oxide containing the preliminarily sorbed molybdenum labelled with the radioactive tracer of ^{99}Mo. The chromatographic column were washed by 0,9% NaCl solution during 14-15 days. Then the desorption of molybdenum from sorbent phase by various solutions such as sulphur acid and ammonium solution as well as the solutions containing hydrogen peroxide was studied. The purification from impurities is carried out by using second chromatographic column containing the resin of quaternary phosphonium alkali (QPhA) in sulphate form:

$$(\text{-}CH_2\text{-}CH\text{-}C_6H_6\text{-}CH_2P^+R)_2 \cdot [SO_4]^{2-},$$

where R=C_3H_7 or C_4H_9.

The investigation results showed that the elution of molybdenum by 1,0 g-eq./l sulphur acid solution at elution rate in less than 2,5 ml/min was the most optimal condition for desorption of molybdenum from the sorbent phase (Al_2O_3).The results obtained are shown in Table1.The plot of molybdenum desorption performed on base of results obtained in static conditions is shown in Fig.1.

The results showing in Table 1 are obtained after elution of chromatographic column by a four free volumes. The elution curve of molybdenum from column is showed in Fig.2. The yield was 87% of all sorbed quantity of molybdenum.

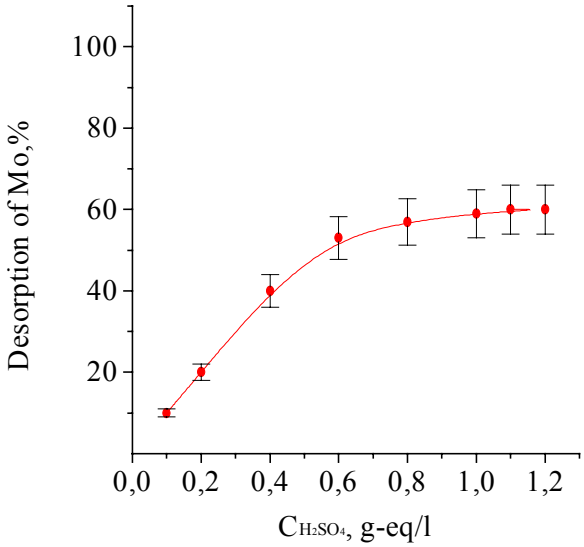


Fig.1. Plot of molybdenum desorption from Al_2O_3 phase in static condition (desorption of molybdenum in 5 ml H_2SO_4).

Table 1

Elution rate, ml/min	Desorption of molybdenum, % of sorbed Mo
0,5	89,9
1,0	89,5
2,0	89,0
2,5	88,0
3,0	82,0
3,5	77,0
4,0	73,0

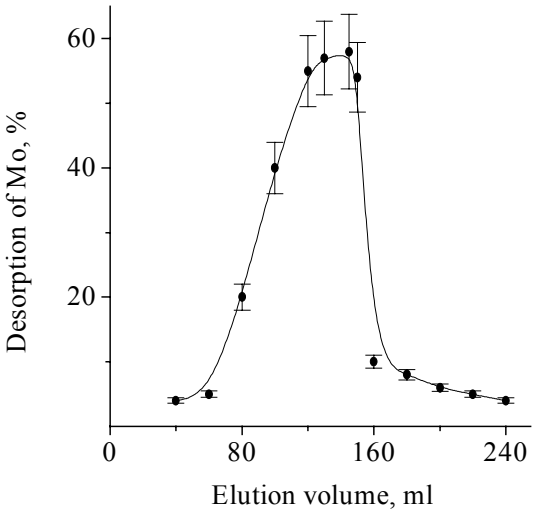


Fig.2. Plot of molybdenum desorption from Al_2O_3 phase in dynamic condition by 1,0 g-eq/l H_2SO_4 solution.

After, the desorbed molybdenum from aluminium oxide phase was purified by using column with QPhA. The molybdenum solution passed through chromatographic column which was preliminarily treated by 1 g-eq/l H_2SO_4 solution. The sorption of molybdenum on the QPhA resin was 95-100% at elution rate in less than 0,4 ml/min (Table 2).

Table 2

Elution rate, ml/min	Sorption of molybdenum, %
0,1	100
0,2	100
0,3	99
0,4	95
0,5	90
1,0	88
2,0	72

The column with sorbed molybdenum was washed by distilled water and 1,0 mol/l NH_4NO_3 solution. Molybdenum desorption from QPhA phase was carried out by 1,0 mol/l NH_4NO_3 + 8% NH_4OH + 10^{-2}% H_2O_2 solution.

Molybdenum yield was 78-80% of its sorbed quantity. The elution profile of molybdenum from the column with QPhA is showed in Fig.3.

The precipitation of molybdenum with following filtration off and its conversion in goods sort of $^{98}MoO_3$. were carried out from the solution obtained. The product obtained was analyzed by emission spectroscopy method.

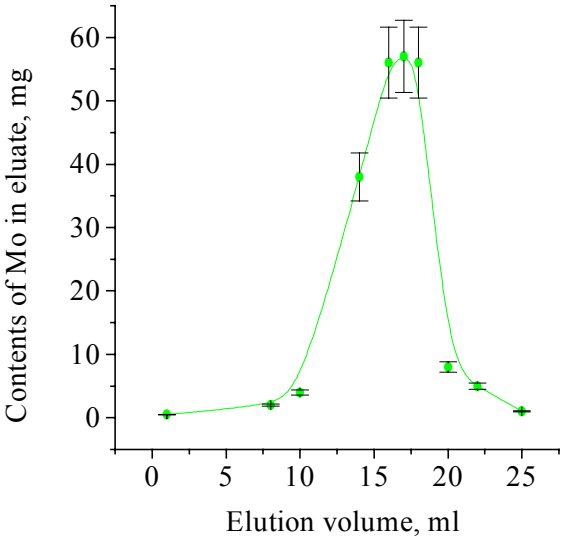


Fig.3. Plot of molybdenum desorption from the column with QPhA in dynamic condition.

SEARCH OF CORRELATION BETWEEN A FLOW LOW ENERGY OF SPACE PARTICLES AND PERTURBATION IN TERRESTRIAL CRUST

M.K. Babaev, A.S. Baigubecov, I.S. Martyanov, T.Kh. Sadykov, N.N. Zastrozhnova

Institute of Physics and Technology, MES RK, Almaty, Kazakhstan

Abstract

The results of the analysis of correlation of a flow of the charged space particles with seismic activity of the Earth are submitted. The experiment was carried out in 8 km. from Almaty on a seismic break in Large Almaty gorge. The experimental data received from counters of ionization G-M and from seismograph were used.

The known forerunners of earthquakes on the experimental control abnormal electromagnetic, hydrogeological effects etc, are practically always observed just before earthquake in expected zone and far not always revealed in epicentral region of expected earthquake and they are not synchronous in time [1].

The searches of forerunners of earthquake will be carried out by complex methods on polygons in seismic regions. The wide network of observations behind forerunners is created, there is a tight cooperation of the scientific different profiles, however problem of prediction of earthquake till now is not solved both actual prognosis of time and place of earthquake was given only once to February 4, 1975 in Northeast of China.

The ways of a short-term prediction of earthquake are known, bound with changes of electromagnetic fields in seismic regions [1,2]. At squeezing and corrupting of mountain breeds there are various electrokinetic effects, which generate variable electric fields under Earth and in an atmosphere, electromagnetic radiations of different sorts in an atmosphere and ionosphere, anomaly of passing of radio waves, sometimes light appearances, there are also perturbations in an ionosphere. Studying of impulses electromagnetic field in an atmosphere, usually register or envelope of high frequency oscillations, or number of impulses. Tens cases of perturbations of a natural electromagnetic field before earthquake, more often after some clocks are marked. Usually before a jolt a level of a field or intensity of impulses are incremented, but sometimes decrease. It, as well as much another in behavior of electromagnetic forerunners yet has no an authentic explanation.

Disadvantage of the given technique is its unreliability, since the abnormal electromagnetic appearances far from being always appear in epicentral region of the future earthquake and are not synchronous in time.

The essence of the concept suggested is follows [3-5]. It‘s evident, that ultralong waves (ULW) have wave directoral character of transmition, where Earth‘s surface is lower wall of spherical wave director while upper wall is lower field of ionosphere (D-field), which altitude fluctuates from 60 km in the afternoon to 100 km in the night. This altitude is comparable with wave‘s length what stipulates wave director character of radio waves transmition in ultralongwave diapason [6]. Heterogeneties appearance in any walls of wave director leads to change of phase speed and ULW attenuation. What should be a spatially scales of these changes in order to be reliably fixed. It‘s evident, that they should be comparable with Frenel zone sizes, which radius is $F = (D\lambda)^{1/2}$, where D - a distance between heterogeneity and observation point, λ - wave length.

If λ=30 km and D=3000 km, F ~ 300 km.

Because of the reason that disturbing origins could be situated not only in the first Frenel zone its expediently to choose characteristic size 3F ~ 1000 km.

For purpose of studing ULW diapason radio wave transmition conditions the most effective method contains of phase measuring and signals amplitude from coherent origins situated in different places of the world. Transmitters signals from phase radionavigation systems of ULW diapason and exact time systems more completely answer these conditions.

Extreme complexity and dearness of a method the realizations, called by necessity, of observations and operating information interchange in an international scale, are its main disadvantage.

The perturbations of an ionosphere are studied which happen 2-3 day prior to jolts and some day after it is prolonged. They can affect all stratums of an ionosphere, changing their electronic density (from here - anomaly at passing radio waves, especially in a short-wave range). Except for effects on an ionosphere, the radiation fields can be affected also. The first indications on possible correlation of streams high energetic of charged particles in a radiation belt with seismic activity of the Earth were obtained in experiment "Maria" on the orbital server “Salute-7” [8], when the geomagnetic field was quiet, there were no tags of solar activity, but triply intensity of charged particles of high energies in a radiation belt of the Earth sharply has jumped up. Was clarified, that on a background of usual geophysical calmness of a planet this day there was a boosted seismic activity on all globe.

The similar legitimacy was revealed by processing of outcomes of experiments on the satellite a “Meteor-3” [9]. The correlation between daily global seismic activity defined by number of earthquakes on all globe and appearance of deviations of intensity of particles (of speed of the score) was parsed. Output from here is made that the streams high energetic of particles are sensitive to manifestation of seismic activity. From 36 cases of increase of intensity of streams of charged particles by a duration from 1 about 8 minutes, 34 came on geomagnetic and solar "calm". However they well have coincided with days of boosted seismicity and 2,5-3,0 hours preceded with intervals earthquakes with

magnitude more than 4 numbers. A disadvantage of this method is inaccurate in definition of a place of earthquake and short period (150-180m) between change of stream of particles and adjustments earth the earth's crust.

In the present operation the description of installation and experimental technique on detection of correlation of streams of charged space particles with seismic activity of the Earth is reduced.

The experiment was carried out in 8 km from Almaty on a seismic break in Major Almaty canyon at height 1700 m above a sea level. For the analysis the data obtained from Geiger-Muller counters (G - M), sensors (M) of a magnetic field of the Earth and seismograph (S) with a seismosensor (SS) (see Fig.1)

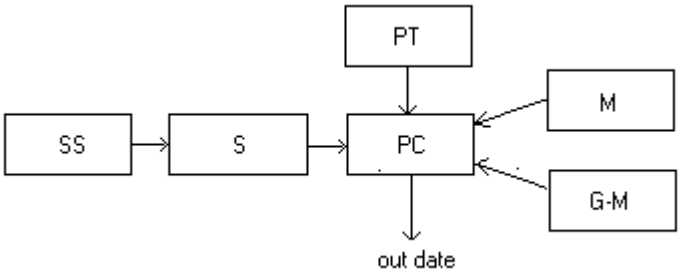


Fig.1

These data were imported to the computer (PC) for processing together with precise time (PT). The installation worked during 1991г. Two detectors G-M were used. One of them, for registration of all incident space particles, consist of 5 counters G-M in length 500mm and diameter 35mm. There was a circuit of self-blanking. The second similar detector allocated under a lead absorbent with width 150mm for an obtruncating low energetic of the soft component of space radiation and registration of muons. Both detectors are located the friend above the friend. The amount of particles in time from 1 about 60 minutes with various intervals was measured, and in case of registration of change of stream of particles score this time and compare it to time of the nearest earthquake with a threshold > 3,5 magnitudes. The continuous monitoring of oscillations earth crust, value of stream low energetic of space particles, magnetic field of the Earth, signals seismograph was carried out.

Reference

1. I.L. Gufeld, E.D. Limarev, V.F. Marenko et al. Search of electromagnetic forerunners of earthquake. M., Science, 1988, c.243.
2. Gangnus. Secret of earth catastrophes. M., Thought, 1985, c.70.
3. I.L. Gufeld, V.F. Marenko. “Short-term forecast of destructive earthquake time with radio wave methods usage. D. Ac. of Scs, 1992, т.323, N6.
4. International information radio wave earthquake forecasting system. Project, Russian Academy of Science. Scientific manager Reutov A.P., 1994.
5. A.P. Reutov, V.F. Marenko. Concept of radio wave earthquake forecasting system building, experimental results. Intern. Informatization Academy-An Associated Member UN, Moscow, 1995.
6. Y.L. Alpert. Spreading of electromagnetic waves in an ionosphere. M., Science, 1972, 564 with.
7. I.L. Gufeld, V.F. Marenko, V.S. Jampolsky. Statistic analysis of connection of perturbation phase of FRNS "Omega" signals with seismotectonic process. Preprint 1, M, IRE AS USSR, 1989.
8. S.A. Voronov, A.M. Galper, V.G. Kirillov-Ugrjumov et al. Registration of increase of streams high of particles in region of the Brazilian magnetic anomaly. 1985г. MIFI, Preprint 006-88, M., 1988.
9. A.M. Galper, V.V. Dmitrienko, I.V. Nikitina et al. Space researches, v.XXVII, issue 5, 1989, p.789.

SEARCH OF THE RESONANCE E_{55}^{+++} IN ANTIPROTON-PROTON INTERACTIONS AT THE MOMENTUM 22.4 GeV/c

Temiraliev T.

Institute of Physics and Technology of MESc RK, Almaty, Kazakhstan

At the beginning of 80-th years was predicted [1] the existence of exotic isobar with isospin *I=5/2*, it was get out from the over-convergence dispersion sum rules for scattering amplitude of redgeon on nucleon resonances. It was shown, that the saturation sum was obtained, if the existence of composite state with isospin *I=5/2,* spin *J=5/2* and positive parity was admitted. Mass E_{55} is connected with mass of the known isobar Δ_{33} and nucleon mass M_N by the expression

$$M_{E_{55}} - M_{\Delta_{33}} \approx M_{\Delta_{33}} - M_N$$

The width $\Gamma_{E_{55}}$ is connected with $\Gamma_{\Delta_{33}}$ by following relation

$$\Gamma_{E_{55}} = \frac{4}{5}\left(\frac{K^*}{K}\right)^3 \Gamma_{\Delta_{33}},$$

where $K^*(K)$ - the momenta of double particle decay in the rest systems $E_{55} \to \Delta_{33}\pi$ and $\Delta_{33} \to N\pi$ respectively. The existence of resonances with *I=5/2* had forecasted at the bag [2] and string [3] models. Since the multiparton nucleon structure is sensitive to the "spin crisis" effect, the search of multiquark hadron state has on principle importance for the ascertain of the inside structure of nucleons.

Search E_{55}^{+++} was carried out in hydrogen bubble chambers, exposed by π^+ - mesons and neutrons at the momentum 4.2 GeV/c and 5.1 GeV/c respectively. Indication on the existence of exotic isobars with mass 1522 MeV, 1640 MeV, 1825 MeV and 1975 MeV was obtained in [4]. Unfortunately, during the next years the more reliable data were not obtained.

Application of the method of image recognition in multidimensional phase space [5], in which full cinematical information on all particles and their interval dynamical correlations is used, can be for obtaining the physically significant results. This method is based on assumption, that the fixed sets of particles are

grouping in different regions of the multidimensional phase space. The regions with high density (clusters) are distinguished by the method of image recognition theory. Search of clusters in multidimensional phase space is carried out by two model-independent and mutually supplementing methods. The comparison of distances between points (events) in multidimentional phase space, corresponding to these events is lied in the basis of this method. The method of cluster distinguishing in multidimensional phase space was discussed in detail in [5].

Search resonance E_{55}^{+++} was carried out in $(p\pi^+\pi^+)$ system (six prong events) in antiproton-proton interactions at momentum 22.4 GeV/c. For analysis 2882 events were choosed with proton identified by ionization dencity (the momentum of proton in laboratory coordinate system ≤ 1,2 GeV/c). If $(p\pi^+\pi^+)$ system two identical pions were observed, then the preliminary numeration of pions (π_1^+, π_2^+), was carried when constructing the minimal covered tree. On the method of "*K* – nearing neighbours" at $K = 5; 7; 10$ and at the critical merging of cluster $N_0 = 20; 30; 45$ the search of clusters was carried out.

In given experiment at $K = 7$ and $N_0 = 30$ the 5 groups of events in $(p\pi^+\pi^+)$ system were discovered, which had small widths ≤ 120 MeV, predicted in Redge model. Corresponding effective masses *M*, widths *Γ*, population *N*, cross sections σ for clusters are given in Table 1.

Table 1: Kinematical cluster characteristics.

Primary momentum	$P_0 = 22{,}4$ GeV/c				
Clusters					
M, GeV/c²	1,547	1,604	1,766	1,864	2,004
Γ, GeV/c	0,091	0,066	0,072	0,091	0,086
N	190	101	100	130	106
σ, μbarn	133 ± 19	70 ± 14	70 ± 14	91 ± 17	74 ± 15

In Fig. 1 the distributions of effective masses $M(p\pi^+\pi^+)$ and two-dimensional distribution of effective masses of double particle $(p\pi_1^+)$ and $(p\pi_2^+)$ sets are given. It can be seen, that the maximums of double particle sets $(p\pi_1^+)$ and $(p\pi_2^+)$ are displaced relatively each other, which contradicts to

supposition about the influence of kinematical interference from $\Delta_{3/2,3/2}$, and the overlapping districts requires for mass values of $(p\pi_1^+)$ and $(p\pi_2^+)$ systems are displaced relatively to field of points in two-dimensional plot. Since, in analysis of effective mass distributions $M(\pi^+\pi^-)$ the ρ – meson production was not observed, the the cinematical reflection from this resonance can be neglected.

If one takes with account that in all cases for three-particle sets the $M(p\pi^+\pi^+)$ well are described by Breight-Wigner curves, it can be supposed that the contribution of background events is not important. In the frames of this approach the E_{55} production cross section , given in table 1, are estimated.

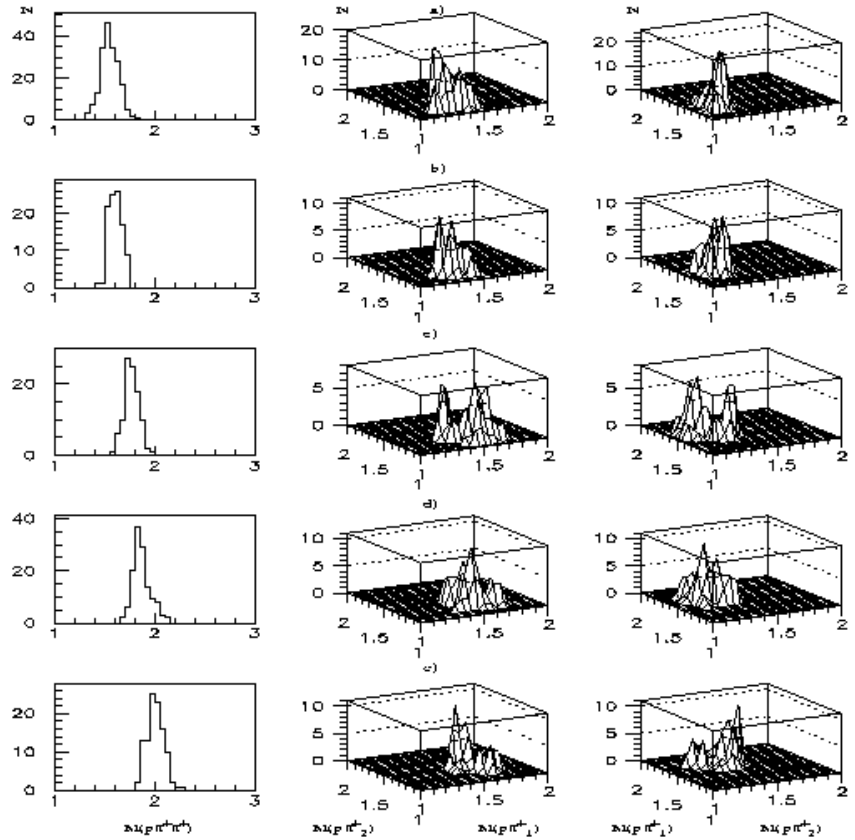


Fig. 1.: a) – E_{1517} ; b) – E_{1601} ; c) – E_{1766} ; d) – E_{1861} ; e) – E_{2001}

Conclusion

The 5 groups of events were discovered with small width (Γ<*120 MeV*) and different effective masses of three-particle sets $M(p\pi^+\pi^+)$, well describing by Breight-Wigner function, which possibly are connected with E_{55}^{+++} production.

References

1. Grigoryan A.A., Kaidalov A.B. // Yad. F., 1980, v. 32, p. 540 (in russian).
2. Ioffe R.Z. // Phys. Rev., 1978, D17, p. 144.
3. Imachi M., Otsuka S. et al. // Progr. Theor. Phys., 1977, v. 55, p. 551.
4. Abdivaliev A., Beshlin K. et al. // Yad. F., 1983, v. 34, p. 629 (in russian).
5. Boos E.G., Vinitsky A.A. et al. // Yad. F., 1991, v. 54, is. 2(8), p. 538 (in russian)

STATUS OF CYCLOTRON BASED RADIOISOTOPES PRODUCTION IN ALMATY

A. Arzumanov, N. Berdinova, A. Borisenko, G. Chumikov, N. Gorodisskaya, A. Knyazev, V. Koptev, Yu. Popov, G. Sychikov, D. Zhetltov

Institute of Nuclear Physics, Almaty, 480082, Kazakhstan

Abstract

The Institute of Nuclear Physics in Almaty is elaborating program the aim of which is developing of technology and production of the most important for Kazakhstan radionuclides, radioactive sealed sources and radiopharmaceuticals to be used in medicine, industry and in radioecological research in Kazakhstan.

Solid and powder targets are irradiated with protons up to 30 MeV and alphas up to 50 MeV using positive ions variable energy isochronous cyclotron. Traditional wet chemistry procedures to extract and purify produced radioisotopes are used.

Regular production of Tl-201, Ga-67, Co-57, Cd-109, Pu-237, Y-88, Sr-85 has already started. It is expected to expand the production of radionuclides as to include Fe-55, In-111, I-123, Rd- 103 and some other radionuclides.

Introduction

First application of the radioactive isotopes dates from 1923 when Hangarian Scientist Haveshi used natural radioactive isotope Pb-212 for studying its distribution in roots, trunk and foliage of some plant (vicia fabe).

Cyclotrons, were very important in the preparation of radioisotopes during the years of 1935 to the end of World War Two.

After World War Two, mainly reactors were used to produce radioisotopes. However, as the techniques for using radiotracers became more sophisticated and advanced, it became clear that reactor radionuclides could not satisfy the growing demands and therefore accelerators were needed to produce new radioisotopes which could be used in new ways.

There are three major reasons the accelerator radioisotopes are used more widely than reactor radionuclides. These are:

1. The reactor radioisotopes may have unfavorable decay characteristics for a particular application.
2. The radioisotope cannot be produced in a reactor with high specific activity.
3. Access to a reactor is limited. The radioisotope has too short a half-life to be transported to the site where it is needed.

The variable-energy isochronous cyclotron U-150 M has been in routine operation in Almaty since June 1967. It was designed and manufactured by V.D.Efremov Institute in Leningrad as “classical” machine with a single beam line and fixed energy per nucleon 10 MeV/nucleon for protons, deuterons and alphas. In 1971-72 it was converted to variable-energy isochronous mode of operation [1]. Now it is a compact pole, three spiral sector, positive ion machine with K=50 MeV. The cyclotron generates beams of protons 6 – 30 MeV, deuterons 12,5 – 25 MeV, helium-3 ions 18,5 – 62 MeV, helium-4 ions 25 – 50 MeV.

Radioisotope Tl-201 has been manufactured in Kazakhstan since 1986 [2]. The short-lived radoioisotope and its labeled compound was supplied to hospitals and research institutes in Almaty and Medical Centers in nearby countries for use as tracers for diagnostic and research purposes.

Now also radionuclides such as Ga-67, Co-57, Cd-109, Pu-237, Y-88, Sr-85 are produced upon request. Wet chemical procedures have been developed for the recovery and purification of various radionuclides from the irradiated targets.

Target preparation

At the present time for isotopes production only solid targets are used at the internal and external beam of the INP isochronous cyclotron. The schematic view of internal target head is shown in Fig.1. Metallic targets prepared by electrodeposition of corresponding metal on a copper substrate of special design are used for production of Tl-201, Ga-67, Cd-109, Co-57 .

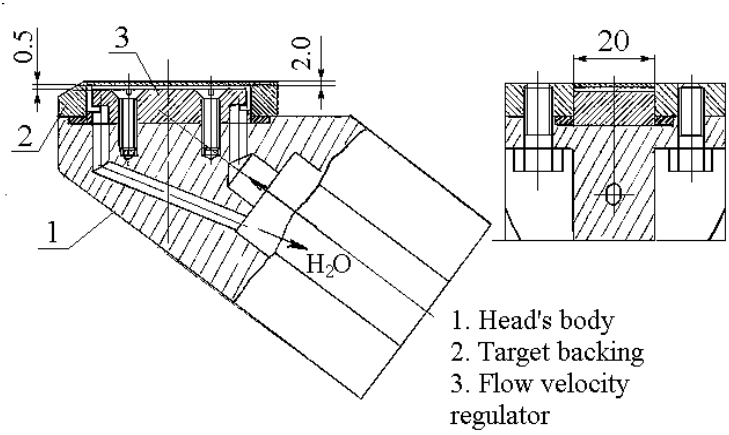


Fig.1 Schematic view of the internal target

Choice of the method for electrolytic deposition depends on the type of metal to be deposited. When prepare a nickel one (Co-57) the galvanostatic mode of deposition with insoluble platinum anode is used. For getting silver (Cd-109) and zinc (Ga-67) layers it is used electrolysis with soluble anode and reverse current what enables to control simultaneously thickness of the deposited layers and spent anode material.

A technology developed by P.Van den Winkel (VUB) and handled over within IAEA Technical Co-operation Project is used for production of thallium targets.

Below, in Table 1, one can find detailed data on metallic targets. Powder targets produced by pressing at ~2500 N/cm^2 of RbCl, SrO and UO_2 into a metallic capsule are used for production of the nuclides Sr-85, Y-88 and Pu-237, correspondingly. In all cases the thickness of the pressed powder is 1-1.5 mm.

Table 1 Summary data on the internal targets prepared by electrolysis.

Radio-nuclide	Target material	Metal layer thickness, μm	Presence of sublayer	Electrolyte type	Current mode
Tl-201	^{203}Tl	160	-	Alkaline EDTA	chopped, sawtooth
Ga-67	^{nat}Zn	350	-	Subacid chloride	Direct with reverse
Cd-109	^{nat}Ag	290	Ag, 2 μm	Thiocyanatous	Direct with reverse
Co-57	^{nat}Ni	240	Au, 10 μm	Sulphate-chloride	direct

For assessment of adhesion due to presence of a diffusion layer a set of experiments was carried out for investigations of the diffusion rate for metal electrically deposited on a copper substrate matrix at different temperatures. Profile of the coated layer prior and after the annealing is determined at the Electrostatic tandem with 1,5 MeV protons by the method PIXE [3]. The investigations have shown that thickness of the diffusion layer comprises 0.5-1 μm at target annealing temperature of 250-300 °C. Therefore, to remove bulk stresses in metal and to increase the diffusion layer thickness the targets are annealed in vacuum at temperature 180-250 °C during 3-5 hours before the irradiation.

Target irradiation

For radionuclides production both external and internal target irradiation are used. Beam intensity on the external target now is equal to 30 μA for protons and deuterons and is limited by beam power dissipation in the electrostatic deflector. In some cases during target irradiation the beam is swept across the

target surface in a circular fashion by means of a stator of electro-motor in order to ensure an even power distribution.

Beam power distribution for the extracted beam spot and for the circularly scanned beam are shown in Fig. 2. When irradiating targets with high intensity internal beam the target is inclined with respect to the beam axis at the angle of 18° in order to reduce beam power density on the target. Thin layer 0,5 mm thick of cooling water, flowing at a velocity of approximately 30 m/s along the target surface is employed to ensure necessary cooling of the target. Cooling water pressure is equal to 20 bar which enables to use irradiation with internal 30 MeV proton beam and intensity up to 500 μA. Summary of the produced radioisotopes is presented in the Table 2.

Table 2 Summary of the produced radioisotopes.

Radio-isotope	Production route	Energy of incident ions, MeV	Beam intensity, μA	Average heat flow, kW/cm^2	Yield of activity (for nat), mCi/μA*h
Tl-201 (72,9 h)	^{203}Tl (p,3n) ^{201}Pb $\rightarrow$ ^{201}Tl	28,5	125	0.7	≥ 0.2
Ga-67 (78,2 h)	^{68}Zn(p,2n)^{67}Ga	30	125	0.8	≥ 1.3
Cd-109 (463 d)	^{109}Ag (p, n) ^{109}Cd	22	250	1.1	≥ 2.6e-3
Co-57 (270 d)	^{58}Ni (p, 2p) ^{57}Co ^{58}Ni (p, pn) ^{57}Ni $\rightarrow$ ^{57}Co	22	300	1.3	≥ 0.3
Pu-237 (45,2 d)	^{235}U(α,2n)^{237}Pu	48 (α)	10	-	≥1.7e-10
Y-88 (106,6 d)	^{88}Sr (p,n) ^{88}Y	22	10	0.044	≥ 0.103
Sr-85 (64,8 d)	^{85}Rb(p,n)^{85}Sr	22	10	0.044	≥0.076

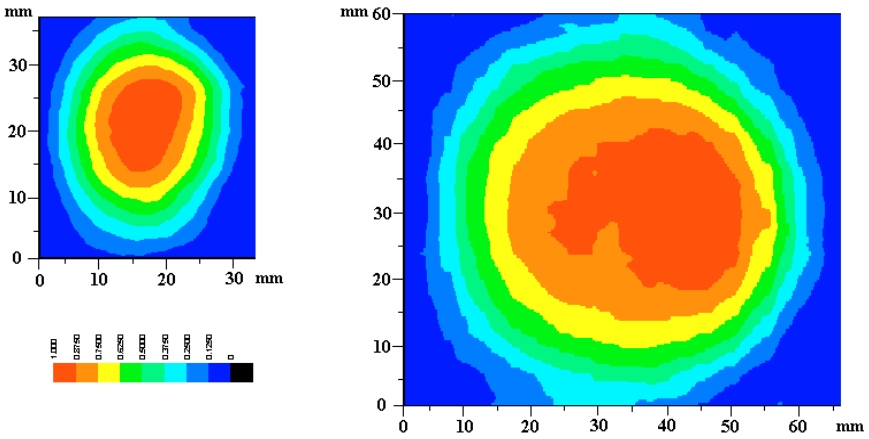


Fig.2 External beam spot (a). Circularly swept beam spot (b).

Radiochemical extraction of radionuclides:

Classical methods of ion exchange and extraction chromatography are used at radiochemical processing of the irradiated targets. Developed on their basis techniques enable to obtain high rate of purification of a desired product both from macrobacking, the irradiated target material, and from accompanying radioactive impurities.

I. **Thallium-201**:

1. Extraction of Pb-201 ($T_{1/2}$ = 9.3 hours) by co-depositing on $SrSO_4$ collector and optimal exposure of the extracted Pb-201 during 26 hours for Tl-201 accumulation.
2. Separation of the accumulated Tl-201 from the parent radionuclide Pb-201 by the extraction method.
3. Thallium-201 transfer to isotonic solution, a base for production of the radiopharmaceutical preparation (RPP).

II. **Gallium-67** [4]:

1. Chemical dilution of a zinc layer at the substrate in 12 N HCl.
2. Separation of Ga-67 from macroamounts of Zn and microelements Fe and Cu by the method of extraction chromatography.
3. Gallium-67 transfer to isotonic solution in form of citrate complex, a base for production of RPP.

III. **Cobalt-57**:

1. Anode dilution of a nickel layer at the substrate in 9 N HCl.

2. Separation of Co-57 from Ni, Fe, Zn-65 by the method of ion exchange chromatography.
3. Cleansing of Cu residue by electrolysis.

IV. **Cadmium-109**:

1. Chemical dilution of a silver layer at the substrate in 7 N HNO_3.
2. Separation of Cd-109 from silver macroamounts by the method of cementation on copper.
3. Separation of Cd-109 from Zn-65, Fe and macroamounts of Cu by the method of ion exchange chromatography.

V. **Yttrium-88** [5]:

1. Dilution of the irradiated powder in weak HNO_3
2. Separation of Y-88 from Zn-65, Fe, Cu and macroamounts of Sr by the method of extraction chromatography.

VI. **Strontium-85** [5]:

1. Dilution of the irradiated powder in weak KOH and filtration.
2. Separation of Sr-85 from Zn-65 and macroamounts of Rb by the method of ion exchange chromatography at activated charcoal.

VII. **Plutonium-237** [5]:

1. Dilution of the irradiated powder in concentrated HNO_3.
2. Pu (III) oxidation to Pu (IV).
3. Extraction of Pu by the method of extraction chromatography.

Recovery

Recovery of the target material occurs in two cases only:

1. Recuperation of enriched ^{203}Tl in metal form to the Tl target production cycle from the spent solutions and the electrolyte. The procedure implies electrolysis with controlled cathode potential (CCPE). The recovery rate is ≥99.5 %.
2. Recuperation ^{nat}Ag in metal form to the Ag target production cycle from the worked out for ~80 A·h/l thiocyanate electrolyte. The reductioned silver is used as dissolved anodes. The recovery is also carried out by CCPE with the recovery rate ≥99 %.

Electron beam stand

The electron beam test facility was created for preliminary heat load targets examination before their irradiation at the cyclotron.

This facility also enables to expedite development of technologies for isotope target production.

Electron blocks of beam focussing and deflection in vertical and horizontal directions provide obtaining of beam dimensions of ∅ 1,5 mm and its scanning against the target surface. Scanning frequencies are the horizontal one – 50 Hz and vertical one – 1200 Hz that provides homogenous target heating. There is an opportunity of fixed beam spot moving at any point of the target surface. Electron

beam has following parameters: electrons energy up to 25 keV, beam intensity up to 200 mA. The water pressure in cooling system is equal to 20 bar that provides water velocity in the cooling channel equal to 30 m/s.

Target tests at the stand enable to determine maximal allowed heat flows which are fixed in melting point of target material. Energy loss caused by reflected and second electrons are accounted on basis of known reference data.

Conclusion

Cyclotron internal beam intensity is increased up to 500 μA for 30 MeV protons. Internal target design enables to irradiate it for some materials with beam current of 350 μA. Sweeping system is inserted in the beam line to produce homogeneous irradiation of the external target. Many radioisotopes to be used in medicine, industry etc. can be produced in Kazakhstan using K = 50 MeV cyclotron to meet need of the Republic.

Acknowledgement

The authors would like to express their gratitude to IAEA for support of this work.

References

1. Arzumanov, A.A., Nemenov, L.M., *Nucl. Instr. And Meth.* **106**, №2, 201-202 (1973).
2. Malinin, A.B., Kozlova, M.D. et al., *Int. J. Appl. Radiat. Isotopes*. 685 (1984).
3. Arzumanov, A.A., Borisenko, A.N. et al., "Application of electrostatic tandem in Almaty for analysis of beryllium foils and radioactive particulates", 6-th EPAC, 1998, 2433 - 2435.
4. Arzumanov, A.A., Batischev, V.N., et al., " Development of cyclotron based high beam current technique for Ga-67 production", 7-th EPAC, 2000, 2498 - 2499.
5. Arzumanov, A.A., Batischev, V.N., et al.,"Production of Plutonium, Yttrium and Strontium tracers for using in environmental research", 16-th Conf. on Cycl. and their Appl., 34 – 36.

STUDY OF FINAL STATE RESONANCE IN PHOTODESINTEGRATION REACTIONS

Takibayev N.Zh., Lennik S.G., Livetsova A.S.

Almaty, Kazakhstan

Induced resonance states as well as long-range effects arise from special conditions in three-body systems [1-3]. They can appear due to interference of two-body resonance in subsystems.

Considering at low energy the α-particle as structureless one we come to three-body problem for d-α system. It is known that amplitude of elastic d-α scattering has a resonance behavior. There is a resonance state ~ 1 Mev, induced by effective potentials of N, α-subsystem.

Can we find any more induced resonances in the system? The existence of such resonances may be very important for nuclear astrophysics.

The low-energy resonances in d-α systems can be investigated in ^{6}Li(γ,d)α reaction. The fact is that nuclear clusters just after action of initial photon absorption come into being at small distances. Then they go out with interaction between each other's in final state. So, it's possible to study the interaction at energies near or below Coulomb repulsive barrier.

A photo-disintegration process can be represented in form: $\gamma + A \rightarrow \sum B_k$, where B_k is a nuclear cluster of number k. It is known that rules of electromagnetic transition result in definite quantum states for final nuclear cluster systems. So, it gives a chance to research corresponding quantum states in more details.

Moreover, using a perturbation theory in respect of electromagnetic forces give us a high accuracy in calculations of this part. Besides, reducing of initial photon energy can shorten a number of open channels in final state. There is only d, α - final state in energy region 1,47 MeV < E_γ < 3,7 MeV.

General formulas of nucleus photodisintegration

It is easy to describe of photodisintegration process at low energy within framework of the two potential scattering theories. Then, $V_{tot} = V_{nucl} + V_\gamma$ and electromagnetic interaction V_γ is taken as additional with respect to nuclear one V_{nucl}. In this case the amplitude of transition can be factorized in form:

$$f_{fi} = -\sum_s \left\langle \varphi_f^{(-)} \middle| \xi_s^{(+)} \right\rangle \cdot \left\langle \xi_s^{(+)} \middle| V_\gamma \middle| \Psi_i^{(+)} \right\rangle = -\sum D_{fs} M_{si}, \qquad (1)$$

where $\Psi_i^{(+)}$ is the wave-function of initial state, $\varphi_f^{(-)}$ - final state of nuclear cluster system, $\xi_s^{(+)}$ - a full set of normalized functions $\sum_s \left|\xi_s^{(+)}\right\rangle\left\langle\xi_s^{(+)}\right| = I$. The set $\xi_s^{(+)}$ should be chosen like two-body one describing free motion of clusters, where χ_s - the wave functions.

Further, the consideration will be restricted by the lowest power of V_γ. Then the gain factor - D will contain only nuclear interaction and can be expressed through off-shell nuclear amplitude $F_{fs} = \left\langle \varphi_f^{(-)} \middle| V_{nucl} \middle| \chi_s \right\rangle$ as follows:

$$D_{fs} = \left\langle \varphi_f^{(-)} \middle| \chi_s \right\rangle = \delta_{fs} - \frac{F_{fs}}{E_f - E_s + i0}. \qquad (2)$$

The matrix $M_{fi} = \left\langle \chi_f \middle| V_\gamma \middle| \varphi_i^{(+)} \right\rangle$ corresponds to probability of photodisintegration process on two free nuclear clusters.

In case of process $\gamma + A \to B_1 + B_2$ at low energy it would be enough to consider a model, when absorption of photon occurs one of the virtual clusters. As a result of this the nuclear system will be excited and dissociated on two free clusters (Fig. 1).

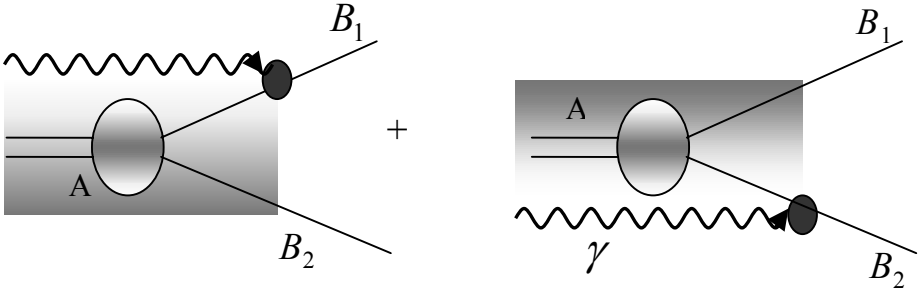


Fig.1. Process of photo-absorption with one of the virtual nuclear clusters

So, the amplitude of nucleus photodisintegration can be written in simple form:

$$f_{fi} = -M_{fi} - \Delta f_{fi}, \qquad (3)$$

where the adjustment

$$\Delta f_{fi} = \sum_{s} \frac{F_{fs} \cdot M_{si}}{E_f - E_s + i0}. \tag{4}$$

contains the cluster interaction in final state.

It is supposed that effective interaction between these clusters gives a result of ground bound energy of system corresponding to energy of initial nuclei. So, the bound energy of B_1 and B_2 cluster system is equal: $E_A = -\kappa^2 / 2\mu$, which may be small and $\kappa r_0 << 1$, where r_0 - radius of effective cluster interaction. Then, the wave function of this state can be written in form:

$$\left|\Psi_A\right\rangle = \left|\varphi(r)\chi\left(S_1 S_2; S_A\right)\chi\left(T_1 T_2; T_A\right)\right\rangle, \tag{5}$$

where

$$\varphi(r) = N \exp(-\kappa r)/r \tag{6}$$

looks like a main part of deuteron wave function at low energy. Here, S and T are spin-isospin quantum numbers, N – normalization constant.

It is clear that above-stated simplification is justified in case of initial photon energy E_γ is lower than energies of high level excitations.

Using perturbation theory M_{fi} can be calculated without difficulties [4,5] and this expression can be written formally in simple form:

$$M_{fi}^{\lambda} = \left(M_{fi}^{\lambda}\right)^{conv} + \left(M_{fi}^{\lambda}\right)^{spin}. \tag{7}$$

$\left(M_{fi}^{\lambda}\right)^{conv}$ is corresponding to interaction between photon and cluster charge currents, and $\left(M_{fi}^{\lambda}\right)^{spin}$ - interaction between owns magnetic moments of photon and clusters.

Choosing energy of initial photon and fixing its polarization one can make a selection of final cluster states and investigate their nuclear interaction at very low energy. In order to compare an experimental data with results of calculations it is possible to approximate nuclear interactions of clusters. These calculations may be as exact solutions of three-body problem or rough two-body approximations.

In case of rough approximation it is very convenient to use separable potentials to describe effective clusters interactions. Indeed, the separable potential

$V_{fs}^{L} = \left| \chi_f \right\rangle g \left\langle \chi_s \right|$ gives the amplitude in the exact formula $F_{fs}^{L} = \left| \chi_f \right\rangle \eta(E) \left\langle \chi_s \right|$, where

$$\eta(E) = \left[g^{-1} - \int \frac{d\vec{k} \left| \chi \right|^2}{E - E_s + i0} \right]. \qquad (8)$$

This approximation leads to success when cluster system has a resonant state, i.e. a pole of scattering amplitude is situated near physical region. A separable potential may be rank of $n \geq 1$ and its parameters are usually easy fixed, so to describe satisfactory experimental data at low energy.

Photo-disintegration of ^{6}Li to $d - \alpha$ cluster system

It is known that nucleus of ^{6}Li has expressly clustered structure. So, a reaction of ^{6}Li photodisintegration is suitable to study the $d - \alpha$ cluster system. The threshold of reaction $^{6}Li + \gamma \rightarrow d + \alpha$ is very small in nuclear scale: E_{th}=*1.47 MeV*. Next one is the deuteron break-up threshold at energy $E_{th,1}$=*3.7 MeV*. This allows using a representation (6) for nucleus of ^{6}Li as a rough approximation of ground state of d, α system.

Partial waves of $\left(M_{fi}^{\lambda} \right)$ are given by Fig.2. They can be taken as a background in respect of cluster interaction in final states. It should be noted that in the region E_{γ}<3 *MeV* all components of $\left(M_{fi}^{\lambda} \right)$ are dynamically suppressed excluding state with L=0 and S=1.

This fact can be taken into account as main argument to investigate S-wave resonance states of d,α system at very low energy. For example, it is possible to study $(d, \alpha)^{*}$ resonances with S=1, L=0 especially the state situated below Coulomb barrier.

In case of existence of the resonance the quantity Δf_{fi} come to the form

$$\Delta f_{fi} \approx \frac{M_{fi} E_0}{(E_f - E_0 + i\Gamma/2)} \tag{9}$$

where energy E_f is close to E_0 (the resonant energy $E_{res} = E_0 - i\Gamma/2$). Thus, it is a well-known Breit-Wigner's curve.

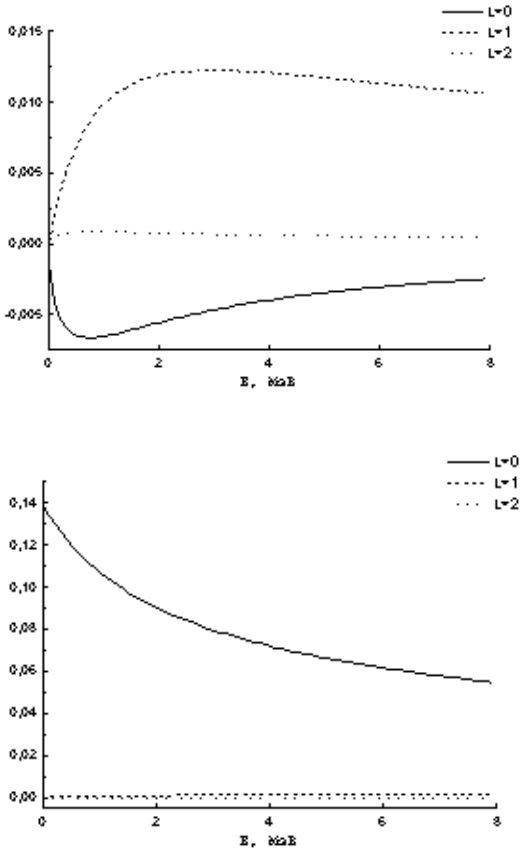


Fig. 2

Using effective potentials, which reproduce N,α scattering experimental data, parameters of d,α states can be obtained in frame of three-body calculations [4-7]. It is important to note that there are a lot of sets of potential parameters leading to satisfactory description of d,α scattering experiments at low energy [6-7]. Our calculations with some of these parameters give $(d,\alpha)^*$ resonance at energy below Coulomb barrier. But a position of the resonance is very sensitive to S-wave interactions in N,α systems.

Meanwhile, $(d,\alpha)^*$ resonances take placed at energy region above Coulomb barrier. So, the amplitudes of d,α scattering with L=2 have a distinctive resonant behavior (Fig.3). Due to three-body calculations this resonant state is obtained as stable one and depends mainly upon parameters of P-wave N,α resonances.

Conclusions

The investigation of nuclear clusters systems at energy below Coulomb barrier can be carried out using photodisintegration reactions. Using of electrodisintegration reactions can complicate them.

Existence of resonance states below Coulomb barrier, for instance, $(d,\alpha)^*$ resonance can give a new possibility in nuclear astrophysics. First of all, it may be interesting for x -Process and for nuclear equation of state. On other hand, using of three-body calculations in cluster physics it should be remarkable to compare them with experimental results.

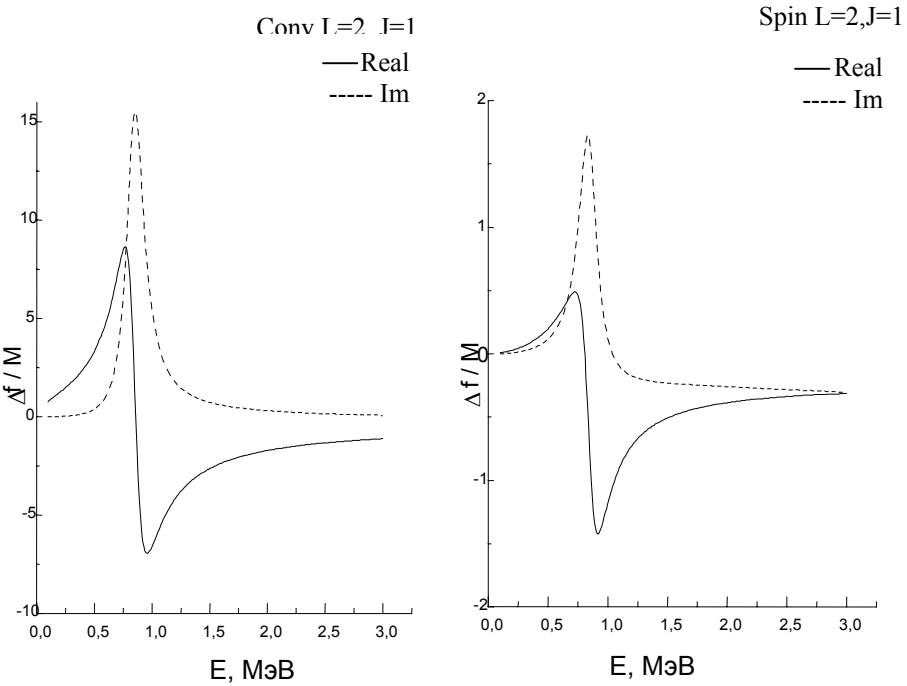


Fig.3

References

1. Proceeding of XIV European Conference on Few-Body Problems in Physics'93, Amsterdam. Few-Body Systems. Supplement 7, Springer-Verlag/Wien, 1994.
2. Efimov V. , Sov. J. Nucl. Phys., V 12, 589, 1971.
3. Pen'kov F., Takibayev N., Phys. At. Nucl., V 57, 1232, 1994
4. Takibayev N., Liventsova A., Lennik S. // Proc. III - International Conference on Nuclear and Radiation Physics, V 1, p 274, 2001, Almaty, Kazakhstan
5. Ajzenberg-Selove F. // Nucl.Phys.A, 1988, v. 490, p.5
6. Grueble W. at. al.// Nucl.Phys.A, 1975, v. 242, p.265
7. Kukulin V.I. at al.// Phys.Rev.C, 1998, v. 57, p.2462

THE QUARK BAG FORMFACTOR IN THE MODEL OF INDEPENDENT PARTICLES

Rasulov E.A.,

Baku State University, Azerbaijan, Baku

Abstract: Assuming existence of quark bags in nuclei we describe the formfactor of nuclei and structure function of inelastic scattering of triton in nuclei. By taking explicitly into the account the composite structure of hadrons and the effects of quark exchange some discrepancies between the theory and the data were recently pointed out were eliminated.

Introduction

A nucleus in the quark bag (cluster) model is described as a system of many bags-completely antisymmetrized with respect to the quark variables. Each bag consists of three quarks and of the nucleon quantum number, namely it has symmetry for spin-isospin, symmetry for colour and symmetry for radial part.

Using the light-cone formalism developed in ref.[1] where the formfactors are calculated starting from the good component of the current we obtained for the charge formfactor of the bag. The bag structure function contains the contribution of valence quarks and that of sea quarks. The sea component of the bag structure function is unknown but its contribution can be noticed at $z \leq 0.2$ only, where z is Bjorken variable. We assume for simplicity that distribution of u – and d – quarks in the quark bag are identical. In principle for bags with non-zero isospin it can be not true.

In the model of the formfactor under consideration no minimum in the $q > fm^{-1}$ region in contrast to standard models where only the nude on component is taken into consideration and the negative sign of the formfactor is predicted, to the right from the minimum. In this model the formfactor at large momentum transfers is positive, so the observed structure is most probably a deep minimum than a zero.

So in the framework of the hypothesis concerning the existence of quark bag in nuclei we managed to describe the behaviour of the formfactors of nuclei at large q and structure functions of nuclei. The parameters of quark distribution in the bag at $k >> k_0$ (the parameter k_0 may in principle be different for different bags) extracted from the data on formfactors and on deep inelastic scattering of nucleons on nuclei proved to be very close.

1. Quark bag model

A nucleus in the quark cluster model is described as a system of many clusters- completely anti symmetrized with respect to the quark variables. Each cluster consists of three quarks and he» the nucleon quantum number, namely it has symmetry for spin-isospin SU(4), symmetry for colour SU(3), and SU(3) symmetry for the radial part [2]

$$| N >=| q^3, [3]_{sr}\, S = 1/2, T = 1/2, [1^3]_c > \Phi \tag{1.1}$$

The radial wave function for a nucleon is taken to be a usual function of the oscillator –cluster model:

$$\Phi = \phi(r_1)\,\phi(r_2)\;\phi(r_3)\,\chi(R) \tag{1.2}$$

where r_1, r_2, r_3 and R are the internal and centre-of-mass coordinates, respectively.

$$R = \frac{(r_1 + r_2 + r_3)}{3}. \tag{1.3}$$

The wave function for the t-particle, |t> consisting of three clusters, is given by

$$| t >= \Gamma_t \left\{ (| N >^{(\sigma r c)})^3 \right\}_{s=0, r=o} \Phi(R_1)\Phi(R_2)\Phi(R_3)\ \text{x}$$
$$\text{x}\ \chi(\tilde{R}_1, \tilde{R}_2, \tilde{R}_3), \quad N = 1/\sqrt{< t \,|\, \Gamma_t \,|\, t >}, \tag{1.4}$$

where Γ_t is antisymmetrization operator among quarks in different clusters for the t -particle.

In eq.(1.2), we use a normalised gaussian:

$$\phi(r) = (\sqrt{\pi} R_h^2) \exp(-r^2 / R_h^2). \tag{1.5}$$

Then for wave function (1.4) we have:

$$| t >= \Gamma_t \left\{ (| N >^{(\sigma c)})^3 \right\} \frac{N}{(2\pi)^4} \quad \exp[-\frac{s_1^2 + s_2^2 + ... + s_9^2}{R_h^2} -$$
$$-4(\frac{1}{R_t^2} - \frac{1}{R_h^2})(R_1^2 + R_2^2 + R_3^2) \quad + i\vec{\xi}\,(\vec{s}_1^{\,2} + \vec{s}_2^{\,2} + ... + \vec{s}_9^{\,2})]. \tag{1.6}$$

Next, using the representation:

$$e^{-a^2 R_i^2} = (\sqrt{\pi / a})^{3/2} \int e^{-2i\vec{\beta}_i \vec{R}_i a - \beta^2 a} d^3\beta \tag{1.7}$$

we can write (1.6) in formally factorized form for space coordinates.

2. Formfactor of nuclei

The momentum distribution of quarks in multiquark bags is discussed usually in the framework of oscillator quark models [3]. Both these schemes are rather rough approximations. Indeed, the real quark distribution may differ from the one predicted by bag model due to a number of reasons such as smearing of bag boundaries, interaction of quarks accompanied by the emission of gluons and quark-antiquark pairs and also due to incomplete suppression of the vacuum fluctuations in the bag interior.

Let us assume as a first approximation that quarks in a multiquark bag embedded in the nuclear matter possess some equilibrium distribution. Such distribution can result from the vacuum pressure on the bag walls as well as from the interaction of quarks with each other and with the walls. The number of quark-antiquark pairs and gluons in the finite bag volume being large enough one can use for describing their momentum distribution the statistical physics methods.

We suppose for simplicity that *u*- and *d* – quark distribution in a multiquark bag for large *k* reads

$$\phi_u^2(k) = \phi_d^2(k) = N^2 e^{-k/k_0} \tag{2.1}$$

But it is reasonable to expect that difference in *u*- and *d*-quark distributions in the multiquark bag are much less pronounced than in the nucleon where they are due to the proximity to the kinematical boundary $z \to 1$.

The momentum *k* of the massless quark can be presented in terms of these variables as

$$|\mathbf{k}| = \frac{1}{2} m_b x \left[1 + \frac{1}{m_b^2} \left(\mathbf{q} - \frac{\mathbf{k}_\perp}{x} \right)^2 \right], \tag{2.2}$$

where **q** is transversal momentum, m_b - mass of the bag, *x* -the fraction of bag momentum.

The bag function F_b per nucleon can be expressed in the momentum distribution of quark in bag

$$F_b(z) = \frac{m_n}{m_b} \int \sum_i \phi_i^2(z, k_\perp) d^2 k_\perp , \tag{2.3}$$

where m_n -mass of the nucleon.

For the bag formfactor in the model in independent particles we obtain

$$F_b = \int \sum_i d^2 k_\perp \phi_i^*(\mathbf{k}_\perp, \mathbf{x}) \phi_i(\mathbf{k}_\perp + \mathbf{1} - x). \tag{2.4}$$

The integration over $d^2 k_\perp$ is done analytically

$$F_b = e^{-x} \left[1 - q_\perp \left(1 + q_\perp^2 / 4 m_b^2 \right)^{1/2} \right] / 2 m_b . \tag{2.5}$$

In our model the formfactor at large momentum transfers is positive, so the observed structure is most probably a deep minimum rather than a zero.

According to the Glauber theory [4] the scattering amplitude of a composite object with A constituents on a system of B constituents is determined by the following expression:

$$F_{AB}(q) = \frac{ik}{2\pi} \int d^2 b e^{i\vec{q}\vec{b}} < \psi_A \psi_B | [1 - \prod_{i=1}^{A} \prod_{j=1}^{B} (1 - \gamma(\mathbf{b} - \mathbf{k}_\perp + \mathbf{r}_j))] | \psi_A \psi_B > \tag{2.6}$$

where ψ_A and ψ_B are wave functions of the target-projectile systems, s_i, r_j are the coordinates of the constituents of projectiles and targets within the plane of the impact parameter b. Inserting (1.4) into (2.6) and using parameterisation

$$\gamma(\mathbf{b}) = \exp(-b^2 / 2B) \tag{2.7}$$

we have direct integral:

$$F_{p,t}(q) = \frac{ik}{2\pi} \exp(q^2 R_h^2 / 9) \sum_{i>j>m>} N_i N_j N_m \frac{N\tilde{N}}{Det\Re(i,j,m)} \text{ x}$$

$$\text{x } (\gamma^{(Q_i + Q_j + Q_m)} \exp[-\frac{q^2}{3} \frac{DetQ(i,j,m)}{Det\Re(i,j,m)}], \tag{2.8}$$

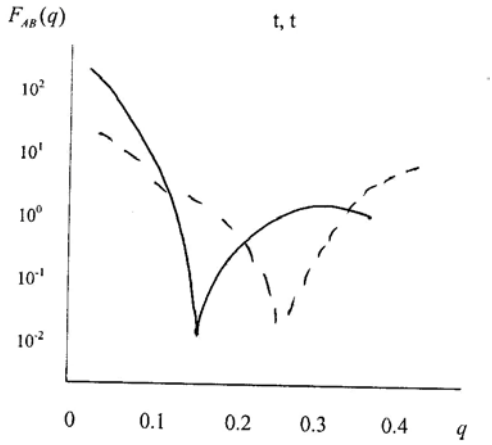
where

$$Q(i,j,m) = \begin{pmatrix} T_i 000 Q_i G_1 \\ 0 T_j 00 Q_j G_2 \\ 00 T_m 0 Q_m G_3 \end{pmatrix},+$$

The structure of matrices T_i , G_i , Q_i and N_i are given in the Appendix.

Conclusion

We show that that the exiting experimental data can be described in a unified way provided



The figure compares the differential cross section calculated from eq. (2.8) with the experimental data for (t,t) scattering. The solid line corresponds to the cross section calculated using eq. (2.8). The dashed line corresponds to the cross section calculated in ref.[5] for the case of point-like nucleons.
The figure shows that the quark cluster model gives good agreement and the Glauber approach extended to nucleus-nucleus scattering leads to satisfactory consistency of the calculated cross sections and their t-dependence with those obtained experimentally.

Our results can be summarized as follows:

- -Taking into accounts the quark structure of nucleons we have significantly improved the description of the data, thus restoring the agreement between the theory and the experiment;

- The quark exchange effects is not negligible for this case.
- Taking into account the quark structure of nucleons we have significantly improved the description of the data, thus restoring the agreement between the Glauber theory and the experiment.
- The quark exchange effect is not negligible for the this case.

Appendix

$$Q_i = q_i \frac{1}{2B};\ q_1 = \begin{pmatrix} 000 \\ 000 \\ 000 \end{pmatrix};\ q_2 = \begin{pmatrix} 100 \\ 000 \\ 000 \end{pmatrix};\ q_3 = \begin{pmatrix} 100 \\ 010 \\ 000 \end{pmatrix};\ q_4 = \begin{pmatrix} 110 \\ 000 \\ 000 \end{pmatrix};\ q_5 = \begin{pmatrix} 100 \\ 100 \\ 000 \end{pmatrix};\ q_6 = \begin{pmatrix} 100 \\ 010 \\ 001 \end{pmatrix};$$

$$q_7 = \begin{pmatrix} 110 \\ 001 \\ 000 \end{pmatrix};\ q_8 = \begin{pmatrix} 110 \\ 010 \\ 000 \end{pmatrix};\ q_9 = \begin{pmatrix} 100 \\ 100 \\ 010 \end{pmatrix};\ G_1 = \begin{pmatrix} 100 \\ 100 \\ 100 \end{pmatrix};\ G_2 = \begin{pmatrix} 010 \\ 010 \\ 010 \end{pmatrix};\ G_3 = \begin{pmatrix} 001 \\ 001 \\ 001 \end{pmatrix};$$

$$T_i = \begin{pmatrix} \frac{1}{R_h^2}00 \\ 0\frac{1}{R_h^2}0 \\ 00\frac{1}{R_h^2} \end{pmatrix} + Q_i;\quad \Re(i,j,m) = \begin{pmatrix} t \\ t \\ Q(i,j,m) \end{pmatrix};\quad t = \left(\frac{1}{R_h^2} \frac{1}{R_h^2} \frac{1}{R_h^2} \right).$$

$N_1 = N_9 = 1$; $N_2 = N_7 = 9$; $N_3 = N_5 = N_8 = -18$; $N_4 = N_6 = 3$.

References

1. Abdulvahabova S.K.//First International Conference on Technical & Physical Problems in Power Engineering, Baku, 2002, p.452
2. Blagojevic M.,Lalovic D..// Prog. Theor. Phys.,1974, 51, p.1152
3. Robson R //Progr. in Part. and Nucl. Phys. 1982, 8, p.257
4. Glauber R.G.//In:Lecture in "Theoretical Physics" New-York,1959, p.315
5. AbdulvagabovaS.K.// " Physics",1995 N 1, p.20

THE H_N METHOD FOR SOLVING LINEAR TRANSPORT EQUATION: THEORY AND APPLICATIONS

Tezcan C., Kaşkaş A. and Güleçyüz M. Ç.

Ankara, Turkey

Introduction

In F_N method [1,2,3,4], the exit distributions, which were obtained from the integro-differential form of the neutron transport equation were considered for both half-space and slab problems. These equations were multiplied by singular eigenfunctions of the method of elementary solutions [5,6,7] and integrated over full range of $\mu \varepsilon [-1,+1]$. It is well-known that the method yields concise equations that can be solved numerically even more efficiently and is based on an equal spacing scheme of the singular eigenvalues.

Integro-differential form of the one-speed neutron transport equation for half-space problems is,

$$\mu \frac{\partial \Psi(x,\mu)}{\partial x} + \Psi(x,\mu) = c\int_{-1}^{+1} f(\mu,\mu')\,\Psi(x,\mu')\,d\mu' + s(x,\mu) \qquad (1)$$

Here $\Psi(x,\mu)$ is the neutron angular density corresponding to the source function $s(x,\mu)$. c is the mean number of secondary neutrons per collision. μ is in optical units means the direction cosine of the propagating neutrons. $f(\mu,\mu')$ is the scattering function and is normalised to unity.

Placzek lemma [6,8] states that any finite medium problem can be extended to infinite medium for which suitable distribution of neutron sources is located at the position of the boundary of finite medium. Therefore Eq.(1) for isotropic scattering is related to the infinite medium problems defined by

$$\mu \frac{\partial \Psi_1(x,\mu)}{\partial x} + \Psi_1(x,\mu) = \qquad (2)$$

$$= \frac{c}{2}\int_{-1}^{+1} \Psi_1(x,\mu')\,d\mu' + s(x,\mu)H(x) + \mu\,\Psi(0,\mu)\delta(x)$$

where the following equation for the infinite medium angular flux

$$\Psi_1(x,\mu) = H(x)\Psi(x,\mu)$$

$$H(x) = \begin{cases} 1 & for \quad x\varepsilon(0,\infty) \\ 0 & otherwise \end{cases} \tag{3}$$

satisfies

$$\Psi_1(x,\mu) = \int_{-1}^{1} d\mu_0 \int_0^{\infty} dx_0\, G(x_0 \to x;\mu_0 \to \mu) \begin{bmatrix} H(x_0)s(x_0,\mu_0) + \\ +\mu_0\Psi(0,\mu_0)\delta(x_0) \end{bmatrix} \tag{4}$$

Where $G(x_0 \to x;\mu_0 \to \mu)$ represents the infinite medium Green's function and denotes to angular flux at x in the direction μ in an infinite medium produced by a plane source at x_0 emitting in the direction μ_0 and is the solution of the following integro-differential equation [5].

$$\frac{\partial G\left(x_0 \to x;\mu_0 \to \mu\right)}{\partial x} + G(x_0 \to x;\mu_0 \to \mu) = \\ = \frac{c}{2}\int_{-1}^{1} G(x_0 \to x;\mu_0 \to \mu')d\mu' + \delta(x - x_0)\delta(\mu - \mu_0) \tag{5}$$

The infinite medium Green's function as mentioned above can be used to describe solutions to problems including finite media. Equations (3) , (4) lead to

$$\Psi(x,\mu) = \int_{-1}^{1} d\mu_0 \begin{bmatrix} \int_0^{\infty} dx_0\, G(x_0 \to x;\mu_0 \to \mu)s(x_0,\mu_0) + \\ +G(x_0 \to x;\mu_0 \to \mu)\mu_0\Psi(0,\mu_0) \end{bmatrix}. \tag{6}$$

The infinite medium Green's function in terms of singular eigenfunctions of the method of elementary solutions is as the following form [5] for the isotropic scattering

$$G^{\mp}(x_0 \to x;\mu_0 \to \mu) = \frac{\varphi(\mp\nu_0,\mu)\,\varphi(\mp\nu_0,\mu_0)}{N(\nu_0)} e^{-\frac{|x-x_0|}{\nu_0}} + \\ + \int_0^1 \frac{\varphi(\mp\nu,\mu)\,\varphi(\pm\nu,\mu_0)}{N(\nu)} e^{-\frac{|x-x_0|}{\nu}} d\nu \tag{7}$$

Where $\pm\nu_0$ are the two discrete eigenvalues with eigenfunctions $\varphi(\pm\nu_0,\mu)$ and ν are the continuum eigenvalues on the range [-1,+1] with eigenfunctions $\varphi(\nu,\mu)$.

$$\varphi(\pm\nu_0,\mu)=\pm\frac{c\nu_0}{2}\frac{1}{\pm\nu_0-\mu} \quad , \quad \varphi(\nu,\mu)=\frac{c\nu}{2}P\frac{1}{\nu-\mu}+\lambda(\nu)\delta(\nu-\mu) \tag{8}$$

The normalization constants corresponding to discrete and continuum modes respectively are

$$N(\pm\nu_0)=\pm\frac{c\nu_0^3}{2}\left[\frac{c}{\nu_0^2-1}-\frac{1}{\nu_0^2}\right] \quad , \quad N(\nu)=\nu\left\{\left(1-c\nu\tanh^{-1}\nu\right)^2+\frac{c^2\pi^2\nu^2}{4}\right\} \tag{9}$$

$$\lambda(\nu)=1-c\nu\tanh^{-1}\nu\ . \tag{10}$$

For finite slab problems the corresponding equation for infinite medium is

$$\begin{aligned}\mu\frac{\partial\Psi_1(x,\mu)}{\partial x}+\Psi_1(x,\mu)&=\frac{c}{2}\int_{-1}^{+1}\Psi_1(x,\mu')\,d\mu'+s(x,\mu)H^*(x)\\&+\mu\Psi(x,\mu)\left[\delta(x+a)-\delta(x-a)\right]\end{aligned} \tag{11}$$

where

$$\Psi_1(x,\mu)=H^*(x)\Psi(x,\mu) \tag{12}$$

$$H^*(x)=\begin{cases}1 & for \quad x\,\varepsilon\,[-1,+1]\\ 0 & otherwise\end{cases}$$

The function $\Psi_1(x,\mu)$ in Eq.(11) as in Eq.(4) is given by

$$\Psi_1(x,\mu)=\int_{-1}^{1}d\mu_0\int_0^{\infty}dx_0\begin{bmatrix}G(x_0\to x;\mu_0\to\mu)s(x_0,\mu_0)+\\+G(-a\to x;\mu_0\to\mu)\mu_0\Psi(-a,\mu_0)-\\-G(a\to x;\mu_0\to\mu)\mu_0\Psi(a,\mu_0)\end{bmatrix} \tag{13}$$

For $x\,\varepsilon\,[-a,+a]$ using Eq.(12), Eq.(13) becomes

$$\begin{aligned}&\Psi_1(x,\mu)=\int_{-1}^{1}d\mu_0\int_0^{\infty}dx_0\,G(x_0\to x;\mu_0\to\mu)s(x_0,\mu_0)\\&-\int_0^1 d\mu_0 G(-a\to x;-\mu_0\to\mu)\mu_0\Psi(-a,-\mu_0)+\\&+\int_0^1 d\mu_0 G(-a\to x;\mu_0\to\mu)\mu_0\Psi(-a,\mu_0)+\\&+\int_0^1 d\mu_0 G(a\to x;-\mu_0\to\mu)\mu_0\Psi(a,-\mu_0)-\\&-\int_0^1 d\mu_0 G(a\to x;\mu_0\to\mu)\mu_0\Psi(a,\mu_0)\end{aligned} \tag{14}$$

I. The Hybrid (H_N) Method

In the method that we introduce here, the exit distributions as in F_N method obtained from the angular singular integral equations as a result of Placzek lemma are used. Expansions of the angular distributions are considered as in the F_N and C_N methods [9-12]. Infinite medium Green function and the singular eigenfunctions of the elementary solutions together with the calculation procedure as in [12-16] are also used. Therefore we call its name as Hybrid (H_N) method.

A. Half – space Problems

For an half-space $0 \le x \le \infty$ from Eq.(6), the exit distribution at $x = 0$ can be written as

$$\Psi(0,-\mu) = \int_{-1}^{1} d\mu_0 \int_0^{\infty} dx_0 G(x_0 \to 0; \mu_0 \to -\mu) s(x_0, \mu_0) +$$

$$+ \int_0^1 d\mu_0 G(0 \to 0^+; \mu_0 \to -\mu) \mu_0 \Psi(0, \mu_0) -$$

$$- \int_0^1 d\mu_0 G(0 \to 0^+; -\mu_0 \to -\mu) \mu_0 \Psi(0, -\mu_0) \qquad \mu > 0 \qquad (15)$$

B. Finite Slab Problems

For a slab thickness *2a*, $-a \le x \le a$ from Eq.(14), the exit distributions at $x = \pm a$ respectively are

$$\Psi(-a,-\mu) = \int_{-1}^{1} d\mu_0 \int_0^{\infty} dx_0 \, G(x_0 \to -a; \mu_0 \to -\mu) s(x_0, \mu_0)$$
$$- \int_0^1 d\mu_0 G(-a \to -a^+; -\mu_0 \to -\mu) \mu_0 \Psi(-a, -\mu_0) +$$
$$+ \int_0^1 d\mu_0 G(-a \to -a^+; \mu_0 \to -\mu) \mu_0 \Psi(-a, \mu_0) + \qquad (16)$$
$$+ \int_0^1 d\mu_0 G(a \to -a; -\mu_0 \to -\mu) \mu_0 \Psi(a, -\mu_0) -$$
$$- \int_0^1 d\mu_0 G(a \to -a; \mu_0 \to -\mu) \mu_0 \Psi(a, \mu_0) \quad , \qquad \mu > 0$$

$$\Psi(a,\mu) = \int_{-1}^{1} d\mu_0 \int_0^{\infty} dx_0 \, G(x_0 \to a; \mu_0 \to \mu) s(x_0, \mu_0)$$
$$- \int_0^1 d\mu_0 G(-a \to -a^+; -\mu_0 \to \mu) \mu_0 \Psi(-a, -\mu_0) +$$
$$+ \int_0^1 d\mu_0 G(-a \to a; \mu_0 \to \mu) \mu_0 \Psi(-a, \mu_0) + \qquad (17)$$
$$+ \int_0^1 d\mu_0 G(a \to a^-; -\mu_0 \to \mu) \mu_0 \Psi(a, -\mu_0) -$$
$$- \int_0^1 d\mu_0 G(a \to a^-; \mu_0 \to \mu) \mu_0 \Psi(a, \mu_0) \quad , \qquad \mu > 0$$

One may consider the entering distributions together with exit distributions.

II. Applications

A. Half-space Albedo Problem

The problem is to obtained the angular neutron density everywhere in a source free half-space $0 \le x \le \infty$ for a beam incident on the surface at *x=0*, that is for;

$$s(x,\mu) = 0 \tag{18}$$

$$\Psi(0,\mu) = \mu^{\gamma} \quad , \quad \mu > 0 \tag{19}$$

where $\gamma = 0, 1, 2....$, using the representation

$$\Psi(0,-\mu) = \sum_{\alpha=0}^{N} a_{\alpha}\mu^{\alpha} \quad , \quad \mu > 0 \tag{20}$$

multiplying the exit distribution in Eq.(6) by μ^{m+1} and integrating over $\mu\ \varepsilon\ [0,1]$, we obtain

$$\sum_{\alpha=0}^{N} a_{\alpha} T_{m\alpha} = R_{m\gamma} \tag{21}$$

where

$$T_{m\alpha} = \frac{1}{m+\alpha+2} + \frac{c^2 \nu_0^{\,2}}{4N(\nu_0)} A_m(\nu_0) A_{\alpha}(\nu_0) + \frac{c^2}{4} I^{AA}_{m,\alpha} \tag{22}$$

$$R_{m\gamma} = \frac{c^2 \nu_0^{\,2}}{4N(\nu_0)} A_m(\nu_0) B_{\gamma}(\nu_0) + \frac{c^2}{4} I^{AB}_{m,\gamma} \tag{23}$$

$$A_{\alpha}(\nu_0) = \frac{2}{c\nu_0}\int_0^1 \mu^{\alpha+1}\varphi(-\nu_0, \mu)d\mu = \frac{1}{\alpha+1} - \nu_0\, A_{\alpha-1}(\nu_0) \tag{24}$$

$$A_0(\nu_0) = 1 - \nu_0 \log\left(1 + \frac{1}{\nu_0}\right) \tag{25}$$

$$B_{\alpha}(\nu_0) = \frac{2}{c\nu_0}\int_0^1 \mu^{\alpha+1}\varphi(\nu_0, \mu)d\mu = \nu_0\, B_{\alpha-1}(\nu_0) - \frac{1}{\alpha+1} \tag{26}$$

$$B_0(\nu_0) = \frac{2}{c} - 1 - \nu_0 \log\left(1 + \frac{1}{\nu_0}\right) \tag{27}$$

$$I^{AA}_{m\,\alpha} = \int_0^1 \frac{\nu^2\, A_m(\nu) A_{\alpha}(\nu)}{N(\nu)}\, d\nu \tag{28}$$

Albedo is given by

$$A^* = (\gamma+2)\int_0^1 \Psi(0,-\mu)\,\mu\,d\mu = (\gamma+2)\sum_{\alpha=0}^{N}\frac{a_\alpha}{\alpha+2} \tag{29}$$

B. Slab Albedo Problem

As in previous part we consider the finite slab thickness *2a* defined by,

$$s(x,\mu) = 0 \tag{30}$$

$$\Psi(-a,\mu) = \mu^\gamma \quad , \quad \mu > 0 \tag{31}$$

$$\Psi(a,-\mu) = 0 \quad , \quad \mu > 0 \tag{32}$$

Where $\gamma = 0,1,2\ldots$Multiplying the exit distributions in Eqs. (12), (13) by μ^{m+1} and integrate over $\mu\ \varepsilon\ [0,1]$, using the expansions

$$\Psi(-a,-\mu) = \sum_{\alpha=0}^{N} a_\alpha \mu^\alpha \quad , \quad \mu > 0 \tag{33}$$

$$\Psi(a,\mu) = \sum_{\alpha=0}^{N} b_\alpha \mu^\alpha \quad , \quad \mu > 0 \tag{34}$$

we have

$$\begin{aligned}&\sum_{\alpha=0}^{N} a_\alpha\left[\frac{1}{m+\alpha+2} + \frac{c^2\nu_0^{\,2}}{4}\frac{A_m(\nu_0)\,A_\alpha(\nu_0)}{N(\nu_0)} + \frac{c^2}{4}I^{AA}_{m\alpha}\right] + \\ &+ \sum_{\alpha=0}^{N} b_\alpha\left[\frac{c^2\nu_0^{\,2}}{4}\frac{A_\alpha(\nu_0)\,B_m(\nu_0)\exp(-\frac{2a}{\nu_0})}{N(\nu_0)} + \frac{c^2}{4}I^{ABE}_{\alpha m}\right] = \\ &= \frac{c^2\nu_0^{\,2}}{4}\frac{A_m(\nu_0)\,B_\beta(\nu_0)}{N(\nu_0)} + \frac{c^2}{4}I^{AB}_{m\gamma}\end{aligned} \tag{35}$$

and

$$\sum_{\alpha=0}^{N} a_\alpha \left[\frac{c^2 {\nu_0}^2}{4} \frac{A_\alpha(\nu_0)\, B_m(\nu_0) \exp(-\frac{2a}{\nu_0})}{N(\nu_0)} + \frac{c^2}{4} I_{\alpha m}^{ABE} \right]$$

$$+ \sum_{\alpha=0}^{N} b_\alpha \left[\frac{1}{m+\alpha+2} + \frac{c^2 {\nu_0}^2}{4} \frac{A_\alpha(\nu_0)\, A_m(\nu_0)}{N(\nu_0)} + \frac{c^2}{4} I_{\alpha m}^{AA} \right] \tag{36}$$

$$= \frac{c^2 {\nu_0}^2}{4} \frac{B_m(\nu_0)\, B_\beta(\nu_0) \exp(-\frac{2a}{\nu_0})}{N(\nu_0)} + \frac{c^2}{4} I_{m\gamma}^{BBE}$$

Now using Eqs. (31), (32) we can compute the albedo

$$A^* = (\gamma+2)\int_0^1 \Psi(-a,-\mu)\, \mu\, d\mu = (\gamma+2) \sum_{\alpha=0}^{N} \frac{a_\alpha}{\alpha+2} \tag{37}$$

and the transmission factor.

$$B^* = (\gamma+2)\int_0^1 \Psi(a,\mu)\, \mu\, d\mu = (\gamma+2) \sum_{\alpha=0}^{N} \frac{b_\alpha}{\alpha+2} \tag{38}$$

Conclusions

It is well known that C_N method solves the integral equations of Fredholm type (third form the transport equation) obtained from Placzek lemma. These equations are related with the angular flux at the boundary of the medium. F_N method which is a modified version of the C_N method solves integro-differential form of the linear transport equation and is based on equal spacing scheme of the singular eigenvalues. In C_N method the infinite medium Green's function obtained by the Fourier transform technique is used. On the other hand in F_N method the infinite medium Green's function and the exit distributions in terms of the singular eigenfunctions of the method of elementary solutions are used.

In the new approach for solving the third form of the transport equation [12], we have used the infinite medium Green's function in terms of singular eigenfunctions in C_N equations.

Here our aim using the exit distributions obtained by Placzek lemma is to follow the same procedure as in “the new approach" [12]. That is,we multiply the exit distributions with the powers of μ and integrate over the appropriate regions. For example for the albedo problem we multiply $\Psi(0,\mu), \mu > 0$ by μ^{m+1} and integrate over [-1,0] or $\Psi(0,-\mu), \mu > 0$ by μ^{m+1} and integrate over [0,1]. The same procedure can also be used for a slab for the exit distributions $\Psi(a,\mu)$ and $\Psi(-a,-\mu)$. We see that the analytical results for the albedo and slab albedo

problems are the same with the results derived in our recent publications [12,15,16]. Therefore here we report the same, fast convergent numerical results. The accuracy of our numerical result, even in the lowest order is shown in tables.

Table 1 Half-space albedo for γ=0

N	c=0,1	c=0,2	c=0,3	c=0,4	c=0,5	c=0,6	c=0,7	c=0,8	c=0,9
0	0,0217	0,04628	0,07448	0,1074	0,1467	0,1950	0,2571	0,3428	0,4794
1	0,0217	0,04627	0,07445	0,1074	0,1466	0,1947	0,2566	0,3419	0,4780
2	0,0217	0,04627	0,07445	0,1073	0,1466	0,1947	0,2566	0,3419	0,4780
3	0,0217	0,04827	0,07445	0,1073	0,1466	0,1947	0,2566	0,3419	0,4780
4	0,0217	0,04627	0,07445	0,1073	0,1466	0,1947	0,2566	0,3419	0,4780
Exact	0,0217	0,04626	0,07445	0,1073	0,1465	0,1947	0,2566	0,3419	0,4780

Table 2 Half-space albedo problem for c = 0,8 and γ = 0

N	F_N	C_N (First kind of Eq.)	C_N (Second kind of Eq.)	H_N
0	0,3284	0,3489	0,3428	0,3428
1	0,3503	0,3415	0,3419	0,3419
2	0,3442	0,3419	0,3419	0,3419
3	0,3420	0,3419	0,3419	0,3419
4	0,3420	0,3419	0,3419	0,3419
5	0.3419	0,3419	0,3419	0,3419
Exact		0,3419		

Table 3 Albedo and transmission factor for c = 0,8, $2a$ = 1 and γ = 0.

	Albedo			Transmission		
N	F_N	C_N (System 2)	H_N	F_N	C_N (System 2)	H_N
0	0,2557	0,2794	0,2794	0,4502	0,4158	0,4158
1	0,2896	0,2802	0,2802	0,4142	0,4163	0,4163
2	0,2813	0,2802	0,2802	0,4189	0,4162	0,4162
3	0,2803	0,2802	0,2802	0,4161	0,4162	0,4162
4	0,2803	0,2802	0,2802	0,4161	0,4162	0,4162
Exact		0,2802			0,4162	

References

1. Siewert CE,. Astrophysics and Space Science 1978; 58:131.
2. Siewert CE and Benoist P, Nucl. Sci. Engng 1979;69:156.
3. Grandjean P and Siewert CE, Nucl. Sci. Engng 1979;69:161.
4. Garcia RDM., Transp. Theory Stat. Phys. 1985;14(4):391.
5. Case K.M and Zweifel P.F, Linear Transport Theory, Addition-Wesley, Reading Mass.1967.
6. Bell GI and Glastone S, Nuclear Reactor Theory,Van Nostrand-Reinhold, New York, N.Y. 1972.
7. Case K.M, Ann Phys., 1960;9:1.
8. Case K.M, Hoffmann FD and Placzek G, Introduction to the Theory of Neutron Diffusion, Vol I, Los Alamos, 1953.
9. Benoist P and Kavenoky A, Nucl. Sci. Engng 1968;32:225.
10. Kavenoky A, Nucl. Sci. Engng 1978;65:209.
11. Kavenoky A, Nucl. Sci. Engng 1978;65:514.
12. Tezcan C, Güleçyüz M. Ç. and Erdoğan F, J Quant Spectrosc Radiat Transfer 1996; 55: 251.
13. Erdoğan F., Güleçyüz M.Ç., Kaşkaş A and Tezcan C, Ann Nucl Energy 1996;23:533.
14. Güleçyüz M. Ç., Kaşkaş A. and Tezcan C., J Quant Spectrosc Radiat Transfer 2001; 70,55.
15. Kaşkaş A, Gülecyüz M Ç and Tezcan C, Ann Nucl Energy 1996;23(17):1371.
16. Kaşkaş A, Tezcan C and Güleçyüz M C, J Quant Spectrosc Radiat Transfer 2000;66:519.

THE SIMPLE METHOD FOR ADAPT TIME SAMPLING OF THE ANALOG SIGNAL

M.K. Babaev, A.S. Baigubecov, Yu.G. Kalinin, I.S. Martyanov, T.Kh. Sadykov N.N. Zastrozhnova

Institute of Physics and Technology, MES RK, Almaty, Kazakhstan

It is most simple the method of the analog signals time sampling by means of the sampling theorem (Kotelnikov- Shannon theorem) (see, e.g., ref. [1]). In accordance with it band-limit signal is determined completely by the set his momentary significance, which are periodical. In order to have faithfully reproduced of the signal at the highest frequencies of the spectra, the number of the samples will be enough big. On the other hand, very small the sampling intervals lead to the correlation date. This reduce efficient of the information in view of appearance superfluous of the information.

It is well known that in accordance with the sampling theorem the speed of the samples on the band-limit signals must to satisfy to the Nyquist‘s criterion $f_c > 2f_m$, where f_c is the frequency of the sampling, f_m is the highest frequency of the signal spectra. The lower frequency of the samples for the functions with the band-limit spectra is $2f_m$ (the Nyquist‘s frequency). For reduction of the number samples it is necessary to lower the frequency of the samples for the permissible limit in order avoid of the errors due to ”masking” of the frequencies.

The theoretical limit with double samples for the period change of the signal put into practice is use very seldom and the lower frequency of the samples is depending on specific of the applications and the duration of the research process.

Usually the frequency of the samples is 2,5-5 more than highest frequency of the signal spectra. This is result of the compromise between aspiration to raise the frequency samples with the purpose to increase accurate reproduced of the initial signal and to lower the bandwidth of the frequencies. In principle are three limit cases:

– $1/T=2f_m$ - it is ideal case, by which errors at the reproduction of the initial signals is absent.

– $1/T>2f_m$ - it is necessary expansion the bandwidth of the frequencies.

– $1/T<2f_m$ - it is the reverse case. There is “masking” of the frequencies because of the spectra are crossed.

A simple method of the analog signals adapt time sampling and quantization has been developed [2] - than more is speed of the signal change, so much the short of the sampling intervals. Thus this time sampling is nonlinear. This allow, assuming that $f_c > 2f_m$ for the highest frequency f_m of the signal or for

the minimal sample interval to provide fulfillment the same criterion and for the frequencies smaller then f_m. At the same time the superfluous information at the lower frequencies of the spectra increase not to be, since with decrease of the frequency is increase the sampling intervals. At the Fig.1 is shown the block diagram of the schematic for the realization of the adapt sampling, at the Fig.2 is shown the time diagram of the voltages in the circuit.

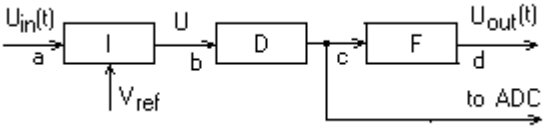


Fig. 1

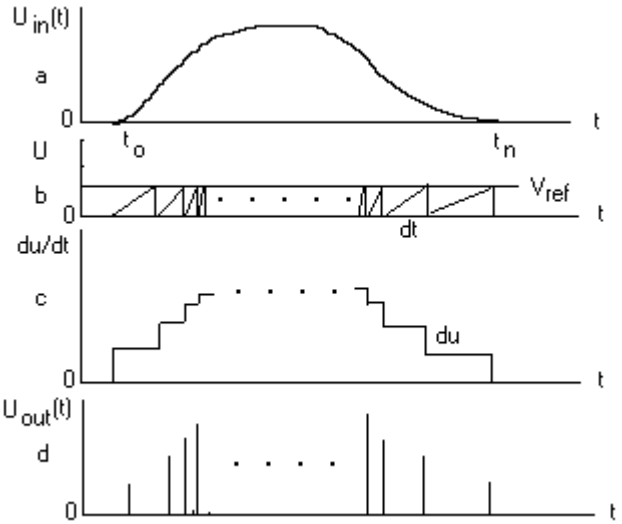


Fig. 2

The algorithm of the processing signals is: the unit “I” is integrated of the input signal. By arrived of the unit output voltage U to the reference voltage V the integrated capacitor of the unit “I” is discharged linearity to the noughted level of the voltage (U=0, see Fig.2). Further is repeated in series these cycles of the sampled integration and are continued theirs to the time moment t_n. At the same time with beginning first integration cycle are differentiated by the unit “D” output voltage and are formed the output pulses in the samples points by the unit “F”. Since the durations of the sampling intervals T are depend on both the values of the

reference voltage V and the integral constant, the latest are choose according to the Nyquist‘s criterion for the minimal sampling intervals.
Thus, the sampling speed is proportional to the signal change speed, by this the superfluous information at the lower frequencies of the spectra is absent.

It should be noted here, that at the same time is implementing quantization of the signal level, and what‘s more the value dU of the quantum is proportional to the signal change.

Thus, the amplitude quantizing the same as the time sampling is nonlinear too. The unit “D” output voltage is sent to the input of the analog-to-digital converter (ADC) and besides there the special pulse stretcher for stretching of the signal pulse peaks is absent.

References

1. J. Max. Methodes et techniques de traitement du signal et applications aux mesures, physiques. V1, p.67. Masson. Paris, New-York. 1981.
2. I.S.Mart‘yanov. The method of the analog signal time sampling. Patent KZ No 5824. Bull. Invent. No 1, 1998.

THE STATIONARY GENERATOR OF THE TECHNETIUM - 99M.

U.T. Ashrapov, S. Khujaev

Institute of Nuclear Physics of the Academy of Sciences of Republic Uzbekistan

A radionuclide of technetium – 99m is one of the basic radionuclide of nuclear medicine, which typically is obtained from its generator [1,2,3]. The Tc-99m generator is manufactured at nuclear centers and then transferred to clinics. At places Tc-99m is eluted in the form of pertechnetatum
(Tc – 99m) sodium solution. In large cities with numerous clinics for providing of clinics by ready pertechnetatum (Tc – 99m) sodium solution the stationary generator technetium – 99m as alternative type of generator can be chosen. In the latter case a necessary product of pertechnetatum (Tc – 99m) sodium solution can be delivered to the nuclear medicine clinics by centralize way.

At the Institute of Nuclear Physics the technological process of the flow diagram for manufacturing of stationary generator Tc – 99m had been developed which is based on sorption of Mo-99 on aluminum oxide with activity of maternal Mo-99 nuclide is not less than 10 Curie per generator.

The maternal nuclide Mo-99 was been obtained by the thermal neutrons irradiation of molybdenum trioxide enriched on Mo-98 in 98 % by the nuclear reaction Mo-98 (n, γ) Mo-99 at the research reactor WWR-SM.

The Mo-99 maternal nuclide sorption processes on aluminum oxide and elution processes of

Tc – 99m from an equilibrium mixture Mo-99/Tc-99m were investigated.

The technetium – 99m stationary generator is sterile glass column ($\varnothing$ = 33 mm, h = 330 mm), which is contain of the aluminum oxide with sorpted of Mo-99 within and supplied with communications system for eluant solution feeding and for pertechnetatum (Tc – 99m) sodium solution elution. The aluminum oxide weight is 110 g, sorbent layer height is 280 mm. For sorption of Mo-99 on the aluminum oxide through the generator column was passed of izopolymolybdatum solution with content of molybdenum 20 mg/ml with flow rate is
5-6 (ml $cm^{-2}min^{-1}$).

The molybdenum sorption was more than 99 % at sorbent loading average is no more 30 mg/g.

The pertechnetatum (Tc – 99m) sodium solution from experimental stationary generator was been the following parameters: eluant volume is 100 ml, volumetric activity is not less than 70 mCi/ml, pH = 4,5, radiochemical purity is not less than 99,9 %, content of Mo-99 in relation to Tc – 99m is no more $0{,}6 \cdot 10^{-4}$ %.

Experimental

The target of molybdenum trioxide enriched on Mo-98 was irradiated in regular channel of reactor WWR-SM during 200 hours by the thermal neutron flux $5 \cdot 10^{13}$ neutron / sm^2 sec. Under these conditions the specific activity of the Mo-99 was 6 Ci/g. The irradiated target was dissolved in 1 N NaOH solution, than was acidulated to pH=3-4. Izopolymolybdatum solution was dynamic sorpted on aluminum oxide of stationary generator column. The aluminum oxide was specially transformation to the anion form.

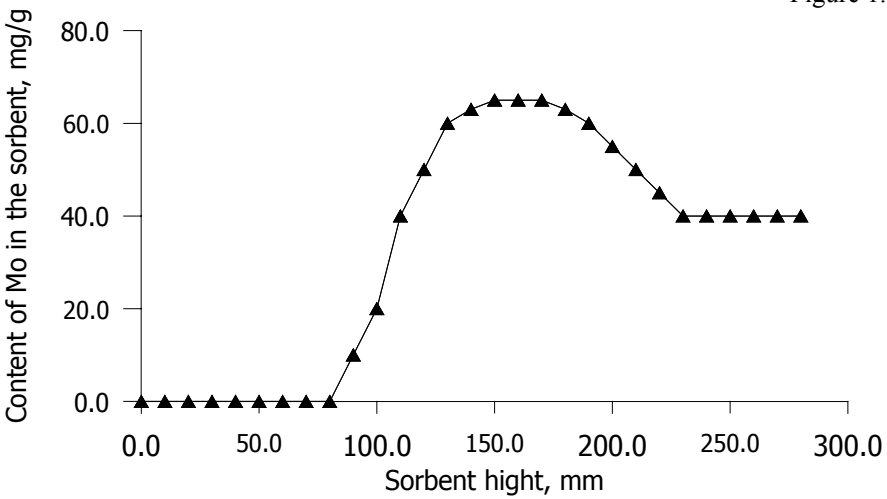
The stationary generators were made with activity of Mo-99: 2,7 Ci, 14,5 Ci, 3,0 Ci . Every day the generators were eluted during 25-30 days by the standard salt solution (0,9 % NaCl, pH=3,0), containing nitrate sodium. As the additive the nitrate sodium is provided reliable protection of

Tc-99m (VII) from its reduced and has been used for its full washing away from the generator column. The Tc-99m radioactivity in the eluates was measured by using of multi channel impulses analyzer.

Results and discussion

The Fig.1 shows the molybdenum distributed in the aluminum oxide column of stationary generator Tc-99m. This results was obtained by radioactive analyze of aluminum oxide obtained from the stationary generator column to remove of sorbent by layer-by-layer method.

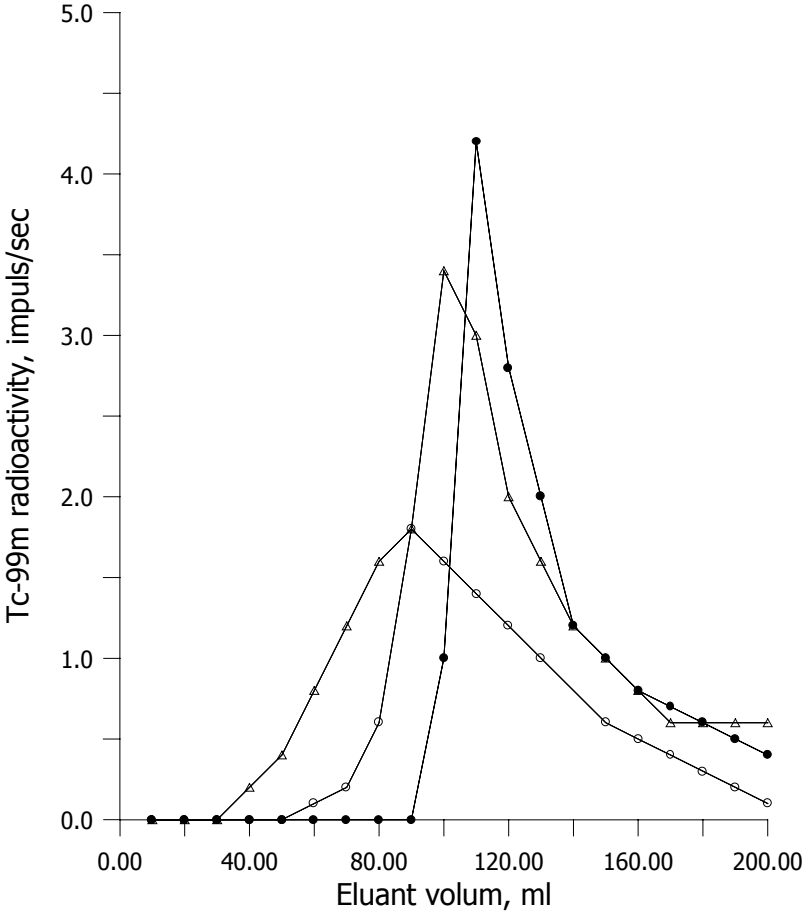
Figure 1.



The basic part of izopolymolibdatum is located on the top of column (110-300 mm) at sorbent weight 66 g (60 %) and molybdenum content 46,3 mg/g. The partly izopolymolibdatum is located also in average column part (h=80-110 mm) at the sorbent weight 13 g (12 %) and the molybdenum content 18,7 mg/g. In the bottom column part (0-80 mm) the izopolymolibdatum is completely absent at sorbent weight 31 g (28 %). This conduction provided obtain from generator column the pertechnetatum (Tc - 99м) sodium solution with high radionuclide purity.

The Fig.2 shows curves of Tc-99m eluant solution obtained from experimental stationary generator column in start, in middle and in finish operation term. It can be shown that the curve of Tc-99m elution daily was constant during 15 days. This result is testified about operational reliability of the stationary generator.

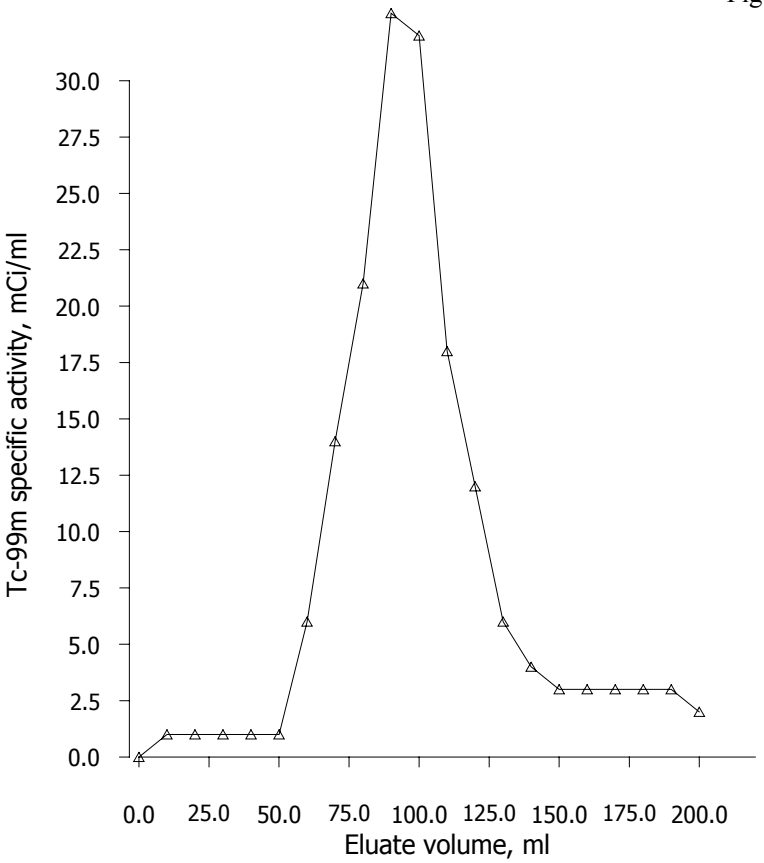
Figure 2.



Elution curve of Tc - 99м from experimental Tc-99m stationary generator is graphically shown in (Fig.3). The first part (50 ml) of eluant does not contain of Tc- 99м.

We can see sharp increase of Tc- 99м radioactivity since volume 50 ml and main part of Tc- 99м radioactivity (75 %) is obtained at the eluant volume 80 ml. The basic part Tc - 99м radioactivity is washed away from the generator column at eluant volume 120 ml and total eluant volume 150-160 ml.

Figure 3.



The operating performances of the experimental stationary generators of the Tc-99m are presented in Table 1.

Table 1.

Eluate parameters	Generator #1	Generator #2	Generator #3
Appearance	Colorless transparent solution	Colorless transparent solution	Colorless transparent solution
Total volume, ml	120	100	100
Volumetric activity, mCi/ml	15,0	71,0	16,0
Radiochemical purity, %	99,0	99,9	99,7
Tc – 99m eluation efficiency mean, %	86,0	70,0	87,0
Content of Mo-99 in relation to Tc – 99m, %	$1{,}5\cdot10^{-4}$	$0{,}6\cdot10^{-4}$	$1{,}5\cdot10^{-3}$
Content of Al^{+3}, mg/ml	3,5	2,5	2,5
Content of Fe^{+2}, mg/ml	1,5	0,5	0,5
Content of Cu^{+2}, mg/ml	0,05	0,06	-

As its shows in Tab.1, eluant quality from the experimental stationary generators is responded with eluant quality from the universal portable generator Tc-99m.

Conclusion.

A stationary generator of the Tc-99m is relative not expensive, convenience in operate generator for provide clinics by high active ready pertechnetatum (Tc-99m) sodium solution.

Parametric testing results of the pertechnetatum (Tc-99m) sodium solution from experimental stationary generators for a long operation time confirm, that the quality of pertechnetatum sodium (Tc-99m) solution obtain from stationary generator is corresponded to requirements of pharmacopoeia and its can be successfully used in practical nuclear medicine.

References.

[1] J. Vucina, S.Milenkovic. Isotopenpraxis. 1988, v.24, p.320.
[2] Sokolov V.A. " The generators of shot time life radioactive isotopes ". Moscow, Atomizdat, 1975, p. 112.
[3] Patent of Russian Federation, №2028679, 1995.

THE VIBRATIONAL STATES IN THE SKYRME MODEL

Abdulvagabova S.K.

Baku State University, Baku, Azerbaijan

Abstract : The vibrational states are described by a SU(5) algebra. On this basis a collective Hamiltonian with Skyrme potential appear in terms of a few constants. The collective Hamiltonian is applied to the transitional nuclei ^{150,152}Nd, $^{150,\ 152}$Sm and ^{152}Gd, where the constants are determined by fitting the experimental spectra, the relative $E2$ transition probabilities and the spectroscopic factors for the two-particle transitions to the ground and excited 0^+ states.

Introduction

The description of collective motion in nuclear has been and still is one of the most challenging subjects in theoretical physics. Generally speaking, the theory has been comparatively successful for deformed nuclei, but less for the spherical, or vibration nuclei. An important feature of the collective motion in nuclei is that, unlike other many-body systems, the excitation energies associated with vibrations and rotations are not very different from each other.

Different methods are used to describe collective motion. One of the methods is group theory method. A.Arima and F.Iachello [1] first proposed description of collective quadrupole states in even-even nuclei in terms of representations of a boson SU(6) group. They showed that within this model both the vibrational and the rotational limit can be recovered.

In this paper an algebraic method for the construction of the collective Hamiltionian of the Skyrme model is treated. The Skyrme model has some phenomenological success in describing the static properties of nucleons and their interactions.

The first case we have discussed here is only vibrational spectra in the framework of the subgroup SU(5). Exploiting the related symmetry group SU(5) we have been able to obtain simple analytic expressions for the eigenvalues of the boson Hamiltonian and for the intraband transition matrix elements as well as for side feeding from one band to the other. Back-bending occurs naturally as the crossing of two bands and it can be predicted from the relative spacing of the low excited states.

The algebraic properties of the collective variable lead to a new quantum number N which implies in the boson representation the maximum number of phonons contained in the vibrational states. Because the boson-boson interaction in SU(5) invariant Hamiltonian splits the degeneracy of the multiplets, this limit describes an anharmonic vibrator. It should be noted, we describe finite

dimensional systems in contrast with the geometrical description in which $N \to \infty$. It is worth noting that the knowledge of the invariance properties of the Hamiltonian provides directly a solution to the eigenvalue problem.

The transformation into the intrinsic frame of reference has been performed explicitly. Thus, the formulae for the potential energy, the quadrupole moments are obtained as well as the spectroscopic factors for 0^+ state excitation in the two-nucleon transfer reactions. The proposed collective Hamiltonian is applied to the transitional nuclei Nd, Sm and Gd.

1. Derivation of the collective Hamiltonian

The symmetry structure of the nuclear many body system is in general very complex. However, since only few degrees of freedom play a dominant role in the description of the collective states, it is hoped that the Hamiltonian of the system when written in terms of these degrees of freedom has simple symmetry properties. We have suggested [1] that these symmetry properties are those of the six dimensional special unitary group SU(6) acting on a boson space.

To begin with, we claim that a number of positive-parity states can be generated in even-even nuclei as states of a system of N bosons having no intrinsic spin but able to occupy two levels, a ground-state level with angular momentum $L = 0$, and an excited state with angular momentum $L = 2$. In the case in which the two levels are degenerate and there is no interaction between bosons, the five components of the excited $L = 2$ state, called d for convenience, and the single component of the ground $L = 0$ state, called s, span a six – dimensional vector space which provides the basis for the representations of the unitary group SU(6).

According to the group reduction [2]:

$$SU(6) \supset SU(5) \otimes U(1), \qquad (1.1)$$

the first case we will consider is that of the group SU(5) spanned by the 5 components of the d state alone. Only five labels are needed to classify the states. Three of them are the total boson number N, the total angular momentum L and its z – component M. The fourth is the seniority v. Instead of v one can introduce another quantum number n_β, which counts boson pairs coupled to zero angular momentum. n_β is related to v by

$$v = N - 2n_\beta . \qquad (1.2)$$

The representations of SU(5)contained in [N] are all symmetric representations

$$[n_\beta = 0],\ [n_\beta = 1],\ [n_\beta = 2],\ \text{up to}\ [n_\beta = N].$$

Finally one can introduce a fifth quantum number n_Δ, which counts boson triplets coupled to zero angular momentum. The total number N is partitioned by n_β and n_Δ as

$$N = 2n_\beta + 3n_\Delta + \lambda, \tag{1.3}$$

and the possible values of the total angular momentum L are given in terms of λ by

$$L = \lambda,\ \lambda+1,\ \lambda+2,\ldots,\ 2\lambda-2,\ 2\lambda. \tag{1.4}$$

The energy levels can be found by diagonalizing the model Hamiltonian

$$H = \varepsilon \sum_m d_m^+ d_m + \sum_\lambda q_\lambda \left[\left[d^+ d^+\right]_\mu^\lambda \left[dd\right]_0^0\right], \tag{1.5}$$

with eigenvalues

$$E([N], n_\beta, v, n_\Delta, L, M) = \varepsilon n_\beta + \frac{1}{14}(3q_4 + 4q_2)N(N-1) + \tag{1.6}$$
$$\frac{1}{10}\left[q_0 - \left(\frac{1}{7}(3q_0 + 4q_2)\right) + \frac{7}{6}(q_0 - q_2)\right](N-v)(N+v+3) + \frac{1}{14}(q_0 - q_2)\left[L(L+1) - 6N\right],$$

where $d^+(d)$ is the creation (annihilation) operator for a d – bosons and

$$q_\lambda = \left\langle d^2\ \lambda\,\mu \middle| V \middle| d^2\ \lambda\,\mu \right\rangle. \tag{1.7}$$

For our considerations the algebraic properties of the binary operators dd, d^+d^+, d^+d are important. Obviously, in a given configuration space these operators from Lie algebra. In what follows our basic assumption is, that this Lie algebra there exists subalgebra, which contains all operators for a construction of the collective variables as well as collective Hamiltonian and the collective states. In general, such algebra does not exist. However, for our aim it is satisfactory, if this subalgebra exists with respect to the subspace of the collective vibrational states only, in which we are interested.

It is important to notice that our collective Hamiltonian yields a finite energy matrix for a given value of N and a definite spin. This is a consequence of the symmetry properties of our collective operators. Hence one can really find exact solutions for the Hamiltonian (1.5).

Because the boson-boson interaction in (1.5) splits the degeneracy of the multiplets, this limit describes an enharmonic vibrator. It should be noted that here

and in (1.6) $0 \le n_\beta \le N$, and thus we describes finite dimensional systems in contrast with the geometrical description in which $N \to \infty$. It is worth nothing that the knowledge of the invariance properties of the Hamiltonian provides directly a solution to the eigenvalue problem.

2. E2 – Matrix Elements

Now the application of the collective Hamiltonian (1.5) to the transitional nuclei ^{150,152}Nd, $^{150,\ 152}$Sm and ^{152}Gd is presented. In general the qualitative structure of the energy spectrum obtained from our Hamiltonian is not significantly influenced by the other order terms. Hence the energy spectrum and the wave functions are determined by the constants q_0, q_2, q_4 and the maximal phonon number N. The numbers of valence nucleons in ^{150,152}Nd, $^{150,\ 152}$Sm and ^{152}Gd are equal to 18,20,18, 20, 20 respectively. Hence for those nuclei, N must be less than 9, 10, 9, 10, 10, respectively. Besides, one has to take into account the fact that N must increase, or one approaches the region of stable deformation, i.e. N must be larger in ^{152}Sm than in ^{150}Sm. For both cases ^{150}Sm and ^{152}Gd we took N =7, because their properties are similar. In ^{152}Sm we put N =9.

For the calculation of the E2 transitions the following expression of the electric quadrupole operator is used:

$$M(E2) = \frac{1}{7}(3q_4 + 4q_2)(d^+s + s^+d)^2_m + \frac{1}{70}(13q_0 - 10q_2 - 3q_4)(d^+d)^2_m \,. \qquad (2.1)$$

This operator has a part $(d^+s + s^+d)$ satisfying the selection rule $\Delta n_\beta = \pm 1$, and a part (d^+d) satisfying $\Delta n_\beta = 0$. In the SU(5) vibrational limit the first term gives rise to transitions form one n_β multiplet to another, while the second term gives rise to transitions within the same multiplet and to quadrupole moments. Of particular importance are those between members of the ground state band, for which one obtains

$$B(E2; I+2 \to I) = \frac{1}{196}(3q_4 + 4q_2)^2 (I+2)(2N-I) = \frac{1}{4}\frac{(I+2)(2N-I)}{N} B(E2; 2 \to 0) \cdot \qquad (2.2)$$

From the structure of (2.2) it also follows that in the SU(5) limit there are no $\Delta n_\beta = 2$ transitions and yet the quadrupole moment of the first excited 2^+ state can be different from zero because of the $\Delta n_\beta = 0$ term. Thus the observed large quadrupole moments may be compatible with the observed retardation of the $\Delta n_\beta = 2$ transitions. The theoretical and experimental ratios of the B (E2) values for $^{150,\ 152}$Nd, $^{150,\ 152}$Sm and ^{152}Gd are shown in table 1. The agreement between

this theory and experimental results is good. The experimental data are taken from [3].

3. Spectroscopic factors for two-nucleon transfer reactions

We have studied the spectroscopic factors for the two-particle transitions to the ground and excited 0^+ states in the model with pairing and quadrupole forces [4]. The transitions operators was taken to be of the form, for e.g. (p,t) reaction

$$\Gamma(p,t) = \sum_{\nu} b_{\tilde{\nu}} b_{\nu} , \tag{3.1}$$

where b_{ν} is the annihilation operator of the nucleon in the state $|\nu\rangle$. Then the spectroscopic for the transition to the ground state is

$$S_0 = (\Delta / G)^2 \tag{3.2}$$

where G is the strength parameter of the pairing force, Δ - energy gap.

The corresponding formula is too cumbersome to be given here. Therefore we present only the approximate expressions for two cases

$\omega \approx 2\Delta$ (pairing vibration)

$$S / S_0 \approx v^2 (N-5)^2 . \tag{3.3}$$

$0 < \omega < 2\Delta$ (pairing + quadrupole force)

$$S / S_0 \approx \frac{c_2^2}{4} (N - n_{\beta} + \nu)^2 (N - n_{\Delta} + 2)^2 . \tag{3.4}$$

One can see from eq. (3.4) the strong dependence of the ratio S / S_0 on the distribution of the single-particle moments. Therefore the low energy 0^+ states are expected to be populated strongly in nuclei having large single-particle quadrupole moments of the same sign in the vicinity of the chemical potential [4].

The theoretical and experimental ratios of the S / S_0 values for $^{150,\,152}$Nd, $^{150,\,152}$Sm and ^{152}Gd are shown in table 1. The experimental data are taken from [5].

4. Summary and conclusions

It is proposed to describe the collective vibrational degree of freedom by an algebra, which is formed by five components. This algebra proves to be the algebra of the group SU(5). This description stresses the symmetry rather than the

geometry of the intrinsic system. The symmetry properties of the model Hamiltonian have played an important role in the development of other branches of physics and it is hoped that they may as well elucidate the description of the collective nuclear states.

Table 1

Theoretical and experimental ratios of the B(E2) and S / S_0 values for nuclei ^{150,152}Nd, ^{150,152}Sm and ^{152}Gd

		^{150}Nd		^{152}Nd		^{150}Sm		^{152}Sm		^{152}Gd	
		Theor	Exp.	Theor.	Exp.	Theor.	Exp.	Theor.	Exp.	Theor.	Exp.
$\frac{B(E2; I+2 \to 2)}{B(E2; 2 \to 0)}$		4.52	5± 0.3	5.05	-	18	13±2	5.66	6± 0.4	46	52±5
S / S_0 (t,p)	I)*	2.76	1.20	1.16	0.70	1.32	0.08	2.63	0.74	2.13	-
	II)*	1.09		0.68		0.93		1.38		1.40	
S / S_0 (p,t)	I	3.66	-	1.22	-	1,35	-	5.50	0.28	3.35	0.13
	II	1.44		0.72		0.49		2.63		1.40	

I)* with pairing force; II)* with pairing + quadrupole forces .

In the resultant collective Hamiltonian the information about single particle energies and matrix elements of the interaction involves few constants. Hence the general properties of the collective Hamiltonian can be easily discussed in terms of these constants. The algebraic properties of collective variables lead to a quantum member N, which implies in the boson representation the maximum number of phonons contained in the collective states. The proposed collective Hamiltonian is applied to the transitional nuclei ^{150,152}Nd, ^{150,152}Sm and ^{152}Gd, where the constants are determined by fitting the experimental spectra, the relative E2 transition probabilities and the spectroscopic factors for the two-particle transitions to the ground and excited 0^+ states. The agreement between the experimental data and the theoretical description is good.

References

1. A.Arima, F.Iachello// Phys. Rev. Lett. 1985, V36, Number 16, p. 1069.
2. A.Arima, F.Iachello// Phys. Lett. 1974, V53B, p. 309.
3. K.Kumar// Phys. Rev. Lett. 1977, V26, Number 9, p. 269.
4. S.Abdulvagabova// Phys. . Lett. 1986, V38 B, p. 215.
5. M.Oouthoudt, N.Hints// Phys. Lett. 1984, 32B, p. 270

UPGRADE OF THE GIBS SPECTROMETER AT THE NUCLOTRON ACCELERATOR FOR INVESTIGATION OF CHARGE EXCHANGE REACTIONS

V.D.Aksinenko[a], V.P. Kondratiev[в], L.V. Krasnov[в], J. Lukstins[a], V.T. Matyushin[a], N.N.Nurgoz- hin[c], V.S.Richvitsky[a], I.S. Saitov[a], O.Yu Tyatyushkina[a].

a Joint Institute for Nuclear Reseach, Dubna, Russia
b Institute of Physics, St-Petersburg State University, St- Petersburg, Russia
c Institute of Physics and Technology, MES RK, Almaty, Kazakhstan.

In the last few years the Nuclotron, a new superconducting accelerator of the Laboratory of High Energies at JINR, has been developed step by step to reach the designed specifications. The ultimate aim of this machine is 12 GeV energy for protons but the accelerator will be generally used as a source of nuclear beams (up to the energy of 6 GeV per nucleon). The research program [1] for the new machine contains proposals aimed to solve actual problems of the relativistic nuclear physics. In this context we present some results on the GIBS spectrometer [2] upgrade dedicated to carry out charge exchange experiments in tritium beams. In our previous experiment [3] there was an evidence of unusual charge exchange reaction channels which should be analyzed in more details. Indeed, a surplus of high longitudinal momentum pions was observed when pion spectra were investigated in the reaction A(t, ^{3}He). Analysis has shown that coherent processes, projectile excitation and massive isobars N(1440) or N(1520) besides Δ(1232) can be a source of these pions. However, the statistic of events was too low to separate these possible channels unambiguously. Moreover, the setup did not allow event-by-event measurement of the tritium momentum. More precise measurement of ^{3}He momentum is also desirable. While time of flight spectrometer and proportional chambers will be used to measure projectile and ejectile momenta, it is necessary to use filmless readout system for the streamer chamber [4] where pions in 4π geometry are registered and measured.

Until recently at the magnetic spectrometer GIBS a stereo camera was used for particle track registration in the streamer chamber. At all virtues the photography essentially complicates and elongates the process of experimental data obtaining and collecting, requires special devices for chemical and optical treating, and also devices for measuring events registered on a film.

Fast progressing of computer techniques and television systems using CDC-matrix allows one to realize picking up the information from the streamer chamber without film process- sing and events measuring. As before, basic performances of a recording device are photosensibility and resolution capability, as a track luminosity in the streamer chamber is gentle. And if the process of

progressing of electron avalanches is interrupted in the chamber at the earlier stage then better quality of tracks can be achieved and their background accompaniment can be reduced.

Quick readout and effective data processing codes presented an effective possibility to study dependence of streamer production process on different conditions. The results presented to the Conference allow one to choose the most effective streamer chamber operation regime and give new information on the streamer formation mechanism.

Up to now there was only one successive experience of TV system used to register tracks of low brightness in the streamer chamber [5]. However, they [5] use expensive high gain and resolution TV cameras. Meanwhile, our Monte-Carlo calculations have shown that simple TV cameras with 500x480 pixel matrix can be used to measure pion momentum in the streamer chamber with an accuracy of 0.5-1.0% that is a good result for the task.

If the resolution capability can be evaluated, knowing the sizes of CDC-matrix and a pixel (sensitive element of the matrix) then its real track sensivity introduces doubtless concern.

For the correspondent measuring we used a setup [6] with a small streamer chamber with volume of 36 liters filled with a gas, similar on composition to the gas of the spectrometer GIBS chamber. Usually it is neon with small impurity of air to reduce the memory time.

The power supply of the chamber was carried out from the two-polar generator of high-voltage impulses with duration of 18 ns. The charging voltage was maintained at one level (±52±0.3 kV). The pulse amplitude on electrodes of the chamber was a little bit less because of losses in a spark gap (according to our estimations it equals to 85 kV).

The gap between electrodes of the chamber could be changed in the wide limits (0÷10 cm) without failure of its sealing.

In addition the streamer chamber was furnished with the system for registration of track light exit. It consisted of an MIR-1 type objective permitting to change angular apertures in wide limits (32 times), light scattering shield, a PMT-85 type photomultiplier and a V4-17 type impulse digital voltmeter. Such system has allowed to obtain a linear interval for registration of light radiation from tracks which was larger than two orders.

The chamber was triggered by electrons from a β-source ^{106}Ru. The total time delay of the chamber concerning the moment of an electron passing was equal to 0.5 μs.

The tracks on the matrix were recorded to scale 1:30, and all pictures of the tracks were displayed by the computer almost life-sized (more precisely - enlarged 1.15 times), i.e. the diameter of one pixel on a CDC-matrix is 0.4 mm in the chamber and on the screen of the monitor. Thus, the limiting resolution in the chamber in these conditions is ≈0.4 mm.

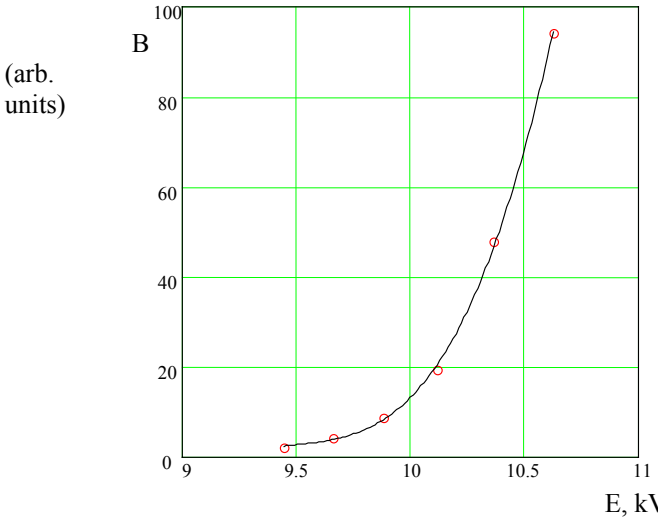


Fig.1. Intensity B of light emitted from streamer chamber as a function of electric field strength E.

In Fig. 1 the dependence of light output from tracks B (in arbitrary units) on the electric field strength E in the chamber is given. Reliable photo registration of tracks by the television system is possible at E=9.3 kV/cm while with the most sensible films only at E = 10.7 kV/cm.

Such conditions of the chamber operation appear more favorable, as the possibility of appearance of background discharges both inside the chamber, and outside of it is sharply abbreviated. The latter usually occur at corona of high-voltage electrodes. Weakening of corona results in better stabilizing of high-voltage impulse parameters in the chamber, that, in turn, ensures better stabilization of a track regime in the chamber. The ability of a television system to register tracks at the earlier stage of progressing (almost two order for the light output, Fig.1) contributes to better stabilization of track regime too, because in fact registration of tracks is carried out at the stage of electron avalanches' progressing the speed of which is one order less than the streamers' speed while the light radiating of tracks grows exponentially with the field intensity E.

Thus, the real photosensibility of a television system is almost two orders more than photographic one, however resolution for large streamer chambers will be dependent on the sizes of a CDC-matrix.

In Fig. 2 the dependence of the average density of avalanche clusters on the field intensity in the chamber is presented. The fall of the density after reaching a maximum with increasing the field is explained by confluence of separate avalanches and overlapping of their images on a CDC-matrix. The tracks step-by-

step become uninterrupted. It is visually mapped in Fig. 3, where the dependence of the decreasing of relative density of single electron avalanches n_1 (n - average density of clusters) on the growth of the electrical field tension E is given. The registration may be considered as optimal inside an interval where the density of clusters grows and where the separate clusters yet do not join. The record of a typical track of an electron in the chamber is presented in Fig. 4, where its cluster pattern is clearly scanned.

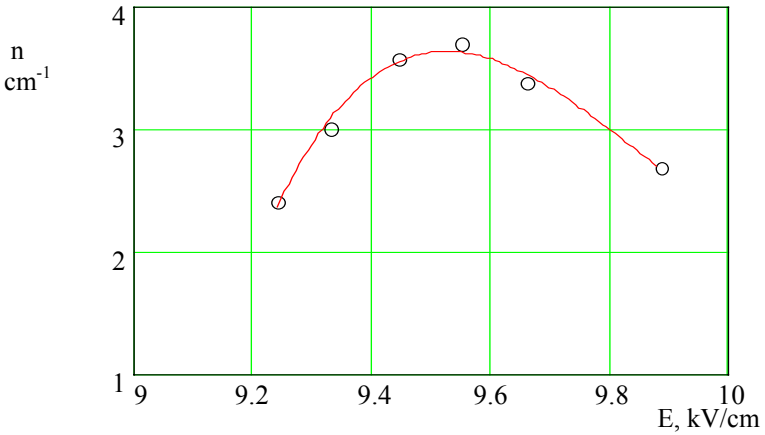


Fig.2. The number of avalanch clusters–n as a function of electric field strength-E.

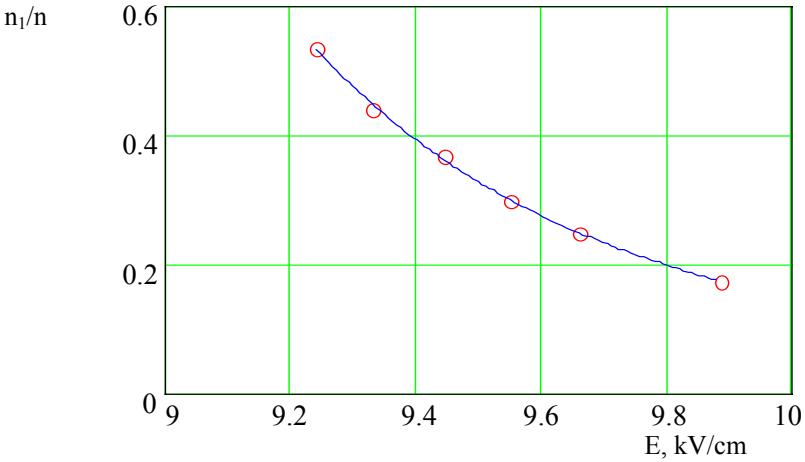


Fig.3. The relative number of single electron avalanches – n_1/n as a function of electric field strength - E.

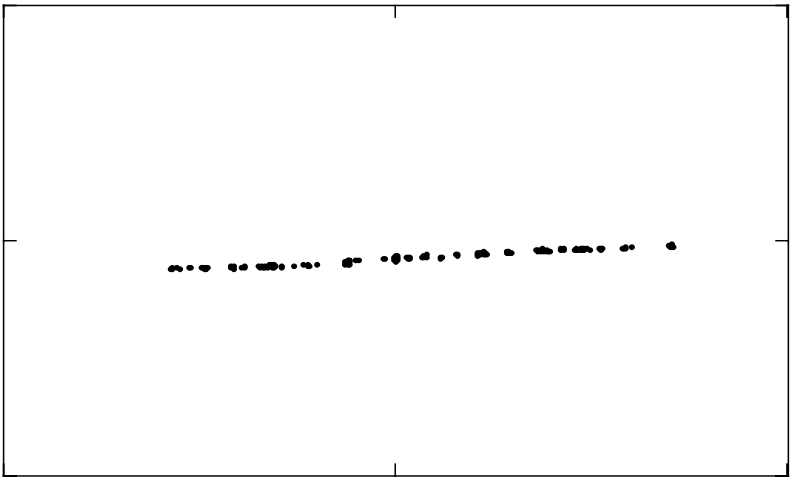


Fig. 4. Typical minimum ionization (electron) track recorded in the test streamer chamber.

In Fig. 5 the integrated distribution of cluster density for 23 tracks is shown. The size of cluster - m was defined by the number of the lighted pixels, and clusters were considered as separate if between them there was at least one empty line.

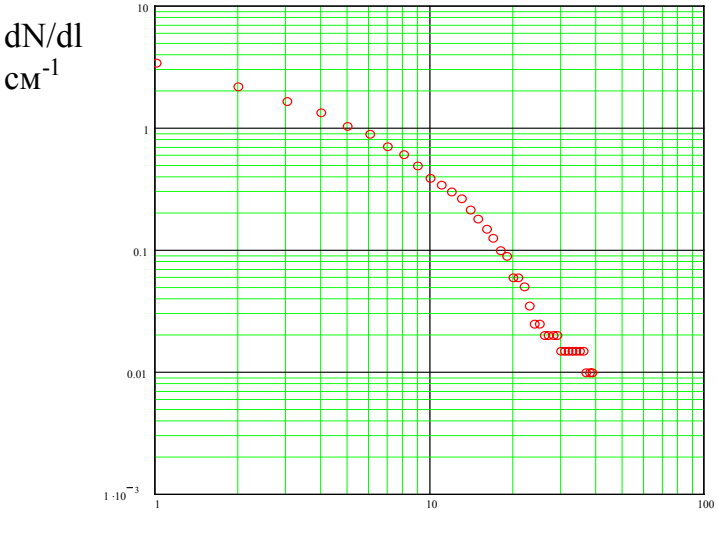


Fig.5. The integral distribution of cluster density - dN/dl as a function of the clusters' size - m in the streamer chamber.

References.

1. Research Program of the Laboratory of High Energies, JINR, Dubna, 1999.
2. S.A.Avramenko et al. Prib. Tech. Exsp. 3 (1999), 27.
3. S.A.Avramenko et al., Nucl. Phys. A596 (1996) 355.
4. S.A.Avramenko et al. I. Eurasia Conference on Nuclear Science and its Application (23-27 October 2000, Izmir Turkey) Presentations, vol.2, p.943, Turkish Atomic Energy Authority, Ankara - Turkey 2001.
5. E.M.Andreev et. al., Nucl. Phys. A684 (2001) 420c.
6. V.D.Volodin et al Prib. Tech.Exsp., 1983, 4, p.60

AUTHOR INDEX

Abdulvagabova S.K.	504
Adalioğlu Ulvi	91
Afanasiev S.V.	169
Aitmuhambetov A.A.	432, 438
Aksinenko V.D.	510
Aksu Levent M.	105
Alkozhaev N.	273
Anisimov Yu.S.	169
Antonova V.P.	378
Arikan İbrahim	91
Artemov S.V.	111
Arzumanov A.	329, 362, 417, 467
Ashimov D.S.	401
Ashirov R.R.	432
Ashrapov U.T.	455, 499
Atila Berrak	105
Aykol Fethiye	105
Babaev M.K.	459, 496
Babenkov M.I.	267
Baigubekov A.S.	378, 459, 496
Baizhanova Zh.	176
Baykal Adnan	91, 367
Berdieva M.	455
Berdinova N.	467
Berger V.	417
Bezzubtsev V.S.	28
Bimurzaev S.B.	288, 295
Blokhintsev L.D.	190
Bondarev V.K.	169
Boos E.G.	305, 373
Borisenko A.	329, 467
Bozkurt A.	422
Boztosun I.	139, 385
Burtebayev N.	111, 139, 385
Çetiner B.	202, 335
Çetiner M.A.	202, 335, 347, 422
Cherepnin Yu.S.	28
Chikhray Y.	49
Chubenko A.P.	378

Chumikov G.	467
Demirbaş A.	422
Demircioğlu B.	202
Demirel H.	202, 422
Dimovasili E.	159
Dineykhan M.	176, 401
Djuraev Sh.Kh.	216
Driablov D.K.	169
Duysebaev A.D.	111
Dzhazairov-Kakhramanov V.	139
Elengeev A.K.	273
Erduran M. Nizamettin	367
Esanniyazov Sh.F.	216
Fazio G.	444
Fazylov M.I.	216, 235
Fazylova Z.F.	235
Gabaraev B.A.	28
Giardina G.	444
Glickman L.G.	326
Gnilozub I.A.	163
Gorkovets M.	362
Gorodisskaya N.	417, 467
Güleçyüz M. Ç.	487
Hangül Gökhan	105
Hasbi Yavuz	85
Ibadov R.M.	277
Ibadova Umida	151
Ibraeva E.T.	244
Imambekov O.	244
Ioannou P.	159
Iskakova Z.D.	295
Ismatov Ye.I.	216, 235
Isupov A.Yu.	169
Ivanov V.I.	169
Izbasarov M.	305
Jahanshir A.	176, 401
Jovliev U.	181, 342
Kadyrzhanov K.K.	111
Kalinin Yu.G.	496
Karadağ M.	347
Karadeniz H.	202, 335

Kartashov V.M.	196
Kaşkaş A.	487
Kazkenov Ye.K.	432
Kenzhin E.	49
Khugaev A.V.	159, 181, 342
Khujaev S.	455, 499
Kim A.	11
Knyazev A.	417, 467
Koblik Yu.N.	159, 181, 342
Kondratiev V.P.	510
Koptev V.	362, 467
Krasnov L.V.	510
Kryukov S.V.	378
Kuchin I.A.	410
Kukhtina I.N.	250, 309
Kulsartov T.	49
Kupchishin A.I.	378
Kurgalin S.D	163
Kuterbekov K.A.	216, 235, 250, 309
Lamberto A.,	444
Lennik S.G.	474
Litvinenko A.G.	169
Livetsova A.S.	474
Lukstins J.	510
Malakhov A.I.	169
Mansurov K.Zh.	438
Martyanov I.S.	459, 496
Matyushin V.T.	510
Migulina I.I.	169
Mirzaeva N.A.	455
Mit' A.G.	273, 326
Mukhambetzhan A.	250, 309
Muminov A.I.	181, 342, 444
Nasirov A.K.	181, 342, 444
Nazarenko L.M.	273
Nurgozhin N.N.	510
Nushtaeva L.B.	455
Öner Önder	18
Oskomov V.V.	378
Oya Özdere Gülol	59
Özgür İ.	335

Özkan Reşat	105
Özmen A.	202, 335, 347, 422
Palamara R.	444
Pavliy K.V.	181, 342
Penev V.N.	169
Penionzhkevich Yu.E.	250, 309
Peterson R.J.	128
Pikul V.P.	159, 181, 342
Pokrovsky N.S.	373
Polyak Yu.V.	181, 342
Popov Yu.	417, 467
Rasulov E.A.	481
Reyhancan Iskender Atilla	367
Richvitsky V.S.	510
Ruggeri R.	444
Sadykov B.M.	250, 309
Sadykov T.Kh.	135, 378, 459, 496
Safarova Zamira	151
Saitov I.S.	510
Sakhyev S.K.	176, 401
Samoilov V.V.	373
Sanfirova A.B.	244
Sarsenbaeva N.S.	295
Serikbaeva G.S.	288
Shepetov A.L.	378
Shestakov V.	49
Stakhov O.V.	273
Starikov A.Yu.	169
Strigina S.B.	216
Sychikov G.	467
Takibayev N. Zh.	145, 474
Tan M.	347
Tarantin N.I.	266
Tarcan Gökçe	367
Taskin F.	385
Tayfun Büke	71, 85
Tchuvil'sky Yu.M	163
Temiraliev T.	373, 463
Tezcan C.	487
Titov O.A.	169
Troitskaya A.G.	196

Turgut Mehmet Hulusi	97
Turhan Ş.	422
Tyatyushkina O.Yu.	510
Üner Çolak	59
Vdovkin P.O.	181
Vetrov V. A.	78
Vildanova L.I.	378
Yakhshiev U.T.	444
Yakushev E.M.	273, 288
Yarmukhamedov R.	111
Yavuz H.	33, 91
Yeligbayeva G.	11
Yesın A.O.	41
Yılmazer A.	33
Yücel H.	202, 335, 347, 422
Yuldashev B.S.	111, 235
Yurtseven İ.	202
Zastrozhnova N.N.	305, 378, 459, 496
Zhantikin T.	11
Zhdanov V.S.	267
Zhetltov D.	467
Zholdybayev T.K.	250, 309
Zhusupov M.A.	244